

Aha Huliko'a



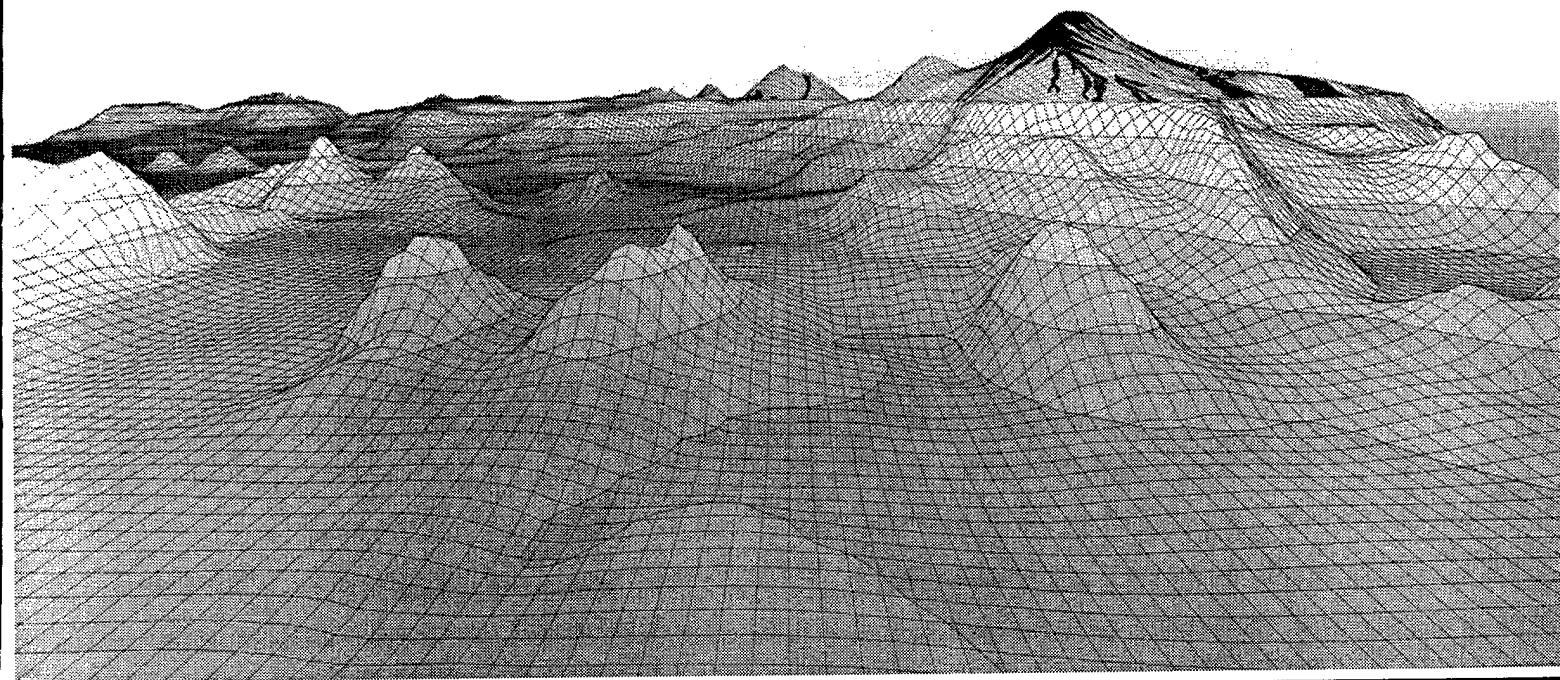
INTERNAL GRAVITY WAVES, II

DISTRIBUTION STATEMENT A
Approved for Public Release
Distribution Unlimited

Proceedings
Hawaiian Winter Workshop
University of Hawaii at Manoa
January 18–22, 1999

REPORT DOCUMENTATION PAGE			Form Approved OMB No. 0704-0188	
<small>Public reporting burden for this collection of information is estimated to average 1 hour per response, including the time for reviewing instructions, searching data sources, gathering and maintaining the data needed, and completing and reviewing the collection of information. Send comments regarding this burden estimate or any other aspect of this collection of information, including suggestions for reducing this burden to Washington Headquarters Service, Directorate for Information Operations and Reports, 1215 Jefferson Davis Highway, Suite 1204, Arlington, VA 22202-4302, and to the Office of Management and Budget, Paperwork Reduction Project (0704-0188) Washington, DC 20503.</small> PLEASE DO NOT RETURN YOUR FORM TO THE ABOVE ADDRESS.				
1. REPORT DATE (DD-MM-YYYY) 10/05/99		2. REPORT DATE 10/05/99		3. DATES COVERED (From - To) 10/02/97-12/31/99
4. TITLE AND SUBTITLE 'Aha Huliko'a Workshop Series Proceedings: "Dynamics of Oceanic Internal Gravity Waves, II"			5a. CONTRACT NUMBER	
			5b. GRANT NUMBER ONR N00014-98-1-0207	
			5c. PROGRAM ELEMENT NUMBER	
			5d. PROJECT NUMBER	
6. AUTHOR(S) Muller, Peter and Henderson, Diane (eds)			5e. TASK NUMBER	
			5f. WORK UNIT NUMBER	
7. PERFORMING ORGANIZATION NAME(S) AND ADDRESS(ES) University of Hawaii/SOEST/Dept of Oceanography 2530 Dole St., SAK D-200 Honolulu, HI 96822			8. PERFORMING ORGANIZATION REPORT NUMBER	
9. SPONSORING/MONITORING AGENCY NAME(S) AND ADDRESS(ES) Office of Naval Research Dept. of the Navy 800 North Quincy Street Arlington, VA 22217			10. SPONSOR/MONITOR'S ACRONYM(S) ONR	
			11. SPONSORING/MONITORING AGENCY REPORT NUMBER	
12. DISTRIBUTION AVAILABILITY STATEMENT Approved for public release; distribution unlimited				
13. SUPPLEMENTARY NOTES Proceedings, 'Aha Huliko'a Hawaiian Winter Workshop, January 1999 Honolulu, HI.				
14. ABSTRACT The proceedings contain the lectures given at the eleventh 'Aha Huliko'a Hawaiian Winter Workshop on the "Dynamics of Internal Gravity Waves, II" and a meeting report. The lectures cover observations, theoretical analyses and numerical modeling results of dynamic processes that affect internal waves, especially near topography.				
15. SUBJECT TERMS Internal gravity waves, internal tides, near-inertial waves, dynamic balance boundary mixing, interaction with topography.				
16. SECURITY CLASSIFICATION OF:			17. LIMITATION OF ABSTRACT	18. NUMBER OF PAGES
a. REPORT UNCL	b. ABSTRACT	c. THIS PAGE		294
			19a. NAME OF RESPONSIBLE PERSON Peter Muller	
			19b. TELEPHONE NUMBER (Include area code) (808)956-8081	

'Aha Huliko'a



DYNAMICS OF OCEANIC

INTERNAL GRAVITY WAVES, II

PROCEEDINGS
'Aha Huliko'a
Hawaiian Winter Workshop
University of Hawaii at Manoa
January 18-22, 1999

19991110 045

PETER MÜLLER
DIANE HENDERSON
editors

Sponsored by the U.S. Office of Naval Research,
the School of Ocean and Earth Science and Technology,
and the Department of Oceanography, University of Hawaii

(Cover image from Dynamic Graphics)

DTIC QUALITY INSPECTED 4

SOEST Special Publication • 1999

FOREWORD

The eleventh 'Aha Huliko'a[†] Hawaiian Winter Workshop was held from January 19-22, 1999, at the Imin Conference Center in Honolulu, Hawaii. The workshop continued the in-depth discussions of the dynamics of oceanic internal gravity waves. Previous workshops on this topic were held in 1984 and 1991.

The 1999 workshop focused on processes near or at topographic boundaries: the generation of internal waves by currents flowing over rough topography, the conversion of surface to internal tidal energy at topography, and the reflection and scattering of internal waves at topography. A primary concern was the extent to which these processes contribute to boundary mixing. In addition, the workshop considered the generation of internal waves by wind, mixed layer turbulence, and continuous geostrophic adjustment; the transfer of wave energy across the spectrum; and the wave-turbulence transition region. The workshop showed that a clear distinction must be made between the near-inertial peak, the tidal peaks, and the continuum, since their dynamics differ. It also advocated a view of the oceanic internal wave field as a radiative phenomenon. In oceanic general circulation models, the internal wave field should be treated as an additional radiative field, similar to the way that light from the sun is treated in atmospheric general circulation models.

The lectures of the workshop are published in these proceedings. The order of the papers loosely follows the agenda of the workshop, covering observations, theoretical analyses, and numerical modeling results. Also included is a summary of the workshop.

The workshop was supported by the Office of Naval Research grant number N00014-98-1-0207. It was hosted by the Department of Oceanography, School of Ocean and Earth Science and Technology, University of Hawaii. The excellent facilities and the capable staff of the Imin Conference Center contributed greatly to the success of the meeting. The local organization and logistical arrangements were expertly handled by Ms. Sharon Sakamoto. This proceedings volume came into existence through the creative and dedicated research of scientists who gathered in Hawaii and provided the articles that follow.

Peter Müller	Department of Oceanography
Diane Henderson	School of Ocean and Earth Science and Technology
	1000 Pope Road
	University of Hawaii
	Honolulu, Hawaii 96822

[†]'Aha Huliko'a is a Hawaiian phrase meaning an assembly that seeks into the depth of a matter.



PARTICIPANTS

M. Hendershott (in the tree)

S. Thorpe, C. Eriksen

D. Farmer, G. Carnevale, J. Lerczak

K. Polzin, T. Nakamura, R. Pinkel, E. Kunze, D. Horn, R. Kloosterziel, C. Garrett, M. Levine

L. Goodman, D. Durran, F. Henyey, J. Paduan, L. Rosenfeld, M. Gregg, D. Luther, E. D'Asaro

S. Sakamoto, M. Merrifield, T. Hibiya, P. Holloway, M. Alford, D. Slinn, M. Briscoe, S. Legg, B. Garwood, D. Wang,
K. Winters, A. Stigebrandt, P. Müller

CONTENTS

Internal Waves on the Continental Shelf <i>Murray D. Levine</i>	1
Observations of the Internal Tide on the Southern California Shelf <i>James A. Lerczak, Myrl C. Hendershott, and Clinton D. Winant</i>	9
Internal Wave Energetics at a Seamount on the California Continental Borderland <i>Robert Pinkel and Matthew Alford</i>	21
Internal Wave Measurements in Mamala Bay, Oahu, Hawaii <i>Patrick K. Sullivan and Dayananda Vithinage</i>	29
Mixing over Shelves and Slopes <i>M. C. Gregg, D. W. Winkel, J. A. MacKinnon, and R. C. Lien</i>	35
Modeling Internal Tide Generation and Evolution into Internal Solitary Waves on the Australian North West Shelf <i>Peter E. Holloway, Efim Pelinovsky, and Tatyana Talipova</i>	43
Internal Tide Generation at Open Ocean Topographies <i>Mark A. Merrifield and Peter E. Holloway</i>	51
The Hawaii Ocean Mixing Experiment (HOME) Is the Abyssal Stratification Maintained by Tidalgenic Mixing? <i>D. S. Luther and the HOME PIs</i>	57
Numerical Simulations and Observations of the Internal Tide in a Submarine Canyon <i>Leslie K. Rosenfeld, Jeffrey D. Paduan, Emil T. Petruncio, and J. Eduardo Goncalves</i>	63
Baroclinic Wave Drag and Barotropic to Baroclinic Energy Transfer at Sills as Evidenced by Tidal Retardation, Seiche Damping, and Diapycnal Mixing in Fjords <i>Anders Stigebrandt</i>	73
Stratified Flow Over Topography and the Generation of Internal Solitary Waves <i>David M. Farmer and Laurence Armi</i>	83
Exact Solitary Wave Solutions in Shallow Water <i>Frank S. Henyey</i>	89
Internal Solitary Waves in Lakes—a Closure Problem for Hydrostatic Models <i>D. A. Horn, J. Imberger, and G. N. Ivey</i>	95

Vertical Mixing Induced by Tidally Generated Internal Waves in the Kuril Straits <i>Tomohiro Nakamura, Toshiyuki Awaji, Takaki Hatayama, Kazunori Akitomo, Takatoshi Takizawa, Tokihiro Kono, and Masao Fukazawa</i>	103
A Rough Recipe for the Energy Balance of Quasi-Steady Internal Lee Waves <i>Kurt Polzin</i>	117
75 + 25 = 99 ±1, or Some of What We Still Don't Know: Wave Groups and Boundary Processes <i>S. A. Thorpe</i>	129
Mixing Generated by Internal Waves Interacting with Rough Topography <i>Sonya Legg and Carl Wunsch</i>	137
Along-Slope Current Generation by Obliquely Incident Internal Waves <i>Donald N. Slinn</i>	141
Turbulent Properties in a Wave-Energized Benthic Boundary Layer on a Slope <i>Kraig B. Winters and Gregory N. Ivey</i>	149
On Redistributed Energy Fluxes in Topographic Scattering Problems <i>Peter Müller</i>	155
A Comparison of Highly Nonlinear Gravity-Wave Generation by Two and Three Dimensional Obstacles <i>Dale R. Durran and Craig Epifanio</i>	163
Short-Term Directional Variability of the Continuum Range in the Deep-Ocean Internal Wave Field <i>Melbourne G. Briscoe</i>	169
Observations of Low-Latitude, Near-Inertial Gravity Waves Forced by Westerly Wind Bursts <i>Charles C. Eriksen</i>	173
Internal Wave Generation in the Equatorial Undercurrent <i>Dailin Wang and Peter Müller</i>	181
Large-Eddy Simulation of Pressure Transport Below the Mixed Layer <i>Roland W. Garwood, Jr. and Ramsey R. Harcourt</i>	189
Near-Inertial Wave Generation on an Unsteady Ocean Current <i>M.-Pascale Lelong, Timothy J. Dunkerton, and David S. Darr</i>	197

Model Predicted Distribution of Internal Wave Energy for Diapycnal Mixing Processes in the Deep Waters of the North Pacific <i>Tohiyuki Hibiya, Maki Nagasawa, and Yoshihiro Niwa</i>	205
What is the "Near-Inertial" Band and Why is it Different? <i>Chris Garrett</i>	215
The Role of Vertical Divergence in Internal Wave/Wave Interactions <i>Eric Kunze and Haili Sun</i>	223
Observations of Fine-Scale Richardson Number, Strain, and Effective Strain Rate Conditions Accompanying Overturning Events in the Thermocline <i>Matthew Alford and Robert Pinkel</i>	253
Waves, Turbulence, and Mixing Parameterizations <i>E. A. D'Asaro and R. C. Lien</i>	269
Large Eddy Simulation of Oceanic Fine Structure <i>G. F. Carnevale and M. Briscolini</i>	279
Diapycnal Mixing and Internal Waves <i>Peter Müller and Melbourne Briscoe</i>	289

Internal Waves on the Continental Shelf

Murray D. Levine

College of Oceanic & Atmospheric Sciences, Oregon State University, Corvallis, OR

Abstract. The Garrett-Munk spectral description of the deep-ocean internal wave field is re-scaled for straightforward application to the shallower water of the continental slope and shelf. Two new parameters are introduced to replace some of the GM parameters: spectral level E_0 and vertical waveguide scale D . The new scaling is applied to some observed spectra, as a first step toward a climatology of internal waves on the shelf. The consistency of the latitudinal scaling of the GM spectrum is also discussed, leading to a modified frequency dependence.

1. Introduction

Oceanic internal gravity waves can be generated by a myriad of forcing mechanisms. The nature of these internal waves will depend on the spatial and temporal characteristics of the forcing. Sometimes it is possible to relate the observed waves to a specific forcing mechanism. For example, the barotropic tide generates a periodic internal tide, and traveling storm fronts generate near-inertial waves. However, because of the complexity of nonlinear interactions and the general confusion of three-dimensional motion, the relationship between the observed wave field and the source is often obscured.

In the early 70s *Garrett and Munk* (1972; 1975) made a remarkable observation: Oceanic fluctuations over a wide range of time and space scales are strikingly stationary and homogeneous, and can be described statistically as an ensemble of random waves which are consistent with the kinematics governing internal waves. This description of the variability is often referred to as the Garrett-Munk (GM) spectrum. Although the GM spectrum does not explain the dynamics affecting the wave field and does not specifically include the tidal or near-inertial bands, it remains a useful description of the internal wave field in the open ocean. If asked to predict the basic statistics of internal waves at a particular location, the GM spectrum would be the prescription of choice.

On the continental slope and shelf the applicability of the GM spectrum is uncertain. However, there are many reasons why an internal wave description in shallow water would be useful. One reason is that differences from the deep ocean wave field may provide clues about which processes are most important in maintaining oceanic internal waves. Another reason to understand the shallow water internal wave field is because of its potential importance in generating turbulence. Knowledge of the role of internal waves in mixing could lead to improved parameterizations of turbulent processes in numerical models of coastal circulation. Over the steep topography of the slope, mixing

enhanced by internal waves may play an important role in mixing the abyssal interior of the ocean (*Munk and Wunsch*, 1998). For a variety of applied concerns, it is important to know how the internal wave field on the shelf affects acoustic propagation and optical properties.

The purpose of this paper is to look briefly at some observations of internal waves on the shelf and suggest a statistical framework with which to view these observations.

We begin with a review of the GM spectrum and suggest modifications and re-scalings needed to formulate a spectral description suitable for shallow water, called Aha99. Several other issues not included in this framework are also discussed.

2. Garrett-Munk spectrum: re-scaling from the deep ocean to the shelf

The GM spectrum is based on observations in deep water. To construct a spectrum applicable for shallow water, we start with the GM deep-water parameterizations and attempt to re-scale (Figure 1). There are many forms of the GM spectrum in the literature; we choose the one called GM79 presented in *Munk* (1981). The essence of the GM spectrum is contained in the expression for the energy distribution of the wave field written here in frequency ω and mode number j space:

$$S_{GM79}(\omega, j) = Eb^2 N_0^2 \left[\frac{N(z)}{N_0} \right] B(\omega) H(j) \quad (1)$$

where
$$B(\omega) = \frac{2}{\pi} \frac{f}{\omega(\omega^2 - f^2)^{1/2}} \quad (2)$$

and
$$H(j) = \frac{1}{J} \frac{1}{(j^2 + j_*^2)} \quad (3)$$

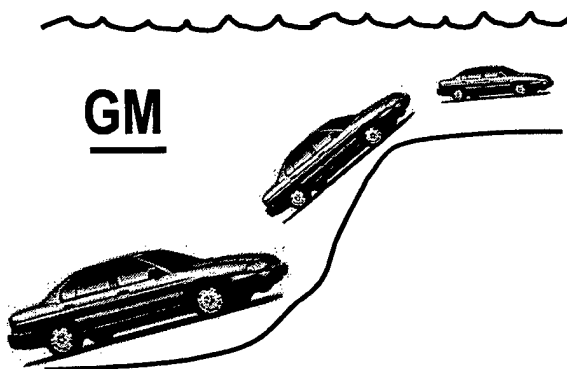


Figure 1. Re-scaling GM from deep ocean to shelf.

where $\int_0^N B(\omega) d\omega = 1$ and J is a constant such that

$$\sum_{j=1}^{\infty} H(j) = 1.$$

This distribution function is derived assuming a random wave field with vertical symmetry, horizontal isotropy, and temporal stationarity. All useful spectral quantities can be derived from this function. The collection of constants $E b^2 N_0^2$ has the dimensions of energy / mass [J/kg] and sets the energy level of the wave field. The constant E is nondimensional; the scales for length and time are given by b [m] and N_0 [s⁻¹] and are linked by GM to an exponential form describing the profile of buoyancy frequency:

$$N(z) = N_0 e^{-z/b}$$

The functions B and H describing the frequency and mode number dependence are separable—this is an assumption of GM, but is not essential to the re-scaling proposed below. Although discrete vertical modes are used in specifying the wavenumber energy distribution H , the depth dependence is given simply as $[N(z) / N_0]$, following a simplified WKB approximation where the energy scales as $N(z)$ relative to some reference N_0 .

The length b is used also to scale the dimensional vertical wavenumber as $m(z) = \frac{j\pi N(z)}{b N_0}$, which is a slowly

varying function of z . It would, of course, be more realistic to use actual modal wavefunctions to describe the vertical dependence instead of WKB, but for this discussion we retain the simplicity of the WKB scaling.

Two new parameters are defined to aid in re-scaling for shallow water: E_0 , the dimensional energy / mass and $D(\omega)$, the scale of the vertical waveguide (Table 1).

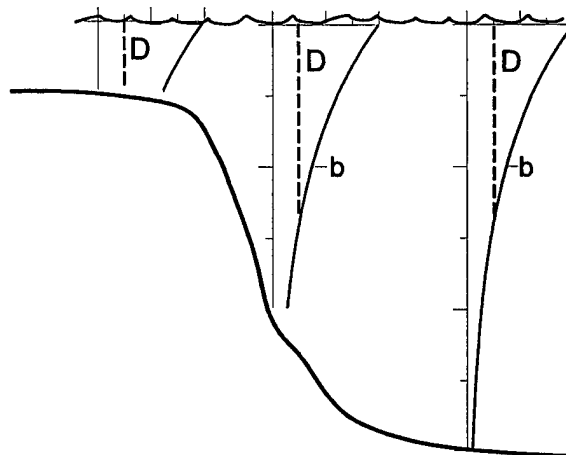


Figure 2. Example showing how the N profile can have the same vertical scale b , but the scale of the vertical waveguide D can vary from the deep ocean to the shelf.

The function D is the effective depth range over which internal waves can propagate as free waves, i.e., where $\omega < N(z)$. In GM the length of the waveguide is a constant b which makes a re-scaling for shallow water unclear. This is because the depth of the ocean does not appear explicitly as an independent parameter in the GM formulation—which is satisfactory as long as the depth of the ocean is much greater than b . Using another parameter D is more straightforward and accommodates variations in the vertical waveguide due to both stratification and ocean depth. For example, suppose that the same exponential form of stratification exists in both shallow and deep water (Figure 2). This is a reasonable first-order description since the ocean gets “shallower from the bottom up” (M. Briscoe, personal communication). In this example b is the same at each location as it describes the form of the stratification, but D is not, as it is affected by the depth of the ocean.

Table 1. Parameters re-scaled from GM79 to Aha99.

Quantity	GM79	Aha99	units
Energy/mass	$E b^2 N_0^2$	E_0	J / kg
Vertical wavenumber	$\frac{j\pi N(z)}{b N_0}$	$\frac{j\pi N(z)}{D(\omega) N_0}$	m ⁻¹

3. Observations

To determine if this re-scaled form of the GM formulation is useful for shallow water, we look to the data. The results shown here are based on a limited number of observations, and therefore this note should be considered a preliminary discussion.

Examples of rotary velocity spectra from the Mid-Atlantic Bight (MAB) and the Oregon Shelf (OS) are compared with the GM spectrum in Figure 3. The details of each data set are given in Table 2 and in *Boyd et al. (1997)* and *Pillsbury et al. (1974)*.

Table 2. Estimates of E_0 from MAB and OS.

Mid-Atlantic Bight 28 Jul - 27 Aug 1996 80 m water depth Sontek ADP current meter- 2 minute sampling		
Depth, m	Average $N(z)$, s^{-1}	E_0 , (J/kg) / 10^{-3}
7	0.026	1.6
15	0.029	0.9
23	0.025	0.6
31	0.018	0.7
35	0.013	1.0
43	0.012	1.0
51	0.011	1.3
Oregon Continental Shelf 29 June - 26 August 1973 100 m water depth Aanderaa current meters- 10 minute sampling		
Depth, m	Average $N(z)$, s^{-1}	E_0 , (J/kg) / 10^{-3}
20	0.022	3.1
40	0.015	3.4
60	0.010	4.2
80	0.008	3.1
95	0.007	1.8

There are peaks at the tide and f and a whitening of the spectrum at high frequency forming a spectral shoulder. The level of the GM spectrum was shifted subjectively to fit the observations in the continuum range above the tide and below the high frequencies. The shape of the GM continuum reasonably follows the observations, and the ratio of the CW and CCW components is also fairly consistent. Estimates of E_0 can then be made from equation (1) for various depths at MAB and OS using local values of $N(z)$ (Table 2). Representative values for MAB and OS are 1 and 3 mJ/kg respectively.

How does this compare with the energy level of GM79 before re-scaling: that is how does E_0 compare with $Eb^2N_0^2$? In attempting to answer this question one realizes the

difficulty in using the existing GM parameterizations—what should be used for b and N_0 ? Should one use the b and N_0 that fit the shelf stratification? This would not make sense physically as b and N_0 in this expression really only provide dimensional scales. It is more straightforward not to link the parameters specifying the stratification (b , N_0) with the absolute energy level (E_0). Using canonical values for the deep ocean for $E = 6.3 \times 10^{-5}$, $b = 1300$ m, $N_0 = 5.2 \times 10^{-3}$

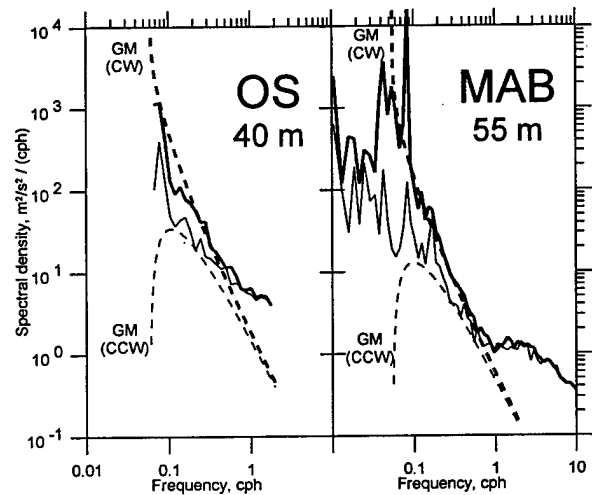


Figure 3. Rotary spectra from OS and MAB (solid lines) compared with GM shape (dashed lines). Clockwise component (CW) is bold; counter-clockwise component (CCW) is thin.

s^{-1} , yields an E_0 of 2.9 mJ/kg. This is relatively close to the levels of the shelf data shown here, i.e., within about a factor of 3. This preliminary result suggests the universality of E_0 in both deep and shallow internal wave fields—without the need to consider the universality of the stratification parameters b and N_0 . Note that since E_0 on the shelf is similar to the deep ocean level and the depth of the shelf is much shallower, the total energy per unit area on the shelf is much less than the deep ocean.

The effect of re-scaling the vertical wavenumber by replacing b with D is most dramatically demonstrated by looking at coherences. In the GM spectrum the vertical coherence is independent of frequency and is essentially a monotonic function of the scaled vertical separation $\Delta z/b$ (*Desaubies, 1976*). However, for large vertical separations, $\Delta z > b$, there is evidence of mode 1 dominance as the coherence increases with vertical separation and becomes out of phase (*Blumenthal and Briscoe, 1995*). On the shelf the stratification scale b is not very different from the deep ocean, but the vertical coherence scale is. The observed coherence pattern is consistent with a mode 1 dominant

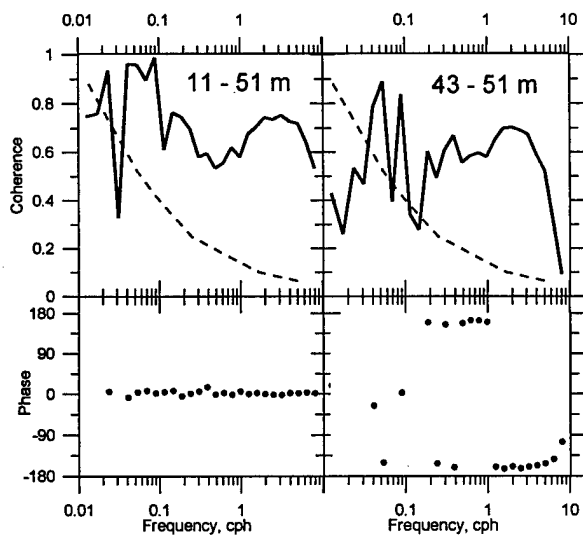


Figure 4. Coherence and phase from MAB between observations at 11 and 51 m (left panel) and 43 and 51 m (right panel). In the continuum, coherence is high for both separations, but becomes out of phase at the larger separation.

wave field, but with a vertical scale, $D \sim$ water depth, that is significantly shorter than the stratification scale $b \sim 1300$ m (Figure 4). Although not demonstrated here, the best fit is given by a $j \sim 1$, rather than 3, which is typical of the deep ocean.

The GM spectrum is horizontally isotropic, a property that is confirmed in observations of the deep ocean. However, on the shelf there is evidence of horizontal anisotropy. This is not surprising given the strong directionality provided by the nearby continental slope. Horizontal anisotropy is easily handled by the GM formalism of random waves—one needs only to parameterize the directional properties of the wave field (e.g., Schott and Willebrand, 1973). The anisotropy may be an important feature that distinguishes the shallow from the deep water wave field. There are clear examples of anisotropy due to domination of cross-shelf propagation (e.g., Winant *et al.*, 1987; Gordon, 1978). This is demonstrated by vertical coherence that is much stronger in the cross-shelf velocity component. However, the universality of the horizontal anisotropy is still under study. Observations from MAB indicate some horizontal anisotropy, but it is not as profound as in these other examples.

4. Other Issues

While the re-scaled GM statistical framework is useful in quantifying some of the properties of the shallow water internal wave field, there are many other issues that are missing in this formulation. In fact it may be that these other

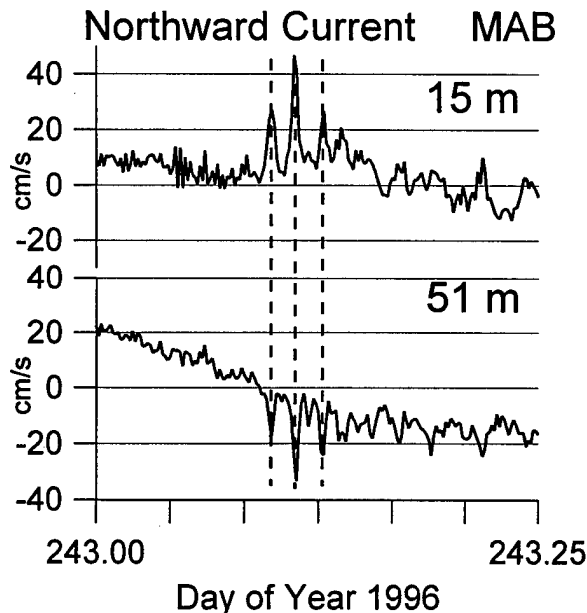


Figure 5. Times series of northward current at 15 and 51 m from MAB showing a packet of nonlinear internal waves with a mode 1 structure.

topics are the most essential to understanding the dynamics of the internal wave field. Perhaps the GM spectrum merely represents the relatively uninteresting background random sea. A few of these other issues are discussed here.

One important issue is temporal variability. While near-inertial motion can be often be associated with storm events in the upper ocean (e.g., D'Asaro *et al.*, 1995), the fluctuations of the energy in the internal wave continuum are more elusive and subtle (e.g., Frankignoul and Joyce, 1979). The wave field has been homogenized to such an extent that tracking observed waves back to their sources is not possible. Somehow the sources are steady enough on average and the nonlinear interactions strong enough so as to maintain a fairly consistent spectral sea of internal waves. Some variability, such as seasonal fluctuations, might be expected as both surface forcing and upper ocean stratification vary. Internal wave energy in the Sargasso Sea shows relatively weak seasonal variation by a factor of 2 to 3 that decrease with depth (Briscoe and Weller, 1984). In shallow water stronger seasonal effects are anticipated as the entire ocean can be considered upper ocean.

Another issue complicating the internal wave field on the shelf is the presence of nonlinear internal wave (NIW) packets. Energetic packets of internal waves are generated owing to the nonlinearity of the shoaling internal tide. NIW have been observed on shelves throughout the world (e.g., Ostrovsky and Stepanyants, 1989), and are sometimes referred to casually as solitary waves, solitons, or solibores. Evidence of these waves can often be seen at the sea surface

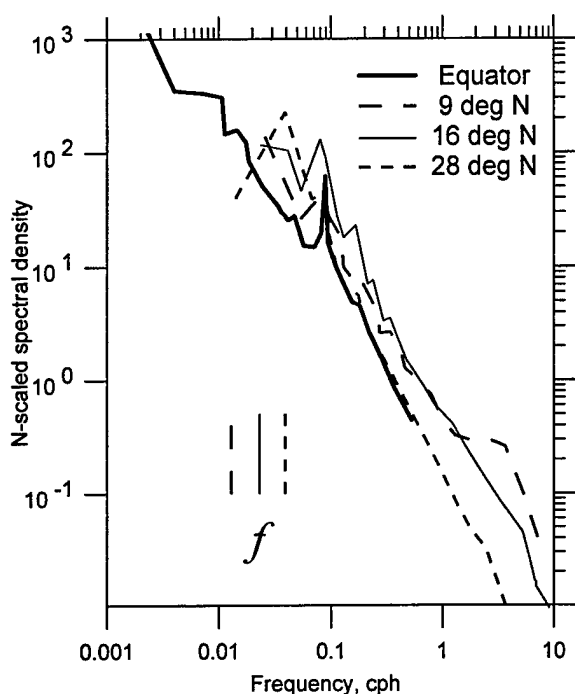


Figure 6. Examples of velocity spectra from different latitudes (Roth *et al.*, 1981); equator (Eriksen, 1985); 9° (Käse *et al.*, 1978); 16°N (Tarbell *et al.*, 1977), 28°N (Briscoe, 1975). Spectra have been scaled based on local N , equation (1).

visually or by surface radar as alternate bands of smooth and rough water. Internally the velocity structure is usually dominated by a mode 1 shape. The packet itself often consists of a collection of "pulses" or solitary-like waves (Figure 5). Nonlinear dynamics tend to create waves of solitary form from any initial wave shape. Despite the regularity of the barotropic tide, the characteristics of NIWs vary in time. The number, amplitudes, and shapes of the individual waves within a packet can vary dramatically from one packet to the next. Spectrally, much of the energy of the NIWs is concentrated at high frequency and contributes to the shoulder in the spectrum. However, the signal from the NIWs is spread over a significant bandwidth—the spectrum is not the best tool to analyze these nonlinear, non-sinusoidal phenomena. It appears that the spectral shoulder is not only due to NIWs, but may be a common feature of the upper ocean (e.g., Levine *et al.*, 1983). Besides obscuring the spectrum of the background internal waves, NIWs may affect dynamically the generation and propagation of other internal waves.

Another interesting issue is the latitudinal scaling in the GM spectrum. While this is not only an issue on the shelf, it does affect the re-scaling of the GM formalism and is

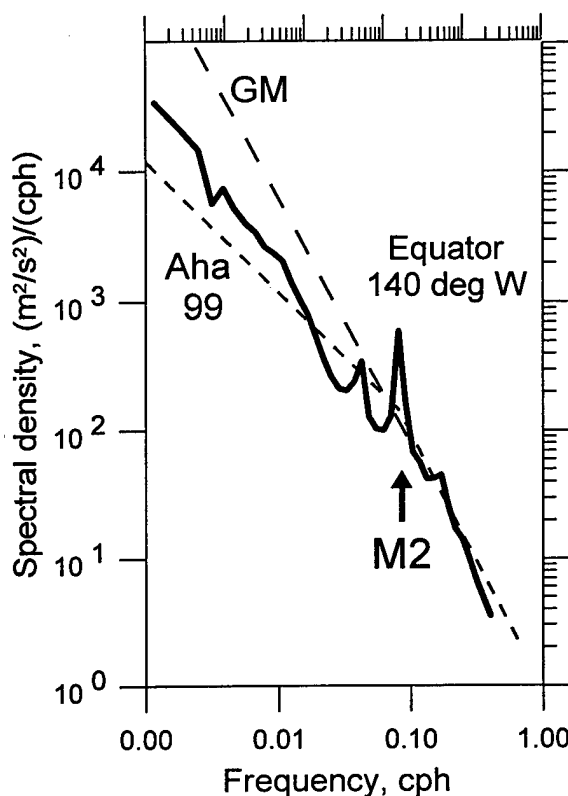


Figure 7. Velocity spectra from the equatorial Pacific Ocean at 140°W measured by NOAA's Tropical Atmosphere Ocean (TAO) array. The spectral slope is less steep than GM below M2, suggesting a modified spectral form called Aha99.

worth mentioning here. The spectral level in GM79 scales as f , which comes from the normalization of B (equation 2). However, observations indicate that the spectral level does not scale with f . Spectra from different latitudes are shown in Figure 6 using WKB to adjust for different $N(z)$. The levels of the continuum are within a factor of 3 without applying any latitudinal scaling; f -scaling actually increases the spread in the data significantly. In a footnote GM79 recognizes this observation and suggests that the f dependence in B be changed to a constant f_0 , at say 30°, to carry the units. While this eliminates the f scaling of the spectral level, the integral of B from f to N is then no longer constant, but is a function of f . This has implications on other statistical measures. For example, the level of the vertical wavenumber spectrum $S(\beta)$, which is a measure of the vertical shear, is set by the integral of B from f to N . In GM79 since $B \sim f$, $S(\beta)$ is not a function of f . This appears to be consistent with observations (Gregg *et al.*, 1993). If one instead uses a spectral level constant with f , as observations of frequency spectra suggest, then $S(\beta)$ goes like $1/f$ and increases dramatically in low latitudes. Both the fre-

quency spectral level and the total energy integrated over all frequencies cannot be independent of f . Hence, the function B needs to be modified.

Looking carefully at observed frequency spectra at low latitude, it is evident that the GM spectral slope does not fit the data at low frequencies (Figure 7). This has been commented on by Eriksen (1985) and even at a previous 'Aha' 'Hulikoa' (Levine, 1991). It appears that there may be a change in spectral slope at the semidiurnal frequency. This perhaps suggests a dynamic link between the high frequency internal wave field and the tide. If the tide is a significant energy source of high frequency internal waves, then this might help explain the remarkable stationarity and homogeneity of the internal wave field, as the tide is everywhere and steady. Recently, there has been renewed interest in the role of the internal tide in mixing the abyssal ocean (Munk and Wunsch, 1998). It may, however, be fortuitous to associate the spectral break with the tidal frequency, but clearly there is less energy below the M2 frequency than in the GM formulation. To fit the observations at low latitude more accurately (Figure 7), a modified functional form B' is proposed for B :

$$B' = B(\omega) \begin{cases} 1 & \omega > M2 \\ \omega/M2 & \omega < M2 \end{cases}$$

Although the fit is not perfect between M2 and f , this simple analytical form does describe the essential shape. The total energy/mass over all frequencies then becomes a function of latitude, and therefore the $S(\beta)$ shear spectrum is still a function of f . However, since the spectral slope is less steep below M2, the f dependence is not as pronounced and is perhaps more realistic. The function B' at least is a consistent compromise to explain the lack or weak f dependence of both S and $S(\beta)$. Further refinement and verification of this modified form for B is needed.

5. Conclusions

The Garrett-Munk spectrum remains a valuable first-order description of the oceanic internal wave field. To obtain an analogous description for the continental slope and shelf, we present the Aha99 form by re-scaling the GM spectrum and defining two new parameters: E_0 and D . The parameter E_0 is the total energy/mass, replacing the collection of constants $E b^2 N_0^2$; the length D scales the vertical waveguide, replacing the b scale. In GM the spectral level and vertical scale are both a function of b , the stratification scale. In the Aha99 these two scales are independent. The waveguide D can then vary with water depth without affecting the spectral level or the depth scaling of the stratification.

Preliminary results on the shelf indicate that the spectral level E_0 of the continuum (between the tide and high frequency) is not very different from the deep ocean. The wavenumber bandwidth in terms of equivalent modes j_* appears to be smaller than the deep ocean. Horizontal anisotropy is more pronounced on the shelves.

Although the apparent universality of the spectral continuum is interesting, other aspects of the wave field may be more important to understanding the dynamics. Other features affecting the climatology of the shelf internal wave field include temporal variability, horizontal anisotropy, and nonlinear internal wave packets. Although not an issue restricted to the continental shelf, the consistency of the latitudinal scaling of the spectrum through f is explored. Observed spectra at low latitude indicate a whiter spectral slope than the GM ω^{-2} at frequencies below M2. To follow these data more closely, a modification of the frequency dependence of the GM spectrum is suggested. The break in the spectral slope at M2 hints at a dynamical relationship between the internal wave continuum and the tide.

Acknowledgments. Many thanks to Peter Müller, Sharon Sakamoto, Di Henderson and the rest of the organizers for an interesting and productive meeting. The enthusiasm of Lou Goodman and the support of the Office of Naval Research under grant N00014-95-1-0534 is greatly appreciated.

References

- Blumenthal, M.B., and M.G. Briscoe, 1995: Distinguishing propagating waves and standing modes: An internal wave model, *J. Phys. Oceanogr.*, 25, 1095-1115.
- Boyd, T., M.D. Levine, and S.R. Gard, 1997: Mooring observations from the Mid-Atlantic Bight, July-September 1996, *Ref. 97-2, Data report 164*, Oregon State University.
- Briscoe, M.G., 1975: Preliminary results from the tri-moored internal wave experiment (IWEX), *J. Geophys. Res.*, 80, 3872-3884.
- Briscoe, M.G., and R.A. Weller, 1984: Preliminary results from the Long-Term Upper-Ocean Study (LOTUS), *Dyn. Atm. Oceans*, 243-265.
- D'Asaro, E. A., C. C. Eriksen, M. D. Levine, P. P. Niiler, C. A. Paulson and P. Van Meurs, 1995: Upper ocean inertial currents forced by a strong storm. I: Data comparisons with linear theory, *J. Phys. Oceanogr.*, 25, 2909-2936.
- Desaubies, Y.J.F., 1976: Analytical representation of internal wave spectra, *J. Phys. Oceanogr.*, 6, 976-981.
- Eriksen, C.C., 1985: Some characteristics of internal gravity waves in the equatorial Pacific, *J. Geophys. Res.*, 90, 7243-7255.
- Frankignoul, C., and T.M. Joyce, 1979: On the internal wave variability during the Internal Wave Experiment (IWEX), *J. Geophys. Res.*, 84, 769-776.
- Garrett, C.J., and W. Munk, 1972: Space-time scales of internal waves, *Geophys. Astrophys. Fluid Dyn.*, 2, 255-264.
- Garrett, C.J., and W. Munk, 1975: Space-time scales of internal waves: A progress report, *J. Geophys. Res.*, 80, 291-297.
- Gordon, R. L., 1978: Internal wave climate near the coast of northwest Africa during JOINT-1, *Deep-Sea Res.*, 25, 625-643.

- Gregg, M.C., D.P. Winkel, and T.B. Sanford, 1993: Varieties of fully resolved spectra of vertical shear, *J. Phys. Oceanogr.*, **23**, 124-141.
- Käse, R.H., H. Peters, G. Siedler and W. Zenk, 1978: A compilation of current, temperature and conductivity data from moorings F1 and F2 in the GATE C-area, *Meteor. Forschungsergeb. Reihe A*, **20**, 13-48.
- Levine, M.D., 1991: Observing oceanic internal waves: What have we learned? What can we learn?, in Dynamics of Oceanic Internal Gravity Waves, Proceedings of the Hawaiian Winter Workshop, P. Muller and D. Henderson (eds.), University of Hawaii, Honolulu, HI, pp. 467-479.
- Levine, M. D., C. A. Paulson, M. G. Briscoe, R. A. Weller and H. Peters, 1983: Internal waves in JASIN, *Phil. Trans. Royal Soc.*, **A308**, 389-405.
- Munk, W., 1981: Internal waves and small-scale processes, in *Evolution of Physical Oceanography*, edited by B.A. Warren and C. Wunsch, pp. 264-290, MIT Press, Cambridge, Mass.
- Munk, W., and C. Wunsch, 1998: Abyssal recipes II: energetics of tidal and wind mixing, *Deep-Sea Res. I*, **45**, 1977-2010.
- Ostrovsky, L.A., and Yu.A. Stepanyants, 1989: Do internal solitons exist in the ocean? *Rev. Geophys.*, **27**, 293-310.
- Pillsbury, R.D., J.S. Bottero, R.E. Still and W.E. Gilbert, 1974: A compilation of observations from moored current meters, vol. VII, Oregon continental shelf, July-August 1973, *Data Rep. 58, Ref. 74-7*, 87 pp. School of Oceanography, Oregon State Univ.
- Roth, M.W., M.G. Briscoe, and C.H. McComas III, 1981: Internal waves in the upper ocean, *J. Phys. Oceanogr.*, **11**, 1234-1247.
- Schott, F., and J. Willebrand, 1973: On the determination of internal-wave directional spectra from moored instruments, *J. Marine Res.*, **31**, 116-134.
- Tarbell, S., S. Payne and R. Walden, 1977: A compilation of moored current meter data and associated mooring action data from mooring 592. Vol XIV, WHOI-77-41, Woods Hole Oceanographic Inst., 122 pp.
- Winant, C. D., R. C. Beardsley, and R. E. Davis, 1987: Moored Wind, Temperature, and Current Observations Made During Coastal Ocean Dynamics Experiments 1 and 2 Over the Northern California Shelf and Upper Slope, *J. Geophys. Res.*, **92**, 1569-1604.

Observations of the Internal Tide on the Southern California Shelf

James A. Lerczak, Myrl C. Hendershott, and Clinton D. Winant

Scripps Institution of Oceanography, University of California at San Diego, La Jolla, California

Abstract. The nature of tidal band (0.030 to 0.17 cph) variability on the narrow (~ 10 km) continental shelf and slope off of Mission Beach, California was studied using data from mooring arrays deployed during the summer and fall months of 1996 and 1997. Tidal variability was intermittent, and its strength was not obviously correlated with the fortnightly cycle of the surface tide or low-frequency changes in background currents or stratification. Surprisingly, strong baroclinic, diurnal (0.042 cph) currents were present on the slope and shelf, even though this frequency was slightly sub-inertial (inertial frequency = 0.045 cph). The spatial structure of the tidal variability was studied separately for the diurnal (0.030 to 0.056 cph) and semi-diurnal (0.056 to 0.11 cph) frequency bands using complex empirical orthogonal functions (cEOFs). Most of the variability in each band was explained by a single cEOF mode. However, the structure of the first mode was strikingly different for the two bands. Diurnal currents were surface enhanced and decayed gradually from the slope to the nearshore of the shelf. They were clockwise, circularly polarized, and generally had a slow upward phase propagation (~ 0.5 mm/s). This upward phase propagation was surprising for motions that were apparently sub-inertial, and therefore evanescent, at this location. The driving mechanism for these oscillations is presumed to be the local sea-breeze, which had a very prominent diurnal peak. The strength of semi-diurnal currents was stronger on the shelf than on the slope. These currents, roughly, had a mode one structure in the cross-isobath direction. However, bottom currents were linearly polarized in the cross-isobath direction, while the surface currents were clockwise, circularly polarized. There was no apparent vertical phase propagation for these waves. The relative phase between cross-isobath, semi-diurnal currents at different depths and temperature fluctuations was consonant with a cross-shore standing wave. The near bottom, semi-diurnal currents on the slope (350 m water depth) were an exception to this general description. Here, the semi-diurnal currents were bottom enhanced, linearly polarized in the long-isobath direction, and apparently coupled to the fortnightly cycle of the surface tide.

Introduction

Tidal currents are often very energetic on continental shelves. In fact, cross-shore currents are frequently dominated by tidal band (here defined as between $\frac{1}{33}$ and $\frac{1}{9}$ cycles per hour) variability. Yet, the tidal variability is often intermittent, and not obviously correlated with the regular and predictable surface tide, which is presumably forcing the currents. This lack of correlation is apparently caused by the presence of energetic baroclinic tidal motions. Baroclinic tides may be intermittent for several reasons. Their generation may be sensitive to the stratification at the generation sites (Baines, 1982; and Rosenfeld, 1990), and stratification on continental shelves varies seasonally as well as at faster time scales due to upwelling events (Rosenfeld, 1990) and the passage of vigorous storms. Multiple generation sites are likely to be present near con-

tinental shelves with complicated topographic features. The presence of low-frequency currents and stratification variability on and near the shelf may act to focus and defocus the internal waves at a given location at different times.

Here we report on a study of the nature of the baroclinic tide on the narrow (~ 10 km) continental shelf and slope off of Mission Beach, California using data from the 1996 and 1997 Internal Waves on the Continental Margin (*IWAVES*) experiments, which were designed to study the internal wavefield, across the entire internal wave frequency band, on the continental slope and across the shelf. The main point that we wish to make here is that, while the tidal currents during *IWAVES* were intermittent and this intermittency was not obviously correlated with local low-frequency changes in stratification and currents, their spatial structure remained consistent across the shelf

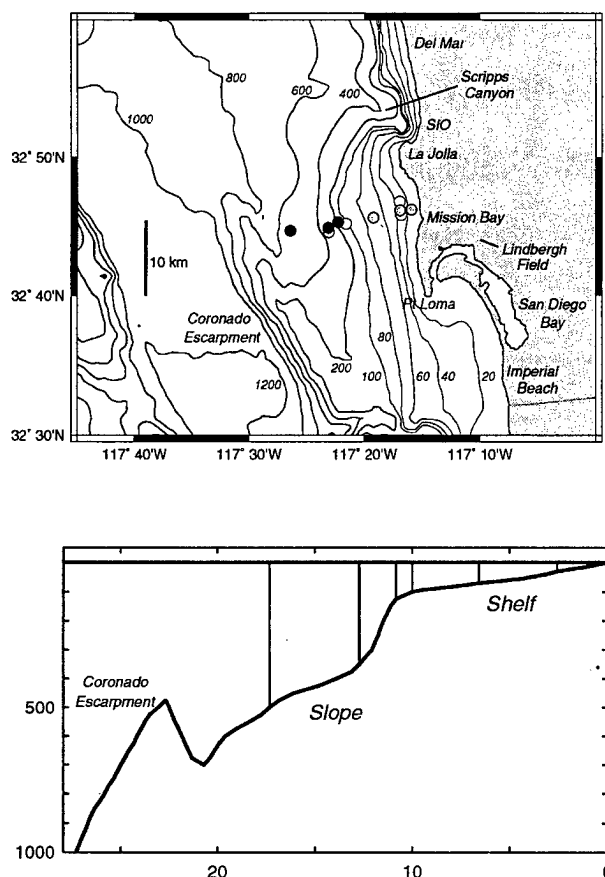


Figure 1. Summer month mooring locations and bathymetry at the Internal Waves on the Continental Margin (*IWAVES*) study site. Circles mark the locations of the moorings of the shelf/slope arrays. Unfilled circles mark moorings deployed in 1996; black-filled mark 1997 moorings; and gray-filled mark moorings deployed in both years. Depths are given in meters, and cross-shore distances are given in kilometers.

and in time and was fairly easy to describe. However, this structure was not consonant with linear flat bottom internal waves nor progressive wave solutions of constant bottom slope models (*Wunsch, 1969*). Further, both diurnal and semi-diurnal variability were present on the shelf, and their respective structures were quite different. The presence of baroclinic diurnal variability in this region was surprising, because this frequency was slightly sub-inertial at this latitude ($32^{\circ} 45' N$). However, we will show that a prominent peak in current variability occurred at the diurnal frequency ($f_d = 0.042$ cph) which was clearly distinguishable from the inertial frequency ($f_i = 0.045$ cph). We propose that the forcing mechanism for the diurnal motions was not the

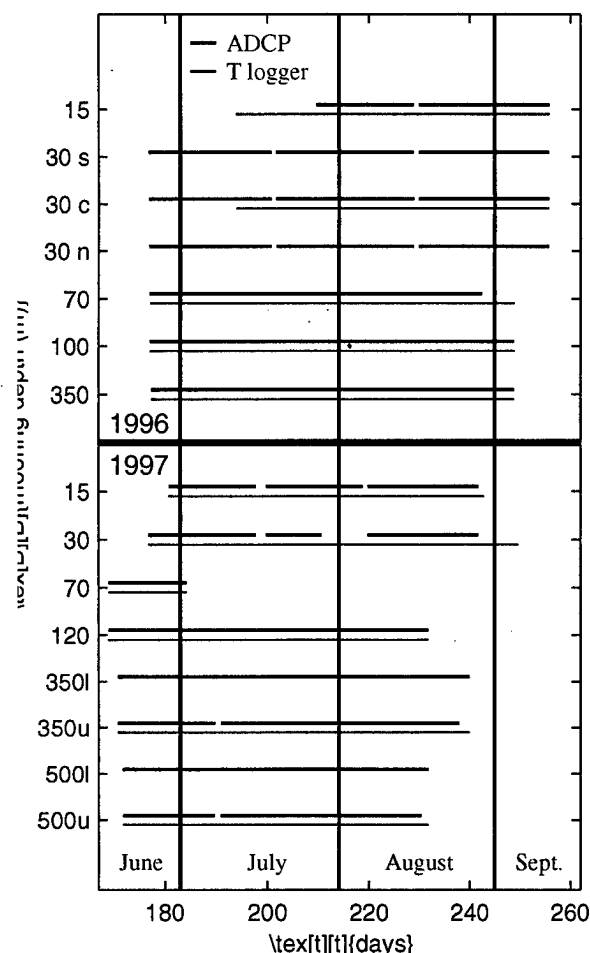


Figure 2. Time line of the 1996 and 1997 summer mooring deployment of the Internal Waves on the Continental Margin (*IWAVES*) experiment. The 30 m moorings of 1996 are labelled s, c, and n to indicate the south, center and north moorings deployed that year (Fig. 1). The 350 and 500 m moorings of 1997 are labelled l and u to indicate the lower (upward-looking) and upper (downward-looking) ADCPs deployed on those mooring lines.

barotropic tide, but the wind stress associated with the local sea-breeze.

After briefly describing the *IWAVES* experiments, three analyses of the data are presented. First, the vertically averaged, diurnal and semi-diurnal kinetic energy at each mooring is described and compared to the low-frequency and super-tidal kinetic energy levels. Next, the vertical structure of the horizontal current rotary spectra is described. Finally, the structure of the dominant modes of variability obtained from complex empirical orthogonal functions (cEOFs) at selected moorings is presented for the diurnal and semi-diurnal frequency bands. The differences in the structure of the two bands is emphasized. Time series of the mode one

CEOFS at different moorings show the intermittent nature of the variability. These time series are compared to the fortnightly cycle of the surface tide, slow changes in stratification at the moorings, and the cross-shore winds measured near the study site.

Field Studies

Arrays were deployed off of Mission Beach, California (Fig. 1) to study internal wave dynamics during the 1996 and 1997 *IWAVES* experiments. The arrays were deployed twice each year with different configurations. From approximately the end of June to the end of August each year (Fig. 2), the array spanned depths from 15 m to 500 m covering a cross-shore range of approximately 15 km (Fig. 1). During the late summer and early fall, moorings were tightly spaced in shallow, nearshore depths ranging from 15 to 30 m. This study focuses on data from the broad shelf/slope arrays deployed in the summer months of both years.

Each mooring was instrumented with at least one acoustic doppler current profiler (ADCP) to measure the three components of velocity as a function of depth. On the shelf, between 67 and 80% of the water column was covered by the ADCPs (Table 1). On the slope, the full water column could not be sampled because of ADCP range limitations. In 1996, the deeper portion of the water column was sampled at the 350 m mooring. In 1997, two ADCPs (a deep upward-looking, and a shallow downward-looking) were deployed on the 350 and 500 m mooring lines. Together, they approximately covered the upper 50% of the water column at each mooring. Vertical resolution ranged from four to 16 m on the slope, and one to 4 m on the shelf. Sampling intervals ranged from one to four min.

Four to 12 temperature loggers (TLs) were evenly spaced on the lines of each mooring. These instruments sampled once every 15 seconds. Bottom-mounted and near-surface pressure sensors (sample interval = one min) were deployed on some of the moorings. Wind speed and direction was monitored from Scripps pier (approximately 12 km north of the study site) during the experiments and was also obtained from NOAA weather stations at Lindbergh Field and Imperial Beach. In addition, continuous CTD yoyo's were conducted at the mooring locations on numerous occasions for periods ranging from 4 to 24 hours.

The shelf was approximately 10 km wide at the study site (Fig. 1). Its bottom slope was approximately planar, with a value of approximately 0.01. The continental slope topography was somewhat more complex, having a shallow bank to the southwest (which shoaled to a depth of approximately 125 m) and then dropping off precipitously at the Coronado Escarpment. Scripps

Canyon impinged on the shelf approximately 14 km north of the study site, drastically changing the shelf geometry there.

Energetics

First we summarize the vertically averaged, horizontal kinetic energy of the tidal currents obtained by the ADCPs in relation to the low-frequency and super-tidal currents on the slope and shelf (Table 1). Long-isobath currents were distinguished from cross-isobath, and the long-isobath direction (approximately 10° W of N at each mooring) was defined by the local bathymetry at each mooring. Low-frequency currents ($f < \frac{1}{33}$ cph) were most energetic in the upper 100 m of the water column. They were highly elliptical, with most energy directed in the long-isobath direction. Currents decayed monotonically from the continental slope to the nearshore, and slope and outer-shelf currents were an order of magnitude more energetic than the nearshore currents.

Diurnal ($\frac{1}{33} < f < \frac{1}{18}$ cph) currents were also surface enhanced. Slope and outer-shelf variability was nearly equal in the cross- and long-isobath directions. The energy decayed towards the shore and became slightly elliptical in the long-isobath direction. In contrast, semi-diurnal ($\frac{1}{18} < f < \frac{1}{9}$ cph) energy increased from the slope to the shelf. It was greatest at mid-shelf depths (30-70 m), and decreased slightly inshore of 30 m. The variability changed from being slightly elliptical in the long-isobath direction at the shelf and outer-slope to slightly elliptical in the cross-isobath direction on the mid- and inner-shelf. Super-tidal ($f > \frac{1}{9}$ cph) currents were most energetic in the nearshore, where they were most elliptical in the cross-isobath direction.

The near-bottom currents at the 350 m mooring, which were sampled in 1996, were at variance with the foregoing general description. The semi-diurnal currents were energetic, while diurnal currents were weak. All currents were nearly linearly polarized in the long-isobath direction. We will show that the structure and temporal variability of these currents differed markedly from the surface to mid-depth currents on the slope and shelf.

Rotary Spectra

We begin our description of the spatial structure of the tidal currents with a look at the horizontal current rotary spectra at each mooring. Spectra were calculated at different vertical bins spanning the depth range of the ADCPs. Each time series was first band-passed of the ADCPs. Each time series was first band-passed between $\frac{1}{33}$ and $\frac{1}{4}$ cph. The data were then subsampled to obtain time series with sample intervals of one hour.

Table 1. Depth-averaged Kinetic Energy

Moor. depth (m)	Range (m)	Low-freq.		Diurnal		Semi-Diurnal		Super-tidal		Noise
		Long- isobath	Cross- isobath	Long- isobath	Cross- isobath	Long- isobath	Cross- isobath	Long- isobath	Cross- isobath	
1996										
350	151-327	24.8	1.39	3.66	0.620	12.3	2.33	2.31	3.32	1.36
100	20-88	102	5.93	9.62	10.7	5.38	5.32	3.75	5.61	0.989
70	6-62	75.9	3.74	9.37	9.61	8.33	12.3	3.35	5.98	1.02
30 <i>c</i>	4-24	17.6	2.72	5.17	3.18	8.09	10.9	6.73	11.4	2.56
15	2-13	9.17	3.64	5.78	2.35	7.72	11.9	7.14	14.9	1.92
1997										
500 <i>u</i>	17-85	214	44.7	14.5	16.1	9.81	8.04	5.45	5.93	2.18
500 <i>l</i>	143-279	29.9	22.9	4.48	4.31	5.27	5.24	2.43	2.82	4.85
350 <i>u</i>	13-89	131	33.2	10.9	10.7	9.22	6.16	4.44	5.41	1.72
350 <i>l</i>	116-196	46.9	4.75	3.73	1.72	7.36	4.28	3.46	4.67	0.612
120	24-108	119	28.1	9.06	8.24	7.81	7.03	4.46	6.81	2.04
30	3-27	21.9	3.14	5.46	2.88	8.50	15.9	7.68	15.0	2.70
15	2-13	11.2	1.69	5.69	1.71	7.08	9.40	4.77	15.0	4.41

Depth-averaged velocity variance (cm^2/s^2) for the ADCPs of the shelf/slope array deployments during the summers of 1996 and 1997. The frequency ranges for the low-frequency, diurnal, semi-diurnal, and super-tidal bands were $0-\frac{1}{33}$, $\frac{1}{33}-\frac{1}{18}$, $\frac{1}{18}-\frac{1}{9}$, and $\frac{1}{9}-f_N$ cph, respectively, where f_N was the Nyquist frequency for each instrument. Long-isobath directions were defined by the local bathymetry at each mooring, and were roughly 10° west of true north. The rms noise variance was removed from the estimates within each frequency band. The noise was assumed to be white-noise, and was estimated from the level floor at the high-frequency end of the horizontal current power spectra. Variances were estimated over the common time range 25 June to 29 August in 1996 (except for the 15 m mooring for which the range 27 July to 29 August was used) and 28 June to 17 August in 1997. The designations *c*, *u* and *l* for the mooring depths are explained in Figure 2.

Finally, a Hanning window was applied to each time series. For most moorings, in order to obtain the highest possible spectral resolution, the full time series were used, and the spectra were neither frequency-band nor ensemble averaged. For the 500 and 350 m moorings of 1997, only the longer of the two continuous time series were used (~ 40 days, Fig. 2). Data from the 30 and 15 m moorings were broken into two to three nearly equal time blocks, because instrument batteries were replaced during the experiments (Fig. 2). For these moorings, spectra were calculated separately for each time block and then averaged. Consequently, the spectral resolution was not as fine for them as that for the outer shelf and slope moorings.

The spectra from the 1996 and 1997 experiments are summarized in figures 3 and 4, respectively. At all moorings, the diurnal variability was well-resolved and clearly distinguishable from inertial variability. Diurnal currents were clockwise-circularly, polarized at all depths and always surface enhanced, falling to near-

background levels at the bottom of the shelf, or at a water depth of about 150 m on the slope. For example, the diurnal band variance at the 1996, 70 m mooring fell from $34 \text{ cm}^2/\text{s}^2$ at a depth of 8 m to $5.8 \text{ cm}^2/\text{s}^2$ at a depth of 60 m. The shape of the peak on the shelf was characterized by a tall, sharp line with broad, background shoulders. On the slope (350 and 500 m), the line was less distinguishable from the shoulders. The widths of the peaks can be compared to spectra of the surface tide, calculated for comparable time periods (Fig. 5).

The semi-diurnal currents were more difficult to generalize. Both clockwise (cw) and counter-clockwise (ccw) semi-diurnal energy were present in the spectra, though the ccw peak tended to be sharper than the cw. In general, the ratio of ccw to cw variance increased with depth on the shelf. We will subsequently show that this was due to the bottom currents being onshore, linearly polarized, while the surface currents were clockwise, elliptically polarized. In contrast, on the slope in

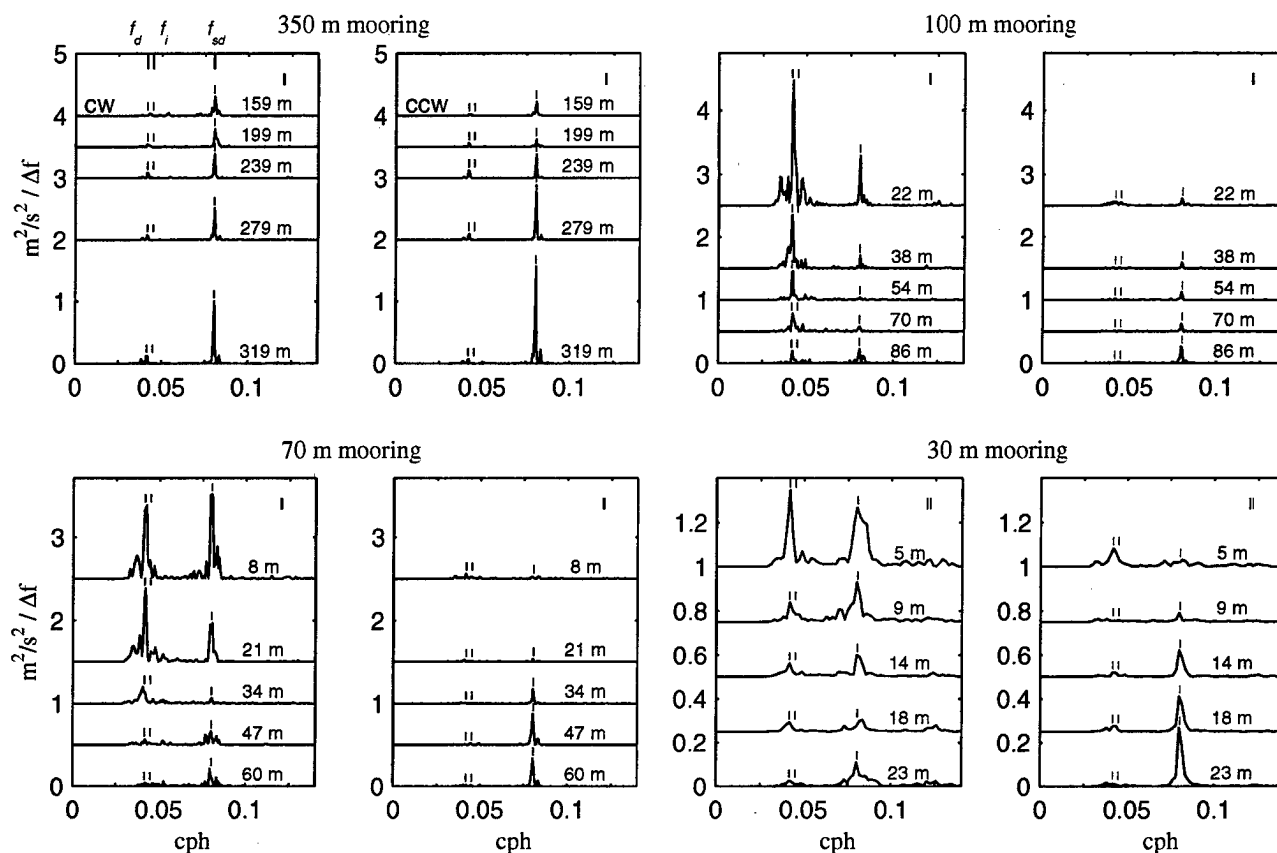


Figure 3. Rotary spectra of horizontal current time series from the 1996 *IWAVES* experiment. Clockwise (cw) and counter-clockwise (ccw) spectra are shown for selected moorings at different depths spanning the range of the ADCPs. Axes are linear, and spectra from different depths are offset by varying amounts. The diurnal (f_d), inertial (f_i) and semi-diurnal (f_{sd}) frequencies are marked by small vertical lines above each spectrum. The spectral resolution (Δf) is indicated by the gap between two vertical lines at the upper-right of each panel. The two lines are almost indistinguishable for most spectra. The resolution of the spectra vary from mooring to mooring because the length of the time series vary.

the upper portion of the water column (500 and 350 m moorings of 1997), the ratio of ccw to cw variance decreased with depth.

Spectra from the bottom half of the water column at the 350 m (1996 deployment) differed from all the others. Here, very little diurnal energy was present, and the semi-diurnal peaks were very sharp and bottom enhanced. We will show that the semi-diurnal variance here was linearly polarized in the long-isobath direction and was not obviously coherent with the tidal variability at the other moorings.

Complex Empirical Orthogonal Functions

To study the vertical structure of the tidal currents in more detail, we employed complex empirical orthogonal functions (cEOFs; *Wallace and Dickinson, 1972*). Complex EOFs, in various forms, have been used by nu-

merous investigators (*Gordon, 1978; Denbo and Allen, 1984; Bratkovich, 1985; and Rosenfeld, 1990*) to study the dominant modes of variability in the tidal frequency bands on continental slopes and shelves. With cEOFs, the dominant, statistically independent modes of variability within a specified frequency band from a collection of time series (e.g., horizontal current time series at different locations) can be identified. An advantage of cEOFs over time-domain EOFs, when studying propagating wave phenomena, is that the relative phase between different locations is not fixed. For example, when a cEOF is calculated for a propagating plane wave sampled at different locations, all the variance will be contained in a single cEOF mode, and the amplitude at each location will be the same (equal to the amplitude of the wave). The relative phase gives the time difference in the arrival of wave crests at different locations.

The strong differences in the nature of the diurnal and semi-diurnal peaks in the spectra suggest that the

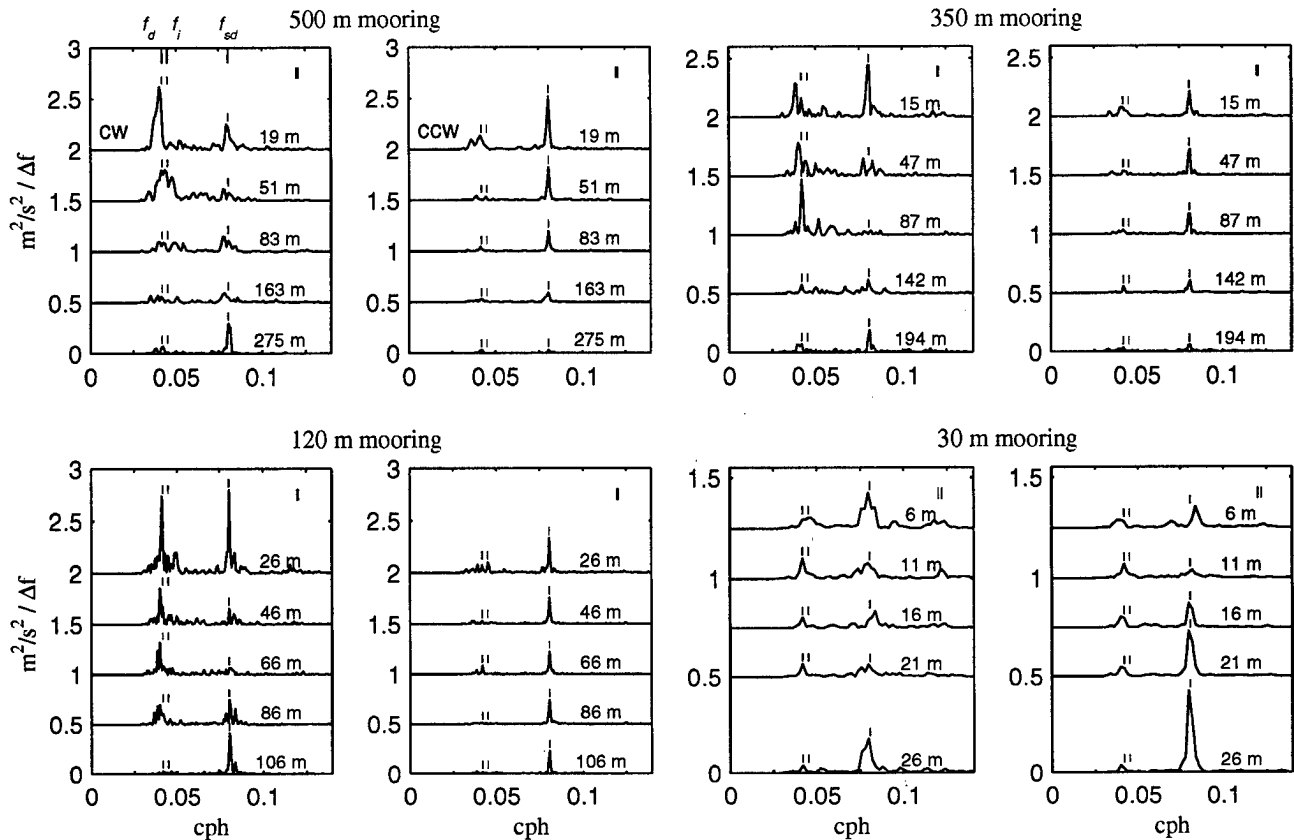


Figure 4. Same as Figure 3, but for selected moorings from the 1997 IWAVES experiment.

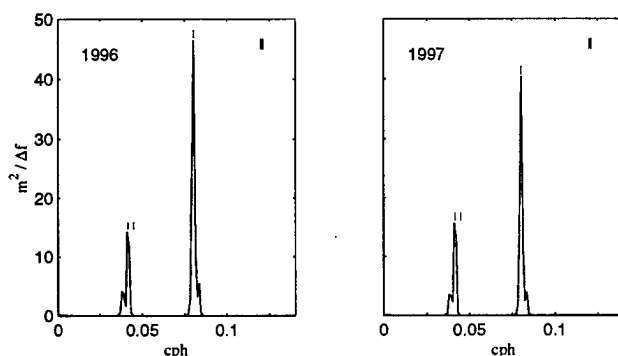


Figure 5. Surface tide power spectra calculated using data from the bottom-mounted pressure gauge at the 15 m mooring deployed during the summer months of the 1996 and 1997 IWAVES experiments. Spectra were calculated in the same manner as the rotary spectra of Figures 3 and 4. The sample length used for both the 1996 and 1997 spectra was 40 days (comparable to the period used for the 500 and 350 m rotary spectra of 1997). The separation between the two vertical lines in the upper-right corner of each plot indicates the spectral resolution of the spectra.

dynamics of these two bands were different. We, therefore, calculated separate cEOFs for the diurnal ($\frac{1}{33}$ to $\frac{1}{18}$ cph) and semi-diurnal ($\frac{1}{18}$ to $\frac{1}{9}$ cph) frequency bands. The data were processed in the same manner as was done to calculate the rotary spectra. Here we present results from decompositions of horizontal current data from single moorings.

Single mooring cEOFs

Complex EOFs were calculated using the current data from individual moorings. In each case, the entire time series was used. The most energetic semi-diurnal and diurnal cEOFs from the 70 m mooring of 1996 are summarized in Figures 6, 7 and 8. These modes explained 73 and 67% of the variance within the semi-diurnal and diurnal bands, respectively. The semi-diurnal, cross-isobath variability essentially resembled a mode one wave (Figs. 6a and b). The amplitude was largest at the top and bottom of the water column, and was at a minimum at a depth of approximately 30 m. The upper and lower currents were 180° out of phase. In contrast, the long-isobath variability was greatest at the surface and decayed to near-zero values at the bot-

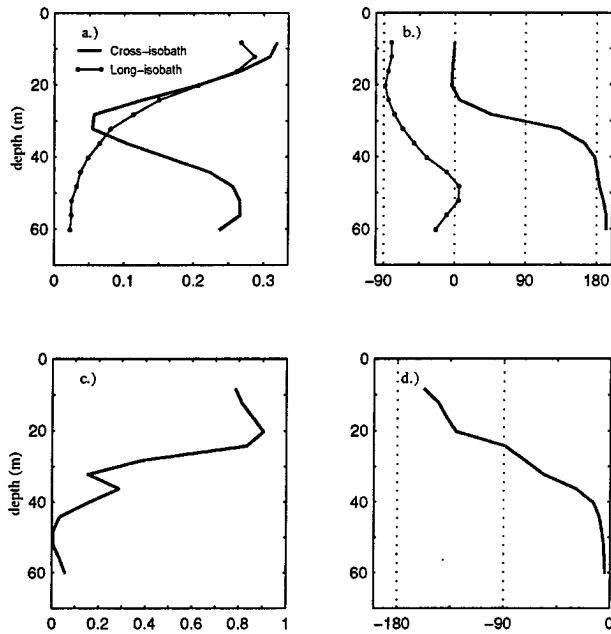


Figure 6. First cEOF mode of semi-diurnal band ($\frac{1}{18}$ to $\frac{1}{9}$ cph), horizontal currents at the 70 m mooring of the 1996 IWAVES experiment. The full time series ($T \approx 65$ days) was used, and a Hanning window was applied to the data before the cross-spectral matrix was calculated. Approximately 73% of the variance within the semi-diurnal band was explained by this mode. a) Relative amplitude of the cross- and long-isobath currents vs. depth. b) Phase of the currents relative to the cross-isobath currents in the upper most depth bin. c) Ratio of the minor to major axes of the current ellipses. d) Angle of the major axis (0° is cross-isobath)

tom. At the surface, long- and cross-isobath currents were 90° out of phase, with the long-isobath currents leading the cross-isobath. The ratio of minor to major current ellipse axes was close to one at the surface (Fig. 6c), consistent clockwise, circular polarization. At the bottom, currents were linearly polarized and directed in the cross-isobath direction (Figs. 6c and d).

The relative phases, at the semi-diurnal frequency, between temperature fluctuations at a depth of 45 m and cross- and long-isobath currents at different depths were calculated for the 1996, 70 m mooring (Fig. 9). Temperature fluctuations (used here as a proxy for vertical isopycnal displacement fluctuations) led (lagged) cross-isobath currents by approximately 90° near the bottom (surface). This was consistent with a cross-shore standing wave.

The amplitudes of the long- and cross-isobath diurnal currents were essentially equal to each other at all depths (Fig. 7a). They were maximum at a depth of 20 m and decayed to near zero values at the bottom.

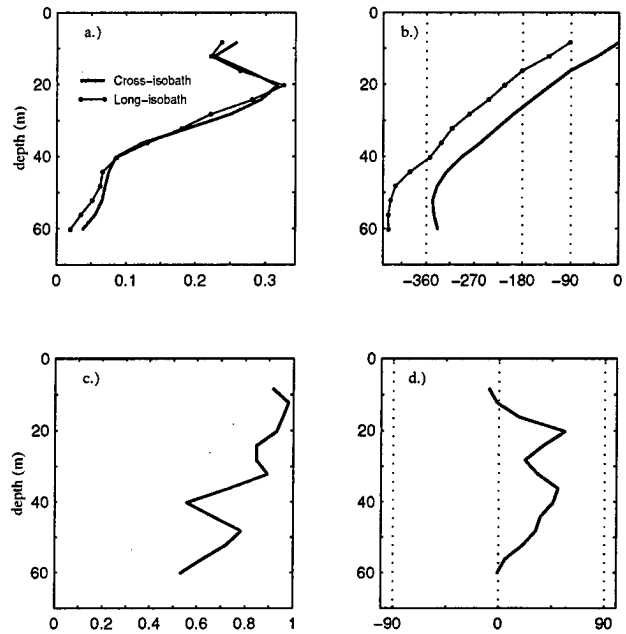


Figure 7. Same as Figure 6, but for the diurnal band ($\frac{1}{33}$ to $\frac{1}{18}$ cph). This first cEOF mode explained 67% of the variance within the band.

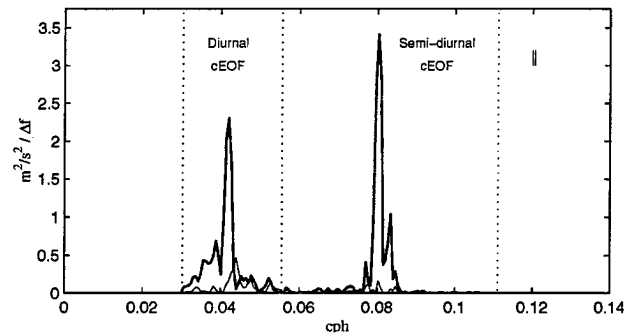


Figure 8. Spectra of the first (bold) and second (light) modes of the diurnal and semi-diurnal cEOF decompositions (Figs. 6 and 7). For the diurnal band, the first two modes explained 67 and 16% of the variance, respectively. For the semidiurnal band, the first two modes explained 73 and 6.8% of the variance, respectively. The dotted lines mark the range of frequencies used in the decompositions. The separation between the two vertical lines in the upper-right corner of each plot indicates the spectral resolution of the spectra.

The phases of both increased linearly with depth (Fig. 7b), with the long-isobath leading the cross-isobath by 90° . This was consistent with upward phase propagation, with a speed of 0.45 mm/s. The ratio of minor to major current ellipse axes was close to one at all depths (Fig. 7c), consistent with clockwise, circular polarization.

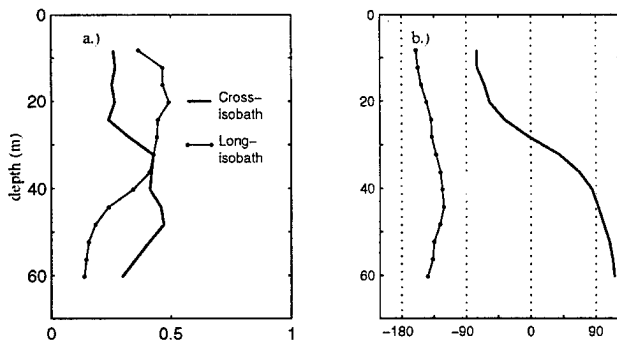


Figure 9. Coherency-squared (a) and relative phase (b) at the semi-diurnal frequency between temperature fluctuations at a depth of 45 m and cross- and long-isobath currents at different depths at the 70 m mooring of the 1996 *IWAVES* experiment. The 65 day time period common to the temperature and current time series was broken into 10 blocks (a Hanning window was applied to each block), giving 20 degrees of freedom in the estimate of the cross-spectra.

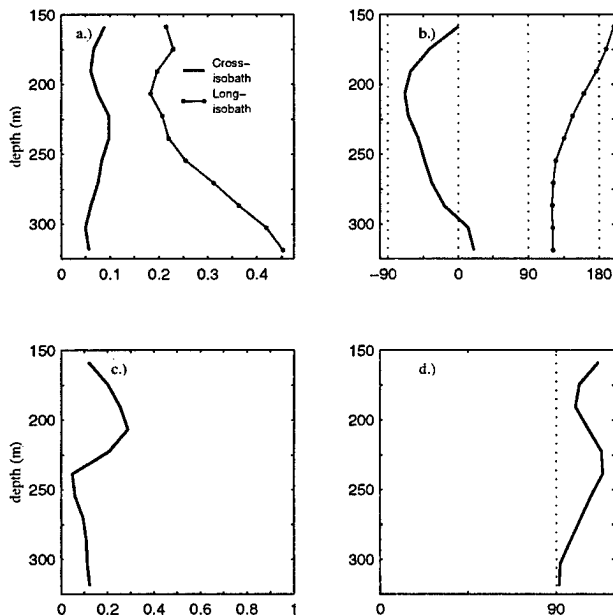


Figure 10. Same as Figure 6, but for the semi-diurnal band first cEOF mode of horizontal currents from the 350 m mooring of the 1996 *IWAVES* experiment. This first cEOF mode explained 74% of the variance within the band.

Not surprisingly, the dominant cEOF modes captured most of the variance in diurnal and semi-diurnal spectral peaks (Fig. 8). While the second cEOF modes explained 6.8 and 16% of the variance in the diurnal and semi-diurnal bands, respectively, their variance was spread more uniformly across each band (Fig. 8.). This suggested that all modes but the first captured the variance of the background and noise within each band,

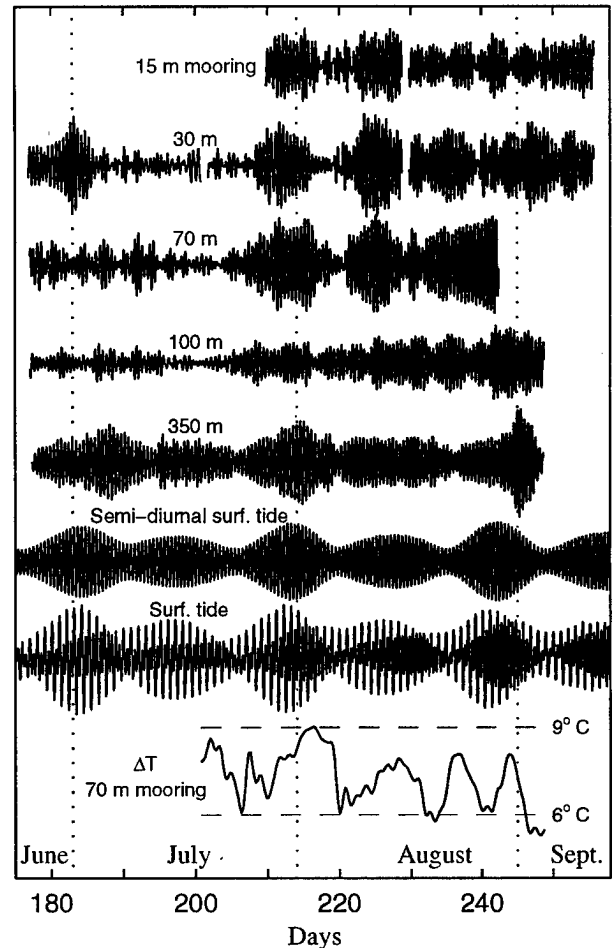


Figure 11. Time series of the first, semi-diurnal band cEOF modes calculated separately for the horizontal currents at the 15, 30, 70, 100 and 350 m moorings of the 1996 *IWAVES* experiment. These modes explained 51, 62, 73, 51, and 74%, respectively, of the variance within the semi-diurnal band at each mooring. The time series are scaled to give a relative measure of the vertically averaged variance of the mode. The semi-diurnal band-passed and unfiltered surface tide are plotted below the cEOF time series. The maximum tidal range was 2.75 m. The final time series is the low-passed ($f < \frac{1}{33}$ cph) temperature difference between the topmost ($z = -1$ m) and bottom ($z = -68$ m) temperature loggers on the 70 m mooring line.

while the first modes were effective at capturing most of the variance in the peaks and their shoulders.

The structure of the first mode cEOFs of all shelf moorings (100 to 15 m water depth) were similar to the 70 m mooring cEOFs described above. In contrast, the mode one, semi-diurnal cEOF from the 350 m mooring of 1996 (Fig. 10) looked quite different. Since the diurnal peaks were comparatively small at this mooring, we focused only on the semidiurnal cEOF.

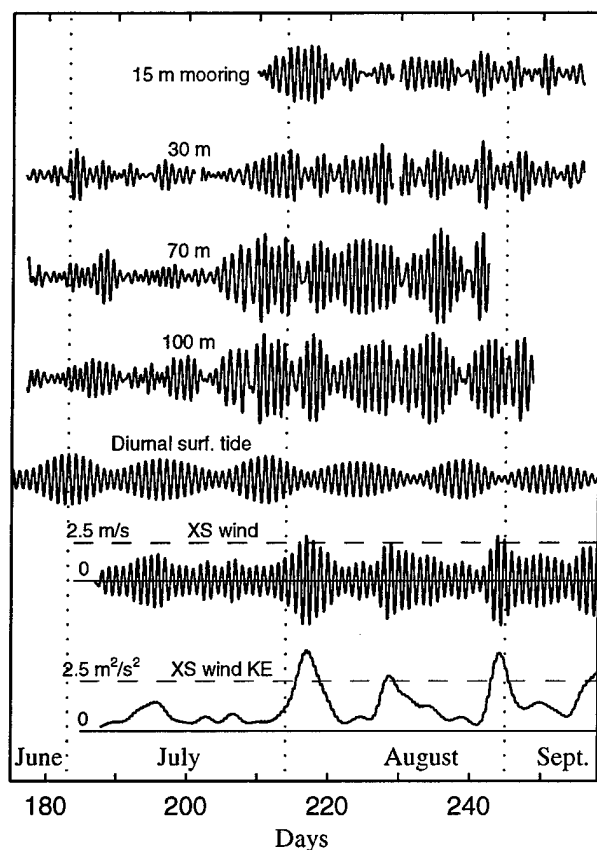


Figure 12. Time series of the first, diurnal band cEOF modes calculated separately for the horizontal currents at the 15, 30, 70, and 100 m moorings of the 1996 *IWAVES* experiment. These modes explained 73, 59, 67, and 66%, respectively, of the variance within the diurnal band at each mooring. The time series are scaled to give a relative measure of the vertically averaged variance of the mode. The diurnal band-passed, surface tide is plotted below the cEOF time series. The lowest two time series are the cross-shore diurnal band wind speed and its variance (running-mean filtered with a boxcar of length 2 days) measured at the end of the Scripps pier, approximately 12 km N of the *IWAVES* study site. Approximately 66% of the cross-shore wind variance was contained in the diurnal frequency band.

Only the lower half of the water column was sampled here. The currents were nearly linearly polarized in the long-isobath direction (Fig. 10c). Further, they were bottom-intensified, with the near-bottom, long-isobath currents being approximately twice the amplitude of those at mid-column.

Time series of the mode one, semi-diurnal cEOFs at each mooring of the 1996 *IWAVE* experiment (Figs. 11) revealed a reasonable correspondence between semi-diurnal currents on the shelf (15 to 70 m). A puzzle was the burst of semi-diurnal variability at the 30 m moor-

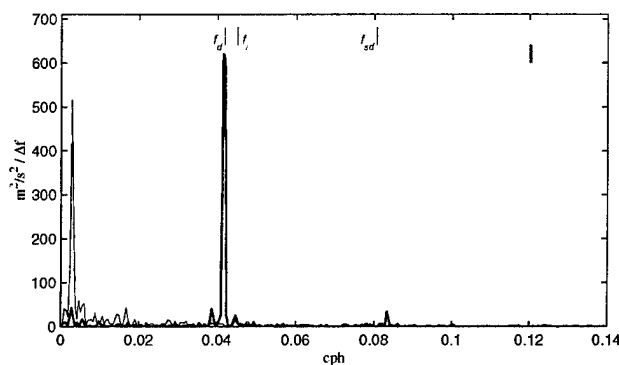


Figure 13. Power spectra of the cross-shore (bold) and long-shore (thin) winds at the Scripps pier (Fig. 1, approximately 12 km north of the *IWAVES* study site) during the summer months of 1996. Vertical lines indicate the diurnal, inertial and semi-diurnal frequencies. The separation between the two vertical lines in the upper-right corner indicates the spectral resolution of the spectra.

ing at the end of June that was not obviously apparent at the moorings further offshore. Shelf variability was generally low through most of July and increased significantly by the end of the month. Thereafter, several pulses with durations of approximately 10 to 15 days passed through. However, correlation with the fortnightly cycle of the surface tide was not obvious. Further, there was not an obvious correlation between the shelf variability and the low frequency changes in the temperature difference between the upper and lower water column (used as a proxy for stratification) at the 70 m mooring. Variability at the 100 m mooring was weaker than and not obviously correlated with that on the shelf. Variability at the 350 m mooring (bottom depths) remained high throughout the summer. Correspondence between the semi-diurnal variability here and the fortnightly beating of the semi-diurnal surface tide was comparatively higher than that on the shelf.

The energy in the mode one cEOF diurnal currents (Fig. 12) on the shelf had a similar temporal modulation as the semi-diurnal energy. Currents were weak at the beginning to mid-July, picked up at the end of July and remained high through August. Packets of diurnal variability also had a temporal width of 10 to 15 days. Correspondence between these currents and the diurnal, surface tide was weak. There was also no obvious correlation between diurnal currents and the strength of the diurnal, cross-shore winds measured at the Scripps pier (Fig. 1). However, the variance in the winds were modulated on a similar slow time-scale as the diurnal currents (10 to 15 days), and the spectrum of the cross-shore winds revealed a very sharp peak at the diurnal frequency (Fig. 13).

During periods of energetic, tidal band motions, the difference in the structure of diurnal and semi-diurnal currents was dramatic, and was clearly seen in the band-passed time series (Fig. 14), without the aid of statistical decompositions like cEOFs.

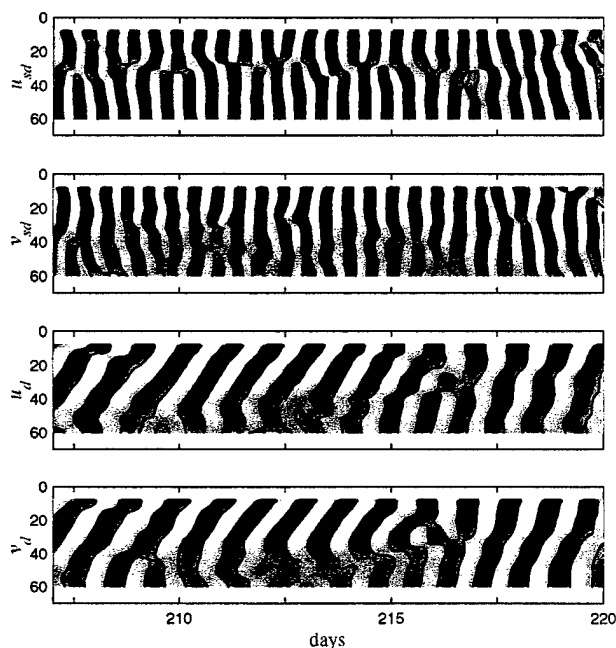


Figure 14. Thirteen day time series of semi-diurnal (*sd*) and diurnal (*d*) band-passed long- and cross-isobath currents (*u* and *v*) at the 70 m mooring of the 1996 IWAVES experiment. Zero current values are contoured. The maximum amplitude of the currents over this time range was 12 cm/s for both frequency bands. The time scale is the same as used in Figures 11 and 12.

Discussion

Semi-diurnal variability

Semi-diurnal variability on continental shelves is often dominated by a low-mode baroclinic structure (Baines, 1986; Rosenfeld, 1990; Braktovich, 1985; Denbo and Allen, 1984; Sherwin, 1988; and Gordon, 1979). Rosenfeld (1990) showed that semi-diurnal currents on the northern California shelf, at the CODE experiment site, had a structure similar to mode one, flat bottom waves (single minimum near the middle of the water column, and 180° phase shift between upper and lower currents) during periods of elevated tidal energy. The phase relationship between cross-shore currents and temperature revealed that the waves were propagating on-shore. Currents were generally elliptical in both the upper and lower water column, possibly with the upper-column ellipses being more circular than the lower-column el-

lipses. Braktovich (1985), who conducted tidal current studies on the shelf off of Del Mar, California (Fig. 1, approximately 25 km north of our study site), revealed a dominant, summer-time, semi-diurnal structure that was similar to mode one internal waves in the cross-isobath direction, with the lower currents enhanced relative to the near-surface currents. Long-isobath currents were uniform in amplitude with depth, and were as energetic as bottom, cross-isobath currents. Relative phases between the two horizontal current components were not determined. At a water depth of 15 m, bottom, cross-shore currents and temperature fluctuations were 90° out of phase with respect to each other at the semi-diurnal frequency, consistent with standing waves (Winant and Braktovich, 1981). Denbo and Allen (1984) distinguished between clockwise and counter-clockwise rotating semi-diurnal coherent structures using data obtained on the Oregon continental shelf. The clockwise rotating structure was mode one-like, and propagated onshore, while the counter-clockwise amplitude and phase were nearly depth independent and weaker than the clockwise amplitude at all depths.

The semi-diurnal cEOFs described above had similarities to each other and to those observed at the IWAVES site, particularly in their cross-shore structure. However, details were different. In particular, the purely cross-isobath, linear polarization in the bottom half of the water column observed here was not observed in the other studies. This structure is a puzzle. It is not consistent with flat bottom internal waves, for which the ellipticity is independent of depth. Nor is it consistent with cross-shore, progressive waves in which there is no long-shore dependence (e.g., Wunsch, 1969). In that case, the ellipticity would also be independent of depth. It seems unlikely that the semi-diurnal motions were the result of a phase-locked, superposition of internal tide and surface tide currents, as assumed by Denbo and Allen 1984. Barotropic currents were much less energetic than the baroclinic currents and appeared to play an insignificant role in tidal band motions. For example, at the 1996, 70 m mooring, the variance of the depth-averaged, long- and cross-isobath, tidal band currents was a factor of 0.18 smaller than the depth-averaged variance of the residual tidal band currents. An argument against the relative unimportance of barotropic motions is that the barotropic and baroclinic tides might conspire to, at times, destructively interfere (end of June to mid-July, 1996, Fig. 11), wiping out the semi-diurnal current signal across the water column, and at other times constructively interfere (end of July through August, 1996, Fig. 11) to produce the energetic packets observed on the shelf.

It is likely that the semidiurnal currents have strong long-shore dependence. The bathymetry varied in the

long-coast direction on length scales comparable to internal-tide, horizontal wavelengths (~ 10 km). Prominent topographic features (e.g., the shallow bank to the southwest of the *IWAVES* study site, Fig. 1) may have acted as local generation sites of internal waves, and our study site may be in the near-field of this generation. Studies of the long- and cross-isobath phase propagation and energy fluxes of the semi-diurnal motions are presently being conducted.

Diurnal variability

Surface enhanced, upward phase propagating (downward energy propagation), near inertial motions are prominent in many regions of the ocean, even continental shelves (Baines, 1986 and Denbo and Allen, 1984). Variability in the near-inertial band is typically at a frequency about 8% higher than f_i (Baines, 1986), and are presumed to be driven by winds. Denbo and Allen (1984) observed an upward phase speed of 1.4 mm/s for these waves on the Oregon shelf ($f_i = 0.059$ cph). They also observed a small peak (compared to the inertial and semi-diurnal peaks) at diurnal frequencies. The currents within this band were clockwise, circularly polarized, and were strong in the upper 15 m of the water column and weak below (water depth = 100 m). There was no apparent vertical phase propagation. These motions were coherent with the wind stress measured at the mooring site and were interpreted as near-surface, wind-driven motions, with weak, rectilinear, compensating, cross-shelf transport below. At our study site, a prominent peak at the diurnal frequency was observed, and was clearly distinguished from the nearby, but slightly higher, inertial frequency. These motions were observed at all locations on the slope and shelf. The currents were clockwise, circularly polarized and had an upward phase speed of 0.45 mm/s. Therefore, diurnal energy was propagating down from the surface, and its source was probably at the surface. A possible surface source for these motions was the cross-shelf wind stress, which had a very prominent diurnal sea-breeze peak (Fig. 13). Correlation between the modulation of cross-shelf wind variance observed at Scripps pier and the modulation of diurnal motions at the 70 m mooring was not apparent. However, the sea-breeze observed at Scripps pier did have a comparable time scale in the modulation of its intensity (10 to 15 days) to that of the diurnal current motions. Further, the winds at Scripps pier may not be representative of the winds directly at the *IWAVES* study site.

An interesting feature of the diurnal peaks in the ro-

tary spectra were their broad shoulders. These shoulders were not present in either the surface tide nor the wind spectra. The proximity of f_d to f_i may cause the diurnal motions to have a high Q and be nearly resonantly driven. Local, slowly varying currents may act to Doppler-shift the diurnal motions from the frequency at which they were forced and, thus, cause the broad shoulders. The downward phase propagation, however, is a puzzle. These sub-inertial, evanescent motions should not propagate. It is possible that the relative vorticity associated with background currents shifted the apparent inertial frequency "felt" by the waves to low enough values to make the diurnal frequency "super-inertial". Changes in relative vorticity could therefore act as a switch for the diurnal waves. Investigations into these possibilities are being conducted at present.

Acknowledgments. This work was sponsored by the Office of Naval Research (grant number N00014-96-1-0031).

References

- Baines, P. G. 1986: Internal tides, internal waves and near-inertial motions, in *Baroclinic Processes on Continental Shelves*, *Coastal Estuarine Sci.*, vol. 3, edited by C. N. K. Mooers, pp. 19-31, AGU, Washington, D.C.
- Bratkovich, A. 1985: Aspects of the tidal variability on the southern California shelf, *J. Phys. Oceanogr.*, 15, 225-239.
- Denbo, D. W. and J. S. Allen. 1984: Rotary empirical orthogonal function analysis of currents near the Oregon coast, *J. Phys. Oceanogr.*, 14, 35-46.
- Gordon, R. L. 1978: Internal wave climate near the coast of northwest Africa during JOINT-1, *Deep-Sea Res.*, 25, 625-643.
- Gordon, R. L. 1979: Tidal interactions in a region of large bottom slope near northwest Africa during JOINT-1, *Deep-Sea Res.*, 26, 199-210.
- Rosenfeld, L. K. 1990: Baroclinic semidiurnal tidal currents over the continental shelf off northern California, *J. Geophys. Res.*, 95, 22,153-22,172.
- Sherwin, T. J. 1988: Analysis of an internal tide observed on the Malin Shelf, north of Ireland, *J. Phys. Oceanogr.*, 18, 1035-1050.
- Wallace, J. M. and R. E. Dickinson. 1972: Empirical orthogonal representation of time series in the frequency domain, *J. App. Met.*, 11, 887-900.
- Winant, C. D., and A. W. Bratkovich. 1981: Temperature and currents on the southern California shelf: A description of the variability, *J. Phys. Oceanogr.*, 11, 71-86.
- Wunsch, C. 1969: Progressive internal waves on slopes, *J. Fluid Mech.*, 35, 131-144.

Internal Wave Energetics at a Seamount on the California Continental Borderland

Robert Pinkel

Marine Physical Laboratory, Scripps Institution of Oceanography, University of San Diego, La Jolla, CA 92093

Matthew Alford

Applied Physics Laboratory, University of Washington, 1013 N.E. 40th Street, Seattle, WA 98105

Abstract. In an effort to document the cascade of energy from large scales to dissipative scales, an intensive density profiling program (0-760 m every 4 minutes) was conducted from the Research Platform FLIP. Data were collected over a 25-day period during August and September 1998, as FLIP was moored near the crest (800 m water depth) of a seamount at the western edge of the California borderland, "overlooking" the deep sea. At this site, internal wave energy levels are a factor of three greater than typical open ocean values. The semi-diurnal internal tide is particularly energetic, with crest to trough amplitudes approaching 70 m and a pronounced fortnightly variation. The variance of vertical velocity, strain and effective strain rate shows weak ($\pm 10\%$) fortnightly variation. Modulation on semi-diurnal and diurnal time scales can also be detected. Vertical wavenumber spectra of these quantities fluctuate by a factor of ten at low wavenumbers (< 0.03 cpm) during a 12.5 day period. At wavenumbers greater than 0.1 cpm the variability is considerably reduced, to at most a factor of three, suggesting that some form of saturation process is active. Spectral levels tend to rise and fall in unison across the wavenumber band. The cross-band cascade of distinct energetic events is not detected.

Introduction

The dominant processes that drive ocean flows are associated with length scales of kilometers or greater. Microscale (cm and less) turbulence ultimately dissipates this energy. The sequence (or sequences) by which energy "cascades" from large to small spatial scales is poorly understood. Observations which span a broad range of space-time scales are necessary to identify the principal phenomena involved.

Here we report on a series of density and velocity measurements obtained at an energetic mixing site. Data were obtained from a Doppler sonar and profiling CTD operated from the Research Platform FLIP while the platform was tri-moored on top of a seamount. Internal wave energy levels are a factor of three greater than deep-sea canonical values. Large scale (> 2 m) overturns are frequently observed.

Following Alford and Pinkel (2000, in press), Alford and Pinkel (1999, this volume), the long-term objectives are to identify the waves that break, and, working up the cascade, to identify the energy sources for these waves. In this paper we explore the possibility of tracking wave energy fluctuations in the depth-time and vertical

wavenumber-time domains. The goal is to detect space-time or wavenumber-time variations in wave energy that correlate with observed breaking.

At large scales, the detection of energy modulation has proven difficult. The characteristic spin-down time of the internal wavefield is of order 50-100 days (e.g., Munk 1981). A 1-2% daily fluctuation in wavefield energy cannot be detected against the statistical noise intrinsic to most point-sampling measurements. The hope is to concentrate on the fine-scale end of the energy cascade. Here, standing wave energy levels are a small fraction of the wavefield total. However, the full cross-scale flux of energy must travel through this spectral region on its way to dissipation scales. Short-term fluctuations in fine-scale energy density might be relatively more robust than at larger, more energetic scales.

There are a number of scenarios concerning the functioning of the cascade process. McComas and Bretherton (1977) and McComas and Müller (1981) have identified the dominant weak-resonant interactions in a continuous spectral wavefield. Of these, the so-called induced diffusion interaction is most cascade-like. Here an energetic small-scale, high-frequency wave interacts with a large-scale low-frequency partner to transfer energy to less en-

ergetic, still smaller, scales. The interaction time associated with this mechanism is a function of overall wave-field energy level. For levels typical of the open ocean, the interaction time is so short that the assumption of a weak interaction is not justified.

In an attempt to deal with stronger interactions, Broutman (1984) and Broutman and Young (1986) consider a small-scale wave in the "propagating background" established by a single large-scale near-inertial wave. If the vertical component of group velocity of the small-scale packet roughly equals the phase velocity of the near inertial background, a strong interaction results.

Recently, Bruhwiler and Kaper (1995) have revisited this model in a numerical simulation. They consider a random field of small-scale waves interacting with a single near inertial "background" wave. They note a net tendency of the test waves to shift to higher frequencies and larger vertical scales in the course of the interaction.

Using eikonal methods, Henyey *et al.* (1986) studied the evolution of an ensemble of small-scale "test waves" as they propagate through a continuous spectral background. The test waves experience sometimes violent evolution, with vertical wavenumbers changing by factors of two in less than a wave period. The test waves are declared to be "self-unstable" if vertical wavelengths drop below 5 m. At this point, the test-waves have typically increased in intrinsic frequency. Sun and Kunze (1999) have re-examined the Henyey *et al.* approach, finding that interaction rates are altered if the vertical divergence, $\partial w / \partial z$, of the background is considered in addition to the shear. The essential scenario is unchanged.

In the Bruhwiler and Kaper (1995) study, individual wave packets also experience rapid evolution of vertical wavenumber and frequency. While eventually being scattered to a larger vertical scale, the test waves can experience significant short term decreases in scale (their Fig 1c). Were these waves to break at this point, the qualitative picture would not be that different than Henyey *et al.* (1986).

We are challenged to establish the relevance of these models to the ocean thermocline. What does a wave, whose wavelength is decreasing by a factor of two in less than a period, actually look like in physical space? Does breaking and turbulence follow this rapid evolution?

In an attempt to identify the mechanisms responsible for cross scale energy transfer, the September 1999 ARL experiment was planned and executed. While results are still in a preliminary state, it is appropriate to present initial findings at this point. The experiment is described briefly below, followed by a presentation of initial results.

The ARL 99 Experiment

The experiment was located on a seamount in the outer continental borderland off southern California (Figure 1). From a minimum depth 600 m below the surface the ter-

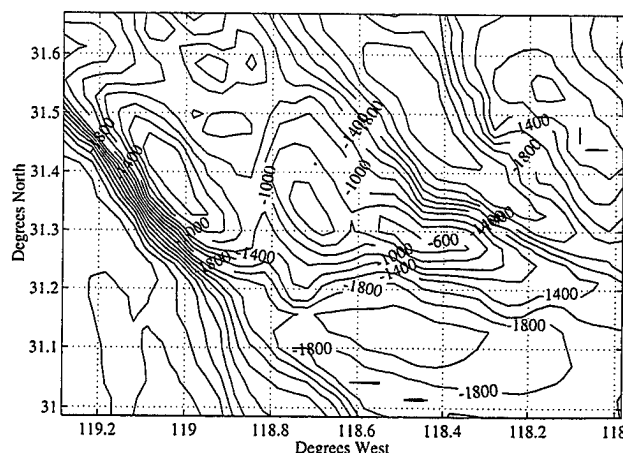


Figure 1. The topography of the ARL 98 site. FLIP was trimmed in 790 m water on the gently sloping north flank of a seamount that crests at 600 m. The Patton Escarpment is to the west. The upper region of the Escarpment swings eastward south of 31.2°N forming a broad south-facing wall.

rain fell to the depths of 2000 m to the south, and to 4000 m moving westward over the Patton Escarpment.

The "southern exposure" of the site is potentially important for tidal scattering. Barotropic M_2 tidal currents flow primarily parallel to the Patton Escarpment (north-west-southeast) in this region. Cross-isobath currents, necessary for baroclinic wave generation, can be driven on the north and south faces of topography. Strong baroclinic tidal activity is thus expected at the site.

Located high on a "cliff" overlooking the deep sea, the site is also ideal for viewing open ocean internal waves as they propagate onto the continental borderland. Waves that propagate at a vertical angle shallower than the slope of the Escarpment will be reflected back to the deep sea. Waves that propagate at a vertical angle steeper than the topographic slope can propagate shoreward. As the water depth decreases, the energy density of these waves should grow correspondingly.

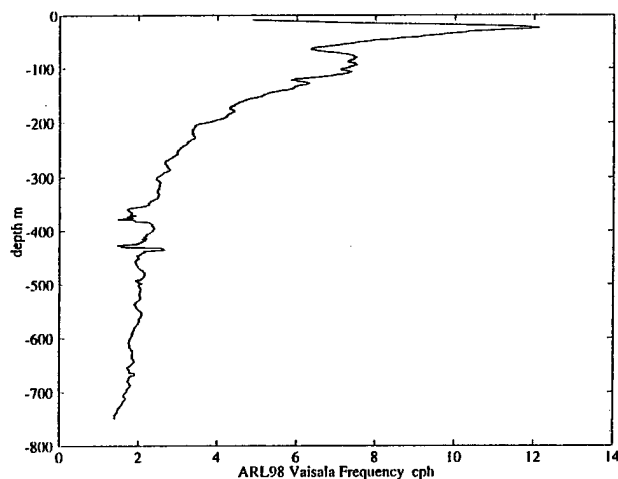
The vertical angle of propagation of a wave is determined by its frequency relative to the local inertial and buoyancy frequencies. For the escarpment, which has maximum slopes of order 0.2, waves of frequency greater than $\sigma = 0.8$ cph¹ can propagate forward up onto the shelf. At the top of the Escarpment one might expect five times the deep-sea energy density (given the five-to-one ratio of water depth). Is this seen?

We would like, of course, to examine the relevance of the various cascade mechanisms. These mechanisms require a spatially homogeneous region of ocean of sufficient extent that the proposed interactions can take place. The ARL site is marginal, at best, in this respect. If established relationships between fine-scale shear and ob-

¹ A buoyancy frequency of 2 cph in the deep sea is assumed.

served dissipation (Gregg, 1989) hold at the ARL site as well as in the deep sea, one might suspect that the underlying mechanisms that regulate the transfer energy down the cascade are quite primal and are not sensitive to the finer aspects of any particular theory.

The Väisälä (buoyancy) frequency profile, $N(z)$, is given in Figure 2. The shallow mixed layer (~30 m) and 12 cph peak value reflect late summer conditions off Southern California. The Väisälä frequency decreases irregularly to ~2 cph at 350 m. Subsequently, it remains roughly constant to 700 m, decreasing slightly below as the top of the seamount is approached.



Observations

Two primary sensing systems, a Doppler sonar and a profiling CTD, collected the principal data. The sonar was mounted at a depth of 87 m, looking downward. It profiled to depths of 400 m, with 3 m depth resolution and 2 min temporal resolution. These data are in a preliminary state of analysis and will not be discussed here.

Seabird SBE911 CTDs profiled from the surface to 760 m at 4-min intervals during ARL. Two profiling systems, operating synchronously at a drop rate of 3.5 ms^{-1} , were required to cover this aperture. Depth resolution is approximately 1.3 m for density measurements. Of the 25-day overall CTD time series, a 12.5-day portion is presently edited and suitable for analysis.

A summary of internal wavefield vertical displacement over this period is presented in Figure 3. The series starts at the peak of the spring tide, with 70 m crest to trough tidal excursions seen in the 600-700 m depth range. The tidal motion is coherent and in phase over the entire water column. In a region where ray-like propagation might be expected, the tide is surprisingly mode-like. As the tide

Figure 2. The Väisälä frequency profile for the site. The profile represents a 12.5 day average formed in an isopycnal following frame, so as to minimize the smoothing associated with Eulerian averages of vertically advected fields.

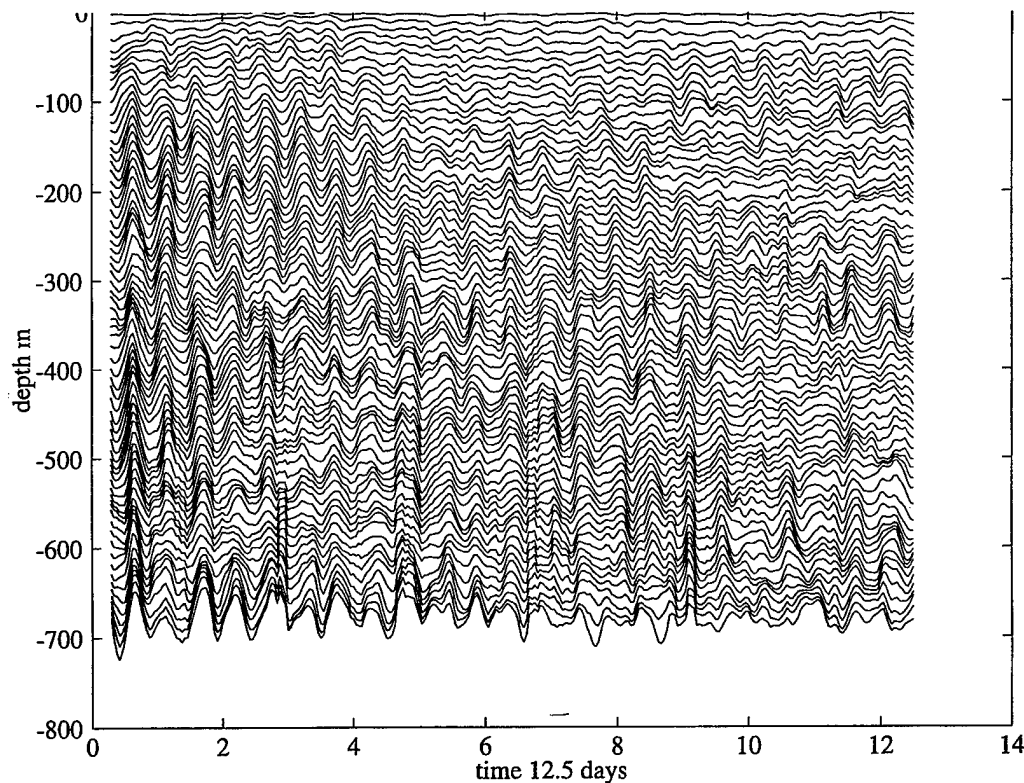


Figure 3. Depth-time fluctuation of isopycnal surfaces during ARL. Isopycnals are spaced at 10-m intervals in depth, on average, and are smoothed by 3 hours in time. Tidal excursions exceeding 50 m amplitude, crest to trough, are seen early in the record. There is some indication that the tidal phase shifts with depth above 150 m.

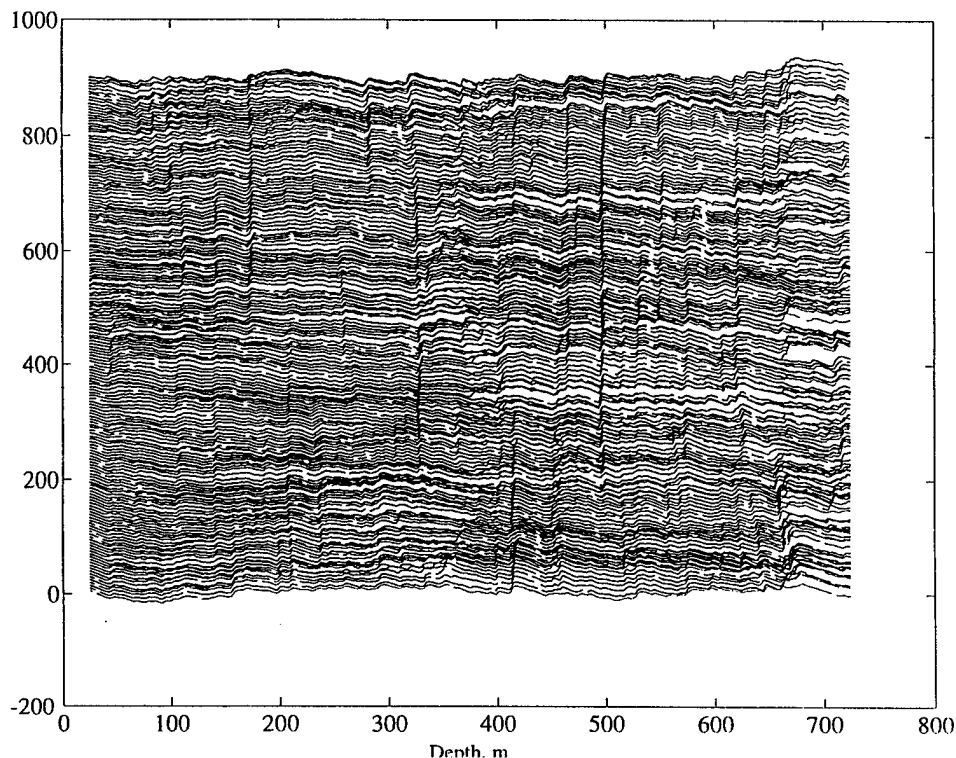


Figure 4. Closeup of a 12.5-hour section of isopycnal displacement data. Displacement is given on the abscissa, with the ordinate indicating the mean depth of the isopycnal. Successive profiles are plotted from left to right, offset by 5 m

diminishes midway through the record, the “background wavefield” reveals a greater variability with depth, a broader effective bandwidth in the vertical wavenumber domain. With the approach of the next spring tide, low mode motions again begin to dominate.

The three-hour smoothing of Figure 3 admits little indication of the finer scales of motion. In Figure 4, a 12-hour closeup is presented. Isopycnal vertical displacement is given in a semi-Lagrangian format. The ordinate is the isopycnal whose (12.5 day) mean depth is at the given value. Vertical displacement is indicated by the lateral position of the vertical lines, with one line representing each 4-min profile. Successive profiles are offset to the right. High-frequency, long vertical wavelength motions are seen as the vertical dark and light bands,

which indicate large-scale changes in vertical displacement from one profile to the next. Layers of (near) constant density water appear as the lateral steps in the record. These can persist for many hours and propagate slowly across isopycnals (vertically, here).

Of particular interest are the regions of rapid vertical and temporal variation. For example, consider the region between 350 and 400 m, midway through the record. *Alford and Pinkel* (1999, this volume) have suggested that this variability is associated with small-scale waves and that these are the waves that subsequently break. The challenge is to determine the energy source for these waves and to compare their evolution to the “test waves” of the various theoretical models.

It is attractive to follow the evolution of the low-

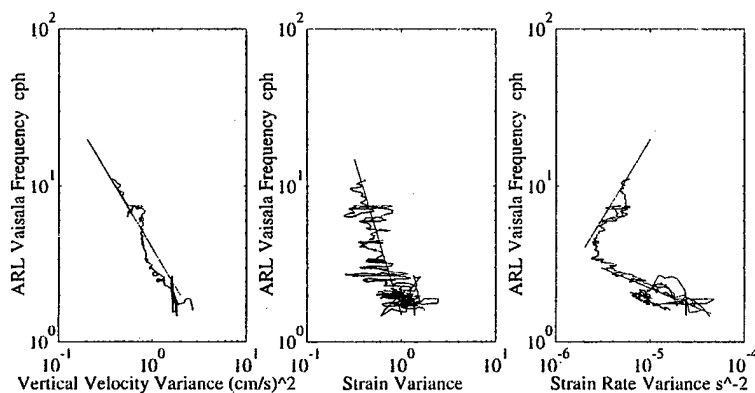


Figure 5. Plots of vertical velocity variance (left), strain variance (center) and strain rate variance (right) as a function of the average Väisälä frequency. Reference lines of N^{-1} and $N^{-1/2}$ are drawn for velocity and strain; N^1 and a N^{-4} line are drawn for strain rate. Increases in strain and strain rate with increasing depth are not seen in the deep sea. A near-bottom source for these fine-scale motions is suggested.

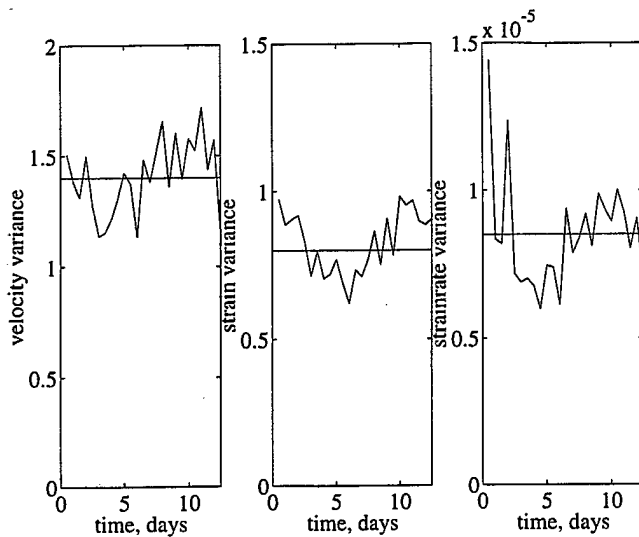


Figure 6. The variance of vertical velocity, strain and strain rate for the 12.5 day record. Averages are taken over the depth region 30-720 m.

frequency small-scale, high-frequency small-scale, and high-frequency large scale fields separately. These can be represented by the finite difference strain, $\gamma_{ij}(t) = (\eta_i - \eta_j) / (\eta_i - \eta_j)$, the effective strain rate, $\partial w / \partial z_{ij} = \gamma_{ij}^{-1} d\gamma_{ij} / dt$, and the vertical velocity, $w_i = d\eta_i / dt$, fields respectively.

In preparation for deterministic case studies, a number of statistical explorations are warranted. In Figure 5 the vertical dependencies of strain, strain rate, and vertical velocity variance are presented. The ordinate is the 12.5-day mean value of N averaged along the set of isopycnals involved in the calculation. Vertical velocity variance (left) is proportional to N^{-1} , consistent with WKB scaling. Strain variance is nearly constant for $N > 3$ cph, consistent with open-ocean experience. At depths greater than 250

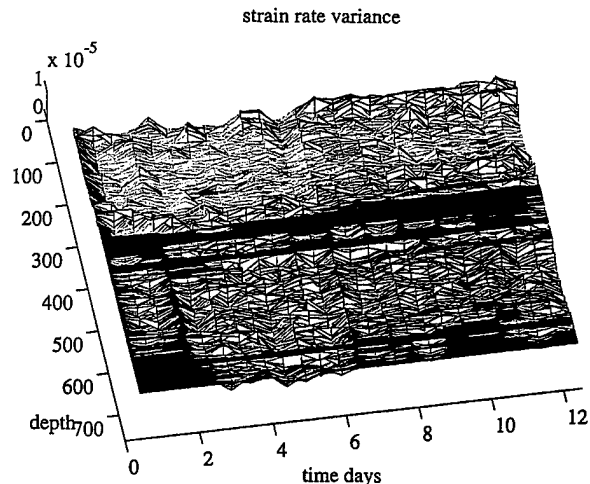
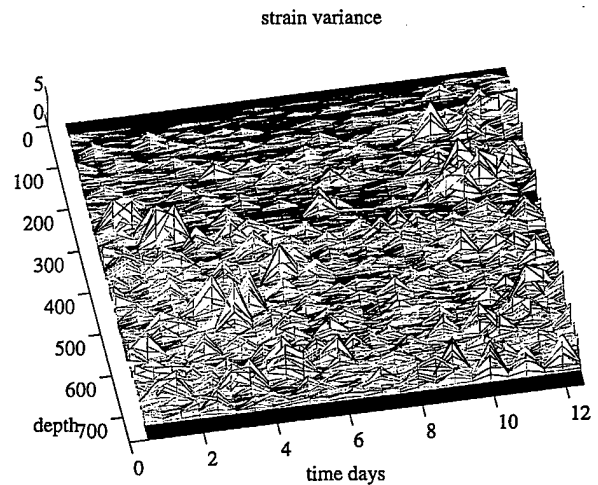
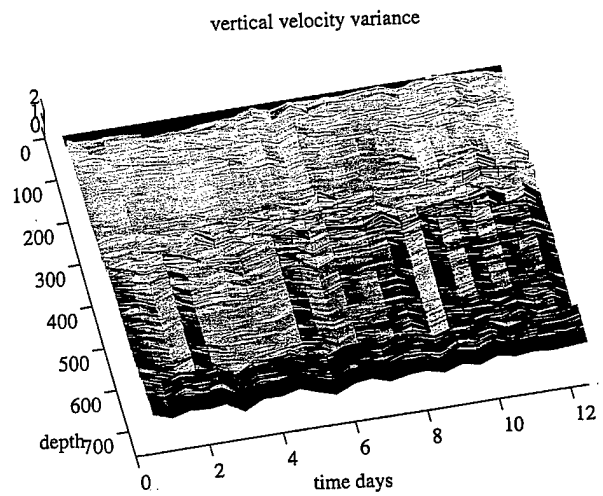


Figure 7. (top right) The variance of vertical velocity, $\text{cm}^2 \text{s}^{-2}$, as a function of depth and time. Variance is calculated with respect to a we-hour by 10-m mean. The depth range 300-400 m is highly irregular. At greater depth, there is significant vertical coherence to the variability of high-frequency, large-scale motion.

Figure 8. (center right) The variance of 2-m strain relative to a 12-hour by 10-m mean. The variability is generally largest early in the record, in the days following the spring tide.

Figure 9. (bottom right). The variance of effective strain rate, s^{-2} , as a function of depth and time. High variance region between 100 and 300 m and below 600 m, early on, are presented in black.

m, strain variance begins to increase. The variance of effective strain rate, $\partial w / \partial z$, right, decreases with depth as N^{+1} until N drops below 4 cph. At this point variance starts to increase, with a N^{-4} dependence at the bottom of the record. The strain rate, which is most sensitive to the high-frequency high-wavenumber portion of the wavefield, shows the greatest departure from open-ocean behavior.

In Figure 6, the time variability of wavefield variance is examined. Averages of vertical velocity, strain and strain rate variance over 30-720 m are presented for successive 12 hour time periods. All records show a modulation of $\pm 10\%$ at a period of 10-15 days. The phase of the vertical velocity modulation tends to lead that of strain and strain rate by several days. In this full-ocean-depth average, contributions from great depth dominate the velocity and strain rate records. The strain average is more uniformly weighted in depth. It will be interesting to see if the apparent fortnightly periodicity is maintained as the full 25 day CTD record becomes available.

Joint depth-time variability can be examined in detail, at the expense of statistical confidence. In Figures 7, 8 and 9, maps of 12-hour velocity, strain and strain rate variance are presented. The variance of vertical velocity (Figure 7) exhibits a large vertical correlation scale. If one depth is undergoing rapid vertical variation over a 12 hour period, depths 200 m above and below probably are as well. Strain variance (Figure 8), in contrast, shows highly localized activity in both depth and time. High levels of activity are seen below 300 m early in the record and in the 100-300 m region at the end. Strain rate-variance (Figure 9) exhibits some degree of coherence with depth. Regions of greatest variability are near the surface and at depth. In addition, between 350-400 m, there is a band of variance greater than $1 \times 10^{-5} \text{ s}^{-2}$ which has been clipped in this figure.

One would like to investigate these fluctuations in the spectral domain, in an attempt to document the cross-scale cascade of energy. To maintain the sense of time evolution, we focus on time changes of vertical wavenumber spectra. These are calculated over 3 hour by 192 m domains. The spectrum of strain emphasizes the low-frequency, small-scale aspects of the wavefield; while the vertical velocity spectrum emphasizes the high-frequency, large scales; and the effective strain rate spectrum focuses on high frequency and small vertical scale. Spectra of all these quantities are formed over depth ranges 100-292 m, 300-492 m and 500-692 m. Here we present the intermediate depth range as representative of the ARL observations. Spectra of velocity, strain and strain rate are plotted in Figure 10.

Each spectrum represents the average of 45 periodograms, one from each 4 min CTD profile. Each is subsequently smoothed by two bands in wave number, formally yielding a 180 degree of freedom spectral estimate. In fact the effective number of degrees of freedom is much

less, as the successive profiles are far from independent. Strain profiles are most highly correlated in time, effective strain rate profiles are least highly correlated.

Velocity spectra generally exhibit a k^{-2} dependence at high wavenumbers. At low wavenumber, the energetic spectra maintain this slope while the lower energy realizations exhibit a decrease.

Strain spectra increase with increasing wavenumbers, to scales of 0.03 cpm (high energy), and to 0.05 cpm (low energy). Spectra decay at a slope in excess of k^{-1} for $k > 0.1$ cpm. Strain rate spectra have a similar behavior, increasing at slopes of order k^1 at low wavenumber and decreasing at k^{-1} slope at high. The spectral maximum shifts from 1/30 cpm for energetic spectra to 1/10 cpm for low variance estimates.

A striking aspect of all three spectra is the greater range of variability at low wavenumber/large scale vs. high wavenumber. The observation is reminiscent of Gregg's (1993) finding that vertical wavenumber spectra of $\langle S^2 \rangle / N^2$, taken from all over the world at a variety of energy levels, all seem to coalesce at 6 m vertical scale.

There are several interpretations possible. If smaller vertical scales are associated with higher temporal frequencies, the effective number of degrees of freedom will vary across the spectrum. From this perspective, the variability seen in Figure 10 might be purely statistical: there is understandably less variability in bands where the ensemble averaging is more effective.

The contrasting view is that the observed variability results from the modulation of the true process variance. This is seen at low wavenumbers, where spectral levels are not dynamically constrained. At higher wavenumbers the spectra are strongly "saturated", limited in magnitude by dynamical processes.

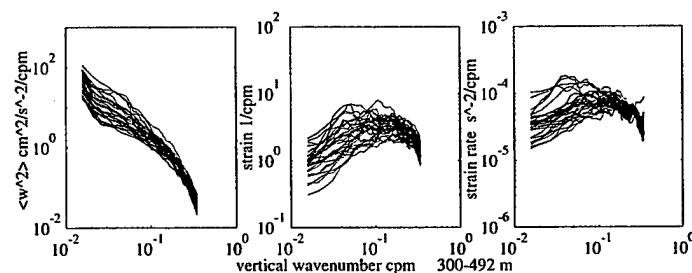


Figure 10. Vertical wavenumber spectra of vertical velocity (left), 2 m strain (center) and strain rate (right) for the depth interval 300-492 m. Spectra are averaged over 3 hr in time and plotted at 10 hour intervals. For all quantities, spectra exhibit a factor of 5-10 variability at low wavenumbers, a factor of 2-3 variability at high.

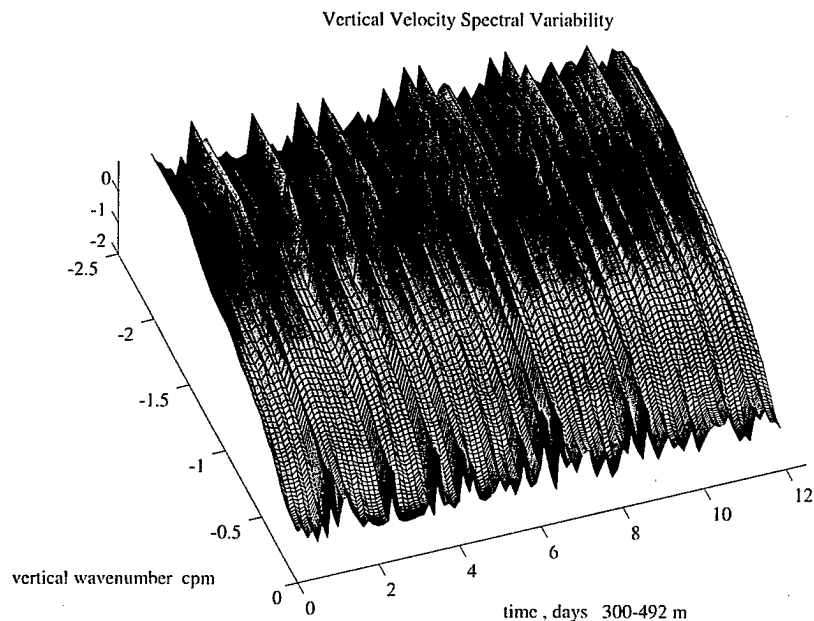
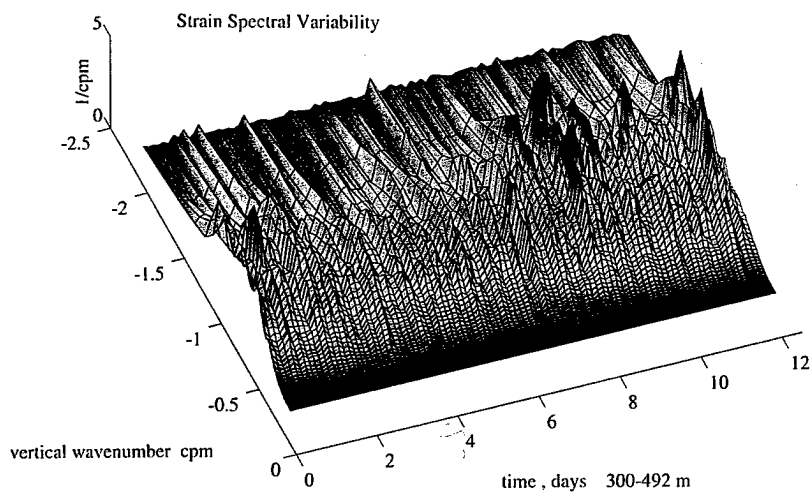
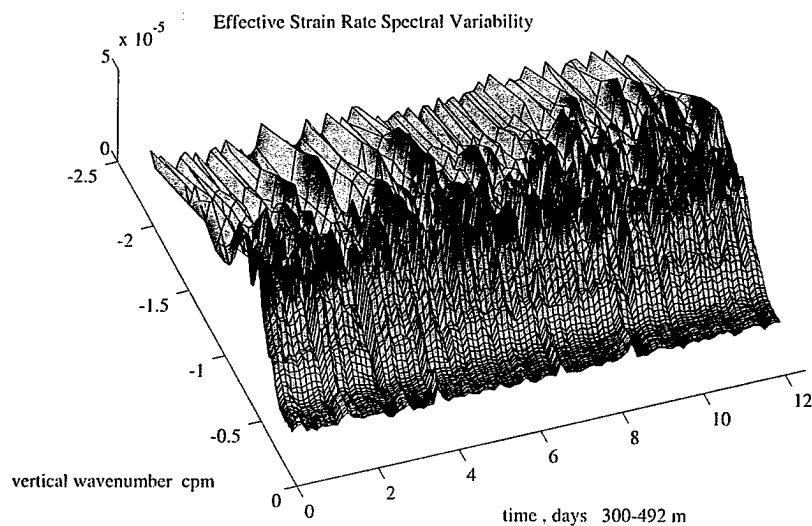


Figure 11. (top left) Time modulation of the vertical wavenumber spectrum of vertical velocity, $\text{cm}^2 \text{s}^{-2}/\text{cpm}$. Spectra are smoother over 3 hr in time and plotted on a linear scale as a function of $\log k$. temporal fluctuations extend across a broad range of wavenumbers, rendering it difficult to follow the "cascade" of an individual energetic event.

Figure 12. (center left) As in 11 for strain, $1/\text{cpm}$.

Figure 13. (bottom left) As in 11, for effective strain rate, s^{-2}/cpm .



Summary

During September 1998, the Research Platform FLIP was anchored at the crest of a seamount on the edge of the Patton Escarpment. Extended (25-day) records of density (0-760 m) and velocity (100-400 m) were obtained. Internal wave energy levels were roughly three times open ocean values. As anticipated, baroclinic tidal amplitudes were large, with crest to trough distances approaching 70 m during the spring tides. Surprisingly, the observed tidal variability appeared "mode like," with large vertical coherence scales, rather than ray-like, as might be expected near topography.

Using a 12.5-day record of isopycnal depth variability, the attempt was made to track cascade-like processes which transfer energy from large to small vertical scales. The variability of strain, vertical velocity, and the effective strain rate was monitored in depth and time. These quantities emphasize the low-frequency small-scale, high frequency large-scale and high frequency small-scale aspects of the overall wavefield.

Depth-time maps of the quantities exhibit considerable variability. Vertical velocity variance is most coherent in depth, variability in strain variance is least coherent. The specific spatial patterns the three fields are quite different. Depth-averaged plots of variance vs. time show a weak ($\pm 10\%$) modulation of a 10-15 day period for all fields (as best determined from a single 12.5-day record). Definitive documentation of this variability awaits analysis of the full data set.

Vertical wavenumber spectra calculated over the depth ranges 100-292 m, 300-492, and 500-692 m reveal few obvious signs of a cascade. Spectral levels fluctuate statistically but also reveal aspects of regular modulation on semi-diurnal and diurnal scales. The degree of fluctuation varies with wavenumber, with the smallest wavenumbers (largest scales) exhibiting the greatest variation. At wavenumbers greater than 1/10 cpm there is very little spectral variability. While the statistical variability in the spectral estimates is decreased at small scale, the observations are suggestive of spectral saturation. The overall variability in the strain spectrum is remarkably similar to the Aha Hulikoa model (for shear) offered by Müller *et al.* (1991).

Along with these classical findings comes the appreciation that with strain and strain-rate variation generally localized in space, variance fluctuations will be distributed broadly in wavenumber. Tracking the cascade of variance across the wavenumber domain will be difficult experimentally. Careful examination of phenomena in the depth-time domain might prove more fruitful.

Acknowledgments. The authors thank Eric Slater, Lloyd Green, Mike Goldin and Chris Neely for the design, construction and operation of the instrumentation used in the cruise. The support of Capt. Tom Golfinos and the crew of the RP FLIP is

much appreciated. This work was supported by the Office of Naval Research under grant N00014-96-1-0297.

References

- Alford, M. A., and R. Pinkel, 2000. The context of ocean mixing, *J. Phys. Oceanogr.*, in press.
- Broutman, D., 1984. The focusing of short internal waves by an internal wave, *Astrophys. Fluid Dyn.*, 30, 199-225.
- Bruhwiller, D., and T. J. Kaper, 1995. Wavenumber transport: scattering of small-scale internal waves by large-scale wave packets, *J. Fluid Mech.*, 289, 379-405.
- Broutman, D. and W. R. Young, 1986. On the interaction of small-scale oceanic internal waves with near-inertial waves, *J. Fluid. Mech.*, 166, 341-358.
- Gregg, M., D. Winkel and T. Sanford, 1993. Varieties of fully resolved spectra of turbulent shear, *J. Phys. Oceanogr.*, 23, 124-141.
- Gregg, M., 1989. Scaling turbulent dissipation in the thermocline, *J. Geophys. Res.*, 94, 9686-9698.
- Heney, F. S., J. Wright and S. M. Flatté, 1986. Energy and action flow through the internal wavefield, *J. Geophys. Res.*, 91, 8487-8495.
- McComas, H., and F. P. Bretherton, 1977. Resonant interaction of oceanic internal waves, *J. Geophys. Res.*, 83, 1397-1412.
- McComas, H. and P. Muller, 1981. Time scales of resonant interactions among oceanic internal waves, *J. Phys. Oceanogr.*, 11, 139-147.
- Müller, P., E. A. d'Asaro and G. Holloway, 1991. Internal gravity waves and mixing, in *Dynamics of Oceanic Internal Gravity Waves: Proceedings of the Aha Hulikoa Hawaiian Winter Workshop*, edited by P. Müller and D. Henderson, pp. 499-508, School of Ocean and Earth Science and Technology, University of Hawaii, Honolulu.
- Munk, W. H., 1981. Internal waves and small scale processes, in *Evolution of Physical Oceanography*, edited by B. A. Warren and C. Wunsch, pp 264-291, MIT Press, Cambridge, MA.
- Pinkel, R., 1975. Upper-ocean internal wave observations from FLIP. *J. Geophys. Res.*, 80, 3892-3910.
- Sherman, J. T., and R. Pinkel, 1991. Estimates of the vertical wavenumber-frequency spectra of vertical shear and strain, *J. Phys. Oceanogr.*, 21, 292-303.
- Sun, H., and E. Kunze, 1999. Internal wave/wave interactions: Part 1. The role of internal wave vertical divergence, *J. Phys. Oceanogr.*, 11, 139-147.

Internal Wave Measurements in Mamala Bay Oahu, Hawaii

Patrick K. Sullivan and Dayananda Vithanage

Oceanit Laboratories, Inc. Honolulu, Hawaii

Abstract. Oceanit Laboratories, Inc. (Oceanit) investigated the influence of internal waves and their impacts on the performance of the municipal wastewater outfall in Mamala Bay, Oahu. Disposal of municipal wastewater through deep ocean outfalls is environmentally acceptable if there is adequate density stratification to keep the wastewater plume from surfacing. Trapped below the surface, the wastewater plume disperses and moves out of the disposal area without adversely impacting surface or coastal waters. However, density stratification variability causes undesirable environmental and public health impacts from wastewater plumes that reach the surface and move to the shore under onshore current and wind conditions. Two major wastewater outfalls discharge close to 100 million gallons per day (mgd) of primary treated wastewater into Mamala Bay on Oahu, Hawaii, through outfalls at depths of around 200 feet. In order to investigate density stratification variability and the effect on the wastewater plume from internal waves, Oceanit conducted current and temperature profile measurements close to the Sand Island outfall in Mamala Bay. Horizontal and vertical components of currents, as well as temperature profiles, were measured at one-minute intervals for a period of 12 months. An acoustic Doppler current profiler (ADCP) and an Applied Microsystems thermistor string were used for the measurements. Conductivity, temperature, and depth (CTD) profiles were measured monthly to supplement data. Current and temperature data were analyzed to investigate high frequency variability of parameters that impact wastewater dilution and dispersion. High-passed data were analyzed to identify high frequency variability and possible internal wave influence. Results showed increasing high-frequency energy in both current and temperature signals with increasing depth. Results also indicated the presence of variance peaks that were related to the semidiurnal tidal period. High-energy peaks were observed in the water column at a period of approximately 40 minutes.

Introduction

Domestic and industrial wastewater from communities is typically collected and treated before disposal into receiving waters such as lakes, rivers or the ocean. All wastewaters, regardless of treatment received, contain substances that pose potential pollution threats to the environment and risk to public health. Wastewater outfalls are designed to operate in about 100 to 200 feet of water. The most important component is the diffuser, which is a few thousand feet in length and directs wastewater flow through a series of holes spaced along the sides of the outfall pipe.

When wastewater enters the marine environment from the diffuser, it is buoyant and tends to rise. This effluent, initially travelling horizontally after leaving the holes in the diffuser, gradually ascends on a vertical path. Throughout this path, the effluent mixes with the ambient seawater by entrainment. The highly concentrated waste-

water becomes progressively more and more diluted with increasing distance from the outfall. This stage of mixing is called initial dilution, and it ceases when the mixed effluent stream reaches vertical equilibrium. In a homogeneous water column, the initial dilution phase ends when the plume reaches the water surface. In a stratified water column, the initial dilution phase ends when the plume reaches vertical equilibrium at some intermediate depth and levels out parallel to the surface.

Once the mixed effluent reaches the sea surface or an intermediate equilibrium depth, it tends to move with the prevailing currents. Further mixing and dilution from eddy diffusion continue at this stage while the plume moves with the ambient current field. The spread of effluent after initial dilution is known as secondary dispersion. The general path of an effluent plume emerging from a diffuser into stratified water is shown in Figure 1.

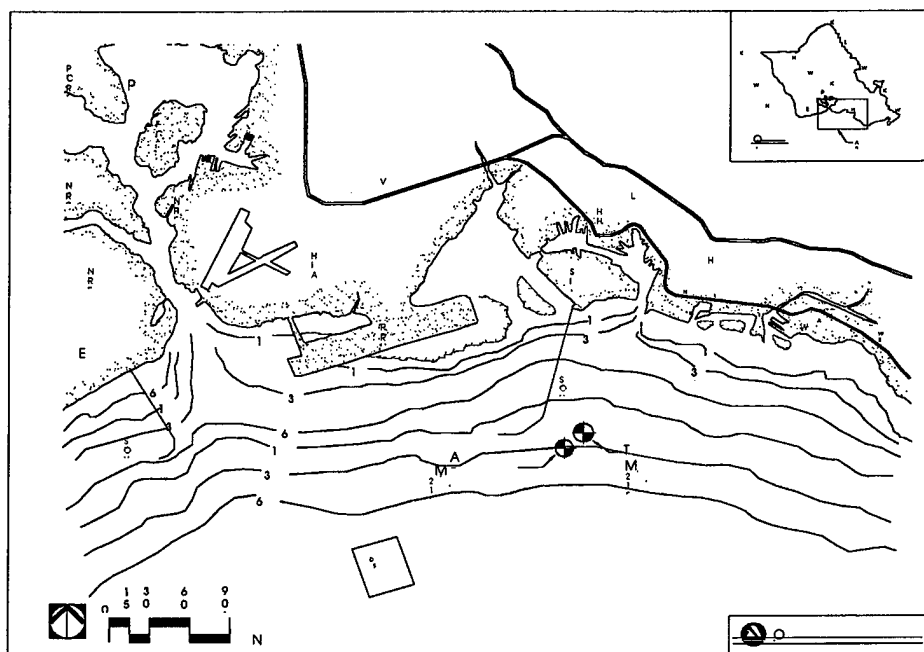
The Sand Island wastewater outfall discharges an average of 75 million gallons per day ($4.47 \text{ m}^3/\text{s}$) of primary

1. Mean flow is steady.
2. The fluid is incompressible and density is included only in the buoyant terms.
3. All other fluid properties are constant.
4. There is no frictional heating.
5. Pressure variations are purely hydrostatic.
6. Ambient turbulence effects are included in the entrainment function only.
7. Flow within the jets before merging is axisymmetric and is a free boundary layer flow type.

depth to measure current and temperature profiles at one-minute intervals. Subsurface buoys moored at a 50-foot depth supported the instrument strings. The velocity and temperature profiles extended from a 50-foot depth to the bottom.

High-frequency data acquisition created large amounts of data that easily exceeded memory and battery capacity, thereby requiring frequent in-field servicing. A cable was attached to the data loggers to enable monthly data downloading. Divers dove to the data logger and retrieved the free end of the data cable for downloading to a portable computer aboard a small boat. Batteries were

Figure 3. Location of instrument moorings relative to outfall.



The model used in this study was developed by the Environmental Protection Agency to calculate dilution and plume trapping depth for different environmental conditions. Results indicated that the probability of any event occurring depended on the sampling interval used for stratification measurements. In the past, only seasonal stratification measurements were taken. However, preliminary field data showed that density stratification occurs at a much higher frequency than earlier assumed. These high-frequency variations are induced by tides and are more energetic close to the bottom in Mamala Bay, indicating some relationship of internal waves with topography.

An experiment was designed to measure the current and temperature profiles close to the outfall diffuser to study the effect of sampling interval on calculated plume surfacing probability. An acoustic Doppler current profiler and a thermistor string were deployed at 200 feet

replaced at three-month intervals by removing the ADCP profiler from the mooring. The thermistor string provided limited data because of flooding. ADCP current profile data were collected for 18 months.

The location of the instrument moorings relative to the outfall is shown in Figure 3. The configurations of the two instrument strings are shown in Figures 4 and 5. Samples of temperature and velocity data are shown in Figure 6.

Data Analysis

Data collected during this effort were used as input into the initial dilution model described earlier. Results of modeling were used to investigate the dependence of the plume surfacing probability on the frequency of data sampling. The model was run at one-minute intervals;

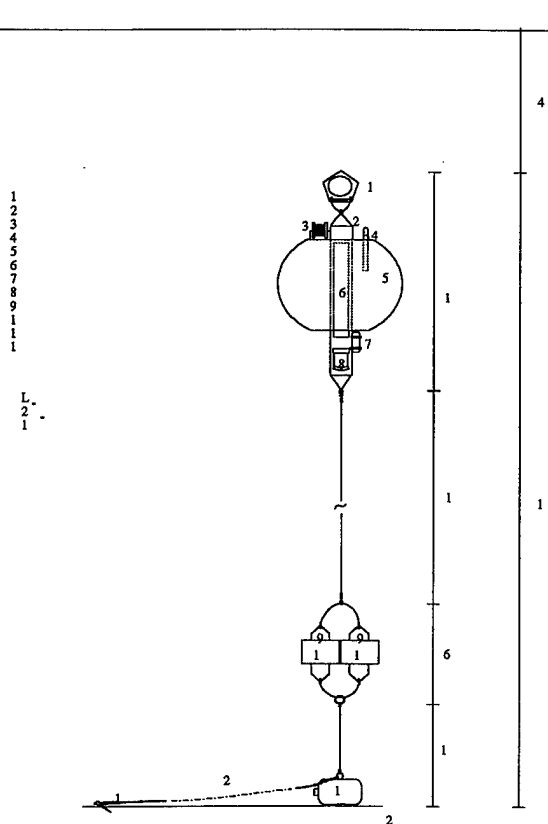


Figure 4. ADCP string mooring.

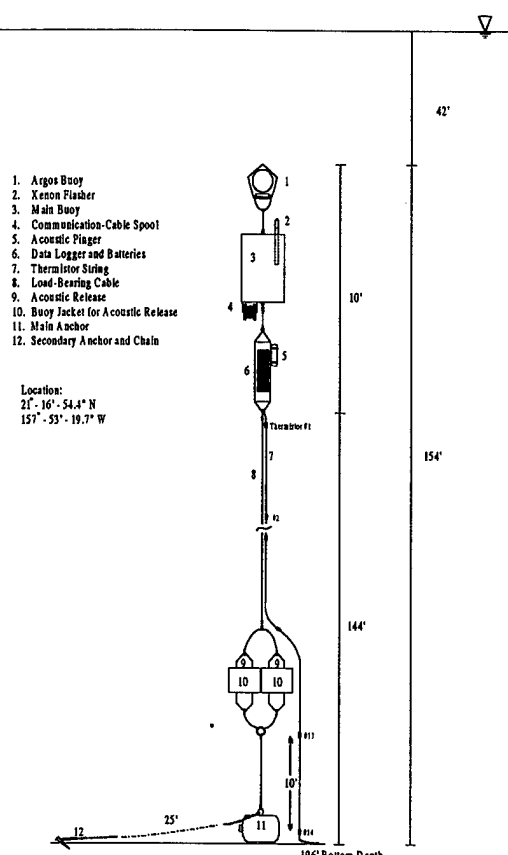


Figure 5. Thermistor string mooring.

results on dilution, plume dimensions, and plume trapping depth were stored for later analysis.

Each parameter (dilution and plume trapping depth) was sampled from the result file at different frequencies

to simulate different data sampling frequencies. Results were evaluated to determine the optimum data sampling frequency for an outfall design. An economic analysis was also made to evaluate cost benefit relations for each combination.

The optimum frequency for measuring receiving water data was found by weighting the cost of data collection with the accuracy of the predictions. Initially, seasonal or monthly stratification was used to determine design parameters for outfalls. In the present analysis, the optimum frequency for environmental data collection was found to be between 15 and 20 minutes.

In order to investigate underlying variations in receiving water parameters that contribute to relatively rapid changes in plume behavior, the data collected were further analyzed using conventional methods. The data set was divided into one-hour sub-samples and the variance of each segment was calculated. Results were plotted as an hourly variance time series as shown in Figure 7 for the month of September 1997.

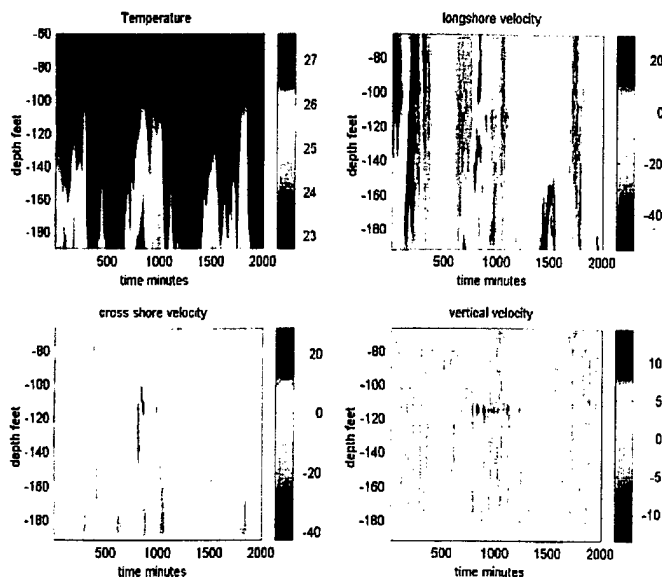


Figure 6. Samples of temperature and velocity data.

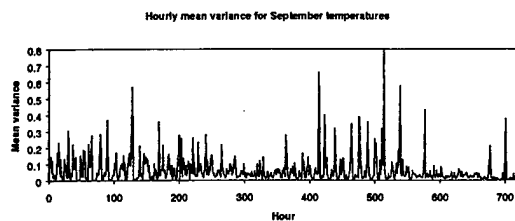


Figure 7. Depth averaged hourly temperature variance for September 1997.

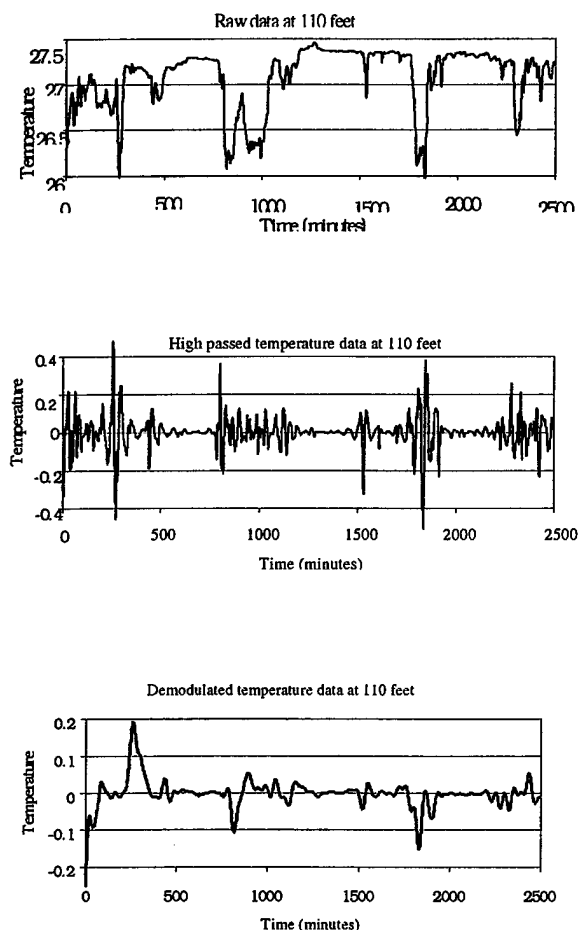


Figure 8. Typical temperature series of raw data, high-passed data, and demodulated high-pass data for temperature at 110 ft depth.

Data were high-passed with a Fourier filter with a cutoff at 60 minutes to filter out low frequency variations that dominated the raw data. A cosine taper was used at the cutoff to reduce data contamination. High-passed temperature data showed a weak periodicity at about 40 minutes. The signal was enhanced by demodulating data at this period. The original high-passed and demodulated, high passed data are shown in Figure 8.

Spectral density of high-passed data at different depths was calculated using a data segment length of 256 minutes. The spectral density distribution of high frequency temperature and velocity data for September 1997 are shown in Figure 9.

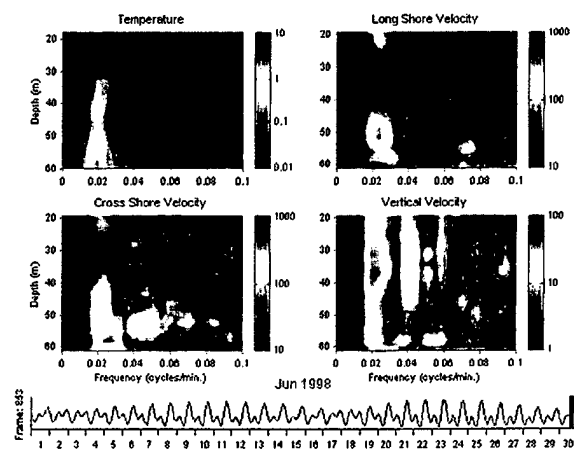


Figure 9. Spectral density of high-frequency temperature and velocity data.

References

- Davis, L. R., 1975. Analysis of multiple cell mechanical draft cooling towers. EPA-660/3-75-039. U.S. Environmental Protection Agency, Corvallis, OR. 39 pp.
- Hirst, E. A., 1971a. Analysis of buoyant jets within the zone of flow establishment. Rep. ORNL-TM-3470. U.S. Atomic Energy Commission, Oak Ridge National Lab., Oak Ridge, TN. 41 pp.
- Hirst, E. A., 1971b. Analysis of round, turbulent, buoyant jets discharged to flowing stratified ambients. Rep. ORNL-TM-4685. U.S. Atomic Energy Commission, Oak Ridge National Lab., Oak Ridge, TN. 37 pp.
- Kanneberg, L. D., and L. R. Davis, 1976. An experimental/analytical investigation of deep submerged multiple buoyant jets. EPA-600/3-76-101. U.S. Environmental Protection Agency, Corvallis, OR. 266 pp.

Mixing over Shelves and Slopes

M. C. Gregg, D. W. Winkel, J.A. MacKinnon, and R. C. Lien

Applied Physics Lab., University of Washington, 1013 NE 40th St., Seattle, WA 98105

Abstract. Recent observations of shear and mixing in the Florida Strait and over several continental shelves and slopes are summarized and compared with earlier observations in the open ocean. Three of the cases have average diapycnal diffusivities 10-100 times greater than background in the open ocean. The most intense mixing occurs in layers tens of meters thick having strong average stratification. In one case, the mixing is produced by the shear of a beam of the internal tide generated at the shelf break.

Introduction

Before shallow-water flows and stratification can be modeled realistically, the climatology of mixing over continental shelves and slopes must be established and the major mixing processes must be identified and parameterized. This sequence is being followed for the open ocean, where the diapycnal fluxes produced by breaking internal waves have been shown to follow theoretically derived parameterizations within a factor of two [Gregg, 1989; Polzin *et al.*, 1995]. Outside boundary layers and away from large average shears, salt fingers seem to be the only other process capable of producing fluxes of equal or greater magnitude.

The situation is not so simple in shallow water, owing to the large number of possible mixing processes. Tidal currents generate prominent bottom boundary layers and may increase shear at mid-depths. Strong barotropic tides flowing over shelf breaks can generate both beams of internal tide propagating into deeper water and solibores propagating back onto the shelf when the tide relaxes. Coastal upwelling and downwelling are also considered capable of generating significant mixing close to coasts.

For the past several years we have been working in shallow water to determine where mixing is important and to learn as much as possible about its characteristics. Here, we summarize four sets of these observations.

Florida Strait

In June 1990 Tom Sanford and I took the Multi-scale Profiler (MSP) to the Florida Strait and repeated the STACS line across the strait at 27°N. We occupied seven stations (Figs. 1 and 2) and obtained about ten profiles at each, although not always sequentially. The profiles ended within 5 to 10 m of the bottom. The east wall of the strait is very steep, sloping at 0.11 in

depths less than 4.5 MPa and at 0.32 near the surface. The western slope is much smaller, 0.015. Upstream, the Miami Terrace juts into the Florida Current and is a likely source of low frequency internal waves, which could be advected by 27°N within a day of being generated at the Terrace.

The 10-m Froude number, $\langle Fr_{10}^2 \rangle$, and the diapycnal diffusivity, K_ρ ,

$$\langle Fr_{10}^2 \rangle \equiv \frac{\langle S_{10}^2 \rangle}{\langle N_{10}^2 \rangle}, \quad K_\rho \equiv \frac{0.2\epsilon_{10}}{\langle N_{10}^2 \rangle} \quad (1)$$

have some similarities, with strong minima in the core of the Florida Current and maxima close to the bottom beneath the core (Figs. 3 and 4). Except for the high-shear zone directly below the core, $\langle Fr_{10}^2 \rangle$ is highest within about 1 MPa of the bottom all across the strait.

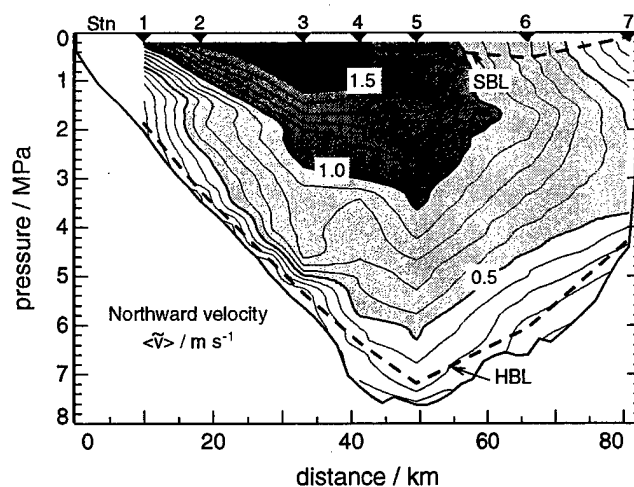


Figure 1. Average northward velocity across the Florida Strait in June 1990. Dashed lines mark maximum extents of homogenous surface and bottom layers.

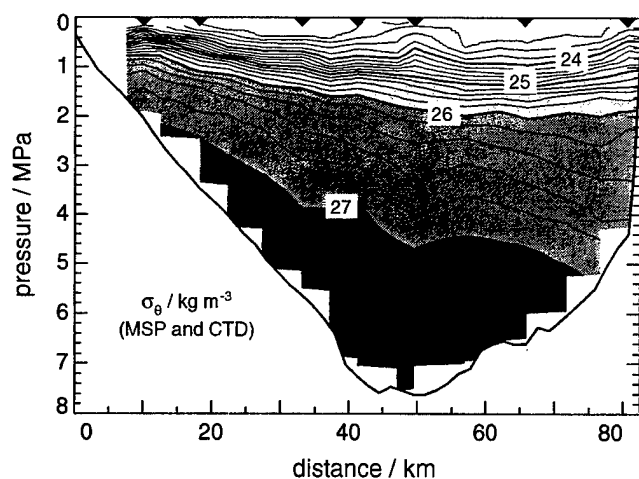


Figure 2. Average potential density across the Florida Strait.

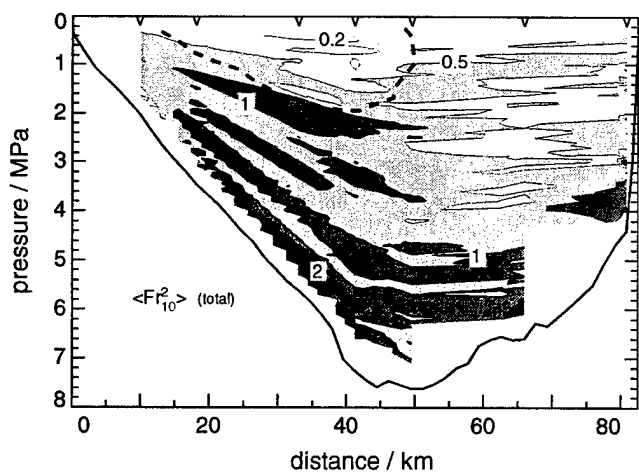


Figure 3. Average Froude number computed with the total 10-m shear variance. The dashed line marks the 1.2 ms^{-1} isotach. Owing to the large spacing between some stations, structures connected by the contouring routine were not necessarily continuous across the strait.

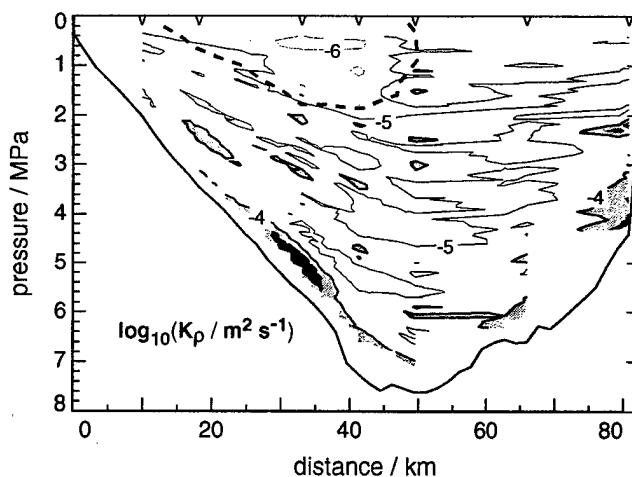


Figure 4. Average diapycnal diffusivity, K_ρ .

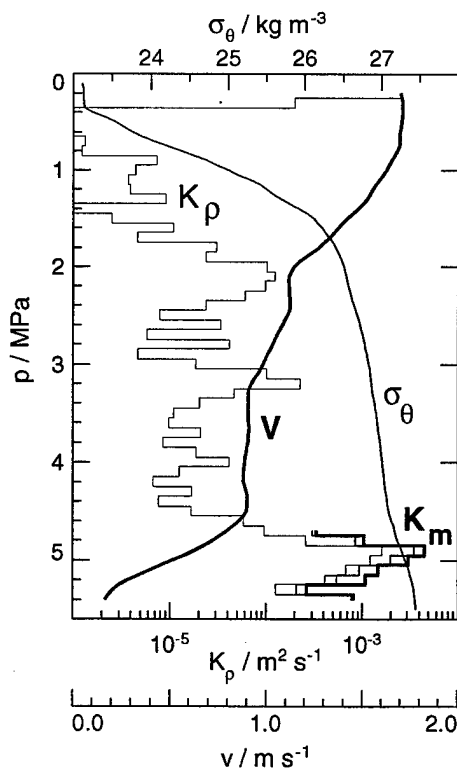


Figure 5. Average profile at station 3, through the core of the Florida Current. Eddy coefficients for momentum (heavy) and for heat (light) are plotted only in the stratified turbulent boundary layer near the bottom.

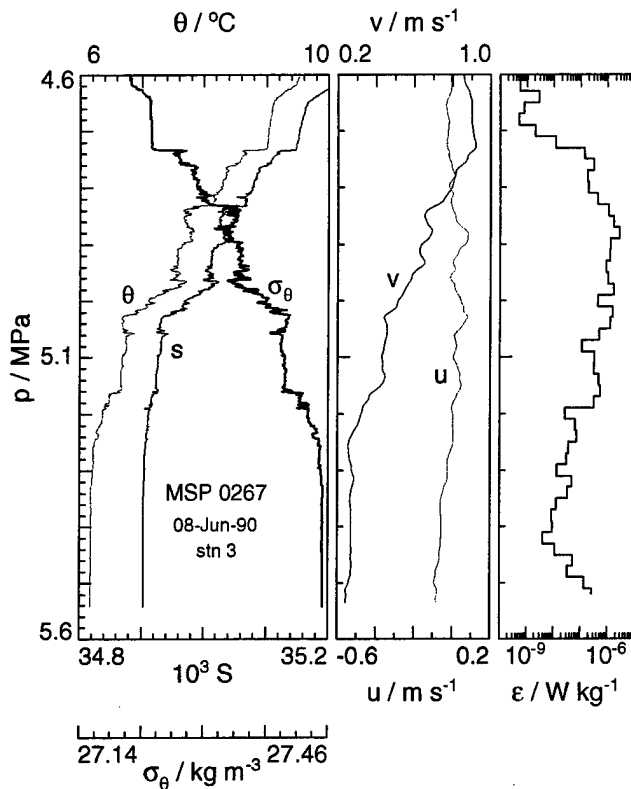


Figure 6. Typical near-bottom profile at station 3, showing a well-stratified region of turbulence above a nearly homogeneous bottom boundary layer.

At station 3, half the mean shear of the Florida Current occurs across this deep zone (Figure 5) and is responsible for most of the total shear. K_ρ is maximum in this deep shear zone, rising above $10^{-3} \text{ m}^2 \text{ s}^{-1}$, in contrast to $\approx 10^{-5} \text{ m}^2 \text{ s}^{-1}$ throughout most of the interior.

Because the average shear contributes most of $(\partial U / \partial z)^2$, it is safe to assume that it also produces most of the turbulence. This allows us to use the dissipation method to calculate the momentum diffusivity, K_m ,

$$K_m \equiv \frac{\epsilon_{10}}{(1 - R_f)(\partial \bar{U}_{10} / \partial z)^2}, \quad K_T \equiv \frac{\chi_T}{2(\partial \bar{T} / \partial z)^2} \quad (2)$$

As seen near the bottom of Figure 5, K_m is slightly larger than K_ρ . K_T , obtained from the temperature gradient variance on the right side of (2), lies between K_ρ and K_m . All three diffusivities peak at $(2 - 4) \times 10^{-3} \text{ m}^2 \text{ s}^{-1}$, a very large value that must represent the primary bottom drag on the Florida Current. By contrast, the upper half of the Florida Current shear occurs between 0.8 and 2 MPa, where K_ρ is much smaller, 10^{-5} to $10^{-4} \text{ m}^2 \text{ s}^{-1}$.

A typical near-bottom profile from station 3 shows the lower high-shear zone between 4.73 and 5.24 MPa

(Fig. 6). It begins at the base of a 10-m-thick homogeneous layer and ends at the top of the homogeneous bottom boundary layer. Density overturns occur throughout, and the largest is 20 m thick. This stratified mixing layer occurs where *Seim et al.* [1999] have identified a benthic front. They speculate that the front separates a bottom Ekman layer on the deeper side from an arrested boundary layer on the shallower side. This lateral convergence may produce the upwelling that appears to compress the stratified water above the bottom boundary layer and produce the high average stratification of the layer.

By comparing K_ρ , $\langle Fr_{10}^2 \rangle$, ratios of clockwise and anti-clockwise velocity rotation, and spectral shapes, we can roughly classify 100-m-thick sections into four categories (Fig. 7).

- **Interior (N):** A large region with moderate K_ρ and $\langle Fr_{10}^2 \rangle$ in which both fluctuating and total shear variance are good predictors of ϵ .
- **High Mean Shear (S):** Restricted regions in which the mean shear is a significant factor producing dissipation. Predicting ϵ using only the fluctuating shear produces serious underestimates.
- **Current Core (C):** Within the 1.2 m s^{-1} mean isotach, the high-velocity core of the Florida Current. This region has the smallest K_ρ , and the fluctuating shear overpredicts ϵ .
- **East Wall (E):** The fluctuating shear is mostly aligned across the strait. Dissipation ranges from low to high and tends to be underpredicted by internal wave scaling.

We applied two approaches to scaling the dissipation rates with internal wave parameters. Using *Polzin et al.* [1995] works well for most of the interior (N) samples but rather badly for many of those in the other categories (Fig. 8, lower). Believing that the discrepancies occur mainly because the spectral approach does not account for turbulence produced by the mean shear, we also applied the *Gregg* [1989] scaling using the 10-m-shear but with the total rather than the fluctuating shear. This reduces the discrepancies to factors of 1/4 to 4 (Fig. 8, upper). Using the total shear is not completely ad hoc because half of the shear dependence in the original model of *Heney et al.* [1986] represented the large-scale, low-frequency background. The large residuals, however, demonstrate that turbulence production by the mean shear is not the entire story and the internal waves differ sufficiently from *Garrett and Munk* [1975] that the limits of the scaling are exceeded.

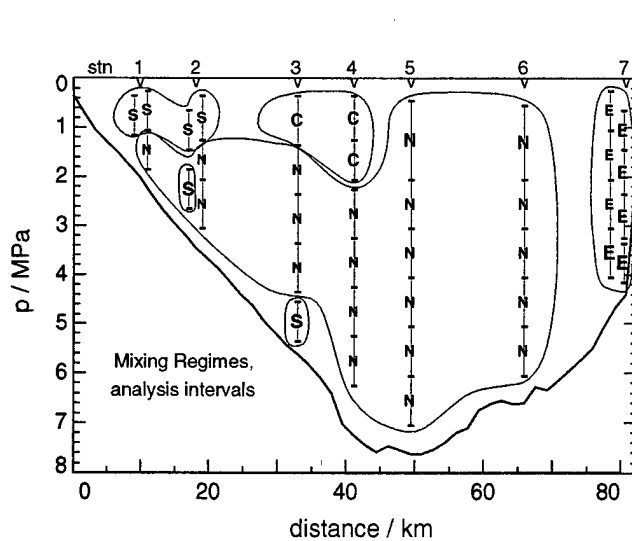


Figure 7. Mixing regimes, in 1 MPa intervals, showing the core (C), interior (N), high-shear zones (S) and east wall (E).

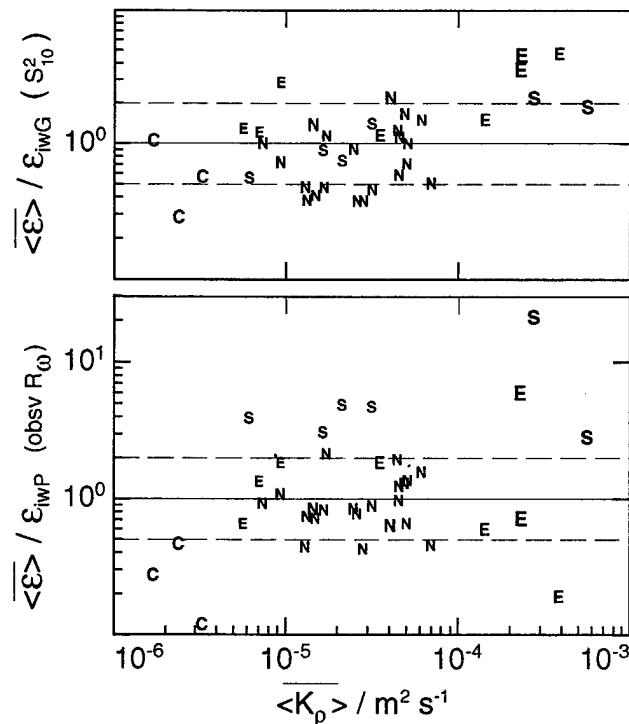


Figure 8. Comparisons of observed ϵ averaged over 1 MPa to predictions based on finestructure. In the upper panel, the prediction of Gregg [1989] is used, but with the total 10 m shear instead of the fluctuating shear. In the lower panel, the prediction of Polzin et al. [1995] is used.

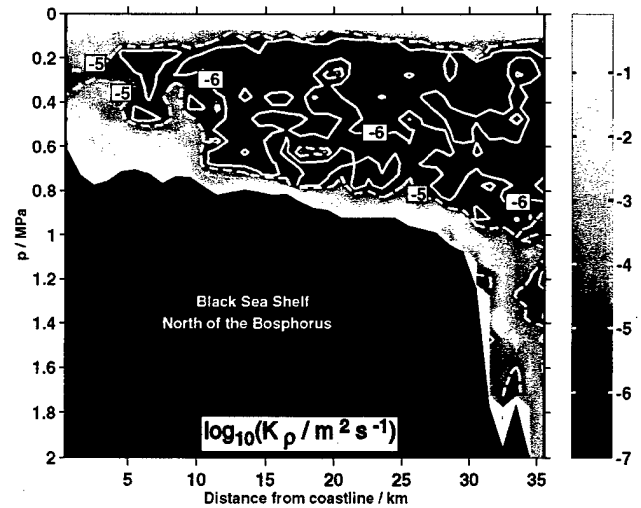


Figure 9. Section of average K_ρ across the Black Sea shelf north of the Bosphorus in September 1994 [Gregg and Özsoy, submitted]. The intense mixing near the bottom is in the dense water flowing out of the Bosphorus.

Black Sea

In September 1994, while following the dense outflow from the Bosphorus, Emin Özsoy and I also observed background mixing rates over the narrow shelf and steep slope of the Black Sea. To produce the section in Figure 9, we averaged profiles taken along the meandering path of the outflow in 1-km bins arranged by their distance from the headlands north of the Bosphorus. Above the intense mixing in the outflow, K_ρ is less than $10^{-6} \text{ m}^2 \text{ s}^{-1}$ in much of the water column and exceeds $10^{-5} \text{ m}^2 \text{ s}^{-1}$ only in the shear zone at the mouth of the strait. These very low levels are likely a lower bound for mixing on shelves; the Black Sea has very small tides (usually no larger than 0.1 m), and winds were very light in September.

New England Shelf

During the Coastal Mixing and Optics Experiment in August 1996, we profiled every night on the New England shelf at 40.5°N , 70.5°W . Using the Modular Microstructure Profiler (MMP), we dropped to within 1-2 m of the bottom at 0.72 MPa and obtained a profile every 6 minutes. Between shallow surface layers and tidally-generated bottom boundary layers penetrating 0.2 MPa above the bottom, N peaked near 0.12 MPa at 0.025 s^{-1} and fell to 0.01 s^{-1} in the bottom half of the water column. Usually $\epsilon \leq 10^{-8} \text{ W kg}^{-1}$ (Fig. 10), but some evenings internal solibores, or their aftermath,

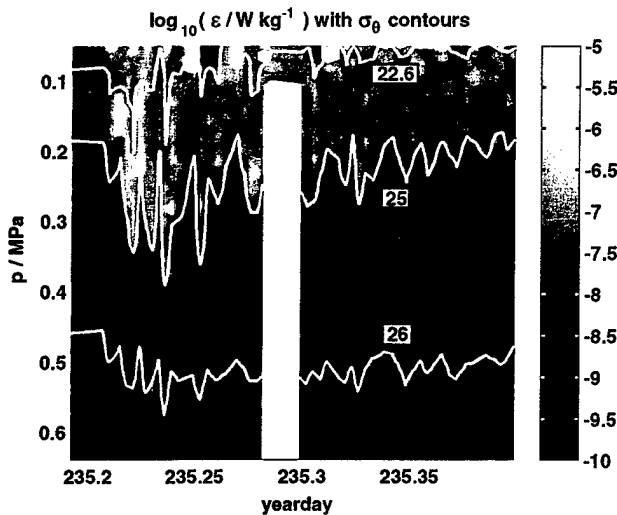


Figure 10. Time series of ϵ during an evening on the New England shelf in August 1996 when no solibores were observed. The bottom was at 0.72 MPa.

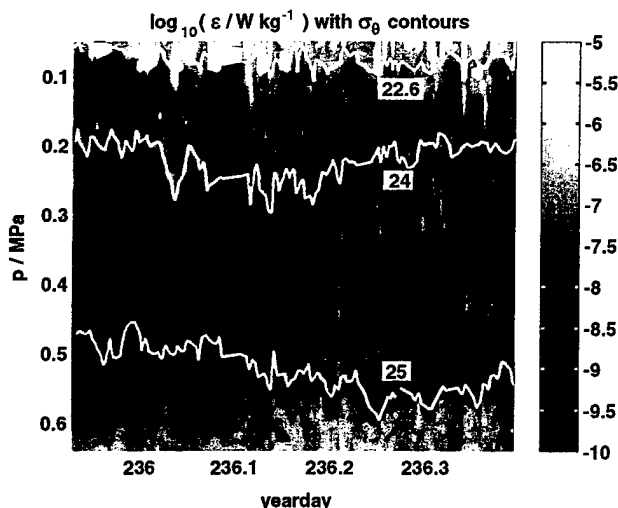


Figure 11. Time series of ϵ on the New England shelf during a night when a solibore appeared in the early evening. Taking a profile every 6 minutes was not sufficiently rapid to resolve the variability produced by the solibore.

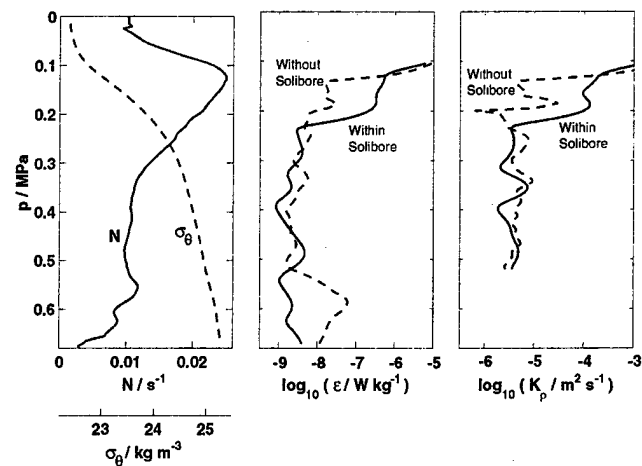


Figure 12. Average profiles when no solibores were present (dashed) and during the solibore on day 235. Averaging of ϵ and K_ρ was done on density surfaces and transformed back to pressure coordinates.

raised ϵ to $10^{-5} \text{ W kg}^{-1}$ in the peak- N region and kept it elevated above background for 4-5 hours (Fig. 11). Our sample interval of 6 minutes did not resolve the solibore waves. Consequently, we cannot determine when mixing resulted directly from the waves or other disturbances associated with them.

Because solibores depress and strain the peak- N region, the mixing they produce is much more compressed between isopycnals than apparent in Figure 11. To represent how the mixing affected the water column, we averaged ϵ on σ_θ and transformed back to pressure in producing the average profiles in Figure 12. The background K_ρ is slightly less than $10^{-5} \text{ m}^2 \text{ s}^{-1}$, but an average during the solibore of day 235 exceeds $10^{-4} \text{ m}^2 \text{ s}^{-1}$ in the peak- N region. Consequently, solibores dominate mixing in the peak- N region, and the average is determined by their frequency and amplitude. Because they did not occur regularly with the tidal cycle, sampling only at night prevented us from estimating a realistic average.

California Shelf

While measuring turbulence in Monterey Canyon, we moved to the north end of Monterey Bay for 21/2 days to examine mixing at the shelf break as part of the Littoral Internal Waves Initiative. During one tidal cycle, we ran a series of lines along the crest of a sea fan and then, for the next cycle, we took sections across the crest. During several of the along-fan sections we found zones of intense mixing along characteristics of the internal tide coming from the shelf break (Fig. 13). The

characteristic slope of the M_2 tide,

$$\frac{dz}{dx} = \left(\frac{\omega_{M_2}^2 - f^2}{N^2(z) - \omega_{M_2}^2} \right)^{1/2} \quad (3)$$

matches the bottom slope at the shelf break (Fig.). The lowest dissipation rates in Figure occur on the shelf. Other minima are found above the beam and below 350 m at the seaward side.

For about 6 km along the beam, the dissipation rate is elevated over 50 m in the vertical. Profiles reveal that ϵ in the beam rises to $10^{-5} \text{ W kg}^{-1}$, more than a 100-fold increase above the background (Fig.). The beam is more weakly stratified than the background, indicating partial homogenization, and it contains a shoreward jet of about 0.15 m s^{-1} . N^2 and S^2 peak on the vertical boundaries of the beam, and $S \approx 2N$, indicating instability. Together with peaks in ϵ , this suggests entrainment of water into the layer from above and below. Forming a crude time series from all data along the fan axis at the depth of the beam shows that ϵ changes by factors of 10-100 with the tidal cycle and is largest during ebb (Fig.). This is additional evidence that the beam is tidally generated.

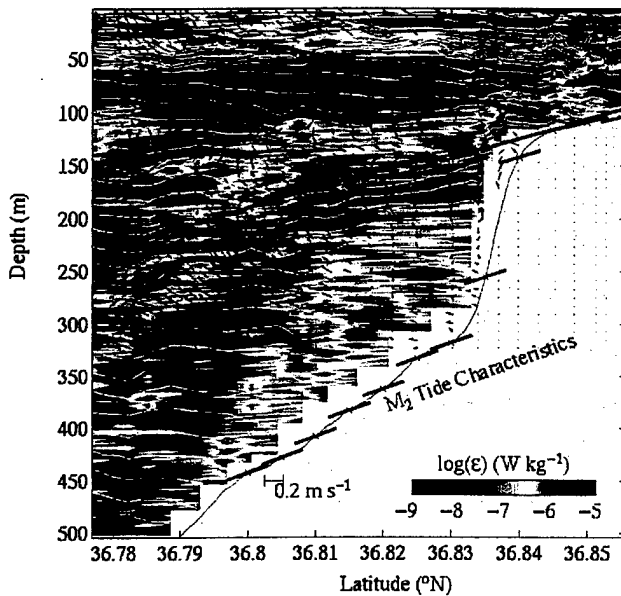


Figure 13. Section of ϵ and velocity along the ridge of a sea fan in the north end of Monterey Bay. Horizontal velocity from a Broadband ADCP operated with 4 m bins is plotted as a vector with north at the top. Solid and dashed lines are characteristics of the internal tide computed using an average N profile (dashed) and using all N profiles (solid). Positions of the AMP drops are shown by ticks at the top, and AMP16304 is marked by an arrow.

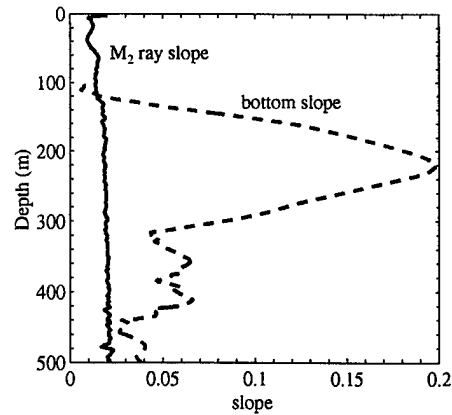


Figure 14. the internal tide (solid). The two match at 120 m, the depth of the shelf break.

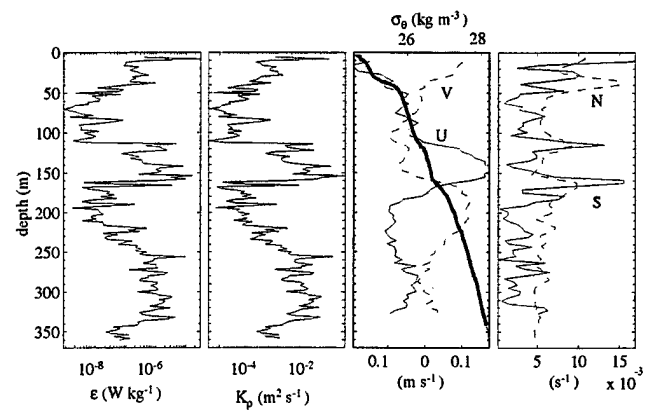


Figure 15. Profiles from AMP16304. Currents are positive inshore (u) and northward (v).

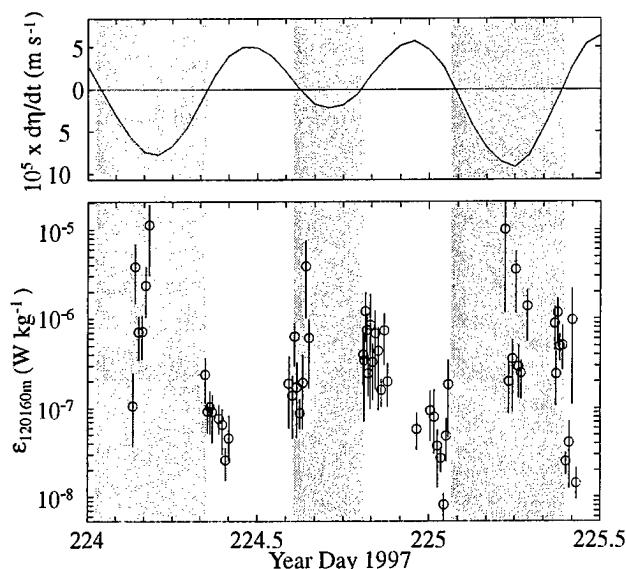


Figure 16. Comparison of surface tide and average ϵ at depths of internal tidal beam. The surface tide is represented by the rate of change of the tidal height in Monterey harbor; ebb tides are shaded. Dissipation rates are 10 to 100 times larger during ebb tides than during flood tides.

The dissipation rate is equally high in an even thicker and more strongly stratified region above the bottom (Figs. 13 and 15). This mixing region seems similar to the turbulent stratified boundary layer observed in the Florida Strait. We are examining across-fan sections and bathymetry to determine if it could be a tidal beam emanating from the bottom. Internal waves reflecting from the sloping topography are another possible source.

Summary

On the Black Sea shelf north of the Bosphorus in September 1994, K_p increased with pressure from slightly above the molecular diffusivity to $10^{-6} \text{ m}^2 \text{ s}^{-1}$. Such low levels likely result from the absence of significant tidal forcing and a seasonal minimum in wind speed.

Except where tides and winds are negligible, mixing on shelves is important, as summarized in Figure 17. Background levels on the New England shelf are $K_p \approx 5 \times 10^{-5} \text{ m}^2 \text{ s}^{-1}$, about 10 times background in the open ocean when internal waves are at the Garrett and Munk (GM) level [Gregg and Sanford, 1988]. Within the solibore, levels average 10 times the local background, i.e., $K_p \approx 5 \times 10^{-4} \text{ m}^2 \text{ s}^{-1}$. Levels are at least that level at two sites on the shelf in Monterey Bay.

In the Florida Strait $K_p \approx 10^{-6} \text{ m}^2 \text{ s}^{-1}$ in the core of

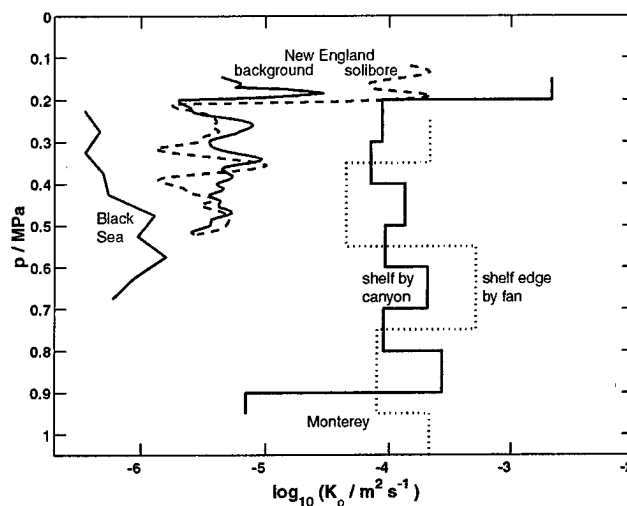


Figure 17. Comparison of average K_p profiles from continental shelves. One of the two Monterey profiles (dotted) is an average of data near the edge of the shelf adjacent to the sea fan. The other Monterey profile (solid) is an average of profiles taken on the shelf a few kilometers north of the canyon. One of the New England profiles is an average of evenings during CMO96 when we observed no solibores (dashed); the other is an average during the solibore on night 235. The Black Sea profile is an average of data between 21 and 35 km from the mouth of the Bosphorus.

the Florida Current; levels so low are only a few times the molecular diffusivity and represent negligible mixing. The diapycnal diffusivity is 1,000 times greater, $K_p \approx 10^{-3} \text{ m}^2 \text{ s}^{-1}$, in a layer with strongly average stratification above the bottom boundary layer. Hence, one profile spans diapycnal diffusivities from among the smallest measured to among the largest (Fig. 18). Half of the vertical shear of the Florida Current occurs across this layer. Intense mixing is also found adjacent to the east wall of the strait. Throughout most of the interior, values average $3.1 \times 10^{-5} \text{ m}^2 \text{ s}^{-1}$, consistent with internal waves 2.5 times GM.

Over a marine fan at the north side of Monterey Bay, K_p exceeds $10^{-3} \text{ m}^2 \text{ s}^{-1}$ in a 50-m-thick beam of the internal tide emanating from the shelf break and in a thicker, stratified, near-bottom layer of uncertain origin. Farther offshore K_p continues to exceed $10^{-4} \text{ m}^2 \text{ s}^{-1}$, indicating that the entire near-shore area is one of strong mixing.

Discussion

Tidal amplitudes, bottom roughness, and wind speeds are probably key parameters determining mixing over continental shelves. Without significant tides and winds, mixing over shelves can drop to nearly molecular levels,

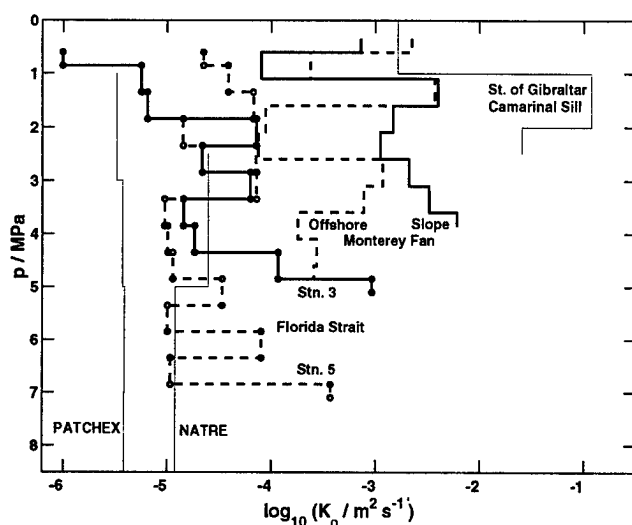


Figure 18. Profiles of average K_p (thick) from the Florida Strait and the continental shelf over the Monterey sea fan compared with a representative values from other locations (thin lines). The references are PATCHEX, in the California Current when internal waves were at GM [Gregg and Sanford 1988]; the North Atlantic Tracer Release (NATRE) in the eastern North Atlantic when internal waves were several times GM [Polzin et al. 1995]; and in a region of large shear instabilities in the lee of Camarinal Sill in the Strait of Gibraltar [Wesson and Gregg 1994].

as demonstrated by the Black Sea observations. In addition to producing turbulent bottom layers and generating internal tides at the shelf break, tidal currents also create internal solibores that mix intensely while propagating across the shelves. The short time and space scales over which mixing varies, sometimes by decades, in response to these processes greatly complicates the observational task of determining averages. For comparison, in the main thermocline of the open ocean, internal wave energy scales vertically with N , is laterally coherent for 10-20 km, and varies in time over periods of weeks to months and only by factors of 2-3 at most. Considerable thought will be required to determine optimum representations of mixing in numerical models of shelves and slopes.

Finding some of the most intense mixing in thick, stratified layers resolves a primary objection Garrett [1979] expressed about the proposal by Armi [1978] that the oceans mix mainly at their boundaries. Garrett

allowed that much energy may be dissipated in boundary layers but argued that mixing in homogenous layers cannot increase potential energy as required for global balances. The data are far too spotty to allow global estimates of the effect of boundary mixing, but they demonstrate that much of it occurs in stratified and not homogenous profiles.

Acknowledgments. The Office of Naval Research funded the collection and analysis of all of these measurements except for those on the shelf alongside Monterey Canyon, which were funded by the National Science Foundation.

References

- Armi, L., Some evidence for boundary mixing, *J. Geophys. Res.*, **83**, 1971-1979, 1978.
- Garrett, C., Comment on 'some evidence for boundary mixing in the deep ocean', *J. Geophys. Res.*, **84**, 5095, 1979.
- Garrett, C. J. R., and W. H. Munk, Space-time scales of internal waves: A progress report, *J. Geophys. Res.*, **80**, 291-297, 1975.
- Gregg, M., Scaling turbulent dissipation in the thermocline, *J. Geophys. Res.*, **94**, 9686-9698, 1989.
- Gregg, M. C., and E. Özsoy, Mixing on the Black Sea shelf north of the Bosphorus, *Geophys. Res. Ltrs.*, submitted, 1999.
- Gregg, M. C., and T. B. Sanford, The dependence of turbulent dissipation on stratification in a diffusively stable thermocline, *J. Geophys. Res.*, **93**, 12,381-12,392, 1988.
- Henyey, F. S., J. Wright, and S. M. Flatté, Energy and action flow through the internal wave field, *J. Geophys. Res.*, **91**, 8487-8495, 1986.
- Polzin, K., J. M. Toole, and R. W. Schmitt, Finescale parameterization of turbulent dissipation, *J. Phys. Oceanogr.*, **25**, 306-328, 1995.
- Seim, H., D. Winkel, G. Gawarkiewicz, and M. Gregg, A benthic front in the Straits of Florida and its relationship to the structure of the Florida Current, *J. Geophys. Res.*, submitted, 1999.
- Wesson, J., and M. Gregg, Mixing at Camarinal Sill in the Strait of Gibraltar, *J. Geophys. Res.*, **99**, 9847-9878, 1994.

This preprint was prepared with AGU's L^AT_EX macros v5.01, with the extension package 'AGU++' by P. W. Daly, version 1.6a from 1999/05/21.

Modeling Internal Tide Generation and Evolution into Internal Solitary Waves on the Australian North West Shelf

Peter E. Holloway

School of Geography and Oceanography, University College, University of New South Wales,
Australian Defence Force Academy, Canberra, Australia

Efim Pelinovsky and Tatyana Talipova

Department of Nonlinear Waves, Institute of Applied Physics, Russian Academy of Science,
Nizhny Novgorod, Russia

Abstract. Internal tide generation by tidal flow over the continental shelf and slope regions on the Australian North West Shelf (NWS) is modeled using a fully three-dimensional, nonlinear, free surface, hydrostatic model, the Princeton Ocean Model. Results show that generation occurs where seabed slopes are similar to those of the internal wave group velocity (critical slopes) and that the generation is characterised by bottom intensification of the flow. The distribution of depth-integrated baroclinic energy flux is highly variable in space with regions of offshore and onshore flux. Three-dimensional topography is found to be important in the generation process with cross-section models tending to underestimate the observed internal tide. Observations from the NWS show a shoreward propagating internal tide near the shelf break that steepens as it shoals and forms a variety of strongly nonlinear waveforms. These include bores and solitons as well as square-wave forms and thick solitons. Such phenomena cannot be adequately described with hydrostatic models. The evolution of a shoaling internal tide is investigated using a Korteweg-de Vries (KdV) model that includes quadratic and cubic nonlinearity, Earth rotation, dissipation, and variable depth and stratification. The initial deep-water waveform is specified as a first mode sinusoidal internal tide and its evolution is strongly dependent on the cross-shelf distribution of the coefficients of the KdV equation. It is shown that rotation, cubic nonlinearity, and dissipation all have a significant influence on the predicted wave evolution. The effects of a background shear flow are also shown to be important as water depth shallows.

1. Introduction

Oscillatory tidal flow moving stratified water over steep topography, such as continental shelves, can generate a propagating long internal wave or internal tide. Such waves are typically a few 10's km in wavelength and 10's m in height. They can be energetic, often associated with bottom intensified currents, and are potentially important contributors to mixing over the continental slope. Additionally, they provide a pathway for barotropic tidal energy to be transferred into internal waves that can be radiated away from the gen-

eration region. These long waves are also observed to steepen and evolve into a variety of strongly nonlinear wave forms including internal solitary waves. Examples drawn from the Australian North West Shelf (NWS) show a large amplitude semi-diurnal internal tide generated over the continental slope, which propagates shoreward and evolves into a variety of strongly nonlinear wave forms with wavelengths of a few 100's m.

This paper describes efforts made at modeling the generation of the semi-diurnal internal tide on the NWS

using a fully 3-dimensional primitive equation, hydrostatic model and also the ability of such a model to predict the nonlinear steepening of the internal tide. The evolution of the internal tide into internal solitary waves is described through the application of a Korteweg-deVries (KdV) model that includes varying topography and stratification, the Earth's rotation, cubic nonlinearity and frictional dissipation. Current meter, thermistor string, and CTD profile observations from the NWS show a variety of internal wave forms.

2. Observations

Observed internal wave forms are presented from observations made on the NWS. Figure 1 shows the region from which observations are presented. The first examples (Figure 2) show isopycnal displacements from three locations, derived from repeated CTD profiles made every 30 minutes over a 13-hr period at each location. At the deepest location shown (115 m water depth), a complex large amplitude semi-diurnal internal tide is seen along with several internal solitary waves. At the middle location similar wave forms are seen with the internal tide showing a near square wave form. At the shallowest location, the internal tide is weak, suggesting dissipation or reflection of the internal tide near the shelf break. A large positive solitary wave is seen at this location while waves of both positive and negative polarity are observed at the other locations.

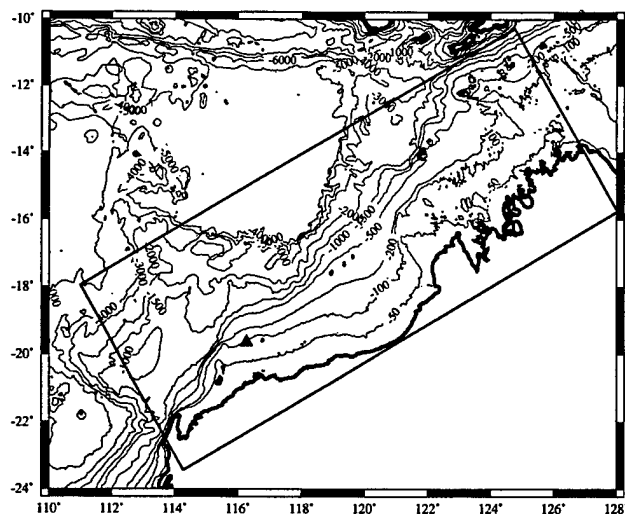


Figure 1. Map of the Australian North West Shelf showing bathymetry and the domain of the internal tide model. The triangle shows the region from which observations are presented.

Current meter observations of internal waves are pre-

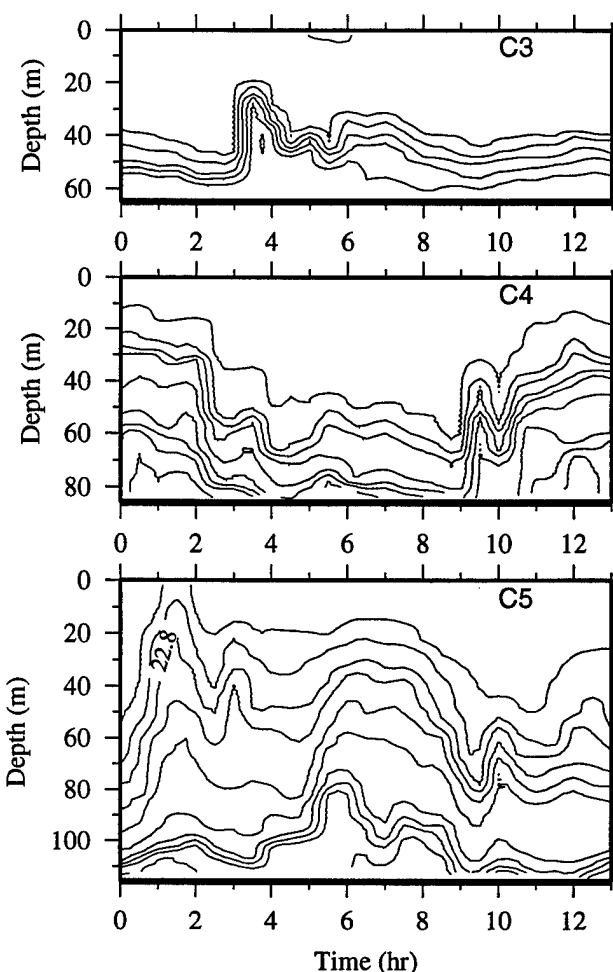


Figure 2. Isopycnal displacements derived from 30 minute repeated CTD casts over 13 hr periods showing observed internal wave forms. Plots show total water depth. Region of observations is shown in Fig. 1.

sented in Fig. 3, as shown by the velocity component flowing across the bathymetry (the dominant wave-propagation direction) and by vertical displacements of isotherms derived from temperature time series at different depths. Measurements are from water 78 m deep close to the shelf break at 19.71°S 116.14°E with instruments sampling at 2-min intervals. Additional examples showing soliton-like wave forms are presented by Holloway et al. (1997). Figure 3a shows a large amplitude wave (peak-trough ~35 m in water 78 m deep) with a downwards shock followed by a number of positive internal solitary waves. At the end of the wave profile when the waveform is again at a crest, negative internal solitary waves are seen. The change in polarity is associated with the dramatic change in the stratification caused by the very large amplitude internal tide. The wave properties are also revealed in the baroclinic

currents (depth average has been removed) at 8 and 68 m depth. the change in direction of flow between upper and lower levels is consistent with a first mode structure.

Figure 3b shows a large upwards jump (~ 40 m) followed by a number of oscillatory waves and a gradual, near linear, decrease in the wave interface. This produces a triangular waveform. Figure 3c shows a small number of internal solitary waves following a weak downward jump. The first wave is "wide" or longer in period than in other examples.

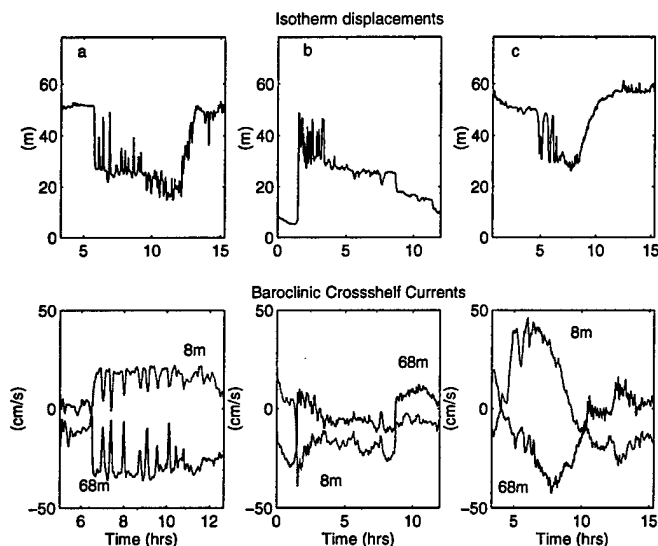


Figure 3. Observed time series of vertical displacements of isotherms and corresponding baroclinic cross-shelf currents on the NWS. Region of observations is shown in Fig. 1.

3. Internal Tide Model

Holloway (1996) describes the application of the Princeton Ocean Model (POM) to modeling the M_2 internal tide over 2D cross sections of topography on the NWS, and Holloway and Merrifield (1999) apply the model in a fully 3D application to idealised topography representing seamounts, ridges and islands. In this paper results are described from a 3D application of the model to the NWS, a region covering 1700 by 700 km (Fig. 1).

The model is forced through the specification of the M_2 tidal elevation along open boundaries, as described by the FES5.2 global tidal model. Real bathymetry, with maximum depth 5500 m, and observed summer stratification, uniform horizontally, are prescribed. The model grid size is 4 km with 51 vertical sigma levels. The model is run over a 4-day simulation with tidal analysis of various fields carried out over the last 24 hr.

The oscillating surface elevations force the barotropic tidal flow, and through the interaction of this flow with bathymetry, a baroclinic, or internal, tide is generated in different locations.

The baroclinic energy flux is calculated from the baroclinic currents, defined as the total flow minus the depth integrated component, and from the vertical displacements, see Holloway and Merrifield (1999). The depth-integrated M_2 baroclinic energy flux (Fig. 4) shows a strong and highly variable internal tide, strongest over the shelf break and continental slope and to the northern part of the NWS. There is energy flux both onshore and offshore although little energy flux is generated or propagates to the inner shelf. The distribution of energy flux shows high spatial variability, much greater than is shown by the barotropic tide, suggesting that small-scale topographic variations have a significant impact on the internal tide. A comparison of these results with those from cross-section model runs shows that the 2D nature of the topography and barotropic tide are important in determining the internal tide generation.

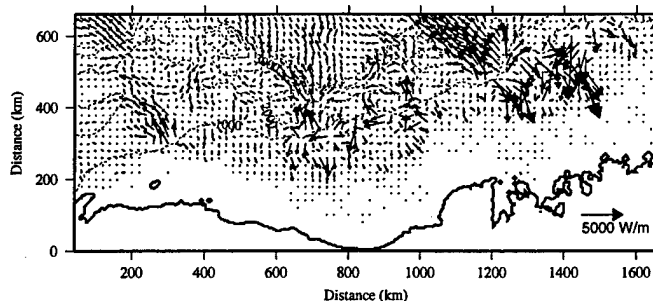


Figure 4. Model-predicted depth integrated M_2 baroclinic energy flux for the NWS.

Observations of the internal tide along a cross section have been made by repeated CTD casts (revealing vertical displacements) and from simultaneous ship mounted ADCP velocity profiles. These are from the region shown in Fig. 1. The observations allow for the calculation of baroclinic energy fluxes. Similarly the energy flux has been computed from moored current meter data in the same region, where month-long records have been analysed to obtain the M_2 values. These observed fluxes are compared to the model-predicted values in Fig. 5. Given the high spatial variability in the energy flux predicted by the model, such comparisons are a demanding test for the model and the observations. Despite this, a reasonable agreement is achieved with directions and the variability in the fluxes is well predicted. The peak observed values are slightly underestimated by the model.

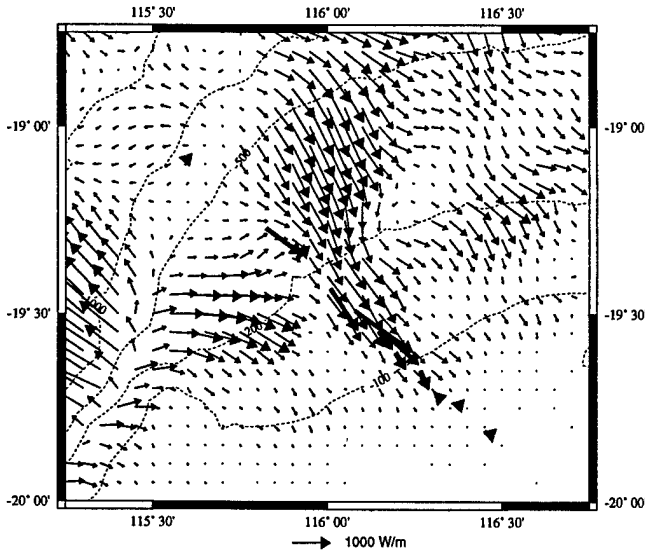


Figure 5. Model predicted depth integrated M_2 baroclinic energy flux for a region on the NWS (dark arrows) along with observed baroclinic energy fluxes (thick arrows).

The model also predicts complex three-dimensional structures of the internal tide. Signals tend to be bottom-intensified near the generation regions and to propagate as beams along characteristic paths (path of the group velocity). This also presents a demanding task for comparison between models and observations, and such data are not presented in this paper.

It is important to know how well hydrostatic models can predict the nonlinear steepening of the internal tide as it shoals over the shelf break. A two-dimensional application of the internal tide model is made to a cross section of bathymetry using fine spatial resolution of 100 m over the shelf break. A snapshot of the density structure is shown in Fig. 6 along with an equivalent output from a 1000-m resolution model simulation. Both runs use 61 vertical sigma levels. The 100-m resolution run shows the nonlinear steepening of the waveform near the shelf break, which is absent in the coarser model run. Some high frequency waves are also seen to form behind the weak bore. This suggests that the hydrostatic model can predict the steepening of the waveform, but without the nonhydrostatic terms the steep waves cannot transform into internal solitary waves. Finer resolution runs allow the “shock” to increase in steepness but, for very steep waveforms, the model can become numerically unstable.

4. Korteweg de-Vries Model

The evolution of internal tides into nonlinear internal solitary waves is studied using a Korteweg de-Vries

(KdV) model. An initial waveform is defined as a sinusoidal long wave, representing an internal tide, and the wave is allowed to propagate over slowly shoaling topography and through arbitrary density stratification. The model includes the effects of rotation, both quadratic and cubic nonlinearity, and dissipation through turbulent bottom friction. Full details are given by Holloway *et al.* (1999).

The model is based on the rotated-modified extended KdV equation (reKdV) which is obtained from a perturbation method in second order in wave amplitude and first order in wavelength and is valid when nonlinearity, dispersion, and rotation are small. The reKdV equation is

$$\frac{\partial}{\partial x} \left(\frac{\partial \eta}{\partial t} + (c + \alpha \eta + \alpha_1 \eta^2) \frac{\partial \eta}{\partial x} + \beta \frac{\partial^3 \eta}{\partial x^3} \right) = \frac{f^2}{2c} \eta \quad (1)$$

where η is the wave profile, x the horizontal coordinate, t time, and f the Coriolis parameter. The phase speed of the linear long wave c is determined by the eigenvalue problem (where f is neglected)

$$\frac{d^2 \Phi}{dz^2} + \frac{N^2(z)}{c^2} \Phi = 0 \quad (2)$$

with boundary conditions $\Phi(0) = \Phi(H) = 0$, normalisation $\Phi_{\max} = 1$ and where H is total water depth and $N(z)$ is the Brunt-Vaisala frequency. The coefficients of dispersion (β), quadratic nonlinearity (α) and cubic nonlinearity (α_1) are (Lamb and Yan, 1996)

$$\beta = \frac{c}{2} \frac{\int \Phi^2 dz}{\int (d\Phi/dz)^2 dz}, \quad (3)$$

$$\alpha = \frac{3c}{2} \frac{\int (d\Phi/dz)^3 dz}{\int (d\Phi/dz)^2 dz}, \quad (4)$$

$$\alpha_1 = -\frac{\alpha^2}{c} + 3c \frac{\int ((d\Phi/dz)^4 - (N\Phi/c)^4) dz}{\int (d\Phi/dz)^2 dz} + 3c \frac{\int \left(c(d\Phi/dz)^2 + \frac{N^2 \Phi^2}{c} - \frac{2\alpha}{3} (d\Phi/dz) \right) \left(\frac{dT}{dz} \right) dz}{\int (d\Phi/dz)^2 dz} \quad (5)$$

where integration is over the total water depth. $T(z)$ is the first correction to the nonlinear wave mode, given by the solution of

$$\frac{d^2 T}{dz^2} + \frac{N^2}{c^2} T = \frac{\alpha N^2}{c^4} \Phi + \frac{dN^2/dz}{c^3} \Phi^2 \quad (6)$$

with $T(0) = T(H) = 0$ and the normalised condition $T(z_{\max}) = 0$, where $\Phi(z_{\max}) = 1$.

The effects of slowly varying depth can be included in (1) by introducing a weak source term, as described

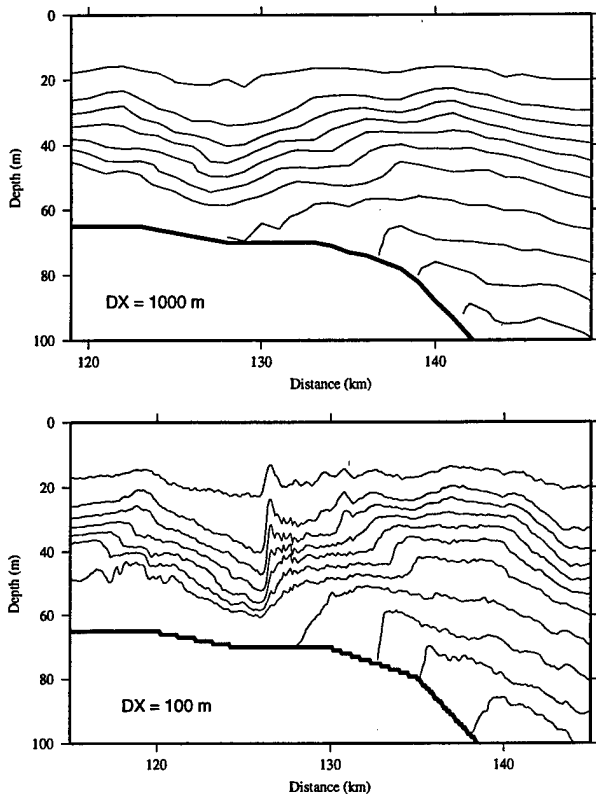


Figure 6. Snapshots of predicted density distributions over the shelf break from a 2-dimensional cross-section internal tide model. Results are from two different horizontal grid resolutions. Both simulations use 61 vertical levels

by Zhou and Grimshaw (1989), defined as

$$Q = \sqrt{\frac{c_0^3 \int (d\Phi_0/dz)^2 dz}{c^3 \int (d\Phi/dz)^2 dz}}, \quad (7)$$

where values with subscript '0' are the values at some origin x_0 . Quadratic bottom friction with a drag coefficient k can also be introduced. Finally, introducing a change in variable $\zeta(x, s) = \frac{\eta(x, t)}{Q(x)}$ and coordinate $s = \int \frac{dx}{c(x)} - t$, the model equation becomes

$$\begin{aligned} \frac{\partial \zeta}{\partial x} + \left(\frac{\alpha Q}{c^2} \zeta + \frac{\alpha_1 Q^2}{c^2} \zeta^2 \right) \frac{\partial \zeta}{\partial s} + \frac{\beta}{c^4} \frac{\partial^3 \zeta}{\partial s^3} + \frac{kcQ}{\beta} \zeta |\zeta| \\ = \frac{f^2}{2c} \int \zeta ds. \end{aligned} \quad (8)$$

Equation (8) is solved numerically with periodic boundary conditions and an initial condition of a sinusoidal internal tide.

5. KdV Model Results

Model results are presented for a bathymetric cross section on the NWS, corresponding to the location of

the observations presented in Section 2. Observed stratification (Fig. 7) from a summer period is used to define the coefficients in the reKdV model.

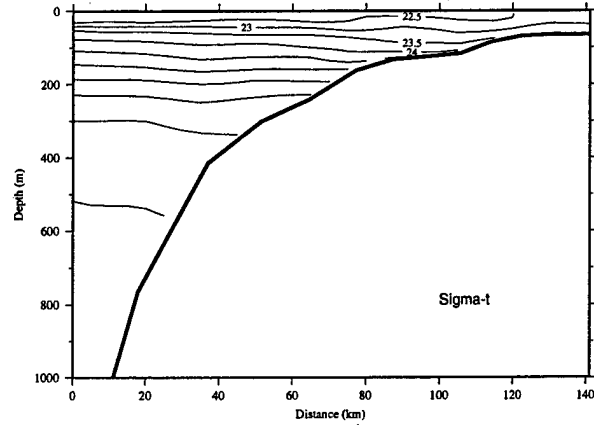


Figure 7. Observed density section from the NWS used to calculate the coefficients of the KdV equation.

The first results presented consider an initial wave of 12 hr period and 2 m amplitude originating in water 500 m deep, although results are insensitive to the initial water depth as little wave transformation occurs in the deep water. Frictional dissipation is also neglected ($k = 0$) in these initial runs. Figure 8 shows the wave forms predicted after the wave has propagated 110 km, to a water depth of ~ 70 m, under different model assumptions. Results are shown neglecting cubic nonlinearity and rotation (KdV model), neglecting only rotation (eKdV model), neglecting only cubic nonlinearity (rKdV model) and including all terms (reKdV model). Solutions without cubic nonlinearity show two solitons forming followed by a train of oscillatory waves. Rotation reduces the phase speed of the long wave (latitude is 20°S). Cubic nonlinearity dramatically changes the form of the solitary waves to produce wide solitons. The full reKdV model produces a nearly square wave form with a train of oscillatory waves. It is clear that both cubic nonlinearity and rotation have significant influences on the wave evolution and that their combined effect is important.

Larger amplitude initial waveforms become unrealistically large as they shoal if dissipation is not included in the model. Figure 9 shows the evolution of a 15-m amplitude wave originating in water 1000 m deep for the same bathymetry and stratification as above using the reKdV model and including dissipation with $k = 0.0013$. A variety of waveforms result showing changing character at different locations as the wave evolves. In 116 m water depth, a large amplitude internal tide is seen with steep leading and trailing faces

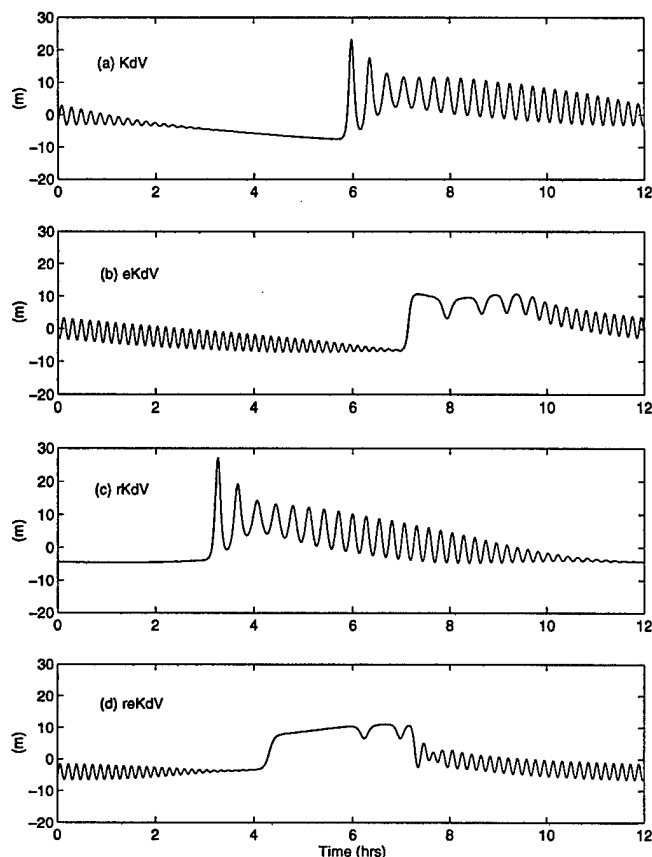


Figure 8. Calculated waveforms, at a depth of ~ 70 m, using different model assumptions with $k = 0$. (a) KdV model, (b) eKdV model, (c) rKdV model, (d) reKdV model.

and numerous oscillatory waves. After further propagation a strong upward bore is produced with a number of solitons and a triangular waveform, similar to the observations shown in Fig. 3b. As this waveform further propagates, a wide soliton is seen, consistent with observations (Fig. 3c).

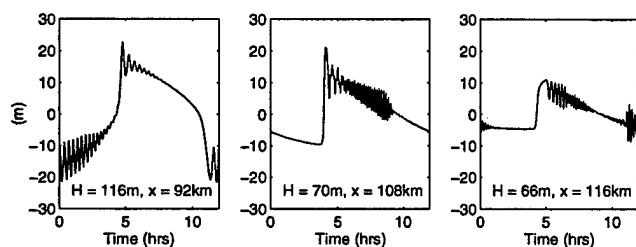


Figure 9. Calculated waveforms from the reKdV model at different depths for an initial wave in water 1000 m deep and amplitude 15 m, with $k = 0.0013$.

6. Effects of Background Shear Flow

The solutions to the KdV models and consequent evolution of nonlinear waveforms are primarily determined by the spatial distribution of the coefficients of the KdV equation. Of the coefficients for the first order KdV equation, the quadratic nonlinear term is the most effected by variability in stratification and background flow. If a background shear flow $U(z)$ is included in the KdV model, the nonlinear coefficient is defined as

$$\alpha = \frac{3}{2} \frac{\int_{-H}^0 (c - U)^2 (d\Phi/dz)^3 dz}{\int_{-H}^0 (c - U) (d\Phi/dz)^2 dz} \quad (9)$$

where the vertical structure of the wave mode $\Phi(z)$ is determined by the solution of the eigenvalue problem

$$\frac{d}{dz}[(c - U)^2 \frac{d\Phi}{dz}] + N^2(z)\Phi = 0 \quad (10)$$

where $\Phi(-H) = \Phi(0) = 0$.

Current meter data from two locations near the shelf break, the region shown in Fig. 1, in 109 and 78 m water depths have been used to compute the variability in the quadratic nonlinear coefficient from (9) and (10). At each location a string of 6 current meters has been used to define stratification and background current profiles using 10-day averages of data. The nonlinear coefficient has been computed including and excluding the background shear flow. At the deeper location there is variability in α in time but the background flow has little effect. At the shallow location, in 78 m depth, the shear flow has at times a pronounced effect on the magnitude of α for both positive and negative values. The shear has reduced the magnitude of positive α and increased the magnitude of negative values of α . It is expected that greater variability would be found if shorter averaging times were selected. This observed influence of shear would have a significant impact on the evolution of an initial waveform.

7. Discussion

Primitive equation, hydrostatic models have been used for many years as tools for modeling barotropic tidal motions over continental shelf and slope regions. Extensions of these models to allow for three-dimensional stratified flows over topography show the generation of internal tides. The predicted internal wave fields for the NWS show a high degree of spatial variability due to variability in the topography. However, owing to the high horizontal and vertical spatial variability in the model predicted fields, and the temporal variability seen in observations, it is a difficult task to obtain sufficient and adequate observations to rigorously validate the internal tide models.

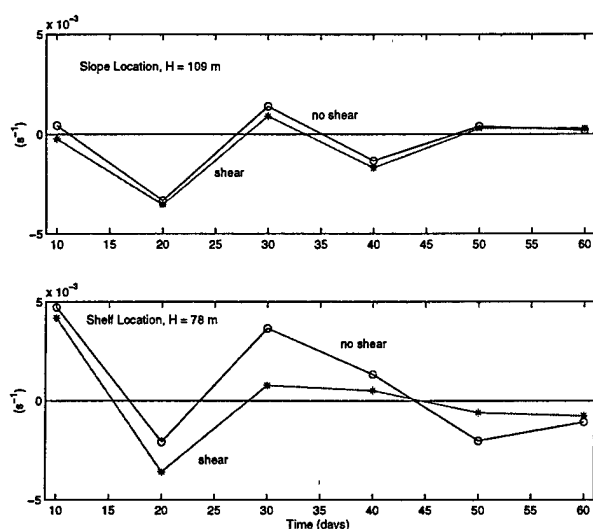


Figure 10. Computed values of the quadratic nonlinear coefficient from the KdV model equations for *slope* and *shelf* locations in 109- and 78-m water depths respectively, the region shown in Fig. 1. Values are computed from 10-day averages of stratification and currents and are shown including and excluding the effects of the background flow.

The hydrostatic models, when run with fine resolution, can provide predictions of the nonlinear steepening of the internal tide as it shoals over the shelf break. Such models, however, cannot predict the evolution of the internal tide into internal solitary waves. Nonhydrostatic models, e.g., Lamb (1994), can be used to model the generation of nonlinear wave forms from tidal flow over topography. The use of KdV-type models is another possible tool for developing an understanding of the way nonlinear internal waves can form from an internal tide and how they can evolve as they propagate. Solutions to KdV models can reproduce a number of features of observed nonlinear waves and demonstrate the importance of frictional dissipation, Earth's rotation and high order nonlinearity in determining the evolution of a waveform. The KdV model applied to the NWS also shows results are sensitive to background stratification and initial wave amplitude. Background shear flow can be important in determining the model solutions by changing the values of the coefficients of the KdV model, particularly in shallow water.

Acknowledgments. Financial support for TT and EP to work in Australia was provided by a Bilateral Science and Technology Grant

References

- Holloway, P. E., Pelinovsky, E., Talipova, T., and Barnes, B. A nonlinear model of internal tide transformation on the Australian North West Shelf. *J. Phys. Oceanogr.*, **27**, 871-896, 1997.
- Holloway, P. E., Pelinovsky, E., and Talipova, T. A generalised Korteweg-de Vries model of internal tide transformation in the coastal zone. *J. Geophys. Res.*, 1999, (submitted).
- Holloway, P. E. and Merrifield, M. Internal tide generation by seamounts, ridges and islands. *J. Geophys. Res.*, 1999, (submitted).
- Lamb, K. G. Numerical experiments of internal wave generation by strong tidal flow across a finite amplitude bank edge. *J. Geophys. Res.*, **99**, 843-864, 1994.
- Lamb, K.G., and Yan, L. The evolution of internal wave undular bores: comparisons of a fully nonlinear numerical model with weakly nonlinear theory. *J. Phys. Oceanogr.*, **26**, 2712-2734, 1996.
- Zhou, X., and Grimshaw, R. The effect of variable currents on internal solitary waves. *Dynamics Atm. Oceans*, **14**, 17-39, 1989.

Internal Tide Generation at Open Ocean Topographies

Mark A. Merrifield

Department of Oceanography, University of Hawaii, Honolulu, Hawaii

Peter E. Holloway

School of Geography and Oceanography, University of New South Wales, Australian Defence Force Academy, Canberra, Australia

Abstract. The generation of internal tides is considered when semi-diurnal barotropic currents encounter three-dimensional, open ocean topographies characteristic of the Hawaiian Ridge. A fully three dimensional, free surface, nonlinear, hydrostatic model (the Princeton Ocean Model) is used to simulate the internal tide generation. Two types of bathymetry are used: idealized Gaussian-shaped seamounts and islands which provide a simplified view of the generation at isolated topographic features, and realistic bathymetric data for the Hawaiian Island region. The generated wave signal for the Gaussian topographies is characterized by tidal beams which emanate from the flanks near the top of the feature. Vertical motions induced by the sloping topography lead to the generation. The strength of this forcing varies considerably depending upon the manner in which the barotropic tide interacts with the three dimensional topography. Preliminary results using the realistic topography show regions of enhanced generation, particularly in the shallow channels between the islands.

Introduction

Recent satellite altimetry [Ray and Mitchum, 1996] and acoustic transmission data [Dushaw *et al.*, 1995] analyses indicate that semidiurnal band internal tides are generated at the Hawaiian Ridge. Ray and Mitchum detect outward propagating waves with mode 1 length scales within 1000 km of the ridge axis. Given that the ridge is not a uniform feature but a chain of largely isolated seamounts and islands (Figure 1), it is plausible that the internal tide signal is a superposition of waves originating from various source topographies rather than a plane wave emanating from a contiguous ridge.

Given this 3-dimensional topography, the question of how the internal waves are generated remains an open issue. For the Hawaiian Ridge, there are several candidates for transferring energy from the barotropic tidal flow to internal tides: the advection of stratified water over sloping bathymetry, tidal flow amplification through the channels causing lee disturbances, and flow convergences around the islands. The former is the primary mechanism for the generation of internal tides at continental slopes [Baines, 1982], and is of particular in-

terest for the Hawaiian Ridge because steep topographic slopes are near-critical for M_2 frequency internal waves at many depth ranges (Figure 1).

In this paper we summarize numerical results obtained using the Princeton Ocean Model (POM) which support the notion that barotropic tidal flow over sloping topography is the primary generation mechanism for the semidiurnal internal tide at the Hawaiian Ridge. These and other POM results are discussed in more detail in Holloway and Merrifield [1999]. We also present new POM results using realistic Hawaiian Island topography.

Model description

A fully three dimensional, nonlinear, free surface, hydrostatic, sigma-coordinate, primitive equation model, incorporating a Mellor Yamada level 2.5 turbulence closure scheme (the Princeton Ocean Model, Blumberg and Mellor [1987] is used in this study). The model is forced at the horizontal boundaries following Flather [1987] which yields a deep water barotropic tidal current in the east-west direction of approximately 1 cm s^{-1} peak amplitude and of 12.42 hour period. The model runs

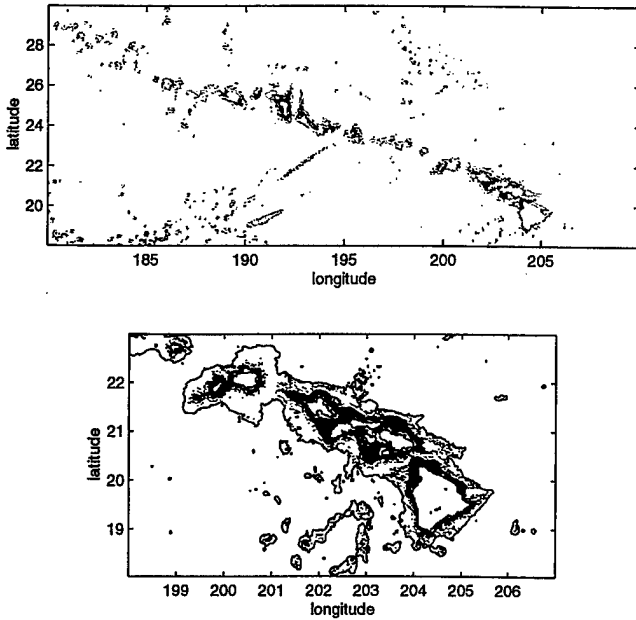


Figure 1. Regions where the topographic slope, in the direction parallel to the deep ocean M_2 tidal current, is within 2° of the M_2 internal wave characteristics as determined from mean stratification data from Levitus. Regions that are located above/below 200 m depth are indicated in blue/red.

are over 4 days, with the forcing gradually increased over a 24 hour ramp period, and the last 24 hours used for the output tidal analysis.

The Gaussian-shaped topography is specified by

$$h(x, y) = H - h_o \exp\left(-\left[\frac{(x - x_o)^2}{a^2} + \frac{(y - y_o)^2}{b^2}\right]\right) \quad (1)$$

where H is the deep water depth, h_o is the height of the topographic feature above the sea bed, $h(x, y)$ is the water depth and (x_o, y_o) is set at the center of the model domain. The values of a and b define the width of the feature. If $a=b$ the feature is referred to as a seamount, or if $h_o > H$ this becomes an island. When $b > a$, the feature becomes a ridge, orientated across the deep water tidal velocity which is in the x -direction. In each run $H=4500$ m, the domain is 600 km in the east-west (x) and north-south (y) directions with a grid spacing of 2 km over the topographic feature (an area 100 by 100 km) which is stretched to 5 km in the deep water and to 10 km near each open boundary. In all runs, 81 vertical levels are used, evenly spaced except for the bottom 5 points that are logarithmically spaced to gain better resolution near the seabed.

The realistic topography is specified by the *Smith and Sandwell* [1997] bathymetry database with a uni-

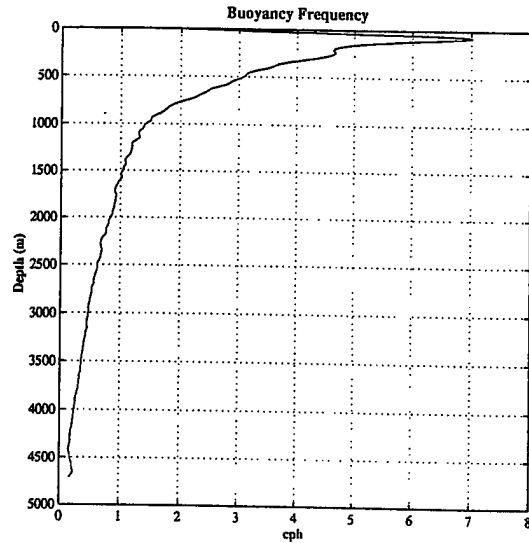


Figure 2. The average stratification profile for the Hawaii region used in the model simulations.

form horizontal grid spacing of 4 km and 61 vertical levels. The semi-diurnal tidal forcing is chosen to simulate the amplitude of the realistic deep ocean tidal flow and its near-normal direction relative to the ridge axis, however, realistic tidal forcing based on a larger-scale model has not been used in these simulations. Such a model run is currently being implemented and will be the subject of a later study.

Stratification for all runs is defined from annual average temperatures and salinities measured in the Hawaiian region (Figure 2). A latitude of 20° N is used to define the Coriolis parameter for all runs.

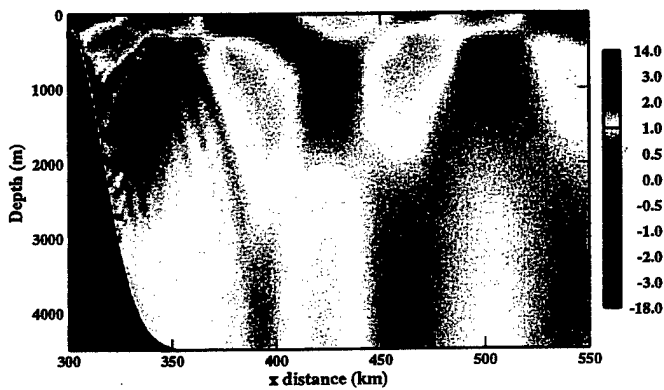
For each model run, time series of horizontal and vertical (mapped from the sigma to z coordinate) velocities and surface elevations are analyzed. The barotropic velocity is defined as the depth-averaged flow; the baroclinic horizontal velocity is the total velocity minus the barotropic component. These time series are harmonically analyzed *Foreman* [1978] to calculate M_2 amplitudes and phases of barotropic and baroclinic tidal velocities and vertical displacements. Energy fluxes are then calculated from the tidal values as described by *Holloway* [1996] and *Holloway and Merrifield* [1999].

Simplified Topography Runs

We begin with a simple Gaussian-shaped seamount to illustrate the structure of the generated internal tide and how changes to this topography affect the am-

plitude of the wave signal. We select a feature submerged 200 m below the surface with width scales of $a=b=23$ km. These values were chosen using a seamount which by inspection seemed to typify the seamounts just north of the main Hawaiian Islands. After 4 days simulation, a cross section of the instantaneous east-west flow field is presented from the center of the domain (top of the topography) looking eastward toward the model boundary (Figure 3a). A dominant tidal beam emanates from the topography with reflections off the sea surface (near 350 km and 500 km) and seabed (425 km). High wave number spatial variability occurs within the first surface-bounce of the main beam. Changing the depth of the seamount to 50 m and 500 m below the surface does not significantly alter current variances from the 200 m run (within 10%).

(a) Seamount U Velocity [cm/s]



(b) Ridge U Velocity [cm/s]

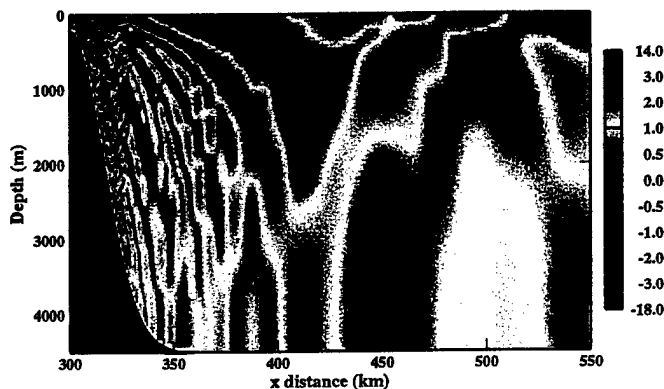


Figure 3. East-west sections (along $y=300$ km) of the u -component of the total velocity after 4 days simulation for (a) a symmetric seamount ($a=b=23$ km), and (b) an elongated ridge ($a=23$ km, $b=69$ km). Both topographies are submerged 200 m below the surface.

The internal tide signal does change significantly when we elongate the seamount in the north-south direction. We hold the east-west scale of the feature fixed at $a=23$ km and alter by a factor of 3 ($b=69$ km) the

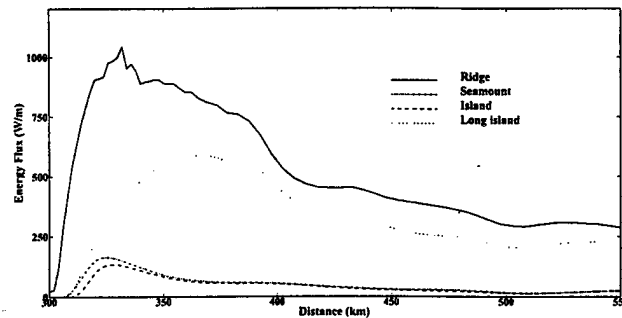


Figure 4. Depth integrated M_2 energy fluxes plotted against distance eastward from the top of the topographic feature ($x=y=300$ km) for the 200 m deep seamount and ridge, and the symmetric ($a=b=23$ km) and long ($a=23$ km, $b=69$ km) island model topographies.

north-south scale creating an asymmetric shape which we call a ridge (Figure 3b). Using the same barotropic current forcing as in the seamount run, the resulting tidal beams are much more energetic for the ridge than the seamount. Again, varying the depth of the feature (50, 500 and 1000 m) results in order 10% changes in current variance.

The contrast between the internal tide amplitude generated from the ridge and seamount runs is readily apparent in the eastward depth-integrated energy flux computed along the center axis of the features (Figure 4a). The internal tide from the ridge topography has nearly an order of magnitude higher peak energy flux, 1000 W m^{-1} compared to 150 W m^{-1} than the symmetric seamount.

Similar model runs are made for surface-piercing topographies, or islands, with symmetric ($a=b=23$ km, $h_o=5000$ m) and asymmetric ($a=23$ km, $b=69$ km, $h_o=500$ m) shapes. Unlike the seamount model tests, the barotropic current now cannot flow over the top of the feature. Again, the elongated shape or long island is a much more efficient internal tide generator than the symmetric shape (Figure 4b) and the energy fluxes are comparable, although weaker, than the submerged test cases. As with the submerged topography runs, the internal tide is characterized by a dominant beam originating at the shallower depths of the island flanks.

As discussed in *Holloway and Merrifield* [1999], the differences in these model runs is attributed to the manner in which the topography perturbs the barotropic tidal flow. To illustrate this point, we examine the forcing term for baroclinic motions caused by oscillatory barotropic flow over a sloping bottom as described by *Baines* [1982]

$$F(x, z) = \frac{N^2(z)w_1(x, z)}{\omega} \quad (2)$$

where N is the buoyancy frequency, w_1 is the vertical velocity that results from the bottom boundary condition of no flow through the sloping boundary, and ω is the frequency of oscillation. Here, F is given as the peak amplitude of the forcing term over a semi-diurnal cycle. In terms of the peak barotropic mass flux, Q , w_1 can be expressed as

$$w_1(x, z) = -Qz(h^{-1})_x \quad (3)$$

where h is bottom depth and the subscript denotes a partial derivative with respect to x . For the model topographies, y derivatives are zero at the center line of the feature ($y=300$ km). The specification of Q is often made on a regional basis under the assumption that the barotropic length scales are much longer than the topographic scales. In such circumstances, F is specified from the bottom slope and stratification in addition to the large-scale Q .

For the seamount and ridge topography runs, Q (in the open ocean away from the topography), N , and h_x along $y=300$ km are identical. Yet, F is an order of magnitude larger for the ridge than the seamount (Figure 5). This seemingly contradictory result is due to the variation of Q near the topography. The ridge shape is apparently more effective than the symmetric seamount in causing the barotropic flow to cross isobaths, thus leading to vertical velocities which generate the internal tide. In Figure 6, the barotropic flow is seen to flow relatively undisturbed around the seamount compared to the more dramatic velocity changes induced by the ridge. The same holds true for the island runs. Thus, the details of the barotropic flow field at the topography are essential for determining the baroclinic response.

Realistic Topography Run

Internal tide generation over realistic topography is investigated for the Hawaiian Islands at the southern end of the chain. The islands are separated by shallow channels (100-500 m) in the center of the group. The islands of Hawaii and Kauai are separated from the central island cluster by deeper passages (1000 m). We force a semidiurnal tidal current orientated perpendicular to the island chain (along the y axis in Figure 7) with a deep ocean speed of approximately 1 cm s^{-1} .

We measure the strength of the generated internal tide by the depth integrated energy flux (Figure 7).

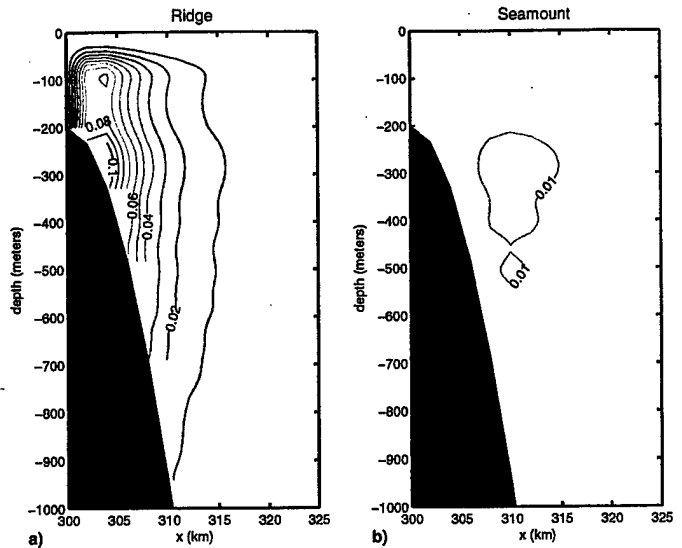


Figure 5. The peak forcing term, F_r in equation 2, for the 200-m deep seamount and ridge. Units are cm s^{-2} .

The strongest generation occurs in the Kauai Channel (200-300 km distance on the x -axis) between the islands of Kauai and Oahu. The strongest energy flux vectors originate from the shallow ridge adjacent to Oahu. Peak amplitudes reach nearly 5000 W m^{-1} near the ridge and fall off below 1000 W m^{-1} after approximately 100 km distance. Weaker internal tides originate from the Kaiwi Channel between Oahu and Molokai ($x=350$ km) and in the Alenuihaha Channel between Maui and Hawaii ($x=550$ km). Strong flux amplitudes but with variable direction occur along the flanks of the island of Hawaii.

This simulation demonstrates that appreciable semi-diurnal internal tide energy can be generated in the island region and that the forcing is highly variable in space. A more realistic simulation will require better boundary conditions for the barotropic forcing based on a regional tide model.

One consideration is whether the internal tide generation for the realistic bathymetry occurs in the same manner as the idealized topography runs, namely the advection of stratified water over sloping bathymetry. The occurrence of large baroclinic energy fluxes in the channels raises the possibility of amplified tidal flows in the constricted passages with associated lee waves. To estimate this effect, we consider the Froude number, $F_r = u/c$ with u the barotropic tidal flow speed and c the internal wave phase speed. In the model simulation, u is approximately 10 cm s^{-1} through the Kauai Channel, an order of magnitude larger than the open water speed. Assuming a water depth in the channel of 100 m and a

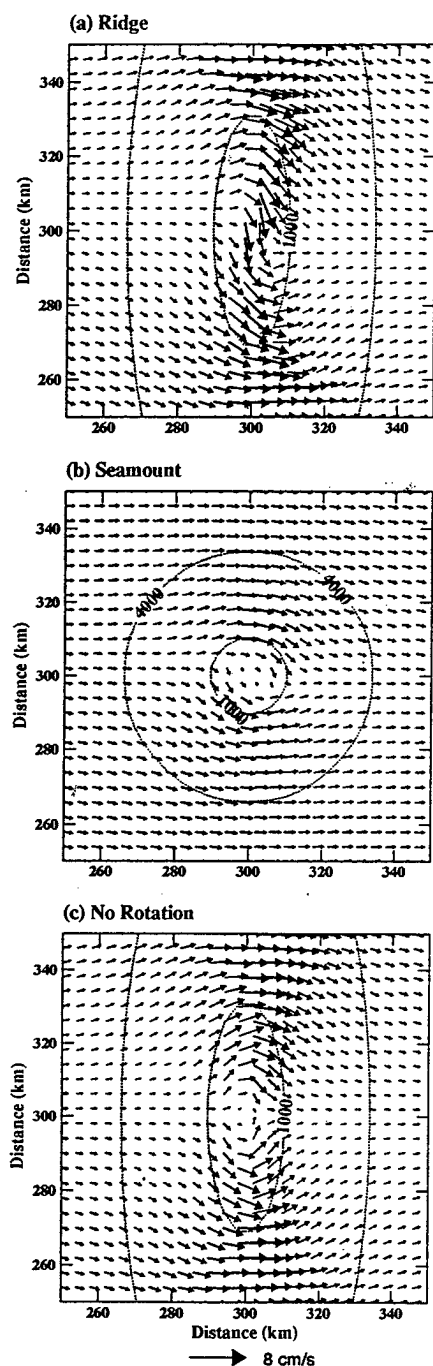


Figure 6. Plan views of the instantaneous barotropic (depth averaged) velocity vectors after 3 days simulation for (a) the 200-m submerged ridge, (b) the 200-m seamount, and (c) the 200-m submerged ridge with the Coriolis parameter set to zero. Depth contours in meters are also shown.

constant stratification of 0.007 s^{-1} , F_r is approximately 0.4. A value in this range may be conducive for weak lee wave generation [e.g., *Maxworthy, 1979*], although the wave amplitude will be sensitive to the details of the stratification and water depth. Further study using realistic tidal forcing is needed to determine the extent to which lee waves contribute to the generated signal in this region.

Summary

The model simulations suggest that tidal flow past a single seamount or island in the Hawaiian Ridge can generate an appreciable internal tide that propagates away to the open ocean. The interaction of the barotropic tide with the three-dimensional topography strongly affects the internal tide amplitude. Using the open ocean current with the local topographic gradient, a method that has been used for more two-dimensional continental slope topographies, can give misleading results when applied to open ocean features. For example, elongating a symmetric seamount to a horizontal aspect ratio of 3:1 increases the energy flux of the generated internal tide by an order of magnitude. The perturbation of the barotropic tidal flow in the near-field of the topography accounts for this difference.

Given the importance of determining the local vertical velocity, two limiting factors for modeling the internal tide at open ocean topographies are the accuracies of the bathymetric data and the regional barotropic tidal models. Recent satellite observations have produced significant improvements in both areas [*Smith and Sandwell, 1997; Egbert, 1997*]. Preliminary model simulations of the Hawaiian Islands using realistic topography with an idealized semi-diurnal tidal forcing indicate internal tide generation occurring preferentially in the major channels between the islands. The possibility of amplified channel currents leading to weak lee wave effects requires further study.

Acknowledgments. We are grateful to Shikiko Nakahara and Holly Dail for assistance with the figures. This work was supported in part by NSF grant OCE-9819519.

References

- Baines, P. G., On internal tide generation models, *Deep Sea Res.*, 29, 307-338, 1982.
- Blumberg, A. F. and G. L. Mellor, A description of a three-dimensional coastal ocean model, p1-16, In: *Three-dimensional coastal ocean models, Vol. 4*, Ed. N. Heaps, pp208, American Geophys. Union, Washington, DC, 1987.
- Dushaw, B. D., B. D. Cornuelle, P. F. Worcester, B. M. Howe, and D. S. Luther, Barotropic and baroclinic tides

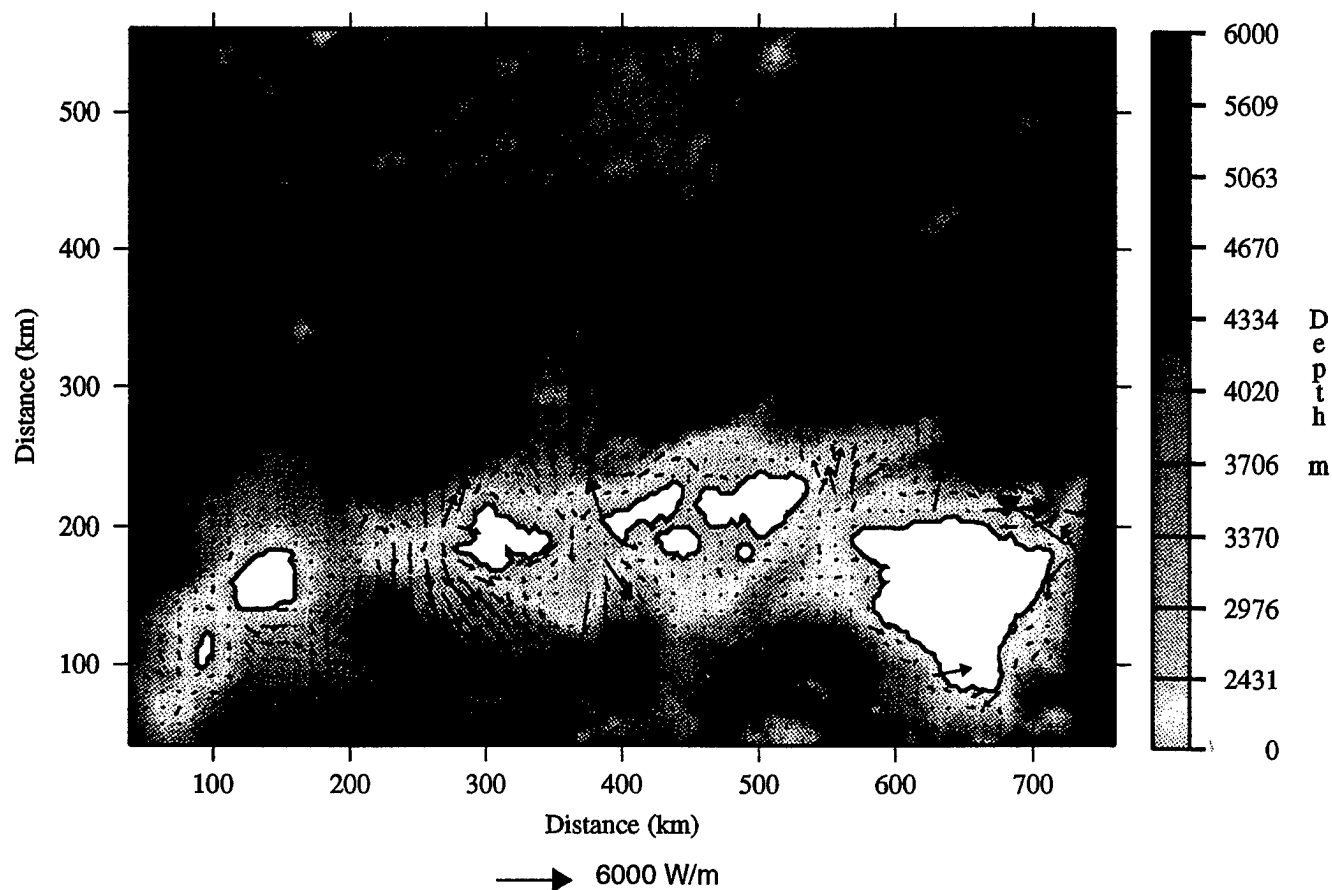


Figure 7. Depth integrated baroclinic energy flux computed for the Hawaiian Islands region for realistic bathymetry and simplified semi-diurnal tidal forcing.

- in the Central North Pacific Ocean determined from long range reciprocal acoustic transmissions, *J. Phys. Oceanogr.*, **25**, 631-647, 1995.
- Egbert, G. D., Tidal data inversion: interpolation and inference, *Prog. Oceanogr.*, **40**, 53-80, 1997.
- Flather, R. A., A tidal model of the northeast Pacific, *Atmos. Ocean*, **25**, 22-45, 1987.
- Foreman, M. C., Manual for tidal current analysis and prediction. Inst. Ocean Sci. Victoria, B.C., *Pacific Marine Sci. Rep.* 78-6, 1978.
- Holloway, P.E., A numerical model of internal tides with application to the Australian North West Shelf, *J. Phys. Oceanogr.*, **26**(1), 21-37, 1996.
- Holloway, P. E., and M. A. Merrifield, Internal tide generation by seamounts, ridges and islands. Submitted to *J. Geophys. Res.*, 1999.
- Maxworthy, T., A note on the internal solitary waves produced by tidal flow over a three-dimensional ridge, *J. Geophys. Res.*, **84**, 338-346, 1979.
- Ray, R. D. and G. T. Mitchum, Surface manifestation of internal tides generated near Hawaii. *Geophys. Res. Lett.* **23**, 2101-2104, 1996.
- Smith, W. H. F., and D. T. Sandwell, Global sea floor topography from satellite altimetry and ship depth soundings, *Science*, **277**, 1956-1962, 1997.

This preprint was prepared with AGU's \LaTeX macros v4, with the extension package 'AGU++' by P. W. Daly, version 1.6a from 1999/05/21.

The Hawaii Ocean Mixing Experiment (HOME): Is the Abyssal Stratification Maintained by Tidalgenic Mixing?

D.S. Luther and the HOME PIs*

School of Ocean and Earth Science and Technology, University of Hawaii, Honolulu, Hawaii

Abstract. Physical processes accounting for the flow of energy from the external tide to small scale turbulence will be studied during this multi-institutional experiment funded by the National Science Foundation. The topography of the Hawaiian Ridge is expected to catalyze these processes. Observations and numerical models will be employed to elucidate the physics and spatial variability of the energy pathways. Direct and indirect techniques will be employed to quantify energy fluxes.

Introduction

HOME is predicated on the assumption that the vertical structure of the abyssal¹ thermal field is maintained primarily by a balance between the downward diffusion of heat by mechanical mixing and the upward advection of cold water. *Munk's* (1966) global budget for this balance has been updated by *Munk and Wunsch* (1998; hereafter, MW98) in an article that is sobering for its enumerations of the large uncertainties in our knowledge of how the abyssal stratification is maintained.

The global vertical advection-diffusion balance requires a diapycnal diffusivity of $K_p \sim 10^{-4} \text{ m}^2/\text{s}$ and a power throughput of $\sim 2 \text{ TeraWatts (TW)}$. Yet in situ mechanical energy sources (mainly internal waves) can generate diapycnal diffusivities of only $\sim 10^{-5} \text{ m}^2/\text{s}$ (e.g., *Gregg*, 1989; *Ledwell et al.*, 1993; *Toole et al.*, 1994). How then is the stratification maintained? Without sufficiently strong downward mixing of heat in the tropics and sub-tropics, the deep ocean should have a weaker vertical temperature gradient, with probably weaker and shallower thermohaline convection cells. Clinging to the in situ mechanical mixing² model, eschewing the possibility of even partial direct ventilation of the abyss (which displaces the required mixing of the abyssal waters from the deep ocean to the surface at high latitudes), higher levels of mixing observed in proximity to constrained, acute and rough topographic features (e.g., *Hogg et al.*, 1982; *Kunze and Toole*, 1997; *Lueck and Mudge*, 1997; *Polzin et al.*, 1997) provide one exit from this quandary as postulated by *Munk* (1966), although quantitatively not an obvious one (e.g., *Kunze and Toole*, 1997). The products of the near-boundary mixing, but not the turbulence itself, are assumed to be advected isopycnally into the ocean's interior (MW98).

Several sources of mechanical energy are available for mixing near sub-thermocline topography, including mean

flows in constricted regions (e.g., sills and fracture zones; *Hogg et al.*, 1982), mesoscale currents (e.g., *Armi*, 1978), external³ and internal tides, and high frequency internal waves (e.g., *Eriksen*, 1985). HOME is focused on the tidal energy sources for several reasons: (i) tidal currents are often the most energetic currents in the deep sea; (ii) recent observations show relatively large internal tides well away from continental boundaries yet close to mid-ocean acute topography (e.g., near Hawaii; *Dushaw et al.*, 1995; *Ray and Mitchum*, 1996); and, (iii) the global application of simple 2-D internal tide generation models (*Sjöberg and Stigebrandt*, 1992; *Morozov*, 1995) and global numerical models (e.g., *Egbert*, 1997) suggest that much more external tide energy is dissipated via the internal tides than the long held estimate of 10% (which is $\sim 4 \text{ TW}$). From a practical point of view, the determinism of the tides should set up temporal (e.g., the spring-neap cycle) and spatial patterns of variability (mixing) that are observationally distinct.

This paper will briefly describe the goals and strategy of HOME. More complete details of the experiment motivation, design and analysis techniques can be found in the full text of the HOME proposal on the web site <http://chowder.ucsd.edu/home/>. A list of HOME participants and their involvement in the various HOME programs is provided in Table 1.

General Goals

HOME investigators have chosen to look for tidally driven (tidalgenic) mixing at a mid-ocean topographic feature, the Hawaiian Ridge, because mid-ocean features are often (and Hawaii in particular is) oriented perpendicular to the principal axes of the external tide currents, which logically should result in the formation of more baroclinic phenomena than at continental borders⁴

¹ "abyssal" is used here to refer to the ocean below the main thermocline that is still well above the bottom.

² "mixing" hereafter refers to diapycnal mixing.

* The HOME PIs are listed in Table 1.

³ "external" refers to the surface (barotropic) tide.

⁴ Whether the corrugations of the continental boundaries are significant sources of barotropic to baroclinic tide energy conversion is an unresolved issue.

Table 1. HOME Principal Investigators

	HOME Programs*				
	HDA	MOD	SUR	FF	NF
NASA					
Richard Ray		X			
NOAA/NMFS					
Russell Brainard	X				
Oregon State Univ.					
Timothy Boyd			X		X
Douglas Caldwell			X		X
Gary Egbert		X			
Murray Levine			X		X
James Moum ‡			X		X
Scripps Inst. of Ocean.					
Bruce Cornuelle				X	
Jean Filloux				X	
Walter Munk				X	X
Robert Pinkel # ‡			X	X	X †
Daniel Rudnick ‡			X †		X
Jeffrey Sherman			X		X
Peter Worcester ‡				X †	
Univ. of Hawaii					
Eric Firing	X				
Pierre Flament					X
Douglas Luther ‡	X †			X	X
Mark Merrifield ‡		X †			X
Univ. of New South Wales					
Peter Holloway		X			
Univ. of Washington					
Brian Dushaw				X	
Michael Gregg			X		X
Bruce Howe				X	
Eric Kunze ‡			X		X
Craig Lee			X		X
Jack Miller			X		X
Thomas Sanford			X		X
Woods Hole Ocean. Inst.					
Alan Chave				X	

Overall HOME Project Coordinator
† Program Leaders
‡ HOME Steering Committee
* HOME Programs:
HDA - Historical Data Analysis
MOD - Modeling
SUR - Survey
FF - Farfield
NF - Nearfield

where the currents tend to oscillate parallel to the boundary. Therefore, the principal HOME goal is to determine whether mid-ocean topographic features such as the Hawaiian Ridge are significant sites of topographically catalyzed, tidalgenic mixing.

There are a number of paths along which energy can travel from the external tides to mechanical mixing, such

as direct generation of boundary layer turbulence by external currents rubbing along the boundaries of channels, or generation of internal tides at sills or critical slopes which propagate away from the source region before losing part of their energy to mixing via instability mechanisms. To obtain a bound on all the possible sinks for tidal energy around the Hawaiian Ridge, a second goal of HOME is to create a simple, quantitative energy budget for Hawaiian tides. Elements of the budget will include the energy lost from the external tide in the vicinity of the Hawaiian Ridge, the energy radiated away from the Hawaiian Ridge in low-mode internal tides, and the observed energy dissipation in tidalgenic mixing in the vicinity of the Hawaiian Ridge.

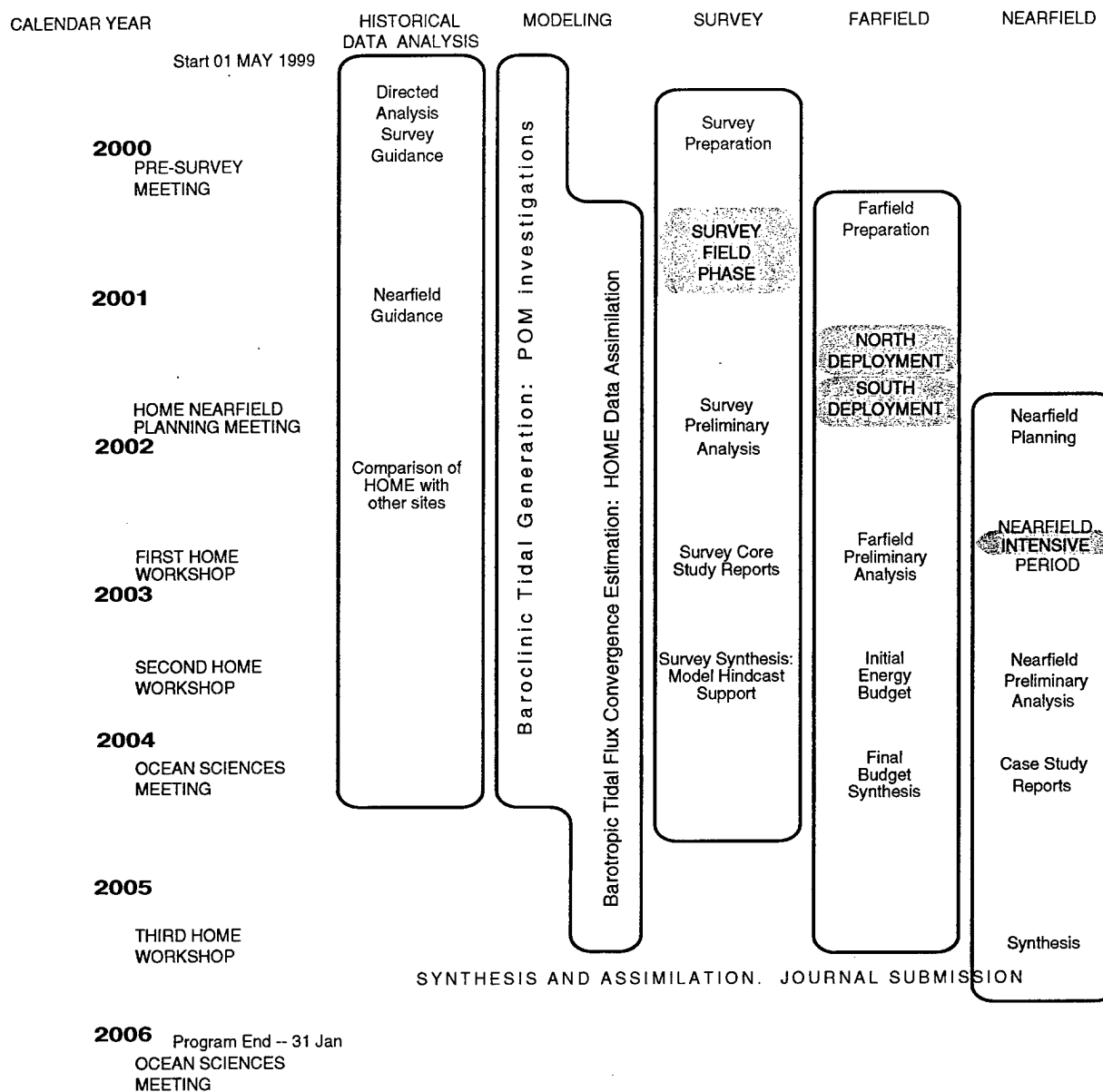
In order to have a hope that the HOME program produces information that can be usefully extrapolated to other topographic environments and that can be employed in improving estimates of the amount of tidal energy available for maintaining the abyssal stratification, the specific mechanisms of energy transfer from the external tide down to the small-scale mixing must be observed. This constitutes the third goal of HOME: to observe the principal mechanisms which transfer energy from the large scale tides to turbulent motions. How do these mechanisms depend on the structure of the topography? Do they work differently in the deep sea versus the upper ocean? How do the depth and lateral dependencies of K_p rely upon the characteristics of the topography and the tides?

Ultimately, global generalization of the HOME results will depend on how well we understand the energy transfer mechanisms, how well we have quantified them, and how well we can model them either directly or parametrically. Thus, the final goal of HOME is to validate numerical models of external tide propagation and dissipation, and models of internal tide generation, propagation and dissipation, all in the presence of acute and irregular topography.

In the best of all possible outcomes, HOME will advance understanding of topographically catalyzed mixing and will contribute significantly to the classical problems of tidal dissipation, global diapycnal mixing, and the maintenance of the abyssal stratification. HOME will contribute to the advancement of tidal models through improved parameterizations of energy dissipation processes. And, HOME will contribute to the advancement of ocean and climate modeling through improved parameterizations of abyssal mixing processes.

Strategy

The HOME goals will be achieved through a judicious integration of modeling and observational enterprises. The timeline for HOME activities is presented in Table 2. HOME begins with a year of analysis of various historical

Table 2. HOME Time-line⁵

data⁶ to provide preliminary information on the locations and strengths of enhanced mixing in relation to topography. Coincident modeling will suggest whether these sites are related to the generation of internal tides.

⁵ Table prepared by R. Pinkel.

⁶ Historical data include the following: near-surface currents from shipboard ADCP transits to/from the Hawaii Ocean Time-series (HOT) stations (see the web site http://www.soest.hawaii.edu/HOT_WOCE/), and to/from Hawaiian ports by various oceanographic vessels, including the R/V *Cromwell* that makes 10 transits a year along the Hawaiian Archipelago (see the ADCP archive <http://ilikai.soest.hawaii.edu/sadcp/>); repeated CTD's from several sites occupied during HOT and Hawaii-to-Tahiti Shuttle cruises; CTD's from oceanographic cruises in the vicinity of the Hawaiian Islands; a variety of nearshore moored current meter data; and more.

This information will be employed in the design of the first field program, the survey.

In the Summer and Fall of 2000, a survey of the ridge from 150° W to 165° W will employ both shallow and deep instruments (towed, dropped, and moored) to gather information on the principal phenomena involved in mixing, their geographic distribution and, to a lesser degree, their temporal variability. A schematic of the survey field work is presented in Figure 1. Table 3 summarizes the participants and tools to be used in the survey. Descriptions of the instrumentation can be found in the HOME proposal on the web page previously cited.

Based on the information obtained from the historical data analysis, modeling and survey efforts, a specific site will be selected for an intensive nearfield experiment.

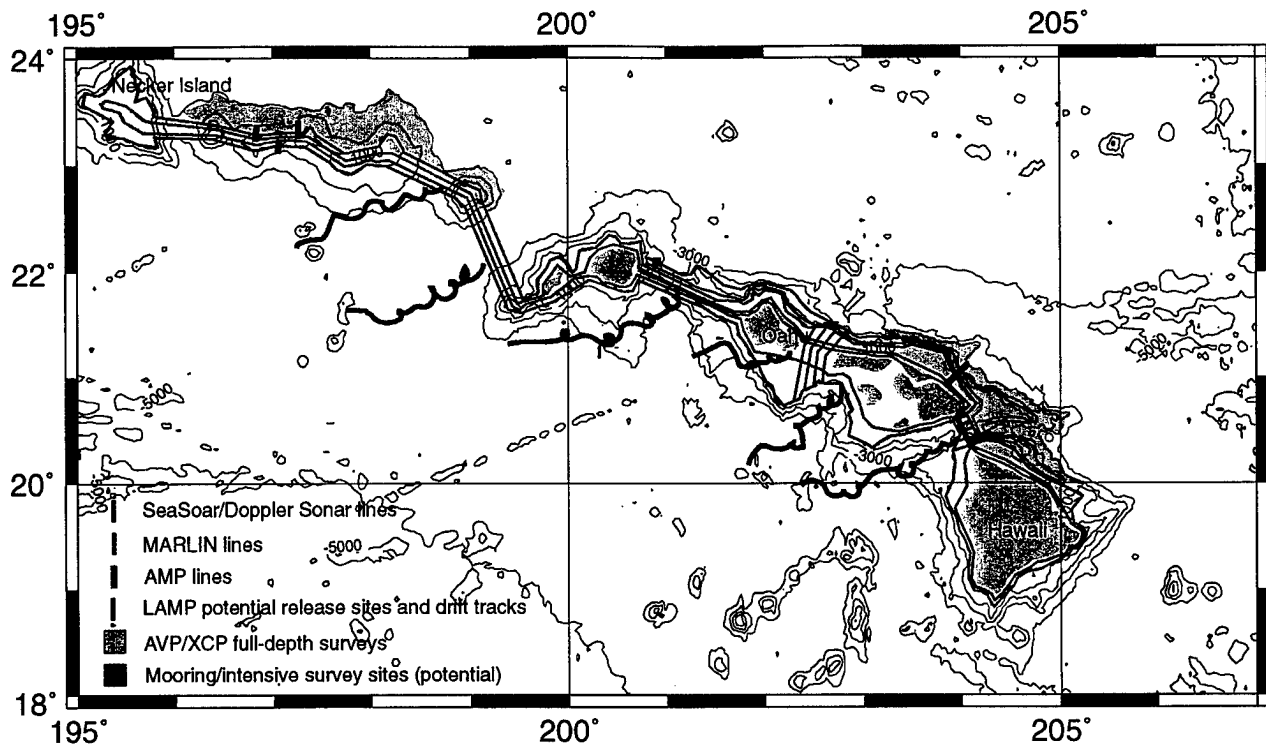


Figure 1. Schematic display of the geographic extent of the survey program sampling. This plan will evolve as information is obtained from the historical data analysis and modeling programs, and from the real-time analysis of the survey data. SeaSoar Doppler Sonar and MARLIN lines represent towed sampling, while AMP and AVP/XCP regions mark areas for sampling by dropped profilers. LAMP drifter tracks are represented by wiggly lines. Moorings (red squares) will be deployed for 3 months. See Table 3 for a list of instrumentation, variables to be measured, and sampling characteristics. (Figure prepared by C. Lee and D. Rudnick.)

This site will encompass topography ranging from 500 m to over 3000 m in depth, over which significant tidalgenic mixing will have been observed. The nearfield program will study the spatial and temporal structures of mixing processes in detail in order to understand the mechanisms involved, quantify mixing rates, determine the explicit connections between the mixing and the deep sea environment, and develop parameterizations of the dominant processes.

As part of the nearfield program, moorings and a high frequency radar system (e.g., Paduan and Rosenfeld, 1996) will be deployed for a full year to establish the long-term surface and sub-surface environmental characteristics of the site. During the Fall, 2002, a six-week intensive observation period will be undertaken using much of the same instrumentation as employed during the survey (Table 3), but concentrated in the smaller nearfield site to achieve greater spatial and temporal definition.

A farfield component of HOME will be deployed in 2001, between the survey and nearfield experiments (Table 2). The farfield experiment will obtain measurements of the external tidal energy flux via a combination of bottom pressure (Pb) measurements with measurements of the external tide currents using both

tomographic (e.g., Dushaw et al., 1995) and horizontal electric field (HEM) techniques (e.g., Filloux et al., 1991). Figure 2 displays the farfield array of instruments. Energy flux convergence at the ridge will be estimated directly, but raw fluxes will also be used to tune an external tide model for a potentially more accurate flux divergence calculation.

The outward flux of low mode internal tide energy will also be measured during the farfield experiment, principally by tomography (e.g., Dushaw et al., 1995, Dushaw and Worcester, 1998). The specific vertical modal structure of the internal tides within the farfield array will be determined by high resolution current and stratification profiling from the R/P FLIP.

Throughout the duration of HOME, numerical modeling efforts will be focused on elucidating the generation mechanisms and structures of the internal tides around Hawaii. HOME experimental results (data and analysis products) will be assimilated into regional barotropic and baroclinic tide models in order to rationally extend the HOME tidal energy flux convergence estimates to the whole length of the ridge (and eventually globally) and to study further the structure and decay characteristics of the internal tides as a function of distance from the source regions.

Table 3. Survey Participants and Tools*

P.I.	Instrument	Variables	Vertical Resolution, Range	Horizontal Resolution, Range	Temporal Res., Tow Speed, Profile Time
Rudnick	SeaSoar CTD Transmissometer	T, S, Optical Transmissivity	Sawtooth: 1 m res. 400 m range	Sawtooth 3 km res. Level: 4 m res.	8 knots (86 km in 6 h)
Pinkel	Doppler Sonar	u, v	3 m res. to 400 m 10 m res. to 1 km	3 km res.	8 knots
Sherman	LAMP	T, S, χ_T	400 m range	Determined by current	3 h
Gregg, Miller	AMP	T, S, ϵ , χ_T	1500 m range	1 km	15 min to 300 m
Gregg, Miller	BioSonics echo sounder	Acoustic backscatter	200 m range	8 m	8 knots
Kunze, Sanford, and Lee	AVP	u, v, w, T, S, ϵ , Optical Transmissivity	1-2 m res. 10 m from bottom	15 km	4 h to 4500 m
Kunze, Sanford, and Lee	XCP	u, v, T	O(m) res. 1600 m range	15 km	6 profiles per 12 h night
Moum, Caldwell	MARLIN	u, v, T, S, ϵ , χ_T , χ_S , TKE, Optical Transmissivity	u, v: O(m) res. 200 m range from body to 2500 m	T, S, ϵ , χ : O(m)	2 knots (22 km in 6 h)
Levine, Boyd	Moorings (2) ADCP Temperature Conductivity	u, v, T, S	u, v: 8 m res. bottom 400 m range T: 9/mooring S: 4/mooring	N/A	10 min

* Table prepared by D. Rudnick.

Relevance of HOME

A major assumption motivating HOME, that the structure of the abyssal stratification is fundamentally determined by in situ mechanical mixing rather than ventilation at high latitudes, combined with existing knowledge of the magnitude of mechanical mixing away from topography leads to the hypothesis that the required mixing must occur via phenomena engendered at the water-earth boundary. The existence of such "boundary" mixing, being certainly unevenly distributed in space, could have a fundamental impact on the qualitative character of the ocean circulation, on the strength of the meridional overturning circulation (MOC), and on the role of the ocean in fixing the present climate state as well as past climate states. For example, if boundary mixing provides diapycnal fluxes, the depth-dependence of the large-scale diffusivity cannot be considered to be known; plausible variations in the depth-dependence lead to different signs for the direction of the mean meridional flows in the ocean interior (Gargett, 1984). And, horizontal localization of mixing can produce significant qualitative changes in the expected ocean circulation (e.g., Marotzke, 1997; Samelson, 1998).

The potential importance of abyssal mechanical mixing is firmly advanced by *Munk and Wunsch* (1998): "the strength of the MOC and associated [poleward] heat flux may well be primarily determined not by the high-latitude buoyancy forcing, but by the power available to return the fluid to the surface layers", and "the equator-to-pole heat flux of 2000 TW associated with the meridional overturning circulation would not exist without the comparatively minute [~ 2 TW] mechanical mixing sources. Coupled with the finding that mixing occurs at a few dominant sites, there is a host of questions concerning the maintenance of the present climate state, but also that of paleoclimates and their relation to detailed continental configurations [and bathymetry], the history of the earth-moon system, and a possible great sensitivity to details of the wind system." (Bracketed text inserted by us.)

In simplest terms, if there is no mechanical energy available to mix heat downward from the surface, within a few thousand years the oceans would consist of a very cold nearly isothermal layer beneath a relatively thin, warm surface layer with a stratification that is principally determined by ventilation and which has only a very weak convective circulation. Without a strong MOC, poleward heat flux would be dramatically reduced. In the geologic

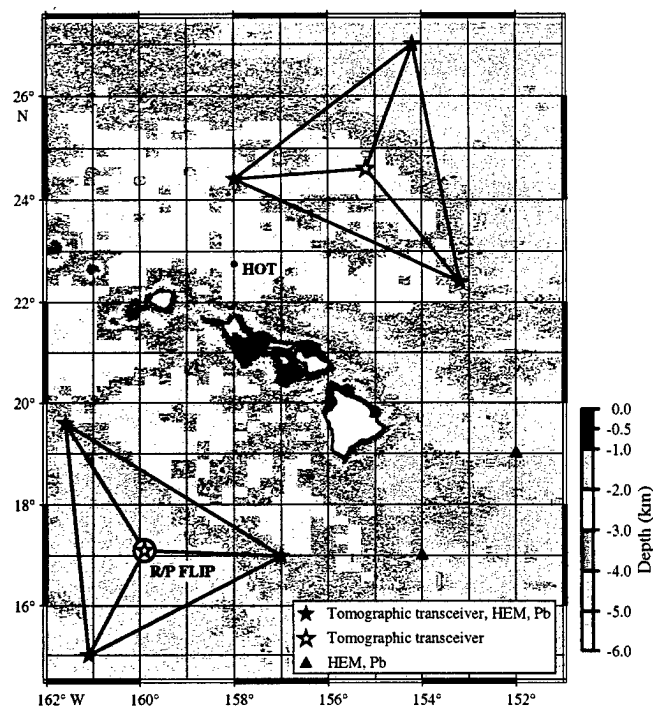


Figure 2. Map of the Hawaiian Islands and vicinity, displaying the probable locations of the tomographic transceivers co-located with the HEM/Pb pairs (solid stars), the tomographic transceivers alone (open stars), the HEM/Pb pairs alone (triangles) and the location where R/P Flip will be moored for a duration of one month (open circle). The shaded topography is taken from the Smith and Sandwell (1997) bathymetric dataset. (Figure prepared by P. Worcester.)

past, tidal dissipation was generally weaker because the tides were less resonant, and mixing in the deep ocean may have been much less energetic than today leading to a significantly different MOC than at present and much different abyssal circulation patterns.

We must emphasize at this point that the processes maintaining the abyssal stratification are poorly understood. How important is direct ventilation? Is it strong enough to obviate the need for more abyssal mechanical mixing than is provided by the internal wave field? On the other hand, if bottom water formation is much greater than the 30 Sv assumed by MW98, both ventilation and significant mechanical mixing at the boundaries may be required to maintain the abyssal stratification. That the maxima in boundary mixing have not yet been observed is certainly likely. What processes lie waiting to be discovered?

References

- Armi, L., 1978: Some evidence of boundary mixing in the deep ocean, *J. Geophys. Res.*, **83**, 1971-1979.
- Dushaw, B.D., B.D. Cornuelle, P.F. Worcester, B.M. Howe and D.S. Luther, 1995: Barotropic and baroclinic tides in the central North Pacific Ocean determined from long-range reciprocal acoustic transmissions, *J. Phys. Oceanogr.*, **25**, 631-647.
- Dushaw, B.D. and P.F. Worcester, 1998: Resonant diurnal internal tides in the North Atlantic, *Geophys. Res. Lett.*, **25**, 2189-2193.
- Egbert, G.D., 1997: Tidal data inversion: interpolation and inference, *Prog. in Oceanogr.*, **40**, 53-80.
- Eriksen, C.C., 1985: Implications of ocean bottom reflection for internal wave spectra and mixing, *J. Phys. Oceanogr.*, **15**, 1145-1156.
- Filloux, J.H., D.S. Luther and A.D. Chave, 1991: Update on seafloor pressure and electric field observations from the north-central and northeast Pacific: tides, infratidal fluctuations, and barotropic flow; in: *Tidal Hydrodyn.*, B. Parker (ed.), New York, John Wiley, pp. 617-640.
- Gargett, A.E., 1984: Vertical eddy diffusivity in the ocean interior, *J. Mar. Res.*, **42**, 359-393.
- Gregg, M.C., 1989: Scaling turbulent dissipation in the thermocline, *J. Geophys. Res.*, **94**, 9686-9698.
- Hogg, N., P. Biscaye, W. Gardner and W.J. Schmitz, 1982: On the transport and modification of Antarctic Bottom Water in the Vema Channel, *J. Mar. Res.*, **40**, 231-263.
- Kunze, E., and J.M. Toole, 1997: Tidally-driven vorticity, diurnal shear and turbulence atop Fieberling Seamount, *J. Phys. Oceanogr.*, **27**, 2663-2693.
- Ledwell, J.R., A.J. Watson and C.S. Law, 1993: Evidence for slow mixing across the pycnocline from an open-ocean tracer-release experiment, *Nature*, **364**, 701-703.
- Lueck, R.G., and T.D. Mudge, 1997: Topographically induced mixing around a shallow seamount, *Science*, **276**, 1831-1833.
- Marotzke, J., 1997: Boundary mixing and the dynamics of 3-dimensional thermocline circulation, *J. Phys. Oceanogr.*, **27**, 1713-1728.
- Morozov, E.G., 1995: Semidiurnal internal wave global field, *Deep-Sea Res.*, **42**, 135-148.
- Munk, W., 1966: Abyssal recipes, *Deep-Sea Res.*, **13**, 707-730.
- Munk, W. and C. Wunsch, 1998: Abyssal recipes II: energetics of tidal and wind mixing, *Deep-Sea Res. I*, **45**, 1978-2010.
- Paduan, J.D. and L.K. Rosenfeld, 1996: Remotely sensed surface currents in Monterey Bay from shore-based HF radar (Coastal Ocean Dynamics Application Radar), *J. Geophys. Res.*, **101**, 20669-20686.
- Polzin, K.L., J.M. Toole, J.R. Ledwell and R.W. Schmitt, 1997: Spatial variability of turbulent mixing in the abyssal ocean, *Science*, **276**, 93-96.
- Ray, R.D., and G.T. Mitchum, 1996: Surface manifestation of internal tides generated near Hawaii, *Geophys. Res. Lett.*, **23**, 2101-2104.
- Samelson, R.M., 1998: Large-scale circulation with locally enhanced vertical mixing, *J. Phys. Oceanogr.*, **28**, 712-726.
- Sjöberg, B. and A. Stigebrandt, 1992: Computation of the geographical distribution of the energy flux to mixing processes via internal tides and the associated vertical circulation in the oceans, *Deep-Sea Res.*, **39**, 269-291.
- Smith, D.K. and D. Sandwell, 1997: Global sea floor topography from satellite altimetry and ship depth soundings, *Science*, **277**, 1956-1962.
- Toole, J.M., K.L. Polzin and R.W. Schmitt, 1994: Estimates of diapycnal mixing in the abyssal ocean, *Science*, **264**, 1120-1123.

Numerical Simulations and Observations of the Internal Tide in a Submarine Canyon

Leslie K. Rosenfeld and Jeffrey D. Paduan

Naval Postgraduate School, Monterey, California

Emil T. Petruncio

Naval Meteorology and Oceanography Command, Stennis Space Center, Mississippi

J. Eduardo Goncalves

University of São Paulo, Brazil

Abstract. Observations and model simulations of internal waves in and around the Monterey Canyon are described here with particular focus on the internal tide generated through interaction of the basin-scale barotropic tide and local topography. Observations reveal strong internal tides along the axis of the canyon near the canyon head. Currents are intensified near the bottom and observed to have both onshore-propagating and standing configurations at different times and stratification conditions. Bottom-mounted ADCP observations from within the canyon axis in depths around 300 m confirm bottom intensified fluctuations throughout the internal wave band. Furthermore, strongly nonlinear fronts or bores are associated with the tidal-band fluctuations. Numerical simulations forced by semidiurnal sea level fluctuations offshore using both idealized and realistic representations of the local topography are used to investigate internal tide generation and propagation in the coastal zone. Canyons with near-critical bottom slopes play a role in bottom intensification, while the actual complex topography leads to significant horizontal variations in the internal wave characteristics on scales of less than 10 km.

1. Introduction

In the proceedings from a previous 'Aha Huliko'a Workshop, Hickey (1995) reviewed what was known about circulation in and around submarine canyons. In this paper we focus on a particular canyon, the Monterey Canyon (MC) off central California (Figure 1). We present the current state of knowledge pertaining to the internal wave field in MC, with emphasis on the internal tide both from an observational and modeling perspective. The head of MC lies within 100 m of Moss Landing harbor (Figure 2). Within the confines of Monterey Bay the axis of the canyon lies, with some meandering, in the cross-shore direction (080°-260°T), bisecting the bay. Between the mouth of the bay and the canyon head, a distance of approximately 20 km, the floor of the canyon rises from 1000 m to 100 m with a slope that varies between 1.7 and 2.6°. Over the same distance, the canyon width (defined as the distance between the 150 m isobaths on the canyon rims) decreases from approximately 11 km to nearly 2 km.

Monterey Bay sea level fluctuations are characterized by a mixed, predominantly semidiurnal tide. The

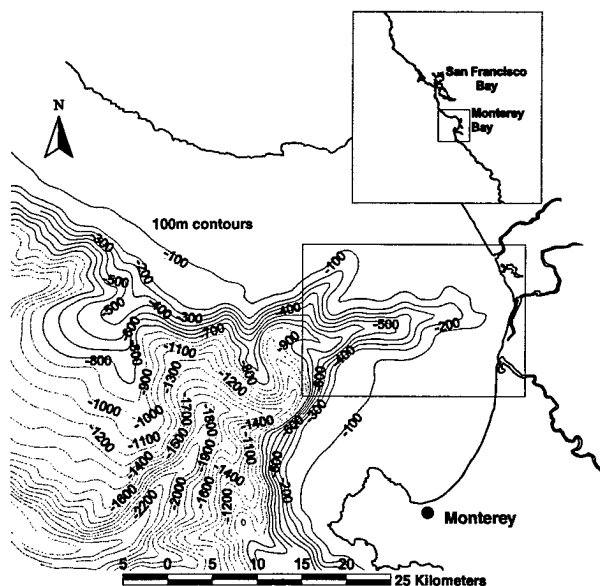


Figure 1. The Monterey Bay, California study site. Canyon measurements described here are from the area within the rectangular box.

oscillates. The largest constituent, M_2 , has an amplitude of 49 cm, and the second largest constituent, K_1 , has an amplitude of 24 cm (Petruncio, 1993). While previous CTD observations indicated the presence of large internal tides in Monterey Canyon (Broenkow and McKain, 1972), it was surface current data derived from HF radar (CODAR) that inspired our interest in this topic. Tidal analysis of several 30-d periods of surface current records revealed semidiurnal currents an order of magnitude larger than expected (10^1 s of cm s^{-1} as opposed to a few cm s^{-1}) based on sea level amplitudes, and perhaps more interestingly, the semidiurnal surface currents were out of phase with what one would expect from looking at sea level; i.e. the surface currents flowed out of the bay during sea level rise (Paduan and Cook, 1997; Petruncio et al., 1998).

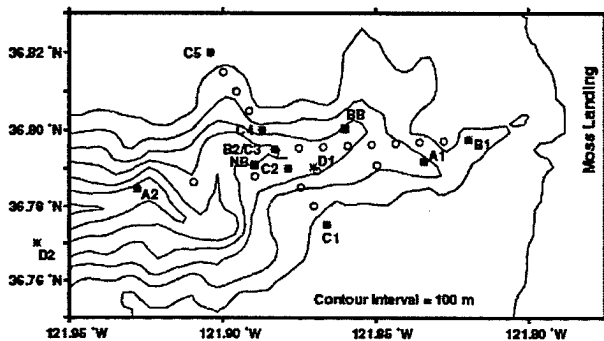


Figure 2. Map showing the locations of the CTD (*) and VM-ADCP (O) measurements made during ITEX1 (A), ITEX2 (B and C) and MCIW (D). Moored ADCP and temperature measurements were made at BB and NB during MCIW. Depth contours relative to the measurement locations are not highly accurate due to the low resolution of the bathymetry in this figure.

It has long been known, both from theory and observations, that submarine canyons may serve as "traps" for internal wave energy (Gordon and Marshall, 1976; Wunsch and Webb, 1979; Hotchkiss and Wunsch, 1982 among others). These environments, being notoriously inhospitable places to make measurements, typically have observations restricted to fairly short durations, on the order of a few days. Where longer time series do exist (Hotchkiss and Wunsch, 1982; Hunkins, 1988; Hickey, 1989; Noble and Butman 1989; Hickey, 1997 among others), the temporal resolution is generally not fine enough to resolve the highly nonlinear aspects of the flow, nor the high frequency end of the spectrum.

2. Internal Tide Experiments – 1994

2.1. Methods

Our initial investigations consisted of 25-50 h time-series of velocity and density constructed from shipboard ADCP and CTD measurements described in Petruncio et al. (1998). During Internal Wave Experiment 1 (ITEX1) in April 1994, CTD stations spaced 8.3 km apart along the canyon axis were occupied every 1.5-2 h for 25 hours (Figure 2). During ITEX2 in October 1994, the CTD stations were located closer together (5.6 km apart) and closer to shore. In ITEX2, the along-canyon measurements were followed by another 25 h of cross-canyon CTD and ADCP surveys. The CTD stations were positioned so that the deeper axial station was common to both the along- and cross-canyon measurements, allowing construction of a time series 50 h in length at that site. The remaining cross-canyon stations were located above the Canyon walls and in the shallow water (60-90 m) on the flanks of the Canyon. The velocity data were spatially averaged by assigning the measurements to evenly spaced along-track geographic bins of 1.5 km for ITEX1 and 0.7 km for ITEX2. The cross-track width of these bins was no more than 0.5 km. The one-minute ensembles in each geographic bin were temporally averaged so that the sampling interval at each de facto ADCP station was the same as that of the CTD stations, 1.5-2 h. A 150 kHz RD Instruments vessel-mounted ADCP with an array of four transducers oriented 30° from the vertical in a Janus configuration was used. Although the ADCP is capable of measuring to depths greater than 400 m, data within the lower 20-30% of the water column can not be used due to side lobe interference from reflections off the Canyon floor and walls.

2.2. Results

Both experiments revealed that semidiurnal kinetic and potential energy was elevated in a 150-200 m-thick band centered 150 m above the bottom, with current amplitudes of $15\text{-}20 \text{ cm s}^{-1}$ (Figure 3). This conclusion is limited however by the vertical extent of the velocity data, which did not include the lower part of the water column. The angle the characteristic ray paths, or beams, make with the horizontal was computed from the velocity and density time-series five different ways, and all gave an answer close to 2.3° (Petruncio et al., 1998). Energy maxima lay nearly parallel to the large-scale canyon floor slope, as do the ray paths computed from linear theory using the measured averaged N^2 profiles. The horizontal wavelengths were estimated to be 30 km, and the group velocities $50\text{-}55 \text{ cm s}^{-1}$. A significant difference between the two experiments is

that, in the first, energy appeared to propagate shoreward parallel to the canyon floor and was best described as a beam. In the second experiment, while the energy maxima were still parallel to the canyon floor, the amplitude and phase structures indicated a standing wave (Figure 4), more easily described in terms of a small number of low modes. At the time we speculated that this difference in vertical structure might be due to seasonal differences in stratification. There is also some evidence to suggest that there is phase-locking between the surface and internal tide. Higher energy levels were observed during the spring tide conditions of ITEX1, versus the neap tide conditions of ITEX2. Cross-canyon measurements

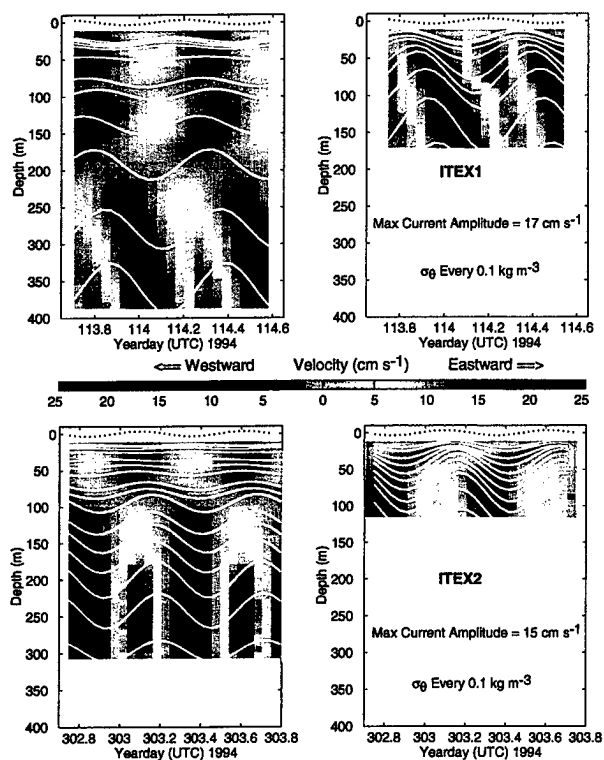


Figure 3. Time series of semidiurnal component, as determined from least-squares fit to the M_2 frequency, of east-west velocity component and isopycnal displacements for deep station A2 (upper left) and shallow station A1 (upper right) during ITEX1 and deep station B2 (lower left) and shallow station B1 (lower right) during ITEX2. Demeaned M_2 sea level oscillations exaggerated by a factor of 10 (dashed lines) are also shown.

made during ITEX2 revealed the internal tide can act to transport cold dense water up onto the shelves to the sides of the Canyon as suggested by *Shea and Broenkow* (1982).

It is difficult to determine whether the internal tide energy in MC is locally generated, or propagates in from another region, and then is concentrated there due

to the steep canyon walls and near-critical bottom slope. The fact that the observed energy maxima were elevated above the canyon floor provides some indication of non-local generation. Figure 5 shows the ray paths emanating from an area to the west of the ITEX sites where the bathymetry is near critical for the M_2 frequency over a large spatial area. We speculated that "Smooth Ridge" could have been the source for the internal tide energy we observed. The figure also illustrates the significant sensitivity of the M_2 ray paths to the different stratifications observed in ITEX1 and ITEX2.

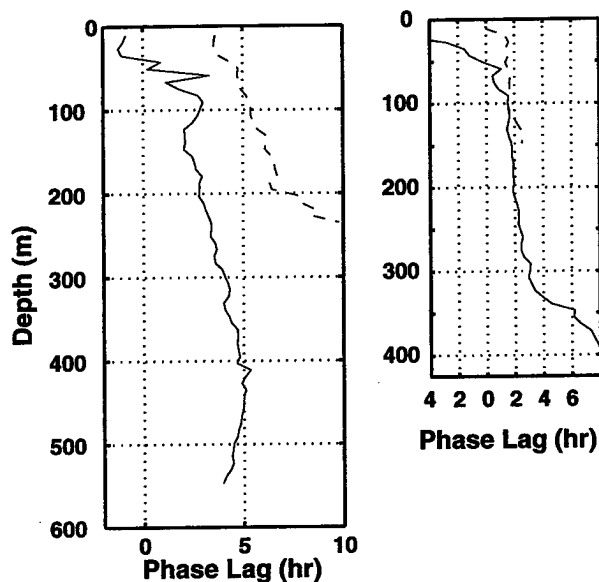


Figure 4. Phase of M_2 component of isopycnal displacement for the deep (solid; A2, B2) and shallow (dashed; A1, B1) CTD time-series stations made over the Monterey Canyon axis during ITEX1 (left) and ITEX2 (right).

3. Model Simulations with Idealized Bathymetry

In order to investigate further internal tide generation and propagation in a submarine canyon, we used a primitive equation numerical model, the Princeton Ocean Model (POM). At least two previous investigators have used POM to investigate internal tides in the coastal ocean. *Holloway* (1996) used a two-dimensional implementation to study internal tide generation and propagation on the Australian North West Shelf. *Cummins and Oey* (1997) used a fully three-dimensional implementation to look at barotropic and baroclinic tides off northern British Columbia.

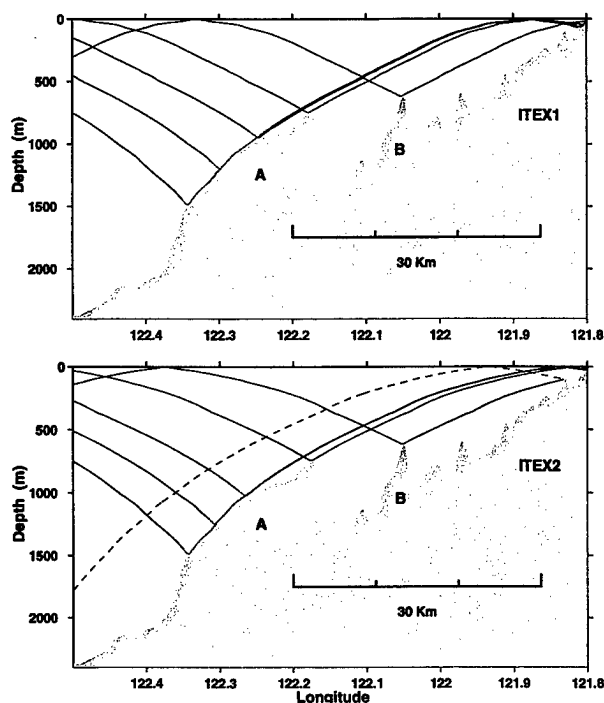


Figure 5. M_2 characteristics calculated from the linear internal wave dispersion relation showing possible paths of energy propagation from Smooth Ridge (A) and Steep Ridge (B) into MC. The dashed line represents a reflected ray.

3.1. Model Setup

We used a 70 km x 70 km domain with a simplified geometry including a 2500 m deep basin, a continental slope with a maximum gradient of 7.15° , and a 20 km wide shelf, 100 m in depth (Figure 6). The eastern boundary of the domain, which represents the coast, was the only closed boundary. The shelf and slope were incised by a single canyon perpendicular to the coast. In the case discussed here, the canyon floor was inclined 1.55° from the horizontal and was 3 km wide. The width across the top of the canyon varied along its length from 11 km at the mouth to 3 km at the head. Horizontal resolution of 1 km x 1 km with 30 σ -levels was used throughout the domain. The σ -levels were logarithmically distributed near the surface and bottom, with vertical resolution in the boundary layers ranging from 12.5 m over the basin to 0.5 m over the shelf. In the middle of the water column (σ -levels 5-26), vertical resolution ranged from 107.5 m over the basin to 4.3 m over the shelf. An external time step of 2 s and an internal time step of 120 s were used. The initial temperature and salinity fields were constant in the horizontal but had vertical dependence typical of summertime stratification conditions in the vicinity of Monterey Bay.

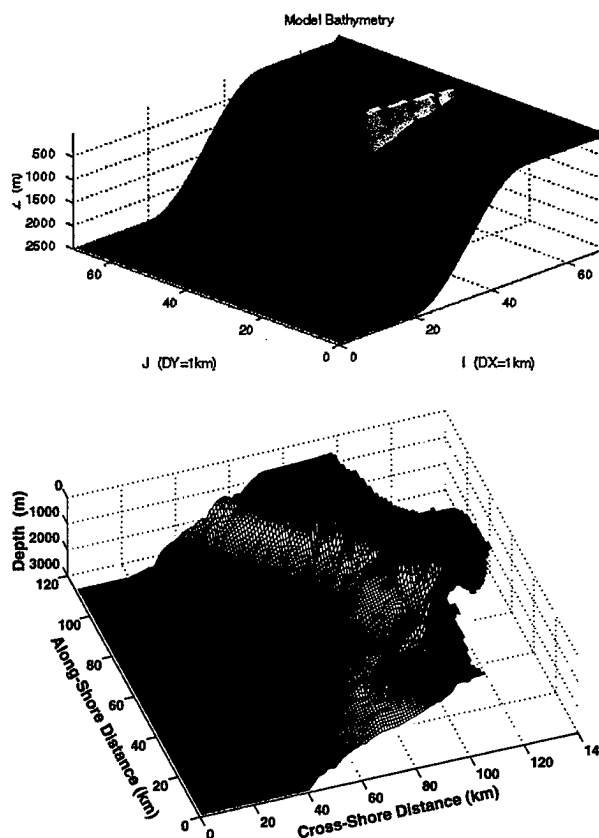


Figure 6. Model geometry and bathymetry for the idealized case (top) featuring a straight coast and shelf with a canyon incising the slope and shelf at a right angle, and a realistic case (bottom) featuring the Monterey Canyon and Bay.

A complete description of these model runs can be found in *Petruncio* (1996). The model was forced with only one tidal constituent, the M_2 , applied as a 0.5 m-amplitude cosine wave to sea level at the western boundary. The model was run for four days with output from the last three semidiurnal cycles used in the analyses summarized below. A mixture of boundary conditions were used. Radiation conditions were applied to the external mode velocities and to the internal mode velocities on the northern and southern boundaries. On the offshore (western) boundary, internal mode velocities and density gradients were decayed exponentially to zero over a 10 km-wide sponge region parallel to the boundary.

3.2. Model Results

Figure 7 shows that in the model results the energy maximum lies at, or near, the canyon floor and is bounded on the upper side by the characteristic emanating from the foot of the canyon. The characteristic

lies nearly parallel to the canyon floor, thus trapping energy generated at the foot along the bottom. In addition, internal tide energy is generated along the portion of the canyon floor critical with respect to the M_2 frequency. (The canyon floor slope is constant but the density stratification varies with depth, thus making only that part of the canyon floor near 300 m depth critical.) A comparison between ITEX1 observations and the model results is shown in Figure 8. Although the model underpredicts the current amplitude by about 50% (due to a combination of simplifications in the model bathymetry, forcing, and density variability relative to the real ocean), the structure looks very much the same, indicating upcanyon energy propagation parallel to the canyon floor. The phase lag between the model currents and sea level is within 1/4 cycle of that observed in ITEX1; near the head of the canyon, maximum shoreward flow occurs in the lower half of the water column, close to the time of high tide. It is not surprising that the phase difference between sea level and maximum upcanyon current is different in the model than the observations since this is so strongly a function of where the measurement site is relative to the generation site.

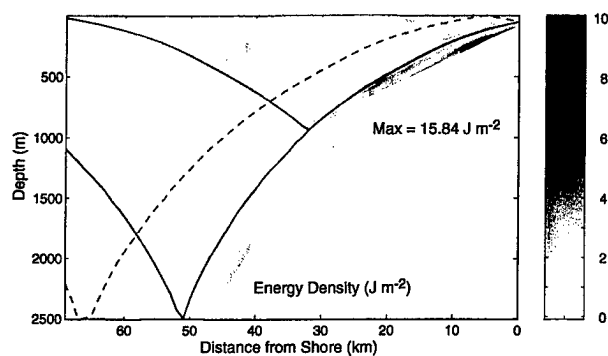


Figure 7. Along-canyon section of M_2 energy density with characteristics emanating from the shelf break (solid lines) and reflecting from the coastal boundary (dashed lines).

As suggested by the observations, isopycnal displacements associated with the internal tides (5–10 m in the model) move water from beneath the canyon rim up onto the shelf. As the isopycnals sink back down below the rim, lenses of dense water pinch off and remain on the shelf in the manner suggested by *Shea and Broenkow* (1982). This “tidal pumping” along the rim of the model canyon near its head is clearly a source of along-shore-propagating internal tides (not shown), which transition from beam-like near the generation site at the canyon rims to first-mode-like near the model boundaries. The density field in the bottom boundary layer at 200–300 m depth reveals that upcanyon-propagating

bore-like surges occur along the canyon floor during rising tide, resulting in isopycnal displacements of 5–10 m. This boundary layer activity is consistent with the 2-D numerical simulations of *Slinn and Riley* (1996), who observed that critical angle internal wave reflection on floors with shallow slopes (3.4° – 9°) resulted in the upslope propagation of thermal fronts in the bottom boundary layer.

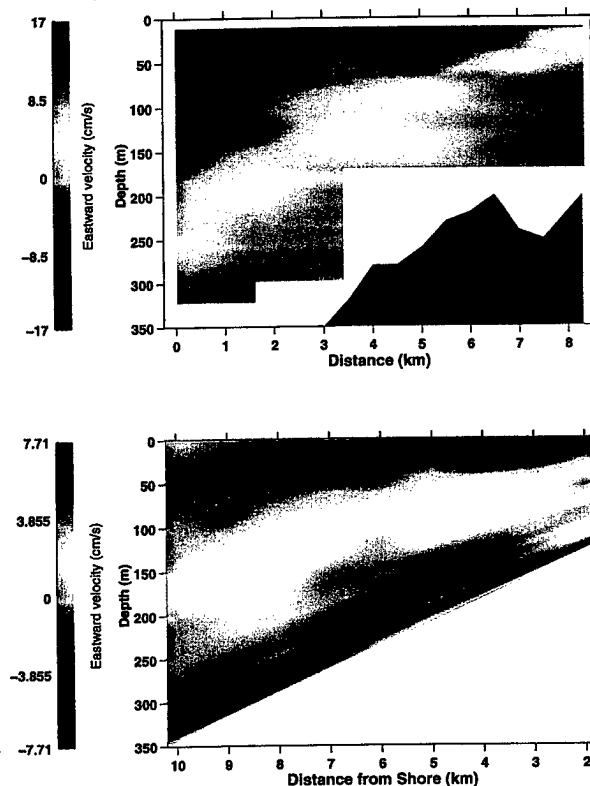


Figure 8. Along-canyon section of the model u at time of high tide (lower), and the u 2.5 h after M_2 high tide observed during ITEX1 (upper).

4. Internal Wave Experiment – 1997

At the conclusion of the previously described work, it was clear that the near-bottom region, undersampled in the previous studies, was likely to contain high levels of energy and shear associated with internal wave generation, trapping, and reflection. In August–September 1997, as part of the Monterey Canyon Internal Wave Experiment (MCIW), Rosenfeld deployed two moorings at 390 and 337 m depth with upward-looking ADCPs and near-bottom thermistors, in the same vicinity of MC where ITEX1 and ITEX2 took place (Figure 2). Twelve-hour CTD time series with 30-min resolution were made about halfway between the two moor-

ings at station D1 on 9 August and 21 August. The 34-d velocity and temperature records, with temporal resolution of 1-3 minutes, confirmed the bottom-intensification of the internal tide, but also revealed for the first time the highly nonlinear character of the signal. High-resolution bathymetry data (vertical resolution of 0.1% of water depth and horizontal resolution of 2% of water depth) obtained by the Monterey Bay Aquarium Research Institute during the summer of 1998, shows that the shallower mooring, BB, was located near a bend in the canyon, thus explaining the highly asymmetric flow measured there (Figure 9). "Along-canyon" flow was calculated for the deepest 4-m bin, centered 12 m above the bottom, by projecting the velocity vectors in the northeast and southwest quadrants onto the major principal axis computed from all the points in the northeast quadrant (positive eastward), and projecting the velocity vectors in the northwest and southeast quadrants onto the major principal axis computed from all the points in the northwest quadrant (negative westward). This results in a scalar time series with upcanyon (eastward) flow being positive and downcanyon (westward) flow being negative.

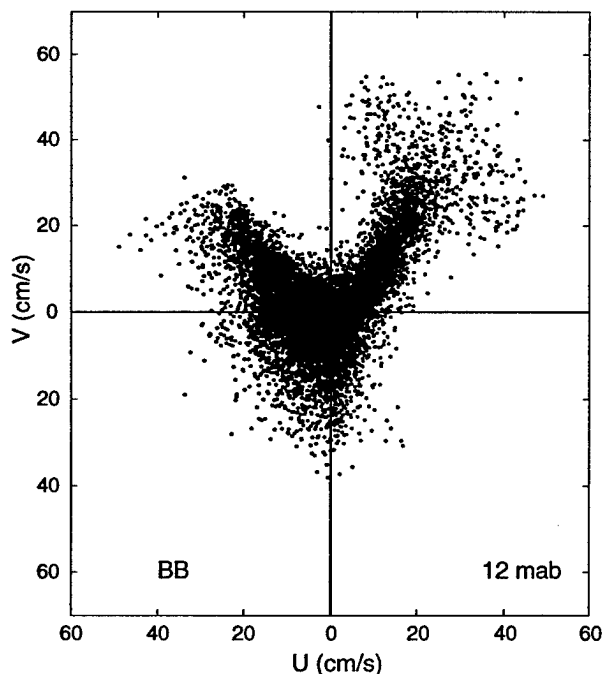


Figure 9. Scatter plot of velocity from the deepest 4-m bin, centered 12 m above the bottom, at mooring BB. Every third 1.5-min data point from the 34-d time-series is plotted.

"Internal bores," visible as sharp drops in temperature with coincident accelerations in the along-canyon velocity (Figure 10) occur at 11-13 h intervals throughout much of the record at mooring BB. They are particularly prominent and do not coincide with the times of maximum tidal range in sea level. There is also circumstantial evidence from a 12-h CTD time series taken between the two moorings that a decrease in light transmission follows the bore passage. At the deeper mooring, NB, the temperature drop takes place as two smaller steps.

These data clearly show that the kinetic energy in the internal wave band throughout the lower third of the water column (the entire range measured by these bottom-mounted upward-looking ADCPs) is elevated above the G-M spectra (Figure 11) calculated according to

$$E_{GM} = \left[\frac{E_0 b^2}{\pi} \right] \frac{N_0}{N(z)} f \frac{(N^2 - \omega^2)(\omega^2 + f^2)}{\omega^3 \sqrt{\omega^2 - f^2}} \quad (1)$$

using the canonical values (Munk, 1981) for b (1.3 km), N_0 ($5.2 \times 10^{-3} \text{ s}^{-1}$), E_0 (6.3×10^{-5}), the appropriate value of f for this latitude, and $N(z)$ calculated from the two 12-h averaged density profiles. Although G-M predicts slightly lower energy levels at 12 m above bottom relative to 112 m above bottom (based on the density profile), the opposite is observed. The energy decreases as you get further up in the water column, and the tidal signal becomes more linear, as evidenced by the reduction in the energy in the overtides. In general the spectral shape follows a ω^{-2} slope, except for the peaks associated with the tides and overtides.

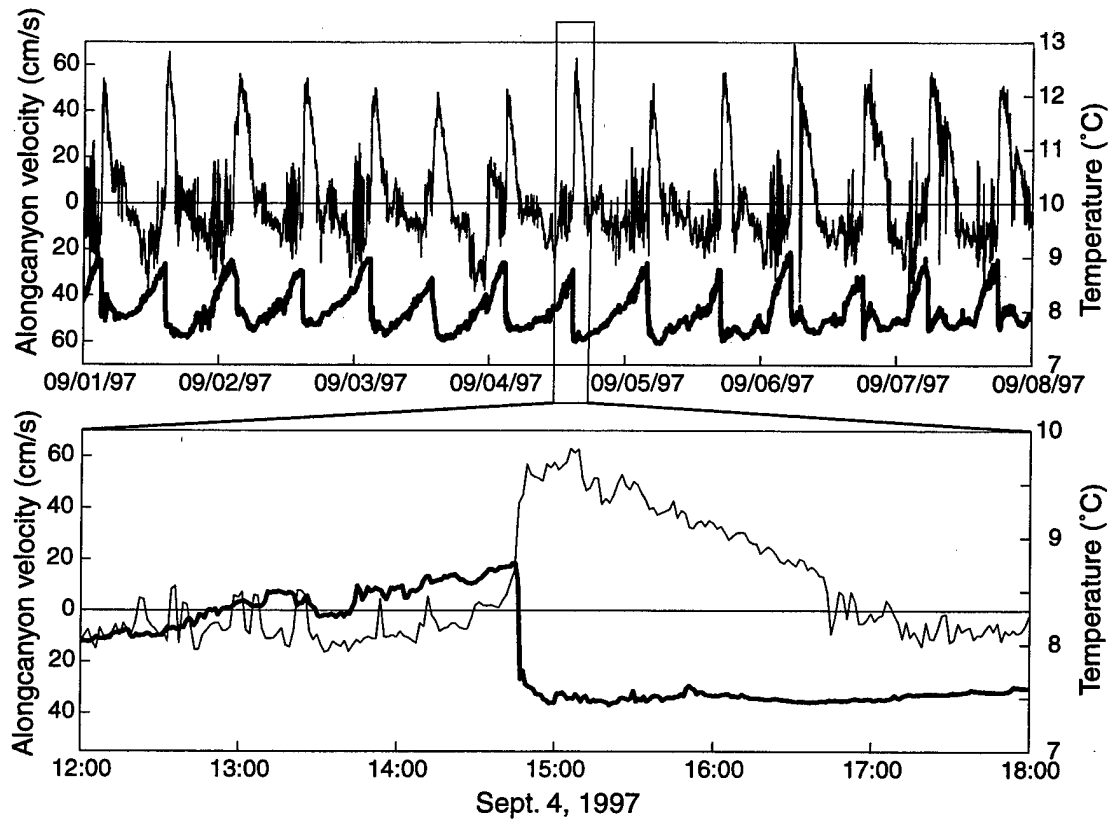


Figure 10. Temperature (bold line) measured once per minute 4 m above the bottom and along-canyon velocity (light line) averaged over 1.5-min intervals from the deepest 4-m bin, centered 12 m above the bottom, at mooring BB for one week (upper panel) and for a 6-h period within that week (lower panel).

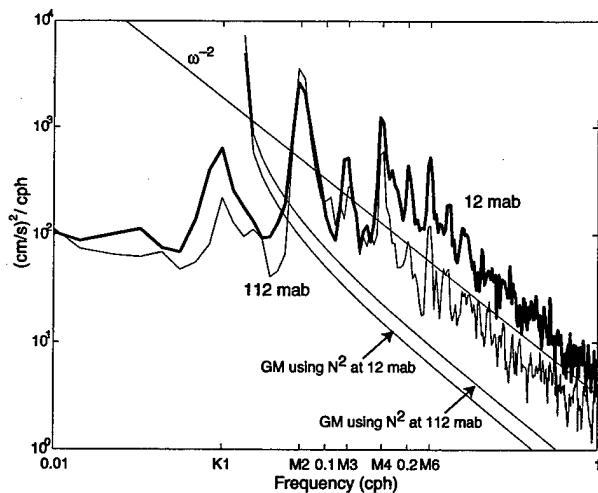


Figure 11. Kinetic energy spectra for the depth bins centered 12 and 112 m above the bottom at mooring BB, together with the G-M spectra calculated using values of N for these depths derived from the nearby CTD time series.

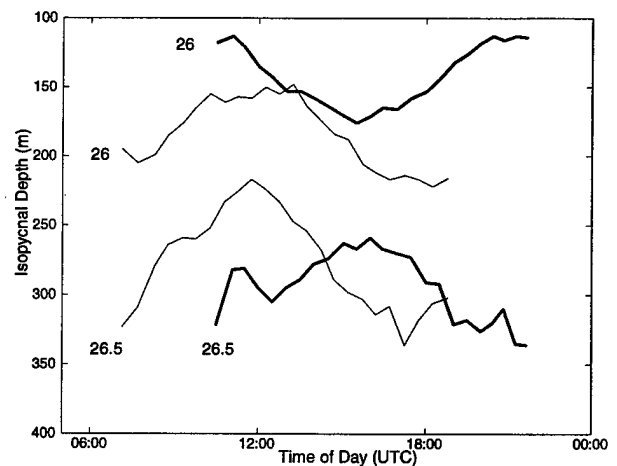


Figure 12. The $\sigma_\theta = 26.0$ and 26.5 isopycnals versus time of day for 9 August (light) and 21 August (heavy) 1997 CTD time series.

We also found that the vertical structure, as seen in isopycnal displacements derived from two CTD time series made just 12 days apart (Figure 12), exhibited changes similar to those observed between ITEX1 and

ITEX2, which differed in time by 6 months. This suggests that the stratification changes responsible for significant alterations to the internal tide may occur on synoptic time scales as well as on seasonal time scales. Indeed, significant changes in the stratification did take place between 9 and 21 August (most probably between 9 and 10 August based on CTD measurements made 10 km west of this site), although they primarily affected the top 250 m of the water column.

5. Model Simulations with Realistic Bathymetry

Coincident with our efforts to obtain more highly resolved observations of the internal wave field in MC, we have been pursuing more realistic model simulations of the same process. Still using POM with 30 vertical σ -levels and the forcing and stratification described above, we adopted a new grid using realistic bathymetry from a 250-m (horizontal) resolution data set (Figure 6). The domain size for these simulations was expanded to 130 km x 113 km and rotated about 20° to minimize land points, and to align the offshore boundary with the, approximate, along-shore direction. Difficulties with the sponge-type open boundary conditions limited the maximum depth in the model to 2500 m for these preliminary simulations.

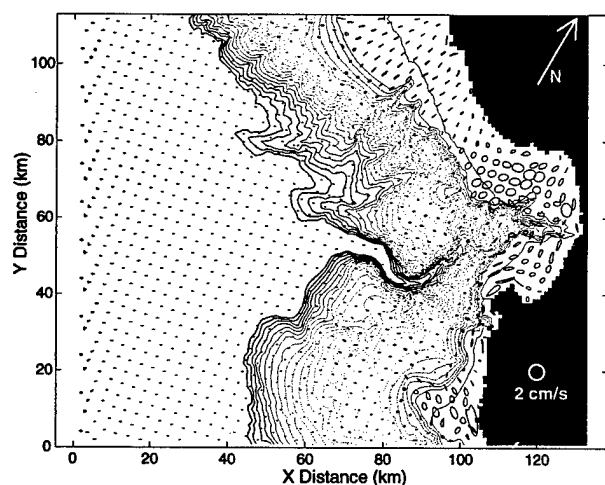


Figure 13. Depth-averaged current hodographs over a semidiurnal tidal cycle on day 10 of the POM simulation. Every 5th model grid point is shown. The contour interval is 100 m and the largest speeds are $\sim 4 \text{ cm s}^{-1}$ over the continental shelf.

The model was run for 10 days and the results of the last M_2 tidal cycle were used in the analyses presented here. Critical to realistic generation of the internal tide for a particular high-resolution topographic domain is an accurate specification of the barotropic forcing, which

interacts with the sloping bottom to generate internal waves.

We verified that the offshore sea level forcing we imposed acted to produce barotropic currents with magnitudes of $1\text{--}4 \text{ cm s}^{-1}$ as expected from what is known about the basin-scale tidal currents (*Battisti and Clarke, 1982*). The depth-averaged current hodographs on day 10 of the model run are shown in Figure 13. In this case, the weak ($< 1 \text{ cm s}^{-1}$) cross-shore currents in the outer portion of the domain are accelerated to a maximum of 4 cm s^{-1} over the continental shelf in the northern part of Monterey Bay. The actual generation of internal waves in the model is proportional to the volume flux vector, $\bar{U}H$, where \bar{U} is the depth-average velocity and H is the water depth (*Baines, 1982*). It is important to note that, although this simulation includes realistic cross-shore forcing, it does not include the along-shore component of the basin-scale tidal forcing. Given the complex topography of the Monterey Bay region, along-shore barotropic currents may be responsible for significant internal tide generation that should be included in future model simulations.

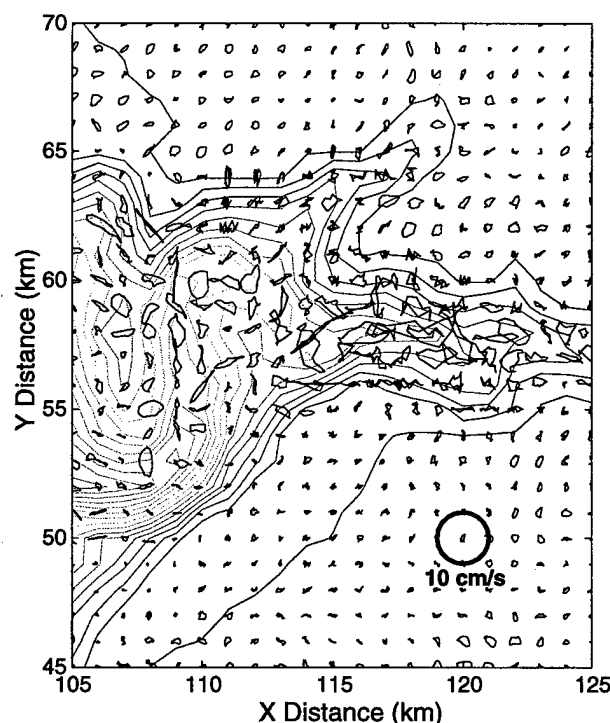


Figure 14. Bottom current hodographs over a semidiurnal tidal cycle on day 10 of the POM simulation. Every grid point is shown for the Monterey Bay portion of the model domain. The contour interval is 100 m and the largest speeds are $\sim 12 \text{ cm s}^{-1}$ in the axis of the canyon.

This preliminary simulation using only offshore forcing does provide insights into the baroclinic response of this region to tidal forcing, particularly in the very interesting confines of the canyon. Hodographs of the near-

bottom currents during a semidiurnal tidal cycle on day 10 of the model simulation are shown in Figure 14 for the subset of the model domain within Monterey Bay. The current patterns are complicated, but they have a strong correlation with the bottom depth contours. The maximum currents exceed 12 cm s^{-1} and are found within the canyon axis near the region of the ITEX measurements described above. These currents are four to ten times larger than the depth-averaged currents produced directly by the M_2 sea level forcing. The near-bottom current hodographs are much less elliptical than those of the depth-averaged currents, which suggests asymmetric flows for the upcanyon and downcanyon portions of the tidal cycle and/or significant nonlinear transfer to high-order tidal harmonics.

6. Conclusions

Large isopycnal oscillations have been reported near the head of Monterey Canyon for more than 25 years (Broenkow and McKain, 1972). It has been shown that the internal tides responsible for these also result in surface currents ten times as large, and of opposite phase, as the barotropic tidal currents (Petruncio, 1993). This is possible because of the bottom-intensified nature of the internal tidal signal (Petruncio et al., 1998) which is a consequence of the slope of the canyon floor being near-critical for the semidiurnal tidal constituents. Very near-bottom high temporal resolution measurements reveal the strongly nonlinear character of the signal. A hydrostatic primitive equation model (POM) is able to replicate many aspects of the observed internal tide; including the bottom-intensification and shoreward propagation of energy nearly parallel to the canyon floor. Further study using the realistic, complex topography should provide more information about the source regions for the internal tide, the dominant horizontal scales of variability, and the sensitivity of internal tide generation to the resolution of the actual bottom features over scales from 1 km to 10 km. However, since the model is hydrostatic, we would not expect it to accurately simulate the bore-like features now known to exist, or the details of the energy cascade within the higher frequency portion of the internal wave band. A combination of hydrostatic modeling at the generation scales with non-hydrostatic modeling of the energy cascade is expected to provide the most insights into the distribution of internal wave energy for a particular coastal regime.

Acknowledgments. We would like to thank Mike Cook, Scott Key, and Fred Bahr for assistance with data processing and display. We also gratefully acknowledge support from a NSF grant to Rosenfeld (OCE-9619466) and an ONR grant to Paduan and Rosenfeld (N00014-97WR-30009).

References

- Baines, P.G., On internal tide generation models, *Deep-Sea Res.*, 29, 307-338, 1982.
- Battisti, D.S., and A.J. Clarke, A simple method for estimating barotropic tidal currents on continental margins with specific application to the M_2 tide off the Atlantic and Pacific Coasts of the United States, *J. Phys. Oceanogr.*, 12, 8-16, 1982.
- Broenkow, W. W., and S. J. McKain, Tidal oscillations at the head of Monterey Submarine Canyon and their relation to oceanographic sampling and the circulation of water in Monterey Bay, Moss Landing Marine Laboratories Tech. Pub. 72-05, 42 pp., 1972.
- Cummins, P. F., and L.-Y. Oey, Simulation of barotropic and baroclinic tides off northern British Columbia, *J. Phys. Oceanogr.*, 27, 762-781, 1997.
- Gordon, R. L., and N. F. Marshall, Submarine canyons: internal wave traps?, *Geophys. Res. Lett.*, 3, 622-624, 1976.
- Hickey, B. M., Patterns and processes of circulation over the Washington continental shelf and slope, in *Coastal Oceanography of Washington and Oregon*, Vol. 47, edited by M. R. Landry and B. M. Hickey, pp. 41-115, Elsevier, Amsterdam, 1989.
- Hickey, B. M., Coastal submarine canyons, in *Proc. 'Aha Huliko'a', Hawaiian Winter Workshop, Topographic Effects in the Ocean*, pp. 95-110, School of Ocean and Earth Science and Technology, Univ. of Hawaii at Manoa, Honolulu, HI, 1995.
- Hickey, B. M., The response of a steep-sided, narrow canyon to time-variable wind forcing, *J. Phys. Oceanogr.*, 27, 697-726, 1997.
- Holloway, P. E., A Numerical Model of Internal Tides with Application to the Australian North West Shelf, *J. Phys. Oceanogr.*, 26, 21-37, 1996.
- Hotchkiss, F. S., and C. H. Wunsch, Internal waves in Hudson Canyon with possible geological implications, *Deep-Sea Res.*, 29, 415-442, 1982.
- Hunkins, K., Mean and tidal currents in Baltimore Canyon, *J. Geophys. Res.*, 93, 6917-6929, 1988.
- Munk, W., Internal waves and small scale processes, in *Evolution of Physical Oceanography*, edited by B. A. Warren and C. Wunsch, pp. 264-291, MIT Press, Cambridge, MA, 1981.
- Noble, M., and B. Butman, The structure of subtidal currents within and around Lydonia Canyon: Evidence for enhanced cross-shelf fluctuations over the mouth of the canyon, *J. Geophys. Res.*, 94, 8091-8110, 1989.
- Paduan, J. D., and M. S. Cook, Mapping surface currents in Monterey Bay with CODAR-type HF radar, *Oceanography*, 10, 49-52, 1997.
- Petruncio, E.T., Characterization of tidal currents in Monterey Bay from remote and in-situ measurements, *M.S. Thesis*, Dept. of Oceanography, Naval Postgraduate School, Monterey, CA, 113 pp., 1993.
- Petruncio, E. T., Observations and modeling of the internal tide in a submarine canyon, *Ph.D. dissertation*, Dept. of Oceanography, Naval Postgraduate School, Monterey, CA, 181 pp., 1996.
- Petruncio, E. T., L. K. Rosenfeld, and J. D. Paduan, Observations of the internal tide in Monterey Canyon, *J. Phys. Oceanogr.*, 28, 1873-1903, 1998.
- Shea, R. E., and W. W. Broenkow, The role of internal tides in the nutrient enrichment of Monterey Bay, California, *Estuarine, Coastal, Shelf Sci.*, 15, 57-66, 1982.
- Slinn, D. N., and J. J. Riley, Turbulent mixing in the oceanic boundary layer caused by internal wave reflection from sloping terrain, *Dyn. Atmos. Oceans*, 24, 51-62, 1996.
- Wunsch, C., and S. Webb, The climatology of deep ocean internal waves, *J. Phys. Oceanogr.*, 9, 235-243, 1979.

Baroclinic Wave Drag and Barotropic to Baroclinic Energy Transfer at Sills as Evidenced by Tidal Retardation, Seiche Damping and Diapycnal Mixing in Fjords

Anders Stigebrandt

Department of Oceanography, Earth Sciences Center, Göteborg University, Göteborg, Sweden

Abstract. Fluctuating barotropic flow over sills in stratified water is subjected to baroclinic wave drag and accompanying barotropic to baroclinic energy transfer. In fjords, this process has notable consequences, for instance, tidal retardation across fjord sills, damping of barotropic seiches and enhanced diapycnal mixing in the basin water. These may be computed from simple models only including local conditions in the sill area. This has been done for numerous fjords with quite satisfactory results as reviewed in this paper. It is therefore concluded that baroclinic wave drag and barotropic to baroclinic energy transfer only depend upon local conditions in the sill area.

Energy transferred from the barotropic tide to baroclinic motions at sills is eventually dissipated by turbulence and diapycnal mixing. If radiated away from the sill by progressive internal waves, the energy may be transferred to turbulence in places remote from the sill. Radiation of baroclinic energy from fjord sills, however, is often less than the energy gain by baroclinic wave drag, so there also seems to be a possibility for a short spatial pathway to dissipation and mixing close to the sill. It is suggested in this paper that the magnitude of the radiated fraction is regulated by the capacity of the fjord basin to dissipate internal waves. In a fjord with small capacity to dissipate internal waves, much of the baroclinic energy gained at the sill has to dissipate close to the sill.

The power for diapycnal mixing in most fjord basins is mainly derived from barotropic tides by baroclinic wave drag at sills. Diapycnal mixing in the abyssal ocean is probably driven in a similar way by baroclinic wave drag at bumps, sills, and ridges on the sea bottom. By analogy with the case in fjords, the energy transfer should be computed using local models. Furthermore, some of the transferred energy probably dissipates close to the topography and the rest is radiated away by internal waves and dissipated in remote places. The total mixing should thus be greater than the mixing related to the field of internal waves sustained by radiation from the topography. Estimates of the total diapycnal mixing in the abyssal ocean should therefore be based on observations covering the whole water column down to the seabed as also suggested by recently published dissipation profiles from the ocean.

1. Introduction

Growing evidence suggests that tides provide much of the power for mixing and the accompanying vertical circulation of the deep ocean, e.g., Munk (1966), Sjöberg and Stigebrandt (1992) and Munk and Wunsch (1998). The vertical mixing is coupled to tides by baroclinic wave drag acting on barotropic tides at sills, bumps and ridges in the bottom, e.g., Cox and Sandström (1962), Bell (1975) and Sjöberg and Stigebrandt (1992). Theoretical estimates of tidal mixing so far largely lack observational verification for the deep ocean. However, recent observations of dissipation in the abyssal ocean show the expected intensification close to rough topography, e.g. Polzin et al. (1997).

Physical processes are much easier to study in fjords than in the deep ocean, thus fjords often are suitable as

ocean process laboratories. Basic knowledge of physical processes obtained from fjord studies may then be applied to other parts of the ocean. As an example, it may be mentioned that the model by Sjöberg and Stigebrandt (1992) is based on results essentially from fjord studies. Energy release from barotropic tides by baroclinic wave drag and pathways of the energy to turbulent dissipation and diapycnal mixing, the focal points of the present paper, might be partly different in the deep ocean and in fjords. Nevertheless, it is believed that elucidation of the mechanics of these processes in fjords might be quite helpful in developing an understanding of the way similar processes work in the deep ocean. The objective of the present paper is to summarize knowledge, gained from work on fjords during the last decades, about barotropic to

baroclinic energy transfer at sills and pathways of the energy to turbulent dissipation and diapycnal mixing.

Barotropic to baroclinic energy transfer at fjord sills due to baroclinic wave drag acting on time-dependent barotropic currents has been modeled with different kinds of stratification and sill topography. The models discussed in the present paper are local in the sense that only conditions in the immediate neighborhood of the sill are invoked. The models may be tested by comparison between predicted and observed estimates of the quantities listed below, which under certain circumstances only are due to baroclinic wave drag (see also Fig. 1).

1. Tidal response in fjords; retardation and amplitude reduction (section 3 below).
2. Damping of barotropic seiches in fjords (section 3).
3. Diapycnal mixing in the basin water of fjords (section 4).
4. Radiation of internal waves from sills in fjords (section 5).

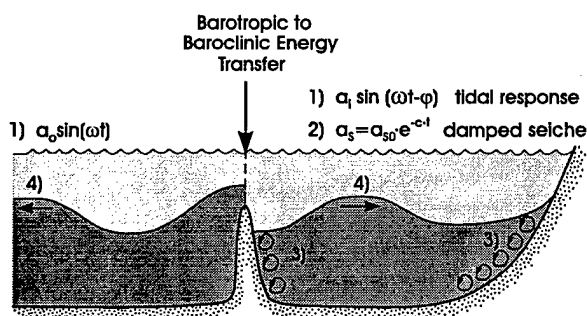


Figure 1. Consequences of baroclinic wave drag and barotropic to baroclinic energy transfer at sills in the mouth of fjords: (1) Tidal response in fjords, (2) damping of barotropic seiches, (3) diapycnal mixing in the basin, and (4) radiation of internal waves from the sill.

It seems that large-scale topographic drag and baroclinic wave drag are mutually exclusive processes in straits, occurring for supercritical and subcritical conditions, respectively. Baroclinic wave drag is the dominating drag acting on barotropic tidal flow in the mouth of most subcritical fjords. It is thus usually much greater than drag due to bottom friction. Baroclinic wave drag was introduced in a model for barotropic strait flow in Stigebrandt (1999). The model explains the observed tidal retardation in fjords where baroclinic wave drag is the dominating resistance to the barotropic flow. Parsmar and Stigebrandt (1997) used the same formulation for barotropic to baroclinic energy transfer at fjord sills to derive the damping coefficient of barotropic seiches in fjords. Their model explained the observed damping of the fundamental barotropic seiche in the Gullmar Fjord.

As further discussed in the present paper, these cases verify that simple, local models describe barotropic to baroclinic energy transfer at sills due to baroclinic wave drag quite well.

From work on a large number of fjords, it is known that the vertical mixing and circulation of the basin water in fjords is driven mainly by barotropic to baroclinic energy transfer at fjord sills. Examples may be found in, for example, Stigebrandt (1976), Stigebrandt and Aure (1989), Simpson and Rippeth (1993), and Tinis (1995). There is an almost constant ratio between the rate of work done by turbulence against the buoyancy forces in the basin water and the energy transfer from barotropic to baroclinic motions at sills as estimated from the simple local models. The fact that the ratio is constant for a wide range of fjords shows that physical dimension and form of a fjord basin are of little or no importance for the energy transfer. A tracer experiment conducted in the Oslo Fjord indicates that dissipation takes place along the rim of the fjord basin, suggesting that energy derived from baroclinic wave drag be dissipated to turbulence close to the sea bottom. This may occur near the sill as well as remotely from the sill by interaction between internal waves and the sea bottom.

The observed radiation of baroclinic energy from fjord sills varies from almost 100% to less than 50% of the energy transfer from the barotropic tide via baroclinic wave drag as estimated by simple models. This suggests that there may be substantial dissipation of tidal energy already close to the sill in many fjords. Radiation of baroclinic energy from a fjord sill is thus generally less than the baroclinic energy gain at the sill. It is suggested in this paper that the magnitude of the radiated fraction should depend on the capacity of the fjord to dissipate internal waves. In a fjord with small capacity to dissipate internal waves (maybe due to highly reflecting side boundaries), much of the energy released by baroclinic wave drag at the sill should accordingly dissipate close to the sill. It was suggested in the preceding paragraph that the physical dimension and form of a fjord basin do not influence the process of baroclinic wave drag. However, physical dimension and form seem to influence radiation of internal waves from sills and thereby the spatial distribution of turbulent dissipation in a fjord basin.

This paper describes observed consequences of baroclinic wave drag and barotropic to baroclinic energy transfer at fjord sills. The theoretical framework for the analysis is given in section 2 where a simple local model for baroclinic wave drag and barotropic to baroclinic energy transfer in subcritical fjords is presented together with some derived consequences of this. In section 3 the simple local model to estimate barotropic to baroclinic energy transfer is verified using data for tidal phase shift from three fjords and the observed damping of the barotropic seiche in one fjord. In section 4 the extensive empirical evidence for tidally forced mixing in the basin water of fjords is presented. The relationship between barotropic to baroclinic energy transfer at fjord sills and

radiation of baroclinic energy into fjords is discussed in section 5. The paper is concluded in section 6 where a number of remaining research questions are asked.

2. Theoretical Framework and Methods

To demonstrate the mechanics of baroclinic wave drag and barotropic to baroclinic energy transfer one may use the simplest possible case, a two-layer stratification with the interface at sill depth. This is actually often a quite good approximation of real fjord stratification because particularly dense water that occasionally refills the basin is trapped by the sill. To keep the discussion simple one may consider the mouth of the fjord to be a rectangular strait of width B , length L and depth h . The velocity of the time dependent barotropic current through the strait is $U_s(t)$.

From basic principles, the momentary rate of energy loss for barotropic flow between two basins, separated by a relatively narrow strait, is

$$\varepsilon = Qg\rho\Delta\eta \quad (1)$$

The flow rate $Q=U_sBh$ has the same sign as $\Delta\eta = h_o - h_i$, h_o (h_i) is the time-dependent sea level in the outer (inner) basin, g the acceleration of gravity, and ρ the density of water. For Eq. (1) to be valid, the barotropic velocities both far upstream and far downstream of the strait have to be small (narrow strait). No essential dynamics are lost by this restriction.

Equation (1) does not reveal, or depend on, the nature of the energy loss and should apply independently of the details of the flow in and around the strait. From time series of Q and $\Delta\eta$, this equation may be used in a diagnostic way to compute the dissipation of barotropic strait flows. However, to study the mechanics of the energy loss a dynamic model for the flow in and around the strait is needed as discussed later in this section.

The following volume budget is applicable to a land-locked basin inside a strait:

$$A_i \frac{dh_i}{dt} = Q + Q_f \quad (2)$$

Here A_i is the horizontal surface area and Q_f the freshwater supply. This equation can be used to compute the barotropic transport from observed time series of h_i and Q_f . For the discussions of baroclinic wave drag in the present paper, possible complications due to freshwater supply, which usually varies on a much longer time scale than tides, will not be considered and thus Q_f will be considered negligible.

If tidal energy is not dissipated in the fjord, co-oscillating barotropic tides should take the shape of standing waves. However, if dissipation occurs, progressive barotropic tidal wave components will appear supporting the energy required by dissipation. The presence of progressive tidal components means that the phase of

the tide increases up-fjord. As already mentioned above, the rate of dissipation of a tidal component may be estimated in a diagnostic way from Eq. (1), provided measurements of h_o and h_i are available. By guessing the functional form of the tidal response h_i in the land-locked basin, an analytic diagnostic relationship between the mean rate of dissipation and the tidal phase shift in the fjord may be derived as discussed below.

2.1 The diagnostic method to estimate tidal dissipation from sea level records

Putting $h_o = a_o \sin(\omega t)$ and assuming that the response in the land-locked basin is $h_i = a_i \sin(\omega t - \varphi)$, the transport Q may be expressed as a function of h_i using Eq. (2) with $Q_f = 0$. The relationship between a_o , a_i and the phase angle φ is readily found to be $a_i = a_o \cos(\varphi)$. Inserting in the expression for momentary dissipation, Eq. (1), and averaging over one tidal cycle, the following expression for the mean dissipation E_{av} may be obtained:

$$E_{av} = \frac{1}{4} \rho g A_i \omega a_o^2 \sin(2\varphi) \quad (3)$$

From harmonic analysis of two time series, h_o and h_i , obtained outside and inside the strait, respectively, one may estimate a_o and φ for the component of frequency ω . Then the mean dissipation of the constituent is directly given by Eq. (3). As can be seen from this equation, maximum dissipation occurs when the phase lag in the land-locked basin equals 45° . The amplitude a_i in the land-locked basin then equals $a_o/2^{1/2}$. This diagnostic method to estimate tidal dissipation from the tidal phase shift has been discussed by a number of authors, for example, *McClimans* (1978), *Farmer and Freeland* (1983), *Stacey* (1984), *Tinis* (1995). The very simple derivation above was presented by *Stigebrandt* (1999) who also showed that the linear response assumed in the derivation of Eq. (3) is consonant with baroclinic wave drag as further discussed below. As already stressed, the diagnostic method may be used to estimate tidal dissipation from sea level records but it does not reveal the nature of the energy loss. To do this, one needs a dynamic model describing the different drag forces and the accompanying energy losses acting on the barotropic current in the strait.

2.2 A dynamic model for barotropic flow in straits with baroclinic wave drag

There are three classes of resistance to barotropic flow causing energy losses in sea straits. Friction against the seabed transfer energy to turbulence in a bottom boundary layer. Large-scale barotropic form drag, caused by contraction-expansion induced by the ends of straits having smaller vertical cross-sectional areas than the adjacent basins, transfer energy to large-scale eddies in the expanding current downstream of the strait. These two kinds of flow resistance have been used frequently in strait

models for barotropic flow, e.g., *Stigebrandt* (1980). Baroclinic wave drag transfer barotropic energy to baroclinic waves in the stratified adjacent basins. To the best of the present author's knowledge, baroclinic wave drag was implemented in a strait flow model for the first time in *Stigebrandt* (1999) where the simple model presented below was derived.

The rate of energy loss suffered by barotropic flow in a rectangular strait, due to these three kinds of resistance, can be described by the expressions given in Eqs. (4), (5) and (6) below. If C_D is the drag coefficient for flow over the seabed and $A_s \approx BL$ the surface area of the strait bed, the rate of frictional energy loss in the strait is

$$\varepsilon_f = \rho C_D U_s^2 BL |U_s| \quad (4)$$

The rate of energy loss due to large-scale barotropic form drag is

$$\varepsilon_a = \frac{\rho}{2} U_s^2 Bh |U_s| \quad (5)$$

For a two-layer stratification the momentary transfer of barotropic energy to baroclinic waves in a stratified basin bordering the strait is

$$\varepsilon_w = \rho \frac{d}{h+d} |U_s| c_g Bh |U_s| \quad (6)$$

Here h , ρ_1 , u_1 (d , ρ_2 , u_2) are thickness, density and orbital velocity of the upper (lower) layer. The internal wave with group velocity c_g has the property that $hu_1 = du_2$ and from the boundary condition of no flow through the sill one obtains $u_1 = U_s d/(h+d)$, see *Stigebrandt* (1976, 1999) for further discussion of ε_w . It should be noted that Eq. (6) gives the barotropic to baroclinic energy transfer at one end of the strait. The total barotropic to baroclinic energy transfer at a strait is usually about twice ε_w because baroclinic wave drag operates at both ends of the strait. However, the magnitude of the two contributions may differ because d and c_g may be different in the two basins bordering the strait.

In Eq. (6) U_s^2 has been expressed as $|U_s|$ times $|U_s|$ to obtain similarity with Eqs. (4) and (5). The quantities multiplying the final $|U_s|$ in Eqs. (4), (5) and (6) are the drag forces due to bed friction, large-scale topographic drag and baroclinic wave drag, respectively. The baroclinic wave drag force was also discussed in *Sjöberg and Stigebrandt* (1992). Using Eqs. (4), (5) and (6) it is easy to estimate the relative magnitude of the three drag forces. It may be interesting to note that large-scale topographic drag dominates over bottom frictional drag if $h/L > 2C_D$ (supercritical flows) and baroclinic wave drag dominates over bottom frictional drag if $h/L > \{C_D U_s (h+d)/(2c_g h)\}$ (subcritical flows).

In the derivation of Eq. (6), the kinematic boundary condition of no flow through the sill (i.e., the end wall of

the fjord at the strait) is satisfied by the barotropic plus the only baroclinic wave mode. A prerequisite for this is that $F_r < 1$ (wave basin - subcritical). Here the Froude number F_r equals U_{sm}/c_g and U_{sm} is the amplitude of the fluctuating barotropic current in the strait. If $F_r > 1$ (jet basin - supercritical) it is assumed that the baroclinic wave drag at the ends of the strait is replaced by large-scale topographic drag developing a jet on the lee side of the strait. The demarcation value between jet and wave generation does not seem to be very sharp and internal waves appear to be generated also for F_r slightly greater than 1, e.g., *Blackford* (1978). However, this will not be discussed further in the present paper but see also a comment in the last paragraph of section 4 below.

Using Eqs. (4), (5) and (6) it is now possible to describe the total energy loss suffered by barotropic flow through a strait. In this paper only a short strait ($\varepsilon_f \ll \varepsilon_w$) with $F_r < 1$ (i.e., $\varepsilon_a = 0$) is discussed for which one obtains $\varepsilon = 2\varepsilon_w$ if the barotropic to baroclinic energy transfers are equally large at the two ends of the strait. It is further assumed that $Q_f = 0$. Eqs. (1), (2) and (6) then give the following relationship between the momentary flow through the strait and sea level difference

$$Q = \frac{g \Delta \eta}{2c_g} \frac{Bh(D+H)}{d} \quad (7)$$

According to this equation, transports through straits are proportional to $\Delta \eta$ if the drag force is due only to baroclinic wave drag. Just for comparison it may be mentioned that if $\varepsilon = \varepsilon_a + \varepsilon_f$ the flow Q through the strait becomes proportional to the square root of $\Delta \eta$, see e.g., *Stigebrandt* (1980) for a discussion of this case including also effects of non-zero values of Q_f .

2.3 Damping of a barotropic seiche by baroclinic wave drag

Equation (6) was used in *Stigebrandt* (1976) and in *Parsmar and Stigebrandt* (1997) to discuss the damping of barotropic seiches in a rectangular fjord with a node in the mouth. If E is the energy of the seiche, the damping coefficient C of the seiche is defined by

$$C = -\frac{1}{E} \frac{dE}{dt} \quad (8)$$

If the damping is due to baroclinic wave drag at the fjord sill one obtains

$$\frac{dE}{dt} = -2\varepsilon_w \quad (9)$$

Here ε_w is given by Eq. (6) and for simplicity it is assumed that the barotropic to baroclinic energy transfers are equally large at both ends of the strait. The energy of

the fundamental (quarter-wave) barotropic seiche is readily found to be, see e.g., *Parsmar and Stigebrandt* (1997),

$$E = \frac{1}{4} \rho g a_i^2 A_f \quad (10)$$

Here a_i is the amplitude of the seiche at the head of the fjord of area A_f . Using Eqs. (6), (8), (9) and (10) one may obtain the following analytical expression for the damping coefficient

$$C = \frac{16d\omega^2 A_f}{\pi^2 g(d+h)Bh} c_g \quad (11)$$

For a discussion of this expression and an estimate of the neglected bottom friction, see *Parsmar and Stigebrandt* (1997).

2.4 Diapycnal mixing in fjord basins driven by barotropic to baroclinic energy transfer

It was suggested in *Stigebrandt* (1976) that most of the diapycnal mixing in the Oslo Fjord is performed by dissipating internal tides generated at the sill in the mouth of the fjord. The time mean barotropic to baroclinic energy transfer, obtained from Eq. (6), is given by

$$E_w = \rho_0 \frac{A_i^2 a_i^2 \omega^2 d}{Bh(h+d)} c_g \quad (12)$$

Here a_i is the amplitude in the fjord of the tidal component of frequency ω . Diapycnic mixing in the basin water is sustained by turbulent dissipation ϵ_d . The relationship between the rate of work against the buoyancy forces due to diapycnic mixing and dissipation is

$$\int_V \kappa N^2 dV = Rf \epsilon_d \quad (13)$$

Here $\kappa = \kappa(z)$ is the horizontal and time (over one tidal cycle) mean vertical diffusivity, $N=N(z)$ is the buoyancy frequency, z the vertical coordinate, V the volume of the basin water and Rf is the efficiency of turbulence with respect to irreversible (diapycnic) work against the buoyancy forces. It was argued in *Stigebrandt* (1976) that all the energy transferred from barotropic to baroclinic motions at the sill dissipates in the basin water. If this is the only energy source for turbulence and mixing in the basin water then $\epsilon_d = E_w$. This is often a quite good approximation although some additional contributions to dissipation may be supplied by other energy sources, see *Stigebrandt and Aure* (1989). Rf should be tantamount to the Richardson flux number. The ratio Rf between the rate of work done against the buoyancy forces in the basin water and the barotropic to baroclinic energy transfer at the fjord sill is further discussed in section 4 below.

To evaluate the integral in Equation (13) one must know the horizontal mean vertical diffusivity $\kappa(z)$ and the

buoyancy frequency $N(z)$. Using the so-called budget method, the horizontal mean vertical diffusivity may be evaluated from vertical profiles of salinity and temperature obtained at different times. The method requires that the basin water has been stagnant in the period between the recordings of the profiles so salinity and temperature changes only are due to vertical diffusion. By stagnant is thus meant that no advective water exchange has taken place in the period. The budget method is further discussed in, e.g., *Gade* (1970), *Gargett* (1984), and *Stigebrandt and Aure* (1989).

The fact that Rf is approximately constant in fjord basins, see section 4, means that Eq. (13) may be used to estimate κ for fjord basins where E_w can be computed from Eq. (12). This was done in *Stigebrandt and Aure* (1989) who empirically determined the distribution of turbulent dissipation as a function of the buoyancy frequency using data from a number of fjords. In this way, they estimated the following expression for κ

$$\kappa = \frac{w}{M^2 \rho_0} c \left(\frac{N}{M} \right)^\delta \quad (14)$$

Here w is the volume mean turbulent dissipation defined by $w = \epsilon_d / V_b$, V_b the volume of the basin water, M the weighted average of N in the basin water, and c and δ are non-dimensional empirical constants depending on the shape of the vertical stratification. For most fjords, the vertical stratification was well behaved and for these cases it was found that $c \approx 1$ and $\delta \approx -1.5$, see *Stigebrandt and Aure* (1989) for details. These fjord results were later used in *Sjöberg and Stigebrandt* (1992) to estimate the vertical variation of $\kappa(x, y, z)$ in the abyssal ocean from estimates of the barotropic to baroclinic energy transfer $E_w(x, y)$.

Local models for barotropic to baroclinic energy transfer due to baroclinic wave drag have also been developed for more complicated stratification, e.g., *Stigebrandt* (1980) and *Stacey* (1984). Finally, it should be noted that the bottom slope of sills in fjords usually is much greater than the critical slope. Direct generation of internal wave rays by sills is therefore probably not very important.

3. Baroclinic wave drag and barotropic to baroclinic energy transfer at fjord sills

The model for barotropic flow in straits with baroclinic wave drag as the only drag force, presented in section 2, can be used to compute the tidal response in fjords. Such computations offer a possibility to verify the model for barotropic to baroclinic energy transfer provided the tidal response in the fjord is known from observations. The model was applied in *Stigebrandt* (1999) to three fjords for which the phase shift of semi-diurnal tides was known. With known sea level outside the sill, $h_o = a_o \sin(\omega t)$ and with $Q_f = 0$, Eqs. (2) and (7) were thus used to

compute the sea level $h_i(t)$ in the fjords. The results for the three cases are discussed below.

The model was applied to the inner Oslo Fjord for which $A_f = 200 \text{ km}^2$, $B = 600 \text{ m}$, $h = 15 \text{ m}$, $d = 65 \text{ m}$, $c_g = 0.8 \text{ m s}^{-1}$. The mouth (the Drøbak Strait) is extremely short and sea bed friction may be neglected (cf. Stigebrandt, 1976). A semidiurnal tide of amplitude 0.15 m is assumed to exist outside the fjord. Using these figures the model predicts that the dissipation is about $2 \times 590 \text{ kW}$ (internal waves emitted from both sides of the sill). The phase lag of the semidiurnal tide in the fjord is predicted to be 22° . This is independent of the amplitude as long as $F_r < 1$ and Equation (7) applies. The phase lag should thus be approximately the same for all semidiurnal components of the tide. For the computation it is assumed that the internal wave speed outside the sill equals that inside which probably is an overestimate since the stratification is weaker outside than inside the sill most of the time. Thus, the predicted phase shift of M_2 across the sill is probably overestimated by some degrees. The observed phase shift is about 15° (Anonymous, 1997).

The model was also applied to Knight Inlet where the inner sill has the width $B = 1250 \text{ m}$ and depth $h = 60 \text{ m}$ while $d = m$ and $A_f = 220 \text{ km}^2$. The tidal component M_2 has the amplitude 1.5 m and for summertime stratification $c_g = 0.83 \text{ (0.50) m s}^{-1}$ for internal wave vertical mode 1 (2) (Webb and Pond, 1986). These authors report that the phase shift of M_2 across the inner sill in Knight Inlet is $2\text{--}3^\circ$ and from time series of velocity and density at different depths in the fjord they find that the internal wave response is a mixture of vertical modes 1 and 2. Stacey (1984) estimated the dissipation inside the sill to about 7 MW under similar conditions of stratification. The present model predicts that the phase shift across the inner sill is 3° (2°) and the dissipation inside the sill is predicted to be 10.1 (5.8) MW for mode 1 (2) internal wave response. With a mixed mode 1 and 2 response, the model thus seems to predict the conditions in Knight Inlet rather well.

The Idefjord, denoted basin 2 in the computations below, is situated at the Skagerrak coast and constitutes part of the border between Sweden and Norway. The mouth of the Idefjord has two narrow ($\sim 70 \text{ m}$) and shallow ($\sim 9 \text{ m}$) sills, at a distance 1.2 km from each other, separated by a wider and deeper small basin (basin 1). It is expected that baroclinic wave drag acts at both sides of both sills as long as $F_r < 1$. Baroclinic wave drag is then much greater than frictional drag. From Munthe Kaas (1970) one may obtain the following numbers: $A_{f1} = 0.27 \text{ km}^2$, $d_1 = 12 \text{ m}$, $h_1 = 9 \text{ m}$, $B_1 = 58 \text{ m}$, $c_{g1} = 0.5 \text{ m s}^{-1}$, $A_{f2} = .4 \text{ km}^2$, $d_2 = 19 \text{ m}$, $h_2 = 9.5 \text{ m}$, $B_2 = 78 \text{ m}$, $c_{g2} = 0.6 \text{ m s}^{-1}$ where subscript 1 (2) refers to basin 1 (2). By simultaneously solving Equations (2) and (7) for basins 1 and 2 coupled in series one obtains for a semidiurnal tidal component a phase shift of 33° between the coastal water and the Idefjord, and the amplitude in the fjord is 83% of that in the coastal water. These results are very close to the observed phase shift

(36°) and amplitude reduction in the fjord (Parsmar, personal communication, 1997).

The damping of the barotropic seiche in the Gullmar Fjord, Sweden, was studied by Parsmar and Stigebrandt (1997). They used the almost one-year-long sea level record from 1985 obtained at Bornö Hydrographical Station, situated in the inner part of the fjord, to estimate the damping coefficient of the barotropic seiche of period of about 2 hours. The seiche was described and modeled by Zeilon (1913). He also described observations of internal waves having the same frequency as the barotropic seiche in the Gullmar Fjord but did not discuss the damping of the seiche (Zeilon, 1912, 1913). Figure 2 shows monthly means of the theoretical, Eq. (11), and the observed damping coefficient in the Gullmar Fjord as estimated by Parsmar and Stigebrandt (1997). It can be seen that the two curves follow each other rather nicely in an annual cycle, caused by the varying vertical stratification, measured once a month the same year in the middle of the fjord (Fig. 3).

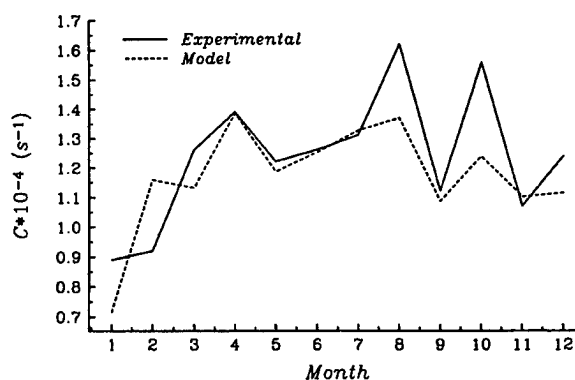


Figure 2. The annual cycle of modeled, Eq. (11), and observed (experimental) damping coefficient for the barotropic seiche in the Gullmar Fjord in 1985. (From Parsmar and Stigebrandt, 1997).

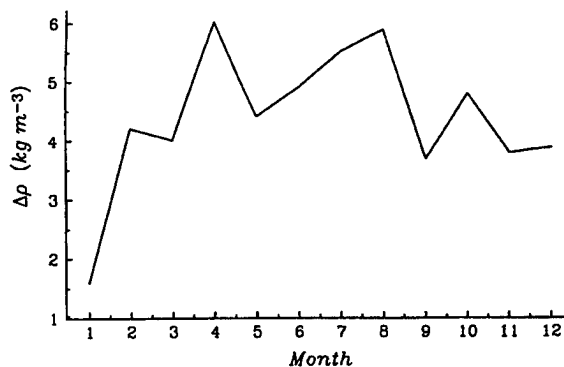


Figure 3. Monthly values of $\Delta \rho$ for a two-layer approximation of the stratification in the Gullmar Fjord in 1985. (From Parsmar and Stigebrandt, 1997).

It seems that the strait flow model with only baroclinic wave drag predicts the observed tidal phase shift quite well for strait flows with $F_r < 1$ and $\epsilon_f \ll \epsilon_w$. From this, one may conclude that the baroclinic wave drag as implemented in the model seems to be quite realistic. In particular it is interesting to note that in spite of the short separation (1.2 km) between the sills in the mouth of the Ide Fjord, baroclinic wave drag is apparently fully developed at both sides of the two sills. The fact that the model for barotropic to baroclinic energy transfer also explains the observed damping of the seiche in the Gullmar Fjord further strengthens the conclusion that the process of baroclinic wave drag should be regarded as a locally controlled process and that the accompanying barotropic to baroclinic energy transfer is well estimated by Eq. (6). It is notable that in some of the studied cases the amplitude of the barotropic flow is near critical but still the linear model for barotropic to baroclinic energy transfer seems to perform well also for these cases.

4. Relationship between barotropic to baroclinic energy transfer and diapycnal mixing in fjord basins

It was suggested in *Stigebrandt* (1976) that most of the diapycnal mixing in the basin water of the Oslo Fjord is performed by dissipating internal tides generated at the sill in the mouth. Using data from this fjord the efficiency factor R_f of turbulent mixing processes was estimated to be about 0.05. *Stigebrandt and Aure* (1989) investigated the mixing efficiency in a large number of fjord basins in Norway. They found that the mixing efficiency equals about 0.056 in fjords where the amplitude of the barotropic current over the sill is subcritical (wave-basins). Figure 4 shows the observed rate of work against the buoyancy forces in the fjords, normalized by the horizontal area of the fjords at sill level, versus the theoretical

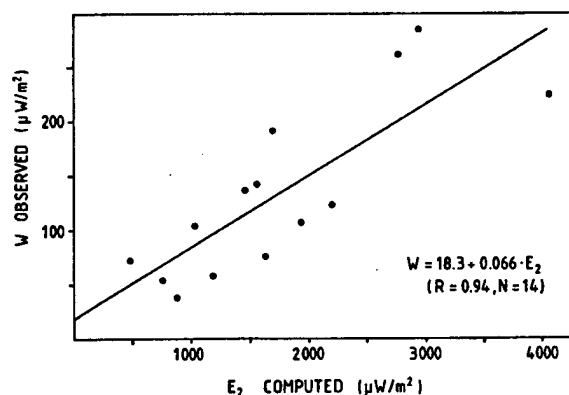


Figure 4. Observed normalized rate of work against the buoyancy forces in the basin water ($w_{observed}$) versus the estimated barotropic to baroclinic energy transfer by semidiurnal tides ($E_2_{computed}$) at the sill for a number of fjords. (From *Stigebrandt and Aure*, 1989).

barotropic to baroclinic energy transfer. Studies in several other fjords confirm that the value of R_f is about 0.06, e.g., *Svensson* (1980), *Simpson and Rippeth* (1993) and *Tinis* (1995).

Based on investigations in a large number of fjords in Scandinavia, Scotland, and Canada, the mixing efficiency ratio R_f thus appears to be about constant and independent of the dimension and form of fjords. Not even the ratio between the volume of the basin water and the total fjord volume seems to have any importance. This supports the assumption, put forward in *Stigebrandt* (1976), that most of the energy released by baroclinic wave drag dissipates in the basin water. Even very short fjords, of lengths that are only small fractions of the wavelengths of internal tides, have the same efficiency ratio as large fjords. This must imply that the process of barotropic to baroclinic energy transfer by baroclinic wave drag at fjord sills should not be influenced by possible reflection of internal tides in the inner reaches of the fjord. This conclusion, implying that baroclinic wave drag is a process determined by the local conditions at the sill, was also drawn in section 3 above from the Ide Fjord case, where the two sills in the mouth separated by a basin only about 1.2 km long, were shown to give rise to full baroclinic wave-drag.

Guided by a simple laboratory experiment, the present author suggested that the baroclinic energy gained at sills by baroclinic wave drag is transferred to turbulence and mixing by the breaking of internal waves against sloping bottoms (*Stigebrandt*, 1976). From this one should expect to find high values of the vertical diffusivity along the rim of the fjord basin (hot spots in the terminology of *Munk*, 1997) and small values in the interior. A boundary-mixing model based on this scenario was described in *Stigebrandt* (1976). An experiment in the Oslo Fjord, with a tracer initially introduced in the interior of the basin water showed that diapycnal mixing in the interior really is much smaller than the basin average, see *Stigebrandt* (1979). This experiment supports the view that diapycnal mixing takes place close to the bottom, either by waves breaking against the bottom, or by wave-bottom interaction creating high local shear in the water column close to the bottom, or by turbulence generated close to the sill. To the best of the present author's knowledge no direct observations of the spatial distribution of turbulent dissipation or mixing in fjord basins have been published.

Stigebrandt and Aure (1989) also investigated the efficiency of diapycnal mixing in the basin water of supercritical so-called jet-fjords, where the amplitude of the barotropic tide over the sill exceeds the speed of internal waves in the fjord. The mixing efficiency for these cases defined by Eq. (13) with ϵ equal to the dissipation of the jet, varied a lot. The mean value was about 0.01, which is much lower than for wave basins. This is because the jet dissipates close to the sea surface and only little of the jet energy is transmitted to deeper layers. However, it seems that internal tides may be generated also in jet-fjords (*Tinis*, 1995, *Allen and Simpson*, 1998). Wave generation

should then not be the result of baroclinic wave drag but be due to a completely different mechanism with the fluctuating jet acting as a piston. Wave generation probably occurs in the vertical cross-section of the fjord where the speed of the declining jet has been reduced to the speed of the lowest internal wave mode.

5. Relationship between barotropic to baroclinic energy transfer at fjord sills and radiation of baroclinic energy into fjords

One might expect that the energy transferred from barotropic to baroclinic motions by baroclinic wave drag at fjord sills would radiate away from the sill by internal waves. If there is no dissipation at or near the sill one should be able to verify models for barotropic to baroclinic energy transfer from estimates of the power of the internal wave radiation. This expectation led the present author to estimate the radiation from the Dröbak sill in the Oslo Fjord. From sparse current measurements it was found that the seaward radiation was about 110% of the expected radiation while the landward radiation was about 80% (Stigebrandt, 1979). However, the estimate of the seaward radiation from the sill was considered uncertain because of uncertainty of the stratification. De Young and Pond (1989) found that radiation of baroclinic energy away from sills in some Canadian fjords was only 50%-80% of the expected radiation. Thus, it seems that there often is a substantial transfer of baroclinic energy to small-scale turbulence in or close to the sills (the short pathway).

The method to compute barotropic to baroclinic energy transfer under the assumption that barotropic and baroclinic modes together satisfy the boundary condition of vanishing normal velocity at non-horizontal topography seems to give quite adequate results for the energy transfer. Evidence based on tidal retardation (phase shift) in three fjords and damping of the barotropic seiche in one fjord was presented in section 3. Further evidence based on the observed constant and the relationship between barotropic and baroclinic energy transfer and the rate of diapycnal mixing in the basin water of fjords was presented in section 4. From all these cases it seems that vertical stratification and the large-scale topography of the sill (height, depth below the sea surface and width) and amplitude and frequency of the barotropic current over the sill are the only properties of the fjord that matter for the topographic barotropic to baroclinic energy transfer. There is no evidence for influence from the field of internal waves in the fjord. It thus appears that the barotropic to baroclinic energy transfer (and the baroclinic wave drag upon the barotropic current) at fjord sills should be considered to be a local process that can be estimated quite well from simple models. The internal wave response in the fjord, however, seems to differ from fjord to fjord.

From presently available information, it is here suggested that the internal wave response to the baroclinic

forcing at the sill depends on the capacity of the fjord basin to dissipate internal waves. In basins with high dissipation capacity, most of the baroclinic energy provided by baroclinic wave drag at the sill may possibly be transmitted by progressive internal waves further into the fjord. In other fjords with low dissipation capacity, only little of the baroclinic energy provided at the sill may be transmitted into the fjord and the rest is dissipated close to the sill. If this view is correct, radiation of internal wave energy from sills is not a good measure of the barotropic to baroclinic energy transfer at sills. It should rather be a measure of the capacity of the inner reaches of a fjord to dissipate internal waves.

6. Concluding remarks

It has been shown that the barotropic to baroclinic energy transfer at fjord sills is well estimated by a simple local model for a large variety of basin conditions. From this, it is concluded that the process of baroclinic wave drag essentially is a local process determined by the topography of the sill, the amplitude and frequency of the fluctuating barotropic flow and the stratification in the fjord. The model applies equally well for a wide range of fjords so the magnitude and form of a fjord basin seem to be of no importance for the process of baroclinic wave drag. The model is based on the assumption that the boundary condition at the sill-fjord junction is satisfied by the barotropic flow together with progressive internal waves. From this, it might seem logical to verify the model by comparing modeled and observed radiation of internal waves from the sill. However, as discussed in the present paper, the net radiation of baroclinic energy into fjords seems to also depend on the capacity of the fjord basin to dissipate internal waves. Contrary to the baroclinic wave drag, the fjord capacity to dissipate internal waves is probably dependent on both the magnitude and form of the fjord basin. Thus, there should be no simple relationship between the barotropic to baroclinic energy transfer at the sill and the net transfer (radiation) of baroclinic energy into a fjord.

The pathways of energy gained by baroclinic wave drag at sills to turbulent dissipation and mixing in fjords are apparently complex. This suggests a number of future investigations to clarify the pathways. How is turbulent dissipation in fjords distributed in time and space? Particular care should be taken to obtain observations near areas of wave generation (sills) and along the rim of the basins where most of the mixing probably occurs. Which factors control the distribution of dissipation of internal waves in fjords? In this paper, it is suggested that the net radiation of internal wave energy into a fjord might be controlled by (and cannot exceed) the capacity of the fjord to dissipate internal waves. Having data from a wide range of fjords, it should be possible to find the key factors determining the capacity of a fjord to dissipate internal waves. As argued earlier in this paper, these key factors are probably related to physical dimension and form

of the fjord basin. By which mechanisms are internal waves dissipated close to sills in fjords where the barotropic to baroclinic energy transfer at the sill exceeds the capacity of the fjord to dissipate internal waves?

The closed character of fjord basins beneath the sill level during stagnant conditions gives an opportunity to estimate the efficiency R_f of turbulence with respect to mixing, using the energy budget in Eq. (13). The dominating energy source for the turbulent mixing processes in most fjord basins is due to baroclinic wave drag at the sill. There may also be energy contributions by other sources, which tend to overestimate R_f if not included in the energy budget. However, these other possible contributions are believed to be small in most fjords. If on the other hand, some of the energy gained by baroclinic wave drag is dissipated above sill level, R_f tends to be underestimated. Estimates in different wave fjords repeatedly give an efficiency of about 0.06. The present author believes that the estimate of R_f from fjord basins actually is the best estimate available in oceanography. However, in oceanographic literature one often uses $R_f = 0.2$ but evidence for this value seems obscure. Fjords are usually salt stratified while most parts of the ocean are dominated by temperature stratification. A possible difference in the mixing efficiency between waters stratified by salt and temperature respectively may then explain the different values of R_f . However, this issue should be investigated further.

Extrapolation of the fjord results to the ocean suggests that (1) barotropic to baroclinic energy transfer should be computed using local models and (2) the radiation of energy away from locations where it is released by baroclinic wave drag might be appreciably less than the barotropic to baroclinic energy transfer. Thus, a substantial part of the dissipation might take place close to the topography where baroclinic wave drag occurs. This was also pointed out in *Sjöberg and Stigebrandt* (1992). Recent observations of dissipation from the deep ocean show enhanced dissipation near the seabed in areas with strong bottom topography, e.g. *Polzin et al.* (1997).

How closely may ridges and bumps be situated to contribute to baroclinic wave drag? One might think that topography with horizontal length scales less than the wavelength of internal tides are unimportant. However, the idea that baroclinic wave drag is a local process and the examples from Ide Fjord and other fjords disprove this! Topographic features of even quite small horizontal length-scales probably contribute to baroclinic wave drag provided the surrounding water is stratified. Thus, small amplitude topography submerged in a homogeneous bottom boundary layer should not contribute very much to baroclinic wave drag.

Baroclinic wave drag on barotropic tides might be the major mechanism to support energy to turbulence and mixing in the deep ocean. However, the contribution by winds is so far not clear, see estimates by e.g., *Kundu* (1993), *Nilsson* (1995) and *Munk and Wunsch* (1998). An attempt to investigate purely wind-driven mixing beneath

the surface layers is presently undertaken in the virtually tide-less Baltic proper by the multinational experiment DIAMIX. High-resolution measurements of currents, density and dissipation will be made during two-week periods in summer and winter. The objective is to describe and parameterize the purely wind-driven mixing of the Baltic proper deepwater. A future goal is to generalize this parameterization and apply it to the open ocean for a comparison between wind-driven and tidally driven mixing. An investigation using the budget method and historic hydrographic data from the Baltic has recently been made by *Axell* (1998) who found a strong seasonal variation in mixing intensity in pace with the wind forcing.

Acknowledgments. This work was supported by the Swedish Natural Science Research Council (NFR). The author wants to thank Peter Müller for the invitation to participate in the 'Aha Huliko'a Workshop on Internal Wave Modeling.

References

- Allen, G.L. and J.H. Simpson, Reflection of the internal tide in the upper Loch Linnhe, a Scottish Fjord. *Estuarine, Coastal Shelf Sci.*, **46**, 683-701, 1998.
- Anonymous, Tidevanntabeller (Tide Tables) for den norske kyst. *Statens Kartverk, Sjøkartverket, Norway*, 80 pp., 1997 [Available from Sjøkartverket, Box 36, N-4001 Stavanger, Norway].
- Axell, L., On the variability of Baltic Sea deepwater mixing. *J. Geophys. Res.*, **103**, 21667-21682, 1998.
- Bell, T.H. Jr., Topographically generated internal waves in the open ocean. *J. Geophys. Res.*, **80**, 320-327, 1975.
- Blackford, B.L., On the generation of internal waves by tidal flow over a sill – a possible nonlinear mechanism. *J. Mar. Res.*, **36**, 529-549, 1978.
- Cox, C. and H. Sandström, Coupling of internal and surface waves in water of variable depth. *J. Oceanogr. Soc. Jpn.*, **20**, 499-513, 1962.
- De Young, and S. Pond, Partition of energy loss from the barotropic tide in fjords. *J. Phys. Oceanogr.*, **19**, 246-252, 1989.
- Farmer, D.M. and H. Freeland, The physical oceanography of fjords. *Prog. Oceanogr.*, **12**, 147-220, 1983.
- Gade, H.G., Hydrographic investigations in the Oslofjord: A study of water circulation and exchange processes. *Rep. 24. Geophys. Inst. Div. A, Univ. of Bergen, Norway*, 193 pp. + figs., 1970.
- Gargett, A.E., Vertical eddy diffusivity in the ocean interior. *J. Mar. Res.*, **42**, 359-393, 1984.
- Kundu, P.K., On internal waves generated by travelling wind. *J. Fluid Mech.*, **254**, 529-560, 1993.
- McClimans, T.A., On the energetics of tidal inlets to landlocked fjords. *Mar. Sci. Commun.*, **4**, 121-137, 1978.
- Munk, W., Abyssal recipes. *Deep-Sea Res.*, **13**, 707-730, 1966.
- Munk, W., Once again: once again – tidal friction. *Prog. Oceanogr.*, **40**, 7-35, 1997.
- Munk, W. and C. Wunsch, Abyssal recipes II: energetics of tidal and wind mixing. *Deep-Sea Res.*, **45**, 1977-2010, 1998.
- Munthe Kaas, H., Iddefjorden og dens forurensningsproblemer. Rapp. Nr. 2: Situasjonsrapport pr. 1 desember 1969. *NIVA, Oslo, Rep. O-113/64*. 33 pp., 1970 [Available from NIVA, Box 173 Kjelsås, N-0411 Oslo, Norway].
- Nilsson, J., On the energy flux from travelling hurricanes to the oceanic internal wave field. *J. Phys. Oceanogr.*, **25**, 558-573, 1995.
- Parsmar, R. and A. Stigebrandt, Observed damping of barotropic seiches through baroclinic wave drag in the Gullmar Fjord. *J. Phys. Oceanogr.*, **27**, 849-857, 1997.

- Polzin, K.L., J. M. Toole, J.R. Ledwell, and R.W. Schmitt, Spatial variability of turbulent mixing in the abyssal ocean. *Science*, 276, 93-96, 1997.
- Simpson, J.H. and T. Rippeth, The Clyde Sea: a model of the seasonal cycle of stratification and mixing. *Estuarine Coastal Shelf Sci.*, 37, 129-144, 1993.
- Sjöberg, B. and A. Stigebrandt, Computations of the geographical distribution of the energy flux to mixing processes via internal tides: its horizontal distribution and the associated vertical circulation in the ocean. *Deep-Sea Res.*, 39, 269-291, 1992.
- Stacey, M.W., The interaction of tides with the sill of a tidally energetic inlet. *J. Phys. Oceanogr.*, 14, 1105-1117, 1984.
- Stigebrandt, A., Vertical diffusion driven by internal waves of tidal origin in a sill fjord. *J. Phys. Oceanogr.*, 6, 486-495, 1976.
- Stigebrandt, A., Observational evidence for vertical diffusion driven by internal waves of tidal origin in the Oslofjord. *J. Phys. Oceanogr.*, 9, 435-441, 1979.
- Stigebrandt, A., Some aspect of tidal interaction with fjord constrictions. *Estuarine Coastal Mar. Sci.*, 13, 197-211, 1980.
- Stigebrandt, A., Resistance to barotropic tidal flow in straits by baroclinic wave drag. *J. Phys. Oceanogr.*, 29, 191-197, 1999.
- Stigebrandt, A. and J. Aure, Vertical mixing in the basin waters of fjords. *J. Phys. Oceanogr.*, 19, 917-926, 1989.
- Svensson, T., Tracer measurement of mixing in the deep water of a small, stratified sill fjord, in *Fjord Oceanography* (H.J. Freeland, D.M. Farmer and C.D. Levings, Eds.). Plenum Press. P. 233-240, 1980.
- Tinis, S.W., The circulation and energetics of the Sechart Inlet System, British Columbia. PhD thesis, Dept. of Oceanography, the University of British Columbia, 173 pp, 1995 [Available from Dept. Of Earth and Ocean Sciences, the University of British Columbia, 6339 Stores Road, Vancouver, British Columbia V6T 1Z4].
- Webb, A.J. and S. Pond, A modal decomposition of the internal tide in a deep, strongly stratified inlet: Knight Inlet, British Columbia. *J. Geophys. Res.*, 91, 9721-9738, 1986.
- Zeilon, N., On the tidal boundary waves and related hydrodynamical problems. *Kungl. Svenska Vetenskapsakademiens Handlingar*, Vol. 47 (4), 46 pp, 1912.
- Zeilon, N., On the seiches of the Gullmar Fjord. *Sven. Hydrogr. Biol. Komm. Skr.*, V, 1-17, 1913.

Stratified Flow Over Topography and the Generation of Internal Solitary Waves

David M. Farmer

Institute of Ocean Sciences, Sidney, BC, Canada

Laurence Armi

Scripps Institution of Oceanography, La Jolla, California

Abstract. Internal solitary waves, which form such a prominent feature in remote sensing images of the coastal zone, are the far field expression of stratified flow over topography. Nonlinear evolution of large amplitude internal tides propagating over the continental shelf is one means by which they might be generated, but detailed observations of wave generation over topography in an inlet illustrate other mechanisms that occur when the topography is abrupt. Tidally forced flow over abrupt topography can lead to streamline splitting. The streamline bifurcation leads to topographic control of the flow beneath the bifurcated layer, even though a simple calculation of the densimetric Froude number using tidal velocities and the unperturbed density field would imply that the flow was subcritical. Its evolution over the changing tidal current is intimately linked to the formation and suppression of boundary layer separation. The split streamlines enclose a slowly moving and weakly stratified layer accompanied by shear flow instability which itself may be a source of nonlinear internal waves. Moreover the collapse of this slowly moving layer as the tidal current slackens generates an internal undular bore. Observations are required to show the generality of these different mechanisms, especially in areas where solitary waves are commonly observed over the continental shelf.

1. Introduction

Internal solitary waves are widespread in the coastal ocean and a prominent feature of remote sensing images of shelf waters, often taking the form of an ordered set of lenticular streaks radiating shoreward. Aside from their fluid dynamical interest as examples of waves of permanent form, internal solitary waves may play a role in cross shelf advection, mixing and the stirring of sediments. Strong currents associated with internal solitary waves may also present a significant hazard to offshore engineering operations. Their prominence in radar and optical images also motivates development of a better understanding of their generation and propagation as remotely sensed signatures of the ocean environment.

The occurrence of internal solitary waves in coastal waters is usually modulated by tidal forcing. It appears that the waves are associated with flow over topographic features such as ridges, canyon walls, and the shelf break; however, the details of the generation process have been investigated in only a few locations. The waves can be generated in the immediate vicinity of the topography due to a strongly nonlinear interaction such as an internal hy-

draulic transition, or they can evolve as a high frequency far-field manifestation of an internal tide. An example of the latter case which has been explored in great detail, is the soliton train forming over the north west Australian shelf (*Holloway et al.*, 1997, *Holloway et al.*, 1999 and elsewhere in this volume). An internal tide of large amplitude propagating across the relatively shallow shelf steepens, leading to growth of high frequency internal solitary waves. Many aspects of the generation and subsequent behavior of the waves appear explainable with the extended KdV equation, including aspects of the dissipation and the effect of rotation and cubic nonlinearity.

Abrupt topography appears to be particularly effective at nonlinear internal wave generation in the near field. Field studies in Knight Inlet have provided very detailed observations of this process, although the complex and nonlinear pattern of topographic response has thus far resisted comprehensive model analysis. Several mechanisms appear responsible for wave generation, including the collapse of an internal hydraulic response which can lead to intrusive undular bores. Nonlinear internal waves can also be formed as an upstream influence of the topography. Unlike the gradual evolution from a steepening

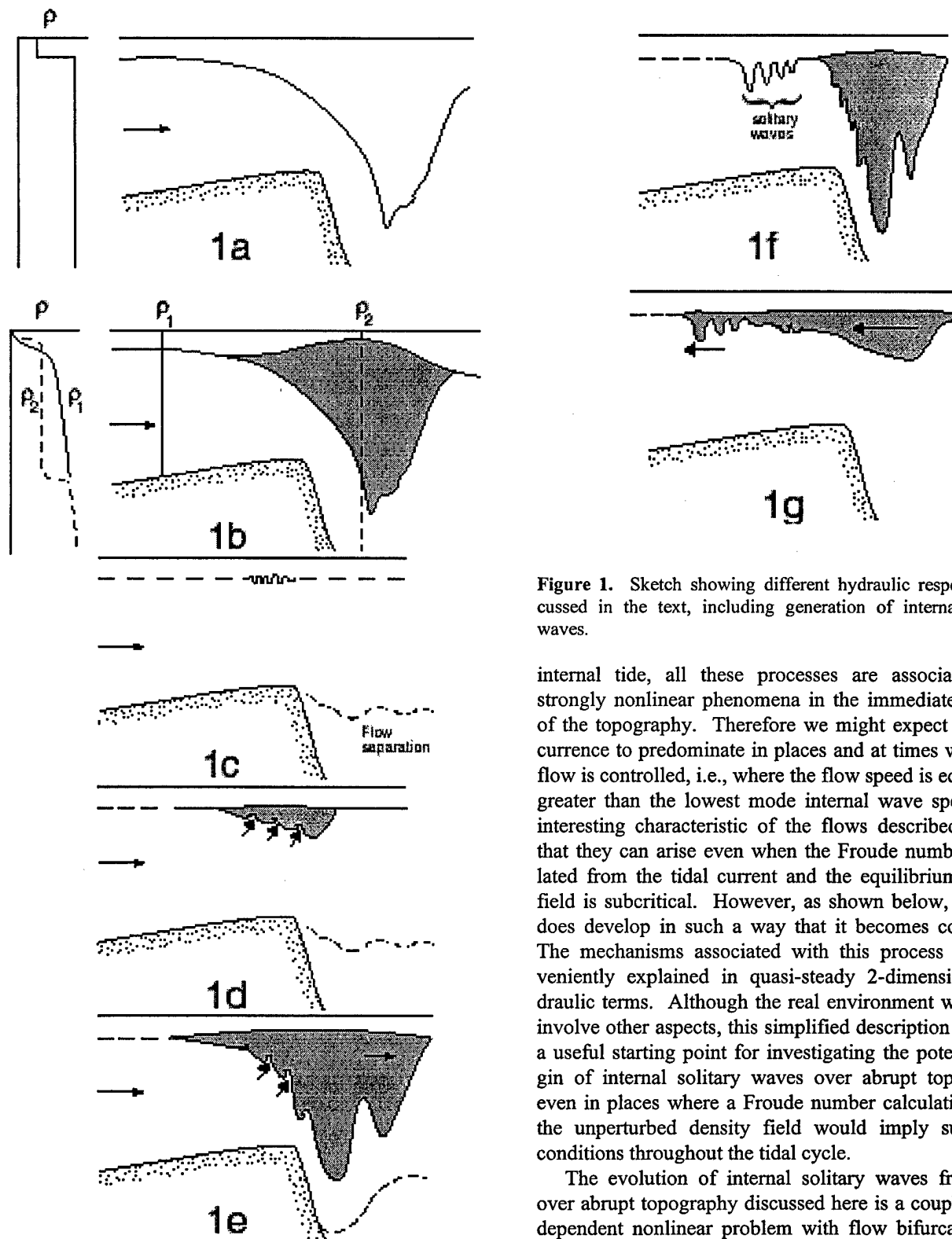


Figure 1. Sketch showing different hydraulic responses discussed in the text, including generation of internal solitary waves.

internal tide, all these processes are associated with strongly nonlinear phenomena in the immediate vicinity of the topography. Therefore we might expect their occurrence to predominate in places and at times where the flow is controlled, i.e., where the flow speed is equal to or greater than the lowest mode internal wave speed. An interesting characteristic of the flows described here is that they can arise even when the Froude number calculated from the tidal current and the equilibrium density field is subcritical. However, as shown below, the flow does develop in such a way that it becomes controlled. The mechanisms associated with this process are conveniently explained in quasi-steady 2-dimensional hydraulic terms. Although the real environment will likely involve other aspects, this simplified description provides a useful starting point for investigating the potential origin of internal solitary waves over abrupt topography, even in places where a Froude number calculation using the unperturbed density field would imply subcritical conditions throughout the tidal cycle.

The evolution of internal solitary waves from flow over abrupt topography discussed here is a coupled time-dependent nonlinear problem with flow bifurcation and boundary layer separation. Despite model analysis of discrete aspects of the flow, there have as yet been no comprehensive models which include all of the essential features. Our purpose here is to illustrate these features with observations acquired in Knight Inlet, British Columbia.

2. Flow separation over abrupt topography

We are concerned with abrupt topography where the flow encounters a sharp increase in total water depth. Unstratified flow past bluff bodies is a widely studied field, with implications for the calculation of drag. Stratified flow over abrupt topography is more complicated and has received relatively less attention (*Huppert and Britter*, 1982), although it has implications for atmospheric flow over mountains. Separation of the boundary layer can occur when there is an adverse pressure gradient caused by high curvature. It results in the formation of a separation 'bubble' downstream of the topography which largely remains isolated from the main flow except for a slow recirculation. The separation has the effect of isolating the main flow from the abrupt feature of the topography and thus reducing the drag. For density stratified conditions development of lee waves or a plunging lower layer can be inhibited by separation. This interaction with the density stratification allows the separation point to move further downslope leading to a progressive transition towards the high drag state.

3. Internal hydraulic response

The steady state internal hydraulic response of stratified flow over topography has been widely studied (*Armi*, 1986). Although the internal hydraulic response to unsteady forcing has been less well studied, some insight into the behavior can be achieved with a quasi-steady model if the time dependence is small enough that the flow can respond locally to the forcing. This will normally be true, for example, if the time required for a density perturbation to propagate across the relevant topographic feature is small compared to the time scale for barotropic forcing.

The steady state hydraulic analysis then identifies the point at which the flow is controlled and describes the asymmetry of the flow about the control characteristic of the nonlinear response. Figure 1a shows this response for a steady two-layer flow, illustrating the asymmetry between the subcritical and supercritical flow. At some point the downstream conditions require that the flow be matched through an internal hydraulic jump. Dissipative effects become important at this location. The jump may be undular, in which case internal waves evolve. These waves can be of large amplitude, comparable to the vertical scale of the topography. In general, coastal flows have more complicated density profiles than the two-layer structure shown in Figure 1a. For example a well defined 3-layer density structure may occur, allowing development of a mode 2 response. This means that an internal hydraulic response can occur, even when a first order

calculation of the densimetric Froude number implies that the flow is subcritical. More generally the stratification is normally continuous, for example with a thin strongly stratified layer overlying weaker stratification. Flow establishment may then take place through a bifurcation as shown in Figure 1b.

4. Flow bifurcation

Bifurcation appears to be a very common characteristic of continuously stratified flow over topography. The experiments carried out by *Long* (1955) show streamline bifurcation forming detached, recirculating flows which are trapped downstream of the obstacle. Long's theoretical analysis appears to predict closed streamlined flow which is qualitatively similar to the laboratory results, but the solutions are not strictly valid in this case. If closed streamline flow occurs or, more generally, if a bifurcation in the flow occurs, the question arises as to the origin of the fluid within the bounding streamline. In other words, how is the flow set up?

This problem is implicit in many studies of atmospheric flow over topography where its significance arises because of the drag of mountain ranges which are thought to account for approximately one half of the total drag of the earth on atmospheric circulation (*Baines*, 1995). The evolution of bifurcating flows has been examined with numerical models and these have motivated explanations of the mechanism (i.e., *Peltier and Clark*, 1979). The problem is difficult to model because of Reynolds number limitations and the atmospheric observations lack the density required for detailed comparison. Tidal flow over a sill provides a useful oceanographic analog to the atmospheric case while also illustrating a mechanism that must be widespread in the coastal ocean.

5. Flow establishment: bifurcation and the suppression of flow separation

Quite detailed measurements of the response of stratified flow to tidal forcing over a sill in Knight Inlet (*Farmer and Armi*, 1999a) show the way in which the bifurcation develops. The tidal current starts with small scale instability and entrainment which then allows a weakly stratified and slowly circulating intermediate layer to form. This layer steadily grows, leading to the establishment of the equilibrium steady state hydraulic response. The process is inextricably linked to the flow separation discussed above. The formation of the slowly moving layer downstream of the bifurcation allows the deeper layer to flow down the lee slope of the topography, suppressing the separation. This transition, however, will occur gradually, since it is coupled to the filling in of the recirculating flow above. Thus the time dependent

evolution involves an initial separation from the crest so that the downstream flow leaves as a horizontal jet (Figure 1c). The strong shear engendered by acceleration over the crest creates instability and the transfer of fluid from the deeper layer up into the weakly stratified flow above. The growing intermediate layer remains trapped above and downstream of the crest (Figure 1d).

As the weakly stratified layer fills in further, the deeper layer starts to descend a little as it passes the sill crest and the separation point moves downstream (Figure 1e). The evolution of this flow therefore represents a coupling between the shear instabilities that transfer fluid into the intermediate layer, the expansion of this intermediate layer, and the suppression of the boundary layer separation.

The location of the bifurcation is determined by the density of the trapped fluid, the surrounding stratification, the shape of the underlying topography and the strength of the barotropic component. If all of these variables are given, the shape of the plunging interface may be derived from the quasi-steady hydraulic equations. The slowly moving intermediate layer is stratified and the resulting variation in the strength of the density step has a significant effect on the resulting shape of the interface. A calculation along these lines is given in *Farmer and Armi* (1999a).

As the barotropic transport continues to increase, the bifurcation will move downstream and may pass over the crest. Analysis of the hydraulic response to a slowly changing tidal current shows that the position of the bifurcation when it is close to the crest is extremely sensitive to the barotropic forcing. A quasi-steady analysis cannot therefore be expected to provide a reliable indication of what happens, but observations confirm that nonlinear internal waves appear just upstream of the bifurcation at the same time as it retreats over the sill crest (Figure 1f and Figure 2). These solitary waves are of first mode and propagate upstream of the bifurcation.

6. Collapse of the intermediate layer and solitary wave generation

As the tidal current slackens, the large mass of nearly stationary fluid that has accumulated over and just downstream of the sill crest collapses. For a short period an exchange flow occurs: the collapsing weakly stratified layer moves upstream while the deeper layer continues downstream. If there is no strong surface stratification, the collapsing upper layer advances upstream as an internal bore which may be undular, thus forming nonlinear internal waves. These have been referred to as 'solibores' (*Henye*, 1998) and have been widely observed in many coastal environments. If the weakly stratified layer is capped by stronger stratification, the upstream flow ad-

vances as an intrusive feature that can be described as a mode 2 internal bore. Again, the bore can be undular and thus exhibit mode 2 nonlinear internal waves (Fig. 1g). If the internal hydraulic jump that had formed during the tidal current downstream of the topography was itself undular, each wave crest can preserve its identity as it moves over the crest, thus producing a train of internal solitary waves that advance upstream (c.f. Figure 9 in *Farmer and Smith*, 1980).

These various outcomes have been well documented and are probably widespread. They depend on control of the flow over the crest. The important point here is that a simple Froude number calculation based on the unperturbed density stratification and predicted tidal current is insufficient to determine whether or not the flow becomes controlled. Bifurcation of the flow allows a single layer 'reduced gravity' hydraulic transition to occur. The formation and relaxation of this flow may then serve as a site for the generation of internal solitary waves.

7. The Generation of internal solitary waves upstream of the control

The formation of mode 1 internal solitary waves upstream of the bifurcation (Figure 1f) represents an example of transcritical wave generation in the sense that the waves are formed upstream of a hydraulic control. It has been observed in both laboratory and numerical models that an instability of the control can generate upstream propagating internal solitary waves, even for steady forcing (*Cummins* 1995, *Melville and Helfrich*, 1987). In addition to the unsteady mechanism illustrated in Figures 1f and 2, it also appears possible for internal solitary waves to be formed on the unstable shear layer associated with bifurcation.

The bifurcation encloses an intermediate layer that moves slowly relative to the deeper flow. The unstable interface between the layers may form waves that can propagate in either direction. If the scale of the waves is such that the wave speed exceeds the local flow speed, then waves travelling against the flow will propagate upstream. Waves that travel with the flow move quickly downstream. The wave speed depends, of course, not only on the stratification, but also on the shear arising from the larger scale topographic response. These waves will be 'transcritical' in the sense that they are formed and propagate upstream of a flow control. However, the formation of upstream propagating waves in this way requires that the instability be of large enough scale to have a speed exceeding that of the background flow speed. This is the speed of a long interfacial wave at the control; just upstream of this point the flow will be subcritical, but short waves propagating against the current will still be swept downstream.

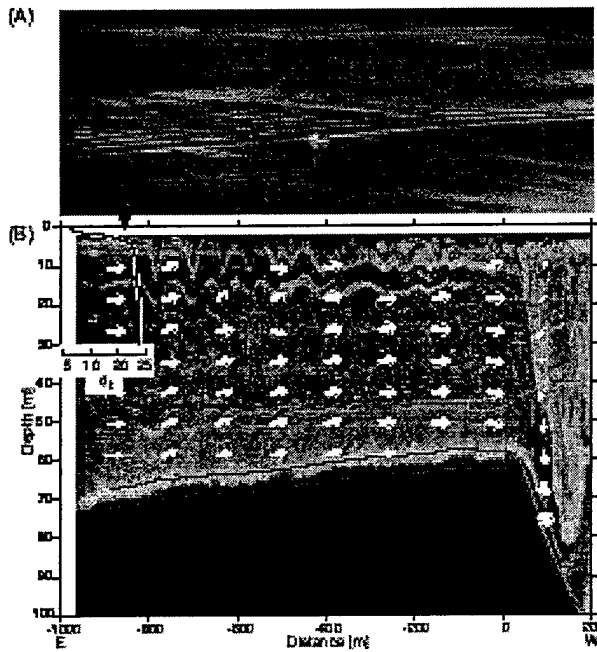


Figure 2. (Above) Air photo of solitary waves in Knight Inlet. (Below) Acoustic image and Doppler velocity field corresponding to the air-photo, showing internal solitary waves. Inset: Upstream density profile.

The scale of the unstable flow is determined by the scale of the fastest growing wave in the unstable shear layer. The resulting wavelength may be too small to produce an upstream propagating wave; however, growing instabilities interact and can therefore generate components having a greater wavelength than the original disturbance. Even if the primary wave is swept downstream, the longer wavelength component, having greater celerity, may still propagate upstream. The stability is found from the dispersion relationship for a stratified flow with shear:

$$c(k) = \left\{ P \pm \left(P - \sum R \left[U_i^2 k^2 R_i + U_3^2 k^2 R_2 - \rho_2 g' k \right] \right)^{1/2} \right\} / k \sum R$$

where $P = k(U_1 R_1 + U_2 R_2)$, U_i is the speed, ρ_i the density and h_i the thickness of the upper and lower layers, $i=1,2$, respectively, k is the wavenumber, $R_i = \rho_i \cotan h(kh_i)$, $\sum R = R_1 + R_2$, g is gravitational acceleration and $g' = g \times (\rho_2 - \rho_1) / \rho_2$ the reduced gravity.

Figure 3a (adapted from Farmer and Armi 1999b) shows observations of an unstable shear layer. There is some indication that the wavelength of the instabilities is greater close to the sill crest. Figure 3b shows the same environment 30 minutes later. Nonlinear interfacial waves appear upstream of the obstacle crest. Since the measurements are not continuous we have no direct

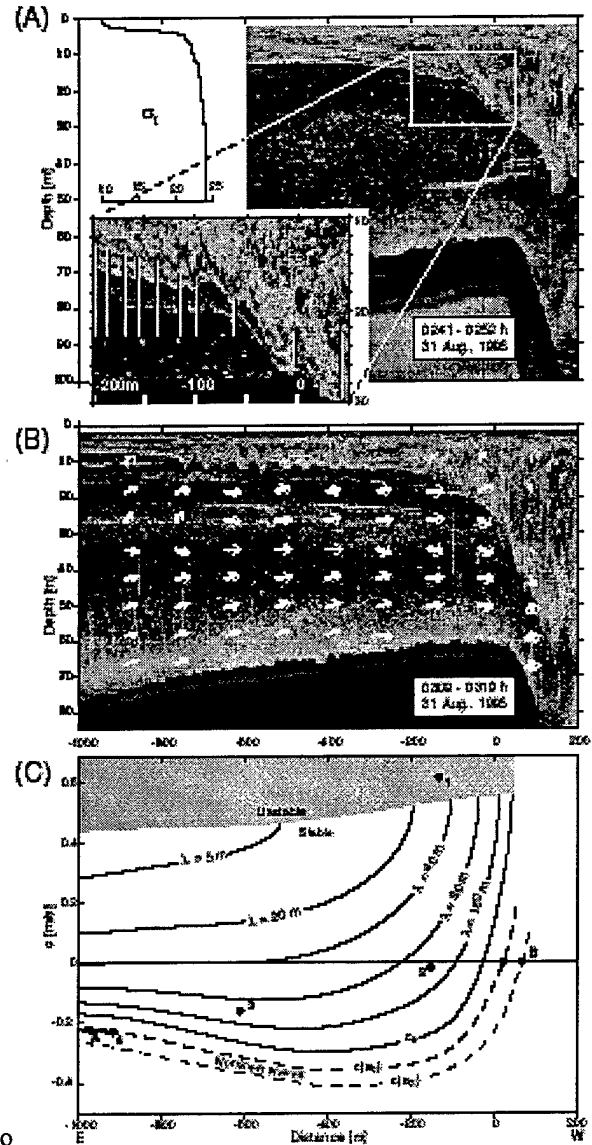


Figure 3. (a) Acoustic image showing bifurcating flow over Knight Inlet and instabilities on the descending shear layer. (Inset: Enlargement to illustrate changing scale of instabilities.) (b) As above, but 30 minutes later. (c) Dispersion relation for upstream propagating waves, showing wave speed as a function of wavelength and position. Instability indicated by area of grey tone.

observation of the origin of the waves. Upstream propagating waves would move along an interface that approaches the surface, thus enhancing the nonlinearity.

Figure 3c shows the stability and wave speed for different wavelengths and positions calculated from the dispersion equation relative to a fixed frame of reference coincident with the figures above. The wave speeds are only shown for waves that travel against the current. Positive speeds correspond to waves that are advected

downstream; only waves with negative speeds can escape upstream. The heavy line identified as c_0 identifies the speed of the long interfacial wave.

Figure 3c also illustrates a possible sequence of wave generation. Shear flow instability at (1) leads to waves that interact to produce longer waves (2) which can propagate upstream (3), eventually evolving into solitary waves (4) as they move up the shoaling interface.

Since an inherent property of internal solitary waves is that they have a greater celerity than long infinitesimal waves, it should be possible for a solitary wave to maintain its position against the background flow speed within the supercritical region just downstream of an internal hydraulic transition. This is illustrated in Figure 3c at position B. Solitary waves have been observed to remain trapped at this location for up to 2 h.

9. Conclusions

The observations discussed here illustrate some of the ways in which internal solitary waves can arise from stratified flow over abrupt topography. The mechanisms are involved and evidently depend on an interaction between shear flow instability and mixing, boundary layer separation and the internal hydraulic response. Thus far we lack the observations required to demonstrate the generality of the Knight Inlet results, but it would appear likely that these wave generation mechanisms occur wherever there are strong tidal currents over abrupt topography.

Acknowledgments. The solitary wave studies in Knight Inlet formed part of a collaborative study carried out with support from the US Office of Naval Research.

References

- Armi L., The hydraulics of two flowing layers with different densities, *J. Fluid Mech.*, 163, 27-58, 1986.
- Baines, P. G. *Topographic effects in stratified flows*, 482 pp., Cambridge University Press, 1995.
- Cummins, P., Numerical simulations of upstream bores and solitons in a two-layer flow past an obstacle, *J. Phys. Oceanogr.*, 25, 1504-1515, 1995.
- Farmer, D. M., and J. Dungan Smith, Tidal interaction of stratified flow with a sill in Knight Inlet, *Deep-Sea Res.*, 27A, 239-254, 1980.
- Farmer, D. M., and L. Armi, The Generation and Trapping of Solitary Waves over Topography, *Science*, 283, no. 5399, 188-190, 1999a.
- Farmer, D. M., and L. Armi, Stratified flow over topography: the role of small scale entrainment and mixing in flow establishment, in press, *Proc. Roy. Soc., Series A*, 1999b.
- Henyey, F. S. and A. Hoering, Energetics of borelike internal waves, *J. Geophys. Res.*, 102, 3323-3330, 1997.
- Holloway, P. E., E. Pelinovsky, T. Talipova, and B. A. Barnes, Nonlinear model of internal tide transformation on the Australian North West Shelf, *J. Phys. Oceanogr.*, 27, 871-896, 1997.
- Huppert, H. E. and R. E. Britter, Separation of hydraulic flow over topography, *J. Hyd. Div, Proc. ASCE*, 108, HY12, 1532-1539, 1982.
- Long, R. R., Some aspects of the flow of stratified fluids. Part III: Continuous density gradient, *Tellus*, 7, 341-357, 1955.
- Melville, W.K., and K. R. Helfrich, Transcritical two-layer flow over topography, *J. Fluid Mech.*, 178, 31-52, 1987.
- Peltier, W. R., and T. L. Clark, The evolution and stability of finite-amplitude mountain waves. Part II. Surface wave drag and severe downslope windstorms, *J. Atmos. Sci.*, 36, 1498-1529, 1979.

Exact Solitary Wave Solutions in Shallow Water

Frank S. Henyey

Applied Physics Lab, Univ. of Washington, Seattle WA

Abstract. Long's equation describes stationary flows to all orders of nonlinearity and dispersion. Dissipation is neglected. In this paper, Long's equation is used to attempt to model the propagation of a solibore -- a train of internal waves in shallow water at the deepening phase of the internal tide.

1. The Solibore Phenomenon

The internal tide in shallow water often has a sawtooth shape rather than a sinusoidal shape. The point of the tooth is not a simple jump as in a turbulent surface tidal bore, but consists of a train of waves. This wave train is called a solibore. The individual waves are often referred to as solitons, because they were originally modeled as solitons in the Korteweg-de Vries (KdV) equation. In many situations, the KdV modeling is highly inaccurate, as in *Stanton and Ostrovsky, 1998*; often an equation called the extended KdV, eKdV, is used. An example of a solibore is shown in Figure 1.

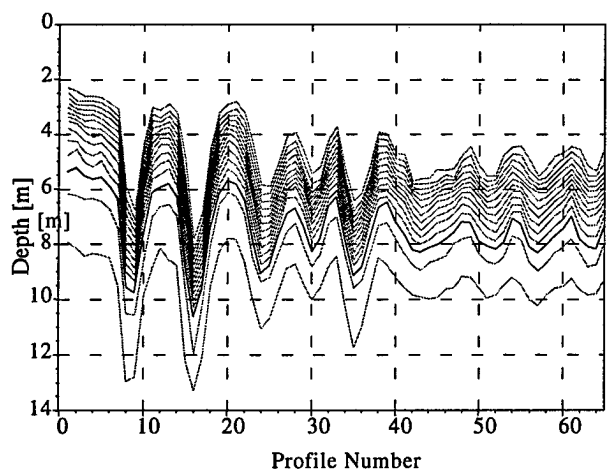


Figure 1. A solibore measured at Knight Inlet, British Columbia. Various isopycnals are shown. It can be seen that each isopycnal ends up lower than it started, forming the tooth of the sawtooth internal tide. The second wave is somewhat larger than the first, in contrast to the rank ordering predicted by the KdV theory. Data from E. D'Asaro.

Solibores are not all the same. Some have only a few waves in them, while others have many. Some are observed to have another solibore crossing them, while others seem to have two solibores merge into one, similar to the behavior of shocks and surface bores. They have a tendency to be very straight or segments of a circle, which

is also the case with shocks and bores. This straightening out requires that dissipation (which may include radiation of smaller-scale waves) is important. This is because a straight line or circle has less entropy than the arbitrary shape that the waves might have been formed with. The only place for that entropy to go to is to smaller scales; small waves, turbulence, or heat. There is a remarkable case that appears to be this loss of entropy in the SAR images of *Fu and Holt 1984, p 36*. In this image, the waves near the source region are made out of many (relatively) small packets, going in various directions. The waves farther from the source region, presumably generated by the previous tide, have organized themselves into one set of waves made of straight lines and circular arcs.

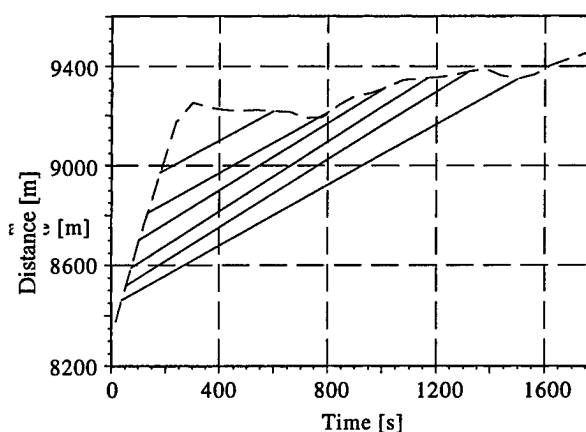


Figure 2 The trajectories of the wave crests of a Knight Inlet solibore. The ship's motion is shown as the dashed curve, and the line segments connect the points at which the ship encountered the crest of one of the waves. On the average, there is no dispersion of the waves, in contrast to KdV. The 3rd, 4th, and 5th waves are actually slightly faster than the others. Another feature of interest is the advection of the ship by the wave-caused surface current.

Another feature of solibores is that there is a tendency not to disperse, except when they are weak. A SARSEX image (*Liu, 1988*) shows four wave packets, generated by four successive tides. The youngest three appear to have

the same wavelength; only the fourth one has clearly dispersed. One may object that these are different solibores, and may have been differently formed. During the 1995 Solibores and Sill flows experiment, Eric D'Asaro made multiple crosses of the same solibore. Figure 2 shows the space-time trajectories for one pair of passes; it can be seen that the velocities of all the waves are nearly the same. Such results contradict assertions commonly made in the literature, which seem to be based more on theoretical prejudice (KdV waves disperse) than on real evidence.

There is a phenomenon in lakes which is similar to the tidally generated solibores. The difference is that the waves in the lakes are generated by an internal seiche rather than an internal tide. The lake solibores warrant additional study (*M. E. Snyder*, private communication.)

The work discussed below started out as an attempt to model the shape of a solibore, but not its longer time dynamics.

2. Long's Equation

There are a number of assumptions made in the model. First are the safe assumptions, which are incompressibility and the Boussinesq approximation. Secondly are simplifying assumptions that are justified by the similarity of the solibore phenomenon in various conditions. Although actual conditions deviate a little from these assumptions, the nature of the solibore does not appear to be controlled by the amount of such deviations. The first such assumption is to neglect the Earth's rotation. This is justified by the absence of any clear dependence on latitude. The second simplifying assumption is that the solibore is two-dimensional. As mentioned above, this assumption is remarkably close to being true in many cases, and solibore properties do not seem to differ much when it is not quite so true. The last simplifying assumption is that there is no shear in the initial state. This assumption is observed to be approximately true in a number of cases, for no particular reason; if there was no net exchange transport over a tidal cycle, one would expect shears of opposite signs before and after the solibore passed. It appears however that the shear during and after the solibore often dominates.

Finally, there are the questionable assumptions that must be put into the category of hypotheses to be tested. There are two such assumptions. The first is to neglect dissipation. Although it is argued above that dissipation is important in the long-time dynamics, the shape of waves is usually determined on a time comparable to the wave period. On this short time, it is reasonable to neglect the dissipation. The second is to assume steady waves. The observed absence of dispersion argues that this assumption is reasonable. Many solibores, especially those with many waves, get longer by adding more waves on the back end of the wave train. This phenomenon is

predicted by KdV, as pointed out by *Apel et al.*, 1997. In that case, the modeling should only apply to the front part of the wave train, which can be assumed steady.

The assumptions listed above lead to Long's equation (*Long*, 1953). Unlike the KdV or eKdV equations, there are no assumptions about the strength of the nonlinearity or the steepness of the waves. Long's equation is a nonlinear, inhomogeneous version of the Helmholtz equation. It has the form

$$b(\nabla^2 + \kappa^2)\zeta = 0$$

In this equation ζ is the vertical displacement of isopycnals. An isopycnal has a constant value of $z - \zeta$. K contains the inhomogeneity and nonlinearity. It is a function of space which depends on the solution ζ . Setting $N(z)$ to be the buoyancy frequency in the initial state, and v to be the speed of the wave, K is given by

$$K = \frac{N(z - \zeta)}{v}$$

In many atmospheric applications, it is assumed that N is a constant, in which case Long's equation reduces to the Helmholtz equation. In the coastal ocean, however, constant N is usually a very poor description of the stratification. When solibores exist, the stratification is much more nearly a 2-layer type stratification. N is large near some depth, and small elsewhere.

The boundary conditions are $\zeta = 0$ at the top and bottom, and in the initial state. The final state ζ is discussed below. The work reported here is based on numerical solutions of Long's equation.

If the assumption of no shear in the initial state is relaxed, v , as well as N , is a function of $z - \zeta$. Now $v(z)$ is the speed of the wave relative to the water in the initial state, and we put $v' = f(dv, dz)$. Long's equation then generalizes to

$$v(\nabla^2 \zeta - v'(\hat{z} - \nabla \zeta)^2 + v') = -N^2 \zeta$$

where N , v , and v' are evaluated at $z - \zeta$.

3. Final State Conditions

One possible final state is $\zeta = 0$. This final state can represent a single solitary wave. Other final states that have $\zeta = 0$ at the top and bottom with $z - \zeta$ a monotonic function of z have solutions on the interior of the computational domain. However, in general, such solutions cannot be continued beyond the computational domain and maintain those properties; $z - \zeta$ will not correspond to any position in the water column. The way to allow the

solution is to have the disturbance localized in the horizontal. Then the final state is independent of the horizontal coordinate x . In order for that to be possible, the final state must obey the ordinary differential equation obtained from Long's equation by dropping the x second derivative:

$$(\partial_z^2 + K^2)\zeta = 0$$

This equation has solutions, one for each number of zero crossings (which are referred to as modes, generalizing the linear mode concept.). Usually, we want to determine the speed v , so for each mode there is a one-parameter family of solutions parameterized by v . For application to most solibores, we are only interested in the lowest mode, with no zero crossing in the interior.

It turns out, however, that there is another condition on the final state. This additional condition can be derived in a number of different ways. It prevents there from being a first x derivative of ζ at the final state. One way to derive the condition, which I have not seen previously in the literature, is by use of a variational principle. Long's equation is the Euler equation for the stationary points of the difference of kinetic energy and potential energy, both expressed in terms of ζ . If the initial and final states are x -independent, then a small horizontal translation δx changes the difference of kinetic energy and potential energy by the vertical integral of the difference of kinetic and potential energy densities in the final state multiplied by δx . (The energy is defined so these densities are zero in the initial state.) Since the solution must be a stationary point, this integral must be zero. By use of the other condition and integration by parts, this integral can be reexpressed in a particularly convenient form (see, e.g., *Lamb and Wan, 1998*) as

$$\int (\partial_z \zeta)^3 dz = 0$$

This additional condition picks out a single member of the one-parameter family; the lowest-mode solution of the two conditions is unique. This solution is called the "conjugate flow."

4. Solutions of Long's equation

The method used to find solutions was a relaxation technique. One guesses a configuration, and the computer code iterates toward a solution, starting from this guess. As a guess, I put in various configurations that resemble observed solibores. In every case, the relaxation technique converged to the same solution, a "kink" connecting $\zeta = 0$ and the conjugate flow, as shown in Figure 3. A set of waves that was present in the first guess would disappear during the relaxation. Assuming that this is the

only solution, Long's equation cannot be used to model solibores. Even if there were a solution resembling a solibore, it is not reasonable to have a unique final state. The final state should be determined by the strength of the internal tide; generally this is weaker than the conjugate flow.

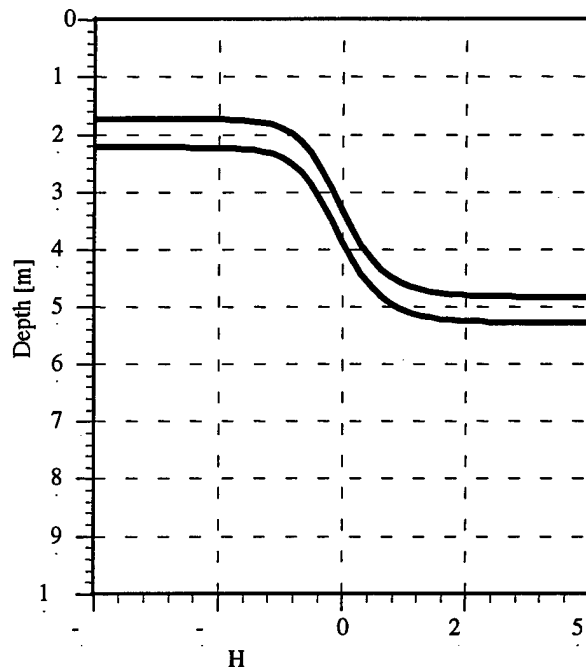


Figure 3. The kink solution of Long's equation. The depth of the water is 100 m, and the initial state (on the left) has a buoyancy profile, which is a Gaussian centered on 20 m depth and a width of 5 m. The isopycnals that start out 2.5 m on either side of the center of the Gaussian are shown.

Perhaps individual waves, rather than the entire solibore, should be modeled as solitary waves. In particular, the first wave in many solibores looks slightly separated from the next one. For individual waves separated from the rest, the appropriate final condition is $\zeta = 0$. However, in this case as well, the conjugate state plays an important role. (The theory of "exact" solitary waves is well known. See, for example, *Lamb and Wan, 1998*. There is a one-parameter family of lowest mode solitary solutions. The parameter can conveniently be taken as the energy of the solitary wave. As the energy varies from zero to infinity, the velocity of the wave varies from the linear wave speed to the kink speed; i. e. that of the conjugate flow. The amplitude varies from zero to that of the conjugate flow. Near the limit, the wave looks like a kink to the conjugate flow, followed after some distance (which asymptotically grows linearly with the energy) by an "an-

antikink" which is the mirror image of the kink. Some of these solitary waves are shown in Figure 4.

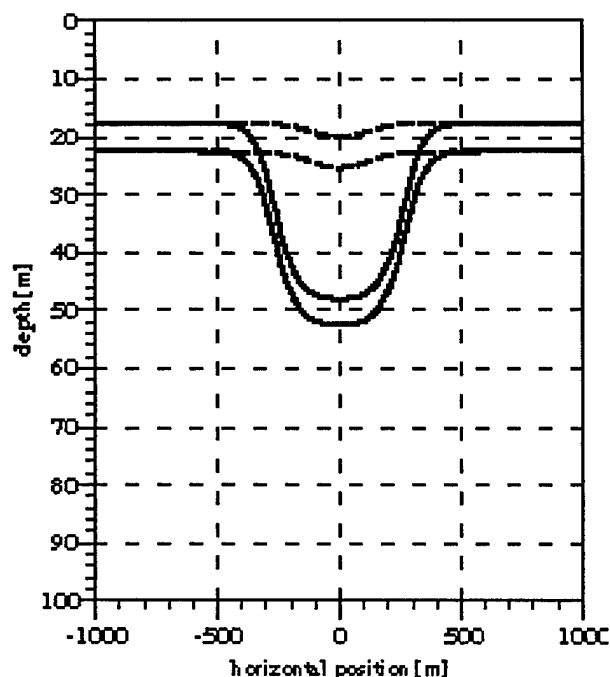


Figure 4. Two solitary waves are shown. The initial state and isopycnals shown are as in Figure 3. The smaller wave is near the limit of validity of KdV, while the larger is very close to the kink-antikink limit.

Thus to understand the family of solitary waves, one must understand the conjugate flow. For the two-layer flow, K^2 is a delta function at the interface. The first condition on the final state then requires ζ to be linear in each layer, with a corner at the interface. The second condition requires that the integrals of the cubes of these slopes be equal (up to the sign). The only way for this to happen is for the two layers to be exactly equal in thickness; the interface is half way through the water column. Calculations with various stratifications typical of shallow water describable as quasi-2 layer all show that this situation is not restricted to the true two-layer case. In all cases, it was found that the maximum stratification in the conjugate flow was extremely close to the mid-depth level. One need not calculate anything to compare to data. An example of such a comparison is with the data of *Podney and Sager, 1979*. The water in this experiment had a very closely to its initial configuration, and stays there for a while until the second wave comes along. The conjugate

state has its maximum stratification at mid-depth, 9 m. However, the observed wave has its maximum stratification at 11 m, and also looks a lot peakier than the kink-good quasi-two-layer stratification, and the total water depth was 18 m. The first wave appears to be the very model of a solitary wave. The stratification returns antikink type configuration. The second wave, not as well separated from what follows it, is even larger, its maximum is about 12.5 m deep, and it also is peaky. These waves are not at all the solitary waves they appear to be!

5. Comparison with KdV and eKdV

The limits of validity of the KdV equation have been examined by a number of investigators. Our calculations support the results others have obtained. The nondimensional parameter used to describe the validity of KdV in a quasi-two-layer stratification has been chosen as the ratio of the wave amplitude to the thickness of the thinner layer, usually the upper layer. For values of this parameter less than 0.1, KdV works fairly well. By the time the parameter reaches 0.2, the nonlinear part of KdV fails. In the COPE wave analyzed by *Stanton and Ostrovsky, 1998*, this parameter is about 4, and, as they show, KdV is extremely far off.

They claim, however, that it fits the eKdV model. Here we analyze that claim, using the formulas and values from their paper. The eKdV model also has a kink-antikink limiting wave, given by their equation 4. Unlike the full Long's equation, the position of the interface in the eKdV "conjugate flow" is not half way through the water column, but at a lesser amplitude. The curve for this limiting interface position, calculated from equations 2-4 of *Stanton and Ostrovsky* is shown in Figure 5. They quote the water depth as 147 m. In their table 1 they state an initial interface depth as 7 m, while their figure 5 shows it at 6 m. The limiting position, with these values is 27.4m if the initial interface depth is 7 m, and 24.3 m if the initial interface depth is 6 m. Their wave has a maximum interface depth of 30.5 m, in excess of the limit for either choice of parameter. (Their theoretical curve in Figure 5 also exceeds this bound, so it doesn't agree with the 147 m depth.) Since the wave is so close to the eKdV limit, one expects it to be fatter in that theory than one expects in the true theory. Indeed, their theoretical curve is clearly fatter than the data. It would be interesting to compare their data to the Long's equation solution. Thus, eKdV also doesn't work for this wave.

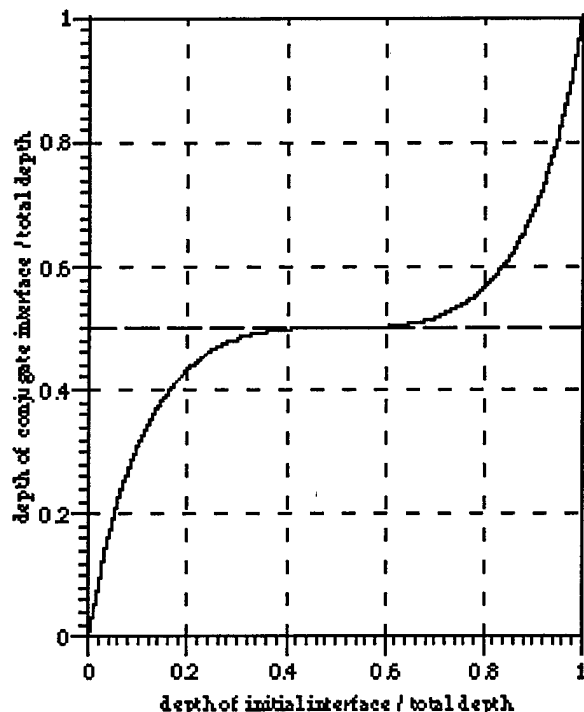


Figure 5. The limiting interface position of the "kink-antikink" wave for the 2-layer case, as a fraction of the total depth. The solid curve is for the eKdV equation, while the dashed line at half the total depth is the actual value given by Long's equation. the * symbol marks the COPE wave values; it exceeds the eKdV limit but is only slightly in excess of 40% of the true limit.

6. Summary

Long's equation makes the assumptions of steadiness and lack of dissipation. With these assumptions it cannot describe the entire solibore wave train, nor, in at least one case one of the waves from a solibore that looks very much as if it should be a solitary wave.

The time-independent versions of KdV and eKdV, which are solved by solitons, make the same assumptions, but in addition, assume small amplitude. Therefore, comparison with Long's equation solutions can test if the amplitude is small enough. In many cases, the amplitudes are too large for either of these two equations.

The KdV equation predicts rank ordering and dispersion of the waves in the packet, both of which are often violated.

The conclusion that I draw from these considerations is that we do not have an adequate theoretical description of solibores; either dissipation or unsteadiness (or both) is important. My guess is that it is the dissipation that will prove to be the missing ingredient; data suggests it is present, but supports the assumption of steadiness.

Acknowledgments. This work was supported by the Office of Naval Research. Steve Reynolds assisted in the numerical calculations.

References

- Apel, J. R., M. Badiey, C. S. Chiu, S. Finette, R. Headrick, J. Kemp, J. F. Lynch, A. Newhall, M. H. Orr, B. H. Pasewark, and D. Tielburger, An overview of the 1995 SWARM shallow-water internal wave acoustic scattering experiment, *IEEE J. Ocean. Eng.*, 22, 465-500, 1997
- D'Asaro, E., and R-C. Lien, Lagrangian Measurements of Waves and Turbulence in Stratified Flows, *J. Phys. Oceanogr.*, in press (1999)
- Fu, L., and B. Holt, Seasat Views Oceans and Sea Ice With Synthetic Aperture Radar, *Jet Propulsion Laboratory Publ.*, 81-120, 1982
- Lamb, K. G., and B. Wan, Conjugate flows and flat solitary waves for a continuously stratified fluid, *Phys. Fluid*, 10, 2061-2079, 1998
- Liu, A. K., Analysis of Nonlinear Internal Waves in the New York Bight, *J. Geophys. Res.*, 93, 12,317-12,329, 1988.
- Long, R. R., Some aspects of the flow of stratified fluids. I. A theoretical investigation, *Tellus*, 5, 542-558, 1953.
- Podney, W., and R. Sager, Measurement of fluctuating magnetic gradients originating from oceanic internal waves, *Science*, 205, 1381-1382, 1979.
- Stanton, T. P., and L. A. Ostrovsky, Observations of highly nonlinear internal solitons over the Continental Shelf, *Geophys. Res. Lett.*, 25, 2695-2698, 1998

Internal Solitary Waves in Lakes – a Closure Problem for Hydrostatic Models

D. A. Horn, J. Imberger, and G. N. Ivey

Centre for Water Research, The University of Western Australia, Australia

Abstract.

Laboratory experiments and field observations suggest that the degeneration of basin-scale internal standing waves into packets of solitary waves is an important mechanism for the transfer of energy within the internal wavefield in lakes. Since these shorter solitary waves break at the boundaries, this process provides a flux path from the wind to the turbulent benthic boundary layer. However, numerical models that make the hydrostatic approximation cannot simulate the evolution or propagation of internal solitary waves and therefore capture this important energy flux path. The feasibility of parameterising the important effects of solitary waves in hydrostatic models is discussed. Using a simple KdV model, some initial steps are suggested towards the development of such a solitary wave closure scheme.

Introduction

The internal wave field in a lake is energized by wind blowing over the surface, generating basin-scale waves or seiches. Horn *et al.* (1999) have shown that, for many lakes, an initial basin-scale seiche will steepen due to nonlinear effects until the steepening is balanced by dispersive effects, generating internal solitary waves. Packets of such solitary waves are frequently observed in lakes (Thorpe *et al.*, 1972; Farmer, 1978; Hunkins and Fliegel, 1973). The shoaling and breaking of these solitary waves is an important energy sink for the internal wave field and plays a major role in driving mixing in stratified lakes (Imberger, 1998). Importantly, the turbulent mixing events caused by the shoaling of internal solitary waves are local in both time and space. Unlike basin-scale waves, which gradually decay as they dissipate energy in the benthic boundary layer over the whole basin, internal solitary waves break on their first encounter with the sloping boundaries of a lake, dissipating most of their energy in a single breaking event (Michallet and Ivey, 1999).

Since the water quality and ecology of a lake are dependent on the vertical mixing of nutrients, oxygen and other biological agents, it is important that our models include this energy flux path: from the wind, to basin-scale internal waves, to shorter solitary waves, to turbulence in the benthic boundary layer (this is not to say that there are not other energy flux paths that result in mixing in the benthic boundary layer). Furthermore, it may not be sufficient to only reproduce the basin-wide

rate of vertical mixing; it may be necessary to reproduce the spatial and temporal variability of mixing events, for it is these events that control many biogeochemical processes. It is likely that in many cases current hydrodynamic models of lakes do not correctly reproduce the cascade of energy from the basin-scale internal waves to solitary waves and hence do not reproduce the spatially and temporally local boundary mixing driven by the shoaling of these waves. The reasons for this shortcoming are twofold: (a) many hydrodynamic models of lakes make the hydrostatic assumption and therefore neglect the physics that allows the generation and propagation of solitary waves, and (b) in many cases the solitary waves would be sub-grid scale.

In this paper we address only the first of these shortcomings; we discuss the feasibility of parameterising the important effects of solitary waves in hydrostatic models. We make use of a simple inviscid two-layer Korteweg-de Vries model to describe the nonhydrostatic evolution of some simple initial conditions, comparing the evolution with that observed in an equivalent hydrostatic model. Some initial steps are suggested towards the development of a solitary wave closure scheme.

A KdV model of long internal waves

Hydrostatic models cannot reproduce the evolution and propagation of internal solitary waves because they neglect the vertical accelerations that generate these waves. The simplest model to include both weak nonlinearity and dispersion is the Korteweg-de Vries (KdV)

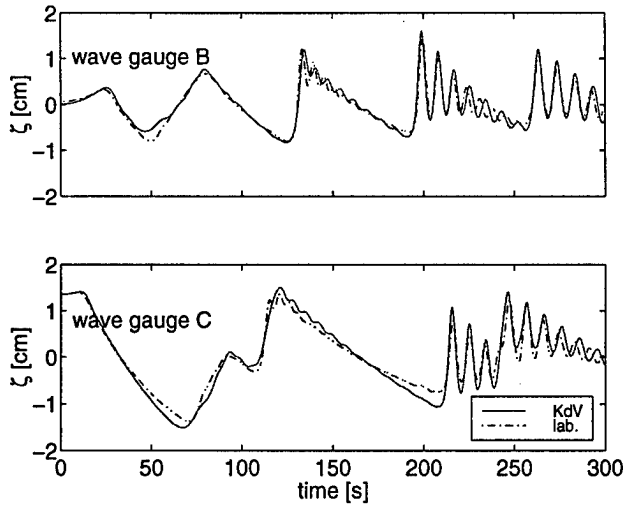


Figure 1. A comparison of the KdV model with laboratory experiment (from *Horn et al.*, 1999a).

equation (for a general review of the KdV equation see *Miles*, 1981). The KdV equation describes the evolution of weakly nonlinear long waves while assuming that nonlinear effects enter the equation at the same order as dispersive effects; solitary waves evolve when nonlinear effects are balanced by dispersive effects. In an inviscid two-layer system consisting of a fluid of depth h_1 and density ρ_1 overlying a fluid of depth h_2 and density ρ_2 , and making the Boussinesq approximation, the KdV equation can be written as

$$\eta_t + c_o \eta_x + \alpha \eta \eta_x + \beta \eta_{xxx} = 0 \quad (1)$$

where $\eta(x, t)$ is the interface displacement, $c_o = (g' \frac{h_1 h_2}{h_1 + h_2})^{1/2}$ is the linear long-wave speed, $\alpha = \frac{3}{2} c_o (h_1 - h_2) / h_1 h_2$ and $\beta = \frac{1}{6} c_o h_1 h_2$. The solitary wave solution to (1) is given by

$$\eta(x, t) = a \operatorname{sech}^2 \left(\frac{x - ct}{\lambda} \right) \quad (2)$$

where a is the solitary wave amplitude, $\lambda = (\frac{12}{a} \frac{\beta}{\alpha})^{1/2}$ is the characteristic wavelength and $c = c_o + \frac{a\alpha}{3}$ is the solitary wave speed.

The KdV equation has been applied to observations of internal waves in lakes (e.g., *Hunkins and Fliegel*, 1973) and has been shown to agree well with experimental data (e.g., *Koop and Butler*, 1981; *Horn et al.*, 1999a). Figure 1 shows the very close agreement between the pseudo-spectral KdV model of *Horn et al.* (1999a) and a laboratory experiment designed to investigate the nonlinear steepening of standing internal waves. Given this close agreement between the KdV model and the laboratory experiments, we use the KdV

model below to investigate the steepening of a number of different initial conditions. A useful feature of the KdV model is that by setting the dispersive term to zero ($\beta = 0$) in (1), the model becomes an equivalent hydrostatic model, allowing direct comparisons between the evolution under the hydrostatic and KdV equations.

Steepening time scale

To highlight the major differences between the behaviour of hydrostatic models and our KdV approximation of the real world, we first consider the evolution of a simple cosine initial condition. Figure 2 shows the evolution of such an initial condition in a frame of reference moving at the linear long wave phase speed. It can be seen that the initial condition evolves in a similar way in each model until a time $t = T_s$, by which time the initial cosine has steepened until the front face is almost vertical. T_s is the steepening time scale derived by *Horn et al.* (1999). The initial steepening of a long wave is described by the nonlinear hydrostatic wave equation (*Long*, 1972)

$$\eta_t + c_o \eta_x + \alpha \eta \eta_x = 0 \quad (3)$$

where α is the nonlinear coefficient from (1). Equation (3) is just the KdV equation (1), neglecting the dispersive term. Balancing the unsteady and nonlinear terms, while moving in a frame of reference with the long-wave, the steepening time scale is defined as

$$T_s \sim \frac{\lambda}{\alpha \eta_o} \quad (4)$$

where λ is some characteristic wavelength and η_o is the initial amplitude. In the absence of dispersion, T_s is the time that it takes for a line of slope η_o/λ to steepen and become vertical. In a series of laboratory experiments, *Horn et al.* (1999) observed that solitary waves emerged from an initial condition at time T_s .

In both systems the horizontal length scale of the wave is initially long compared with the depth of the fluid, so the hydrostatic approximation is valid and the initial steepening is well described by (3). However, as the wave steepens, its horizontal length scale decreases until the vertical accelerations, and hence dispersive effects, become significant, eventually balancing the nonlinear steepening. The internal solitary waves subsequently evolve owing to this balance between nonlinear steepening and dispersion. The behaviour of the models diverge for $t > T_s$ because the hydrostatic model continues to neglect the vertical accelerations when they are clearly important.

In a hydrostatic model the wave would continue to steepen until breaking unless diffusion dissipates the

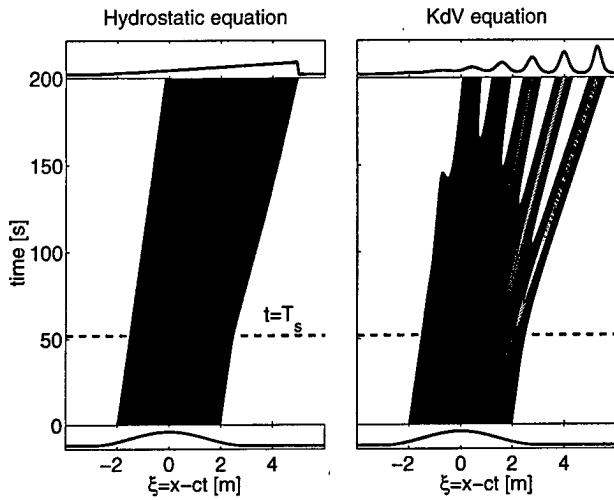


Figure 2. The evolution of a cosine initial condition under a hydrostatic equation and the KdV equation. The contours are of interface displacement. The initial and final interface profiles are shown below and above the X - T contour plots.

shock. In the pseudo-spectral code used for these simulations, wave-breaking is prevented by a prescribed hyper-viscosity that dissipates the high wavenumber energy of the sharp front. In most finite-difference schemes numerical diffusion plays a similar role. The result is that in a hydrostatic model the wave continues to propagate as a steep fronted feature, dissipating energy as it travels, so that its amplitude quickly decays. In contrast, in the KdV model dispersive effects are retained and lead to the evolution of solitary waves at time $t = T_s$.

The propagation and the dissipation of internal wave energy are very different in the two models. In the hydrostatic model, energy is dissipated in the interior of the lake by diffusion across the sharp front. In the KdV model, the initial internal wave energy is re-packaged into coherent high energy-density solitons that propagate without loss until they encounter a boundary. In a real lake the propagation of solitons will be accompanied by some viscous losses and may even induce some local shear instabilities, but the fundamental difference remains that the hydrostatic model will always dissipate energy within the interior of the lake that would otherwise be dissipated at the boundaries.

To consider the effect of the shape and slope of an initial condition on the steepening process we let four simple initial shapes evolve under the KdV equation. Each of the shapes shown in Figure 3 was chosen to have the same vertical and horizontal length scales and the same area, but the front face of each shape has a different slope. The steepening time scale for each shape can then be defined as $T_s = 1/(\alpha S_o)$, where S_o is the

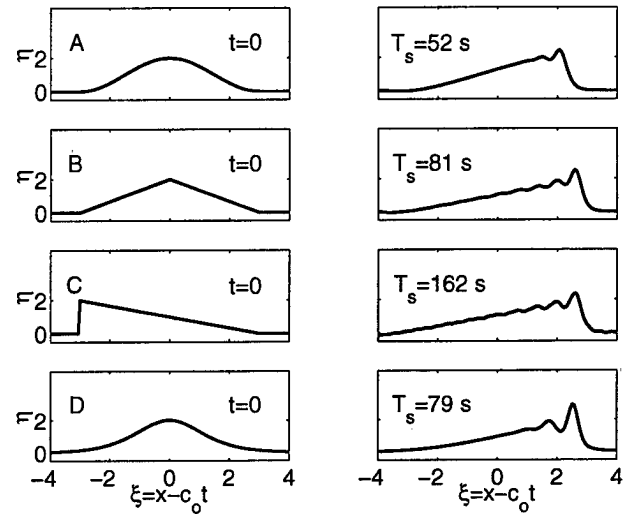


Figure 3. The evolution of four simple initial conditions under the KdV equation. The second column of panels represent the waves at $t = T_s$, where T_s has been calculated for each initial condition from (4).

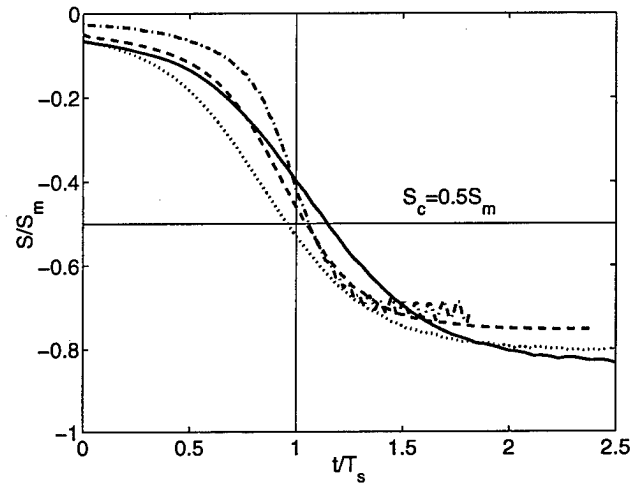


Figure 4. The maximum slope of the front face at any time t of each of the initial conditions in Figure 3. Time is nondimensionalized by the steepening time scale given by (4) and the slope is nondimensionalized by the maximum possible slope given by (6).

maximum slope of the front face. Figure 3 shows that at $t = T_s$ each of the shapes has evolved into the same steep-fronted wave.

Figure 4 plots the maximum slope of the front face of each of the waves as they steepen. Each shape steepens in a similar way, achieving approximately the same slope at $t = T_s$ and asymptotically approaching the same maximum slope. It is this similar steepening that is important in the development of a solitary wave clo-

sure scheme. Although the steepening time scale is a useful parameter in determining *when* solitary waves will emerge, it requires some knowledge of the initial shape at $t = 0$ (specifically the initial slope S_0); information that is not available when implementing a closure scheme. However, since all of the shapes evolve to a common form with a similar frontal slope at $t = T_s$, it is possible to define the time and place at which solitary waves will emerge in terms of some critical slope, S_c . So what determines this critical slope?

Critical wave slope

Using the inverse scattering transform to solve the initial-value problem for the KdV equation, it is possible to determine the number and amplitude of the solitons that will emerge from some simple initial conditions (*Drazin and Johnson, 1989*). *Horn et al. (1999b)* used this method to investigate the solitons emerging from an idealised depression of the thermocline in a lake which they modelled as the triangular initial condition C shown in Figure 3. Figure 5 plots a series of curves representing the amplitudes of each of the solitons that emerge as a function of the size and shape of the initial triangle. It can be seen that the scaled amplitude parameter $K/\sqrt{u_m}$ of the leading soliton (given by the first curve) very quickly approaches a value of unity. Here K^2 represents an eigenvalue of the scattering problem and is related to the solitary wave amplitude and $u_m = a_0/h_1$ is the scaled amplitude of the initial condition. When the scaling is removed it can be shown that if $K/\sqrt{u_m} \sim 1$, the soliton amplitude is given by

$$a = 2K^2 h_1 \sim 2a_0 \quad (5)$$

Since KdV solitary waves are one parameter waves described by (2), the amplitude of the leading soliton determines its shape and maximum interfacial slope

$$S_m = \frac{4\sqrt{2}}{9} \left(a_0^3 \frac{\alpha}{\beta} \right)^{1/2} \quad (6)$$

This is the maximum slope that any initial condition can reach through nonlinear steepening in the presence of dispersion. The wave-slopes plotted in Figure 4 have been non-dimensionalized by this maximum slope, S_m , and the figure shows that at $t = T_s$ the front wave-slope is approximately $-0.5 S_m$. We define the *critical slope* as $S_c = -0.5 S_m$. If any wave steepens beyond this critical slope it will evolve into a packet of solitons. Any solitary wave closure scheme would be implemented when a slope exceeding S_c was detected in the model.

The appearance of the amplitude, a_0 , of the initial condition in the right hand side of (6) raises a number

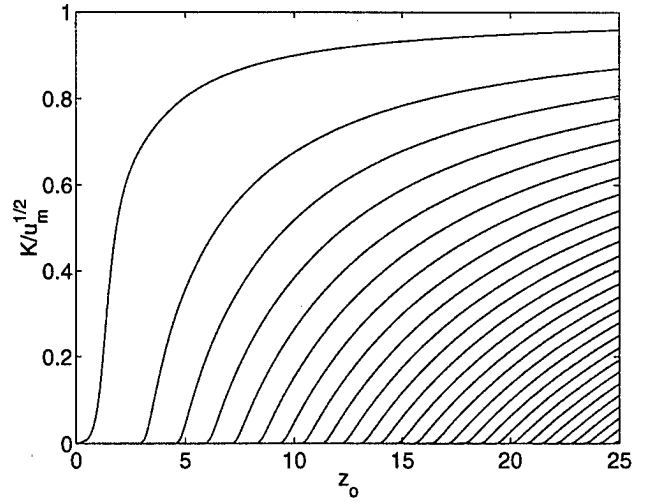


Figure 5. Curves representing the scaled amplitude of the solitons emerging from a triangular initial condition similar to C in Figure 3. z_0 is a geometric parameter representing the area and shape of the triangle (from *Horn et al., 1999b*).

of issues. Firstly, if the implementation of the closure scheme requires the detection of waves with some critical slope, S_c , this implies some measure of the amplitude of the initial condition. We have already acknowledged that any practical closure scheme will have no such knowledge of the initial conditions, even if these initial conditions could be defined in a developing system. The process of nonlinear steepening does not increase the amplitude of the initial condition until after the emergence of solitons at $t = T_s$. Therefore, the initial amplitude, a_0 , can be assumed to be the amplitude of the wave at $t = T_s$, the time at which it will reach its critical slope. However, the calculation of the critical slope still requires knowledge of the initial amplitude of the wave. Any closure scheme must first define some characteristic amplitude for a feature and then use this amplitude to calculate the critical slope. If the front face of the feature exceeds the critical slope, then the closure scheme would be invoked.

The dependence of S_c on a_0 is not initially obvious. Equation (4) confirms that the steepening time scale depends only on the initial slope of the wave and is independent of the initial amplitude. However, (6) shows that the steepness of the front at $t = T_s$ is dependent on the initial amplitude of the wave and is independent of the initial slope. The consistency of these statements can be confirmed by recalling that for KdV solitary waves the wavelength is inversely proportional to the square-root of the amplitude; large amplitude solitons are narrower and steeper than small amplitude solitons. Therefore, a small amplitude initial condition will evolve into small amplitude solitary waves that will

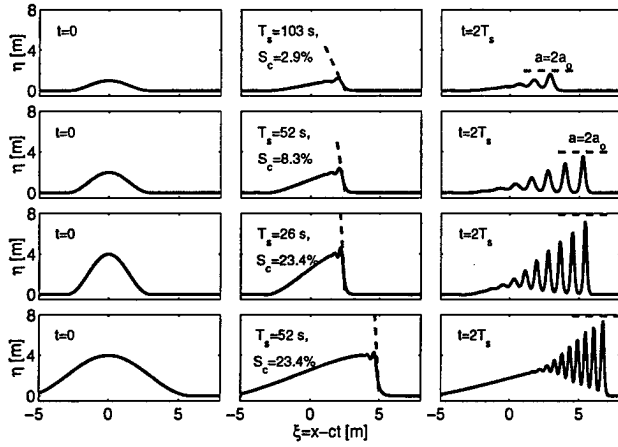


Figure 6. The evolution of four cosine initial conditions under the KdV equation. The second column of panels represent the waves at $t = T_s$, where T_s has been calculated for each initial condition from (4). The critical slope, $S_c = -0.5 S_m$ is marked on each wave (where S_m is calculated from (6)). The third column of panels show the evolving packet of solitons at $t = 2T_s$. The dashed line in these panels represents the predicted amplitude $a = 2a_0$.

have relatively small slopes.

Figure 6 shows the evolution of four cosine initial conditions with different amplitudes and initial slopes. The figure confirms that at $t = T_s$ (where T_s is calculated for each initial condition) the wave has evolved into a steep front with a slope given by S_c (where S_c is calculated for each initial condition). S_c appears to be a good indicator of the time and place of the emergence of solitons.

Energy propagation

In most stratified lakes the thermocline is above mid-depth so any solitary waves are waves of depression. Although an initial disturbance can consist of both a depression and elevation of the thermocline (as in the case of a basin-scale internal seiche), it is the volume of the depression of the thermocline that determines the energy that is transferred from the initial condition to the emerging solitary waves (Horn *et al.*, 1999b). As a first approximation, all of the energy in that part of an initial condition that is comprised of a depression of the isopycnals will be transferred to the solitary waves. Assuming that there is an equipartition of potential and kinetic energy in the initial steep-fronted wave, the total energy per unit width of the initial wave can be estimated by

$$E_0 = \Delta \rho g \int_{x_1}^{x_2} \eta_0^2(x) dx \quad (7)$$

where η_0 is the interface displacement at the time when the wave-slope first exceeds S_c (where $S_c > 0$ for a wave of depression), and $\eta_0 < 0$ over $[x_1, x_2]$ (for the case of a thin upper layer).

Given, from (5), the amplitude of the leading soliton that will emerge from the steep-fronted initial condition, and its shape from (2), we can determine the energy per unit width (to $O(a/H)$)

$$E = \frac{4}{3} \Delta \rho g a^2 \lambda \quad (8)$$

and its propagation speed

$$c = c_0 + \frac{a\alpha}{3} \quad (9)$$

We have now built up a reasonably detailed picture of the formation of solitons from some simple initial conditions. We know when and where solitons will emerge from an initial conditions, we know the energy that will be transferred from the initial condition to the solitons, and we know the amplitude, shape, energy and speed of the leading soliton. Let us now consider a simple energy propagation model.

The motivation for developing a solitary wave closure scheme is to ensure that energy that is incorrectly dissipated in the interior of a lake by hydrostatic models is dissipated at the boundaries. This requires that, once invoked by the detection of a wave with a slope exceeding the critical slope, the closure scheme must (i) prevent any incorrect mixing in the interior of the lake, (ii) propagate the energy of the initial wave to the boundary at the correct speed, and (iii) dissipate the energy at the boundary, with the correct distribution between turbulent dissipation, mixing (and possibly reflection).

To prevent any further mixing in the interior, the closure scheme must effectively and rapidly reduce the diffusion caused by the steep front. The simplest method would be to remove the initial steep-fronted wave from the domain as quickly as possible. This could be achieved by directly resorting the vertical density profile over the extent of the wave, previously identified as the domain $[x_1, x_2]$. Alternatively, the initial wave could be rapidly damped with a locally enhanced *virtual* viscosity, provided that this enhanced viscosity was not associated with any diffusion of density. The rapid removal of the initial wave from the model ensures that the total energy of the system is conserved, since the energy of the initial wave has by then been transferred to the closure scheme for propagation to the boundary.

The propagation of the energy to the boundary can be achieved by advecting the energy of the solitary wave packet through the domain as a parameter. In the KdV

model the packet of solitary waves gradually disperses, with the front of the packet propagating with the speed of the leading wave, c , given by (9), and the rear of the packet propagating at the long-wave speed, c_o . However, it is unlikely that the length of the solitary wave packet will spread beyond two or three grid cells (1–2 km) in most models before encountering a boundary. The energy of the solitary wave packet can therefore be parameterized by a single value that is propagated through the domain at the speed of the leading soliton.

From a series of laboratory experiments investigating mixing due to internal solitary waves breaking on a slope, Michallet and Ivey (1999) determined the mixing efficiency and reflection coefficient as functions of the beach slope and the wave-slope. We have already determined an estimate of the wave-slope, S_m , for the leading wave. Although the wave-slopes of solitons towards the rear of the packet may not be as steep, S_m provides a reasonable approximation of a characteristic wave-slope for the packet that could then be used to estimate the mixing efficiency and reflection coefficient when the solitary wave packet encounters a sloping boundary.

The discussion so far has assumed that all of the energy transferred to the solitary waves is propagated to the boundary without loss. However, in a lake there are a number of mechanisms that might lead to some internal dissipation and mixing as the solitary waves propagate. These include bottom boundary layer losses (Leone *et al.*, 1982), shear induced decay (Bogucki and Garrett, 1993) and wave-wave interactions. The first two of these are well understood and could be included in any solitary wave closure scheme by allowing the parameterized amplitude and energy to decay as they propagate through the lake.

Conclusions

Laboratory experiments and field observations suggest that the generation of internal solitary waves may be an important mechanism for the transfer of energy from basin-scale internal waves, energized by the wind, to turbulence in the benthic boundary layer in lakes. However, hydrostatic models, which are widely used to model the hydrodynamics of lakes, cannot simulate this important process because they neglect the vertical accelerations that are necessary to generate solitary waves. Furthermore, for many *engineering* models of lakes, internal solitary waves will not be resolved at practical grid-scales. If these models are to be used to simulate the spatial and temporal variability of mixing events in lakes, it will be necessary to parameterize the effects of the evolution, propagation and dissipation of internal solitary waves. By considering the evolution of

some simple initial conditions in a KdV model, we have suggested the first steps that could lead to the development of such a solitary wave closure scheme.

If such a solitary wave closure scheme is to be feasible, it must include some method of determining where and when in the model domain solitary waves will evolve. We have defined a critical wave slope, S_c , at which solitary waves emerge from an initial condition. This critical slope is dependent on the amplitude of the initial condition and on the background stratification. The proposed method would search the domain for a wave-front, the amplitude of the wave would be determined and the critical slope calculated. If the maximum slope of the wave-front exceeded the critical slope the closure scheme would be invoked.

Once invoked, the closure scheme must calculate the energy contained in the portion of the initial condition that contributes to solitary wave generation (that part of the wave in which isopycnals are below their equilibrium position for most cases) using (7). This energy would then be advected through the model as a parameter. The amplitude of the initial condition that invoked the closure scheme would be used to determine the amplitude of the leading soliton in the packet (5), and hence the speed at which the parameterized energy should be advected (9) and the reflection coefficient and mixing efficiency applied when the packet encountered a sloping boundary. The closure scheme could include the gradual decay of the solitons due to boundary layer losses and shear.

Although the principles of the proposed closure model have been applied to simple initial conditions propagating along an interface, the challenge is to apply these ideas to more complex initial conditions in a continuously stratified, three-dimensional model with complex topography.

Acknowledgments. The first author is grateful to Peter Müller for the opportunity to participate in the workshop. This research was supported by the Centre for Environmental Fluids and the Australian Research Council. This paper is Centre for Water Research reference ED 1477 DH.

References

- Bogucki, D., and C. Garrett, A Simple Model for the Shear-induced Decay of an Internal Solitary Wave, *J. Phys. Oceanogr.*, 23 1767-1776, 1993.
- Drazin, P. G., and R. S. Johnson, Solitons: an introduction, Cambridge University Press, 1989.
- Farmer, D. M., Observations of long nonlinear internal waves in a lake, *J. Phys. Oceanogr.*, 8, 63-73, 1978.
- Horn, D. A., J. Imberger, and G. N. Ivey, The degeneration of basin-scale internal gravity waves in lakes, submitted

- to *J. Fluid Mech.*, 1999.
- Horn, D. A., J. Imberger, and G. N. Ivey, and L. G. Redekopp A KdV model of basin-scale internal waves in lakes, *in preparation*, 1999a.
- Horn, D. A., L. G. Redekopp, J. Imberger, and G. N. Ivey, Internal wave evolution in a space-time varying field, submitted to *J. Fluid Mech.*, 1999b.
- Hunkins, K., and M. Fliegel, Internal undular surges in Seneca Lake: A natural occurrence of solitons, *J. Geophys. Res.*, **78**, 539-548, 1973.
- Imberger, J., Flux Paths in a Stratified Lake: A Review, in *Physical Processes in Lakes and Oceans*, edited by J. Imberger, pp. 1-17, AGU, 1998.
- Koop, C. G., and G. Butler, An investigation of internal solitary waves in a two-fluid system, *J. Fluid Mech.* **112**, 225-251, 1981.
- Leone, C., H. Segur and J. L. Hammack, Viscous decay of long internal waves, *Phys. Fluids* **25**, 942-944, 1982.
- Long, R. R., The steepening of long internal waves, *Tellus* **24**, 88-99, 1972.
- Michallet, H., and G. N. Ivey, Experiments on mixing due to internal solitary waves breaking on a uniform slope, *J. Geophys. Res.*, *in press*, 1999.
- Thorpe, S. A., A. J. Hall, and I. Croft, The internal surge in Loch Ness, *Nature* **237**, 96-98, 1972.

This preprint was prepared with AGU's L^AT_EX macros v5.01, with the extension package 'AGU++' by P. W. Daly, version 1.6a from 1999/05/21.

Vertical Mixing Induced by Tidally Generated Internal Waves in the Kuril Straits

Tomohiro Nakamura, Toshiyuki Awaji, Takaki Hatayama,
and Kazunori Akitomo

Department of Geophysics, Kyoto University, Kyoto 606-8502, Japan

Takatoshi Takizawa

Japan Marine Science and Technology Center, Yokosuka 237, Japan

Tokihiro Kono

Hokkaido National Fisheries Research Institute, Kushiro 085, Japan

Masao Fukazawa

School of Marine Science and Technology, University of Tokai, Shizuoka 424, Japan

Abstract. Numerical experiments with a 2-dimensional nonhydrostatic model are performed to investigate tidally generated internal waves in the Kuril Straits and their effect on vertical mixing. The results show that in contrast to previous theories, intense short internal waves are generated at the sill breaks by the subinertial K_1 tidal flow, and propagate upstream as the tidal flow slackens. These short waves are identified as unsteady lee waves. Our theoretical consideration showed that tidally generated internal waves can be classified into (1) unsteady lee waves (when $\frac{kU_0}{\sigma_f} \gg 1$), (2) mixed tidal lee waves ($\frac{kU_0}{\sigma_f} \sim 1$), and (3) internal tides ($\frac{kU_0}{\sigma_f} \ll 1$), where k is the curvature of topography, U is the flow speed, and σ_f is the frequency of tidal flow. Different from internal tides, unsteady lee waves have a tendency to be trapped in the generation region and grow into large-amplitude waves. Superposition of a propagating unsteady lee wave and a newly generated lee wave over a sill causes significant wave breaking. Owing to these processes, the estimated vertical diffusivity reaches $\sim 10^3 \text{ cm}^2 \text{ s}^{-1}$. This quite intense mixing extends to the density layer of the North Pacific Intermediate Water (NPIW), suggesting the possibility that generation of lee waves through interactions between the K_1 current and the bottom topography of the Kuril Straits affects the formation of the NPIW.

1. Introduction

Generation of large-amplitude internal waves by tidal currents is a major cause of the boundary mixing process, which is a subject of increasing interest. As revealed by recent studies, mixing at open-ocean boundaries can significantly affect a large-scale circulation in the open ocean (e.g., Samelson 1998). Interaction between the Okhotsk Sea and the North Pacific Ocean via the Kuril Straits is one example of such boundary

mixing problems.

In the Okhotsk Sea, a pycnocline around $26.8 \sigma_\theta$ named the Okhotsk Sea Mode Water (OSMW), is formed by the isopycnal mixing of the cold fresh water subducted in the northern Okhotsk Sea and the warm saline water from the North Pacific (Kitani 1973) and the dense Soya Warm Current Water (Watanabe and Wakatsuchi 1998). Assuming that the OSMW flows out without modification owing to mixing, Yasuda (1997) indicated that the NPIW salinity minimum centered

on $26.8\sigma_\theta$ has a close relation to the pycnostad of the OSMW and concluded that the origin of the NPIW lies within the Okhotsk Sea.

However, recent detailed observations (e.g., *Kawasaki and Kono* 1994) show the presence of intense vertical mixing in the Kuril Straits, implying that the outflowing OSMW may be subjected to water modification in the Kuril Straits. Thus it is necessary to take into account such mixing in order to fully comprehend the impact of the Okhotsk Sea. Past studies suggested tidal mixing could be responsible for this mixing (e.g., *Talley* 1991). However, the actual physical mechanisms are still unknown.

According to observations, the currents in the Kuril Straits are dominated by the diurnal tidal components, and the semidiurnal components are rather weak. Swift K_1 currents have been thought to cause intense vertical mixing through interactions with the large-amplitude sills in the Straits. However, the situation in the Kuril Straits is out of the range of previous theories for the growth of tidally generated internal waves because these studies focused on internal waves of its tidal frequency (internal tides). Since the diurnal tides are sub-inertial around this high latitude ($\sim 47^\circ\text{N}$), internal tides of the K_1 frequency cannot propagate freely. This fact prevents us from applying the previous theoretical models. For example, *Hibiya's* (1986) theory assumes that internal tides propagating upstream are trapped at the generation point and amplified when the barotropic flow is critical for the corresponding vertical mode. For the same reason, interpretations of wave growth by the critical slope theory (e.g., *Wunsch* 1969) or the nonlinear steepening effect (e.g., *Lee and Beardsley* 1974; *Gerkema and Zimmerman* 1995) are also inapplicable to the K_1 internal tides.

Thus, as a first step toward clarifying the dynamics responsible for the vertical mixing in the Kuril Straits at high latitude, we performed numerical experiments to investigate tidally generated internal waves and have estimated the vertical mixing induced by those waves.

2. Numerical model

The model bottom topography (Fig. 1) is representative of the sills in the northeastern part of the Kuril Straits, where tidal currents are so strong that they could cause considerable mixing. Although there are a variety of sill depths (ranging between tens to several thousand meters) in the Kuril Straits, the present sill topography is of a basic form so that simulation results may be qualitatively applied to cover other cases. In order to simulate vertical mixing by internal waves, we used a nonhydrostatic model with horizontal and vertical grid sizes of 500 m and 10 m, respectively. The

eddy viscosity and diffusivity coefficients are assigned to the relatively small values of $0.1\text{ cm}^2\text{s}^{-1}$ vertically and $2 \times 10^5\text{ cm}^2\text{s}^{-1}$ horizontally, so that their effect on mixing is small enough to demonstrate the wave mixing clearly. As basic forcing terms for internal wave generation, barotropic K_1 and M_2 currents are given at both lateral boundaries. Their maximum speeds at the sill top are 0.5 ms^{-1} for the K_1 case and 0.2 ms^{-1} for the M_2 case, as determined from our preceding barotropic tidal simulations (*Nakamura et al.* 1999). We took account of the effect of rotation by adapting an f plane approximation to distinguish the physics of waves generated by the subinertial K_1 flow from that of the superinertial M_2 flow in the Kuril Straits. Thus the governing equations of our 2-dimensional model are these:

$$\frac{\partial u}{\partial t} + u \frac{\partial u}{\partial x} + w \frac{\partial u}{\partial z} - f v = -\frac{1}{\rho_0} \frac{\partial p}{\partial x} + \nu_H \frac{\partial^2 u}{\partial x^2} + \nu_Z \frac{\partial^2 u}{\partial z^2}, \quad (1)$$

$$\frac{\partial v}{\partial t} + u \frac{\partial v}{\partial x} + w \frac{\partial v}{\partial z} + f u = \nu_H \frac{\partial^2 v}{\partial x^2} + \nu_Z \frac{\partial^2 v}{\partial z^2}, \quad (2)$$

$$\frac{\partial w}{\partial t} + u \frac{\partial w}{\partial x} + w \frac{\partial w}{\partial z} = -\frac{1}{\rho_0} \frac{\partial p}{\partial z} - \frac{\rho}{\rho_0} g + \nu_H \frac{\partial^2 w}{\partial x^2} + \nu_Z \frac{\partial^2 w}{\partial z^2}, \quad (3)$$

$$\frac{\partial u}{\partial x} + \frac{\partial w}{\partial z} = 0, \quad (4)$$

$$\frac{\partial \theta}{\partial t} + u \frac{\partial \theta}{\partial x} + w \frac{\partial \theta}{\partial z} = \kappa_H \frac{\partial^2 \theta}{\partial x^2} + \kappa_Z \frac{\partial^2 \theta}{\partial z^2}, \quad (5)$$

$$\frac{\partial S}{\partial t} + u \frac{\partial S}{\partial x} + w \frac{\partial S}{\partial z} = \kappa_H \frac{\partial^2 S}{\partial x^2} + \kappa_Z \frac{\partial^2 S}{\partial z^2}, \quad (6)$$

$$\rho = \rho(\theta, S, p), \quad (7)$$

where (x, y, z) are the across-sill, along-sill, and vertical coordinates, respectively; (u, v, w) are the velocities in the (x, y, z) directions; p is pressure; ρ is density variation; θ is potential temperature; S is salinity; $f (= 1.07 \times 10^{-4}\text{ s}^{-1})$ is the Coriolis parameter at 47°N ; ρ_0 is the reference density; g is the gravity acceleration; and ν and κ are the coefficients of eddy viscosity and eddy diffusivity, respectively, with the subscripts H and Z for the horizontal and vertical direction. The equation of state used is based on *Bryan and Cox* (1972). In performing the model calculation, we solve the equation for the vorticity $\zeta = \frac{\partial w}{\partial x} - \frac{\partial u}{\partial z}$ derived from Eqs. (1) and (3) as

$$\frac{\partial \zeta}{\partial t} + u \frac{\partial \zeta}{\partial x} + w \frac{\partial \zeta}{\partial z} + f \frac{\partial v}{\partial z} = -\frac{g}{\rho_0} \frac{\partial \rho}{\partial x} + \nu_H \frac{\partial^2 \zeta}{\partial x^2} + \nu_Z \frac{\partial^2 \zeta}{\partial z^2}, \quad (8)$$

and the Poisson equation for the stream function ψ as

$$\frac{\partial^2 \psi}{\partial x^2} + \frac{\partial^2 \psi}{\partial z^2} = \zeta, \quad (9)$$

where the stream function ψ is defined as

$$u = -\frac{\partial \psi}{\partial z}, \quad w = \frac{\partial \psi}{\partial x}. \quad (10)$$

At the bottom boundary, a no-slip condition is imposed in the sill region and a free-slip condition is imposed in the deep region with the flat bottom. A rigid-lid approximation is used at the surface. Although the time variation of the tidal flow in the model occurs completely in phase throughout the entire domain as a result of the rigid lid approximation and the incompressibility assumption, the approximation is still valid because we are concerned only with the internal wave generation over a sill, where the phase of the barotropic tidal flow varies only slightly. In fact, the incoming K_1 tidal waves take at most 10 minutes to propagate across the sill region, a time much smaller than the K_1 period. For a similar reason, many previous studies such as *Hibiya* (1988) and *Lamb* (1994) successfully reproduced topographic internal wave processes using the rigid lid approximation. To avoid numerical noise, sponge zones are set near the lateral boundaries.

The initial vertical profiles of temperature and salinity are from summer time climatology in the Okhotsk Sea (not shown). Model calculations start at the beginning of rightward flow so that wave generation processes can be seen clearly.

3. Model results

Figure 2 shows the temporal evolution of the internal mode stream function defined by *Lamb* (1994) during the 2nd period in the M_2 case (the definition of internal mode stream function will be described in the Appendix). As past studies show, the 1st-mode internal waves are generated on the slopes of the sill by the rightward flow (Fig. 2a) and propagate away from the sill in both directions. In the half period of leftward flow (Figs. 2c,d), almost the same sequence of events can be observed, but with their phase reversed. Using the linear dispersion relation, the frequency of these 1st mode waves is estimated as $1.4 \times 10^{-4} \text{ s}^{-1}$, almost equal to the M_2 frequency. Thus, these waves can be identified as typical internal tides at the M_2 frequency.

Since the amplitude of the barotropic M_2 flow is small and most of the internal mode energy generated by the M_2 flow propagates away from the sill as 1st-mode internal tides and dissipates gradually, large-amplitude internal waves are not formed and breaking

is absent in the M_2 case. Consequently, vertical mixing induced by waves generated by the M_2 flow is probably not strong enough to cause significant mixing in the Kuril Straits.

The time series of the internal mode stream function in the K_1 case (Fig. 3) shows a quite different behavior from that of the M_2 case, mainly because the Kuril Straits are located over the critical latitude for the K_1 tide. Sill-scale cells do not propagate away, and intense disturbances are present on small scales.

We pay attention to these smaller-scale disturbances because short internal waves are favorable to causing mixing, considering the fact that shorter wavelengths induce stronger dissipation and so release energy for mixing and that wave breaking takes place at smaller amplitudes for waves of shorter wavelengths.

Figure 3 clearly shows the movement of these small-scale disturbances, labeled as R_{1-4} and $L_{1,2}$ from left to right, with the direction of the tidal flow at the time of their generation indicated by R (rightward) and L (leftward). Their propagation speeds estimated from Fig. 3 ($0.3 \sim 1.4 \text{ ms}^{-1}$) are different from the tidal flow speed (less than 0.125 ms^{-1} in the deep water region). This fact means that they are freely propagating internal waves. Thus, their frequencies must be larger than the inertial frequency, despite the fact that the K_1 frequency is subinertial. Furthermore, these waves generated by right-(left-) ward flow propagate left-(right-) ward, indicating that these move only in the upstream direction as determined at their generation time. This is also inconsistent with the character of internal tides which propagate in both directions. From these considerations, it is inferred that the intense short waves in our model cannot be internal tides. In fact, the above two qualities are characteristics of lee waves, and thus we reinvestigate the excitation mechanism of internal waves by a tidal flow in the next section, to show that unsteady lee waves (which are capable of propagating away) can be excited by an oscillating flow.

4. Excitation mechanism of unsteady lee waves

To investigate the wave excitation properly, it is necessary to consider the total time-variation of the forcing to which fluid parcels are subjected. Representing the forcing as F , the total time-variation of the forcing DF/Dt is given in Eulerian variables as

$$\frac{DF}{Dt} = \frac{\partial F}{\partial t} + U_i \frac{\partial F}{\partial x_i}, \quad (11)$$

where U_i represents the velocity of the basic flow in the x_i direction. Most of the previous theories of internal

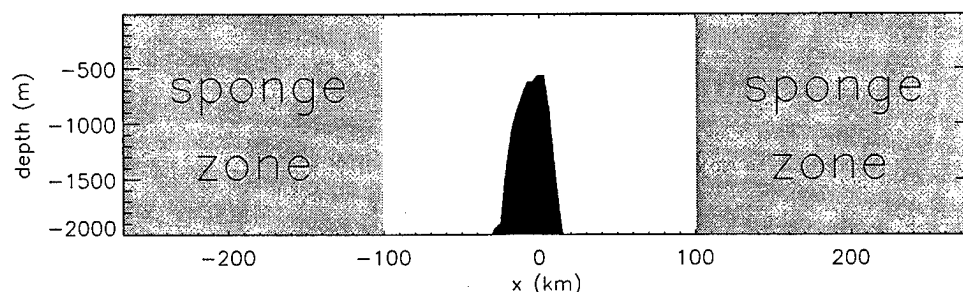


Figure 1. The model topography, representing the vertical cross section of a strait in the northeastern part of the Kuril Islands, where tidal currents are strong enough to cause considerable mixing.

waves generated by an oscillating tidal flow have neglected the advection effect (the second term) in wave-excitation. However, Eq. (11) shows that in regions where the tidal flow is strong and the horizontal scale of forcing is small, such as sill-tops or shelf breaks, wave excitation cannot be fully taken into account unless the advection effect on wave-excitation is incorporated.

To easily specify the nature and structure of tidally generated internal waves, our discussion is restricted to the vertical 2-dimensional case ($\frac{\partial}{\partial y} = 0$), and we assume that the basic flow varies as a single harmonic component of frequency σ_f in time. Then the linearized bottom boundary condition gives the vertical velocity at the bottom as

$$W(x, t) = U_0(x) e^{i\sigma_f t} \frac{\partial h(x)}{\partial x} = e^{i\sigma_f t} \int_{-\infty}^{\infty} \hat{W}_0(k) e^{-ikx} dk, \quad (12)$$

using a Fourier transformation, where U_0 is the tidal current amplitude and h is the sill height. We describe the vertical velocity W in the moving frame X using the approximation

$$x \simeq X + U(x_0, t_0)(t - t_0), \quad (13)$$

in the neighborhood of $x = x_0$ and $t = t_0$. This is equivalent to a local Doppler shift in time and space. After some manipulation, the vertical velocity W splits into the sum of travelling waves propagating with two different phase velocities (corresponding to upper and lower signs) as

$$W(x, t) = \int_0^{\infty} \hat{W}_0(\pm k) e^{i\sigma_f t_0} \times \exp[\mp i\{kX + (kU(x_0, t_0) \pm \sigma_f)\tau\}] dk. \quad (14)$$

This expression shows that the internal wave excited in the neighborhood of $x = x_0$ and $t = t_0$ by the basic flow (U, W) is composed of a sum of monochromatic waves with intrinsic frequency of $-kU(x_0, t_0) \pm \sigma_f$ and horizontal wavenumber of k . Their vertical wavenumber

m is determined so as to satisfy the governing equations and the condition that their energy propagates upward. The total wave field is formed by the superposition of these monochromatic waves excited at various times and positions by a tidal flow over topography.

The terms $-kU(x_0, t_0)$ and $\pm\sigma_f$, which compose the frequencies of the monochromatic waves, relate to the lee waves and the internal tides, respectively. Thus, according to the nondimensional parameter kU_0/σ_f , we can classify internal waves excited by an oscillating flow into unsteady lee waves (when $kU_0/\sigma_f \gg 1$) and "mixed tidal lee waves" (when $kU_0/\sigma_f \sim 1$), in addition to the internal tides (when $kU_0/\sigma_f \ll 1$) which previous theoretical models have focused on.

The properties of these three types of tidally generated internal waves are summarized in Table 1. Unsteady lee waves have the intrinsic frequencies of $-kU(t)$, and their relative phase velocities are $-U(t)$. Thus, unsteady lee waves can propagate in the upstream direction at their excitation time. The amplitudes of unsteady lee waves depend on the magnitude of the forcing at the time of their excitation. Such unsteady lee waves are excited in a region where the curvature of topography is sufficiently large, such as shelf breaks. In contrast, internal tides have a frequency of σ_f and a constant phase velocity of $\pm\sigma_f/k$, and propagate in both directions, as shown in previous studies. In the intermediate range, excited waves have intermediate properties between those of lee waves and internal tides, and we name such waves "mixed tidal lee waves."

Consideration of the intrinsic frequency of these new waves allows us to explain the reason why the sub-inertial K_1 flow can generate super-inertial internal waves propagating in the only one direction. Figure 4 shows the potential density and (original) vertical velocity in the K_1 case around the sill top up to 0.5 period, when the generation process of intense short waves can be seen clearly. For example, as the K_1 current flows rightward, large downward velocity is induced at sudden changes in the sill slope on the downstream side

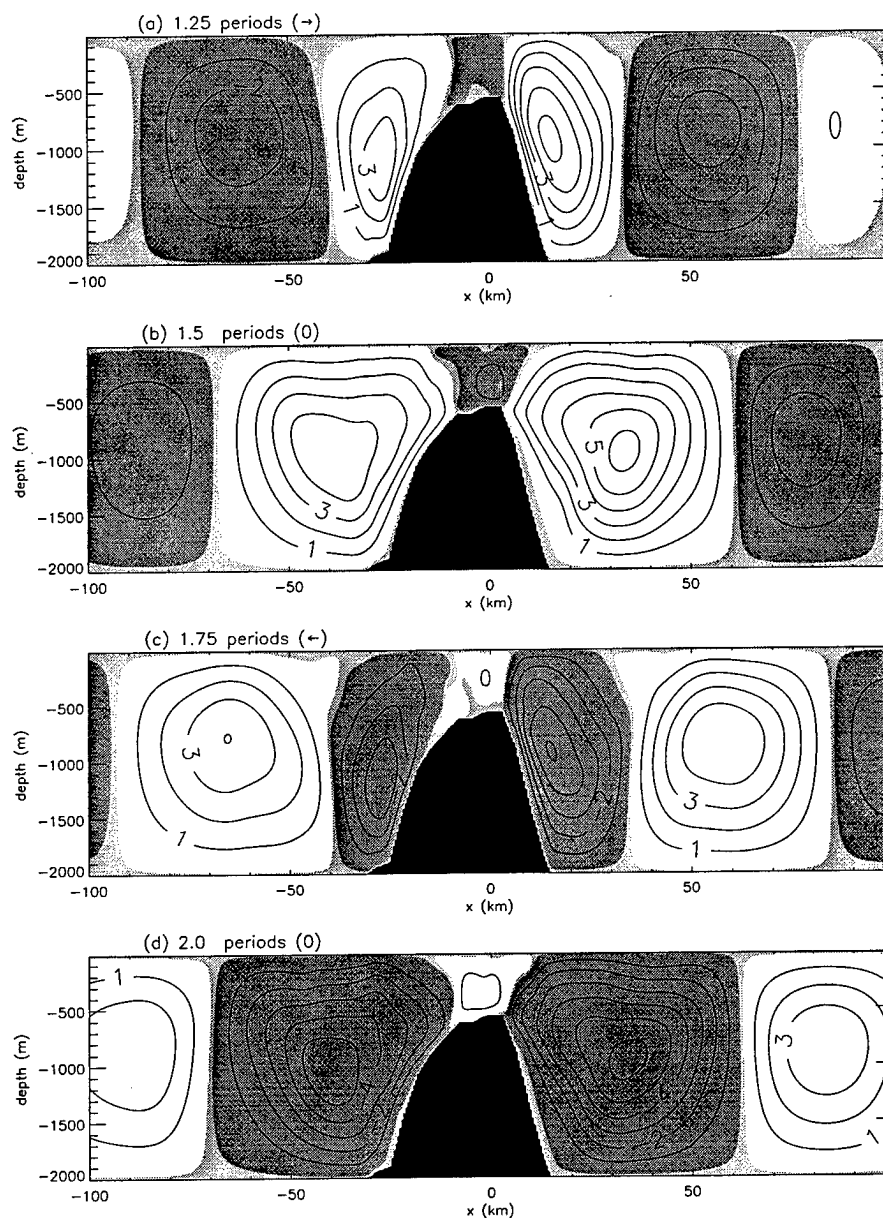


Figure 2. The time series of the internal mode stream function in the M_2 case during the second tidal period; after (a) 1.25, (b) 1.5, (c) 1.75, and (d) 2.0 periods. The contour interval is $1.0 \times 10^5 \text{ cm}^2 \text{ s}^{-1}$. Values in nonshaded areas and the thicker shaded areas are positive and negative, respectively, and the absolute values in the thinner shaded areas are less than $1.0 \times 10^4 \text{ cm}^2 \text{ s}^{-1}$.

Table 1. Properties of Tidally Generated Internal Waves

regime	$\frac{kU_0}{\sigma_f} \gg 1$	$\frac{kU_0}{\sigma_f} \sim 1$	$\frac{kU_0}{\sigma_f} \ll 1$
wave type	unsteady lee waves	mixed tidal lee waves	internal tides
intrinsic frequency	$-kU(t)$	$-kU(t) \pm \sigma_f$	$\pm \sigma_f$
relative phase velocity	$-U(t)$	$-U(t) \pm \sigma_f/k$	$\pm \sigma_f/k$

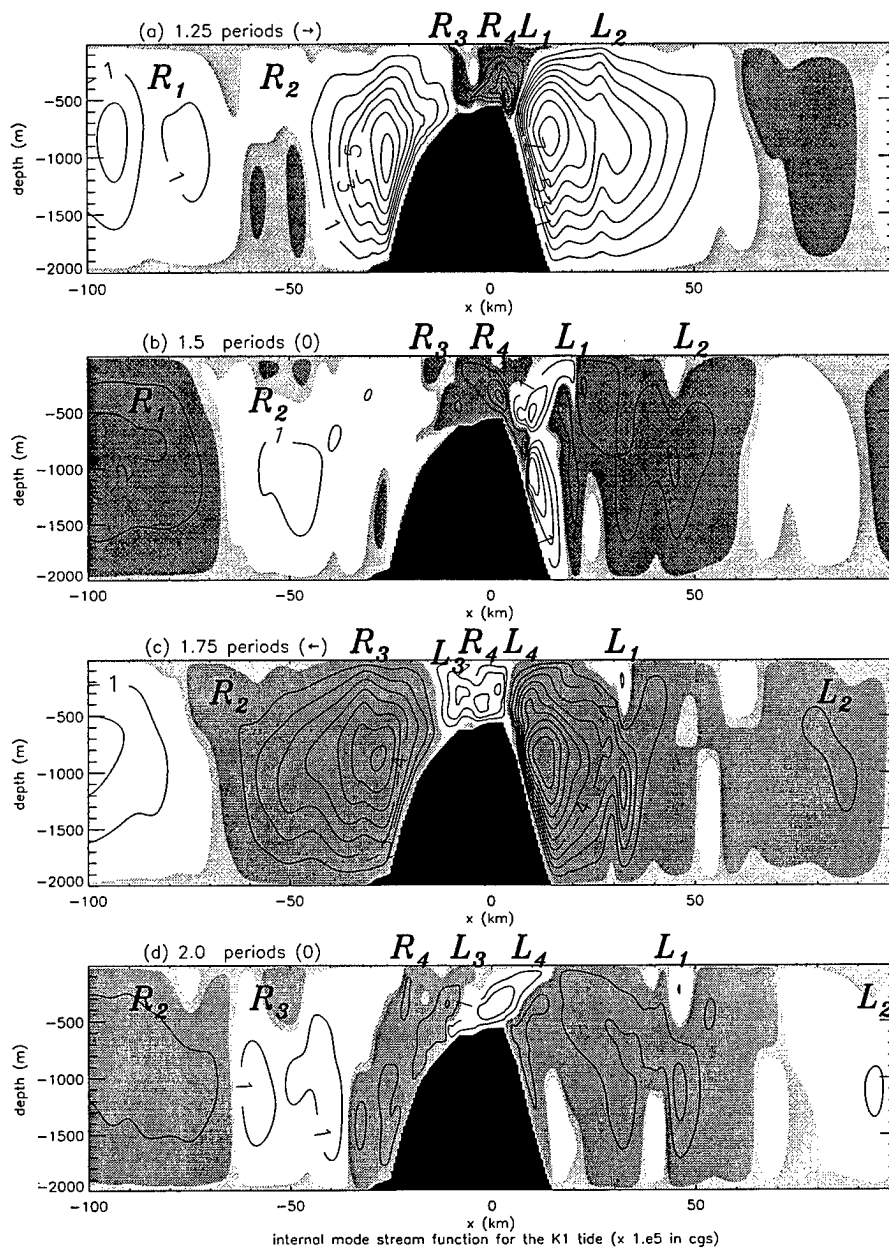


Figure 3. Same as in Fig. 2 but for the K_1 case.

(Fig. 4a). This small-scale downward current produces a large depression at the right-hand break, which grows to form a distinct wave pattern (Fig. 4b,c), as expected from our theoretical model. Since $\frac{kU_0}{\sigma_f} = 5.4$, this wave can be roughly classed as an unsteady lee wave. An estimate of its frequency based on Eq. (14) $((3.9 \pm 0.73) \times 10^{-4} \text{s}^{-1})$ shows good agreement with that based on the linear dispersion relation $(4.6 \times 10^{-4} \text{s}^{-1})$. The co-phase lines of these short waves extend in one direction, consistent with the character of unsteady lee waves. Thus, we conclude that the intense short waves simulated in the K_1 case are unsteady lee waves.

The displacement at the right-hand break continues to grow until the end of the rightward flow to form a large-amplitude (~ 100 m) wave (Fig. 4d). As the flow ceases, the upper part propagates upstream (leftward) while the lower part of the wave stays at almost the same place, and the co-phase line of vertical velocity leans toward the upstream side. This indicates that modal waves have not yet been formed and hence the modal wave approximation could be inappropriate for understanding the growth mechanism of this wave.

5. Growth mechanism of tidally generated internal waves

Another interesting implication of our theoretical model is that the wave-growth mechanism depends on the non-dimensional parameter $\frac{kU_0}{\sigma_f}$. This is because the intrinsic horizontal phase velocities are different according to the wave types, as shown in Table 1.

Ray tracing of individual wave components generated at various instants of time demonstrates this fact clearly. To see the fundamental growth-mechanism, the following simplifications are made. (1) The basic flow and stratification are uniform, (2) modal waves still have not been formed, as in the K_1 case (Fig. 4), so that wavenumbers can be determined from the horizontal scale of forcing and the dispersion relation, and (3) the group speed $|c_g|$ is nearly equal to the phase speed $|c_p|$ (the ratio $|c_g|/|c_p|$ is about 0.9 for the unsteady lee waves in the K_1 case). Then, the positions, $x^\pm(t)$, of the wave components excited at $t = t_0$ are

$$x^\pm(t) \simeq (-U(t_0) \pm \sigma_f/k)(t - t_0) + \int_{t_0}^t U(\tau) d\tau. \quad (15)$$

Figure 5 shows the loci of individual wave components during one tidal cycle for these three wave types. The amplitudes of the components are represented by line thickness. The basic flow is given as $U(t) = U_0 \sin(\sigma_f t)$, which begins to flow rightward at $t = 0$.

In the unsteady lee wave regime ($kU_0/\sigma_f \gg 1$), a large-amplitude wave is formed around the time of max-

imum flow and propagates upstream. This wave growth is mainly caused by the following two reasons. One is that the absolute phase velocity (i.e., the phase velocity in the frame fixed to the ground) of unsteady lee waves is zero at the generation time. Thus, individual waves generated are trapped to superpose at the generation point when the time variation in the basic flow is small (i.e., the time of maximum flow). This mechanism is, in a sense, an extension of the modal wave theories such as *Hibiya* (1986) to individual unsteady lee waves. Another is that because the amplitudes are in proportion to the basic flow speed, individual waves generated in this duration have largest amplitudes and thus have the major portion of the energy extracted as unsteady lee waves in the half period. In the K_1 case, the growth process to the large-amplitude wave can be understood by the above mechanism because $\frac{kU_0}{\sigma_f} = 5.4$.

For the internal tides ($kU_0/\sigma_f \ll 1$), the intrinsic horizontal phase velocities are always almost equal to $\pm \sigma_f/k$. The effect of advection is negligible since the ratio of the maximum current speed to intrinsic phase speed of internal tides is kU_0/σ_f , which is much less than unity. Accordingly, these components are not superposed and wave-amplification never occurs.

When the magnitudes of lee-wave ($-U(t)$) and internal-tide ($\pm \sigma_f/k$) constituents are comparable (Fig. 5b), the loci of wave components for x^+ and those for x^- are quite different. Thus, we separate wave components on the basis of whether the phase velocity of their internal-tide constituent is in the same direction as the lee-wave constituent (i.e., $c_{px} = c_{px}^f = -U + \text{sgn}(-U)\frac{\sigma_f}{k}$) or in the opposite direction (i.e., $c_{px} = c_{px}^s = -U + \text{sgn}(+U)\frac{\sigma_f}{k}$). We name the waves with phase velocities c_{px}^f and c_{px}^s "fast mixed tidal lee waves" and "slow mixed tidal lee waves", respectively. The superposition is, in effect, of fast (slow) mixed wave components generated in the acceleration (deceleration) stage before (after) the maximum flow.

The vertical positions of wave components z^\pm at time t under consideration are

$$z^\pm \simeq \frac{k}{N} (c_{px}^\pm(t_0))^2 (t - t_0). \quad (16)$$

This equation indicates that the loci in $z - t$ space (not shown) are straight lines, and show basically similar tendencies to those in $x - t$ space except for the advection effect, since vertical phase speeds depend on (intrinsic) horizontal phase speeds. The vertical phase speed of internal tides is the fastest among three wave types. Unsteady lee waves are faster than fast mixed tidal lee waves. This is because we change the value of kU_0/σ_f keeping σ_f constant so that the maximum vertical group speed $c_{gz}^+ (\simeq \frac{1}{Nk}(kU_0 + \sigma_f)^2)$ increases with increasing kU_0 . Slow mixed tidal lee waves have very small vertical

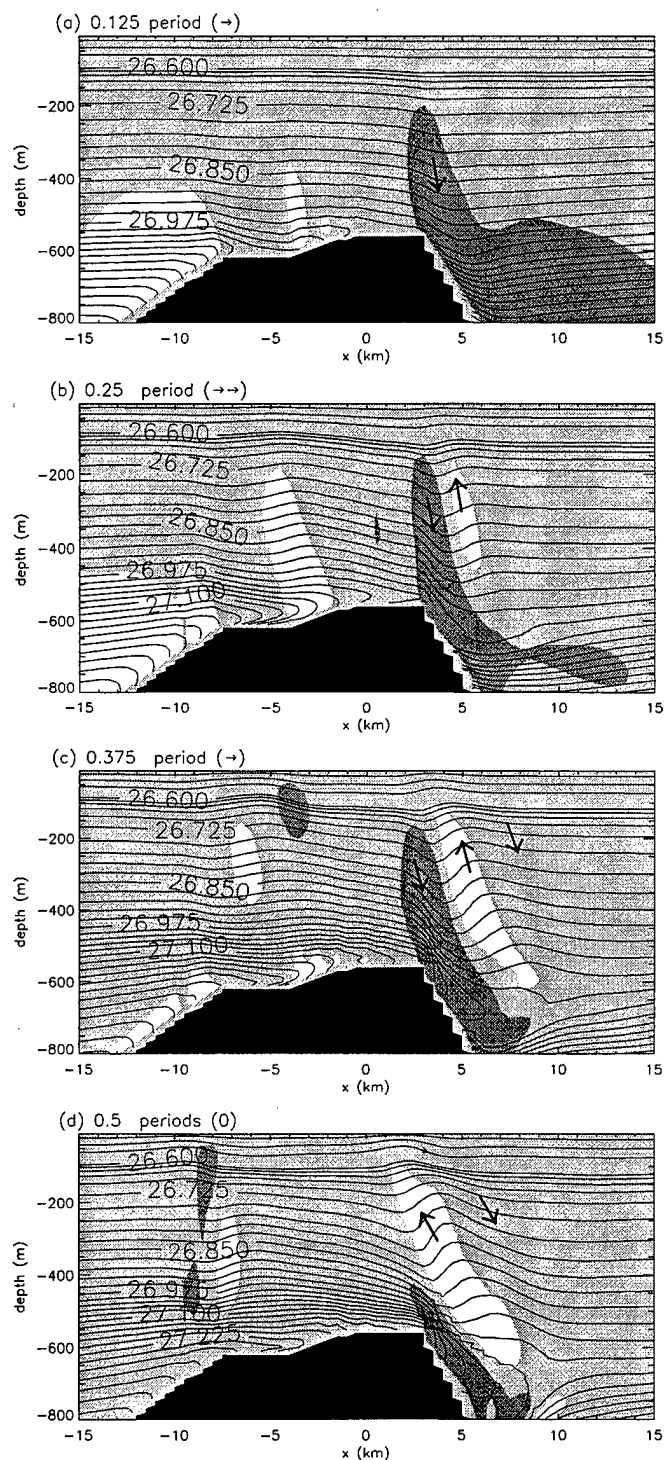


Figure 4. The evolution of potential density (σ_θ) and vertical velocity (w) around the sill top in the K_1 case, during the 1st period; after (a) 0.125, (b) 0.25, (c) 0.375, and (d) 0.5 period. Vertical velocity is greater than 0.5cm s^{-1} in the non shaded areas and less than -0.5cm s^{-1} in the thicker shaded areas. For $\sigma_\theta < 26.6$, the contour interval is $0.2 \sigma_\theta$. For $\sigma_\theta \geq 26.6$, the contour interval is $0.025 \sigma_\theta$.

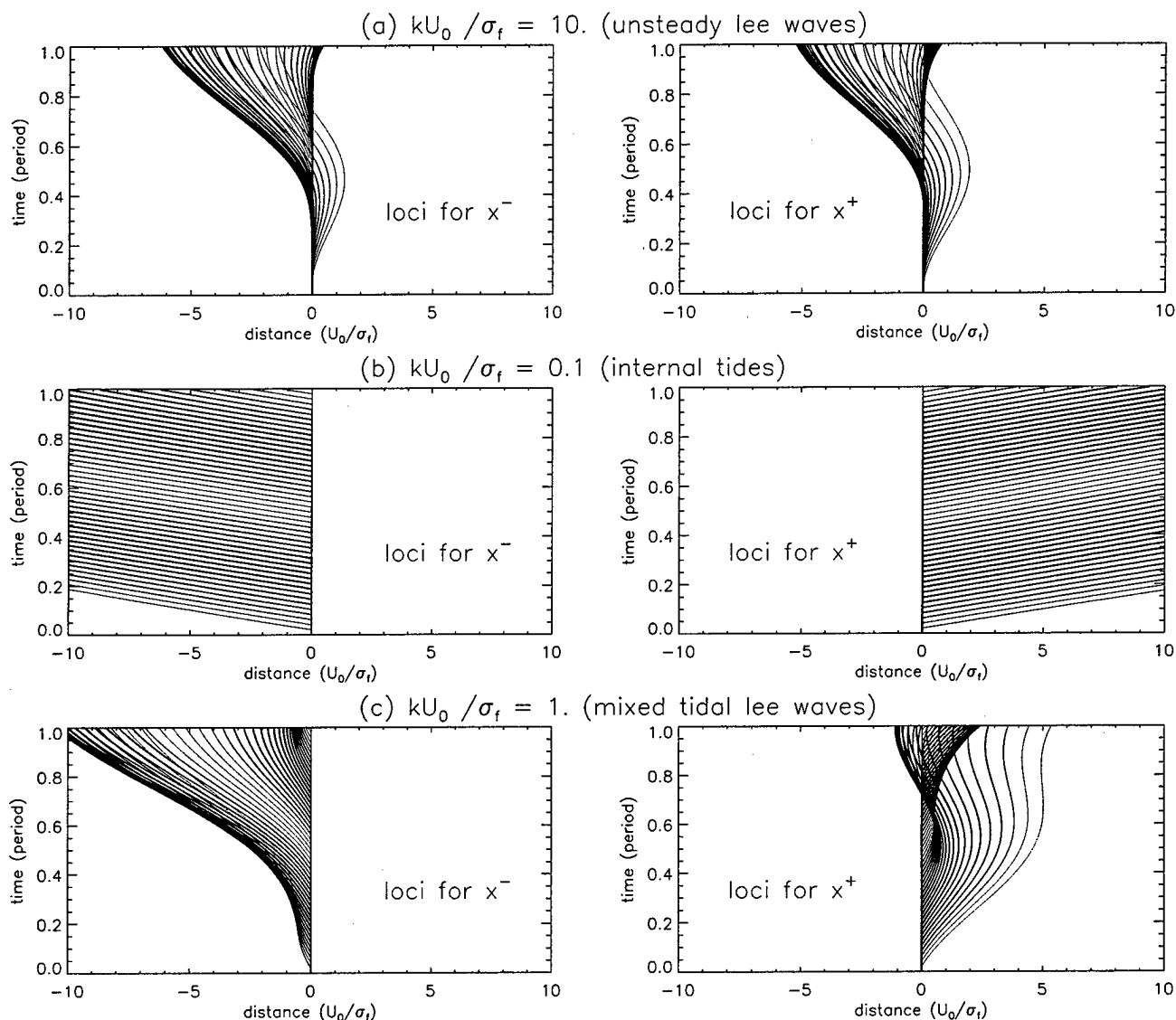


Figure 5. The loci of individual wave components in $x-t$ space during 1 tidal cycle, when the parameter $\frac{kU_0}{\sigma_f}$ is (a) 10, (b) 1, and (c) 0.1. Those for x^+ and x^- are shown in left and right columns. Waves are generated at $x = 0$, the basic current flows rightward during $0 \leq \text{period} < 0.5$ and leftward during $0.5 \leq \text{period} < 1$, and the amplitudes of individual waves are represented by line thickness (for the case of $\hat{W}(k) = \hat{W}(-k)$). The horizontal scale is non-dimensionalized using the tidal excursion $\frac{U_0}{\sigma_f}$.

phase speeds. Thus, superposition of wave components during the period of their generation occurs mostly in the horizontal direction for the unsteady lee wave case and in the vertical direction for the mixed tidal lee wave case.

6. Vertical mixing induced by internal waves

Figure 6 shows the subsequent evolution of the large-amplitude unsteady lee waves. As the flow turns to the left, the large-amplitude wave generated at the right-hand break (Fig. 4d) propagates across the sill and encounters an unsteady lee wave newly generated at the left-hand break (after 0.75 period). This event produces a large-amplitude isopycnal elevation at the foot of the unsteady lee waves (Fig. 6b). As the flow turns to the right, this elevation gradually breaks, propagating rightward, and causes vigorous vertical mixing over the sill top.

The superposition of the unsteady lee waves forms a distinct V-shape (Fig. 6c), inducing density inversion (Fig. 6d). Again, a large-amplitude unsteady-lee wave is generated at the right-hand break by the rightward flow, showing that the lee-wave response is not an artifact of the initial spin-up of the model. In this way, large-amplitude unsteady-lee waves induce intense vertical mixing repeatedly, and relatively vertically-uniform water is produced over the sill top in the K_1 case as is seen in Fig. 7a. The feature of this map has good similarities with that of observations (Fig. 7b), supporting our model's realism.

We estimate the intensity of the resulting vertical mixing in terms of diffusivity. To relate the result to the parameterizations used in general circulation models, we estimate the vertical diffusivity K_z from an Eulerian point of view using the following Fickian formulation,

$$K_z = |\overline{S'w'} / \frac{dS_0}{dz}| \quad (17)$$

where dS_0/dz is the vertical gradient of the initial salinity profile, and $\overline{S'w'}$ is salinity flux induced by perturbations, averaged over one tidal period. In the M_2 case, the estimated diffusivity using the calculated velocity fields in the 2nd period is not so large ($\sim 10 \text{ cm}^2 \text{ s}^{-1}$), as expected earlier. In contrast, the value in the K_1 case is very large around the sill ($\sim 10^3 \text{ cm}^2 \text{ s}^{-1}$) and relatively small in other regions. This is mainly due to large-amplitude unsteady lee waves propagating over the sill and their superposition on unsteady lee waves newly generated by the reversed flow leading to prominent wave breaking.

7. Summary and discussion

In order to clarify the mechanism responsible for the intense vertical mixing in the Kuril Straits and the associated modification of water properties, we numerically investigated internal waves generated through the interaction between the tidal currents (predominant in the Kuril Straits) and the sill and their effect on mixing, using a nonhydrostatic f -plane model.

The model results reveal the following. Although internal waves at the tidal frequency (internal tides) generated by the subinertial K_1 flow are trapped to the sill, large-amplitude free-propagating internal waves of short wavelengths are repeatedly generated and break around the sill top, thus producing relatively vertically-uniform water over the sill top. In the M_2 case, most of the generated internal waves propagate away as 1st-mode internal tides, conveying energy away from the sill. Moreover, because the barotropic flow amplitude is small, the amplitudes of waves do not become so large as to cause wave breaking. As a result, the M_2 tidal current did not cause significant vertical mixing in this case.

Our theoretical consideration identifies the large-amplitude short waves in the K_1 case as unsteady lee waves, which have been neglected in previous theories for tidally generated internal waves. Interestingly, unsteady lee waves are always amplified when the group speeds are nearly equal to the phase speeds, because their individual wave components generated around the time of maximum flow have maximum amplitude and are always trapped to superpose in the generation region. Furthermore, the superposition of a propagating unsteady lee wave and a newly generated lee wave over the sill generates a large-amplitude internal wave, which causes wave breaking and induces intense vertical mixing over the sill top.

The estimated vertical diffusivity in the K_1 case is very large around the sill in both cases, reaching a maximum value of $10^3 \text{ cm}^2 \text{ s}^{-1}$. Such intense mixing occurs from the sill to the surface, reaching down to the density core of the NPIW ($\sim 26.8\sigma_\theta$). Thus it is suggested that large-amplitude unsteady lee waves generated by the K_1 tidal current and their breaking is one possible mechanism for the observed water modification in the Kuril Straits.

Although internal tides have a secondary effect on vertical mixing in the Kuril Straits at high latitudes, these are expected to induce significant vertical mixing in the subtropical and tropical regions, where the superinertial semidiurnal tides dominate. In such regions, not only unsteady lee waves but also internal tides are likely to be effectively amplified. The latter is especially

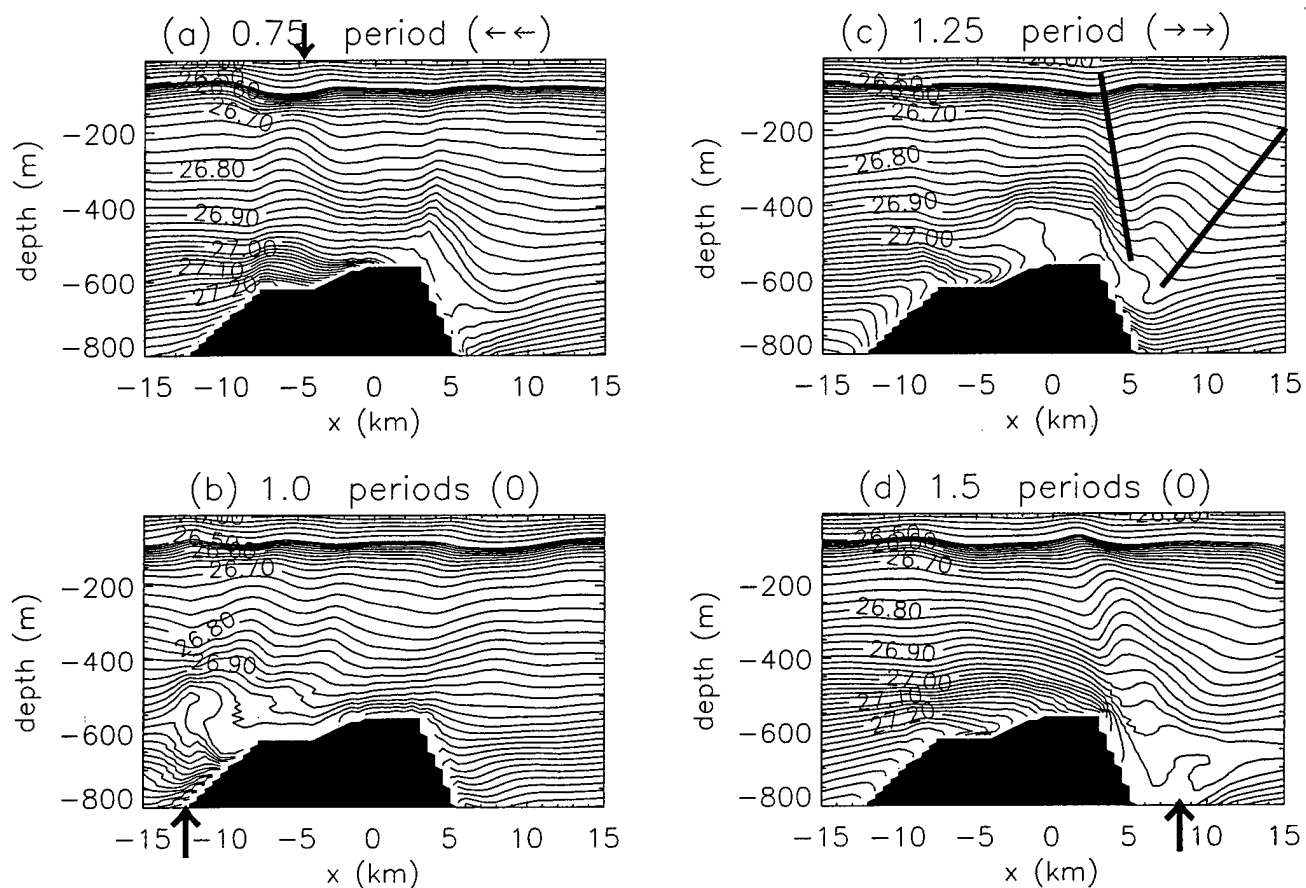


Figure 6. The subsequent evolution of potential density (σ_θ) around the sill top in the K_1 case; after (a) 0.75, (b) .0, (c) 1.25, (d) 1.5 periods. The contour intervals are the same as in Fig. 4.

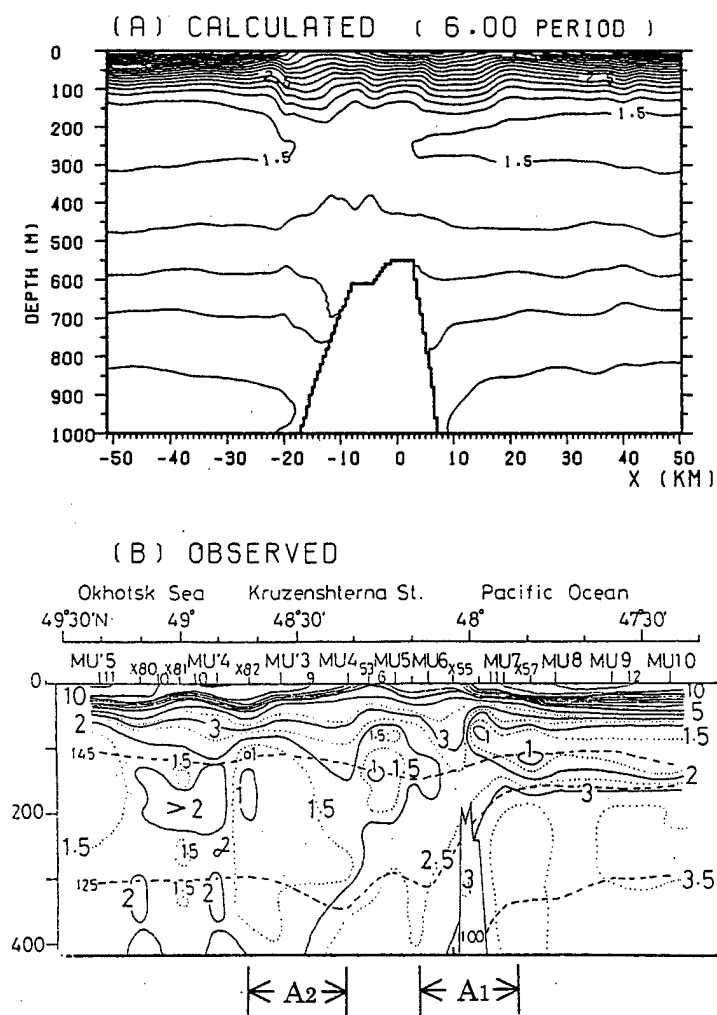


Figure 7. (a) The calculated potential temperature distribution after 6 periods (contour interval is 0.2°C), and (b) the observed potential temperature distribution in the Kruzenshterna Strait (A_2) together with a shallow bank (A_1), observed by the Hokkaido National Fisheries Research Institute in 1994. Dashed lines indicate isopycnal surfaces of 145, 125, and 100 cl/ton (26.6 , 26.8 , $27.1 \sigma_\theta$).

so when the condition of the critical slope (e.g., Wunsch 1969) and/or the critical Froude number (Hibiya 1986) is satisfied. The combined effects of these waves are interesting problems for future theoretical and observational studies.

Since we use a vertically 2-dimensional model, the sub-inertial K_1 internal tides are not properly reproduced. To roughly examine the influence of longitudinal wave-radiation, we performed a numerical experiment in which the horizontal eddy viscosity and diffusivity coefficients are increased by a factor of 4 relative to those in the original case. The result reveals that the lee-wave processes are basically the same and the estimated diffusivity is still of the order of $10 \sim 100$ (cm^2s^{-1}). This suggests the importance of tidal mixing on the freshening of the intermediate layer in the actual Kuril Straits. However, further modifications are required to our numerical model since quantitative estimation of the actual role of vertical mixing at the Kurils on the formation of the NPIW is beyond the power of a 2-dimensional model and should be investigated using a 3-dimensional model. Nevertheless the qualitative similarities between the observational results and our simulations point to the importance of strong vertical mixing in the water modification between the Okhotsk Sea and the North Pacific.

8. Appendix

The internal mode stream function is defined as the difference between the original solutions and the solutions obtained by setting $g = 0$. Since the $g = 0$ solution gives approximately the barotropic flow which acts as the forcing (Lamb 1994), internal mode processes can be seen in terms of internal mode stream functions. This is not exactly true, since the $g = 0$ flow satisfies the no-slip condition at the sill by viscous effects, whereas in the full solution this boundary condition is satisfied by a combination of viscous effects and internal waves. Hence, the viscous effects are not the same in the two cases, and hence internal mode stream functions do not represent the true baroclinic response but also include some reminiscent effects of viscosity from the $g=0$ case. However, since the thickness of the bottom Ekman layer ($\sim (\nu_z/f)^{1/2}$) is less than 10m in the present case, the effect of a no-slip condition is significant in only a few grids from the bottom. Thus, the current field of the

$g=0$ solution in the K_1 case is vertically uniform except very near the bottom (not shown). Therefore, the baroclinic response can be fairly well described by internal mode stream functions.

Acknowledgment. We wish to express our thanks to Prof. P. Müller for his kind acceptance of our presentation in 'Aha Huliko'a Hawaiian Winter Workshop.

References

- Bryan, K., and M. D. Cox, 1972: A numerical method for the study of the circulation. *J. Phys. Oceanogr.*, **2**, 510-514.
- Gerkema, T. and J. T. F. Zimmerman, 1995: Generation of nonlinear internal tides and solitary waves. *J. Phys. Oceanogr.*, **25**, 1081-1094.
- Hibiya, T., 1986: Generation mechanism of internal waves by tidal flow over a sill. *J. Geophys. Res.*, **91**, 7696-7708.
- Hibiya, T., 1988: The generation of internal waves by tidal flow over Stellwagen Bank. *J. Geophys. Res.*, **93**, 533-542.
- Kawasaki, Y. and T. Kono, 1994: Distribution and transport of Subarctic Waters around the middle of Kuril Islands. *Sea and Sky*, **70**, 71-84 (in Japanese).
- Kitani, K., 1973: An oceanographic study of the Okhotsk Sea - particularly in regard to cold waters. *Bulletin of the Far Seas Fisheries Research Laboratory*, **9**, 45-77.
- Lamb, K. G., 1994: Numerical experiments of internal wave generation by strong tidal flow across a finite amplitude bank edge. *J. Geophys. Res.*, **99**, 843-864.
- Lee, C.-Y. and R. C. Beardsley, 1974: The generation of long nonlinear internal waves in a weakly stratified shear flow. *J. Geophys. Res.*, **79**, 453-462.
- Lott, F. and H. Teitelbaum, 1993: Linear unsteady mountain waves. *Tellus*, **45A**, 201-220.
- Nakamura, T., T. Awaji, T. Hatayama, K. Akitomo, and T. Takizawa, 1999: Tidal exchange through the Kuril Straits. *submitted to J. Phys. Oceanogr.*
- Samelson, R. M., 1998: Large-scale circulation with locally enhanced vertical mixing. *J. Phys. Oceanogr.*, **28**, 712-726.
- Talley, L. D., 1991: An Okhotsk Sea water anomaly: implications for ventilation in the North Pacific. *Deep-Sea Res.*, **38**, s171-190.
- Watanabe, T., and M. Wakatsuchi, 1998: Formation of 26.8 σ_θ water in the Kuril Basin of the Sea of Okhotsk as a possible origin of North Pacific Intermediate Water. *J. Geophys. Res.*, **103**, 2849-2865.
- Wunsch, C., 1969: Progressive internal waves on slopes. *J. Fluid Mech.*, **35**, 131-144.
- Yasuda, I., 1997: The origin of the North Pacific intermediate water. *J. Geophys. Res.*, **102**, 893-910.

A Rough Recipe for the Energy Balance of Quasi-Steady Internal Lee Waves

Kurt Polzin

Woods Hole Oceanographic Institution, Woods Hole, MA 02543

Abstract. Recent fine- and microstructure observations indicate enhanced finescale shear and strain in conjunction with bottom intensified turbulent dissipation above regions of rough bathymetry. Such observations implicate the bottom boundary as an energy source for the finescale internal wavefield. They also pose a question. Can the vertical profile of turbulent dissipation be predicted from a model of wave generation which serves as input to a model describing how internal wave energy is transferred to dissipation scales as waves propagate away from their source region? This paper attempts to address that question in the context of quasi-steady lee wave generation and dissipation.

1 Introduction

The intensity, spatial distribution and casual physical mechanisms of diapycnal mixing in the deep ocean have been the subject of much speculation. Advective heat budgets in semi-enclosed basins (e.g., *Hogg et al.*, 1982) typically return estimates of $K \sim 1 - 10 \times 10^{-4} \text{ m}^2 \text{ s}^{-1}$, similar to estimates of $K \sim 1 \times 10^{-4} \text{ m}^2 \text{ s}^{-1}$ obtained from vertical advection/diffusion models (*Wyrtki* 1962, *Munk* 1966). These estimates, however, do not appear to be appropriate for the stratified upper ocean, for which a purposeful tracer release experiment (*Ledwell et al.* 1993) and microstructure measurements (*Gregg* 1987) suggest $K \sim 0.1 \times 10^{-4} \text{ m}^2 \text{ s}^{-1}$. Validation studies (*Polzin et al.* 1995, *Gregg* 1989) of internal wave-wave interaction models indicate that the empirical Garrett and Munk (GM, *Garrett and Munk* 1975, as modified by *Cairns and Williams*, 1976) spectral description of the background internal wave state supports only weak ($K \leq 0.1 \times 10^{-4} \text{ m}^2 \text{ s}^{-1}$) mixing which is independent of the background stratification rate, N^2 .

In order for internal wave-driven mixing to explain the results of advective heat budgets in abyssal basins, the abyssal internal wave spectrum needs to depart substantially from the GM specification. As abyssal internal wave observations were used to help construct the GM model, significant spatial variability of the abyssal wavefield is implied. Neither departures of the abyssal internal wavefield from GM nor diffusivities in excess of $1 \times 10^{-4} \text{ m}^2 \text{ s}^{-1}$ are apparent above smoothly sloping abyssal plains and Continental Rise regions (*Toole et al.* 1994, *Kunze and Sanford* 1996, *Polzin et al.*

1997). Significant departures are, however, found above rough bathymetry (*Polzin et al.* 1997, *Polzin and Firing* 1997).

What, then, are the mechanisms which support enhanced mixing above rough topography? *Polzin et al.* (1997) proposed that the enhanced mixing above rough topography in the Brazil Basin was associated with a direct conversion of barotropic tidal energy into baroclinic tidal energy having horizontal scales which were characteristic of the bottom topographic roughness ($\lambda_h < 6 - 10 \text{ km}$). Linear internal wave kinematics ($\lambda_v \sim \lambda_h N/\omega$) implies the baroclinic response to be band-limited to vertical wavelengths ($\lambda_v < 600 - 1000 \text{ m}$). If so band-limited, an internal wavefield can exhibit both relatively modest velocities and significant shear ($S^2 > N^2$, where S^2 is the shear variance and N^2 is the buoyancy frequency squared) over large vertical length scales. Both are essential considerations. Energetic arguments suggest baroclinic tidal velocities should not exceed barotropic, and barotropic tidal velocities in the open ocean typically are only $0.02 - 0.03 \text{ m s}^{-1}$. Turbulent production from internal wave breaking is quadratically dependent upon the length scale over which $S^2 > N^2$ (*Polzin*, 1996). In the background wavefield, $m^2 U^2 = S^2 = N^2$ for a vertical scale $2\pi/\lambda_v = 1/m$ of 1 meter. If a single vertical scale characterizes both the shear and velocity fields of the baroclinic response, $U/N = 20 \text{ m}$ for $U = 0.02 \text{ m s}^{-1}$ and $N = 0.001 \text{ s}^{-1}$. It is entirely possible to obtain turbulent dissipation rates that are two orders of magnitude larger than background values from the breaking of an internal tide having relatively modest velocities which are characteristic of the open

ocean barotropic tidal velocity field. The trick is that the baroclinic response needs to have a small vertical scale. This small scale response is effectively and efficiently provided by flow over topographic roughness. Data obtained during an additional cruise to the Brazil Basin further supports this proposed mechanism (*Ledwell et al.*, submitted). Depth-averaged dissipation data document a fortnightly modulation in the turbulence intensity that lags the amplitude of the barotropic tide by 1–2 days. The fortnightly modulation and small phase lag imply a spatially local balance between internal tide generation and dissipation, rather than generation of low modes at the shelf break of the Brazilian coast (*Baines* 1982) and subsequent propagation and scattering (*Müller and Xu* 1992) into smaller spatial scales above rough bathymetry.

Polzin and Firing (1997) infer depth-averaged dissipation rates above rough topography on the Southeast Indian Ridge which have a similar enhancement as the data obtained above the Mid-Atlantic Ridge in the South Atlantic. They cite deep sub-inertial flows associated with the Antarctic Circumpolar Current as being responsible for the generation of small vertical scale internal lee waves. As with baroclinic tide generation, the issue is that wave energy resides at sufficiently small scales that waves dissipate near their source. How the magnitude and decay scale of turbulent production via wave breaking relates to the amplitude and spatial scales of the wavefield is defined by the competing and coupled effects of propagation in an inhomogeneous environment and nonlinear transfers. The amplitude and spatial scale of the wavefield can, in turn, be viewed as a product of wave generation at the bottom boundary.

The motivation for this study is to better define and understand those processes which contribute most significantly to the closure of the abyssal heat budget. The predisposition is to view generation of small vertical wavelength internal waves and their subsequent dissipation as the dominant process. The objective of this research is to develop quantitative, predictive models for the spatial evolution of the finescale wavefield and associated turbulent mixing. The problem of quasi-steady lee wave generation and dissipation is formulated in the following section and addressed below.

2 Problem statement

The turbulent fluxes associated with wave breaking can be viewed as the end result of a systematic, downscale transport of energy by adiabatic mechanisms at larger spatial scales. The downscale transport can result from a variety of mechanisms such as buoyancy scaling, wave-mean flow or wave-wave interactions. Wave-wave interactions are the most problematic of

these. While the downscale transport of energy associated with either buoyancy or wave-mean flow interactions can be defined for a single internal wave, defining a transport model for fluxes associated with wave-wave interactions necessitates a statistical, spectral framework if the wavefield exhibits a broad-banded character in the vertical wavenumber domain.

A conceptual diagram of the problem appears in Figure 1. Internal waves are assumed to be generated at the bottom boundary ($z = 0$) by sub-inertial flow $U(z)$ impinging upon topographic roughness. In view of the statistical framework, the bathymetry is described in terms of a 2-D spectrum $H(k, l)$, where k and l are horizontal wavenumbers and the flow is assumed to be aligned in the 'k' direction. The sub-inertial flow is assumed here to be steady. A spectral model of wave generation is employed to specify the distribution of energy flux into the wavefield as a source function, $S_o(k, l)$, which can simply be viewed as a product of the bathymetric spectrum and a transfer function. A dispersion relation is then used to transfer the source function into the vertical wavenumber (m) and intrinsic frequency ($\omega = \sigma - kU$) domain, $S_o(m, \omega)$. This source function then serves as a bottom boundary condition for an interior wavefield having both upward (E^+) and downward (E^-) propagating components, Section 8.

Evaluating the vertical evolution of the wavefield requires defining the relative effects of vertical propagation and transport in a vertical wavenumber (m), intrinsic frequency (ω), height above boundary (z) coordinate system. Here, transport is used to denote transfers of energy (or wave action) in the vertical wavenumber (F) and intrinsic frequency (G) domain associated with buoyancy scaling, wave-wave and wave-mean flow interactions. An equation governing the evolution of the wave spectrum is derived in Section 3, and transport models are discussed in Section 4.

Solutions for the internal wave spectrum are determined by solving the wavefield evolution equation subject to appropriate boundary conditions on E^+ and E^- . In Section 6 a radiation condition is used. Solutions described in Section 7 assume an upward (downward) propagating wavefield reflects from the surface, $z = H$ (and bottom, $z = 0$). Surface generation and scattering from non-uniform bathymetry or reflection from a sloping boundary are neglected. Complicating the analysis is the potential need to incorporate the interaction between upward [$E^+(m, \omega, z)$] and downward [$E^-(m, \omega, z)$] propagating waves. Direct transfers of energy between upward and downward propagating waves are ignored here. The two components of the wavefield are assumed to be simply coupled by the dependence of downscale transfers F upon the total wavefield,

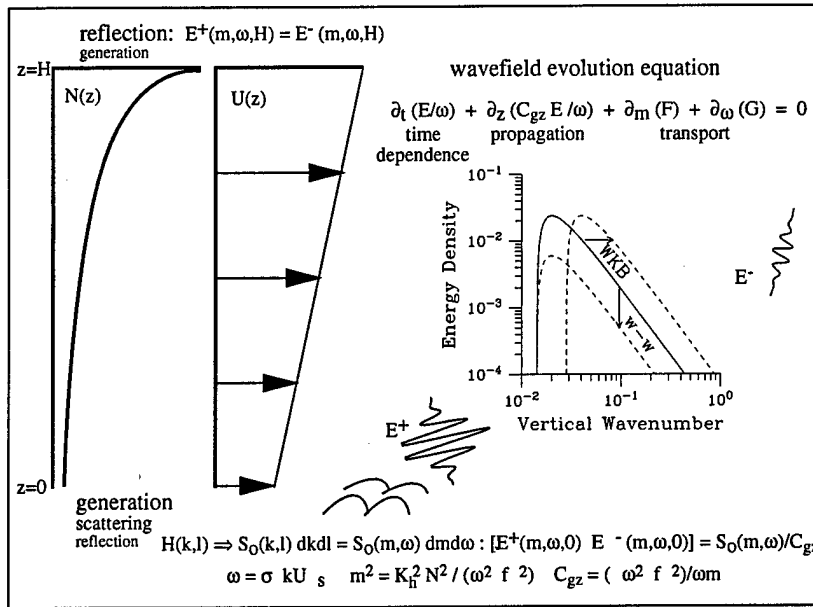


Figure 1. A conceptual process diagram. The shape of the solution in the vertical wavenumber domain is depicted at the center of the figure. Propagation of this spectrum into a region of increasing $N(z)$ or decreasing $U(z)$ implies a transport of energy to smaller scales depicted by the notation 'WKB'. Transport associated with wave-wave interactions simply results in a decrease of the amplitude of the spectrum with height. The evolution of the spectrum in this case is denoted by 'w-w'. See text for description of the other variables.

$E^+ + E^-$. Finally, estimates of turbulent fluxes can be obtained by evaluating the transport F using the solutions to the wavefield evolution equation.

3 Wavefield Evolution Equation

The intent of this section is to derive an equation from which the relative effects of propagation and transport on the amplitude of the wavefield can be assessed. The wavefield evolution equation represents a wave action conservation statement (e.g., *Bretherton and Garrett 1968*) formulated in the frequency, vertical wavenumber domain.¹ It is the wave stress, rather than energy, which is conserved by waves propagating in a spatially varying background flow (*Bretherton 1966, Jones 1967*). The interaction of the wave stress with the background shear implies a transfer of energy between

the two (*Garrett 1968*). The stress is then expressed as wave action. The hydrostatic approximation is assumed throughout as the transport models for buoyancy scaling and wave-mean flow interactions are based upon the WKB approximation.

Consider a point (m_2, ω_2, z_2) in vertical wavenumber (m), frequency (ω), and vertical coordinate (z) space, Figure 2. The action density in the volume defined by the line segments $\Delta m = m_3 - m_1$, $\Delta \omega = \omega_3 - \omega_1$, $\Delta z = z_3 - z_1$ is $\Delta m \Delta \omega \Delta z E(m_2, \omega_2, z_2, t)/\omega_2$, where $E^\pm(m, \omega, z, t)$ is the vertical wavenumber-frequency energy density of either the upward (+) or downward (-) propagating wavefield, and Δm , $\Delta \omega$ and Δz are assumed to be small. The time rate of change of action density in the area, $\Delta m \Delta \omega \Delta z \partial [E^\pm(m_2, \omega_2, z_2, t)/\omega_2] / \partial t$, is balanced by vertical fluxes of action through the surfaces defined by $z = z_1$ and $z = z_3$, $[C_{gz}(m, \omega) E^\pm(m, \omega, z, t)/\omega] \Delta m \Delta \omega$, where $C_{gz} = \mp(\omega^2 - f^2)/\omega m$ is the vertical group velocity; down-scale spectral transfers $F^\pm(m, \omega, z, t) \Delta z \Delta \omega$ of action through the surfaces at $m = m_1$ and $m = m_3$; and spectral transfers in the frequency domain across $\omega = \omega_1$ and $\omega = \omega_3$, $G^\pm(m, \omega, z, t) \Delta m \Delta z$:

$$\Delta m \Delta \omega \Delta z \frac{\partial [E^\pm(m_2, \omega_2, z_2, t)/\omega_2]}{\partial t}$$

¹ $E^\pm(m, \omega, z)$ is the vertical wavenumber-frequency energy density with direction of energy propagation denoted by either + or -. The notation $E^\pm(m, z)$ [or $F^\pm(m, z)$] denotes integration over the frequency domain, $E^\pm(m, z) = \int E^\pm(m, \omega, z) d\omega$. For narrow frequency band solutions discussed below, this distinction is superfluous and the notation is simplified by dropping the explicit ω dependence. Likewise, the absence of the (\pm) superscript denotes summation over both upward and downward propagating wavefields.

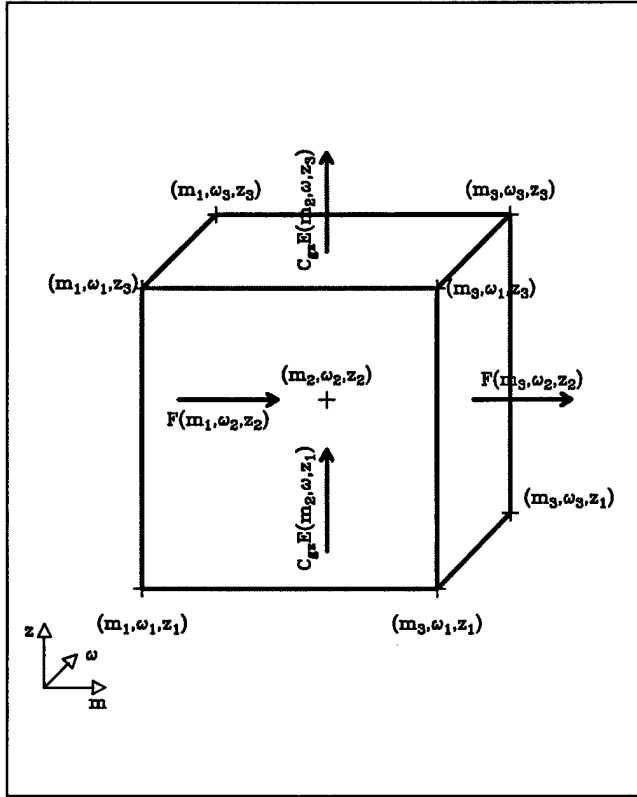


Figure 2. The energy balance for the vertical wavenumber-frequency energy density spectrum, $E(m, \omega, z)$, at vertical wavenumber m_2 , frequency ω_2 and vertical coordinate z_2 . The vertical flux of energy is $C_{gz}E$. Transports of energy to small scales are represented by F . Transports of energy in the frequency domain, G , are not depicted.

$$\begin{aligned}
 & +\Delta m \Delta \omega C_{gz}(m_2, \omega_2, z_1) E^{\pm}(m_2, \omega_2, z_1, t) / \omega_2 \\
 & -\Delta m \Delta \omega C_{gz}(m_2, \omega_2, z_3) E^{\pm}(m_2, \omega_2, z_3, t) / \omega_2 \\
 & +\Delta \omega \Delta z F^{\pm}(m_1, \omega_2, z_2, t) - \Delta \omega \Delta z F^{\pm}(m_3, \omega_2, z_2, t) \\
 & +\Delta m \Delta z G^{\pm}(m_2, \omega_1, z_2, t) - \Delta m \Delta z G^{\pm}(m_2, \omega_3, z_2, t) = 0.
 \end{aligned} \quad (1)$$

Dividing by $\Delta m \Delta \omega \Delta z$ and taking the limit as Δm , $\Delta \omega$ and Δz approach zero results in:

$$\frac{\partial [E^{\pm} / \omega]}{\partial t} \pm \frac{\partial [C_{gz} E^{\pm} / \omega]}{\partial z} + \frac{\partial F^{\pm}}{\partial m} + \frac{\partial G^{\pm}}{\partial \omega} = 0, \quad (2)$$

where C_{gz} has been assumed to be positive definite.

This equation defines the evolution of the vertical wavenumber-frequency action (and energy) density as a function of vertical coordinate and time. It has been assumed that there is no local production or dissipation of action in the volume $\Delta m \Delta \omega \Delta z$. This effectively eliminates the direct exchange of energy between upward E^+ and downward E^- propagating waves. The vertical wavenumber spectrum would seem to be ill-defined because of vertical inhomogeneity implied by

the z -dependence, but it is a well defined construct if one can invoke horizontal homogeneity and a dispersion relation. The need for a plane of statistical homogeneity currently appears to be one of the limitations of the theory. The theory, however, does not demand that the plane of homogeneity be vertical, and in that vein the description of wavefield evolution away from a planar slope is possible. But the description of the evolution of a wavefield from a point source, such as the offshore evolution of a baroclinic tide from the shelf break, is problematic.

4 Transport Models

The flux $F(m, \omega)$ represents the transfer of wave action in vertical wavenumber space associated with a variety of physical mechanisms: wave-wave interactions, buoyancy scaling, and wave-mean flow interactions. These mechanisms are dealt with successively in the following three subsections.

a. Wave-Wave Interactions

This sub-section is dedicated to defining an analytical representation for $F^{\pm}(m, \omega)$ based upon the ray-tracing model of *Henye et al.* (1986, hereafter HWF). In the context of that model, the flux may be represented as

$$F^{\pm}(m, \omega) = \left\langle \frac{E^{\pm}(m, \omega)}{\omega} \frac{d(m)}{dt} \right\rangle \quad (3)$$

with

$$\frac{dm}{dt} = -(kU_z + lV_z).$$

The factors k and l represent horizontal wavenumbers of a test wave packet with vertical wavenumber m propagating in a time dependent background having larger vertical scales and with vertical shear (U_z , V_z). The background in HWF was a stochastic representation of the GM model. HWF assume no correlation between the energy density and time rate of change of vertical wavenumber in (3), so that

$$F^{\pm}(m, \omega) = \frac{E^{\pm}(m, \omega)}{2\omega} \langle k_h \rangle S(m) C(m), \quad (4)$$

where $k_h = (k^2 + l^2)^{1/2}$ and $S(m)$ is the rms shear; $S(m)^2 = 2 \int_0^m m'^2 E_k(m') dm'$ with $E_k(m)$ the vertical wavenumber kinetic energy density spectrum. The factor $C(m)$ is expressed in HWF as $(1-r)/(1+r)$, where r is the ratio of energy flux to higher and lower vertical wavenumber. HWF use Monte-Carlo simulations to estimate $r(m_u)$, where m_u is a high wavenumber limit, beyond which internal waves are considered to break. In extrapolating their numerical results to higher values of $E(m_u)$, HWF suggest that $C(m)$ is a function

only of $S(m)$. *Polzin et al.* (1995) point out that if an inertial subrange exists, implying no convergence of energy flux in vertical wavenumber space, $\int F(m, \omega) d\omega$ is independent of m and one can solve (4) for $C(m)$ by integrating over ω and specifying $E(m)$ as the inertial subrange solution. Both HWF and *McComas and Müller* (1981b) ascribe inertial subrange behavior to the GM spectrum, so that with an m^{-2} dependence for $E(m)$, $C(m) \sim m^{1/2} \sim S(m)$, and (4) may be rewritten as

$$F^\pm(m, \omega) = AmN^{-2}\phi(\omega)E^\pm(m, \omega) \int_0^m m'^2 E(m') dm' \quad (5)$$

with $A = 0.10$ and

$$\phi(\omega) = (\omega^2 + f^2)(\omega^2 - f^2)^{1/2}/\omega^3.$$

In (5), $\phi(\omega)$ accounts for the conversion from horizontal to vertical wavenumber and conversion from shear spectral density to energy density by invoking a linear dispersion relation. The specification of $A = 0.10$ renders (5) to be consistent with *Polzin et al.* (1995).

The expression (5) was utilized by *Polzin et al.* (1995) in a model/data validation study. When evaluated at $m = m_c$, where m_c is the wavenumber at which

$$S^2(m_c) = 2 \int_0^{m_c} m'^2 E_k(m') dm' = 0.7N^2 \quad (6)$$

and with factors involving wave frequency estimated from the shear-strain ratio, (5) accurately predicts the rate of dissipation of turbulent kinetic energy ϵ to within a factor of ± 2 , the approximate statistical uncertainty of the measurements.

The transport of wave action through the frequency domain associated with wave-wave interactions is assumed to be zero,

$$G^\pm(m, \omega) = 0. \quad (7)$$

b. Buoyancy Scaling

Variable stratification adds an additional complication. WKB scaling gives the change with N of vertical wavenumber for a single internal wave as (e.g., *Leaman and Sanford*, 1975):

$$m \cong \hat{m}N(z)/\hat{N}, \quad (8)$$

where \hat{m} and \hat{N} are reference values of m and N . The change of vertical wavenumber implies a transport through the vertical wavenumber spectrum which needs to be accounted for in (2). The appropriate flux law is

$$F^\pm(m, \omega) = \frac{E^\pm(m, \omega)}{\omega} \frac{\partial m}{\partial z} \frac{\partial z}{\partial t}$$

$$= \frac{\omega^2 - f^2}{\omega^2} E^\pm(m, \omega) \frac{\partial N}{\partial z} N^{-1}. \quad (9)$$

c. Wave-Mean Flow interactions

As with buoyancy scaling, internal wave propagation in a vertically inhomogeneous sub-inertial flow implies a transport. For internal waves propagating in a geostrophic background flow, invoking the WKB approximation returns the dispersion relation

$$m \cong N(z)k_h/(\omega^2(z) - f^2)^{1/2}, \quad (10)$$

with

$$\omega(z) = \sigma - kU(z).$$

The derivation of (10) assumes the hydrostatic approximation, $\zeta/f \ll U_z/N \ll k_h N/mf \sim O(1)$, where ζ is the relative vorticity (*Polzin et al.* 1996). The transport in the wavenumber domain is given by the product of the action and the time rate of change of vertical wavenumber for a single wave group:

$$F^\pm(m, \omega) = \frac{E^\pm(m, \omega)}{\omega} \frac{\partial m}{\partial \omega} \frac{\partial \omega}{\partial U} \frac{\partial U}{\partial z} \frac{\partial z}{\partial t} = \frac{E^\pm(m, \omega)}{\omega} \frac{\partial \omega}{\partial U} \frac{\partial U}{\partial z} \quad (11)$$

The transport in the frequency domain is similarly

$$G^\pm(m, \omega) = \frac{\partial \omega}{\partial U} \frac{\partial U}{\partial z} \frac{\partial z}{\partial t} \frac{E^\pm(m, \omega)}{\omega}. \quad (12)$$

5 Approximations

It is a rather simple affair to solve the system defined by (2), (5), (7), (9), (11) and (12) numerically, at least for a steady, unidirectional wavefield. If a numerical solution was one's intent, it is possible to define a more sophisticated and potentially realistic system of equations governing the spatial evolution of the internal wavefield.

For example, the spatial evolution of a wavefield may be influenced by the potential transfer of energy from waves propagating away from a source into those propagating towards the source. A representation of such transfers is given by the elastic scattering mechanism in the formalism of *McComas and Müller* (1981a):

$$\frac{\partial E^\pm(m, \omega_1)}{\partial t} = -\frac{\pi\omega_1 m^3}{N^2} [E^\pm(m, \omega_1) - E^\mp(m, \omega_1)] \times [E^\pm(2m, \omega_2) + E^\mp(2m, \omega_2)]$$

in which the hydrostatic, non-rotating limit has been invoked and $\omega_1 > \omega_2$. Representation of such phenomena

within the eikonal framework is unclear: The transport associated with individual waves is a random variable and (5) is merely an expression for the mean transport in an isotropic wavefield. There is no guarantee that (5) is an adequate representation for evaluating the spatial evolution of an anisotropic wavefield.

The transport (5) does not appear to be a complete representation of transports even within the eikonal model. *Sun and Kunze* (1999, accepted) suggest the need to incorporate a term proportional to the vertical divergence in the evolution of the test wave vertical wavenumber (3). They also indicate a need for relatively sophisticated filtering in the wavenumber domain in order to ensure validity of the methodology. If the intent was to determine numerical solutions to (2), such additional details could be incorporated into the transport terms.

The frequency domain transports associated with wave-wave interactions has been neglected (7). This is certainly an idealization. The transports associated with the GM spectrum are to lower frequency in the weak interaction approximation and to higher frequency in the eikonal model. Not much can be done about this issue unless the equilibrium frequency spectrum is defined and a rule is developed for how quickly perturbed spectra will relax. Implementing such a scheme begs the question of which, if either, of the two models is an accurate representation of wave-wave interactions.

Rather than add such complexity, the intent here is to simplify the transport terms such that (2) can be solved analytically. At this point in time, this implies:

$$\frac{\partial E}{\partial t} = 0, \quad (13)$$

$$\int_0^m m'^2 E(m') dm' \sim m^3 E(m) \text{ and} \quad (14)$$

$$\omega = \hat{\omega} U(z) / \hat{U}, \quad (15)$$

where $\hat{\omega}$ and \hat{U} are reference values of ω and U .

The approximation (14) states that the shear variance in the wavenumber band $0 < m' < m$ is dominated by contributions at $m' \sim m$. The relation (14) is exact if $m^2 E(m)$ is independent of m , which is approximately true at high wavenumbers for the Garrett and Munk spectrum. While this represents an approximation of the transport in (5), the reader should note that the author does not attach inordinate significance to the specific functional dependence of F upon m in (5), despite apparent agreement between (5) and dissipation data in the validation study of *Polzin et al.* (1995). Roughly the same degree of agreement was found between (5) and an equivalent representation of the transport under the weak interaction approximation, with

the exception that the triad based transport estimate tended to overestimate the observed dissipation rates by a factor of 2-3. That estimate was based upon a scale argument. No numerical results exist to provide a more definitive result. It is an open question which, if either, of these two theories represents a better description of the transport.

With this question in mind, it is worth noting that the two theories share important similarities. The transport F depends upon buoyancy frequency as N^2 and is quadratically nonlinear in amplitude, $F \sim E^2$. Both theories predict faster interaction rates for higher frequency waves. Both theories suggest the GM spectrum is in equilibrium with respect to the nonlinear interactions at high wavenumber, with the implication that spectra which are perturbed from the GM specification of $E(m) \sim m^{-2}$ are relaxed back to that power law. The approximation of the shear variance in (14) retains these features common to both models and the estimate of transport at high wavenumber is not quantitatively altered if $m_c \gg m_o$.

The specification of the depth dependence of the intrinsic frequency in (15) is clearly an idealization. In the context of steady flow over topography, it describes the linear propagation of the largest scales in the problem. This approximation cannot be construed to imply linear propagation of a steady wavefield at all scales, however. Physically, (15) states that the intrinsic frequency is independent of vertical scale, which would be true if the energy appearing at small scales obtained its characteristic frequency by transport from larger scales at that depth and the transport in the frequency domain associated with wave-wave interactions was negligible. Mathematically, the approximation (15) eliminates ω as an independent variable. The parametric specification of ω in terms of $U(z)$ is accounted for by taking 'z' derivatives in the spatial flux divergence term.

Finally, (15) represents the wavefield as a narrow frequency band process. The existence of a broad-frequency band wavefield is fundamental to the triad description of wave-wave interactions and the importance of such a frequency spectrum has not been addressed within the eikonal framework. In terms of the dynamics of wave-wave interactions, it could matter greatly if the wavefield was narrow- or broad-banded. However, the problem of wave generation at the bottom boundary, be it either tidal or lee wave, characteristically involves a response at more than a single frequency (e.g., *Bell* 1975a,b). The idealization of narrow frequency band solutions is an *ad hoc* characterization of the generation process rather than an extrapolation of theoretical results for the flux representation which were based upon a broad-frequency band wavefield. The derivation

above does not exclude the possibility of a broad-band frequency wavefield.

6 A Unidirectional Solution

With the approximations given in Section (5), the wavefield evolution equation for a uni-directional (upward propagating) wavefield becomes

$$\begin{aligned} & \frac{\partial}{\partial z} \left[\left[\frac{\omega^2 - f^2}{\omega^2 m} \right] E^+(m, z) \right] \\ & + \frac{\partial}{\partial m} \left[\left[\frac{\omega^2 - f^2}{\omega^2} \frac{N_z}{N} - \frac{U_z}{U} \right] E^+(m, z) \right] + \\ & \frac{a(\omega^2 + f^2)(\omega^2 - f^2)^{1/2}}{N^2 \omega^3} m^4 E^{+2}(m, z) = 0. \end{aligned} \quad (16)$$

A solution to (16) is

$$E^+(m, z) = b^+ A^+(z) \frac{\omega^2}{\omega^2 - f^2} \alpha(m, z) \left[1 - \frac{\alpha(m, z)}{2} \right] \quad (17)$$

with

$$\begin{aligned} \alpha(m, z) &= \frac{m^2 N^2 (\omega^2 - f^2)}{m^2 N_o^2 (\omega_o^2 - f^2)}, \\ A^+(z) &= \frac{1}{1 + b^+ \int_0^z \beta(z') dz'}, \text{ and} \\ \beta(z) &= 2a N^2 \frac{\omega(\omega^2 + f^2)}{(\omega^2 - f^2)^{3/2}} \frac{(\omega_o^2 - f^2)^2}{(\omega_o^2 - f^2)^2} \frac{m^4}{N_o^4}. \end{aligned}$$

The solution is characterized by an energy containing wavenumber of $m = m_o N (\omega_o^2 - f^2)^{1/2} / N_o (\omega^2 - f^2)^{1/2}$, which varies with height in accordance with WKB scaling. The constants N_o and U_o represent the $N(0)$ and $U(0)$, respectively. The action flux associated with this solution, $\int_0^\infty C_{gz} E^+(m, z) \omega^{-1} dm$, is independent of height in the absence of wave-wave interactions [i.e., $a = 0$]. The basic character of this solution in the absence of wave-mean flow interactions is described in Polzin (1999).

7 A Bidirectional Solution

The addition of an upper boundary results in separate equations for the upward and downward propagating wavefields. These are coupled through the wave-wave interaction transports:

$$\begin{aligned} & \frac{\partial}{\partial z} \left[\left[\frac{\omega^2 - f^2}{\omega^2 m} \right] E^+(m, z) \right] \\ & + \frac{\partial}{\partial m} \left[\left[\frac{\omega^2 - f^2}{\omega^2} \frac{N_z}{N} - \frac{U_z}{U} \right] E^+(m, z) \right] \\ & + \frac{a(\omega^2 + f^2)(\omega^2 - f^2)^{1/2}}{N^2 \omega^3} m^4 E^+(m, z) \\ & \times [E^+(m, z) + E^-(m, z)] = 0. \end{aligned}$$

and

$$\begin{aligned} & \frac{\partial}{\partial z} \left[\left[\frac{\omega^2 - f^2}{\omega^2 m} \right] E^-(m, z) \right] \\ & + \frac{\partial}{\partial m} \left[\left[\frac{\omega^2 - f^2}{\omega^2} \frac{N_z}{N} - \frac{U_z}{U} \right] E^-(m, z) \right] \\ & + \frac{a(\omega^2 + f^2)(\omega^2 - f^2)^{1/2}}{N^2 \omega^3} m^4 E^-(m, z) \\ & \times [E^+(m, z) + E^-(m, z)] = 0. \end{aligned} \quad (18)$$

A solution can be found by specifying

$$E^+(m, z) = b^+ A^+(z) \frac{\omega^2}{\omega^2 - f^2} \alpha(m, z) \left[1 - \frac{\alpha(m, z)}{2} \right] \text{ and}$$

$E^-(m, z) = b^- A^-(z) \frac{\omega^2}{\omega^2 - f^2} \alpha(m, z) \left[1 - \frac{\alpha(m, z)}{2} \right]$, which reduces (18) to a system of ordinary differential equations,

$$b^+ A_z^+ + \beta(z) A^+ b^+ (A^+ b^+ + A^- b^-) = 0 \text{ and}$$

$$b^- A_z^- - \beta(z) A^- b^- (A^+ b^+ + A^- b^-) = 0. \quad (19)$$

The boundary conditions are applied to the difference between the upward and downward propagating spectra. Application of the boundary conditions is simplified by expressing (19) in terms of the sum ($S = A^+ b^+ + A^- b^-$) and difference ($D = A^+ b^+ - A^- b^-$) amplitude functions. The corresponding coupled equations are

$$\begin{aligned} S_z + \beta(z) S D &= 0 \text{ and} \\ D_z + \beta(z) S^2 &= 0. \end{aligned} \quad (20)$$

The non-constant coefficient $\beta(z)$ can be eliminated by defining a stretched coordinate $q(z) = \int_0^z \beta(z') dz'$. The resulting sum and difference equations can be combined to obtain a second order nonlinear equation for D:

$$D_{qq} + 2DD_q = 0. \quad (21)$$

This equation can be solved by noting that (i) it is "exact", and integration returns a Ricatti equation, (ii) the Ricatti equation can be transformed into a Bernoulli equation with the substitution $D(q) = D_2(q) + \gamma_1$, where γ_1 is a constant, and (iii) transforming the Bernoulli equation for $D_2(q)$ into a first order, linear equation (e.g., Bender and Orszag 1978). After application of the upper boundary condition that $D(q = q_H = \int_0^H \beta(z') dz') = 0$ [i.e., perfect reflection at the upper boundary],

$$D(q) = -\gamma \tan[\gamma(q - q_H)], \text{ and}$$

$$S(q) = \gamma / \cos[\gamma(q - q_H)]. \quad (22)$$

The coefficient γ is then determined by equating the difference spectrum with a source spectrum at the bottom boundary.

8 Bottom Boundary Condition

The bottom boundary condition is viewed here to be set by the process of quasi-steady lee-wave generation. The scales of interest are typically small. A vertically propagating response is obtained only for intrinsic frequencies $f < kU < N$, implying horizontal wavelengths $2\pi U/N < \lambda_h < 2\pi U/f$, or 600-6000 m for $U = 0.1 \text{ m s}^{-1}$, $f = 1 \times 10^{-4} \text{ s}^{-1}$, and $N = 1 \times 10^{-3} \text{ s}^{-1}$. Faulting and volcanism at mid-ocean ridge crests are the dominant sources of seafloor roughness having these scales. This roughness has been characterized in terms of a 2-D, anisotropic spectral representation, $H(k, l)$ (Goff and Jordon 1988). Extant models of quasi-steady lee-wave generation (e.g., Bretherton 1969) can then be used with such 2-D representations of seafloor topography to define the vertical wavenumber, intrinsic frequency domain wave response, which can then be mapped onto the interior solution. This mapping process is not straightforward, as the solutions to the wave generation problem may not be expressible in terms of the solution to the nonlinear wave evolution equation. This relationship will be described in detail at a later time.

For now, however, it suffices to note the following: First, the internal wave dispersion relation is $m = k_h(N^2 - \omega^2)^{1/2}/(\omega^2 - f^2)^{1/2}$. In the case of steady flow normally incident upon bathymetry, $\omega = -kU$, $k_h = k$, and the dispersion relation in the hydrostatic, non-rotating limit reduces to $m = N/U$. The internal wave response will exhibit a well defined peak at $m = N/U$ under these conditions. An increased response at slightly higher vertical wavenumber is anticipated with the addition of rotation and non-normal incidence. Second, for flow normally incident upon 1-D topography, the vertical flux of energy associated with the internal wavefield is

$$E_{flux} = \frac{2U(0)}{\pi} \int_{f/U(0)}^{N(0)/U(0)} [N(0)^2 - k^2 U(0)^2]^{1/2} \times [k^2 U(0)^2 - f^2]^{1/2} H(k) dk \quad (23)$$

(e.g., Bell 1975a). The amplitude of the solution to the wavefield evolution equation can then be defined by equating E_{flux} with the vertical energy flux of the wavefield at the bottom boundary,

$$\int_{m_o/\sqrt{2}}^{\infty} C_{gz} [E^+(m, 0) - E^-(m, z)] dm = D(0) \frac{\omega_o}{2} = E_{flux} \quad (24)$$

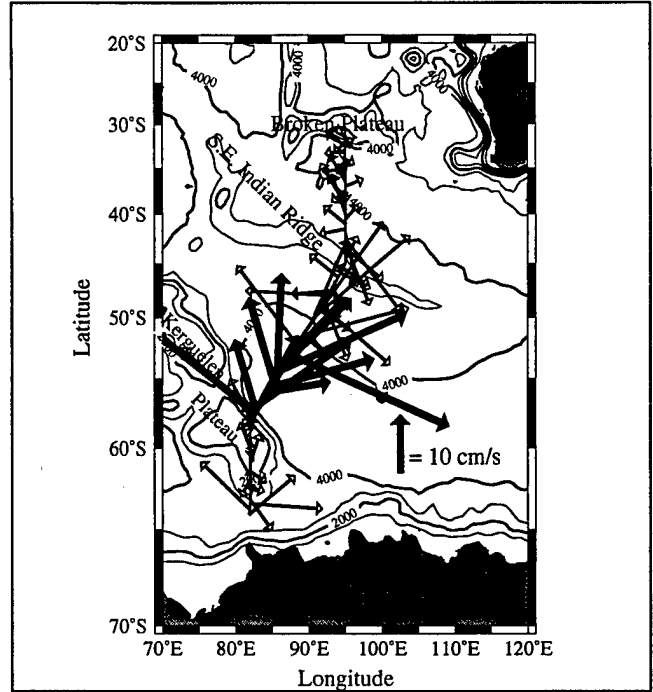


Figure 3. Bathymetry and depth-averaged current vectors along the I8S section line. The analysis focuses upon a group of 12 profiles centered about 55° S. These stations are denoted with bold current vectors. The bathymetric contour interval is 1000 m, with thick contours every 2000 m.

9 Comparison

Numerous full-water-depth, lowered ADCP (LADCP) profiles of relative velocity have been collected coincident with CTD profiles along WOCE hydrographic lines. The velocity profiles, in principle, resolve oceanic currents having vertical wavelengths from full water depth down to about 50 m (Kunze *et al.* in preparation), and the barotropic component can be estimated by a method similar to utilized with shipboard Dopplers (Fischer and Visbeck, 1993). These data afford the opportunity to investigate the spatial characteristics of the finescale internal wavefield and groundtruth the theoretical development presented in the previous sections. Application of finescale parameterizations permits corresponding estimates of the turbulent dissipation rate (ϵ) and diapycnal eddy diffusivity (K_ρ).

Finestructure estimates were made with data from the I8S hydrographic section, Figure 3. The section extends from 30° S, 90° E on the Broken Plateau, across the SE Indian Ridge to 64° S, 82° E, south of the Kerguelen Plateau. This section cuts across the Antarctic Circumpolar Current (ACC) in a region of particularly strong eddy energy and topographic influence. A group of 12 stations centered about 55° S is examined. Further discussion of the data appears in Polzin and Firing

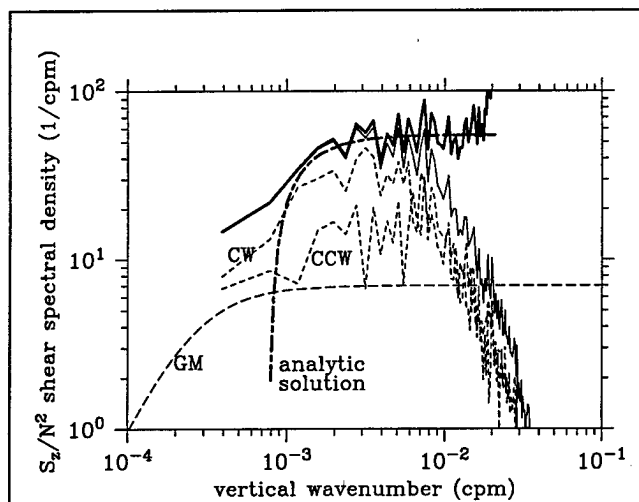


Figure 4. Buoyancy frequency normalized shear spectra. The thin solid line represents the observed LADCP spectrum from depths of 1000–3560 m. The thin, short-dashed lines are the rotary (CW and CCW) components. The thick solid line depicts the LADCP shear spectrum after correction for the effects of spatial averaging. The GM spectrum is represented by the thin, long-dashed line. The thick, long-dashed line is the analytical solution.

(1997).

Shear spectra from 55°S differ markedly from the background GM internal wavefield, Figure 4. Mid-depth shear spectra reveal (i) significantly larger high wavenumber spectral levels, (ii) excess clockwise (CW) versus counter-clockwise (CCW) phase rotation with depth, and (iii) a low wavenumber roll-off at smaller vertical wavelengths than the GM model. Mid-depth (1000–3500 m) spectral levels are 7–8 times larger than GM for vertical wavelengths 1000 < λ_v < 100 m. The GM model is vertically isotropic, implying no net vertical energy flux. The observed enhancement of CW phase rotation with depth implies an excess of upward energy propagation in the southern hemisphere for near-inertial internal waves (Leaman and Sanford, 1975). The GM shear spectrum is characterized by an increasing spectral level for vertical wavelengths larger than mode 3 and is independent of vertical wavelength at smaller scales. Buoyancy scaling and the observed N^2 profile imply mode 3 is equivalent to a vertical wavelength of 4000 m over the depth range in question. In contrast, the observed spectrum is bandwidth limited to vertical wavelengths smaller than 1000 m.

Estimates of turbulent dissipation and diffusivity were made with the finestructure data using (5) following the method outlined in Polzin *et al.*, 1995. In this observational approach, turbulent production is equated with the spectral energy transport at high ver-

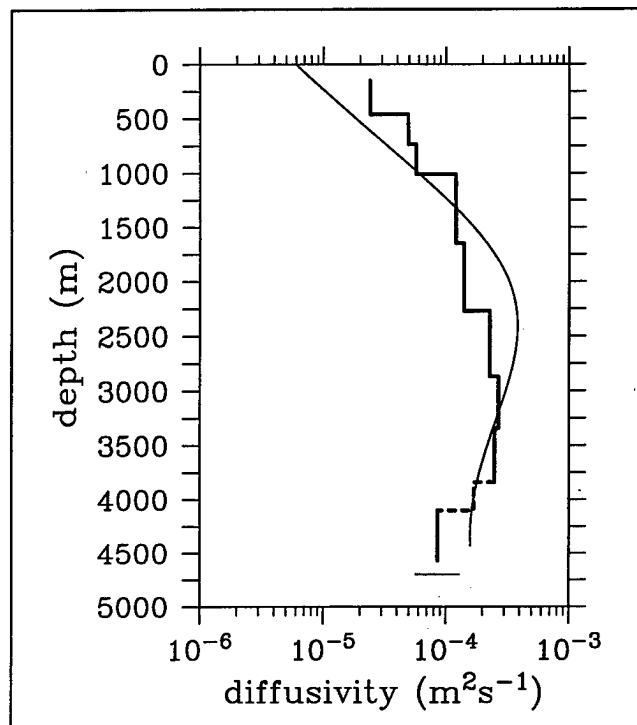


Figure 5. Vertical profiles of finestructure derived (thick) and theoretical (thin) diffusivity. The dashed line represents a region where no data are available and the diffusivity estimate has been interpolated. The thin horizontal line at the bottom of the finestructure profile represents the average bottom depth. No data are available in the bottom most 130 m of each profile. Finestructure based diffusivity estimates were calculated in a height above bottom coordinate system in the deepest 1400 m.

tical wavenumber,

$$\epsilon = (1 - R_f)F(m_c) \text{ and } K_p = R_f F(m_c)/N^2, \quad (25)$$

where $R_f \sim 0.2$ is the flux Richardson number which expresses the partitioning of turbulent production into potential energy fluxes and dissipation. Below 1000 m depth, the average diapycnal eddy diffusivity is $2 \times 10^{-4} \text{ m}^2 \text{ s}^{-1}$, 20 times larger than that for a GM wavefield, Figure 5. Shear spectral levels and diffusivity estimates decay towards GM levels above 1000 m. The heightened diffusivity corresponds to shear spectral levels a factor of 5–8 above GM. The enhanced spectral levels, excess of CW variance and heightened levels of turbulent mixing inferred from (25) are interpreted as the product of quasi-steady internal lee wave generation associated with the flow of large depth-averaged velocities over rough bathymetry and the consequent breaking of the waves as they propagate away from the bottom boundary.

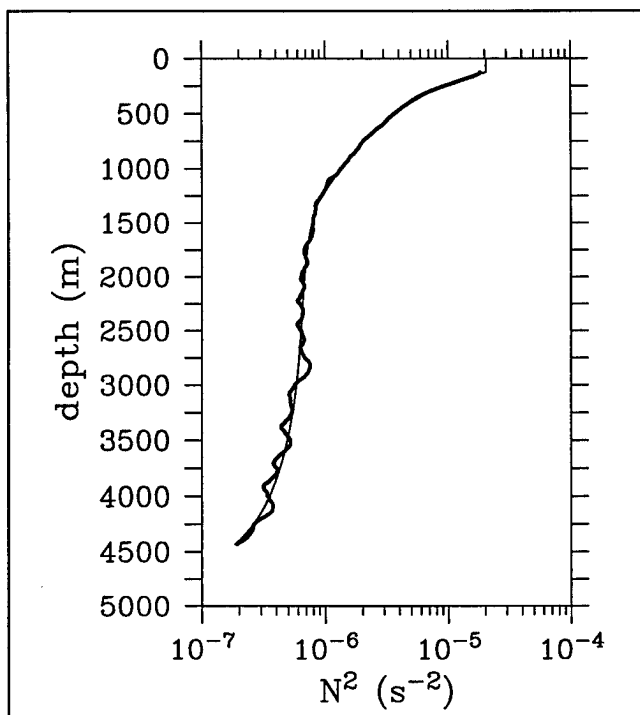


Figure 6. Vertical profile of N^2 defined as an average over the group of twelve stations. The thin line represents a polynomial fit and is used in the theoretical analysis.

Vertical variability in turbulent production associated with wave breaking is defined by the competing and coupled effects of propagation in an inhomogeneous environment and nonlinear transports. Solutions to the wavefield evolution equation detailed above suggest that profiles of turbulent quantities can be estimated once a buoyancy profile $N(z)$, a velocity profile $U(z)$, and bottom boundary conditions on the energy containing scale m_o , intrinsic frequency ω_o , and vertical flux of energy associated with the generation process, E_{flux} , are specified. The velocity and buoyancy profiles are obtained by averaging the station data and fitting with low order polynomials, Figure 6 and 7. The latter three constants represent the output of a generation model. These constants depend quantitatively upon issues such as whether the bathymetry is characterized as either 1- or 2-D and the direction of the background current relative to the orientation of the bathymetry. Defining an adequate generation model to deal with such complexities and producing an entirely theoretical estimate for the diffusivity profile will be addressed at a later date. Here it is simply noted that a qualitatively robust feature of wave generation by steady flow over bathymetry represented by a red spectrum is a dominant response at a vertical scale slightly smaller than U/N . Given the smoothed velocity and buoyancy profiles, the model parameter m_o

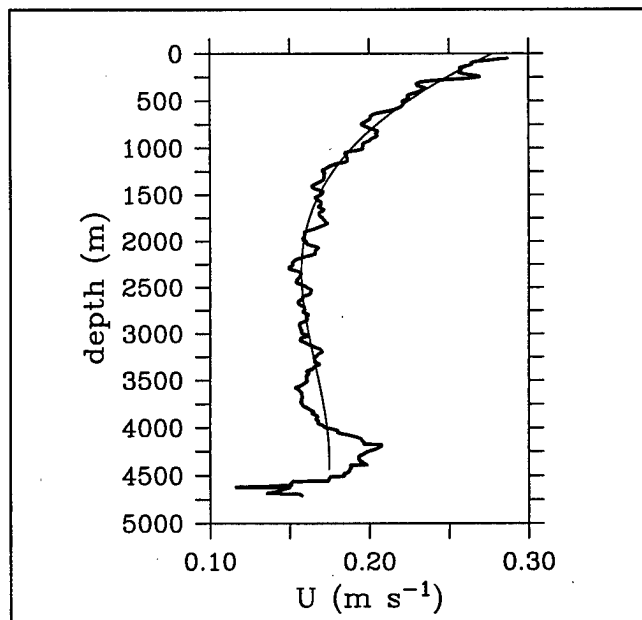


Figure 7. Vertical profile of horizontal velocity U averaged over the group of twelve stations. The thin line represents a polynomial fit and is used in the theoretical analysis. The velocity data were analyzed in a depth coordinate system. The bottom ($z = 0$) is defined as the greatest depth for which data are available for eleven of the twelve stations.

is identified as $m_o = \frac{N}{U}(\omega_o^2 - f^2)^{1/2} = 0.0011$ cpm, with $\omega_o = 1.5f$, from a fit to the observed mid-depth shear spectrum, Figure 4. The amplitude is set here by specifying the net vertical flux of energy at the bottom boundary as being proportional to the depth integrated dissipation rate inferred from the observed finestructure, $E_{flux} = (3 \text{ mW/m}^2)/\rho$. This value for the energy flux is somewhat smaller than would be anticipated on the basis of flow normally incident upon 1-D topography (23), where the bathymetric spectrum is prescribed in terms of a 1-D representation of the 2-D model spectrum proposed by Goff and Jordan (1988): $H(k) \propto 1/(k_0^2 + k^2)^{-\nu}$. Appropriate values for the South East Indian Ridge crest at 100° E are $k_0 = 0.002 \text{ m}^{-1}$ and rms height of 60 m (Goff et al. 1997) with $\nu = 1.45$ (John Goff, personal communication 1999). With a value of $\nu = 1.5$, (23) returns an estimate of $E_{flux} = (11 \text{ mW/m}^2)/\rho$. While there may be some spatial variability in the spectral parameters and uncertainty in the adequacy of the generation model, it is reassuring that the theoretical estimate of E_{flux} is much larger than that identified from the finescale observations.

After applying the bottom boundary condition to determine the constant γ , the theoretical estimate of the diffusivity profile is simply

$$K(z) = \lim_{m \rightarrow \infty} \frac{R_f \omega F(m, z)}{N^2} \quad (26)$$

The degree of agreement with the diffusivity profile inferred from the finestructure estimates is amazing, Figure 5.

10 Summary

The ultimate goal of this research is the specification of turbulent flux profiles in terms of limited inputs: a background velocity profile, a buoyancy profile and a spectrum of bottom topography. This problem has been reduced here to the specification of three constants: an energy containing scale, a frequency, and an energy flux. Future work will focus on an entirely theoretical prescription for these constants.

Acknowledgments. The LADCP data were obtained by Eric Firing. His interest in this finestructure analysis is appreciated. Financial support from the National Science Foundation (Grant No. OCE94-15589) and the Office of Naval Research (grant No. N00014097-1-0087) is gratefully acknowledged.

References

- Baines, P., 1982: On internal tide generation models. *Deep-Sea Res.*, **29**, 307-338.
- Bell, T. H., 1975a: Topographically-generated internal waves in the open ocean. *J. Geophys. Res.*, **80**, 320-327.
- Bell, T. H. 1975b: Lee waves in stratified flows with simple harmonic time dependence. *J. Fluid Mech.*, **67**, 705-722.
- Bender, C. M. and S. A. Orzag: *Advanced Mathematical Methods for Scientists and Engineers*. McGraw-Hill, New York, 593 pp.
- Bretherton F. P., 1966: The propagation of groups of internal gravity waves in a shear flow. *Quart. J. R. Met. Soc.*, **92**, 466-480.
- Bretherton F. P., 1969: Momentum transport by gravity waves. *Q. J. R. Meteorol. Soc.*, Ser. A **302**, 529-554.
- Bretherton, F. P. and C. J. R. Garrett, 1968: Wavetrains in inhomogeneous moving media. *Proc. Roy. Soc.*, **A. 320**, 529-554.
- Cairns, J. L., and G. O. Williams, 1976: Internal wave observations from a midwater float, 2. *J. Geophys. Res.*, **81**, 1943-1950.
- Fischer, J. and M. Visbeck, 1993: Deep velocity profiling with self-contained ADCPs. *J. Atmos. Oceanic Tech.*, **10**, 765-773.
- Garrett, C. J. R., 1968: On the interaction between internal gravity waves and a shear flow. *J. Fluid Mech.*, **34**, 711-720.
- Garrett, C. J. R., and W. H. Munk, 1975: Space-time scales of internal waves: A progress report. *J. Geophys. Res.*, **80**, 291-297.
- Goff, J. A., Y. Ma, A. Shah, J. R. Cochran, and J-C. Semper, 1997: Stochastic analysis of seafloor morphology on the flank of the Southeast Indian Ridge: The influence of ridge morphology on the formation of abyssal hills. *J. Geophys. Res.*, **102**, 15521-15534.
- Goff, J. A. and T. H. Jordan, 1988: Stochastic modeling of seafloor morphology: Inversion of Sea Beam data for second-order statistics, *J. Geophys. Res.*, **93**, 13589-13608.
- Gregg, M. C., 1987: Diapycnal mixing in the thermocline: A review. *J. Geophys. Res.*, **92**, 5249-5286.
- Gregg, M. C., 1989: Scaling turbulent dissipation in the thermocline. *J. Geophys. Res.*, **94**, 9686-9698.
- Heney, F. S., J. Wright and S. M. Flatte, 1986: Energy and action flow through the internal wave field: An eikonal approach. *J. Geophys. Res.*, **91**, 8487-8495.
- Hogg, N., P. Biscaye, W. Gardner and W. J. Schmitz Jr., 1982: On the transport and modification of Antarctic Bottom Water in the Vema Channel. *J. Mar. Res.*, **40**, (Suppl.), 231-263.
- Jones, W. L., 1967: Propagation of internal gravity waves in fluids with shear and rotation. *J. Fluid Mech.*, **30**, 439-448.
- Kunze, E., and T. B. Sanford, 1996: Abyssal mixing. Where it isn't. *J. Phys. Oceanogr.*, **26**, 2286-2296.
- Kunze, E., K. Polzin, J. Hummon and E. Firing: Comparison of lowered ADCP and XCP velocity profiles. in preparation.
- Leaman, K. D., and T. B. Sanford, 1975. Vertical energy propagation of inertial waves: A vector spectral analysis of velocity profiles, *J. Geophys. Res.*, **80**, 1975-1978.
- Ledwell, J. R., A. J. Watson and C.S. Law, 1993: Evidence of slow mixing across the pycnocline from an open-ocean tracer-release experiment. *Nature*, **364**, 701-703.
- Ledwell, J. R., K. L. Polzin, L. C. St. Laurent, R. W. Schmitt and J. M. Toole, 1999: Mixing over rough topography in the Brazil Basin. submitted to *Science*.
- McComas, C. H., and P. Müller, 1981a. Time scales of resonant interactions among oceanic internal waves, *J. Phys. Oceanogr.*, **11**, 139-147.
- McComas, C. H., and P. Müller, 1981b. The dynamic balance of internal waves, *J. Phys. Oceanogr.*, **11**, 970-986.
- Müller, P., and N. Xu, 1992: Scattering of oceanic internal gravity waves off random bottom topography. *J. Phys. Oceanogr.*, **22**, 474-488.

- Munk, W., 1966. Abyssal recipes, *Deep-Sea Res.*, **13**, 707-730.
- Polzin, K. L., 1996: Statistics of the Richardson Number: Mixing models and Finestructure. *J. Phys. Oceanogr.*, **26**, 1409-1425.
- Polzin, K. L., 1999: Inertial subrange solutions for the energy balance of the finescale internal wavefield. submitted.
- Polzin, K. L., J. M. Toole and R. W. Schmitt, 1995: Finescale parameterizations of turbulent dissipation. *J. Phys. Oceanogr.*, **25**, 306-328.
- Polzin, K. L., N. S. Oakey, J. M. Toole and R. W. Schmitt, 1996: Fine- and micro-structure characteristics across the Northwest Atlantic Subtropical front. *J. Geophys. Res.*, **101**, 14,111-14,124.
- Polzin, K. L., J. M. Toole, J. R. Ledwell and R. W. Schmitt, 1997: Spatial variability of turbulent mixing in the abyssal ocean. *Science*, **276**, 93-96.
- Polzin, K. L. and E. Firing, 1997: Estimates of diapycnal mixing using LADCP and CTD data from I8S. *WOCE International Newsletter*, **29**, 39-42.
- Sun, H. and E. Kunze, 1999: Internal wave/wave interactions: Part I. The role of internal wave vertical divergence. *J. Phys. Oceanogr.*, accepted.
- Toole, J. M., K. L. Polzin, R. W. Schmitt, 1994a: Estimates of diapycnal mixing in the abyssal ocean. *Science*, **264**, 1120-1123.
- Wyrtki, K., 1961. The thermohaline circulation in relation to the general circulation in the oceans, *Deep-Sea Res.*, 39-64.

75 + 25 = 99±1, or Some of What we Still Don't Know: Wave Groups and Boundary Processes

S.A.Thorpe

School of Ocean and Earth Science, Southampton Oceanography Centre, European Way, Southampton, SO14 3ZH, UK

Abstract. The intermittent generation of internal waves at ocean boundaries, the air-sea interface or benthic topography, leads to the formation of packets or *groups* of internal waves which, in the deep ocean, are then prevalent in the vicinity of the generation sites, if not throughout the water column. A consequence is that wave breaking, either of the groups themselves or that induced by their presence as they travel through the background wave field, has structure and periodicity depending on the properties of the wave groups. Wave breaking in downward travelling groups of frequency $2^{1/2} f/[1+(f/N)^2]^{1/2}$ may lead to the generation of waves of the same period, but travelling upwards. The reflection and dissipation of internal waves at topography leads to a variety of processes. Amongst these is the generation of alongslope currents which, because of the sporadic temporal and spatial momentum transfer produced by the breaking of the incident waves, results in regions of convergence in the benthic boundary layer, flow ejection from the boundary layer, and possibly the formation of vortical modes communicating into the ocean interior.

1. Prologue

It is probably a mistake to look back at one's past papers or to add up the years. Time is rarely kind. The ideas in the papers are often naive, plain wrong or, to be milder, misguided, and sums are prone to be incorrect too! Whilst the former may not be too great a fault provided that the work eventually had the result of stimulating a quest for further knowledge, the arithmetic may, at least, be a cause of uncertainty and confusion; after all, the paper in question (Thorpe, 1975) was actually given at an AGU meeting 1974, not 1975, and the present document is being prepared in 1998, not 1999, the year of the present Aha Huliko'a Winter Workshop.

The work referred to above and written *about* a quarter of a century ago, is a review of what was I thought was then known of the excitation, dissipation, and interaction of internal waves in the deep ocean. Garrett said that it would have been enough if I had just presented the cartoon (Thorpe, 1975, fig.5) showing the processes affecting internal waves. As usual, Chris was quite right; this is the only part of my paper which others have found worthy of recall and criticism (e.g., LeBlond and Mysak, 1980, use it as figure 53.6 in their text book but they make the fish, my obviously ambiguous symbol of the ocean, generate internal waves! Perhaps it is their proxy for what was once described as a 'cigar-shaped body'? Walter Munk complains that although there is a Sun, there is no Moon and the tides are consequently under-represented.)

One element which seems to be right about the cartoon is that it implicitly suggests that internal waves are inter-

mittent in space and time. Their breaking and association with mixing is explicit, although here still lies the uncertainty of how waves break. What is most obviously missing is the importance of processes at sloping ocean boundaries. (Lee wave generation by flow over topography is represented, but nothing more.) This is a serious omission in view of recent observations of high dissipation and mixing near rough topography (Polzin *et al.*, 1997; Toole *et al.*, 1997). In a belated attempt to correct matters, Figure 1 shows some of the wave-related processes now recognised as occurring on slopes.

Moving from the top left to right these are (i) lee wave generation by flow over topography (e.g., Bell, 1975; Thorpe, 1996), (ii) wave generation by oscillatory flow, particularly those of tidal period at or near the shelf break or where the slope and stratification lead to critical conditions (e.g., Baines, 1974, 1982; New, 1988), (iii) resonant interaction between incident and reflected waves (Thorpe, 1987, 1997), (iv) wave breaking when the incident wave is at or near critical (e.g., Eriksen, 1982, 1985, 1998; Ivey and Nokes, 1989; Taylor, 1993). The second row, left to right shows (v) wave steepening and the formation of fronts on reflection (e.g., Thorpe, 1992, 1999a; Slinn and Riley, 1998), (vi) the generation of upslope Eulerian flows, V_E , and along-slope Lagrangian flows, U_L , as waves reflect (Thorpe, 1987, 1997, 1999b), and (vii) mixing produced by reflecting subcritical waves when the first harmonic is near critical (Thorpe, 1999a). The final illustration, bottom left, represents along-slope Eulerian flows, U_E , generated by waves which break and loose

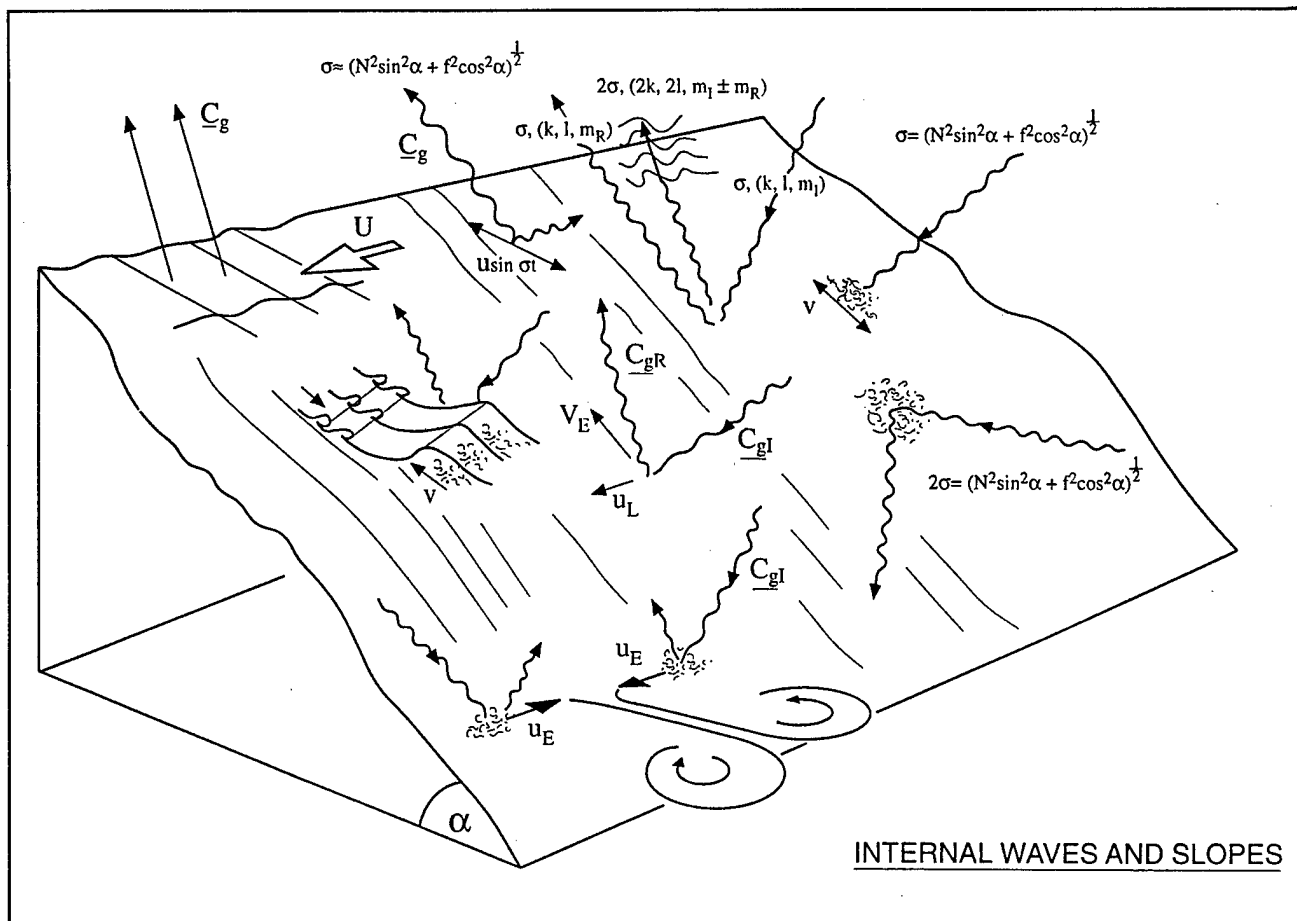


Figure 1 Physical processes involving the interaction of internal waves on sloping topography.

momentum at the boundary (Dunkerton *et al.*, 1998; Thorpe, 1999c; Slinn, 1999). Since the wave field is irregular and intermittent, waves will approach the boundary from different directions and break sporadically, leading to convergence at the boundary and the ejection of mixed fluid, and possibly the formation of vortical modes (Müller *et al.*, 1986) as illustrated. These processes are poorly known, and as the dates of references imply, are a subject of current research.

My 1975 review began by saying that we have very little knowledge about which physical processes are most important in controlling internal gravity waves in the deep ocean. It remarks that "The complexity of three-dimensional propagation in a medium which is itself moving in the mean at speeds" which vary in the vertical by amounts "which are comparable to the speed of the waves, the uncertainty of the processes which dominate generation and dissipation, and the changes which the

waves themselves make to the mean density structure of the medium—all these contrive to make this problem far more difficult than that of surface waves." (I was even then seeking to learn about internal waves by thinking of the properties and characteristics of their surface equivalents, and I shall follow this methodology in the section which follows.) Peter Müller's generous invitation to this workshop refers to modeling, "... to what extent we understand and are able to model the observed internal wave field." I don't know about modeling but am interested in "the internal wave field" and its appropriate representation, particularly near generation sites. This is related to the question "How does diapycnal mixing occur in the ocean?" Representing mixing in models in an appropriate way, one which is responsive to physical, temporal and spatial variation (and possibly also to the nature of the quantity being transferred by the mixing) does seem to be important.

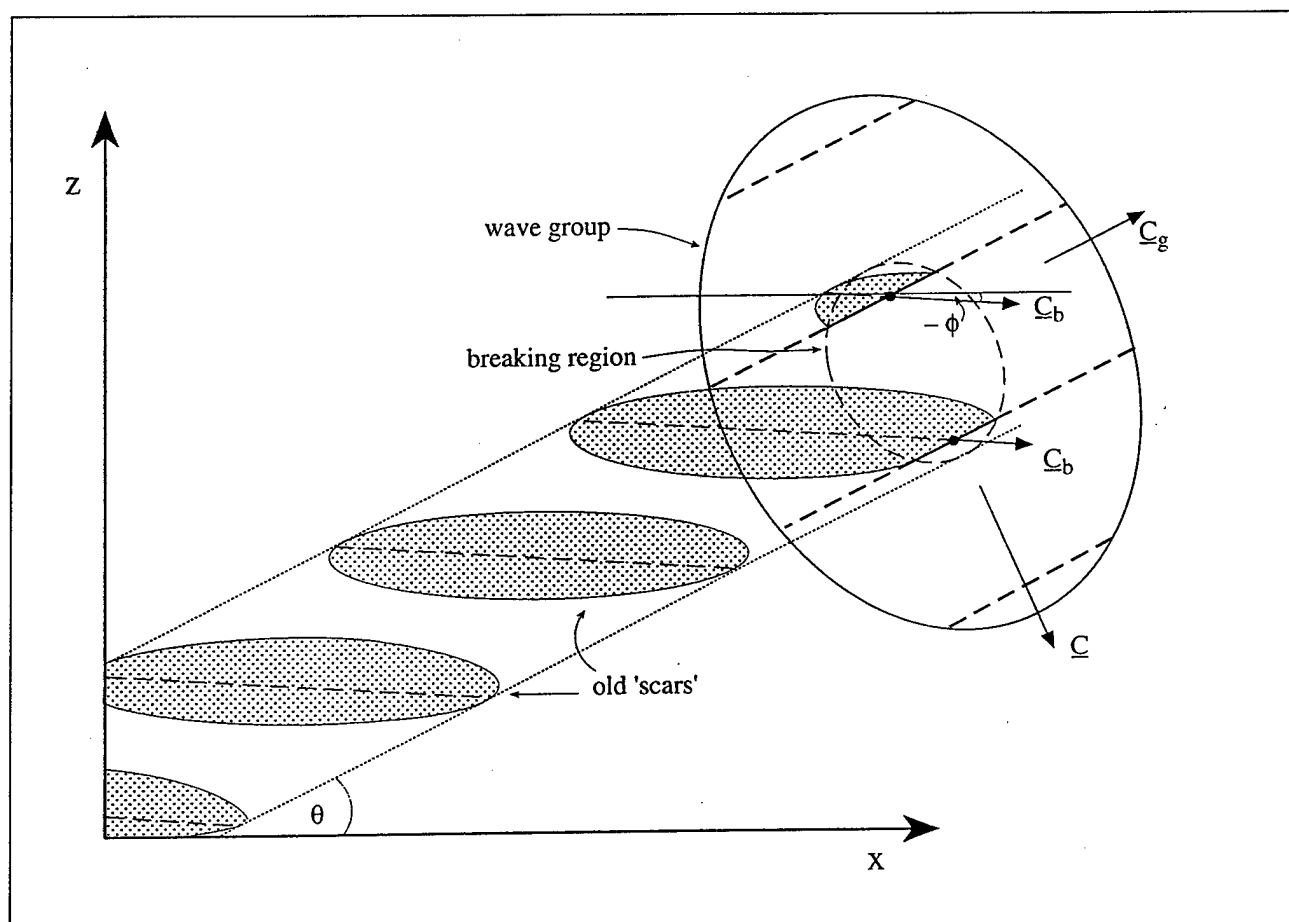


Figure 2 A wave group, the dashed constant phase lines within the solid-line contour, propagating with velocity c_g , at an angle θ to the horizontal x axis. The wave phase advances in direction c . Waves break (where constant phase lines are solid) within the breaking region moving with the group, producing scars (stippled). Breaking regions advance in direction c_b , inclined to the horizontal at angle ϕ . Here the stippled regions do not overlap; conditions for (2) are not satisfied.

2. Internal wave groups and turbulent patches

It is evident to anyone who watches surface gravity waves breaking in deep water that often breaking is repeated after a short interval of time in almost the same location, but slightly ahead (in the direction of wave propagation) of the first breaker. The explanation of this was given by *Donelan et al.* (1973); it is because of the tendency for waves to travel in groups. The group velocity is in the same direction as the phase speed, but is only half its size, and in consequence waves advance through a wave group at a speed which, in relation to the group, is half their phase speed. The time required for a wave to reach the location within its group at which its predecessor, one wavelength ahead, began to break, is therefore twice the wave period. This is the time interval between breaking or, by just the same argument, the time interval between waves reaching a position in a wave group where the wave properties (e.g., wave height or the currents they

produce) may reach some particular, or "critical," value; it is the period between "extreme events." The locations at which breaking first occurs as waves break are separated by one wavelength (the first wave breaks one wavelength ahead of the second wave which then travels forward two wavelengths in the two wave periods before it begins to break). It may be that the way in which the wind forces the waves has something to do with the development of wave groups and their breaking, rather than an instability of a periodic wave train in which the wind plays no part, but there is (surprisingly) no theory of wave generation which takes due regards of the presence, shape, and properties of wave groups. Particularly large waves are, however, known to develop when the wind speed happens to be in the same direction and to correspond roughly to the group speed of pre-existing swell (e.g., winds in m/s of about $0.78T$, where T is the swell period in s), conditions in which energy can be fed continuously into the wave

field from the wind. Rather little is known of the lifetime of wave groups, but it is possible that groups have properties which make them more robust than are waves in a uniform wave train—which are subject to instability (e.g., the Benjamin-Feir instability, *Benjamin*, 1967).

As we have seen, the presence of wave groups on the sea surface impresses particular properties on the location and periodicity of breakers. If breaking continues for more than one wave period, regions in which the waves have broken, producing patches of turbulence and the clouds of bubbles, will overlap in space; the breakers will produce an extended area of turbulent water at the sea surface, although within the area the intensity of turbulence will vary according to the variation of the rate of energy dissipation during the course of wave breaking. There will however be gaps in time between successive breakers unless the duration of breaking, τ , exceeds $2T$, the interval between the onset of breaking in successive waves. The detection by photography of breaking in a wave group or as groups pass fixed measurement points therefore depends on the ratio, τ/T . (In practice, the duration of wave breaking is generally less than T , and bubble clouds from successive breakers are separate in both time and space; e.g., see *Thorpe and Hall*, 1983). Breaking, once initiated in a surface gravity wave, may spread laterally along its crest, but the main direction of advance is in the direction of the phase and group velocity, which of course are the same.

A natural question to ask is whether internal waves may also have group-like structure which dictates the properties of their breaking. There is plentiful evidence that groups of internal waves exist, at least at near-inertial frequencies where the waves are most energetic and, perhaps because the signal is strongest, groups are often evident (e.g., see *Leaman and Sanford*, 1975; *Pinkel*, 1983). Spring-neap modulations in internal tidal waves found at a distance from the wave source may also imply a group-like structure. Recent careful analysis by *Alford and Pinkel* (1999) demonstrates the existence of groups of relatively high frequency internal waves and associated instability or wave breaking. The intermittent nature of wave forcing at the surface or by topography points to the generation of wave packets rather than 'uniform trains'. Indeed the known instability of wave trains (e.g., *Borisenko et al.*, 1976; *Thorpe*, 1977) dictates that waves will not be regular. Can more be inferred about the nature or distribution of turbulent regions produced by internal waves breaking in groups from what is known of surface wave breaking?

For internal waves in the deep near-uniformly stratified ocean, the phase, c , and group, c_g , velocities are at right angles. The time interval between 'breaking' in wave

groups (or between the reoccurrence of extreme events, which for internal waves may be large amplitude, large amplitude, large current shear, high strain, low Richardson number, high wave steepness, etc.) is the wave period (*Thorpe*, 1988). The direction in which the "breaking" develops (the direction in which the centre of a patch advances) is given by $c_b = c_g + c$ (Fig. 2). If θ is the inclination of the group velocity vector to the horizontal, then the inclination of the breaking zone is approximately given by

$$\tan \phi = -(f/N)^2 \cot \theta. \quad (1)$$

As in the case of surface waves, the properties of the patches of water, or "scars," produced by a group of breaking waves depends on the ratio of the time of duration of breaking (or how long a period of time an extreme value is exceeded), τ , and the wave period T (*Thorpe*, 1999d). The ability of different sampling methods to detect mixing is related to the extent of these patches, whether there are gaps left between them in the horizontal (which will affect whether they are sampled by vertical profiles) or in the vertical (for, say towed arrays). Scars will overlap in space if

$$\tau/T > (\tau/T)_c = (c_g/c) A/B \quad (2)$$

where $(\tau/T)_c$ is a critical value, and A/B is the aspect ratio of the region (here assumed elliptical) within a wave group in which 'breaking' occurs, the ratio of the length parallel to the group velocity, A , divided by that in the direction of the phase vector, B . Estimates of A/B from oceanic observations are at best approximate. It appears probable however that whilst inertial waves, and internal tides generated at the shelf break, will be quite effective in producing connected scars or 'breaking' patches if the criterion for 'breaking' is exceeded somewhere in the group, since the critical value is small, internal lee waves have high critical values and are less likely to promote connected patches of, say, mixed fluid even if breaking occurs within a wave group (*Thorpe*, 1999d).

The scars left by a wave group of one frequency may have the same inclination to the horizontal as the wave group vector of another wave frequency, i.e., using (1), there may exist waves which have group inclination β such that $\tan \beta = -(f/N)^2 \cot \theta$. In this case the scars could be misinterpreted in observations as being group of waves of a different frequency. The relation between the apparent frequency, σ_A , and the true frequency of the wave group producing the scars is found using the dispersion relation $\sigma^2 = N^2 \sin^2 \theta + f^2 \cos^2 \theta$, and is

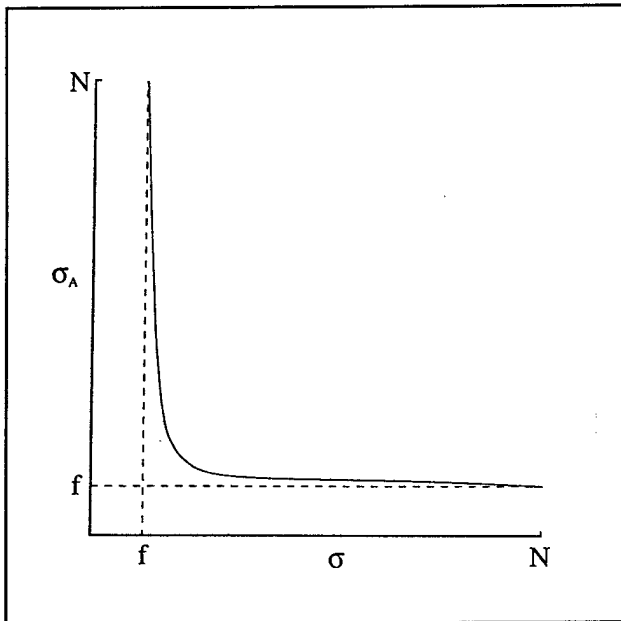


Figure 3 Sketch of the graph σ vs. σ_A . N is the buoyancy frequency and f the Coriolis frequency.

$$\sigma_A^2 = \left[\sigma^2 (f/N)^2 \right] / \left\{ \sigma^2 \left[1 + (f/N)^2 \right] - f^2 \right\} \quad (3)$$

This is sketched in Figure 3. Generally the wave periods of the apparent and 'true' wave groups will not be the same. Only when $\sigma_A = \sigma = 2^{1/2} f / [1 + (f/N)^2]^{1/2}$ will the periods match, and the scars are forced, as in resonance, at a frequency which corresponds to a wave with inclination β . In these circumstances it appears possible that if, for example, the wave group is promoting regions of, say, shear in which smaller waves become critical and break, transferring their momentum to the mean flow, then conditions are favourable for energy transfer into a packet with the same frequency as the initial group, but travelling in the opposite vertical sense.

To first order, a wave group reflecting from an inclined plane will retain its frequency and hence the inclination of its group velocity inclination to the horizontal, θ . The ratio, (c_g/c) , is a function only of θ , and is therefore conserved. During interaction with the wall, waves will be produced in the reflected group for the same length of time as the incident waves arrive; it follows that the reflected length corresponding to the region of exceedence, A , is A times the ratio of the reflected to the incident group velocities. If the number of waves is conserved in the group, the corresponding length in the direction of the reflected phase vector will be B times the ratio of the re-

flected to incident wavelengths, or since the period is conserved, the ratio of the reflected to incident phase speeds. The reflected aspect ratio of the group can therefore be found in terms of the incident. Since c_g/c is a function only of θ , it follows that the aspect ratio of the region within the wave in which a particular value is exceeded (i.e., A/B) is unchanged on reflection and so is $(\tau/T)_c$ (see 2). Because wavelength and shear change on reflection (Eriksen, 1985), the area of the reflected wave group in which 'breaking' may occur may be increased, as too may be its duration, and the likelihood of the reflected wave group producing overlapping scars will be enhanced.

3. Discussion

a. The persistence and survival of wave groups

Internal wave groups or packets are generated by intermittent generation. It is not known whether there are circumstances in which internal wave groups are robust against disintegration through wave interactions. We know little about groups because the usual methods of data analysis or measurement are not tuned to reveal their existence. (Would the relations of wave breaking to surface wave groups be known yet if only wave data were available, and not visual images?) The process of continual forcing of waves, or possibly wave groups, which can occur in surface waves driven by wind, may have no equivalent for internal waves. These are usually physically separated from the sources of energy which lead to their generation. Internal wave groups may therefore have a relatively more transient existence and be more susceptible to decay or disintegration by non-linear wave interactions (and at second rather than third order!) than are surface wave groups. Their presence and consequent effect may be most pronounced near generation sites, e.g., close to topography, where groups of lee waves may be formed. It may not however be necessary for wave groups to loose energy in producing a breaking region; they may simply promote conditions of shear or stratification in which other, perhaps smaller, waves may break (e.g., Thorpe, 1989). There is also the possibility that such interactions may *reinforce* wave groups, either by resonance or through the injection of momentum at appropriate phase in the waves forming the group by the breaking of smaller waves, and so sustain the groups as they propagate through the ocean.

b. Models and wave breaking

Perhaps for modeling ocean circulation it doesn't matter very much whether or not internal waves break in groups, but it may if, for example, the goal of prediction is to forecast the mean distribution of active mixing re-

gions, the recurrence of extreme events which are caused by internal waves, or even the probability of their detection by different sampling strategies. It seems quite possible that existing models of non-linear interactions do not account properly for waves with a group-like structure. Calculations of resonant interaction are sensitive to dissipation, the strength of interactions becoming uncertain when dissipation occurs; breaking and dissipation are still poorly understood and weakly constrained by observations. The conditions in which internal waves break is an area of great uncertainty. Even in the case of a simple uniform wavetrain travelling through a uniformly stratified ocean, let alone the case of time-dependent waves in a wave group, knowledge is imperfect. The pendulum of understanding about instability has swung from favouring convective overturn (*Orlanski and Bryan, 1969*), to shear (Kelvin-Helmholtz) instability (*Garrett and Munk, 1972*), to parametric instability (*McEwan and Robinson, 1975*), and now towards possibly all three depending on the relative wave, buoyancy and inertial frequencies (*Lombard and Riley, 1996; Thorpe, 1999e*). The development of instability and its transition to turbulence are even more poorly known although advances via numerical methods, directed primarily towards understanding of wave breaking in the atmosphere, have provided considerable insight into the processes following the onset of convective instability (e.g., see *Fritts et al., 1996*). Questions of how turbulent regions are produced by breaking waves cannot be separated from that of how instability occurs in individual internal waves, or, for example, whether collective instability spanning several waves is possible. If however the dynamics of the ocean interior at the scale of internal waves is dominated by wave groups, then it follows that turbulence at smaller scales, those at which breaking and diapycnal diffusion occur, is controlled by the wave groups, occurs in association with them and has an intensity which is related to wave groups parameters.

c. Boundary generation

There is certainly a need to discover more about the processes near boundaries. What is most needed are observations capable of resolving the temporal and spatial structure of currents and density variations (i.e., the internal wave field, including its directional and dissipative properties) near a sloping boundary. A pre-requisite is that the bathymetry is known, at least to a scale at which internal waves may be generated. Polzin and colleagues at WHOI and elsewhere have undertaken an observational study in a region off the U.S. eastern seaboard to begin addressing these requirements. The cartoon in Fig.1 illustrates some of the internal wave-related phenomena at sloping boundaries (but not groups!), including the possible ejection of fluid in regions where convergence occurs

on isopycnal surfaces, akin to rip currents in the surf zone. This provides a presently unquantified means of connection between the boundary layer and the interior, a mechanism whereby the boundary processes can influence the interior, perhaps via the generation of vortical modes.

4. Epilogue

Discussion at the workshop included the suggestion that the internal wave field in the ocean is similar to that of the light field in a cloud where multiple scattering results in an almost isotropic directional field of light, even though the primary external source is highly directional, coming from the Sun. This received some opposition, since the internal wave generation sources are intermittent whilst the Sun shines continuously. Briscoe remembered that the IWEX data showed evidence that packets of waves could sometimes be observed propagating from one sensor to another through the array over distances of about 1 km. Where wave packets (or groups) are best observed is near the source of the two prominent narrow band frequency oscillations, diurnal tides and inertial waves. The propagation distance of wave packets of different frequency and mode number appears to be still uncertain. Whether 'groups' can retain form within an ambient wave field and against its interaction appears still uncertain, but sufficiently close to generation sites (i.e., for waves of low frequency, at least within about 1 km of the ocean surface and regions of rough benthic topography) it is known that wave packets can survive. It is in this zone that mixing (large ϵ and K_v) is greatest. Here the internal wave field appears akin to a light field in which flashes (possibly of different colour) come intermittently from nearby generation zones. It is likely that, in the deep ocean, there is often a blue pulsation due to tidal generation, although this may be tinged with lighter and redder hues which correspond to topographic structure, the short, high frequency, lee waves generated by tidal flow over the small-scale topography. We need to know more about mode structure in these near-generation regions, for which there is no obvious light analogue, as well as frequency. A central question for observations and models is "Is the ocean full of internal waves or internal wave groups?"

The only certain conclusion is that those of you still here in 25 years time will then be able to recall how wrong people were 25 years ago, and how little they knew which was of use to help solve the then-important problems. You will however probably understand better what should really be known, but isn't yet.

References

- Alford, M. and R. Pinkel, R. 1999, Observations of overturning in the thermocline: the context of mixing. Submitted to *J. Geophys. Res.*
- Baines, P.G. 1974, The generation of internal tides over steep continental slopes. *Phil. Trans. R. Soc. Lond. A*, **277**, 27-58.
- Baines, P.G., 1982, On internal tidal generation models. *Deep-Sea Res.*, **29**, 307-338.
- Bell, T.H., 1975, Topographically generated internal waves in the open ocean. *J. Geophys. Res.*, **80**, 320-327.
- Benjamin, T.B., 1967, Instability of periodic wavetrains in non-linear dispersive systems. *Proc. R. Soc. Lond. A*, **299**, 59-75.
- Borisenko, Yu.D., A.G. Voronovich, A.I. Leonov and Yu.Z. Miropolskiy, 1976, Towards a theory of non-stationary weakly nonlinear internal waves in a stratified fluid. *Atmos. Oceanic Phys.*, **12**, 174-179.
- Donelan, M., M.S. Longuet-Higgins and J.S. Turner, 1973, Periodicity in whitecaps. *Nature*, **239**, 255-261.
- Dunkerton, T.J., D.P. Delisi and M.-P. Lelong, 1998, Along-slope current generated by obliquely incident internal waves. *Geophys. Res. Lett.*, **25**, 3871-3874.
- Eriksen, C.C., 1982, Observations of internal wave reflection off sloping bottoms. *J. Geophys. Res.*, **87**, 525-538.
- Eriksen, C.C., 1985, Implications of ocean bottom reflection for internal wave spectra and mixing. *J. Phys. Oceanogr.*, **15**, 1145-1156.
- Eriksen, C.C., 1998, Internal wave reflection and mixing at Fieberling Guyot. *J. Geophys. Res.*, **103**, 2977-2994.
- Fritts, D.C., J.F. Garten and O. Andreasson, 1996, Wave breaking and transition to turbulence in stratified shear flows. *J. Atmos. Sci.*, **53**, 1057-1085.
- Garrett, C. and W. Munk, 1972, Oceanic mixing by breaking internal waves. *Deep-Sea Res.*, **19**, 823-832.
- Ivey, G.N. and R.I. Nokes, 1989, Vertical mixing due to breaking of critical internal waves on sloping boundaries. *J. Fluid Mech.*, **204**, 479-500.
- Leaman, K.D. and T.B. Sanford, 1975, Vertical energy propagation of inertial waves: a vector spectral analysis of velocity profiles. *J. Geophys. Res.*, **80**, 1975-1978.
- LeBlond, P.H. and L.A. Mysak, 1978, *Waves in the Ocean*. Amsterdam, Elsevier, 602 pp.
- Lombard, P.N. and J.J. Riley, 1996, On the breakdown into turbulence of propagating internal waves. *Dyn. Atmos. Oceans*, **23**, 345-356.
- McEwan, A.D. and R.M. Robinson, 1975, Parametric instability of internal gravity waves. *J. Fluid Mech.*, **67**, 667-687.
- Muller, P., G. Holloway, F. Henyey and N. Pomphrey, 1986, Nonlinear interactions among internal gravity waves. *Rev. Geophys. Space Phys.*, **24**, 493-536.
- New, A.L., 1988, Internal tidal mixing in the Bay of Biscay. *Deep-Sea Res.*, **35**, 691-709.
- Orlanski, I. and K. Bryan, 1969, Formation of the thermocline step structure by large-amplitude internal gravity waves. *J. Geophys. Res.*, **74**, 6975-6983.
- Pinkel, R., 1983 Doppler sonar observations of internal waves: wave-field structure. *J. Phys. Oceanogr.*, **13**, 804-815.
- Polzin, K.L., J.M. Toole, J.R. Ledwell and R.W. Schmitt, 1997, Spatial variability of turbulent mixing in the abyssal ocean. *Science*, **276**, 93-96.
- Slinn, D.A. and J.J. Riley, 1998, Turbulent dynamics of critically reflecting internal gravity wave. *Theor. Comput. Fluid Dyn.*, **11**, 281-304.
- Taylor, J. R., 1993, Turbulence and mixing in the boundary layer generated by shoaling internal waves. *Dyn. Atmospheres. Oceans*, **19**, 233-258.
- Thorpe, S.A., 1975, The excitation, dissipation, and interaction of internal waves in the deep ocean. *J. Geophys. Res.*, **80**, 328-338.
- Thorpe, S.A., 1977, On the stability of internal wavetrains. In 'A voyage of discovery: G. Deacon 70th anniversary vol.', Ed. M. Angel. Pergamon Press, Oxford, 199-212.
- Thorpe, S.A., 1987, On the reflection of a train of finite amplitude internal waves from a uniform slope. *J. Fluid Mech.*, **178**, 279-302.
- Thorpe, S.A., 1988, A note on breaking waves. *Proc. R. Soc. Lond. A*, **419**, 323-335.
- Thorpe, S.A., 1989, The distortion of short internal waves produced by a long wave, with applications to ocean boundary mixing. *J. Fluid Mech.*, **208**, 395-415.
- Thorpe, S.A., 1992, Thermal fronts generated by internal gravity waves reflecting from a slope. *J. Phys. Oceanogr.*, **22**, 105-108.
- Thorpe, S.A., 1996, The cross-slope transport of momentum by internal waves generated by along-slope currents over topography. *J. Phys. Oceanogr.*, **26**, 191-204.
- Thorpe, S.A., 1997, On the interactions of internal waves reflecting from slopes. *J. Phys. Oceanogr.*, **27**, 2072-2078.
- Thorpe, S.A., 1999a, Fronts formed by obliquely reflecting internal waves at a sloping boundary. Submitted to *J. Phys. Oceanogr.*
- Thorpe, S.A., 1999b, The effects of rotation on the non-linear reflection of internal waves from a slope. Submitted to *J. Phys. Oceanogr.*
- Thorpe, S.A., 1999c, The generation of along-slope currents by breaking internal waves. *J. Phys. Oceanogr.*, **29**, 29-38.
- Thorpe, S.A., 1999d, On internal wave groups. In press, *J. Phys. Oceanogr.*
- Thorpe, S.A., 1999e, A note on the breaking of internal waves in the ocean. In press, *J. Phys. Oceanogr.*
- Thorpe, S.A. and A.J. Hall, 1983, The characteristics of breaking waves, bubble clouds, and near-surface currents observed using side-scan sonar. *Cont. Shelf Res.*, **1**, 353-384.
- Toole, J.M., R.W. Schmitt and K.L. Polzin, 1997, Near-bottom mixing above the flanks of a midlatitude seamount. *J. Geophys. Res.*, **102**, 947-959.

Mixing Generated by Internal Waves Interacting with Rough Topography

Sonya Legg

Woods Hole Oceanographic Institution

Carl Wunsch

Department of Earth, Atmospheric and Planetary Sciences, Massachusetts Institute of Technology

Abstract. The reflection of internal waves from a slope where the slope angle is close to the angle of the wave energy propagation has long been postulated as a mechanism for transfer of wave energy to smaller scales, leading to mixing through the enhancement of shear. Recent laboratory experiments and numerical simulations have examined the mixing generated when an internal wave reflects from a uniform slope at the critical angle. Here we perform simulations of interactions between internal waves and variable slope, using a novel numerical model which combines 3-dimensional topographic variations and non-hydrostatic dynamics.

Introduction

In regions of complex topography, observed diapycnal mixing [Polzin *et al.*, 1997] is several orders of magnitude greater than observed in the ocean interior [Ledwell *et al.*, 1993; Toole *et al.*, 1994]. This enhanced diapycnal mixing plays an important role in the ocean general circulation [Munk, 1966; Munk and Wunsch, 1998] as well as being of local significance for the biogeochemistry of coastal regions. Hence a greater understanding of the factors which determine the distribution and magnitude of topographically generated mixing are of great importance for both local and global ocean prediction.

One mechanism for generating diapycnal mixing at topographic features is through the interaction between internal waves and topography. When internal waves are reflected from sloping topography the angle θ between the propagation direction and horizontal is preserved. If the topography slopes at an angle α close to θ , the reflected wave has a higher energy density than the incident wave, the vertical length scales are reduced, and shear is increased. Richardson numbers may be sufficiently reduced that instability results, leading to overturning and mixing. Mixing generated by the interaction of an internal wave with a uniform slope at the critical angle ($\alpha = \theta$) has been studied in the laboratory [Cacchione and Wunsch, 1974; Ivey and Nokes, 1989; De Silva *et al.*, 1997] and through numerical simulation [Slinn and Riley, 1996]. It is yet not understood how

3-dimensional variations in slope may modify the mixing efficiency. In particular variable topography may confine the mixing to particular locations.

The mixing on the sloping topography can have a significant effect on the interior of the ocean only if mixed fluid is exported away from the boundary, and the mixing region replenished with stratified fluid. Such export mechanisms include the large-scale secondary circulation [Ivey and Nokes, 1989] and the periodic replenishment of the boundary layer fluid by the oscillating current itself [Slinn and Riley, 1996]. In the presence of rotation, baroclinic instability of the along slope currents established by mixing [Ivey, 1987] may contribute to the export process. If mixing is spatially variable, for example, in response to variable topography, lateral transports of mixed fluid may be enhanced. Hence the focus of our study is on the effects of variable topography on the mixing generated by internal wave reflection.

Numerical model formulation

Our tool for this study of internal waves interacting with variable topography is a numerical model which combines both non-hydrostatic physics (essential to capture the instability and overturning which lead to mixing) and arbitrary 3-dimensional topography [Figure 1]. Previous numerical studies have employed models which either parameterize the mixing [Holloway and Barnes, 1998] or explicitly resolve mixing in a model limited to uniform slope [Slinn and Riley, 1996]. We em-

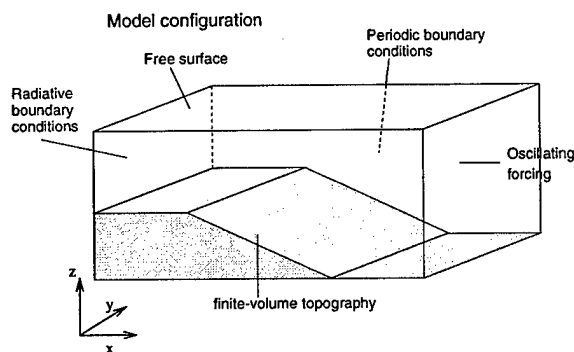


Figure 1. Schematic of the numerical model

ploy the MIT Ocean Model [Marshall *et al.*, 1997a,b], a 3-dimensional non-hydrostatic Boussinesq model which includes topography through a finite-volume formulation [Adcroft *et al.*, 1997]. The variant of the model which we use includes open boundary conditions and a free-surface: we force internal waves at the off-shore boundary and allow them to propagate toward the sloping topography.

Preliminary results: comparison between critical wave reflection on linear, concave and convex slopes

To demonstrate the capability of this model to include subtle topographic variations, and as a first step to examining the role of variable topography in determining mixing location and strength, we have carried out 3 simulations of an internal wave reflecting from a slope. In all three cases the parameters are identical apart from the curvature of the slope - in one case the slope is linear, and at the critical angle, while the other two cases are concave and convex respectively, with the same average slope as the linear case. These preliminary calculations are carried out in only 2-dimensions, with all derivatives in the y -direction set to zero. The stratification is initially uniform, with $N^2 = 10^{-6} \text{s}^{-2}$. The total depth of the volume is 200 m, and the gravest mode internal wave is forced at $x = 0$ at the M_2 tidal frequency $1.41 \times 10^{-4} \text{s}^{-1}$, with an velocity amplitude of $U_{max} = 0.024 \text{m s}^{-1}$. The coriolis parameter $f = 10^{-4} \text{s}^{-1}$. A uniform resolution of 3.33 m is used in the vertical, while in the horizontal a stretched grid is applied, with a total of 640 grid points. Maximum horizontal resolution occurs over the slope, where $\Delta x = 7$ m. The calculations are carried out for a total of 9 tidal cycles.

As shown in previous studies, when the internal wave encounters the critical slope a bore-like feature develops in the density field (Figure 2), which leads to overturn-

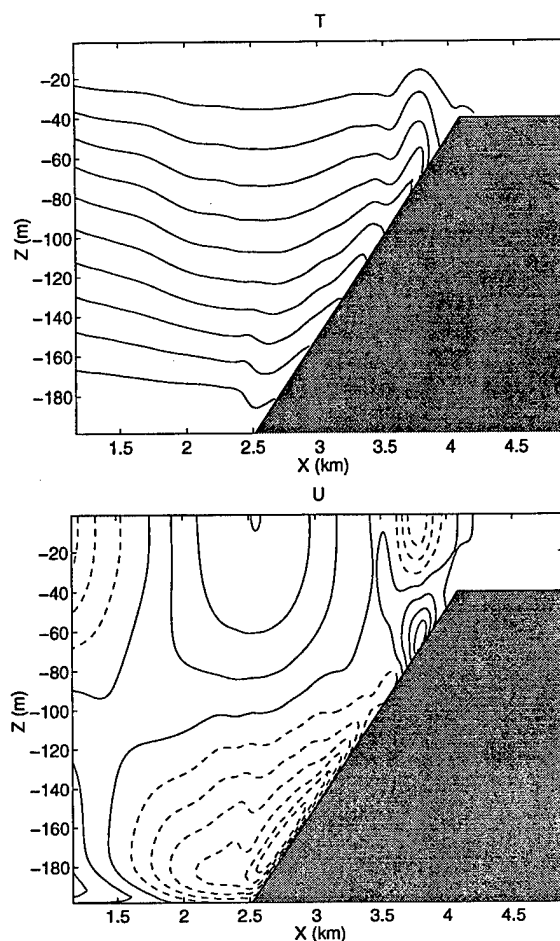


Figure 2. (a) The temperature field and (b) horizontal cross-slope velocity field as an internal wave undergoes a critical reflection at a uniformly sloping boundary. The contour spacing is (a) 0.01 K and (b) 0.0065 m s^{-1} . Negative values of velocity are indicated by dashed contours, positive values by solid contours.

ing and mixing, as dense fluid is pulled up the slope over less dense fluid. We average the fields over 6 tidal cycles, following the encounter of the wave with the slope, and compare the time averaged fields for the 3 different cases (Figure 3). All three cases have features in common - an Eulerian averaged flow which flows downslope right adjacent to the boundary, and upslope a short distance away. The along-slope velocity, generated as a result of finite rotation, is strongly sheared, with negative flow adjacent to the slope and positive flow just above. The temperature field has been strongly modified, with isotherms dragged upwards at the slope, bent downwards a short distance away, particularly toward the bottom of the slope, and bent upwards further in the interior and towards the top of the slope. The net effect of these isotherm distortions is a weakening of the

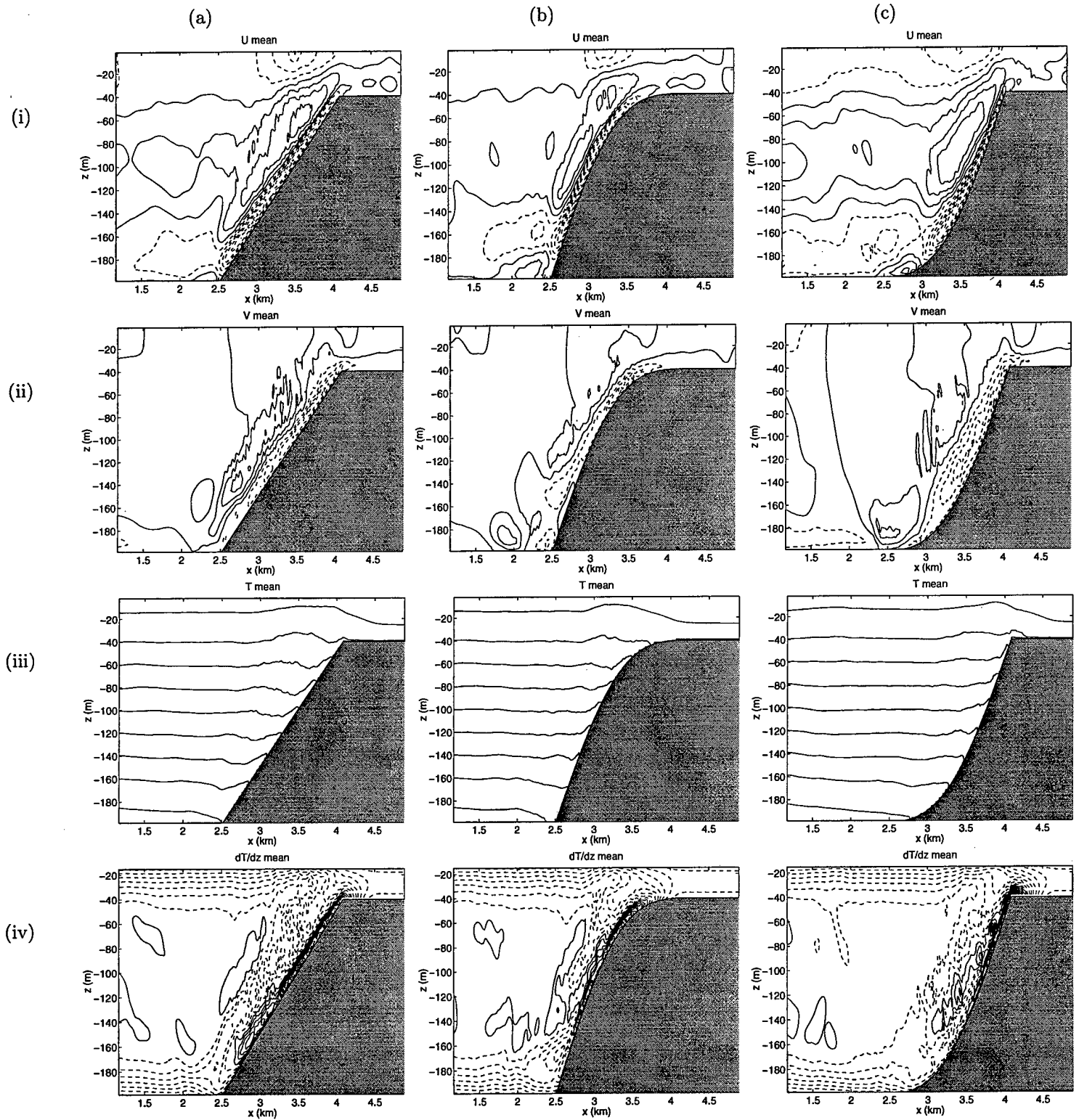


Figure 3. The fields at the slope, averaged over 6 wave-periods. (i) The cross-slope velocity field U , (ii) the along-slope velocity field V , (iii) the temperature field T , (iv) the change in the vertical gradient of the temperature field dT/dz , shown for (a) linear slope, (b) convex slope, (c) concave slope. Contour spacing is (i,ii) 0.0025 m s^{-1} , (iii) 0.01 K , (iv) $5 \times 10^{-5} \text{ K m}^{-1}$. Negative values are indicated by dashed contours, positive values by solid contours.

stratification in a broad band parallel to the slope (indicated by dashed contours), in the uniform slope case, with narrower regions of increased stratification at the slope itself and further in the interior (solid contours). Hence most of the mixing appears to take place not at the boundary, but a short distance into the interior.

Despite these broad similarities, there are differences between the 3 cases, particularly in the net changes in temperature and stratification. The concave slope simulation shows much less distortion of the isotherms than the other two cases, while the convex slope case has weakened stratification concentrated near the top of the slope, where the slope is critical. Note that the concave slope is critical toward the bottom of the slope, where the temperature perturbations associated with the 1st mode internal wave are small.

Discussion

These preliminary calculations show that variations in the slope can have a significant influence on the location and magnitude of mixing generated by internal wave reflection. Naturally the importance of such variations must depend on the relative scales of the topography variations compared to the wave motions: higher vertical modes might be less influenced by the broad topography variations studied here than the gravest mode.

Later calculations in 3-dimensions will examine along-slope variations in topography and the exchange of fluid between the boundary regions and interior initiated by 3-dimensional motion. Our ultimate aim is the development of parameterizations of mixing and its dependence on the topography and waves.

Acknowledgments. This study is funded by ONR grant N00014-98-1-0096.

References

- Adcroft, A., C. Hill and J. Marshall, 1997. Representation of topography by shaved cells in a height coordinate ocean model. *Mon. Wea. Review*, **125**, 2293–2315.
- Cacchione, D., and C. Wunsch, 1974. Experimental study of internal waves over a slope. *J. Fluid Mech.*, **66**, 223–239.
- De Silva, I.P.D., J. Imberger, and G.N. Ivey, 1997. Localized mixing due to a breaking internal wave ray at a sloping bed. *J. Fluid Mech.*, **350**, 1–27.
- Holloway, P.E., and B. Barnes, 1998. A numerical investigation into the bottom boundary layer flow and vertical structure of internal waves on a continental slope. *Cont. Shelf Res.*, **18**, 31–65.
- Ivey, G. N., 1987. Boundary mixing in a rotating stratified fluid. *J. Fluid Mech.*, **183**, 25–44.
- Ivey, G. N., and R. I. Nokes, 1989. Vertical mixing due to the breaking of critical internal waves on sloping boundaries. *J. Fluid Mech.*, **204**, 479–500.
- Ledwell, J. R., A. J. Watson and C. S. Law, 1993. Evidence for slow mixing across the pycnocline from an open-ocean tracer-release experiment. *Nature*, **364**, 701–703.
- Marshall, J., A. Adcroft, C. Hill, L. Perelman and C. Heisey, 1997a. A finite-volume, incompressible Navier Stokes model for studies of the ocean on parallel computers. *J. Geophys. Res.*, **102**, 5753.
- Marshall, J., C. Hill, L. Perelman and A. Adcroft, 1997b. Hydrostatic, quasi-hydrostatic and non-hydrostatic ocean modeling. *J. Geophys. Res.*, **102**, 5733.
- Munk, W., 1966. Abyssal recipes. *Deep Sea Res.*, **13**, 707–730.
- Munk, W., and C. Wunsch, 1998. Abyssal recipes II: energetics of tidal and wind mixing. *Deep Sea Res.* **45**, 1977–2010.
- Polzin, K. L., J. M. Toole and R. W. Schmitt, 1997. Spatial variability of turbulent mixing in the abyssal ocean. *Science*, **276**, 93.
- Slinn, D. N., and J. J. Riley, 1996. Turbulent mixing in the oceanic boundary layer caused by internal wave reflection from sloping terrain. *Dyn. Atmos. Oceans*, **24**, 51–62.
- Toole, J. M., K. L. Polzin and R. W. Schmitt, 1994. Estimates of diapycnal mixing in the abyssal ocean. *Science*, **264**, 1120.

S. Legg, WHOI, Woods Hole, MA 02543

This preprint was prepared with AGU's L^AT_EX macros v4. File ahatext formatted August 19, 1999.

With the extension package 'AGU++' by P.W.Daly, version 1.5 from 1996/08/20

Along-Slope Current Generation by Obliquely Incident Internal Waves

Donald N. Slinn

Florida Atlantic University, Boca Raton, FL 33431

Abstract.

Numerical studies of internal wave reflection from sloping boundaries are presented. Previous work (*Slinn and Riley, 1996, 1998a, 1998b, 1999*) has restricted attention to internal waves that approach the bottom slope in a plane normal to the boundary (normal incidence). This work extends the scope of the three-dimensional time-dependent numerical experiments to examine internal waves that approach the slope at an oblique angle ϕ out of the plane normal to the boundary. These preliminary studies with obliquely incident waves at the critical frequency have shown that strong alongslope mean currents are generated near the boundary by the flux of incident wave momentum when wave breakdown occurs in a turbulent layer above the slope. After a short time the mean boundary currents interact with the oncoming wave field in a complex fashion. The waves break down near the upper interface of the current and no longer penetrate to the slope. Turbulent mixing near the boundary is nearly extinguished, and a new turbulent layer is produced at the upper interface of the shear layer. At this point the flux of wave momentum into the water column occurs farther from the wall, and the net result is a steady thickening of the alongslope boundary current. For the moderate wave parameters used in an illustrative example, within ten wave periods after the onset of wave breaking the mean current is approximately two vertical wavelengths thick and has a velocity close to the phase speed of the oncoming waves in the alongslope direction.

Introduction

Past numerical studies of internal wave reflection from slopes have examined mixing in turbulent boundary layers that are created when internal wave energy is focused near boundaries (e.g., *Slinn and Riley, 1996, 1998a, 1998b*). Gaining improved understanding of diapycnal (vertical) mixing in the ocean is the underlying motivation for these experiments. In nature, vertical mixing is inhibited by the ocean's stable stratification. *Munk (1966)* shows that a basin-averaged vertical eddy diffusivity of roughly $\kappa = 10^{-4} \text{ m}^2 \text{ s}^{-1}$ must exist to balance the effects of upwelling and downward diffusion. Field studies, however, have failed to observe such large vertical diffusivities in the ocean interior, falling short by approximately an order of magnitude. The conclusion from the field experiments is that 80-90% of the vertical mixing is not taking place in the ocean interior. Instead, the mixing is expected to occur near bound-

aries in turbulent benthic boundary layers.

Recent field experiments (*Eriksen 1985, 1998*) have suggested that the oceanic internal wave field can provide sufficient energy to activate strong mixing near sloping boundaries, which can in turn account for a significant portion of the overall oceanic vertical mixing. One mechanism by which this may occur is the breaking of internal gravity waves, as they reflect off the continental shelf or off other sloping boundaries near islands or seamounts. When an internal wave of frequency ω propagating in a uniformly stratified environment reflects from a larger-scale, sloping boundary, its angle of propagation with respect to the horizontal, θ , is preserved (*Phillips, 1977*). The angle between the group velocity vector and the horizontal depends upon the wave frequency, ω , and the background density stratification according to the dispersion relation $\omega = N \sin \theta$, where N is the buoyancy frequency defined by $N^2 = (-g/\rho_0)(\partial \rho / \partial z)$. This reflection from

a sloping boundary can lead to an increase in the energy density of the wave, as the energy in the oncoming wave is concentrated into a more narrow ray tube upon reflection.

The situation probably most effective for boundary mixing arises when an oncoming wave reflects from a bottom slope α that nearly matches the angle of wave propagation θ . In this case linear theory suggests that a small amplitude oncoming wave may be reflected with large amplitude, thus exhibiting nonlinear behavior and possibly wave breaking and turbulence. The flux of reflected energy from the slope is adjusted in two ways during reflection. The wave energy is transferred to shorter wavelength (higher wave number) and the group velocity decreases. At the critical condition, $\theta = \alpha$, linear wave theory predicts a reflected wave of infinite amplitude, infinitesimal wavelength, and zero group velocity, leading to the trapping of oncoming wave energy in the boundary region. In such a case, nonlinearities and turbulence must come into play.

Previous numerical and laboratory experiments have primarily examined internal waves that approach the slope in the plane normal to the boundary. Field observations, of course, contain incident waves that approach the slope from a full spectrum of incident angles. The purpose here is to begin to bridge this gap by conducting numerical experiments of internal wave reflection for waves that approach the boundary at varying angles of oblique incidence.

Results

Numerical simulations of the three-dimensional Navier-Stokes equations are utilized to complement other methods of investigation; the advantage compared to field measurements is the ability to isolate a single physical process and examine its behavior in different parameter ranges. The numerical model is described in detail in *Slinn and Riley (1998b)*.

This model simulates forced, dissipative, incompressible, stratified flow within the Boussinesq approximation (*Phillips, 1977*) and incorporates advanced numerical techniques. For a sloping ocean floor, the coordinate system used in the numerical simulation is rotated to align with the slope. The x' -direction is upslope, the y -direction is along or across the slope, the z' -direction is normal to the slope, and z is in the true vertical direction opposite gravity. The model is periodic in the x' - and y -directions and bounded by a plane wall at the bottom boundary. Note that the background density and pressure fields are not periodic at the lateral boundaries in x' . If the remaining perturbation density and pressure fields are initially periodic in the x' -direction, however, they will remain so, because the background

fields are subtracted from the governing equations. The important nondimensional parameters are the Richardson, Reynolds, and Prandtl numbers.

During simulations, incoming waves are forced continuously from inside the computational domain, utilizing spatially localized forcing terms. The two-dimensional forcing method of *Slinn and Riley (1998b)* has been generalized by *Lombard and Riley (1998, private communication)* to include the three-dimensional case of oblique wave incidence.

$$F_u = \frac{A}{k^2 \cos \alpha - mk \sin \alpha + l^2 \cos \alpha} \times [F(z)(l^2 \sin \alpha - km \cos \alpha + m^2 \sin \alpha) \cos \Phi - F'(z)(k \cos \alpha - m \sin \alpha) \sin \Phi],$$

$$F_v = -\frac{A}{k^2 \cos \alpha - mk \sin \alpha + l^2 \cos \alpha} \times [F(z)(ml \cos \alpha + kl \sin \alpha) \cos \Phi + F'(z)l \cos \alpha \sin \Phi],$$

$$F_w = AF(z) \cos \Phi,$$

$$F_p = -\frac{A[(k \cos \alpha - m \sin \alpha)^2 + l^2]}{\omega(k^2 \cos \alpha - mk \sin \alpha + l^2 \cos \alpha)} \times [F(z) \sin \Phi + F'(z) \sin \alpha (k \cos \alpha - m \sin \alpha) \cos \Phi],$$

where $\Phi = kx + ly + mz - \omega t$ and the forcing localization terms, $F(z)$ and $F'(z)$, and wave numbers in the rotated coordinate system, $\kappa = (k, l, m)$, are as defined in *Slinn and Riley (1998b)*. For $l = 0$ these expressions simplify to those used previously for normally incident waves.

Both the velocity and density fields are locally forced (F_u, F_v, F_w , and F_p are added to the rhs. of the momentum and density equations) in a region several wavelengths above the boundary in a manner that generates one or more monochromatic wave trains with specified frequency and wavenumber vectors incident upon the sloping terrain. No-slip boundary conditions on velocity are employed at the bottom boundary, while a zero flux boundary condition is used for the density field.

For moderate Reynolds number experiments, *e.g.*, for $Re < 2000$, all of the scales of motion are well resolved and the numerical experiments represent a direct numerical simulation (DNS). Typical grid resolutions used in the experiments are $256 \times 128 \times 200$ grid points. For the higher Reynolds number experiments,

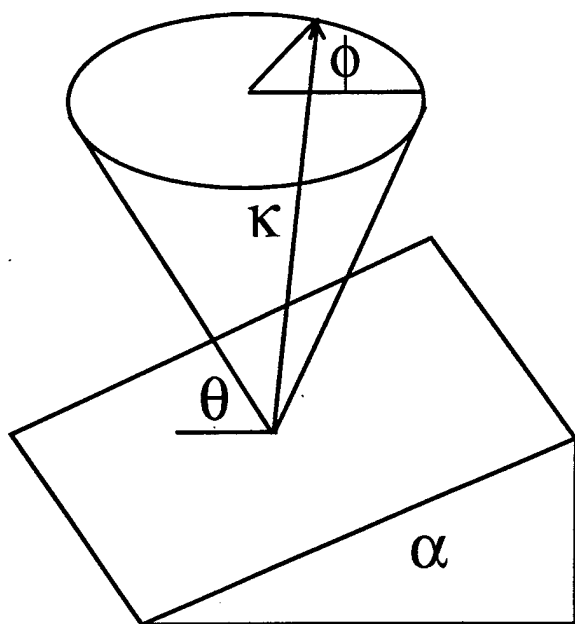


Figure 1. Definition sketch of geometry: with bottom slope α , the wave number vector κ lies on the cone with angle θ from the horizontal, and ϕ is the direction of the incident wave vector from normal to the slope.

e.g., for $2000 < Re < 10,000$, the model incorporates additional numerical dissipation at the smallest resolved length scales (*e.g.*, a simple sub-grid-scale model).

Results from an oblique reflection experiment at the critical frequency with $Re = \lambda U_w / \nu = 2000$, $Ri = N\lambda / U_w = 120$, bottom slope $\alpha = 20^\circ$, and angle from normal incidence $\phi = \tan^{-1}(k/l) = 52.5^\circ$ (Eriksen, 1982) are presented here. This experiment shows a very different flow results for oblique waves compared to normally incident waves. The major difference is the generation of a strong mean alongslope current in the y -direction. We use the terminology “alongslope” to mean a v -velocity component along or across the slope, as opposed to an upslope or downslope current that would appear in the u' -velocity component in the x' direction. Aspects of the generation of a mean current by obliquely incident internal waves have been predicted by Hogg (1971), Wunsch (1973), and Thorpe (1997).

In the present studies the forcing is turned on at $t = -6.5$, where time is nondimensionalized by the wave period. Between $-6.5 < t < 0$ the wave train approaches the wall, and we intentionally maintain a zero mean v -velocity in the model by subtracting the mean flow at each time level. This is done because during the period of initial transients, as the leading edge of the wave train approaches the wall, the amplitude of the wave train is not constant in space. Hence,

the gradient of the Reynolds stress $(\rho uv)_z$ is nonzero and will generate a weak mean v -velocity. While this transient mean velocity is small compared to the later development of the mean flow from wave breakdown, it is cleaner to “start” the experiment when the uniform wave train has reached the boundary. At this point, $t = 0$, the artificial constraint on the mean is removed below the forcing region, and a flux of momentum from breaking waves produces an alongslope current.

An analogous process occurs for surface wave breakdown at the shore when waves approach the beach at an oblique angle. An alongshore current (*e.g.*, Slinn *et al.*, 1998, 1999) can develop in the surf zone from the flux of surface wave momentum. This process has been explained using the concept of the radiation stress (Bowen, 1969). Simply stated, if a reflected wave train does not carry as much momentum away from a boundary as is carried toward the boundary by an incident wave train, then there will be a compensating flux of momentum to a mean flow.

The picture that emerges from the preliminary oblique internal wave reflection experiments is that at early time ($0 < t < 3$) wave breakdown occurs in a fashion similar to the case of normal incidence in a turbulent layer with $\delta < \lambda_z/2$. During this period an alongslope current is generated in this region with maximum local velocities approximately equal to the component of the phase speed of the oncoming wave in the y -direction, C_{phy} , and a horizontally averaged v -velocity of approximately $0.6C_{phy}$. After approximately three wave periods the location of wave breakdown separates from the bottom boundary and occurs instead at the upper surface of the mean current, where the oncoming wave experiences a shear flow. During this period the flux of wave momentum to the mean flow occurs farther from the slope, and the mean boundary layer grows thicker. By $t = 10$ (wave periods) the boundary layer thickness is $\delta \approx 2\lambda_z$, and the mean velocity for $z' < 2\lambda_z$ is $\bar{v}(z') \approx 0.6C_{phy}$. As the mean flow strengthens only a small portion of the oncoming wave energy appears to penetrate through the shear layer and reach the boundary.

The process is illustrated in Figure 2. Panels in the left column show fields at $t = 1$, and panels in the right column are for $t = 10$. The top row shows isopycnals in a two-dimensional cross-section (an x - z plane). At $t = 1$ wave breakdown at the boundary is visible from the density surfaces for $z' < 0.5\lambda_z$. The direction of propagation of the group velocity of the oncoming waves is downward, to the right, and into the page in this experiment. The full domain extends to a height of $z' = 6\lambda_z$, and the wave forcing region is located between $3\lambda_z < z' < 5\lambda_z$. By $t = 10$ the isopycnals near the

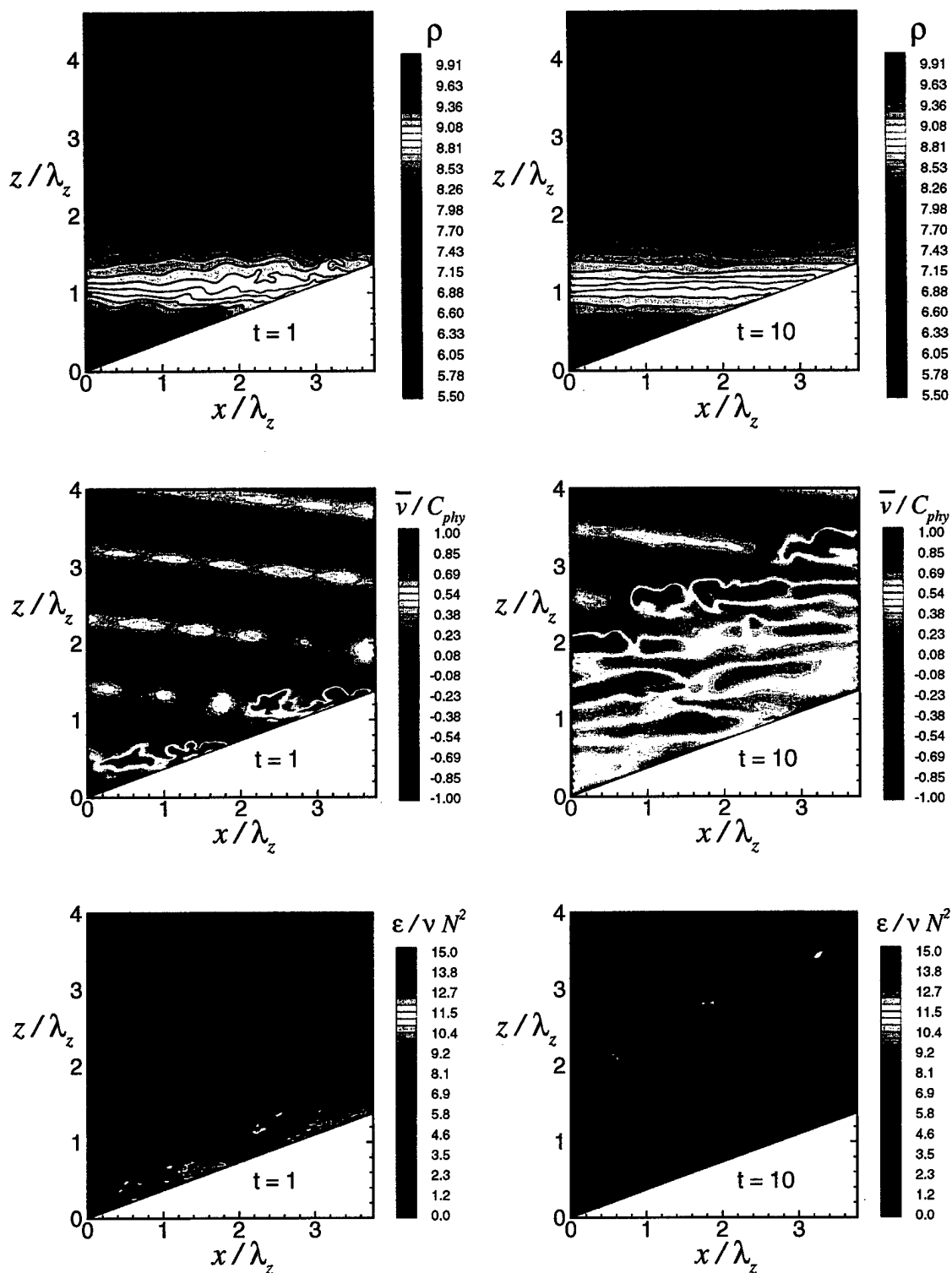


Figure 2. Isopycnals (top), v -velocity contours (middle), and kinetic energy dissipation rates $\epsilon/\nu N^2$ (bottom), In an $x - z$ plane one and ten wave periods after the beginning of wave breakdown in the bottom boundary layer for obliquely incident internal waves at the critical frequency with a bottom slope of 20° and $RE = 2000$.

boundary are relatively flat while the region near $z' = 2\lambda_z$ exhibits overturned isopycnals.

The middle row of panels in Figure 2 show cross sections of the v -velocity component normalized by C_{phy} . At $t = 1$ the dominant signal is that of the uniform oncoming waves with disturbances of comparatively large positive values of v developing near the wall where wave breaking is active. The bottom two panels show the normalized kinetic energy dissipation rate $\epsilon/\nu N^2$ that indicates regions of strongest wave energy dissipation. The lower right panel shows that the region of wave breaking is separated from the wall at $t = 10$. The middle right panel, v at $t = 10$, shows that a thick layer of v -velocity has developed. The strongest currents are localized at the shear layer at the interface between the boundary current and the oncoming wave field. There is an apparent layering of the velocity structure within the mean boundary layer that may be due to the superposition of the mean flow with residual wave energy that penetrates through the region of wave breaking. This is not clear because the layers do not retain the characteristic slope of the oncoming wave field. It would be expected, however, that the slope of the waves would change to conserve the apparent frequency $(\omega + \vec{k} \cdot \vec{u})$ where the mean velocity is nonzero (Phillips, 1977). This is an area for further investigation.

Additional features of the oblique wave experiment are shown in Figure 3. The top two panels of Figure 3 show $\epsilon/\nu N^2$ in an $x'-y$ plane parallel to the boundary located at a height of $z' = 0.12\lambda_z$ at $t = 1$ and 10. At $t = 1$ the orientation of the wave fronts, perpendicular to ϕ , are evident in the dissipation rate contours. Flow visualizations show that these wave fronts sweep through the boundary layer in a uniform manner until the mean velocity becomes relatively strong, at which point a combination of wave propagation and drift in the y -direction operate. By $t = 10$ dissipation near the wall has essentially shut down, (shown in the upper right panel of Figure 3) and isolated flow features appear to drift with \bar{v} .

The lower left panel of Figure 3 shows the horizontally ($x'-y$) averaged \bar{v} velocity as a function of distance from the boundary (z'/λ_z) at $t = 2, 4, 6, 8$, and 10. The approximately steady thickening of the boundary layer in time with nearly constant \bar{v} -velocity of $0.6 C_{phy}$ is the main feature. The lower right panel shows the volume averaged kinetic, potential, and total energies in the experiment. In addition, the time integrated net buoyancy flux is shown. The increasingly negative values of the time integrated buoyancy flux indicate a flux of wave potential to kinetic energy. For normally incident waves the kinetic and potential energies remain approximately equipartitioned during wave breakdown.

The relative increase of average kinetic energy over potential energy at longer time indicates the contribution from the mean flow.

The potential energy dissipation rate normalized by the total work input to force the oncoming internal wave, $\eta = \chi/W$, varies with the oblique angle ϕ . In initial experiments, for $\phi = 52.5^\circ$, $\eta = 0.32$; for $\phi = 31.0^\circ$, $\eta = 0.45$; and for $\phi = 0.0^\circ$ $\eta = 0.34$. Additional experiments exploring the dependency of the dissipation rates on the Reynolds and Richardson numbers in addition to ϕ are planned.

Summary

In general, the flows that develop in experiments with obliquely incident waves differ strongly from previous work with normally incident waves. The mean flows are an order of magnitude stronger than the weak circulations that develop for normally incident waves. Density intrusions extending from the turbulent boundary layer that were a robust feature with normal waves are swept alongslope by the mean current as other boundary mixing processes dominate.

Several key questions are being investigated in ongoing work: How do the net mixing properties change when a mean flow is present? How does the flow behavior depend on the oblique angle ϕ for a fixed frequency and bottom slope? Do different flows develop for different steepnesses of slopes? Why does the wave break when approaching the top of the shear layer? Is this flow behavior similar to a wave approaching a critical layer? What continues to support the mean flow near the wall when waves no longer penetrate to the boundary? Will this eventually spin down? How thick will the mean flow boundary layer become before it reaches an equilibrium state for different wave conditions? Can the resulting mean flow properties be predicted by linear models? What is the effect of the wave amplitude? If multiple incident waves with different wave properties approach a boundary how will the mean flow respond? We are pursuing the answers to these and other questions utilizing the numerical experiments.

References

References

- Bowen, A. J., 1969: The generation of longshore currents on a plane beach, *J. Mar. Res.*, 27, 206-215.
- Eriksen, C. C. 1982: Observations of internal wave reflection off sloping bottoms, *J. Geophys. Res.*, 87, 525-538.
- Eriksen, C. C. 1985: Implications of ocean bottom reflection for internal wave spectra and mixing, *J.*

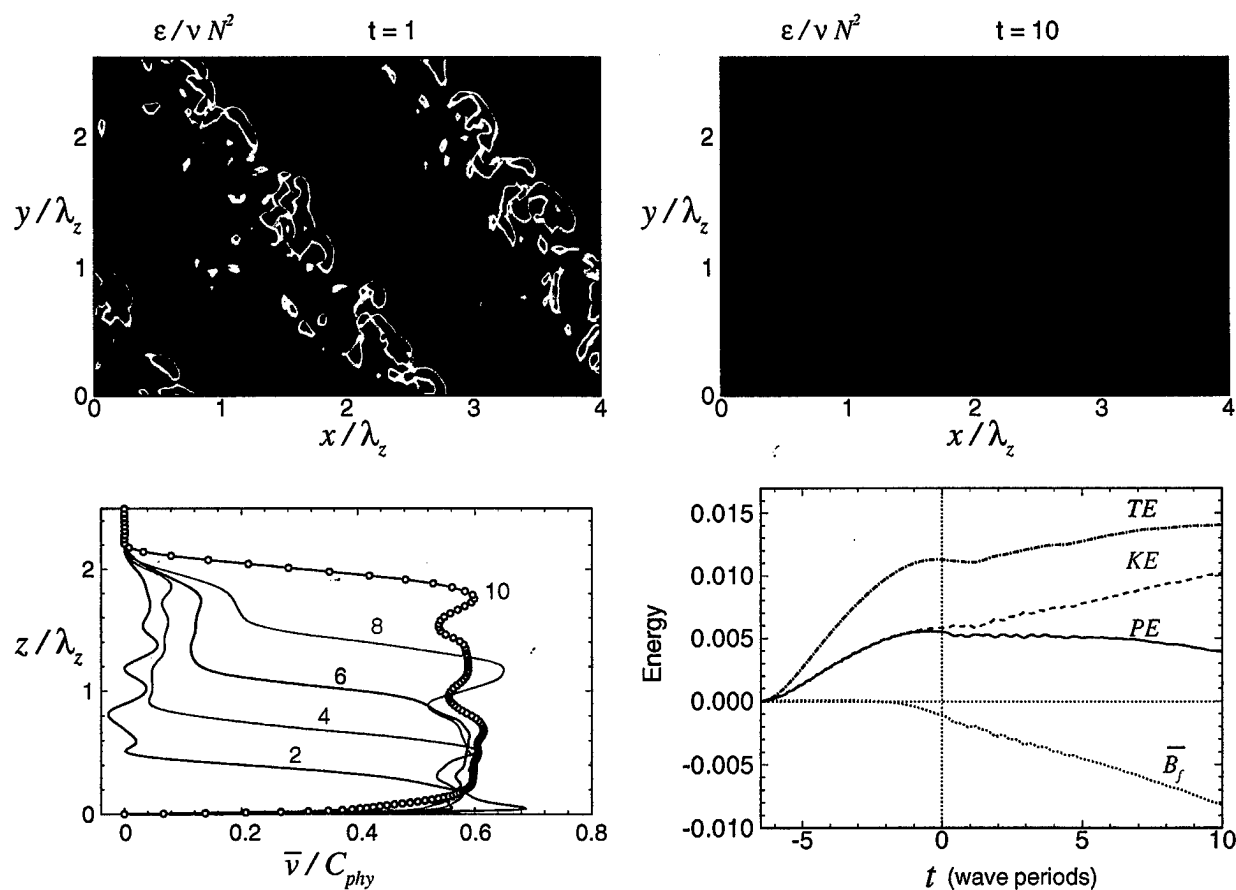


Figure 3. Kinetic energy dissipation rates $\epsilon/\nu N^2$ in a plane parallel to the bottom slope (top row) located at $z = 0.12\lambda_z$, one and ten wave periods after the onset of wave breakdown in the boundary layer for obliquely incident internal waves at the critical frequency for a bottom slope of 20° and $RE = 2000$. Also shown are the mean alongslope v -velocity profiles in the boundary layer at 2, 4, 6, 8 and 10 wave periods after the onset of breaking (lower left), and the volume averages of the kinetic, potential, and total energies and the volume averaged time integrated buoyancy flux (lower right).

- Phys. Oceanogr.*, 15, 9, 1145-1156.
- Eriksen, C. C. 1998: Internal wave reflection and mixing at Fieberling Guyot, *J. Geophys. Res.*, 103, 2977-2994.
- Hogg, N. G., 1971: Longshore currents generated by obliquely incident internal waves, *Geophys. Fluid Dyn.*, 2, 361-376.
- Munk, W. H., 1966, Abyssal Recipes, *Deep-Sea Res.*, 13, 707-730.
- Phillips, O. M., 1977: *The Dynamics of the Upper Ocean*, 2nd ed. (Cambridge University Press, Cambridge, 336 pp.)
- Slinn, D. N., Riley, J. J. 1996. Turbulent mixing in the oceanic boundary layer caused by internal wave reflection from sloping terrain, *Dyn. Atmos. Oceans*, 24, 51-62.
- Slinn, D. N., Riley, J. J. 1998a. Turbulent dynamics of a critically reflecting internal gravity wave, *Theor. Computat. Fluid Dyn.*, 11, 287-310.
- Slinn, D. N., Riley, J. J. 1998b. A model for the simulation of turbulent boundary layers in an incompressible stratified flow, *J. Computat. Phys.*, 144, 550-602.
- Slinn, D. N., Riley, J. J. 1999. Internal wave reflection from sloping boundaries, submitted to *J. Fluid Mech.*
- Slinn, D. N., Allen, J. S., Newberger, P. A., Holman, R. A., 1998, Nonlinear shear instabilities of alongshore currents over barred beaches, *J. Geophys. Res.*, 103, 18,357-18,379.
- Slinn, D. N., Allen, J. S., Holman, R. A., 1999, Along-shore currents over variable beach topography, to appear in *J. Geophys. Res.*
- Thorpe, S. A. 1997: On the interactions of internal waves reflecting from slopes, *J. Phys. Oceanogr.*, 27, 2072-2078.
- Wunsch, C., 1973: On the mean drift in large lakes, *Limnol. Oceanogr.*, 18, 793-795.

Turbulent Properties in a Wave-Energized Benthic Boundary Layer on a Slope

Kraig B. Winters^{1,2} and Gregory N. Ivey²

¹Applied Physics Laboratory, University of Washington, Seattle WA

²Centre for Water Research, University of Western Australia, Australia

Abstract. Laboratory experiments were conducted in which a beam of steadily forced monochromatic internal waves encounters a planar, sloping boundary. Measurements of the rate of dissipation of turbulent kinetic energy ϵ and density flux ρw were made at several locations within the turbulent benthic boundary layer. The observations show that ϵ is approximately constant within a distance h of the bottom and that both h and the average dissipation rate $\langle \epsilon \rangle$ are well predicted by simple scaling arguments. Within the turbulent boundary layer, the time averaged density flux $\langle \rho w \rangle$ is negative. The observed correlation results primarily from motions at frequencies near the forced wave frequency and shows no obvious change in character outside the turbulent boundary layer but within the interaction region of incident and reflecting waves. Motions at frequencies higher than N contribute negligibly to the total correlation. The implications of these results for estimating mixing rates are discussed and a new scaling of the diapycnal diffusivity K_p in terms of ϵ , the fluid viscosity ν and the background stratification N^2 is proposed and applied to the experimental results.

1. Introduction

A series of laboratory experiments was conducted to investigate the properties of boundary layer turbulence generated in a uniformly stratified fluid as a wave beam of finite width forward-reflects from a sloping boundary. The problem is of interest both because sloping boundaries are thought to be preferential locations of wave driven mixing and because such mixing can have important implications for nutrient fluxes in oceans and lakes. The present work is an extension of earlier work (Ivey and Nokes, 1989, Ivey *et al.* 1995) in that turbulent properties of the wave-driven boundary layer are directly measured. In this note we focus in particular on the implications of the measurements for estimating diapycnal mixing. A more complete discussion of these experiments can be found in Ivey *et al.* (1998).

Experiments

2.1. Facility

The experiments were conducted in a glass walled tank with a working section 3 m long by 54 cm wide with a depth of 60 cm. A plexiglass sheet was used to form a uniform sloping bed at angle β as shown in Figure 1.

The tank was filled with linearly stratified salt water to a depth of 50 cm. A folding paddle consisting of eight hinged blades, each 5 cm wide by 53.5 cm long, was os-

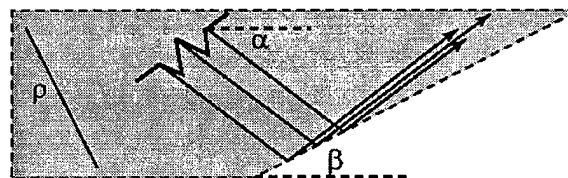


Figure 1. Geometry of experiments. Internal waves propagate at an angle α towards a smooth bed inclined at angle β . The experiments were conducted for forward reflecting waves under steady forcing in uniformly stratified salt water.

cillated at a constant frequency ω_f to excite an internal wave beam propagating toward the sloping bed. The wavelength in the plane of the paddle was 20 cm and the entire paddle assembly was oriented at an adjustable angle α as indicated in the schematic.

The geometric parameter $\gamma = \sin \alpha / \sin \beta$ determines the direction of wave reflection at the sloping boundary. The experiments reported here are for forward-reflecting waves with $1.25 < \gamma < 3.76$.

2.2. Procedure

The experiments were initiated by oscillating the paddle blades at the forcing frequency ω_f . Typical experimental parameters were $N \approx 0.71 \text{ s}^{-1}$, $\omega_f \approx 0.5 \text{ s}^{-1}$ with characteristic wave amplitudes a of 1 cm just above the turbulent

boundary layer. The experiments were run under steady forcing conditions for approximately 5 minutes. Data were recorded throughout each run and analyzed only after initial transients had decayed and quasi-steady conditions had been established.

2.3. Stratification Measurements

Vertical density profiling was accomplished using a fast-response, four-electrode PME microscale conductivity probe, dynamically calibrated via an auxiliary siphoning probe, and a Thermometrics FP07 thermistor. Sensor spacing for the three probes was less than 4 mm. The probes were mounted on a computer-controlled assembly and lowered at a speed of 10 cm/s. Direct and differentiated output from each sensor was sampled and recorded at 100 Hz using a 16-bit A/D converter.

Vertical profiling was carried out continuously throughout the experiments. Differences in N^2 estimated by averaging monotonized profiles taken during the experiments and averages of restratified profiles taken before and after individual experiments were negligible.

2.4. Dissipation Measurements

Estimates of the rate of dissipation of turbulent kinetic energy were made from measurements of temperature gradients along horizontal traverses at fixed distances from the sloping bottom. Horizontal profiling takes advantage of the two-dimensional nature of the wave forcing and results in much longer record lengths than would be possible with vertical profiling. FP07 thermistors were traversed at 10 cm/s and sampled at 100 Hz. Interior segments of 256 mm, sampled over 2.56 seconds, thus yielded 256 data points for spectral analysis. These data were then fit to the theoretical Batchelor spectrum to produce estimates of the dissipation rate ϵ . From the work of *Luketina and Imberger* (1998) we estimate the accuracy of the dissipation estimates to be about 10%.

Measured dissipation rates are plotted as a function of perpendicular distance from the bottom in Figure 2 for several experiments. The distance coordinate is scaled by $h = 0.1 \lambda_p$, where λ_p is the wavelength measured perpendicular to the sloping bottom as discussed in *Ivey et al.* 1995. The dissipation rates are scaled by the quantity $\epsilon_* = E_{in}/hl$ where E_{in} is the incident energy flux and l is the along slope mixing length determined by the intersection region of incident and linearly reflecting wave rays. This scaling implicitly assumes a reflection coefficient of zero. A somewhat better result was obtained for a reflection coefficient of 0.3 but a zero value was used here for simplicity. Scaled dissipation rates are approximately uniform for $z/h < 1$ and decay rapidly with distance for heights $z/h > 1$. The scale h can thus be taken as the defining scale of the turbulent boundary layer. The values

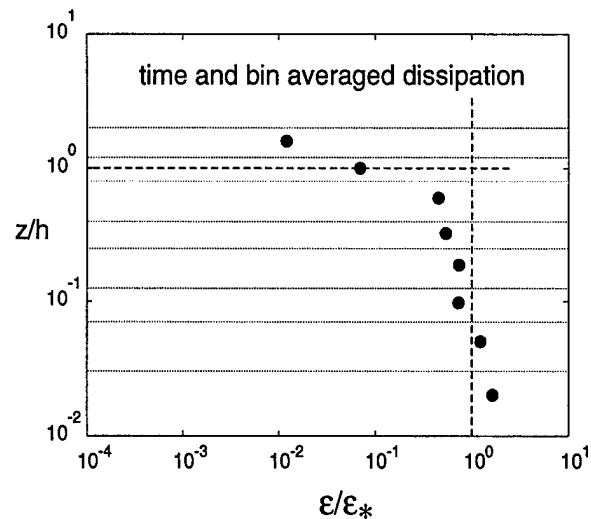


Figure 2. Measured dissipation rates as a function of perpendicular distance from the sloping boundary. Heights are scaled by the estimated boundary layer scale h . Dissipation rates scaled by the scale ϵ_* (see text). The figure summarizes all experiments conducted in which dissipation measurements were made.

shown have been averaged within the vertical bins marked in the figure.

Variability within individual experiments (not shown) is most likely due to a dependence on the phase of the incident waves. To first order, the simple scaling with h and ϵ_* appears to collapse the time-averaged dissipation rates within the boundary layer over a moderate range of the criticality parameter γ . The magnitudes of the unscaled dissipation rates within the boundary layer were generally between 5×10^{-7} and $10^{-6} \text{ m}^2/\text{s}^3$. These values correspond to ϵ/vN^2 of approximately 1 for the range of stratifications used in the experiments.

2.5. Flux Measurements

Time series measurements were made at fixed positions using the Portable Flux Profiler (PFP) (*Imberger and Head*, 1994). The PFP is equipped with duplicate pairs of thermistors and fast response conductivity sensors. A laser Doppler anemometer (LDA) measures two independent components of velocity. The temperature and conductivity sensors were separated by 2.5 mm in the horizontal, the time response and resolution of the thermistors was 12 ms and 0.001 C and those of the conductivity probes 4 ms and 0.0004 S/m. The LDA measured two velocity components along and across the (inclined) probe axis with a resolution of 0.001 m/s. Temperature and conductivity signals were recursively filtered to match the difference in time response. The probe itself

was mounted up-slope of the interaction region, with sensors protruding into the region of interest, to minimize the effects of flow around the probe casing. Fluxes of both mass and momentum were determined from time series of two velocity components, temperature and conductivity over sampling periods of approximately five minutes after the paddle motion was initiated.

Figure 3 shows the co-spectrum of density and vertical velocity Co_{pw} in area-preserving form at four different heights for a typical experiment. The heights are normalized by the boundary layer scale h determined by the dissipation measurements. A negative value of the co-spectrum indicates a release of available potential energy and a transport leading to restratification. The clearest feature for all four heights is the large negative contribution at the forcing frequency ω_f . This feature dominates the total flux with the result that the total flux is negative at all heights measured. Note that even for $z/h = 1.31$, the time series measurements were still made close to the bottom boundary, i.e., within the region where incident and reflected waves can interact according to linear theory (see Figure 1). The magnitude of the flux near ω_f is comparable both inside and outside the boundary layer but decays significantly very close to the bed. The co-spectrum is small in magnitude and can be of either sign at frequencies near and greater than N .

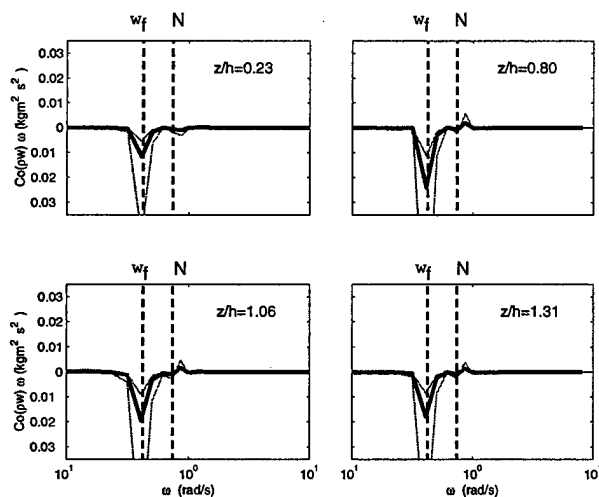


Figure 3. Co-spectrum of vertical velocity and density at four heights for a typical experiment. Spectral analysis was conducted for time series sampled at 100 Hz for approximately 5 minutes. The forced wave and the buoyancy frequencies are indicated on the figure.

3. Interpretation

The benthic boundary layer is turbulent. Typical cycle-averaged dissipation rates within the boundary layer are on the order of $10^{-6} \text{ m}^2/\text{s}^3$. This rate is *much* greater than

the laminar dissipation rate $\epsilon_{\text{wave}} \approx v(ak\omega_f)^2 \approx 10^{-9} \text{ m}^2/\text{s}^3$ characteristic of the incident wave motion. Average dissipation rates are approximately uniform within a distance h of the boundary and decay rapidly to laminar rates at distances greater than h .

Though the enhanced dissipation rates indicate that the flow is turbulent, the parameter $\epsilon/\nu N^2$ is only of order 1. When $\epsilon/\nu N^2$ is equal to 1, the Ozmidov scale $L_O = (\epsilon/N^3)^{1/2}$ is equal to the Kolmogorov scale $L_K = (\nu^3/\epsilon)^{1/4}$. This is usually taken to indicate that there is no bandwidth available for a turbulent cascade. In these experiments however, there is an additional scale ($\approx a$), the scale at which waves overturn and break. Energy is continuously supplied to the boundary layer at this scale. Thus, though $\epsilon/\nu N^2 = 1$, there is a finite range of scales, from L_K to a , within which a nonlinear cascade can occur.

The mass fluxes measured within the boundary layer are signatures of nonlinear interactions between the incident and reflecting waves. The correlation is dominated by frequencies close to the incident wave frequency with little contribution from significantly higher frequency motions. The observed mass fluxes are not spatially correlated with the dissipation rates, which are clear signatures of turbulence intensity. Since the flux is carried primarily by wavelike motions near the forcing frequency, and these motions are not confined to the zone of enhanced dissipation but extend throughout region where incident and reflected waves can interact, the buoyancy flux measured within the turbulent layer is difficult to interpret. It would appear that global rather than local measurements of buoyancy flux are required to remove the wavelike signature, even after long-time averaging.

Inference of diapycnal mixing from the local flux measurements is thus problematic. The observed local correlation $\langle pw \rangle$ is negative within the quasi-steady turbulent mixing zone. If we define a diapycnal diffusivity K_p in terms of the observed flux, i.e., as $\langle pw \rangle / |dp/dz|$, then we must conclude that $K_p < 0$, which is clearly not sensible. It would appear that the (unmeasured) positive fluxes well outside the boundary layer should be included. Unfortunately, this is not possible. It is tempting however to attempt a local analysis based only on the high frequency motions, say for frequencies greater than N . If only these frequencies are included however, the experiments suggest that K_p is negligible. A negligible diffusivity implies that there is a negligible cascade of scalar variance to small scales where molecular diffusion occurs. It is not at all clear how a turbulent flow could sustain a velocity cascade sufficient to enhance laminar dissipation rates by three orders of magnitude but not support a corresponding scalar cascade. We suggest that a properly de-

finned diffusivity should be non-negligible for these experiments. The question is how should we define the diffusivity?

These observations lead to a rather fundamental question: should we always expect *local* measurements of buoyancy flux to be highly correlated with turbulent dissipation and/or mixing when the turbulence is localized in space? After all, in these experiments the waves that carry the flux are clearly not confined to the mixing region. If not, is it reasonable to infer mixing rates from formulae based fundamentally on a *definition* of K_p in terms of the local buoyancy flux $\langle \rho w \rangle$?

These experiments provide an opportunity to re-evaluate some of our fundamental assumptions regarding the link between dissipation, buoyancy flux and irreversible mixing in situations where turbulence is spatially localized and results from the collapse of relatively energetic internal waves. We suggest that these characteristics are not confined to turbulence at sloping boundaries but may also be characteristic of much of the mixing in the interior of stratified basins.

Diapycnal diffusivities K_p are frequently inferred from dissipation rates ϵ using the formula $K_p = 0.2 \epsilon / N^2$. It is worthwhile to remind ourselves that this expression is derived by assuming a local steady balance of turbulent kinetic energy (TKE), with divergence terms neglected and the buoyancy flux acting as a sink for TKE. *Defining* the diffusivity in terms of the local mass flux, i.e., via $K_p = -\langle \rho w \rangle / (d\rho/dz)$ and substituting into the assumed TKE balance leads to an expression which is often simplified to the familiar result $K_p = 0.2 \epsilon / N^2$. It would appear that this result can be no better than the assumption that the diffusivity is reasonably defined in terms of the local buoyancy flux. Since we have already argued that using the measured flux to estimate the diffusivity is problematic in these experiments, it is difficult to justify estimating the diffusivity from $0.2 \epsilon / N^2$.

4. Proposed Scaling of K_p

Many of these conceptual difficulties can be alleviated by returning to first principles and defining a diapycnal diffusivity in terms of irreversible diffusive flux at molecular scales. The average diffusive or diapycnal flux F across an isopycnal surface S is given by (Winters and D'Asaro, 1996)

$$F = \frac{1}{A} \int \kappa |\nabla \rho| dS = \kappa \frac{\langle |\nabla \rho| \rangle^2}{|d\rho/dz_*|} \quad (1)$$

where the quantity z_* is an isopycnal coordinate with dimensions of length, the angled brackets represent a spatial average over the isopycnal surface S , κ is the thermal diffusivity and A is the geometrical projection of S onto a horizontal plane. If we define the diapycnal diffusivity K_p as the average flux F divided by the thermodynamically relevant gradient, i.e., as

$$K_p = \frac{F}{|d\rho/dz_*|} = \kappa \frac{\langle |\nabla \rho| \rangle^2}{|d\rho/dz_*|^2} \quad (2)$$

where $\rho(z_*)$ is the adiabatically resorted reference gradient. Scaling estimates can be obtained for K_p defined in this way by considering an idealized model of turbulent eddies under the influence of buoyancy.

We consider stably stratified fluids with $Pr = (\nu/\kappa) > 1$, an ambient N^2 given by $(-g/\rho_0)(d\rho/dz_*)$ and turbulent motions characterized by eddies of scale L . The maximum density difference $\Delta\rho$ between fluid parcels within an eddy is thus of order $L |d\rho/dz_*|$. Straining or wrapping motions result in a convergence of isopycnal surfaces with the characteristic density difference $\Delta\rho$. The separation distance between two such surfaces will decrease until it becomes comparable to the Batchelor scale L_B at which point molecular diffusion will prevent further enhancement of the gradients. Since the gradient spectra will be concentrated at small scales, this idealized model implies that the characteristic magnitude of the density gradient will be given by

$$\langle |\nabla \rho| \rangle \sim \frac{\Delta\rho}{L_B} \sim \frac{|d\rho/dz_*| L}{L_B} \quad (3)$$

Substituting (3) into (2) yields

$$K_p \sim \kappa \left(\frac{L}{L_B} \right)^2 \quad (4)$$

The characteristic displacement scale L , i.e., the scale that supplies the density contrast in (3) will depend on both fluid and flow properties. We now outline three distinct flow regimes and give scaling relations for the diapycnal diffusivity K_p .

4.1 Laminar flow

In this regime the gradients induced by eddies are not appreciably greater than the background gradient and so $L \approx L_B$ and K_p reduces to the molecular value κ as required.

4.2 Weak density-stratified turbulence

We wish to estimate a scale L proportional to the scalar contrast when the turbulence is weak enough that the fluid viscosity is dynamically important. If the scalar were passive, then the scale could be determined by assuming that $L = L(\epsilon, \nu)$ yielding $L = L_K = (\nu^3/\epsilon)^{1/4}$ as discussed in *Batchelor* (1959). For density-stratified fluids, even small scale motions require work to be done against gravity and we thus expect the buoyancy N to be important and to reduce the characteristic scale L . Assuming that $L = L(\epsilon, \nu, N)$ gives $L = (\nu\epsilon)^{1/4}/N^2$. N will be important when the buoyancy time-scale $1/N$ is less than (or of the same order as) the straining time scale $(\nu/\epsilon)^{1/2}$. This is equivalent to the condition $(\epsilon/\nu N^2)$ is less than or equal to order 1. We note that this scale L approaches L_B as $\epsilon \rightarrow \kappa N^2$ from above and $L \rightarrow L_K$ as $\epsilon \rightarrow \nu N^2$ from below.

Substituting this result into equation (4) yields

$$K_p \sim \frac{\epsilon}{N^2} = \nu \left(\frac{\epsilon}{\nu N^2} \right) \quad (5)$$

This expression is equivalent in form to the familiar expression $K_p = 0.2\epsilon/N^2$ but required no assumptions about the buoyancy flux or the balance of turbulent kinetic energy. The scaling analysis offers no information on the constant of proportionality.

4.3 Energetic density-stratified turbulence

For energetic density-stratified turbulence, the fluid viscosity ν is no longer dynamically relevant. We expect L to be larger than for weak density-stratified turbulence and to depend only on ϵ and N . In this regime buoyancy will act to suppress scales larger than $L_O = (\epsilon/N^3)^{1/2}$ and so an upper bound on the length scale L will thus be the Ozmidov scale L_O . Substitution into (4) gives

$$K_p \sim \nu \left(\frac{\epsilon}{\nu N^2} \right)^{3/2} \quad (6)$$

The requirement that L_O be greater than the maximum L in the weakly turbulent regime is simply that $L_O > L_K$ or $\epsilon/\nu N^2$ is order 1 or greater. In the limit of vanishing N , not only does L_O become unbounded but our simple conceptual picture of the characteristic density contrast in an eddy being proportional to the ambient gradient becomes increasingly inappropriate. We thus expect equation (6) to be an upper bound and to overestimate the diffusivity in the unstratified limit.

5 Application of Scaling to Experiments

The time averaged dissipation rates are in the range $(\epsilon/\nu N^2) \approx 1$ for the experiments under discussion. This regime sits at the upper limit of weak density-stratified turbulence and the lower limit of energetic density-stratified turbulence. Thus, either of equations (5) or (6) can be used to estimate the magnitude of the diapycnal diffusivity K_p . Both formulas are in agreement and give $K_p \approx O(\nu)$ as $\epsilon/\nu N^2 \rightarrow 1$.

Note that ν is equal to Pr times the molecular diffusivity κ and for a salt-stratified fluid $Pr \approx 700$. The scaling results thus predict an enhancement of diffusivity by nearly three orders of magnitude over molecular levels. This result seems reasonable in light of our earlier observations that measured ϵ values were approximately 1000 times the laminar rate ϵ_{wave} . We note however that this interpretation is not consistent with the notion that when $\epsilon/\nu N^2 < 15-25$, turbulence is too weak to support turbulent mixing.

6. Discussion

Experiments were conducted in which nearly monochromatic wave beams in a uniformly stratified fluid forward reflect at a sloping boundary. Under conditions of steady forcing, measurements of the dissipation rate of turbulent kinetic energy revealed the presence of a turbulent benthic boundary layer with nearly uniform time-averaged properties. Despite the simplicity of the experimental set-up, the observations are not readily explained using existing models of stratified turbulence.

The observations underscore the difficulties inherent in separating "wavelike" motions from "turbulent" motions, a notion implicit in existing models. The measured turbulence has $\epsilon/\nu N^2$ of order 1 which implies $L_O = L_K$ and thus (apparently) a vanishing bandwidth for a "turbulent" cascade. In these experiments however, energy is supplied to the boundary layer at the wave scale a which is much larger than L_K . Apparently, the dynamics of breaking waves supports a cascade from a to L_K and thus a greatly enhanced dissipation rate. Are the motions responsible for this cascade "wavelike" or "turbulent"?

The question is not entirely semantic because defining K_p in terms of the buoyancy flux requires that these motions, which are characterized by $\langle p w \rangle < 0$, be regarded as "wavelike" and somehow separated out from the "turbulent" motions before examining the local TKE balance. If such a separation is difficult or impossible in controlled laboratory settings, how useful is the concept when applied to time dependent mixing events in the field? How

much faith should we have in the resulting formula $K_p = 0.2\epsilon/N^2$? Despite the importance of this issue there are no controlled experiments that we are aware of where an appropriately defined diapycnal diffusivity, ϵ and N^2 have been independently measured. What is the relationship between these quantities and how does it depend on flow and fluid properties?

We have attempted to address these difficulties by avoiding the necessity of a wave/turbulence decomposition and defining K_p directly in terms of the average diapycnal flux (2). The resulting formula is diagnostic; it requires the measurement of small-scale density gradients and averaging on isopycnal surfaces. The expression is positive definite, greater than or equal to the molecular diffusivity κ and independent of the sign of the buoyancy flux, all properties that would appear intuitively desirable.

Introducing a simple model for the estimation of the density gradients in (2) results in scaling laws for K_p in terms of ϵ and two fluid properties ν and N . The model, and hence the resulting scaling, is based on two related ideas. The first is that at scales large compared to turbulent eddies, the fluid exists in a state not far from its adiabatic equilibrium and so the characteristic density contrast within eddies is proportional to the product of the eddy scale and the ambient density gradient. The second is that the eddy scale is influenced by buoyant restoring forces and so N must be included in the scaling. Rather than splitting waves and turbulence, these ideas suggest a fundamentally wavelike nature of density-stratified turbulence, i.e., even small-scale vertical motions induce a restoring force. Clearly, these ideas break down in the limit of vanishing N . No insight is gleaned from the analysis regarding an upper limit on the range of validity.

An experimental program in which ϵ , N , and changes in background potential energy were measured in a controlled environment would aid in the clarification of many of these issues.

Acknowledgments. We would like to acknowledge the contributions of Prabath DeSilva who carried out much of the laboratory work. Nicky Grigg also assisted with the preliminary experiments. The flux measurements were made possible by Jorg Imberger who made the PFP available to us. This work was supported by the Office of Naval Research (Code 322 PO), the National Science Foundation and the Australian Research Council.

References

- Batchelor, G. K., Small-scale variation of convected quantities like temperature in a turbulent fluid. Part 1: General discussion and the case of small conductivity, *J. Fluid Mech.*, 5, 113-133, 1959.
- Imberger J., and R. Head, Measurements of turbulent properties in a natural system, in *Fundamentals and advancements in hydraulic measurements and experimentation*, pp. 1-20, ASCE, Buffalo, 1994.
- Ivey, G. N., and R. I. Nokes, Vertical mixing due to the breaking of critical internal waves on sloping boundaries, *J. Fluid Mech.*, 204, 479-500, 1989.
- Ivey, G. N., I. P. D. DeSilva, and J. Imberger, Internal waves, bottom slopes and mixing. *1995 Aha Hulikoa Hawaiian Winter Workshop on Topographic Effects in the Ocean*, pp. 199-205, Honolulu, Hawaii.
- Ivey, G. N., K. B. Winters, and I. P. D. DeSilva, Turbulent mixing in an internal wave energised benthic boundary layer on a slope, *J. Fluid Mech.*, submitted, 1998.
- Luketina, D. and J. Imberger, Determining turbulent kinetic energy dissipation from Batchelor curve fitting, *J. Atmosph. And Oceanic Technology*, (submitted) 1998.
- Winters, K. B. and E. A. D'Asaro, Diascalar flux and the rate of fluid mixing, *J. Fluid Mech.*, 317, 179-193, 1996.

On Redistributed Energy Fluxes in Topographic Scattering Problems

Peter Müller

Department of Oceanography, School of Ocean and Earth Science and Technology,
University of Hawaii, Honolulu

Abstract. The scattering of infinitesimal inviscid internal waves at topography redistributes the incoming energy flux in wave number and physical space. This energy flux redistribution describes the scattering process most succinctly. The definitions of the redistributed energy flux in wave number space and in various subspaces are given. All of the incident energy flux is redistributed in wave number space. The total redistributed energy flux in subspaces is only a fraction of the total incident flux and depends on the choice of subspace. These concepts are illustrated with examples from the scattering at an infinite straight slope, random infinitesimal topography, and finite topography in a finite-depth ocean.

1. Introduction

The energy flux, as opposed to the energy or shear, is the most fundamental quantity in analyzing the scattering of infinitesimal inviscid internal waves at topography. This is because the conservation of energy implies that the total energy flux incident onto the topography equals the total energy flux scattered away from the topography. The incoming energy flux is only redistributed both in physical and wave number space. The details of this redistribution depend on the frequency and wave number of the incident wave and on the topography. The definition and interpretation of the redistributed energy flux is straightforward in the complete space of independent variables that describe the scattering process. In this space all of the incident flux is redistributed. In applications one usually considers the redistribution in some reduced space. The redistributed energy flux in such reduced spaces is smaller than the incident energy flux and depends on the choice of the reduced space. We illustrate these concepts by examples taken from the scattering at random infinitesimal topography, the reflection at an infinite straight slope, and the scattering at finite topography in a finite depth ocean. The incident internal wave field in all these examples is assumed to be a typical deep ocean internal wave field described by the Garrett and Munk spectrum.

2. The Redistributed Energy Flux

The energy flux vector is given by

$$\mathbf{F} = \mathbf{v} E \quad (2.1)$$

where \mathbf{v} is the group velocity vector and E the energy. The flux normal to a surface with normal vector \mathbf{n} is

$$\mathbf{F} \cdot \mathbf{n} = \mathbf{v} \cdot \mathbf{n} E \quad (2.2)$$

Let the slope or vertical inclination of the surface be $\gamma = \tan \varphi_0$. One can then orient the horizontal coordinates such that $0 \leq \varphi_0 \leq \pi/2$ and $\mathbf{n} = (1 + \gamma^2)^{-1/2} (-\gamma, 0, 1)$. The normal vector is assumed to point out of the surface into the fluid. A plane internal wave is characterized by its wave number vector $\mathbf{k} = (k_1, k_2, k_3)$. The frequency ω is given by the dispersion relation. Scattering at topography does not change the frequency. It is therefore advantageous to work in a representation that includes the frequency. Here we choose the frequency ω , the magnitude $\alpha = (k_1^2 + k_2^2)^{1/2}$ of the horizontal wave number vector, the azimuthal direction $\phi = \arctan(k_2/k_1)$, and the sign $s = \text{sgn}(k_3)$ of the vertical wave number component as the independent variables to describe a plane internal wave. Then

$$\mathbf{v} \cdot \mathbf{n} = -\frac{1}{(1 + \gamma^2)^{1/2}} \frac{1}{\alpha} \left(\frac{\omega^2 - f^2}{N^2 - f^2} \right) \left(\frac{N^2 - \omega^2}{\omega^2} \right)^{1/2} \left[\gamma(N^2 - \omega^2) \cos \phi + s(\omega^2 - f^2)^{1/2} \right] \quad (2.3)$$

where f is the Coriolis frequency and N the Brunt-Väisälä frequency. Expressions for other independent variables can be obtained by standard transformations. Figure 1 shows the areas in (ω, ϕ, s) -space for which $\mathbf{v} \cdot \mathbf{n} \geq 0$.

The flux incident on a surface with normal vector \mathbf{n} is

$$F_i(\omega, \alpha, \phi, s) = \begin{cases} |\mathbf{v} \cdot \mathbf{n}| E_i(\omega, \alpha, \phi, s), & \text{if } \mathbf{v} \cdot \mathbf{n} \leq 0 \\ 0, & \text{if } \mathbf{v} \cdot \mathbf{n} \geq 0 \end{cases} \quad (2.4)$$

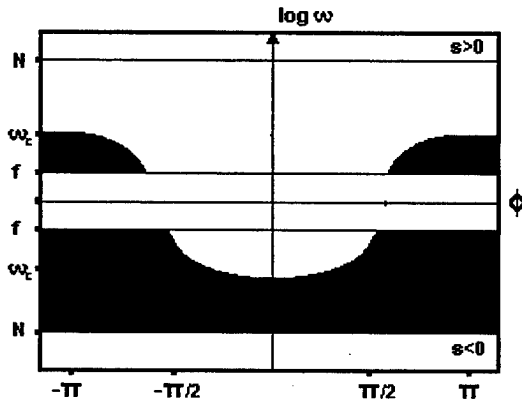


Figure 1. Areas (shaded) in (ω, ϕ, s) -space for which $\mathbf{v} \cdot \mathbf{n} \geq 0$.

The scattered energy flux is

$$F_s(\omega, \alpha, \phi, s) = \begin{cases} |\mathbf{v} \cdot \mathbf{n}| E_s(\omega, \alpha, \phi, s), & \text{if } \mathbf{v} \cdot \mathbf{n} \geq 0 \\ 0, & \text{if } \mathbf{v} \cdot \mathbf{n} \leq 0 \end{cases} \quad (2.5)$$

Here E_i and E_s are the energy spectra of the incident and scattered wave field. Note that F_i and F_s are both defined to be positive. In scattering problems the incident energy spectrum is specified. The scattered energy spectrum is calculated from some scattering theory. In applications the incident energy spectrum is often specified to be

$$\begin{aligned} E_i(\omega, \alpha, \phi, s) &= E_{GM}(\omega, \alpha, \phi, s) \\ &= \frac{1}{2\pi} \frac{1}{2} E_{GM}(\omega, \alpha) \end{aligned}$$

where

$$E_{GM}(\omega, \alpha) = E_0 b^2 N_0 N B(\omega) \frac{A(\frac{\alpha}{\alpha_*})}{\alpha_*} \quad (2.6)$$

is the horizontally isotropic and vertically symmetric Garrett and Munk spectrum (henceforth GM-spectrum, *Munk* 1981), given here in standard notation.

The basic diagnostic tool to describe the effect of scattering is the redistributed energy flux

$$D(\omega, \alpha, \phi, s) = F_s(\omega, \alpha, \phi, s) - F_i(\omega, \alpha, \phi, s) \quad (2.7)$$

Since the incident and scattered $(\omega, \alpha, \phi, s)$ -values are mutually exclusive, a given set of values is either an incoming or a scattered wave. All of the incident flux is redistributed in $(\omega, \alpha, \phi, s)$ -space. The total redistributed energy flux in $(\omega, \alpha, \phi, s)$ -space is defined as the integral over the positive (or negative) lobe of $D(\omega, \alpha, \phi, s)$, i.e., by

$$T = \frac{1}{2} \int d\omega \int d\alpha \int d\phi \sum_s \int |D(\omega, \alpha, \phi, s)| \quad (2.8)$$

and the above statement becomes

$$T = \int d\omega \int d\alpha \int d\phi \sum_s F_i(\omega, \alpha, \phi, s) =: F_i \quad (2.9)$$

One can also determine the redistributed fluxes and the total redistributed fluxes in various reduced spaces such as

$$D(\omega, \alpha) = \int d\phi \sum_s D(\omega, \alpha, \phi, s) \quad (2.10)$$

$$T_1 = \frac{1}{2} \int d\omega \int d\alpha |D(\omega, \alpha)| \quad (2.11)$$

or

$$D(\alpha) = \int d\omega D(\omega, \alpha) \quad (2.12)$$

$$T_2 = \frac{1}{2} \int d\alpha |D(\alpha)| \quad (2.13)$$

For scattering at topography, there is no redistribution in frequency space

$$D(\omega) = \int d\alpha D(\omega, \alpha) \equiv 0 \quad (2.14)$$

Instead one introduces

$$D^+(\omega) = \frac{1}{2} \int d\alpha |D(\omega, \alpha)| \quad (2.15)$$

which describes the frequencies where most of the redistribution occurs.

In the following we illustrate these concepts with a few examples.

3. Reflection at a Flat Bottom

Reflection at a flat bottom $z = 0$ is the most trivial reflection problem. Internal wave kinematics implies that a downward propagating wave $(\omega, \alpha, \phi, s=+1)$ is reflected into an upward propagating wave $(\omega, \alpha, \phi, s=-1)$. Thus

$$F_s(\omega, \alpha, \phi, s) = F_i(\omega, \alpha, \phi, -s) \quad (3.1)$$

and

$$D(\omega, \alpha, \phi, s) = \begin{cases} -F_i(\omega, \alpha, \phi, s), & \text{if } s = +1 \\ F_i(\omega, \alpha, \phi, -s), & \text{if } s = -1 \end{cases} \quad (3.2)$$

The flux is redistributed from downward propagating waves ($s = +1$) to upward propagating waves ($s = -1$). There is no redistribution in (ω, α, ϕ) -space

$$D(\omega, \alpha, \phi) = \sum_s D(\omega, \alpha, \phi, s) \equiv 0 \quad (3.3)$$

The total redistributed energy flux in $(\omega, \alpha, \phi, s)$ -space equals the total downward energy flux

$$T = \int d\omega \int d\alpha \int d\phi F_i(\omega, \alpha, \phi, s=+1) =: F_3 \quad (3.4)$$

For the GM-spectrum (2.6) one finds $F_3 = 17.6 \text{ mW m}^{-2}$, if $N = 0.4 \text{ cph}$ (deep ocean), and $f = 0.042 \text{ cph}$ (mid latitudes).

4. Scattering at Random Infinitesimal Topography

The scattering at random infinitesimal topography has been studied by perturbation methods by various authors (e.g., Cox and Sandstrom, 1962; Rubenstein, 1988; Müller and Xu, 1992). Here we draw on the results of Müller and Xu.

Consider random infinitesimal topography

$$z = h(x, y) \quad (4.1)$$

where $h(x, y)$ is a statistically homogeneous random field with zero mean and spectrum $H(\alpha)$. An incident wave with wave number α that interacts with

bottom component α' is scattered to wave number $\alpha'' = \alpha + \alpha'$ (Bragg scattering). The incident flux is downward. The scattered flux is upward. The total redistributed flux in $(\omega, \alpha, \phi, s)$ -space is thus F_3 which is 17.6 mW m^{-2} for the GM-spectrum.

Figure 2 shows the redistributed energy flux $D(\omega, \alpha)$ in (ω, α) -space. The energy flux is redistributed from low to high wave numbers, most efficiently at low frequencies. The total redistributed energy flux in (ω, α) -space is 1.2 mW m^{-2} , only about 6.8% of the total incoming flux of 17.6 mW m^{-2} .

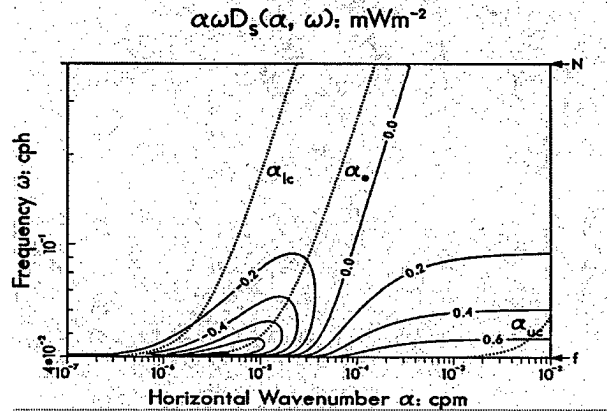


Figure 2. Contours of redistributed energy flux $D(\alpha, \omega)$ horizontal wave number and frequency in a variance-conserving representation. The dotted lines are the low wave number cutoff $\alpha_{lc}(\omega)$, the bandwidth $\alpha(\omega)$ and high wave number cutoff $\alpha_{uc}(\omega)$ of the Garrett and Munk spectrum. (From Müller and Xu, 1992).

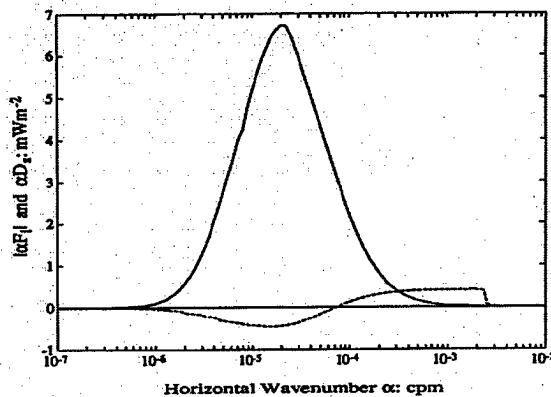


Figure 3. Incident energy flux $F_i(\alpha)$ (solid line) and redistributed energy flux $D(\alpha)$ (dashed line) as a function of horizontal wave number in a variance-conserving representation. (From Müller and Xu, 1992).

Figure 3 shows the incident energy flux $F_i(\alpha)$ and

the redistributed energy flux $D(\alpha)$. $D(\alpha)$ again exhibits the transfer from low to high wave numbers seen in Figure 2. However, the total redistributed energy flux in α -space is 1.14 mW m^{-2} , slightly less than the total redistributed energy flux in (ω, α) -space. During frequency integration of $D(\omega, \alpha)$ some cancellations of positive and negative contributions occur. The zero line of $D(\omega, \alpha)$ depends on frequency and wave number (see Figure 2). The cancellations are, however, small. Figure 4 displays the incident energy flux $F_i(\omega)$ and $D^+(\omega)$ and again shows that most of the redistribution energy occurs at low frequencies.

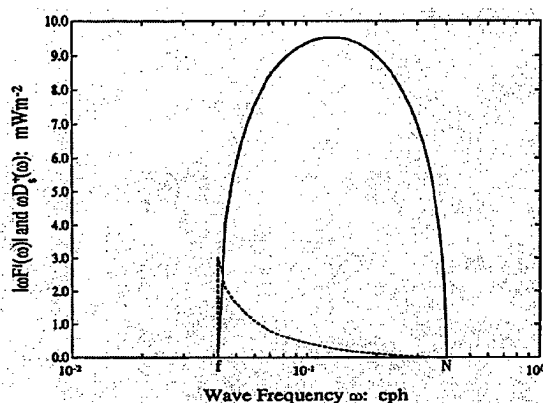


Figure 4. Incident energy flux $F_i(\omega)$ (solid line) and energy flux $D^+(\omega)$ (dashed line) as a function of frequency in a variance-conserving representation. (From Müller and Xu, 1992.)

5. Reflection at an Infinite Straight Slope

The reflection of an incident GM-spectrum off an infinite straight slope was first calculated by Eriksen (1985). Here we use results given in Müller and Xu (1992).

The reflection laws are algebraically quite complex. The case of normal incidence is considered in Figure 5. Both the incident and reflected wave number lie in the (k_1, k_3) -plane. Figure 5 shows the regions of permissible incident waves and the regions to which these incident waves are reflected. A particular role in this diagram is played by the frequency cone that has an inclination $\theta = \arctan(k_3/k_1)$ perpendicular to the bottom slope. This is the cone of critical frequency

$$\omega_c^2 = N^2 \sin^2 \varphi_0 + f^2 \cos^2 \varphi_0 \quad (5.1)$$

Incident waves of critical frequency are reflected to waves with infinite wave number and zero group velocity. The incident energy flux cannot propagate away from the boundary. The energy increases without bound. The behavior of the reflection process is different for sub- and supercritical frequencies. The areas of sub- and supercritical frequencies are also indicated in Figure 5.

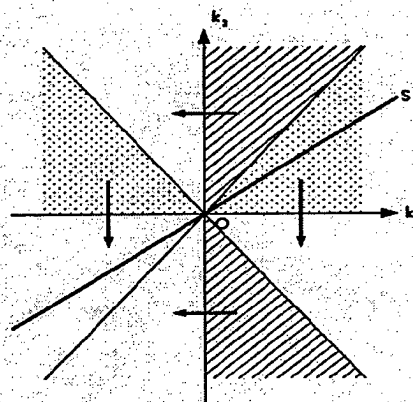


Figure 5. Regions of permissible incident and reflected waves in the horizontal-vertical wave number plane. The heavy solid straight line represents the bottom slope. The light solid lines represent the critical frequency cone. The cross-hatched and stippled regions are permissible incident wave numbers. For the cross-hatched regions the reflection is subcritical, for the stippled region the reflection is supercritical. The regions to which the incident wave numbers become reflected are indicated by the arrows. (From Müller and Xu, 1992).

The incident and redistributed energy fluxes $F_i(\omega, \alpha)$ and $D(\omega, \alpha)$ are shown in Figure 6 as a function of horizontal wave number for three different frequencies. There is a redistribution from medium to low and high wave numbers. The total incident energy flux is the flux normal to the slope. It is 18.2 mW m^{-2} for the GM-spectrum and thus slightly larger than the total vertical energy flux of 17.6 mW m^{-2} considered in the previous section. The total redistributed energy flux in (ω, α) -space is 3.89 mW m^{-2} or about 21% of the incoming flux.

The fluxes $F_i(\alpha)$ and $D(\alpha)$ in wave number space are shown in Figure 7. The flux is mainly redistributed from medium to high wave numbers, with only a small fraction reflected to low wave numbers. The total redistributed flux in wave number space is 2.90 mW m^{-2} or about 16% of the total incoming flux. Most of the redistribution occurs at frequencies around the critical frequency as can be seen in Figure 8 which shows $F_i(\omega)$ and $D^+(\omega)$. Note that

$F_i(\omega)$ shows a characteristic dip at $\omega = \omega_c$ which is absent from the frequency spectrum of the vertical flux shown in Figure 4. The incident wave number spectra $F_i(\alpha)$ on the other hand look very similar for the vertical and normal-to-slope flux (Figure 3 and Figure 7).

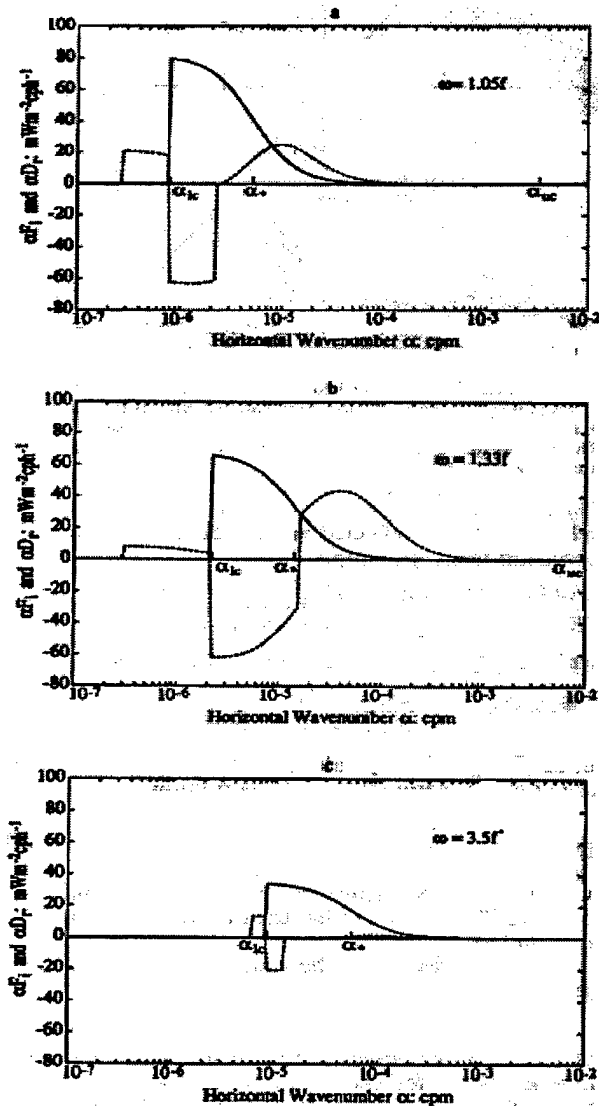


Figure 6. Reflection at a straight slope. Incident energy flux $F_i(\alpha, \omega)$ (solid line) and redistributed energy flux $D(\alpha, \omega)$ (dashed line) as a function of horizontal wave number for three different frequencies in a variance-conserving representation. The bottom slope is $\gamma = 0.07$ and the critical frequency is $\omega_c = 1.2f$. The wave numbers α_{lc} , α_* and α_{uc} are the low wave number cutoff, bandwidth, and high wavenumber cutoff of the Garrett and Munk spectrum. (From Müller and Xu, 1992).

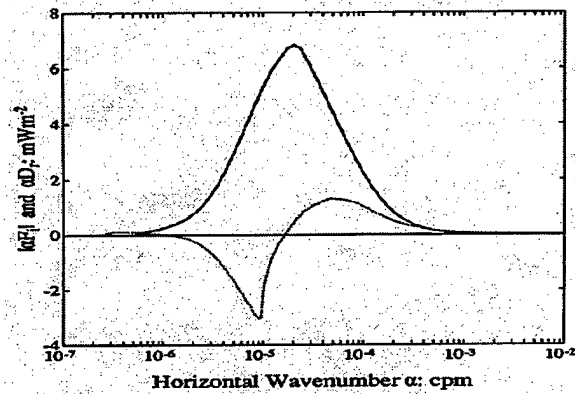


Figure 7. Reflection at a straight slope. Incident energy flux $F_i(\alpha)$ (solid line) and redistributed energy flux $D(\alpha)$ (dotted line) as a function of horizontal wave number in a variance-conserving representation. (From Müller and Xu, 1992).

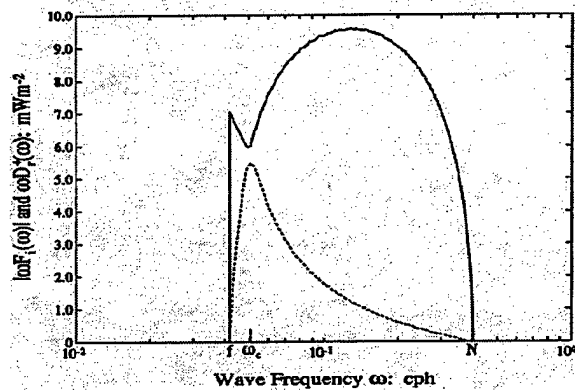


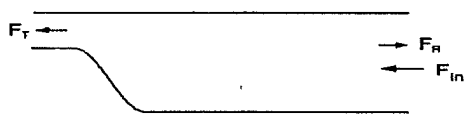
Figure 8. Reflection at a straight slope. Incident energy flux $F_i(\omega)$ (solid line) and energy flux $D^+(\omega)$ (dashed line) as a function of frequency in a variance-conserving plot. The bottom slope is $\gamma = 0.07$ and the critical frequency is $\omega_c = 1.2f$. (From Müller and Xu, 1992).

6. Scattering at Finite Topography

The scattering at finite topography in a finite depth ocean is considered in two papers by Müller and Liu (1999 a, b). The wave field is incident from the side onto either a slope shelf configuration or a ridge configuration (Figure 9). The study is restricted to the two-dimensional case of normal incidence. Modes are used. For the slope shelf configuration the incident wave field comes from the deep ocean side. For the ridge configuration one can consider the incident wave field coming from just one

side or the symmetric situation that the wave field is incident from both sides.

Shelf-Slope configuration



Ridge configuration

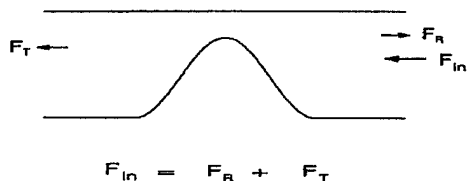


Figure 9. Configurations for the scattering at finite topography.

For the scattering problem one has to distinguish between the waves transmitted (or forward scattered) onto the shelf (or across the ridge) and the waves reflected (or back scattered) to the deep ocean. The energy flux is not only redistributed in wave number but also in physical space. As a complete set of independent variables one may thus use (ω, n, μ, x) where ω is the frequency as before, n the mode number, $\mu = \text{sgn}(k_1)$ the horizontal direction, and $x = \pm \infty$ the location in physical space. Assume that the incident field comes from the right hand side. Then the incident field is characterized by $\mu = -1$ and $x = +\infty$, the transmitted field by $\mu = -1$ and $x = -\infty$, and the reflected field by $\mu = +1$ and $x = +\infty$.

The two-dimensional problem only considers normal incidence. The along-topography wave number k_2 is zero. To complete the problem one also needs to calculate the scattering for oblique incidence. However, a consistent physical problem can be obtained by considering the total energy flux onto the topography, integrated over all azimuthal directions.

$$F(\omega, n) = \int_{-\pi/2}^{\pi/2} d\phi E(\omega, \alpha, \phi) v_h(\omega, n) \cos \phi \quad (6.1)$$

Here v_h is the magnitude of the horizontal group velocity vector. Note that F is a horizontal flux. Assume this integrated flux to be the incident flux in the two-dimensional problem.

$$F_i(\omega, n) = F(\omega, n, \mu = -1, x = +\infty) = F(\omega, n) \quad (6.2)$$

We thus assume that all incident waves are scattered as if they had normal incidence. If we substitute the horizontally isotropic GM-spectrum into (6.1) we find

$$F_i(\omega, n) = \frac{1}{\pi} E_{GM}(\omega, n) v_h(\omega, n) \quad (6.3)$$

This incident flux spectrum together with the reflected flux spectrum

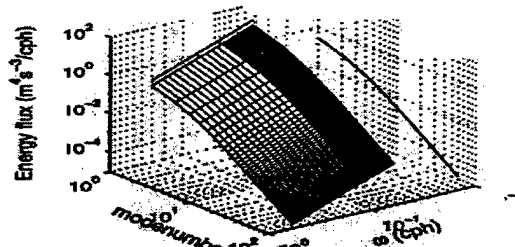
$$F_r(\omega, n) = F(\omega, n, \mu = +1, x = +\infty) \quad (6.4)$$

and the transmitted flux spectrum

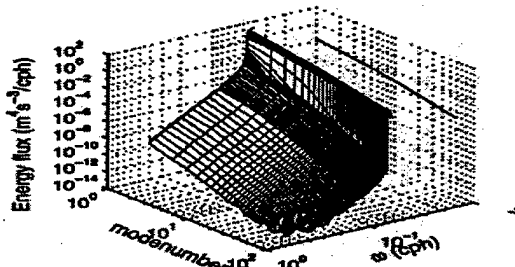
$$F_t(\omega, n) = F(\omega, n, \mu = -1, x = -\infty) \quad (6.5)$$

is shown in Figure 10 for the scattering at a half cosine slope.

(a) Incident flux spectrum, half-cosine slope



(b) Reflected flux spectrum



(c) Transmitted flux spectrum

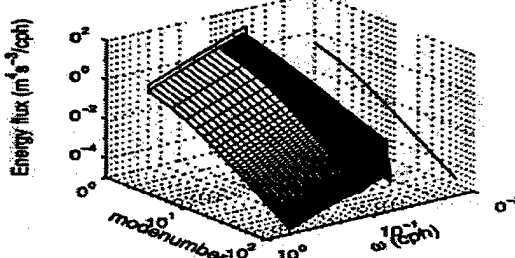


Figure 10. Incident, reflected, and transmitted flux spectrum for a half-cosine slope. (From Müller and Liu, 1999b.)

The total incident flux is 560 W m^{-1} when vertically integrated over the water column. This corresponds to a local flux of the order of 100 mW m^{-2} for a 5 km deep ocean. This horizontal flux is considerably larger than the vertical energy flux of 17.6 mW m^{-2} . In Figure 10, 91.4% of the incident flux is transmitted onto the shelf and 8.6% is reflected back into the deep ocean.

Redistribution in various reduced spaces can now be considered. The redistribution

$$D(\omega, n, \mu) = \sum_{x=\pm\infty} D(\omega, n, \mu, x) \\ = \begin{cases} F_t(\omega, n) - F_i(\omega, n), & \text{if } \mu = -1 \\ F_r(\omega, n), & \text{if } \mu = +1 \end{cases} \quad (6.6)$$

in (ω, n, μ) -space is shown in Figure 11. The redistribution is only significant for low and near critical frequencies. The major redistribution is from low mode number leftward propagating waves to low and medium mode number rightward propagating waves. There is also a transfer from low to medium mode number leftward propagating waves at near critical frequencies. The total redistributed energy flux is about 8.9% of the total incident flux.

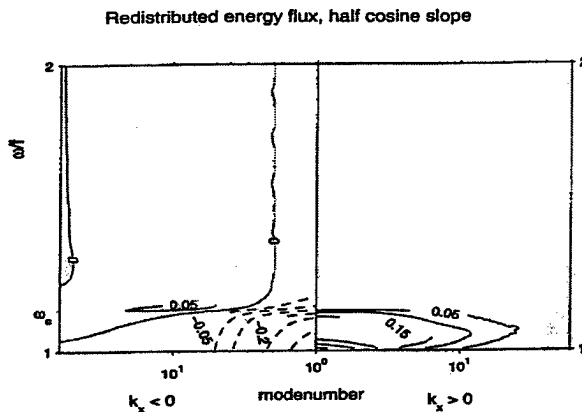


Figure 11. Redistributed energy flux $D(\omega, n, \mu)$ for the half cosine slope of figure 10. (From Müller and Liu, 1999b.)

The redistribution in (ω, n, μ) -space has to be distinguished from the redistributed energy flux

$$D(\omega, n, x) = \sum_{\mu} D(\omega, n, \mu, x) \\ = \begin{cases} F_r(\omega, n) - F_i(\omega, n), & \text{if } x = +\infty \\ F_t(\omega, n), & \text{if } x = -\infty \end{cases} \quad (6.7)$$

in (ω, n, x) -space (not shown).

For a ridge configuration one can consider the symmetric case where a GM-spectrum is incident from both sides. Then

$$D(\omega, n, x) = F_y(\omega, n) + F_t(\omega, n) - F_i(\omega, n) \quad (6.8)$$

for both $x = \pm\infty$. This redistributed energy flux is shown in Figure 12. The redistribution is from low to medium mode numbers at low and near critical frequencies. Figure 13 shows the incident and redistributed energy fluxes $F_i(n, x)$ and $D(n, x)$. The energy flux is redistributed from the first and second mode to mode numbers around 10. The total redistributed energy flux is about 4.3% of the incident flux.

Redistributed energy flux, cosine ridge

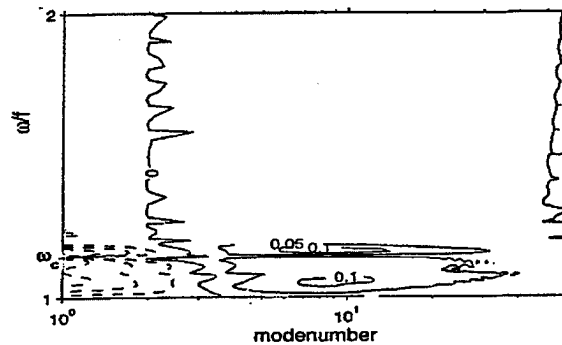


Figure 12. Redistributed energy flux $D(\omega, n, x)$ for a cosine ridge of depth ratio $\delta = 4/3$ and maximum slope $h_{max} = 0.01\pi$. (From Müller and Liu, 1999b.)

Redistributed energy flux, cosine ridge

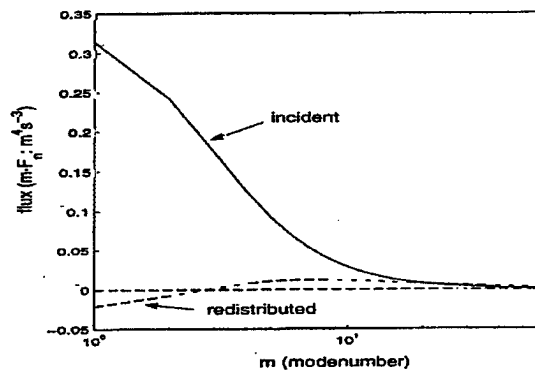


Figure 13. Incident energy flux $F_i(n, x)$ and redistributed energy flux $D(n, x)$ for the cosine ridge of figure 12. (From Müller and Liu, 1999b.)

7. Summary and Conclusions

The scattering of internal waves at topography is most succinctly described by the redistributed energy flux. Energy conservation implies that the total incoming energy flux equals the total outgoing flux. Since incoming and outgoing waves are characterized by different wave number vectors, the total redistribution in wave number space is equal to the total incident flux. Since scattering at topography does not change the frequency it is advantageous to use a representation that involves the frequency instead of the wave number vector. It is also helpful to atune the other components to the geometry of the problem. In some problems the location in physical space must also be considered. For various applications one considers the redistribution of the energy flux in reduced spaces. The total redistributed energy flux in these reduced spaces is only a fraction of the total incident flux and depends on the choice of the reduced space.

Scattering at topography is often implied in causing wave breaking and mixing. The redistributed energy flux is used to calculate the fraction of the incident energy flux that is scattered to high wave numbers beyond a critical wave number. This critical wave number is determined by the condition that the Richardson number of all waves up to that critical wave number is of the order of one. It is then argued that waves scattered to wave numbers higher than the critical wave number are likely to break and cause mixing. There are problems with these calculations. First, the critical wave number is not uniquely defined. Results depend on whether one works in vertical wave number, horizontal wave number or mode number space. Second, it is by no means clear that in a breaking wave field energy is extracted (and then converted to mixing and heat), only from high wave numbers larger than a critical

wave number. Wave breaking is a process that is local in physical space and can be expected to be broad-banded in wave number space.

8. Acknowledgments

The author would like to thank Alexander Adams for his help in the preparation of this manuscript. This work was supported by the Office of Naval Research. This is SOEST Contribution no. 4878.

References

- Cox, D. and H. Sandstrom, 1962: Coupling of internal and surface waves in water of variable depth. *J. Oceanogr. Soc. Japan* (20th Anniversary Volume), 499-513.
- Eriksen, C. C., 1982: Observation of internal wave reflection off sloping bottom. *J. Geophys. Res.*, 87, 525-538.
- Müller, P. and Xu, N., 1992: Scattering of oceanic gravity waves off random bottom topography. *J. Phys. Oceanogr.*, Vol. 22, No. 5.
- Müller, P. and Liu, X., 1999a: Scattering of internal waves at finite topography in two dimensions. Part 1: Theory and case studies. *J. Phys. Oceanogr.* (accepted for publication)
- Müller, P. and Liu, X., 1999b: Scattering of internal waves at finite topography in two dimensions. Part 1: Spectral calculations and boundary mixing. *J. Phys. Oceanogr.* (accepted for publication)
- Munk, W. H., 1981: Internal waves and small-scale processes. *Evolution of Physical Oceanography*, B. A. Warren and C. Wunsch, Eds., MIT Press, 264-291.
- Rubenstein, D., 1988: Scattering of inertial waves by rough bathymetry. *J. Phys. Oceanogr.*, 18, 5-18.

A Comparison of Highly Nonlinear Gravity-Wave Generation by Two and Three Dimensional Obstacles

Dale R. Durran and Craig Epifanio

Department of Atmospheric Sciences, University of Washington, Seattle

Abstract.

A series of idealized experiments are presented comparing internally stratified Boussinesq flow over three-dimensional ridges of varying height and horizontal aspect ratio (i.e., the ratio of cross-stream to stream-wise length scales). Solutions are obtained using linear and weakly nonlinear semi-analytic steady-state models, as well as a fully nonlinear numerical model. In the weakly nonlinear regime, the three-dimensional solution for flow over a long ridge (aspect ratio of order 10) is in relatively close agreement with the classical solution for two-dimensional mountain waves generated by a uniform infinitely long ridge. Substantial deviations from the two-dimensional solution do, however, appear when the mountain is high enough to force gravity wave overturning. Significant three-dimensional effects are apparent in the wave-breaking regime even for very long ridges. The differences between the two-dimensional and three-dimensional solutions appear to result from the lateral diversion of the low-level flow around the ends of the ridge.

Introduction

An extensive body of literature exists exploring both linear and nonlinear stratified flow over two-dimensional obstacles (see reviews in *Smith* [1979]; *Durran* [1986]; *Baines* [1995]). Recent advances in computing power have facilitated several studies of nonlinear flow over three-dimensional obstacles, including *Smolarkiewicz and Rotunno* [1989, 1990]; *Miranda and James* [1992]; *Ólafsson and Bougeault* [1996, 1997]; *Schär and Durran* [1997]. Despite these advances in our understanding of stratified flow over three dimensional obstacles, there has been no systematic estimate of the conditions under which flow perpendicular to a long ridge generates perturbations that can be accurately determined using a two-dimensional model. The goal of this paper is to examine this question.

The upstream flow structure in all the experiments discussed in this paper is characterized by a uniform Brunt-Väisälä frequency $N = 0.012 \text{ s}^{-1}$ and a uniform 8 m s^{-1} cross-mountain wind speed. The topography is a smooth ridge with its ridge line perpendicular to the x -axis defined such that

$$H(x, y) = \begin{cases} \frac{h}{16} [1 + \cos(\pi r)]^4 & \text{for } r \leq 1, \\ 0 & \text{otherwise,} \end{cases}$$

where

$$r^2 = \begin{cases} \left(\frac{x}{4b}\right)^2 + \left(\frac{|y| - (A_r - 1)b}{4b}\right)^2 & \text{for } |y| > (A_r - 1)b, \\ \left(\frac{x}{4b}\right)^2 & \text{otherwise.} \end{cases}$$

In the preceding, b is a characteristic half-width of the slope and A_r is the horizontal aspect ratio, defined as the ratio of the cross-stream to the along-stream width of the topography.

The steady-state linear and weakly nonlinear calculations were performed using fast Fourier transforms on a large horizontally periodic domain. The weakly nonlinear model is accurate to second order in the perturbations and will be described in detail in a forthcoming publication. The fully nonlinear calculations were performed using a three-dimensional version of the nonhydrostatic model described in *Durran and Klemp* [1983], except that the model was modified to solve the compressible Boussinesq equations [*Durran*, 1999, p. 356]. The compressible Boussinesq equations differ from the standard Boussinesq system only in that the prognostic pressure equation

$$\frac{1}{\rho_0} \frac{dp}{dt} + c_s^2 \nabla \cdot \mathbf{v} = 0$$

is retained for computational convenience. In the following simulations $c_s = 331 \text{ m s}^{-1}$.

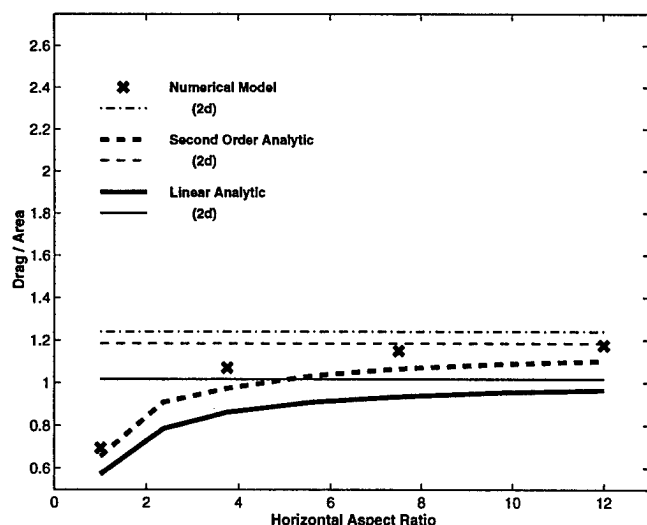


Figure 1. Normalized cross-mountain pressure drag as a function of horizontal aspect ratio for $Nh/U = 0.5$ as predicted by linear theory (solid), weakly nonlinear theory (dashed), and a fully nonlinear numerical model (crosses). The drag for 2d flow corresponding to each of these cases is shown as a thin horizontal line.

Grid nesting is included following the formulation in *Skamarock and Klemp* [1993]. Three levels of nesting were employed such that the mesh spacing and time step were refined by a factor of three at each nested-grid boundary. The horizontal mesh spacing on the finest grid was $\Delta x = \Delta y = 0.18b$. The finest grid occupied the region $|x| \leq 7b$, $|y| \leq (6 + A_r)b$, the intermediate grid covered region $|x| \leq 18b$, $|y| \leq (17 + A_r)b$, and the coarse grid the region $|x| \leq 48.6b$, $|y| \leq 48.6b$. On all grids $\Delta z = 0.27U/N$. The computations were performed using the terrain following coordinate

$$\zeta = z_t \left(\frac{z - H}{z_t - H} \right),$$

where $z_t = 8\pi U/N$ is the top of the model domain. The large and small time steps on the finest mesh were 7 s and 7/3 s, respectively.

Aspect-Ratio Dependence of the Normalized Wave Drag

Figure 1 shows the dependence of the normalized cross-mountain pressure drag D_n on the horizontal aspect ratio of the ridge as predicted by linear, weakly nonlinear, and the full nonlinear models for cases in which the nondimensional mountain height Nh/U is 0.5. In each case, the total pressure drag has been divided by the cross-sectional area of the ridge in the y - z plane normal to the upstream flow, and the

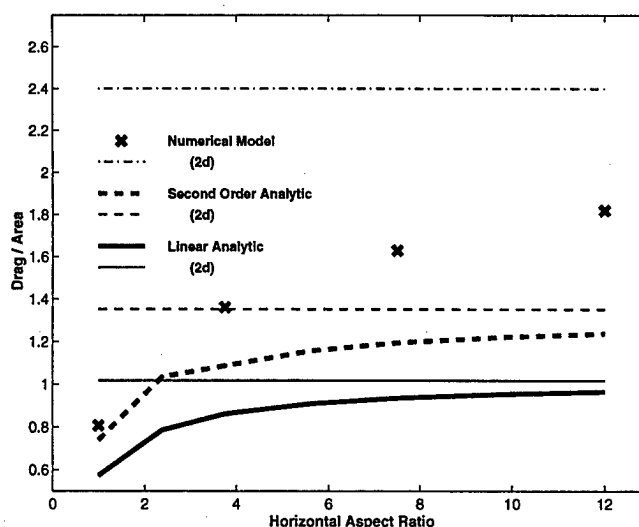


Figure 2. As in Fig. 1 except that $Nh/U = 1.0$.

result has been normalized so that the drag per unit cross-sectional area in the linear solution for the two-dimensional problem is unity. The normalized drag associated with each two-dimensional solution (which, of course, is independent of A_r) is indicated by a thin horizontal line. The drag predicted by the linear, weakly nonlinear, and fully nonlinear models for flow around a circular mountain is significantly weaker than that for a purely two-dimensional ridge, but the D_n predicted by each model appears to asymptote to the result for purely two-dimensional flow as $A_r \rightarrow \infty$. In particular, when $A_r = 12$, each D_n lies close to the value obtained from the corresponding two-dimensional calculation.

When $Nh/U = 0.5$, the flow remains laminar and the wave response is almost linear, as suggested by the close agreement between the second-order weakly nonlinear and the fully nonlinear calculations in Fig. 1. If Nh/U is increased to 1.0 and A_r exceeds 3, the wave breaks; the flow becomes highly nonlinear, and the weakly and fully nonlinear models yield very different solutions. Fig. 2 shows the aspect ratio dependence of D_n when $Nh/U = 1.0$ as predicted by the linear, weakly nonlinear and fully nonlinear models. In contrast to the situation for $Nh/U = 0.5$, when $Nh/U = 1.0$ the normalized cross-mountain pressure drag for the fully nonlinear simulation remains well below the result obtained using a two dimensional model for horizontal aspect ratios at least as large as 12.

As suggested by the data plotted in Figs. 1 and 2, the degree of nonlinear amplification associated with breaking gravity waves in a three-dimensional flow is significantly less than that predicted by a strictly two-dimensional model. This reduction in the nonlinear en-

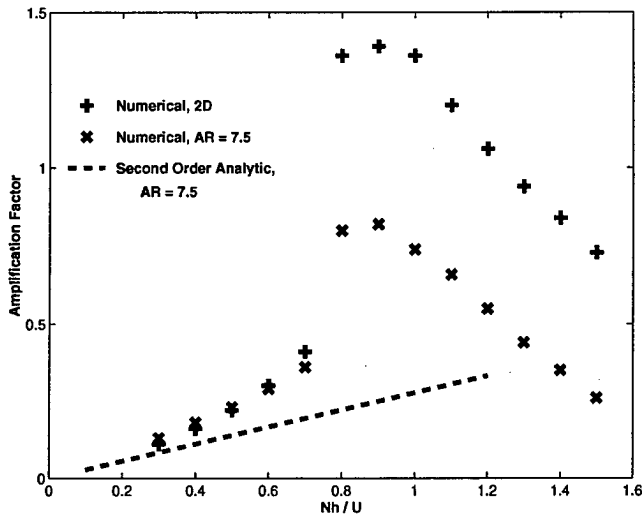


Figure 3. Nonlinear drag amplification δD as a function of Nh/U when $A_r = 7.5$ for the fully nonlinear 2d (plus signs) and 3d (crosses) calculations, and for the weakly nonlinear 3d model (dashed line).

hancement of D_n is more clearly displayed in Fig. 3, which shows plots of the "nonlinear drag amplification"

$$\delta D = \frac{D_n^{(NL)} - D_n^{(L)}}{D_n^{(L)}}$$

as a function of Nh/U for a ridge with $A_r = 7.5$. Here $D_n^{(NL)}$ represents the normalized drag for the nonlinear simulation $D_n^{(NL)}$, and $D_n^{(L)}$ is the drag for the corresponding linear model. As evident in Fig. 3, the enhancement in the cross-mountain pressure drag associated with the onset of wave overturning in a three-dimensional flow with $A_r = 7.5$ is reduced from the two-dimensional result by approximately 50%.

Diversion of the Low-Level Flow

The difference between the drags obtained in the two- and three-dimensional calculations appears to be associated with the lateral diversion of the low-level flow impinging on the finite-length ridge. As illustrated in Fig. 4, the lateral deflection of the low-level flow increases dramatically as Nh/U increases from 0.5 to 1.0.

The aspect ratio of the ridges shown in Fig. 4 is 12. The influence of A_r on low-level flow diversion is illustrated in Fig. 5. The vertical coordinate in Figure 5 is the ratio of the mass flux diverted through the sides of a control volume extending upstream from the ridge crest to the mass flux into the upstream face of the control

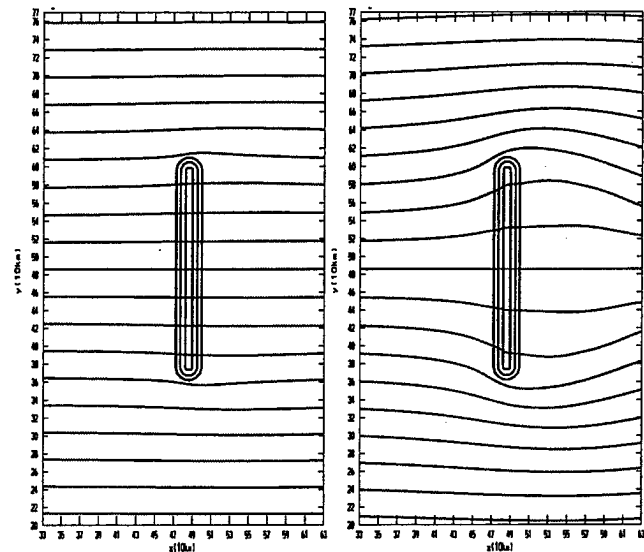


Figure 4. Comparison of lateral diversion of dye lines originating at an upstream elevation of $0.375U/N$ when $A_r = 12$ and Nh/U is (left) 0.5 or (right) 1.0.

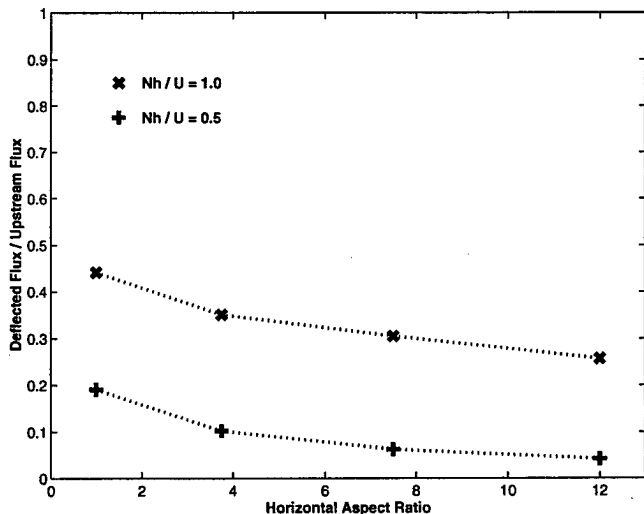


Figure 5. Ratio D_r of the low-level mass flux diverted laterally to the upstream mass flux plotted as a function of A_r for Nh/U equal to 0.5 (plus signs) and 1.0 (crosses).

volume. This control volume is bounded above by a material surface, below by the topography and on the sides by vertical planes. The downstream side of the control volume is a quasi-rectangular area whose bottom edge coincides with the ridge line along the segment where the elevation of the crest is constant. The lateral sides of the control volume are embedded in vertical planes parallel to the x -axis running through each end of the segment along which the elevation of the crest is constant. The upstream side of the control volume is a quasi-rectangular region nominally located at upstream infinity but actually placed at $x = -15b$. The mass budget was computed after the flow had become essentially steady. Defining $\hat{z}(x, y, z_0)$ to be the elevation of the material surface that originates at height z_0 in the undisturbed upstream flow, and assuming that $A_r > 1$, the mass flux through a vertical face within the control volume oriented perpendicular to the mean flow is

$$F(x, z_0) = \int_0^{(A_r-1)b} \int_0^{\hat{z}} \rho u \, dz \, dy.$$

If $A_r = 1$, the mountain is circular, and the integration with respect to y in the preceding is neglected. The ratio of the mass flux diverted through the sides of a control volume upstream of the ridge crest to the total upstream mass flux into the control volume may now be defined as

$$D_r = \frac{F(-15b, z_0) - F(0, z_0)}{F(-15b, z_0)}.$$

In the following, we have chosen $z_0 = 2U/N$, in which case the top of the control volume is coincident with the lowest dye line plotted in Figs. 7 and 8.

As indicated in Fig. 5, substantial low-level mass flux is diverted around the ends of the ridge for all aspect ratios considered in this study when $Nh/U = 1.0$. On the other hand, when $Nh/U = 0.5$ the low-level flow diversion is minimal for all obstacles except the circular mountain. The lateral diversion of the low-level flow increases substantially when overturning waves are present. Figure 6 shows the dependence of the diverted mass flux on Nh/U in a series of simulations with $A_r = 7.5$. The y -velocity component across the lateral sides of the control volume is linearly proportional to h , so the linear solution shows a linear dependence of D_r on Nh/U . In order to highlight the effects of nonlinear processes the normalized mass-flux divergence $D_r U/(Nh)$ is therefore plotted in Fig. 6. A comparison of Fig. 6 with the Fig. 3 indicates that as Nh/U increases past the critical threshold for wave breaking at about $Nh/U = 0.8$, the nonlinear enhancement of both the lateral-flow deflection and the wave-drag increase dramatically.

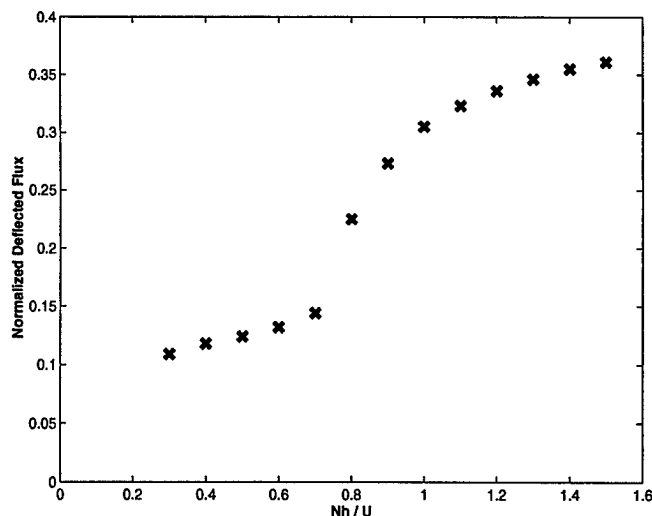


Figure 6. Normalized laterally diverted mass flux $D_r U/(Nh)$ as a function of Nh/U for $A_r = 7.5$.

Lee-Side Troughing and Warming

The pronounced lateral deflection of the low-level flow in those simulations with breaking waves enhances the subsidence of the near-surface flow as it descends the lee slope. As a consequence, the positive buoyancy perturbations just above the surface over the central segment of the lee slope are stronger in the three-dimensional simulations than in those computed using the two-dimensional model. The buoyancy perturbations $-g(\rho - \bar{\rho}(z))/\rho_0$ generated along the centerline of a three-dimensional ridge with $A_r = 12$ and $Nh/U = 1.0$ are compared in Fig. 7 with the corresponding results obtained using a two-dimensional model. Note that the lee-side buoyancy perturbations at the lowest grid level in the model, which is $\Delta z/2$ above the surface, are strongest in the three-dimensional simulation.

Although the near-surface buoyancy perturbations are stronger in the three-dimensional simulations, the decrease in the cross-mountain flow associated with the enhanced low-level diffidence reduces the strength of the mountain-wave-induced buoyancy perturbations throughout most of the lowest one-half wavelength of the wave ($0 \leq z \leq \pi U/N$). The reduction in wave-amplitude can also be seen by comparing the vertical displacement of the top dye line in each panel of Fig. 7. As illustrated in Fig. 8, this reduction in the vertically integrated lee-side buoyancy perturbation reduces the strength of the pressure minimum and lee-side trough relative to that obtained in the two-dimensional simulation. The pronounced reduction in the lee-side pressure minimum is responsible for the previously discussed de-

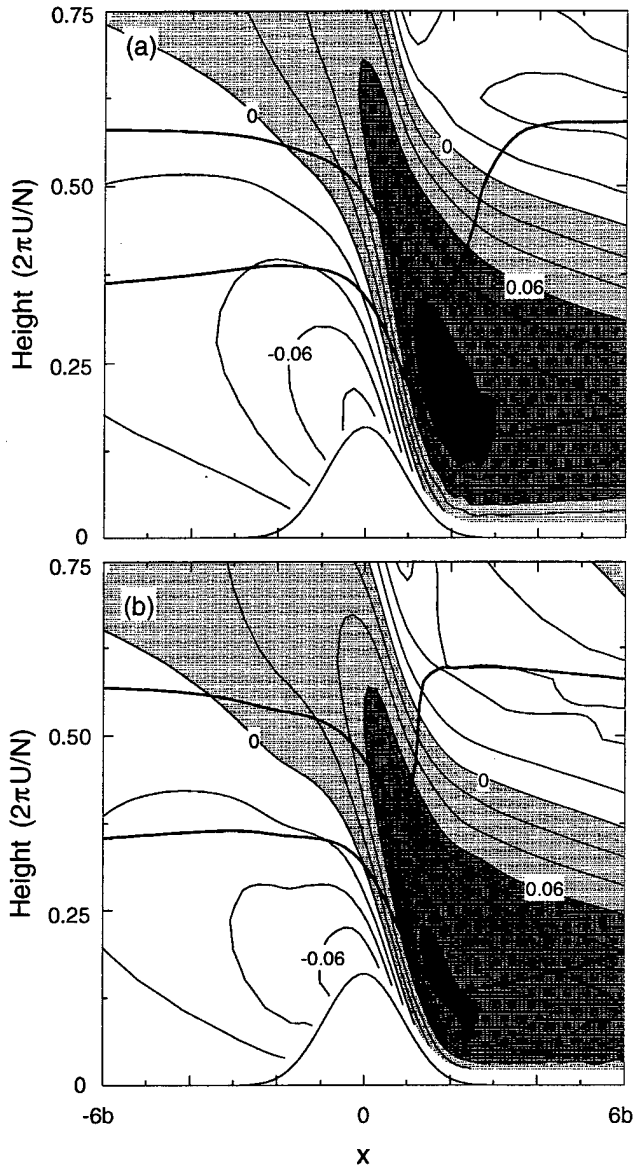


Figure 7. Buoyancy perturbation contoured at intervals of 0.02 ms^{-2} and two material-surface dye lines at $t = 30b/U$ for (a) flow over a two-dimensional ridge, and (b) flow along the centerline of a three-dimensional ridge with $A_r = 12$. In both cases $Nh/U = 1.0$; the darkest shading indicates buoyancy perturbations in excess of 0.12 ms^{-2} ; the dye-lines are the darkest solid lines.

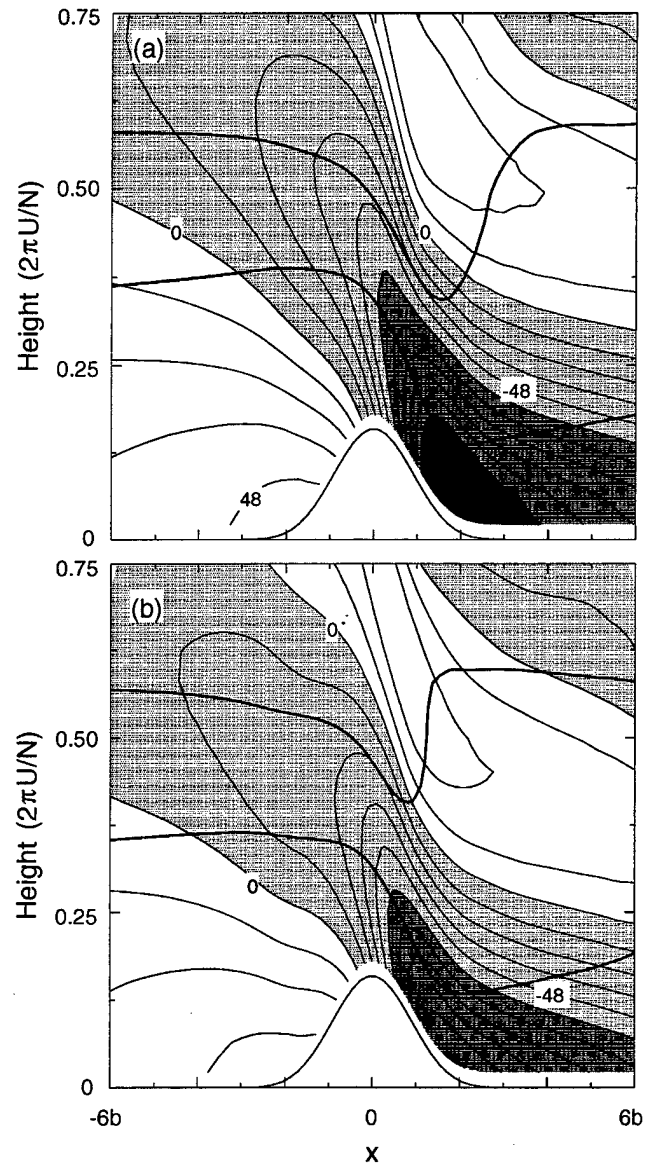


Figure 8. As in Fig. 8 except that p/ρ_0 is contoured at intervals of $12 \text{ m}^2 \text{ s}^{-2}$. The darkest shading indicates pressure perturbations more negative than $-120 \text{ m}^2 \text{ s}^{-2}$.

crease in the cross-mountain pressure drag in the three-dimensional simulations relative to those drags obtained with the two-dimensional model.

Conclusions

This paper has explored the extent to which the disturbances generated by flow over a long, but finite, ridge can be adequately described by a two-dimensional model. Our results indicate that linear and weakly nonlinear disturbances over the central region of the ridge can be well approximated by two-dimensional theory when the horizontal aspect ratio of the ridge is greater than approximately 10. Significant deviations from the two-dimensional solution are, however, apparent when the mountain is high enough to produce breaking waves. In the wave-breaking regime, important differences between the two-dimensional and three-dimensional results remain apparent for mountains with A_r at least as large as 12.

As first noted by Peltier and Clark [1979], the cross-mountain pressure drag is sensitively dependent on the nondimensional mountain height Nh/U when the mountain is close to the critical height required to force wave overturning. Our results for flow over a long three-dimensional ridge suggest that the degree of low-level flow diversion is also a very sensitive function of Nh/U for mountain heights close to the critical height for wave overturning. The deflection of the low-level flow increases dramatically when the mountain becomes large enough to generate breaking waves. As a result, the nonlinear enhancement of the cross-mountain pressure drag associated with the onset of wave overturning in the three-dimensional case is approximately half the strength of the nonlinear enhancement in the two-dimensional problem.

The increased diversion of the low-level flow appears to be the primary factor responsible for the difference between the results obtained using two- and three-dimensional models to simulate highly nonlinear flow over a long ridge. As a consequence of the low-level flow diversion, there is increased subsidence in the lee of the central segment of the ridge, which makes the lee-slope warming stronger in the three-dimensional model. The vertically propagating wave in the three-dimensional solution is, however, weakened by the net reduction in the cross-mountain flow. As a consequence, the positive vertically integrated buoyancy perturbation over the lee slope, the wave-induced lee trough, and the cross-mountain pressure drag are all weaker in the three-dimensional case than in the corresponding two-dimensional problem.

References

- Baines, P. G., *Topographic Effects in Stratified Flows*, Cambridge University Press, Cambridge, 1995.
- Durran, D. R., Mountain waves, in *Mesoscale Meteorology and Forecasting*, edited by P. S. Ray, pp. 472–492, American Meteorological Society, Boston, 1986.
- Durran, D. R., *Numerical Methods for Wave Equations in Geophysical Fluid Dynamics*, Springer-Verlag, New York, 1999.
- Durran, D. R., and J. B. Klemp, A compressible model for the simulation of moist mountain waves, *Mon. Wea. Rev.*, **111**, 2341–2361, 1983.
- Miranda, P. M. A., and I. N. James, Non-linear three-dimensional effects on gravity-wave drag: Splitting flow and breaking waves, *Quart. J. Roy. Meteor. Soc.*, **118**, 1057–1081, 1992.
- Ólafsson, H., and P. Bougeault, Nonlinear flow past an elliptic mountain ridge, *J. Atmos. Sci.*, **53**, 2465–2489, 1996.
- Ólafsson, H., and P. Bougeault, The effect of rotation and surface friction on orographic drag, *J. Atmos. Sci.*, **54**, 193–210, 1997.
- Peltier, W. R., and T. L. Clark, The evolution and stability of finite-amplitude mountain waves. Part II. Surface wave drag and severe downslope windstorms, *J. Atmos. Sci.*, **36**, 1498–1529, 1979.
- Schär, C., and D. R. Durran, Vortex formation and vortex shedding in continuously stratified flows past isolated topography, *J. Atmos. Sci.*, **54**, 534–554, 1997.
- Skamarock, W. C., and J. Klemp, Adaptive grid refinement for two-dimensional and three-dimensional nonhydrostatic atmospheric flow, *Mon. Wea. Rev.*, **121**, 788–804, 1993.
- Smith, R. B., The influence of the mountains on the atmosphere, in *Advances in Geophysics*, edited by B. Saltzman, vol. 21, pp. 87–230, Academic Press, 1979.
- Smolarkiewicz, P. K., and R. Rotunno, Low Froude number flow past three dimensional obstacles, *J. Atmos. Sci.*, **46**, 1154–1164, 1989.
- Smolarkiewicz, P. K., and R. Rotunno, Low Froude number flow past three dimensional obstacles. Part II: Upwind flow reversal zone, *J. Atmos. Sci.*, **47**, 1498–1511, 1990.

This preprint was prepared with AGU's L^AT_EX macros v4. File Durran formatted September 12, 1999.

With the extension package 'AGU++' by P.W.Daly, version 1.5 from 1996/08/20

Short-Term Directional Variability of the Continuum Range in the Deep-Ocean Internal Wave Field

Melbourne G. Briscoe

Office of Naval Research, Arlington, Virginia

Abstract. A simple method (Zalkan, 1970) to examine the directionality of the internal wave field has been applied to temperature data at 1000 m depth from the IWEX trimoor (Briscoe, 1975). Results suggest the concept of a horizontally-isotropic deep-ocean internal wave field is not valid over 75-hour periods, but only over a longer time average. The estimated wavenumbers, for each frequency examined, lie along the calculated dispersion relation for modes 1-4.

1. Background

It is commonly argued that deep-ocean (> 500 m) internal waves are horizontally isotropic (i.e., no preferred direction of propagation), whereas upper-ocean (< 200 m) internal waves tend to occur in intermittent groups that propagate in specific directions. The original reference for the deep result was Garrett and Munk (1972), buttressed by Muller *et al.* (1978); recent results have only differed for the internal tidal frequencies. The seminal references for the upper-ocean result were the numerous papers of Sabinin and his co-workers e.g., Sabinin (1971, 1973) and the observations from FLIP reported originally, for example, by Zalkan (1970) and Pinkel (1975).

Part of the reason for the different views of the deep and upper ocean is simply that the observational techniques and the analysis methods have often been quite different in the two depth regimes, and to a certain extent the differing results have been therefore inevitable. For example, the deep experiments tend to be of long duration and are usually analyzed to yield the mean spectral properties. The upper ocean experiments tend to be quite short, often only a few days, and usually are analyzed in a way that emphasizes the time variability, for example wave packets and significant events.

However, it is possible to find many data that contradict the common view. Briscoe (1974) analyzed IWEX data (1000 m depth) in the same way that Zalkan (1970) looked at upper ocean data and found numerous instances where the deep-ocean internal wave field appeared to be time-varying and directional; those unpublished results are given here, with some extensions and a modern interpretation. Similarly, the detailed thermistor chain tows of Bell (1976) in the upper ocean show no significant horizontal anisotropy. Sabinin (personal communication, 1978) has commented that, contrary to his earlier work, he finds the Garrett-Munk spectrum

to be quite reasonable as a description of the mean state in the upper ocean. His conclusion is consistent with Roth *et al.* (1981) and unpublished work by Levine and co-workers (personal communication, 1999).

2. Introduction

The Internal Wave Experiment (IWEX) in 1973 was a deep-sea three-dimensional mooring array (current meters and temperature sensors) designed to act as an antenna for internal waves in the main thermocline. Briscoe (1975) describes the experiment and basic results; Muller *et al.*

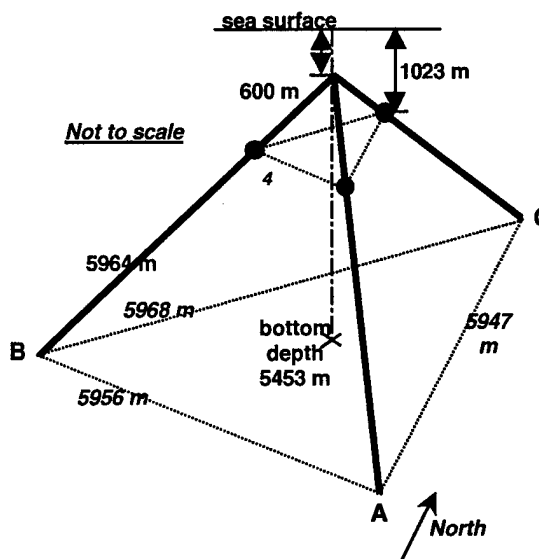


Figure 1. The IWEX Trimoor. The horizontal triangle of temperature sensors at 1023 m depth, separated 450 m, is the source of the data analyzed here. The location of the mooring was $27^{\circ}43.9' N$, $69^{\circ}50.95' W$, on the Hatteras Abyssal Plain south of Woods Hole and east of Scripps. See Briscoe (1975) for details.

(1978) give the detailed analysis for the mean conditions over the 40-day experiment. Figure 1 shows the mooring array shape; instruments were distributed along the three legs of the mooring. Of note is the triangular horizontal triplets of instruments with horizontal spacings of a few meters to about a kilometer.

From the three temperature time-series at the 1000 m-level on the IWEX trimoor (~ 450 m horizontal separation) one may attempt to fit an incoming plane wave to the measured phase differences from the cross-spectra. The technique applied here is copied from Zalkan (1970) who argued for his data that a single plane wave of a single vertical mode was an adequate, perhaps even good, representation of the high-frequency internal wave field for short time intervals.

The argument is not totally convincing, for one may always find a single "wave" that will "best fit" the phase differences, even if multiple waves, non-planar, from various directions are simultaneously present. Zalkan suggested that agreement between the estimated wave number, for a given frequency, and a theoretical wave number calculated from the dispersion relation for some mode, would support the argument. He showed (his Table III) such acceptable solutions and concluded that the relatively high-frequencies are well-fit by a single wave of the first mode. However, the low-frequencies were poorly fit by this approach.

Here I report a simple but illuminating attempt to apply those ideas to a fraction of the IWEX data set.

3. Method

Given three sensors, A-B-C, three possible phase differences for each frequency can be calculated from the three cross-spectral pairs; call the phases ϕ_{AB} , ϕ_{BC} , and ϕ_{CA} . An incoming plane wave of wavenumber \mathbf{K} will project on the A-B-C sensor separations, \mathbf{X} , to yield phase differences:

$$\phi_{ij} = \mathbf{K} \cdot \mathbf{X}_{ij} = K_x X_{ij} + K_y Y_{ij} \quad (1)$$

For the IWEX tri-mooring the sensors A and C were aligned south-north, respectively; B was west of the A-C line and completed an equilateral triangle of side L ; at the 1023 m depth $L = 450$ m.

Consequently,

$$-X_{AB} = X_{BC} = \frac{1}{2} L \quad 3^{1/2}; \quad X_{AC} = 0 \quad (2a)$$

$$+Y_{BC} = Y_{AB} = \frac{1}{2} L \quad Y_{AC} = \frac{1}{2} L \quad (2b)$$

Therefore,

$$\phi_{AB} = -\frac{1}{2} 3^{1/2} L K_x + \frac{1}{2} L K_y \quad (3a)$$

$$\phi_{BC} = +\frac{1}{2} 3^{1/2} L K_x + \frac{1}{2} L K_y \quad (3b)$$

$$\phi_{AC} = L K_y \quad (3c)$$

There are only two unknowns, K_x and K_y , for the incoming plane wave, yet taking equations (3) two at a time yields three different estimates each for K_x and K_y . Hence one writes, following Zalkan,

$$K_{RMS} = \left[\frac{1}{3} \left(\sum_{i=1}^3 K_x^{(i)^2} + \sum_{i=1}^3 K_y^{(i)^2} \right) \right]^{1/2} \quad (4)$$

Similarly, the angle of incidence of the estimated plane wave is

$$\Theta_{RMS} = \arctan \left(\frac{\sum_{i=1}^3 K_y^{(i)}}{\sum_{i=1}^3 K_x^{(i)}} \right) \quad (5)$$

Hence, for each frequency f , one may obtain $K_{RMS}(f)$, and $\Theta_{RMS}(f)$.

4. Data

I broke up the three approximately 40-day temperature records into 13 non-overlapping pieces of 75 hours each (length chosen to give minimal spectral leakage from tidal and inertial bands). Coherences and phases were calculated by smoothing over 14 frequency bands, giving 28 degrees of freedom. The lowest-frequency estimate was consequently $14/75 = 0.187$ cph. Because the coherences dropped with increasing frequency, the phase estimates were stable only for frequencies less than about 1.7 cph. Hence, 1.68 cph was the highest frequency considered.

In a program on a PC the relations (4) and (5) were calculated, using the phase data from the coherence/phase estimates. The frequencies involved were 0.187, 0.373, 0.560, 0.747, 0.933, 1.120, 1.307, 1.493, and 1.680 cph.

5. Results

Figure 2 shows a polar plot (north up) of the $K_{RMS}(f)$, and $\Theta_{RMS}(f)$ results for each of the 9 frequencies and for each of the 13 data pieces. The solid circles are scale-circles having wavenumbers equivalent to 20, 10, 5, 2, 1, and 0.5 km^{-1} , stating from the origin. The radial scale is logarithmic in km^{-1} . Each $K_{RMS} - \Theta_{RMS}$ solution is plotted in the same color for its time segment from which it was obtained, regardless of which frequency it applies to. The plotted direction is the direction from which the wave is incident.

Figure 2 should be viewed as a kind of zoom view of what an average internal wave field looks like: overall, there is no particular directionality, but at any moment for any frequency there is something more distinct happening.

Figure 3 is the same as Figure 2 except only the 9 $K_{RMS} - \Theta_{RMS}$ solutions for the first 75-hour time segment are shown. Here, the waves are clearly incident from either the southwest or the northeast. Other time segments show either no pattern, or their own pattern. For example, time segment 4 (yellow) is mostly propagation from the northwest, and segment 8 is mostly from the southwest.

Figure 4 presents the same data as in Figure 2 but sorted by frequencies rather than time pieces. Again, each $K_{RMS} -$

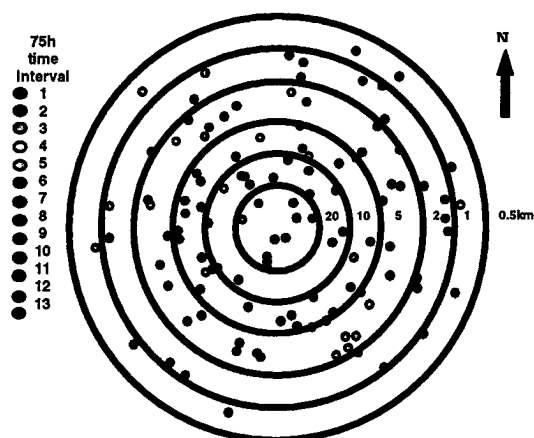


Figure 2. Polar plot of incident wave numbers based on single plane-wave analysis of the temperature coherences. Plot is direction of wave travel (North = \uparrow) versus log wavenumber, given as wavelength. Each color refers to one of 13 consecutive 75-hour time periods. For each time period there are 9 frequencies plotted here. No preferred direction of propagation exists over the total 40-day period.

Θ_{RMS} solution is plotted in the same color for its frequency, regardless of which time segment it came from.

Now some trends are clearer, but the results are mostly just indicative of the dispersion relations for an internal wave field. That is, in a modal framework, a given frequency should have some preferred wavenumbers. This is quickly seen with the red-yellow (lower) frequencies having smaller preferred wave numbers, and the green-blue (higher) frequencies having larger preferred wavenumbers. Figure 5 quantifies this: the average K_{RMS} for each frequency is

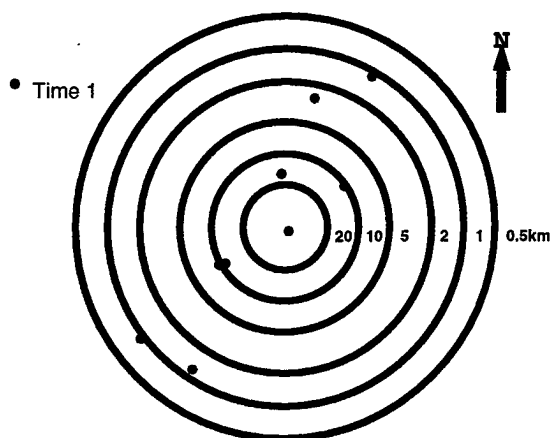


Figure 3. Same as Figure 2, but only the wavenumbers for nine frequencies from the first 75-hour time period are shown, to illustrate strong directionality for all frequencies during that time period.

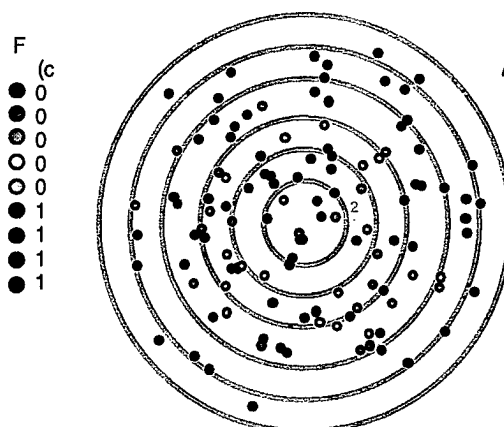


Figure 4. Same as Figure 2, but no each color refers to one of 9 frequency bands. For each frequency band there are 13 consecutive time periods plotted here.

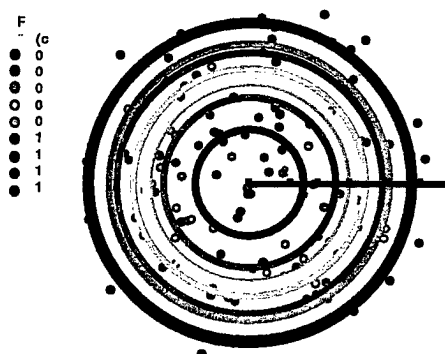


Figure 5. Same as Figure 4, but colored circles are added at the wavenumber magnitude that is the average for each frequency.

plotted as a circle of the same color as that in which the frequencies are coded. (higher) frequencies having larger preferred wavenumbers. Figure 5 quantifies this: the average K_{RMS} for each frequency is plotted as a circle of the same color as that in which the frequencies are coded.

Figure 6 compares the empirical dispersion relation of Figure 5 (the solid black dots are the average K_{RMS} for each frequency) to the theoretical dispersion relations (for the first 4 modes) calculated from the mean buoyancy frequency profile for the IWEX site. The error bars are ± 1 standard deviation (based on the 13 pieces). The K_{RMS} seems to follow the fourth mode for the lower frequencies, and the third mode for the higher frequencies, which is approximately consistent with a Garrett-Munk j_s of 3. The transition occurs at about the wavenumber-frequency of the Eckart

resonance for the IWEX buoyancy frequency (Eckart, 1969; Katz and Briscoe, 1979).

6. Discussion

The same caveats apply here as in Zalkan's work: (1) it is unlikely *a priori* that a single plane wave can account for the observed coherences; (2) the technique cannot distinguish between one plane wave and several in different directions, nor between one and several of different vertical modes.

Nevertheless, the results are consistent with a mono-modal-model in the sense that Zalkan found consistency.

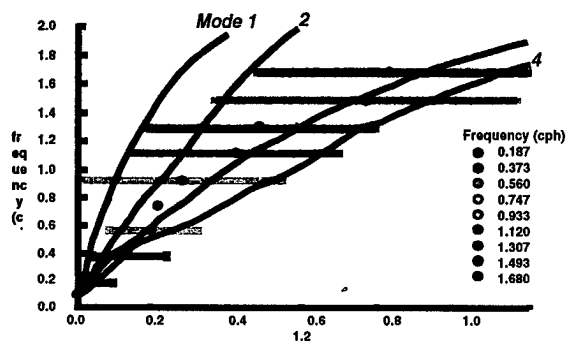


Figure 6. Empirical dispersion curve for the data set, for each of 9 frequencies, versus the average wavenumber from Figure 5. Error bars on wavenumber are ± 1 standard deviation over the 13-piece average. The solid black lines are the calculated dispersion curves for the local mean buoyancy frequency, for the first four modes.

This does not mean that only one mode is present (at each frequency), but rather that during each time segment, only a small number of modes (and lower modes) dominates. Were it otherwise, the estimated wavenumbers for each frequency would not fall so neatly along the low-mode dispersion curves.

Directionality is evident in these 75-hour time periods, but no pattern is obvious from one time period to the next. Thus, this analysis is consistent with internal wave sources being distributed in time and space and arriving at any one point from a variety of directions, but not from all directions at any one time.

Some internal consistency checks of the analysis are possible. When one examines a scatter plot of ϕ_{AB} versus $\phi_{BC} + \phi_{CA}$, most of the points are consistent with the diagonal line that represents perfection. This simplest-possible consistency check works fairly well, and suggests the phases observed are meaningful and interpretable as being due to a simple modal/wave system at each frequency for each time segment.

This analysis means a non-directional internal wave field (at the higher frequencies, in the deep ocean) is true in the average over 40 days but is not certain at all frequencies for

all 3-day periods. Additionally, during the shorter time intervals, the incident internal wave field is composed of a fairly simple modal structure.

From the point of view of using an instantaneous description of the internal wave field as an input to acoustic propagation applications, these data suggest it would be better to include this directionality than to ignore it. The original Garrett-Munk (1972) argument for an isotropic spectrum is true only in the mean; acoustic propagation does not see the mean state.

Acknowledgments. I thank my quarter-century colleague in IWEX, Peter Müller, for a continuing series of stimulating discussions on internal waves. This work was originally performed at Woods Hole Oceanographic Institution, but was written up while at the Office of Naval Research under the Research Opportunities for Program Officers (ROPO) program.

References

- Bell, T. H., Jr., The structure of internal wave spectra as determined from towed thermistor chain measurements, *J. Geophys. Res.*, **81**, 3709-3714, 1976.
- Briscoe, M. G., Directional variability by plane wave analysis, in *Status Report on IWEX - June 1974*, edited by M. G. Briscoe, Woods Hole Oceanographic Institution, 1974. [copy of article available from author]
- Briscoe, M. G., Preliminary results from the trimoored internal wave experiment (IWEX), *J. Geophys. Res.*, **80**, 3872-3884, 1975.
- Eckart, C., Internal waves in the ocean, *Phys. Fluids*, **4**, 791-799, 1961.
- Garrett, C. J. R., and W. H. Munk, Space-time scales of internal waves, *Geophys. Fluid Dyn.*, **2**, 225-264, 1972.
- Katz, E.J., and M.G. Briscoe, Vertical coherence of the internal wavefield from towed sensors, *J. Phys. Oceanogr.*, **9**, 518-530, 1979.
- Muller, P., D. J. Olbers, and J. Willebrand, The IWEX spectrum, *J. Geophys. Res.*, **83**, 479-500, 1978.
- Pinkel, R., Upper ocean internal wave observations from FLIP, *J. Geophys. Res.*, **80**, 3892-3910, 1975.
- Roth, M.W., M.G. Briscoe, and C.H. McComas, Internal waves in the upper ocean, *J. Phys. Oceanogr.*, **11**, 1234-1247, 1981.
- Sabinin, K. D., Measurement of the parameters of internal waves by means of a moving, spatially-separated system of sensors, *Izv., Atm. Oc. Physics*, **7**, 379-381, 1971.
- Sabinin, K. D., Certain features of short-period internal waves in the ocean, *Izv., Atm. Oc. Physics*, **9**, 32-36, 1973.
- Zalkan, R. L., High-frequency internal waves in the Pacific Ocean, *Deep-Sea Res.*, **17**, 91-108, 1970.

Observations of Low-Latitude, Near-Inertial Gravity Waves Forced by Westerly Wind Bursts

Charles C. Eriksen

School of Oceanography, University of Washington, Seattle, Washington

Abstract. The dominant contribution to upper ocean current variance observed over a 4-month period within 2° of the equator in the western tropical Pacific was from motions with periods of a few to several weeks occurring in events coherent across hundreds of meters vertically and hundreds of kilometers meridionally. These can be explained in large part as near-inertial internal gravity waves generated by rapidly translating westerly wind bursts. The spatial and temporal structure of the observed currents can be understood through examination of wave rays. While wind bursts last only a few days, the near-inertial waves they excite propagate slowly away from the sea surface, refracting across the equator as they descend, remaining near the generation site for a few periods.

Introduction

Near-inertial motions are familiar features of oceanic response to wind forcing by storms at mid-latitudes (e.g. D'Asaro *et al.*, 1995). By contrast, wavelike motions in the vicinity of the equator are commonly described as meridionally standing modes. While equatorial modes aptly describe large scale low frequency motions excited winds of comparable scales, they are not very efficient in describing the response of the tropical ocean to short duration wind events. The response to such forcing is more compactly described as the superposition of downward wave beams excited with frequencies that are locally near-inertial at the top of the oceanic pycnocline.

The dominant contribution to upper ocean current variance observed within 2° of the equator in the tropical western Pacific over a 4 month period was from motions with a few weeks period. These occurred in events coherent across hundreds of meters vertically and hundreds of kilometers meridionally. These motions behave as near-inertial internal gravity waves, despite periods quite long compared to those at mid-latitudes. Rapidly translating westerly wind bursts generate a spectrum of waves, the most prominent of which are near-inertial at the latitude of their excitation. The spatial and temporal structure of the observed currents can be understood through examination of wave rays.

We use current profile time series from 7 moorings along 156°E to examine the spatial-temporal structure of upper ocean currents at low latitude. The depth-latitude structure of currents across a range of periods is conveniently described using complex empirical orthogonal functions (CEOFs). Over half the variance of upper ocean currents is contained in a single dominant mode across a range of frequency bands. The structure of these dominant empirical modes can be understood as the superposition of

near-inertial rays descending from both hemispheres and interfering at depth.

Westerly wind bursts generate ocean baroclinic waves whose phase speeds match the wind pattern translation speed. Formally, these may include Rossby, Kelvin and Rossby-gravity modes as well as equatorial gravity modes. Most attention has been given to Kelvin wave generation (e.g. Eriksen *et al.*, 1983, Geise and Harrison, 1990, McPhaden *et al.*, 1992, Kessler *et al.*, 1995). When the wind burst translation speed exceeds the gravest baroclinic mode Kelvin wave speed, gravity and Rossby-gravity modes form most of the response. The slowest of these waves (in group speed) are those which are near-inertial, hence have the highest energy density (in order to carry significant energy flux) so are most prominent in current observations. A linear model projecting idealized westerly wind burst stress onto equatorially trapped dynamical modes predicts currents with the character and amplitude of those observed (Eriksen, 1993). When summed, the dynamical modes reveal a response that at any given latitude is dominated by slightly superinertial wave motion. The dominant feature of the prediction can be understood by considering wave rays on an equatorial β -plane.

Data

Current profile time series along 156°E from 2°N to 2°S collected during the Tropical Ocean Global Atmosphere - Coupled Ocean Atmosphere Response Experiment (TOGA-COARE) Intensive Observing Period (IOP) (November 1992 through February 1993) are the primary data source for this study. These were obtained by a variety of investigators and three different kinds of instruments: acoustic doppler current profilers (ADCPs), multiple vector measuring current meters (VMCMs), and a profiling current meter (PCM). Wind stress records were

collected from the four surface moorings in this line, at 2°N , 0° , and 2°S (part of the TOGA Tropical Atmosphere Ocean (TAO) array maintained by the Pacific Marine Environmental Laboratory) and at $1^{\circ}45'\text{S}$ (Woods Hole Oceanographic Institution). Current records at 2°N and 2°S (Hiroshima and Tokai Universities), $0^{\circ}45'\text{N}$ and $0^{\circ}45'\text{S}$ (University of South Florida), and $1^{\circ}15'\text{S}$ (University of Washington) were collected using subsurface moorings. The wind records from TOGA-TAO moorings along 147°E and 165°E are a secondary source of data for this study. A map of the array is given in Figure 1.

Wind Patterns

Western tropical Pacific winds are of modest strength and exhibit considerable variability. During the boreal winter, trade winds are weak and punctuated by episodes of westerly winds lasting a few days or so. These westerly wind bursts are a manifestation of intraseasonal oscillations, large convective systems that develop over the eastern Indian Ocean and translate eastward with speeds of 10–20 m/s (Nakazawa, 1995, Milliff and Madden, 1996, Wheeler and Kiladis, 1999). Westerly wind bursts appear and disappear at a given surface location within a day or so and stresses associated with them typically reach a few Pa. Bursts have relatively short meridional scales (a few hundred km) but very long zonal scales (several thousand km) (Harrison and Vecchi, 1997). Wind records from the IOP indicate the passage of three such bursts during the last week of December 1992 and the first week of January, 1993, concentrated a few degrees south of the equator. Hourly zonal winds at 1.75°S , 156°E were highly correlated with those at 2°S , 165°E during the IOP at a lag of 15 h, indicating eastward propagation at roughly 18.5 m/s. Stress vector time series from the surface moorings along 156°E are shown in Figure 2.

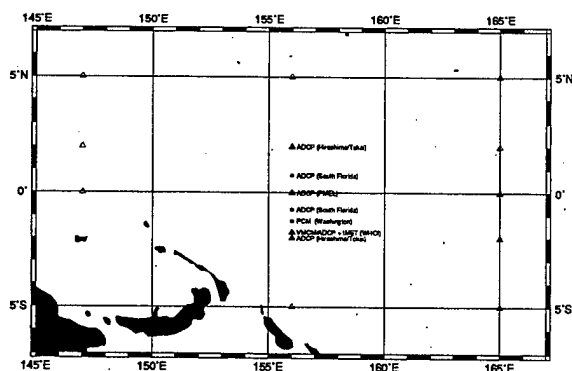


Figure 1: Map showing mooring locations (triangles denote surface, circles denote subsurface moorings).

Current structure

Upper ocean current variance is dominated by motions with periods of 10–40 days within a few degrees of the equator. Current fluctuations are prominent in both zonal and meridional components with the two in near quadrature to produce current vectors which turn anticyclonically at periods slightly shorter than the local inertial period. Both vertical and meridional propagation are prominent in current profile time series. Typical vertical scales and propagation rates are several tens of m and 5–20 m/day. The current vector time series at $1^{\circ}15'\text{S}$ illustrate these tendencies (Figures 3 and 4), where propagation is evident even in the unfiltered time series (Figure 3).

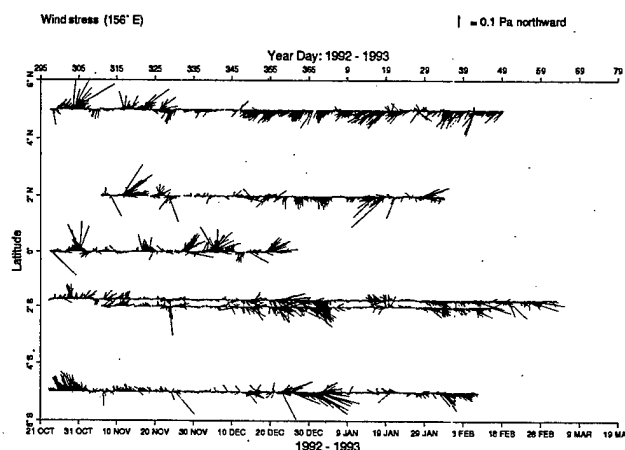


Figure 2: Wind stress time series from surface moorings along 156°E (3 hr averages). A sequence of three westerly wind bursts in late December 1992 is prominent in records from 2 and 5°S .

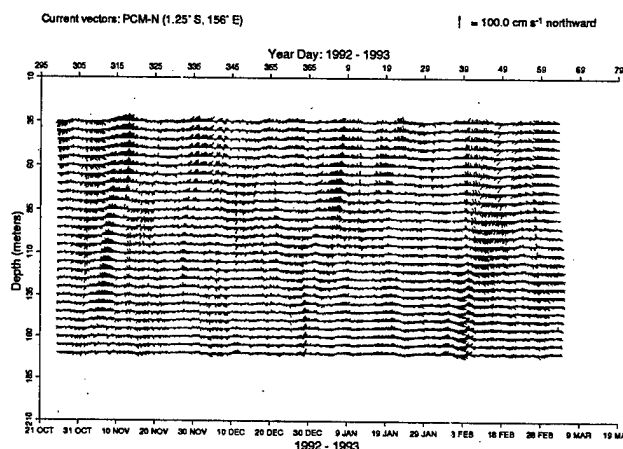


Figure 3: 3 hour current vector time series from $1^{\circ}15'\text{S}$. The local inertial period is 22.9d.

When viewed at common depths, the currents are seen to be coherent meridionally over a few hundred km and to display a tendency for equatorward propagation. As an example, current vector time series at 120m depth in the pycnocline are shown in Figure 5 (raw time series) and Figure 6 (10-20d band pass filtered series). Equatorward propagation is easily seen in the filtered time series to proceed at a few tens of km/d.

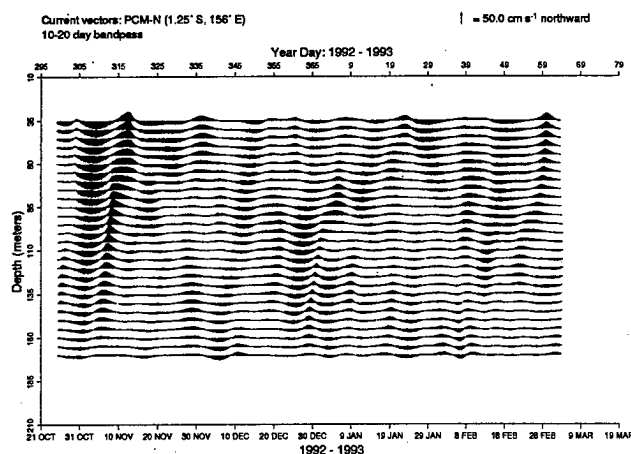


Figure 4: 10-20d bandpass filtered current vector time series from 1°15'S. Note prominent vertical propagation episodes in early November and in late December.

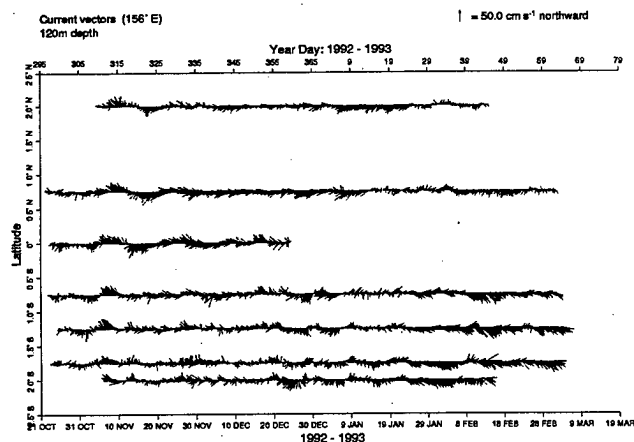


Figure 5: 3h current vector time series at 120 m depth

Vertical-Meridional Current Structure

The coherent structure of currents in the meridional-vertical plane as a function of period is readily given by complex empirical orthogonal functions (CEOFs). CEOFs are obtained from the cross spectral matrix of an array of measurements. To calculate these, the longest common record length over a significant latitude span was chosen (120 d), so that only records at 0°45'N, 0°45'S, 1°15'S, and 1°45'S were used. East and north current time series at 14 depths at the 4 mooring locations were used, and in addition, estimates of vertical velocity based on density

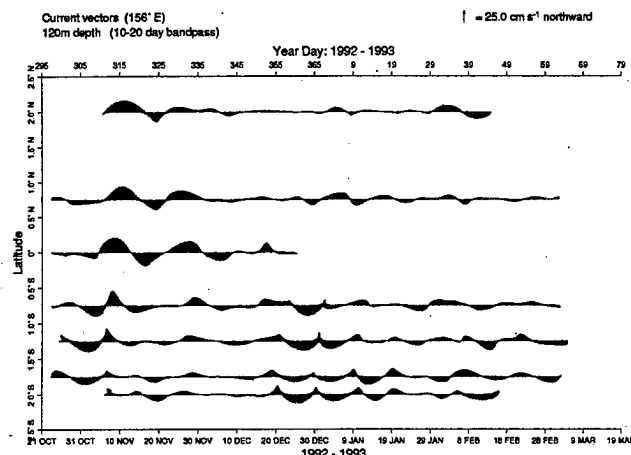


Figure 6: 10-20d band pass filtered current vector time series at 120 m depth. Note the equatorward propagation of current bursts in early November-late December 1992 and early January 1993.

time series at 1°15'S were used. The dominant mode of these 126 time series was clearly evident in 3 adjacent frequency bands (centered at periods of 20, 13.33, and 10d) where more than half of the current variance was explained by a single CEOF mode. The eigenfunctions for the dominant modes are displayed below in two ways.

The dominant CEOF mode eigenfunctions can be displayed as current ellipses for each depth-latitude location (Figure 7). Currents are polarized clockwise to the north and anticlockwise to the south of the equator, but with significant meridional orientation. Current ellipses are nearly circular at shallow depths (i.e. 40 m and shallower) but are elongated and tend to be oriented meridionally within the pycnocline (i.e. 40 m and deeper). In the 20d band, the structure of the dominant mode shows motions that are strongest near the shallowest depths used for the CEOF decomposition, 40-60 m, whereas in the 10d band the most prominent ellipses are at the deepest depths used in the decomposition. At the intermediate period, 13.33d, intermediate depth ellipses are prominent.

The CEOF eigenfunctions can also be plotted component by component, where each component has a magnitude and phase. The eigenfunctions of the east, north, and (for one latitude only, based on density time series) vertical current components at each depth-latitude location are so drawn in Figure 8. The length of each vector indicates relative amplitude, while its orientation indicates phase. The convention is that more clockwise vectors lead in time. An arrowhead is drawn on eigenvector components for which there is significant coherence between the measurements and the CEOF mode. The consistent clockwise turning with increasing depth of these vectors indicates upward phase propagation. Phase propagation is variously northward or southward dependent on depth and frequency. To understand these features, it is useful to examine internal wave ray paths.

Ray Tracing

The vertical-meridional structure of the dominant CEOF modes at the three period bands examined above can be explained by tracing rays on an equatorial β -plane. The fast zonal translation speed of wind patterns (roughly 20 m/s) suggests that waves with very small, purely zonal, wavenumber vectors will be excited at the sea surface. Rays describing such waves will be refracted equatorward as they propagate downward, upward phase propagation being indicative of downward energy propagation. The appearance of relatively high meridional wavenumber components within a short distance from the surface can be understood by recognizing that near-inertial motions at neighboring latitudes will become ever more out of phase as time passes, generating short meridional scale motions. This is the mechanism used by D'Asaro, 1989, to explain growing meridional wavenumber in mid-latitude near-inertial motions. The difference in near-inertial frequencies between adjacent latitudes is comparable to the inertial frequency itself at low latitudes, driving significant convergence and divergence in the meridional direction, in turn forcing vertical motions. Near-equatorial near-inertial waves thus carry substantial vertical velocity signals.

Closed-form solutions to the problem of zonally rapidly propagating wind patterns generating wave motions in the equatorial zone can be found by considering equatorial wave modes, but the resulting solution resembles no particular equatorial mode. When thousands of modes are superimposed, the solution is better described as a continuum of rays propagating as locally near-inertial waves at their generation site (Eriksen, 1993). These rays descend and crisscross in latitude and depth. By tracing rays through the western Pacific pycnocline, an explanation for the apparently complicated patterns of Figures 7 and 8 can be found.

The finite bandwidth of any spectral band means that rays across the range of frequencies over which CEOFs are calculated must be considered. The ray paths for rays starting at the surface at frequencies one percent higher than the local inertial frequency corresponding to the center and edges of each band are plotted in Figure 9. These rays all cross the equator as they descend, reach their turning point in the opposite hemisphere, and refract back across the equator. Ray paths generated on opposite sides of the equator cross more deeply with higher frequency when projected onto the meridional-vertical plane, since lower frequency waves travel along more gently sloping ray paths.

Near-inertial rays generated at the surface with purely zonal wavenumber turn equatorward after descending only a few meters. The more nearly inertial they are, the more meridionally dominated their paths are. Rays corresponding to the center and edges of the frequency band for

which empirical eigenvector structures for meridional current are displayed in Figure 9. The WKB local wavenumber components in the vertical-meridional plane for rays starting at 1% above the local inertial frequency at their point of origin (chosen as the base of the mixed layer) are comparable to wavenumber components inferred from the CEOF structure, as indicated. Ray paths explain the slanted structure of the observed modes as a result of coherently forced near-inertial waves generated in both hemispheres (but primarily in the southern) propagating downward, crossing, and alternately reaching turning points on either side of the equator.

The swaths in depth-latitude space covered by near-inertial rays in Figure 9 first intersect at shallower depth in the 20d band and at deeper depth in the 10d band. Interference between rays descending from opposite hemispheres is a likely explanation for the lack of coherent structure deeper than about 100m in the 20d band. By contrast, near-inertial rays in the 10d band do not intersect the measurement locations until 80-100m depth, explaining why the empirical mode is most prominent at deeper depths in this band.

By differencing phase meridionally and vertically, an estimate of the wavenumber vector can be found (assuming the zonal component is negligible, since the zonal scale of the forcing is very large). These estimates are plotted wherever pairs of adjacent significantly coherent eigenvector estimates, both vertically and meridionally, are found. These estimates are plotted in the panels of Figure 9 as double width lines, scaled by the vertical exaggeration of the plot so that slope is preserved. Thin arrows indicate the corresponding wavenumber projections of the ray traces at the center frequency of each band. These are comparable and generally similarly directed where the estimates can be made.

Discussion

Rapidly translating wind bursts excite internal gravity wave rays at all latitudes lower than the inertial one for a given frequency. Rays from most of these latitudes progress rapidly eastward with the westerly wind burst. The rays whose group velocity is smallest (i.e. near-inertial ones) stay in the vicinity of forcing a substantial time after it has passed. Examples of such rays are given in the panels of Figure 10, where rays locations are plotted every 0.5h starting from the surface at locations initially 0.1° apart along a meridian. The ray closest to the turning latitude in case descends most slowly, indicating phase changes of half a cycle or more in the upper 200 m. These near-inertial rays crisscross the equator most directly and descend most steeply, travelling zonally only modestly in the upper ocean.

The favorable comparison between simple linear ray

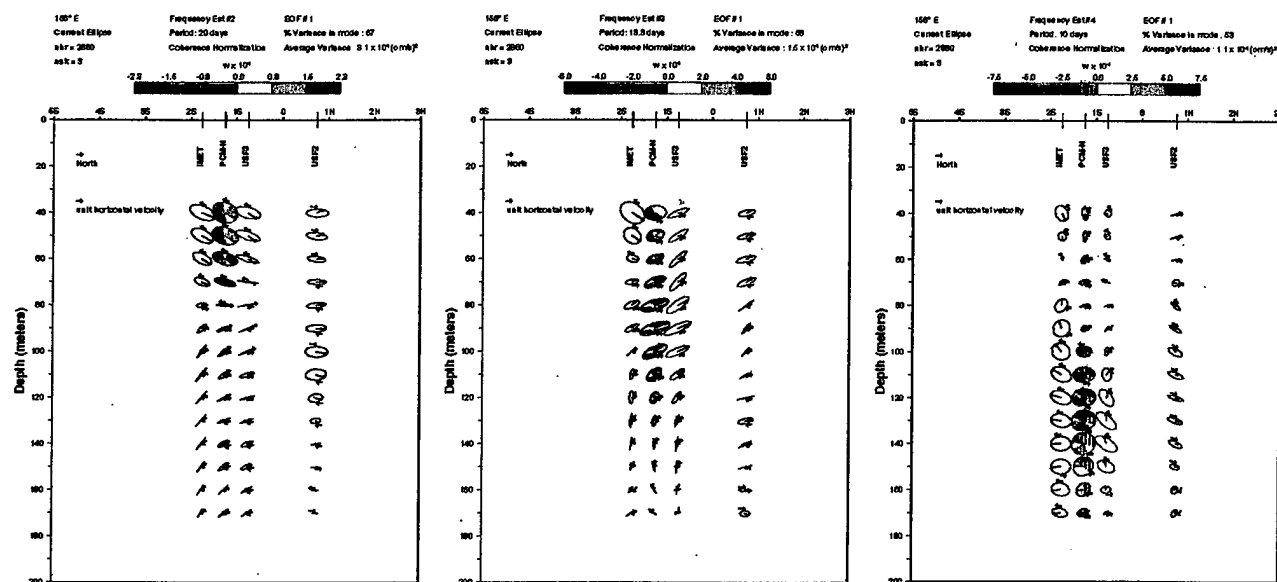


Figure 7: The dominant eigenmode for a CEOF decomposition made from horizontal current records at 14 depths and $1^{\circ}45'S$, $1^{\circ}15'S$, $0^{\circ}45'S$. and $0^{\circ}45'N$ and vertical current inferred from density fluctuations at $1^{\circ}15'S$. The eigenmodes are plotted as horizontal current ellipses oriented with north to the right, east down. Vertical current is indicated by color and is scaled by 10^4 . Current ellipses tend to be oriented meridionally and are more energetic at the shallower depths observed at 20d period and at the deeper depths at 10d period.

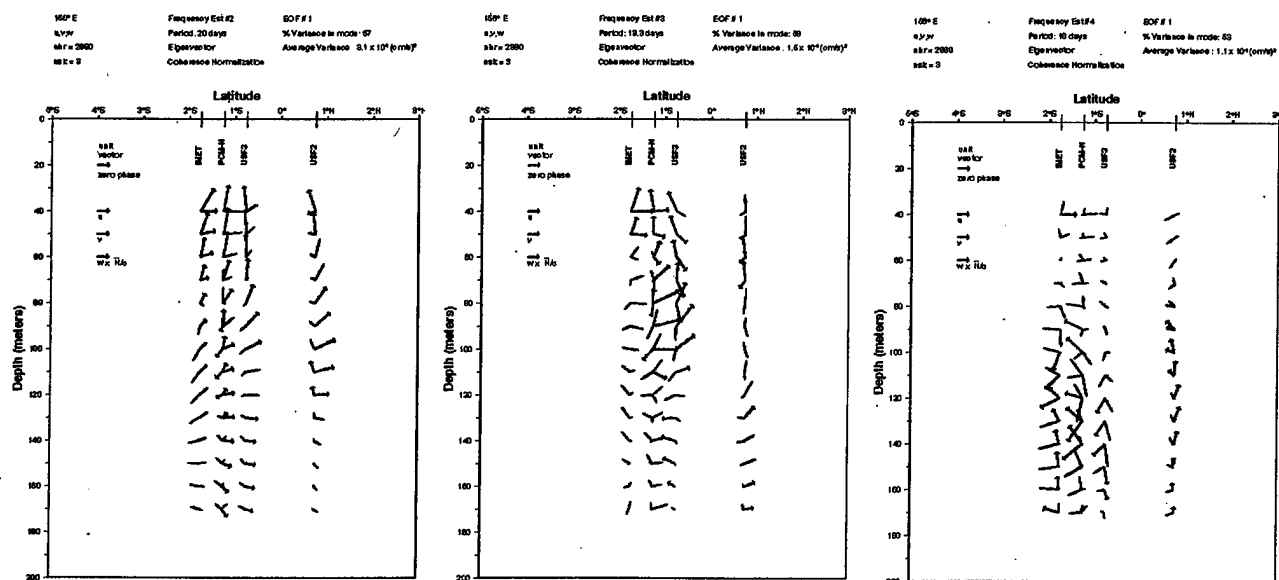


Figure 8: The dominant eigenmode as in Figure 5 but plotted as vectors for each flow component where length indicates magnitude and orientation phase (more clockwise leads). Zonal, meridional, and vertical current components are plotted as red, blue, and green vectors, respectively. Arrow heads are drawn for significant coherence with measured series at 95% confidence. Upward phase propagation is evident throughout but meridional propagation sense varies with position and frequency.

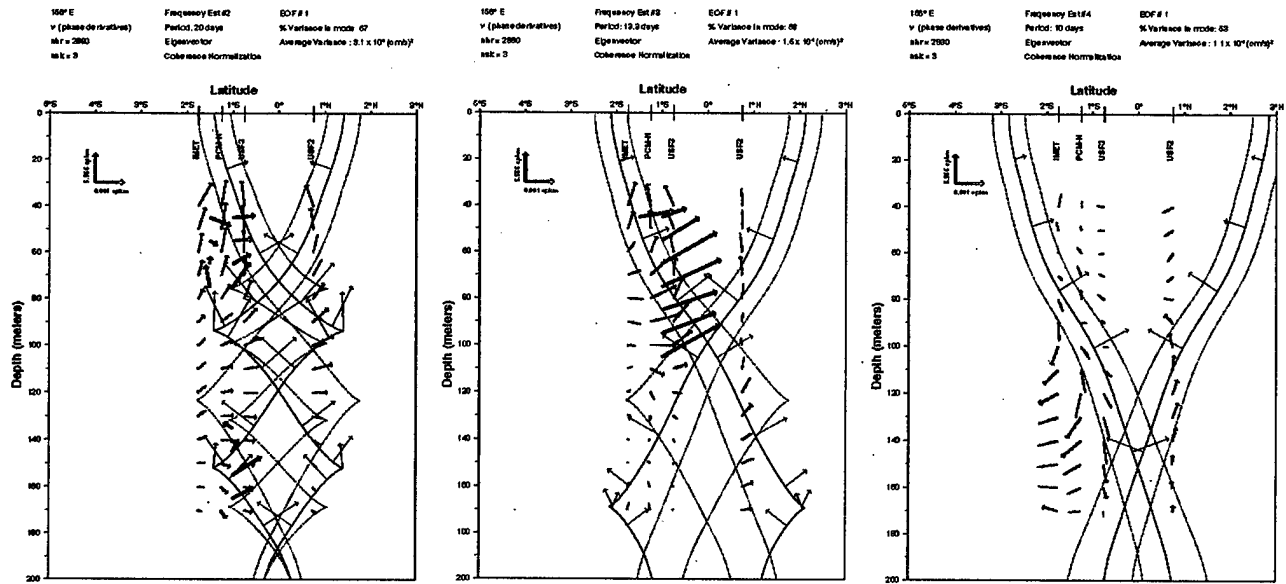


Figure 9: Rays projected onto the vertical-meridional plane for waves starting at the sea surface with purely zonal wavenumber corresponding to zonal propagation at 20 m/s and frequency one percent higher than the local inertial frequency. Heavy curves correspond to rays with the central frequency of the band (20d left panel, 13.33d middle panel, and 10d right panel). Lighter curves correspond to waves with frequencies at the edges of each band. Rays are superimposed upon the dominant eigenfunction describing meridional current (blue vectors, plotted with arrowheads if significantly coherent at 95% confidence). Double arrows indicate wavenumber vectors calculated as finite differences between sites for which current coherence with the CEOF mode is significantly non-zero. These vectors are stretched with the same vertical exaggeration as the figure. Thin arrows indicate the local wavenumber vector calculated from the central band ray at 30° intervals.

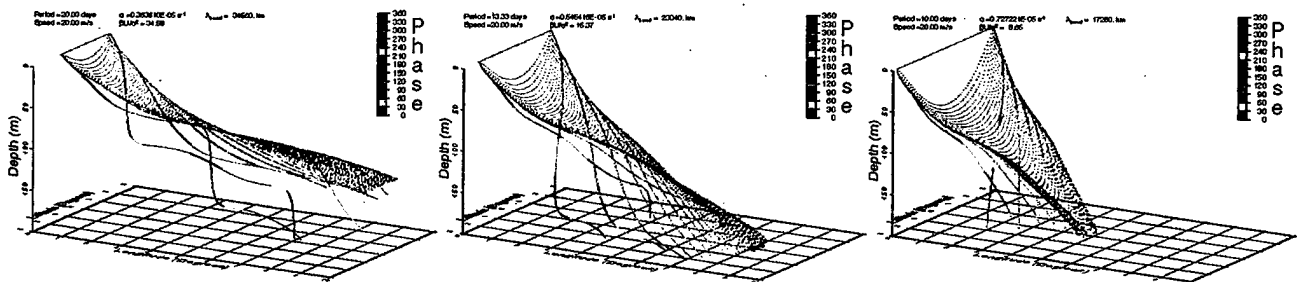


Figure 10: Traces in three dimensions for rays starting at the sea surface with purely zonal wavenumber corresponding to 20 m/s zonal speed at different period (20d left, 13.33d middle, 10d right). Dots are drawn every half hour. Phase is indicated by color. The domain is from 3°S to 3°N over 10° longitude in the top 200 m using the average COARE IOP stratification. Rays starting near the turning points descend most slowly (phase changes through a large fraction of a cycle) and are most meridionally oriented. Because these have smaller group speed than those starting closer to the equator, they have proportionately higher energy density. Waves starting near the turning points remain close to the generation site long after the swift passage of the wind disturbance that generated them.

theory and the observed depth-latitude-frequency current structure confirms that most of the observed variance at periods of a few weeks within a few degrees of the equator is due to near-inertial internal gravity waves. Because of the substantial vertical motions induced by such waves, linear theory is expected to no longer apply after several days, since advection in the vertical-meridional plane becomes important (Eriksen, 1993). Yet before nonlinearities become important, linear theory also predicts that Richardson numbers will fall to 1/4 or below, suggesting the onset of turbulent mixing. It is expected that near-inertial rays will dissipate themselves before flow becomes nonlinear on wave scales.

Acknowledgments

We are grateful for current measurements made by R. Weisberg and A. Kaneko and current and wind measurements made by R. Weller and M. J. McPhaden without which this work could not have been done. This work was supported by N.S.F. under grant OCE-9110537.

References

- D'Asaro, E. A., 1989: Decay of wind-forced mixed layer inertial oscillations due to the β -effect, *J. Geophys. Res.*, **94**, 2045-2056.
- D'Asaro, E. A., C. C. Eriksen, M. D. Levine, P. Niiler, C. A. Paulson, and P. Van Meurs, 1995: Upper-ocean inertial currents forced by a strong storm. Part I: Data and comparisons with linear theory, *J. Phys. Oceanogr.*, **25**, 2909-2936.
- Eriksen, C. C., M. B. Blumenthal, S. P. Hayes, and P. Ripa, 1983: Wind-generated equatorial Kelvin waves observed across the Pacific Ocean, *J. Phys. Oceanogr.*, **13**, 1622-1640.
- Eriksen, C. C., 1993: Equatorial ocean response to rapidly translating wind bursts, *J. Phys. Oceanogr.*, **23**, 1208-1230.
- Geise, B. S., and D. E. Harrison, 1990: Aspects of the Kelvin wave response to episodic wind forcing, *J. Geophys. Res.*, **95**, 7289-7312.
- Harrison, D. E., and G. A. Vecchi, 1997: Westerly wind events in the tropical Pacific, 1986-95, *J. Climate*, **10**, 3131-3156.
- Kessler, W. S., M. J. McPhaden, and K. V. Weickmann, 1995: Forcing of intraseasonal Kelvin waves in the equatorial Pacific, *J. Geophys. Res.*, **100**, 10613-10631.
- McPhaden, M. J., F. Bahr, Y. Du Penhoat, E. Firing, S. P. Hayes, P. P. Niiler, P. L. Richardson, and J. M. Toole, 1992: The response of the western equatorial Pacific Ocean to westerly wind bursts during November 1989 to January 1990, *J. Geophys. Res.*, **97**, 14289-14303.
- Milliff, R. F. and R. A. Madden, 1996: The existence and vertical structure of fast, eastward-moving disturbances in the equatorial troposphere, *J. Atmos. Sci.*, **53**, 586-597.
- Nakazawa, T., 1995: Intraseasonal oscillations during TOGA-COARE IOP, *J. Met. Soc. Japan*, **73**, 305-319.
- Wheeler, M., and G. N. Kiladis, 1999: Convectively-coupled equatorial waves: Analysis of clouds and temperature in the wavenumber-frequency domain, *J. Atmos. Sci.*, **56**, 374-399.

Internal Wave Generation in the Equatorial Undercurrent

Dailin Wang

International Pacific Research Center, School of Ocean and Earth Science and Technology,
University of Hawaii at Manoa, Honolulu, Hawaii

Peter Müller

Department of Oceanography, School of Ocean and Earth Science and Technology, University of
Hawaii at Manoa, Honolulu, Hawaii

Abstract.

The generation of internal waves in the equatorial undercurrent is studied using a large-eddy simulation (LES) model. The model is forced with a constant easterly windstress and diurnal heating and cooling. Internal waves are generated with typical horizontal wavelengths of about 250 m, consistent with observations and comparable to the wavelengths of the most unstable modes from linear instability analysis. The internal waves exhibit a diurnal cycle below the boundary layer, or well below the mixed layer. The equatorial undercurrent (EUC) shear is crucial for the generation of these "long" internal waves. The range of diurnal variation of the wave energy (or equivalently, the isotherm displacement) is also consistent with observations. The wave energy is highly correlated with turbulence dissipation in the stratified regions of the boundary layer, in agreement with observations. The wave energy flux below the boundary layer has a maximum value of about 0.4 mW/m^2 near the core of the EUC. The wave energy flux into the deep ocean is about one order of magnitude smaller. The interaction of nighttime convection with the EUC does not contribute significantly to the internal wave field in the deep ocean.

1. Introduction

It has been well over a decade since the first observations of deep diurnal cycle turbulence at the equator [Gregg *et al.*, 1985; Moum and Caldwell, 1985]. Various mechanisms have been proposed for this deep-cycle turbulence, including Kelvin-Helmholtz instability of the mean and/or local shear and internal wave breaking in the high but stable shear environment. One of the characteristics of the deep-cycle turbulence is the existence of internal waves with typical wavelengths of a few hundred meters below the mixed layer [e.g., McPhaden and Peters, 1992; Lien *et al.*, 1996]. Two dimensional numerical studies [e.g., Skillingstad and Denbo, 1994] also show the existence of such internal waves. The most unstable modes of the EUC system also have these wavelengths, as shown by the linear analyses of Sutherland [1996] and Sun *et al.* [1998]. The linear analyses require the mean shear to be unstable above a certain depth (in the mixed layer and/or in part of the stratified layer be-

low the mixed layer). The vertical wavelengths of the growing waves are, however, much larger than the region of dynamic instability. Sun *et al.* [1998] suggested that these internal waves play a critical role in the generation of the deep-cycle turbulence, although it cannot be deduced from linear analysis whether or not these waves develop into turbulence because of the lack of an active turbulent boundary layer and the infinitesimal growth assumptions.

In a recent study by Wang *et al.*, [1998], who used a large-eddy simulation (LES) model, the deep diurnal cycle of turbulence was qualitatively reproduced. This study suggests that local Kelvin-Helmholtz (K-H) instability is the major cause of the deep-cycle turbulence. It also suggests that the deep-cycle turbulence is a contiguous part of the boundary layer in the presence of the equatorial undercurrent (EUC). Since the model domain size of this study was not large enough to resolve the observed internal waves with wavelengths of a few hundred meters, the results of their study seem

to contradict the suggestion of *Sun et al.* [1998]. Further investigations are warranted of how these internal waves are generated and whether or not these internal waves have any effects on the deep-cycle turbulence.

In this study, we investigate the generation of long internal waves in the equatorial boundary layer using a large-eddy simulation (LES) model with a much larger domain than that used in *Wang et al.* [1998] so that internal waves with wavelengths of a few hundred meters can be resolved (for the remainder of this paper, we shall refer to these internal waves as "long internal waves", to distinguish them from short internal waves, which can also be generated in the LES model). The advantage of a 3-D LES model over 2-D models and linear analyses is that both turbulence (large eddies) and internal waves are resolved simultaneously. Here we focus on the following questions:

Can long internal waves be generated from the interaction of diurnally cycling turbulence and the equatorial undercurrent shear?

What is the generation mechanism of these waves?

Do these waves carry a significant wave energy flux into the deep ocean?

The effects of these long internal waves on the deep-cycle turbulence itself will be discussed elsewhere.

The LES model and numerical experiments are described in section 2. Model results are presented in section 3 and some concluding remarks are made in section 4.

2. Model and Numerical Experiments

The LES model used in this study is based on a newer version [*Sullivan et al.*, 1996] of the LES model originally developed by *Moeng* [1984]. The model employs collocation Fourier method in the horizontal and second order finite difference in the vertical. Some of the large-scale flow terms typical of eastern Pacific conditions are also included: the equatorial undercurrent (EUC), zonal pressure gradient, upwelling, horizontal divergence, zonal temperature gradient, and mesoscale eddy forcing terms for the zonal momentum and the heat equations. The governing equations are

$$\mathbf{u}_t + \mathbf{u} \cdot \nabla \mathbf{u} = -\nabla p - \alpha g T + \nabla \cdot \boldsymbol{\tau} + \mathbf{G}, \quad (1)$$

$$\nabla \cdot \mathbf{u} = 0, \quad (2)$$

$$T_t + \mathbf{u} \cdot \nabla T = \nabla \cdot \mathbf{q} + \frac{1}{C_p} \partial_z I(t, z) + H_T, \quad (3)$$

$$e_t + \mathbf{u} \cdot \nabla e + W e_z = \boldsymbol{\tau} : \nabla \mathbf{u} - \alpha g q_3 - \epsilon + \nabla \cdot 2\mathbf{K} \cdot \nabla e, \quad (4)$$

where $C_p = 4.1 \times 10^6 \text{ J m}^{-3} \text{ K}^{-1}$ is the specific heat of sea water per unit volume and $\alpha = 0.00027 \text{ K}^{-1}$ is the thermal expansion coefficient. The large scale terms \mathbf{G} and H_T are given by

$$\begin{aligned} G_u &= -uU_x - vU_y - Wu_z - P_x + F_u, \\ G_v &= -uV_x - vV_y - Wv_z - P_y + F_v, \\ G_w &= -uW_x - vW_y - Ww_z + F_w, \end{aligned} \quad (5)$$

and

$$H_T = -u\hat{T}_x - v\hat{T}_y - WT_z + F_T, \quad (6)$$

where $\mathbf{F} = (\mathbf{F}_u, \mathbf{F}_v, \mathbf{F}_w)$ and F_T represent mesoscale eddy forcing that is not explicitly contained in the LES model. The variables in upper cases are prescribed. Further details of the model physics and subgrid scale parameterizations (SGS) are given in *Wang et al.* [1998, section 2 and appendices therein].

The model domain size for the present study is $640 \text{ m} \times 160 \text{ m} \times 270 \text{ m}$, with a resolution of $128 \times 32 \times 270$. In the zonal direction, this model domain size is four times that of the largest domain size used in *Wang et al.* [1998]. Ideally, the domain size in the meridional direction should also be 640 m, instead of 160 m as used here. The choice of the smaller domain size in the meridional direction size is purely based on the availability of computing resources. However, with 32 grid points in the meridional direction, the resolved large eddies within the boundary layer are still three dimensional. A 3-D configuration is required. We were unable to generate turbulence in a 2-D configuration without added random forcing at the surface. *Skyllingstad and Denbo* [1994] employed large amplitude (as much as 30% of the prescribed value) random surface forcing in their 2-D study, for as long as a 24-hour period, to facilitate spinup of 2-D large eddies.

The initial condition of the numerical experiment is obtained by repeating 16 times the $16 \times 16 \times 270$ resolution case in *Wang et al.* [1998, experiment I] at 3 p.m. of day five, with some small initial noise (with velocity variance of order $10^{-6} \text{ m}^2/\text{s}^2$) introduced to break the symmetry of the original solution. Without the noise, it would take a very long time for motions with scales larger than the small domain to develop (only possible because of machine truncation errors). The surface forcing are a constant zonal windstress of $\tau = -0.042 \text{ N/m}^2$, a constant cooling rate of $Q = -200 \text{ W/m}^2$, and a sinusoidal penetrative solar heating with noontime maximum insolation of 776 W/m^2 . The model is integrated forward for two days.

We also conducted a pure convection experiment to contrast its solution with that of the experiment de-

scribed above to gain insights into the generation mechanisms of internal waves. The convection experiment employs a domain size of $960 \text{ m} \times 320 \text{ m} \times 270 \text{ m}$, with a resolution of $192 \times 64 \times 270$.

3. Results

3.1. Diurnal Cycle of Internal Waves

The diurnal cycle of the boundary layer is caused by the diurnal solar heating. At night, when solar heating is absent, convection occurs because of surface cooling. The mixed layer deepens and turbulence grows. During the day, restratification of the surface layer due to intense solar heating suppresses convection and turbulence decays despite the windstress forcing. In this section we present evidence of the diurnal cycle of internal wave generation below the boundary layer.

Figure 1 shows a snapshot of vertical velocity in the $x-z$ plane typical of the early morning hours. The mixed layer has a depth of about 30 m. The boundary layer extends to about 80 m depth. The zonal scales of motions below the boundary layer are about 250 m. The vertical scales are on the order of 80-100 meters. Closer examination of the time evolution shows that these large scale features have upward phase propagation and are coherent over a large vertical extent. These large scale features can be traced upward into the boundary layer. For example, the positive vertical velocity region, centered at $x = 130 \text{ m}$, extends from 160 m to about 20 m, with zonal scales of about 80 m at the depth of 80 m. Similar features are also observed for the other two positive velocity regions, centered at 330 m and 550 m, respectively. We interpret these large scale upward propagating features as long internal waves. For internal waves upward phase propagation implies downward energy propagation.

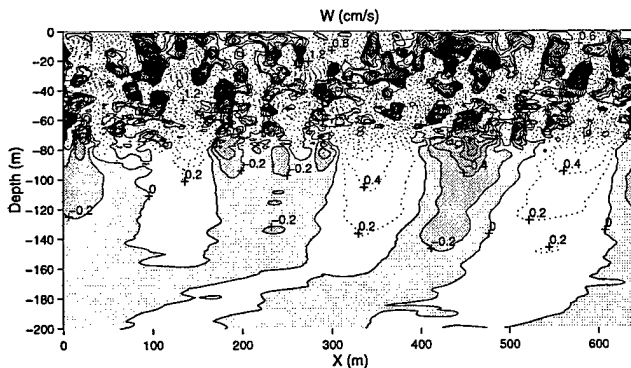


Figure 1. A zonal section of vertical velocity at 6 a.m. Regions with negative vertical velocities are shaded. Positive contours are indicated by dotted lines. The range of vertical velocity is about $[-3, 3] \text{ cm/s}$. Contour interval $= 0.2 \text{ cm/s}$.

The horizontal and vertical scales of resolved motions above 40 m are a few tens of meters and exemplify convective turbulence (of course, if the resolution is still finer, smaller scale motions can also be resolved). The stratified region below 40 m but above 80 m shows somewhat smaller scales of motions, compared to the region above. This is because stratified turbulence tends to have smaller scales in more stable stratification. As described above, these small scales are modulated by the long internal waves extending upward into the boundary layer. Note that the small scale motions are absent in *Skyllingstad and Denbo's* [1994] 2-D simulation. However, long internal waves are still generated. We shall defer the discussion of the generation mechanism of these long internal waves to section 3.3.

We will next address the question whether or not internal waves below the turbulent boundary layer exhibit a diurnal cycle. First we define as a measure of nonlinearity the ratio γ of the rms perturbation temperature gradient to the mean temperature gradient

$$\gamma = \frac{\sqrt{\langle T_z'^2 \rangle}}{\langle T_z \rangle},$$

where triangle brackets denote horizontal averages. Above 80 m, γ tends to be larger than one (except during the daytime decay of turbulence in the mixed layer) and to be smaller than one below 80 m. Therefore, the motions above 80 m are more nonlinear, or more turbulence-like, and the motions below 80 m are more linear, or more wave-like (see also [Wang et al. 1998]). This behavior of γ is another indication that the large scale feature below 80 m are internal waves.

Figure 2 shows the normalized vertical velocity variance $\langle ww \rangle$ as a function of time and depth. The mixed layer depth, defined as the depth at which density differs from that of the surface by 0.01 kg/m^3 , is also shown (dashed line). The mixed layer depth varies from 5 m during the day to 30 m at night. The boundary layer depth, defined as the depth at which the momentum flux or heat flux becomes zero (or a small fraction of the corresponding surface fluxes), is different from that of the mixed layer depth. For example, in the early morning hours, the boundary layer depth is roughly 80 m, while the mixed layer is much shallower.

After sunset and above 80 m (i.e., in the turbulent region), the depth at which the vertical velocity variance is maximal increases with time, a characteristic of turbulent entrainment. It takes time for convective turbulence to reach deeper depths. The growth of turbulence is gradual. It takes many hours for turbulence to reach deeper depths. In contrast, below 80 m (or in the wave region), there is no apparent phase difference between different depths: maximal vertical velocity variance is

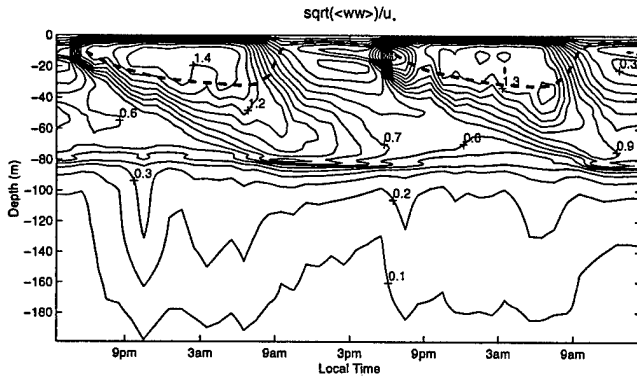


Figure 2. Vertical velocity variance, normalized by the surface friction velocity. The time axis covers two days, starting and ending 3 p.m. local time. The dashed line indicates the depth of the mixed layer, which is defined as the depth at which density differs from that of the surface by 0.01 kg/m^3 .

reached at the same time at all depths, such as the feature near 10 p.m. of the first diurnal cycle and near 8 p.m. of the second diurnal cycle. This is a characteristic of internal waves, of fast vertical propagation. The diurnal cycle of vertical velocity variance below 80 m thus indicates a diurnal cycle of internal wave activity below the boundary layer. In the 2-D study of *Skyllingsstad and Denbo* [1994] there are no separate regions of turbulence and waves. The rms of vertical velocity in their whole region resembles that of the wave region in this study.

3.2. Wave Energy

Observational studies often calculate the normalized displacement variance

$$P_e = N^2 \eta^2, \quad (7)$$

where $\eta^2 = \langle T'^2 \rangle / \langle T_z \rangle^2$. Figure 3 shows time series of P_e at 30, 60, 70, and 80 m. At 30 m and 80 m (solid line and dot-dashed line), P_e varies by a factor of about ten over a diurnal cycle, which is comparable to the observations of *Moum et al.* [1992]. At 60 m and 70 m, the diurnal variations of P_e are much smaller, only about a factor of two. This is small compared to observations. This discrepancy might be due to the fact that environmental conditions used in our model are not exactly comparable to the observations. In terms of gradient Richardson number Ri , a depth of 80 m in our study corresponds to a depth of about 50 m in *Moum et al.* [1992, Figure 7].

Observations also show a high degree of correlation between P_e and turbulence dissipation. Figure 4 shows this correlation coefficient from our numerical simulation. The correlation coefficient is small for the depth

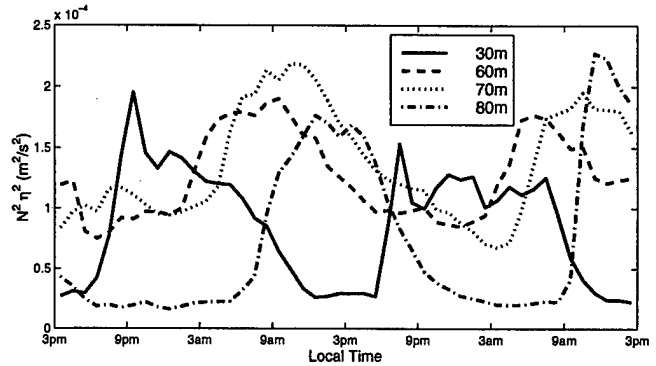


Figure 3. Time series of $N^2 \eta^2$ at 30, 60, 70, and 80 m.

range of 0–10 m, greater than 0.8 for the depth range 15–80 m, and then decreases towards deeper depths. This finding is also comparable to the observations of *Moum et al.* [1992], who found the correlation coefficient to be near 0.8 away from the surface and no significant correlation below the depth of 50 m, which is comparable to the depth of 80 m in our numerical study.

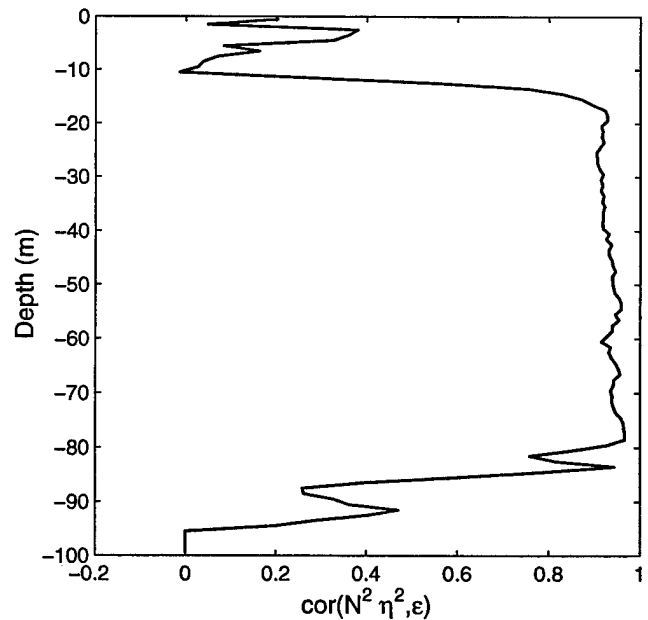


Figure 4. Correlation coefficient between $N^2 \eta^2$ and turbulence dissipation.

The displacement variance P_e defined by (7) is often referred to as internal wave energy in the literature [e.g., *Moum et al.* 1992; *Lien et al.* 1996]. P_e is indeed the total energy of internal waves if one assumes equipartition between potential and kinetic energy, which is the case for high frequency internal waves. Thus P_e represents the wave energy at depth below 80 m. This is not true in the stratified region above 80 m where

we also have turbulence. We have not attempted separating turbulence and waves in this region. *D'Asaro and Lien* [this volume] and *Lien et al. [1998]* suggest a method of separating turbulence and waves according to the Brunt-Väisälä (or buoyancy) frequency N . Motions with Lagrangian frequencies higher than N are considered turbulence while motions with frequencies below N are considered waves. Turbulent large eddies can also have time scales (eddy turnover times) longer than the buoyancy period, and that this distinction might not be fully adequate. We will explore the possible use of this method in diagnosing LES solutions in future studies.

3.3. Mechanisms of Wave Generation

In section 3.1, we showed that long internal waves are generated when the model domain was large enough. One immediate question that follows is whether such long internal waves can be generated without the presence of an equatorial undercurrent shear. To address this question, we conducted a pure convection experiment with the same initial stratification as that of the experiment with the EUC and with the same surface cooling rate of 200 W/m^2 . Figure 5 shows a typical zonal section of vertical velocity. There are internal waves below the boundary layer. The vertical and horizontal scales of these waves, however, are small compared to the case with the EUC shear (compare with Figure 1). The amplitudes of these waves are also much smaller. It is intriguing that the internal waves have smaller scales near the bottom of the boundary layer than well below the boundary layer. We do not yet have an explanation for this behavior. Comparison of the convection experiment and the experiment with the EUC demonstrates that the presence of the EUC shear is crucial for the generation of the long internal waves.

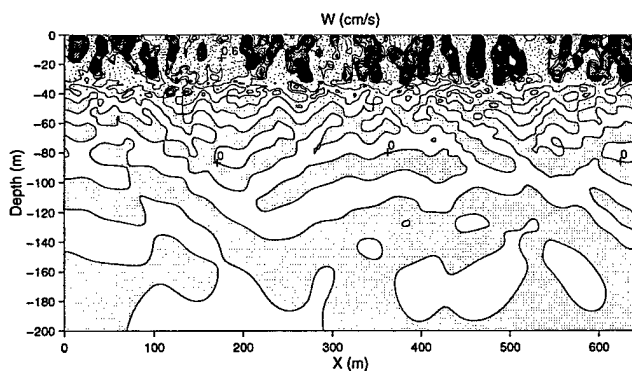


Figure 5. A zonal section of vertical velocity for pure convection experiment at time=210 min. Regions with negative vertical velocities are shaded. Positive contours are indicated by dotted lines. Contour interval=0.2 cm/s.

To investigate the role of the shear in the genera-

tion of long internal waves, Figure 6 shows the gradient Richardson number Ri at 6 a.m. and 6 p.m. At 6 a.m., Ri is near the critical value of $1/4$ for most part of the 0-50 m depth range. At 6 p.m., most of the water column is stable except near the surface, where nighttime convection has already commenced. We conclude that the diurnal cycle of the resolved long internal waves below the boundary layer in our model is a direct result of the diurnal cycle of mean shear instability inside the boundary layer.

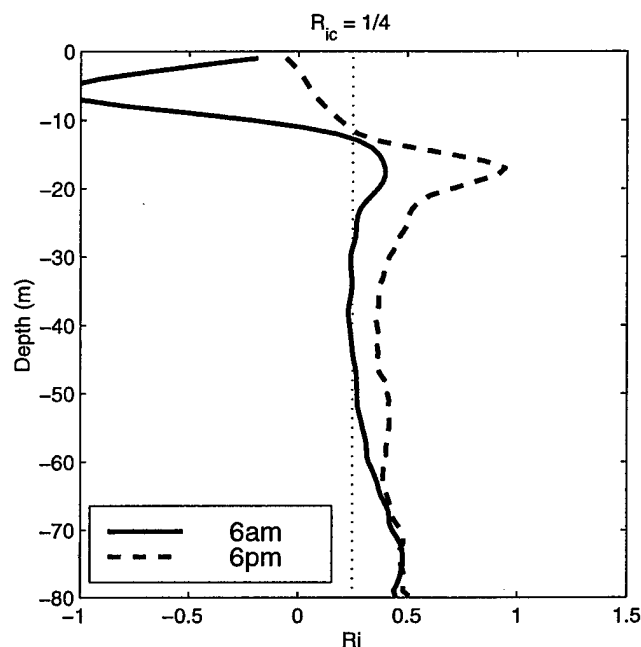


Figure 6. Gradient Richardson number Ri . The dotted line indicates critical Richardson number $Ri_c = 1/4$.

The fact that 2-D studies and linear analyses also show the generation of these long internal waves implies that turbulence convection is not a necessary condition for the generation of the long internal waves. As long as the mean shear is unstable, long internal waves tend to grow given the right scale of disturbances. We further speculate that long internal waves might also be generated due to local K-H instability, in a stable mean environment. Future studies are needed to test this hypothesis.

3.4. Wave Energy Flux into the Deep Ocean

Figure 7 shows a profile of the vertical energy flux $\langle pw \rangle$ at 6 a.m. Its divergence is a small term in the overall turbulent kinetic energy budget. Below 80 m the energy flux is interpreted as an internal wave energy flux. The flux peaks just below the boundary layer, around 110 m, with a value of 0.4 mWm^{-2} , and then decreases with depth. Only a flux of about 0.02 mWm^{-2}

leaves the domain towards the deep ocean. This flux is much smaller than the flux of 1 mWm^{-2} quoted or implied for wind forced and tidally generated internal waves (e.g., Olbers 1983). If the LES code correctly implements the radiation condition at the lower boundary of the model domain then we must conclude that internal waves generated by the interaction of nighttime convection with the EUC shear does not significantly contribute to the deep ocean internal wave field.

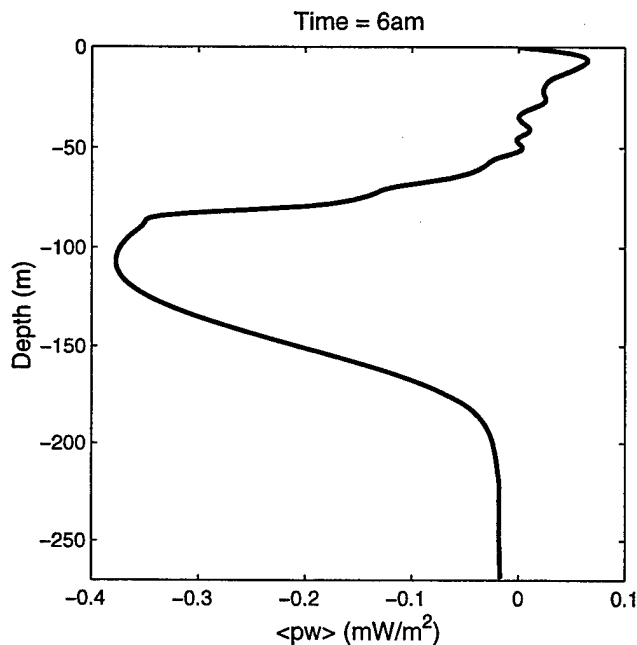


Figure 7. Wave energy flux $\langle pw \rangle$ at 6 a.m.

4. Conclusion

Internal wave generation in the equatorial undercurrent is investigated using a large eddy simulation model with a larger domain size than previous LES studies. It is found that internal waves with typical wavelengths of 250 m are generated as an integral part of the equatorial boundary layer. The equatorial undercurrent shear is crucial for the generation of these waves. The mean shear is more unstable during nighttime convection than during the daytime restratification when only the surface layer is dynamically unstable. This diurnal cycling of the mean shear causes a diurnal cycle in the internal wave energy.

The wave energy flux into the deep ocean is calculated to be of order 0.02 mW/m^2 , which is small compared to energy fluxes for wind and tidally generated internal waves.

We also found that the long internal waves have minor effects on the deep-cycle turbulence. A detailed

examination of this issue will appear elsewhere.

In this and other numerical studies, and also in observations, it is not always clear how to distinguish waves from turbulence and whether or not such a distinction even makes sense in a stratified environment. We ascribed motions within the mixed layer to turbulence and motions well below the boundary layer to waves but made no attempt to separate these components in the transitional layer, or entrainment layer, where turbulence is very intermittent. It is even questionable whether the LES models with resolutions of a few meters adequately resolve these intermittent motions.

Acknowledgments. Funding to D. Wang is provided by Frontier Research System for Global Change. D. Wang is grateful to Humio Mitsudera for his encouragement. This is SOEST contribution no. 4865.

References

- Gregg, M. C., H. Peters, J. C. Wesson, N. S. Oakey, and T. J. Shay, Intensive measurements of turbulence and shear in the equatorial undercurrent, *Nature*, **318**, 140-144, 1985.
- Lien, R.-C., D. J. McPhaden, and M. C. Gregg, High-frequency internal waves at 0° , 140°W and their possible relationship to deep-cycle turbulence, *J. Phys. Oceanogr.*, **26**, 581-600, 1996.
- Lien, R.-C., E. A. D'Asaro, and G. T. Dairiki, Lagrangian frequency spectra of vertical velocity and vorticity in high-Reynolds-number oceanic turbulence, *J. Fluid Mech.*, **362**, 177-198.
- McPhaden, M. J., and H. Peters, Diurnal cycle of internal wave variation in the equatorial Pacific ocean: results from moored observations. *J. Phys. Oceanogr.*, **22**, 1317-1329, 1992.
- Moeng, C. H., A large-eddy-simulation model for the study of planetary boundary-layer turbulence. *J. Atmos. Sci.*, **41**, 2052-2062, 1984.
- Moum, J. N., and D. R. Caldwell, Local influences on the shear-flow turbulence in the equatorial ocean. *Science*, **230**, 315-316, 1985.
- Moum, J. N., D. Hebert, C. A. Paulson, and D. R. Caldwell, Turbulence and internal waves at the equator. Part I: statistics from towed thermistors and a microstructure profiler, *J. Phys. Oceanogr.*, **22**, 1330-1345, 1992.
- Olbers, D.J., Models of the oceanic internal wave field. *Rev. Geophys. Space Phys.*, **21**, 1567-1606, 1983.
- Skyllingstad, E. D., and D. W. Denbo, The role of internal gravity waves in the equatorial current system, *J. Phys. Oceanogr.*, **24**, 2093-2110, 1994.
- Sullivan, P. P., J. C. McWilliams, and C-H Moeng, A grid nesting method for large-eddy simulation of planetary boundary-layer flows, *Boundary-Layer Meteorology*, **80**, 167-202, 1996.
- Sun, C., W. D. Smyth, and J. N. Moum, Dynamic instability of stratified shear flow in the upper equatorial Pacific, *J. Geophys. Res.*, **103**, 10,323-10,338, 1998.
- Sutherland, B. R., Dynamic excitation of internal gravity

- waves in the equatorial oceans. *J. Phys. Oceanogr.*, 26, 2398-2419, 1996.
- Wang, D., W. G. Large, and J. C. McWilliams, Large-eddy simulation of the equatorial ocean boundary layer: diurnal cycling, eddy viscosity, and horizontal rotation. *J. Geophys. Res.*, 101, 3649-3662, 1996.
- Wang, D., J. C. McWilliams, and W. G. Large, Large-eddy simulation of the diurnal cycle of deep equatorial turbulence, *J. Phys. Oceanogr.*, 28, 129-148, 1998.
-

This preprint was prepared with AGU's \LaTeX macros v4, with the extension package 'AGU++' by P. W. Daly, version 1.6a from 1999/05/21.

Large-Eddy Simulation of Pressure Transport Below the Mixed Layer

Roland W. Garwood, Jr. and Ramsey R. Harcourt

Naval Postgraduate School, Monterey, California 93943

Abstract. Deep convection energizes the entire water column. Large-eddy simulation of the oceanic boundary layer system predicts turbulence in the well-mixed layer as well as turbulence-induced internal waves propagating into the underlying stratified water column of the freely convecting wintertime Labrador Sea. Of particular interest is the downward propagation of energy from the turbulent boundary layer by pressure transport and the buildup of internal wave energy in response to local atmospheric forcing. A near equilibrium internal wave spectrum is approached after about two weeks of episodic storm cooling. A broad band omnidirectional internal wave field with peak energy near the buoyancy frequency N is forced mostly by the surface buoyancy flux. The pressure transport of mixed-layer kinetic energy carries about 30 % of the available energy into the stratified zone and causing entrainment. On average, 10^{-4} W/m² or about 1% of the winter Labrador Sea mixed-layer energy escapes into the pycnocline where it is converted into internal wave energy.

1. Introduction

There is much interest in describing the internal wave field and understanding the sources and sinks for this energy in the ocean interior. The capability to predict the variety of phenomena responsible for internal wave generation, propagation and ultimate dissipation and mixing is necessary to understand and predict the distribution of mass, energy and momentum in the ocean interior. At the 1991 Hawaiian Winter Workshop many investigators reported on the broad aspects of the problem, and the meeting proceedings (*Muller and Henderson, 1991*) and subsequent journal articles provide valuable references and an understanding of the complex nature of these non-linear problems.

Here we focus only on a single source and pathway of internal wave energy by asking the question, "How much locally generated kinetic energy escapes the mixed layer to generate internal waves and ultimately to cause mixing and dissipation in the underlying pycnocline?" To answer this question for a specific well-observed case, the dynamical system response of the Labrador Sea water column to realistic surface forcing has been simulated numerically using oceanic large-eddy simulation (*Garwood et al., 1994; Harcourt et al., 1998; Harcourt, 1999*). The Labrador Sea deep convection field experiment, 1996-1998, is yielding a wealth of observations to initialize, force, and ultimately to verify model results (*The Lab Sea Group, 1999*).

2. Numerical Experiment

To focus on the problem here, Figure 1 is presented to define the problem and illustrate the nature of the results. This figure depicts the model-predicted internal wave field generated by the turbulence in the surface mixed layer. At the instant of this picture on Julian day 63 of

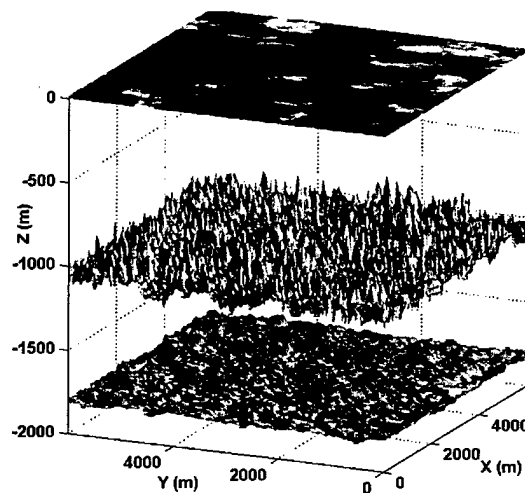


Figure 1. Sea surface temperature showing the surface manifestation of Rayleigh-Benard convection cells above isopycnal surfaces vertically distorted by internal waves in the Labrador Sea pycnocline.

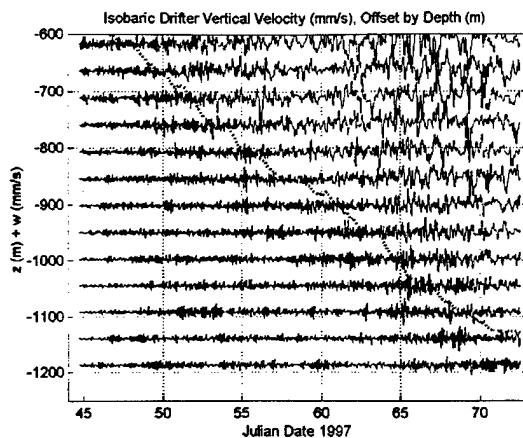


Figure 2. LES-predicted vertical velocity for isobaric drifters (solid) and mixed layer depth (dotted) for winter 1997 in Labrador Sea, from *Harcourt* (1999).

1997, the numerical model had simulated about 20 days of ocean response to synoptic atmospheric forcing. In the picture, the vertical displacements by the internal waves exceed 30 m on the km-deep density iso-surface just beneath the mixed layer. Wave displacements are on the order of 5 m on the iso-surface near $z = -2$ km. A well-mixed layer is at the top of this coupled turbulence-internal gravity wave system. The mixed layer coincides approximately with the fully turbulent boundary layer. It extends from the ocean surface at $z = 0$ downward to the beginning of the nonturbulent pycnocline at $z = -h$. In the course of 28 days during winter 1997 at 57N, 54W in the Labrador Sea, h deepened from less than 600 m to more than 1100 (Figure 2). The vertical velocities shown in this figure were "observed" by simulating freely drifting isobaric floats distributed randomly in the LES domain. Data collected by these floats augment considerably the sampling in time of both the turbulence and the internal waves. The fluctuating vertical velocity and buoyancy above $z = -h$ in Figure 2 are associated with turbulence; below $z = -h$ the vertical velocity and displacement are attributable to internal waves. Figure 3 is a representative N^2 profile. At the time of this profile, Julian day 63, the maximum stratification of $N = 10^{-3} \text{ s}^{-1}$ is at the base of the mixed layer near $z = -950$ m.

Between $z = 0$ and $z = -h$, turbulent kinetic energy (TKE) is produced by shear production (forced convection) and upward buoyancy flux (free convection). This TKE is mostly dissipated or converted to potential energy by downward buoyancy flux in the entrainment zone immediately beneath the well-mixed layer. For the Labrador Sea profile on day 63, the entrainment zone is the region of sharply increased N , which is about 200 m thick. The downward buoyancy flux in this zone is associated with entrainment or "penetrative convection." Typically, up to

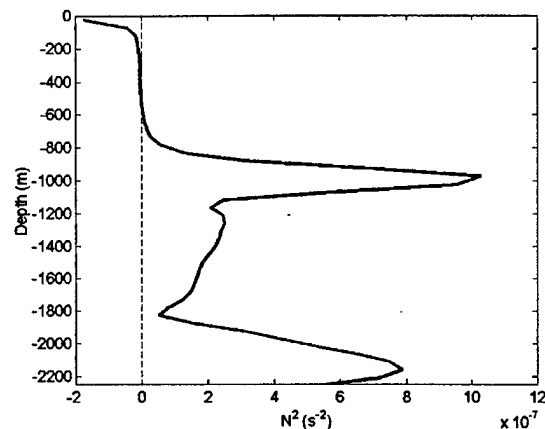


Figure 3. N^2 profile for 1 March 1997.

about 20-30% of the total mixed layer TKE may be converted into potential energy by penetrative convection. But how much energy escapes below the entrainment zone? The purpose of this paper is to answer this question using a nonhydrostatic model for the complete mixed layer-pycnocline system that includes actually observed surface forcing and the most complete model physics available to predict unsteady three-dimensional realization of both turbulence and internal waves.

2.1. Why is Large-Eddy Simulation Needed Here, and What are the Model Requirements?

Large-eddy simulation (LES) is necessary and appropriate for this problem because the same model that was originally developed for robust prediction of geophysical turbulence can predict the nonlinear forcing by wave-wave interactions in the pycnocline. Originally developed to predict three-dimensional unsteady turbulence in the atmosphere (*Deardorff*, 1973; *Moeng*, 1984), LES was extended to oceanic application in the polar seas by *Garwood et al.* (1994). Others including *Skyllingstad and Denbo* (1995) have subsequently conducted nonhydrostatic large-eddy simulation of deep ocean convection, but none of these examine the internal wave field generated by the mixed layer turbulence. Conversely, *Siegel and Domaradski* (1994) simulated internal waves in decaying stratified turbulence, isolated from the original surface forcing.

More recently, oceanic applications (*Harcourt et al.*, 1998; *Harcourt*, 1999) have embedded drifter models of a variety of designs (e.g., *Rossby et al.*, 1986; *Davis et al.*, 1992; *D'Asaro*, 1996) into the LES domain. *Lherminier et al.* (1999) have used these LES drifter predictions to help understand actual drifter observations in the Greenland Sea. Some of these hypothetical drifter results are useful here for understanding internal waves. Another recent

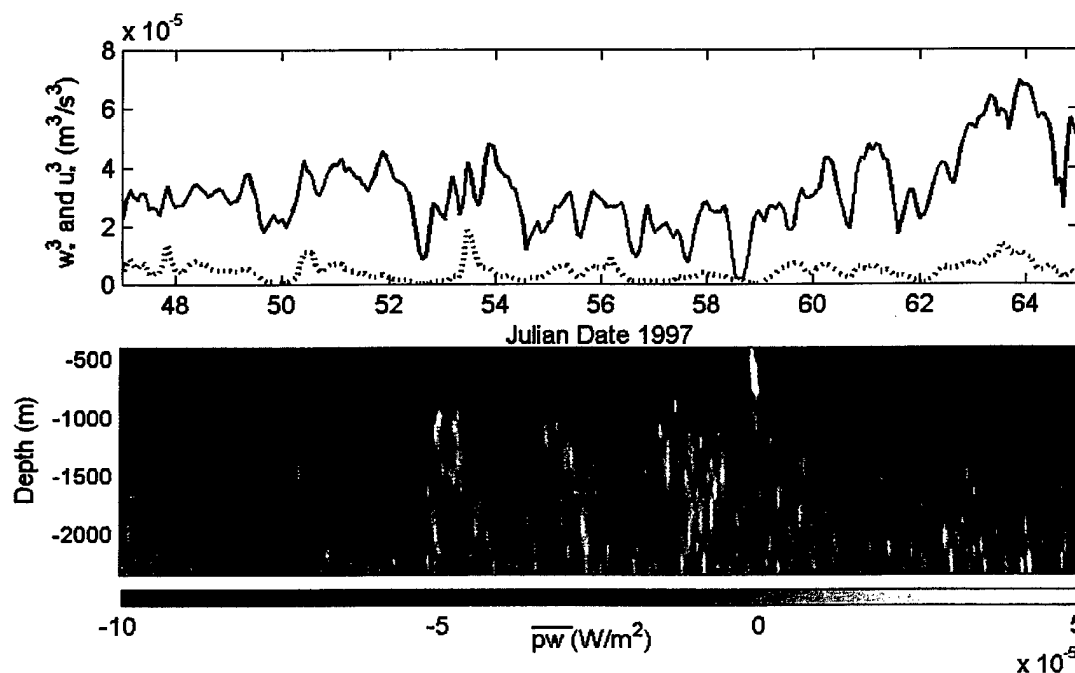


Figure 4. (Upper) Surface forcing: w_*^3 (solid) and u_*^3 (dotted). (Lower) Pressure transport simulated in pycnocline beneath mixed layer during February and March 1997 in the Labrador Sea.

oceanic LES study involves the interaction between surface-forced convection and larger-scale oceanic flows (Stone, 1999), and this may be a precursor of larger-scale

LES investigation of internal wave propagation. Collectively these several references provide more detailed explanations of LES, and computational issues are not emphasized. However, some important LES issues are listed here.

With regard to realistic prediction of the ocean mixed layer, LES needs to include the physical processes of the mixed-layer eddies that contain most of the energy and buoyancy variance of the turbulence. These “large eddies” are responsible for the buoyancy flux and Reynolds stresses. To accomplish this, an LES model must resolve scales from the largest turbulence motion (integral scale) down to and including the upper portion of the inertial subrange of the turbulence, exhibiting the expected $K^{-5/3}$ cascade of energy.

As a practical matter, if the turbulence integral length scale is approximated by h , LES for oceanic free convection is able to accomplish this first objective well with a grid size $\Delta x = \Delta y = \Delta z = h/25$ or smaller. Also required is a proven combination of filtering and application of a realistic TKE budget-based subgrid eddy viscosity/conductivity/diffusivity, $K_{M/T/S}$, in the momentum, potential temperature, and salinity budgets. Then $K_{M/T/S}$ values are kept to a minimum. This “mops up” the high wavenumber variances created by aliasing and the energy cascade, without unduly damping the flux-supporting and energy-containing integral scale eddies. Then the effective model Reynolds number can be sufficiently large ($\text{Re}_M = w_* h / K_M > 2000$) to establish a geophysically real-

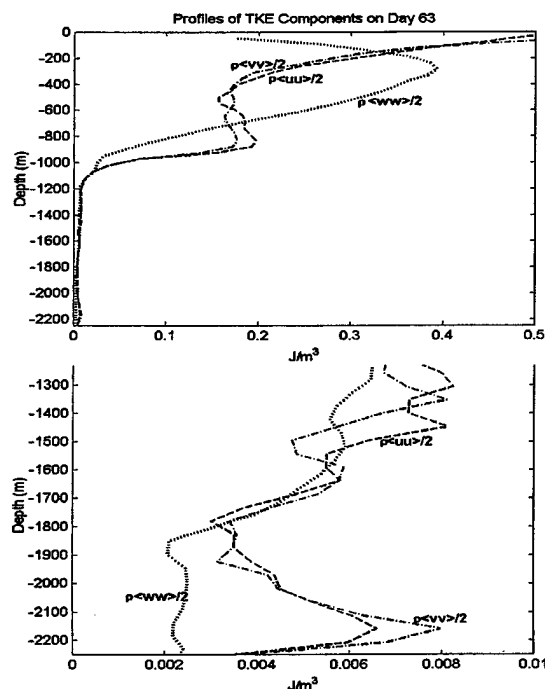


Figure 5. Horizontally averaged TKE profiles on day 63 of 1997 for (a) entire water column, and (b) below mixed layer with expanded scale.

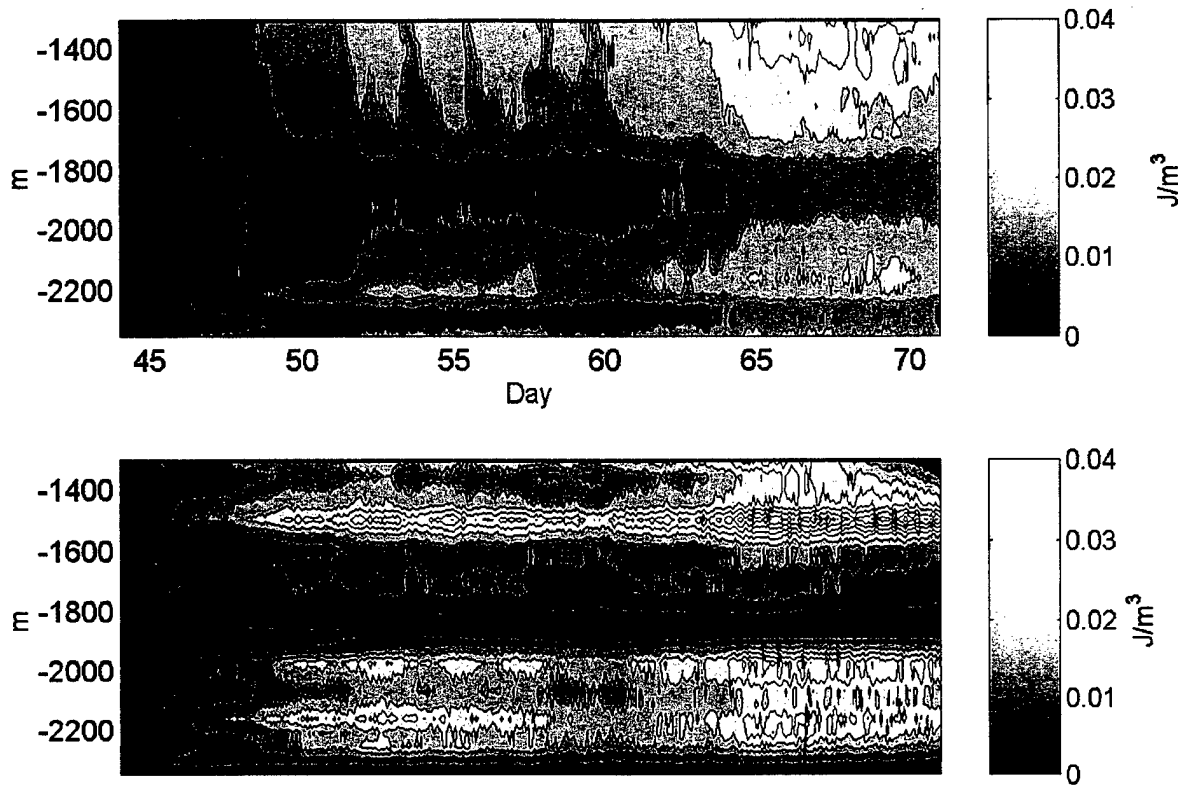


Figure 6. (a) Vertical kinetic energy and (b) wave potential energy versus time and depth in the pycnocline well beneath the surface mixed layer.

istic inertial subrange. Here w_* is the free convection velocity scale that depends upon mixed layer depth and the surface buoyancy flux B_0 . Low-pass filtering during the course of model integration is necessary to reduce aliasing at the highest wavenumbers and to prevent numerical instability.

The horizontal and vertical grid sizes should be equal in order to resolve well the approximately isotropic inertial subrange. Furthermore, to minimize any artificial resonance or a box mode, the scale size L_H of the model horizontal domain needs to be bigger than several integral scales, or $L_H > 5h$. These requirements are satisfied here, with h increasing during the course of the numerical solution from about 600 m to 1000 m, by employing a grid size between 25 m and 50 m with $128 \times 128 \times 50$ grid points in the two horizontal and vertical coordinates, respectively. The model time step Δt is constrained by the c-f-l condition to be less than the resolved length scale divided by the largest resolved convective velocity. For the widely fluctuating intensity of convection during the winter Labrador Sea numerical experiments, a Δt of 2 minutes meets this requirement.

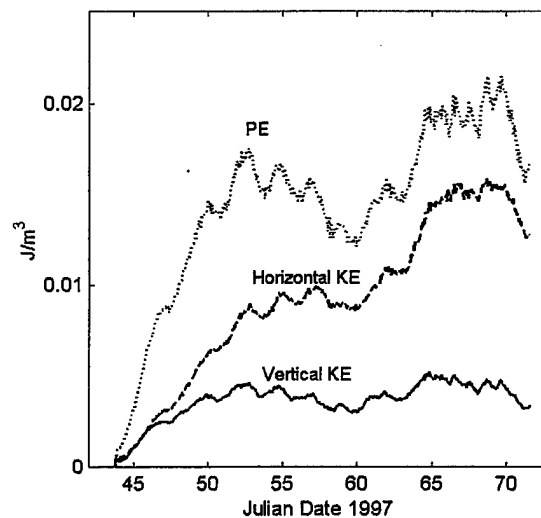


Figure 7. Vertically integrated wave kinetic energy and potential energy, from $z = -2300$ m to $z = -1200$ m.

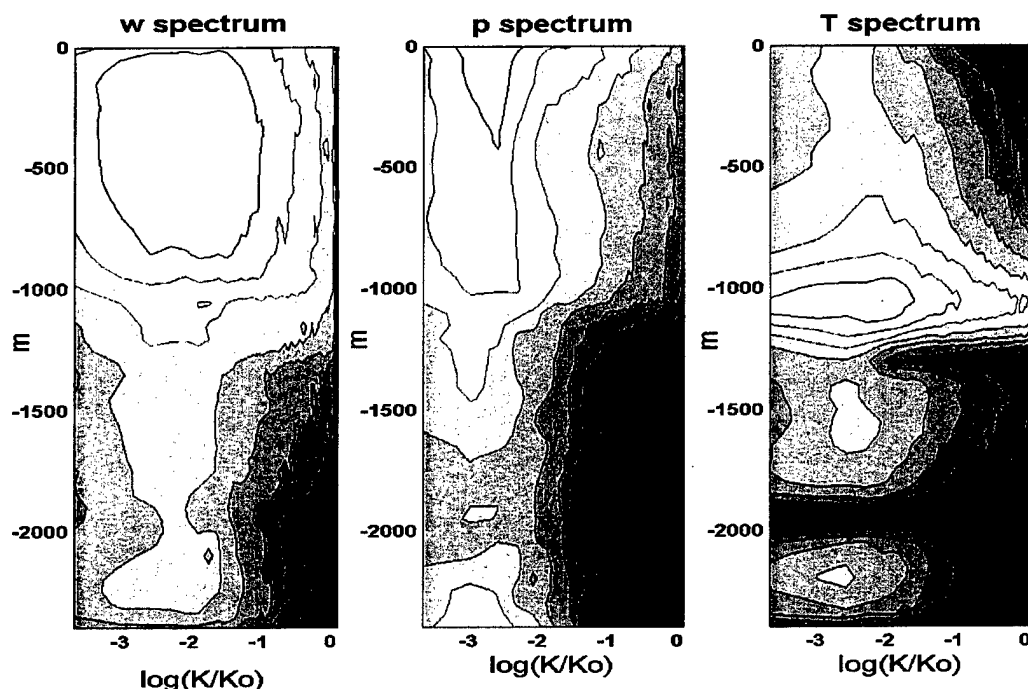


Figure 8. Wavenumber spectra versus depth for 28-day period during winter 1997 in Labrador Sea.

With regard to realistic prediction of internal waves in the pycnocline, Siegel and Domaradski (1994) delineate LES requirements. In short, LES for mixed layer-generated internal waves includes the same nonhydrostatic physics that maintains mixed-layer turbulence. A possible difference in internal wave prediction is that Δt needs to resolve the largest buoyancy frequency N_{\max} , or $\Delta t \ll N_{\max}^{-1}$. For the N^2 profile shown in Figure 3, the N_{\max} is 10^{-3} s^{-1} . Hence the 2-min value of Δt is more than adequate for both mixed layer turbulence and the highest-frequency internal waves of consequence possible at this location in the Labrador Sea.

2.2. Surface Forcing

Surface forcing was provided by time series of the wind stress $\tau(t)$ and the surface buoyancy flux, $B_o(t)$. The period of the numerical experiment coincided with the period of observed forcing in the Labrador Sea experiment during February and March 1997. These time series were calculated *in situ* from the R/V Knorr, as documented by The Lab Sea Group (1999). For the purposes of this study of the energy budgets and propagation of energy into the interior, the surface forcing in Figure 4 is presented in terms of kinematic energy per unit area, or the cube of the forcing velocity scales u_* and w_* . The forced convection velocity scale is $u_* = (\tau/\rho)^{1/2}$, and the free convection velocity scale is $w_* = (B_o h/2)^{1/3}$.

As Figure 4 shows, the free convection forcing is usually several times larger than the forced convection. The largest free convection forcing of $w_*^3 = 6.8 \times 10^{-5} \text{ m}^3/\text{s}^3$ occurred on day 64. This largest forcing was associated with a net upward surface heat loss to the atmosphere and the sky of nearly 700 W/m^2 . This heat flux causes a surface buoyancy flux of $B_o = 1.43 \times 10^{-7} \text{ m}^2/\text{s}^3$, and the mixed layer depth was $h = 949 \text{ m}$ at the time. The time-averaged free convective forcing for the entire numerical experiment was $\langle w_*^3 \rangle = 3.01 \times 10^{-5} \text{ m}^3/\text{s}^3$. The time-average of the forced convection forcing was $\langle u_*^3 \rangle = 0.35 \times 10^{-5} \text{ m}^3/\text{s}^3$, nearly an order of magnitude smaller than the forcing by the buoyancy flux. Both u_* and w_* vary in time with the periodic synoptic storm forcing, and this is important for the transient nature of the mixed layer turbulence and the propagation of energy into the interior by pressure transport, or pressure-velocity correlation, $\langle pw \rangle$. The lower panel of Figure 4 shows $\langle pw \rangle(t, z < -h)$, which was calculated from the LES-predicted fields. The downward pressure transport below the mixed layer is obviously synchronized with the surface forcing.

3. Turbulent and Wave Energy, Budgets and Fluxes

3.1. Turbulent and Wave Kinetic Energy

The fluctuating kinetic energy may be partitioned between turbulent kinetic energy (TKE) and internal wave kinetic energy (IWKE). Figure 5 shows the total turbulent plus internal wave kinetic energy at an instant during day 63. There is a maximum vertical KE at about -300 m and a shoulder just below -1000 m. The maximum energy is entirely TKE. The shoulder is attributable to IWKE and is coincident with the large stratification just beneath the mixed layer. The snapshot in Figure 1 of the internal wave field showed the largest internal waves with amplitudes exceeding 30 m just below the mixed layer. The internal waves in the underlying pycnocline have a root-mean-square amplitude of about 10 m. The peak vertical velocity observed by the isobaric drifters situated in the steep pycnocline just beneath the mixed layer in Figure 2 is about 10 mm/s. This is consistent with a vertical kinetic energy of about 0.02 J/m^3 in the vicinity of $z = -1050 \text{ m}$ in Figure 5.

Figure 6 shows that the wave kinetic and potential energy fields vary considerably in response to the episodic surface forcing. The time series of the vertical averages for wave potential and kinetic energy (Figure 7) show the effect of this episodic forcing. The wave energy has a net growth trend for the 28-day period; however, the wave energy spins up most rapidly during the first couple weeks of the numerical solution.

Variability in internal wave energies in the vertical is linked to stability. As a rule here, the largest values of wave energy are associated with the pycnocline immediately beneath the mixed layer. In both Figures 5 and 6, secondary maxima in wave energies near $z = -2100 \text{ m}$ are associated with a second peak in stability. This second stable zone is remnant from the mixed layer that deepened to about 2000 m during the previous winter, and it is evident in the N^2 profile in Figure 3.

As suggested by Figures 6 and 7, the internal wave field takes about a week to spin up to an approximate equilibrium. Horizontal wavenumber spectra for the vertical velocity, pressure and temperature were calculated from this point in time, day 50, until the end of the numerical experiment. Figure 8 shows the depth dependence of the horizontal wavenumber spectra. Within the mixed layer, spectra of vertical velocity, potential temperature and salinity (not shown) all have a $K^{-5/3}$ inertial subrange that spans a decade of increasing wave number. The peak energy and variances in the mixed layer correspond closely to the wavenumber $K_0 = 1/h$, indicating the strong influence of vertical convection on the horizontal scale of the Rayleigh-Benard convection cells (Carsey and Gar-

wood, 1993). The peak variances at 1100 m and 2100 m depths are especially obvious in the temperature spectra.

Below the mixed layer, the horizontal wavenumber fall off to approximately K^{-1} (Figures 8 and 9a). From the time series of vertical velocity sensed by a simulated drifter beneath the large gradient region, near $z = -1200 \text{ m}$, a frequency spectrum was also calculated (Figure 9b). The frequency spectrum peaks at the buoyancy frequency N for this depth, and it resembles the frequency spectrum of the freely convective atmosphere (Fritts *et al.*, 1990).

3.2 Turbulent and Wave Kinetic Energy Budgets and Fluxes

The dissipation ϵ and the buoyancy flux $\langle bw \rangle$ dominate the TKE budget in most of the freely convecting mixed layer during day 63 (Figure 10a), except near the surface and the entrainment zone. In the upper 100 m, the shear production is the dominant source of turbulence. In the entrainment zone between $z = -780 \text{ m}$ and -1000 m , the buoyancy flux is negative because of entrainment of

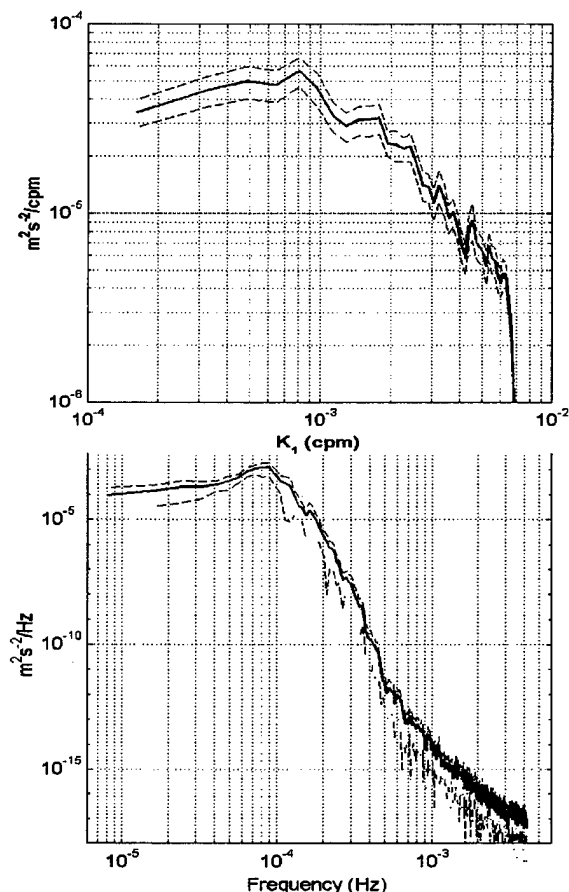


Figure 9. (a) Horizontal wavenumber and (b) frequency spectra at 1200-m depth

dense fluid from below into the mixed layer. In this region there is an approximate balance between the buoyant damping by entrainment and the convergence of pressure and turbulent transport.

Below the mixed layer, the approximate balance between buoyancy flux and the convergence of transport is continued (Figure 10b). An important difference from the entrainment zone, however, is that the buoyancy flux below the mixed layer goes to increase the wave potential energy; in the entrainment zone, the buoyancy flux increases the mean potential energy by mixing. Another important difference is that the transport of energy below the mixed layer is accomplished almost entirely by the pressure transport, $\langle pw \rangle$, while turbulent transport is large only in the overlying turbulent boundary layer (Figure 11a).

Figure 11b plots the pressure transport below the mixed layer, averaged for the entire period of the simulation. The mean downward energy flux is 0.1 mW/m^2 at z

$= -1100 \text{ m}$ and is reduced to half this value by $z = -1300 \text{ m}$. Included in Figure 11b is the pressure transport for an instant during day 63. The pulse-like form is caused by the episodic nature of the surface forcing. The slanted structure in the $\langle pw \rangle(t, z)$ field (Figure 4) is attributable to this phase lag, and its slope corresponds to a downward propagation of energy-transporting events at a speed of approximately 1 km/day . Figures 4 and 11b together demonstrate the importance of episodic storms, causing order of magnitude temporal and spatial fluctuations in the energy flux downward.

4. Conclusions

Verification of these model results is yet to be accomplished but will be done by comparison with the Labrador Sea drifters deployed during 1997 and 1998 (designs of Rossby *et al.*, 1986; Davis *et al.*, 1992; D'Asaro, 1996). However, some conclusions may be readily drawn. In

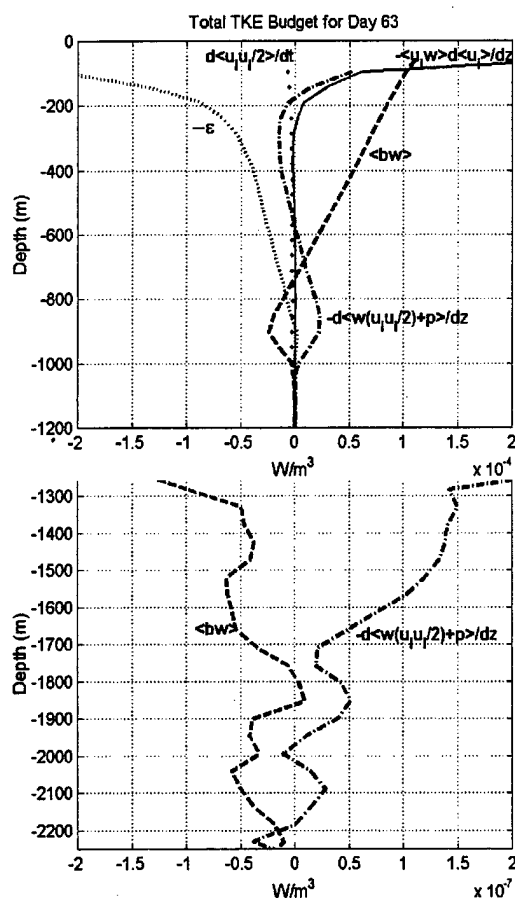


Figure 10. Average TKE budget for 28-day period for (a) upper 1200 m of water column, and (b) below mixed layer with expanded scale.

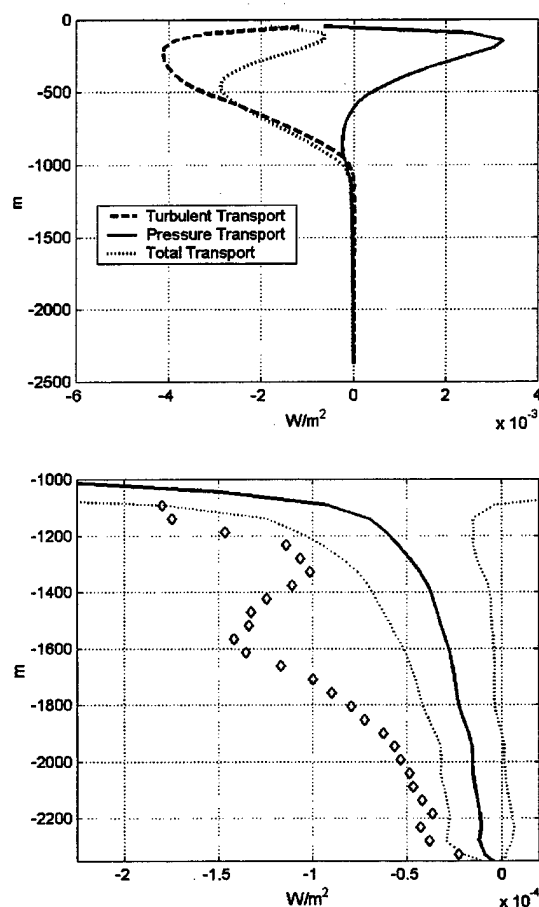


Figure 11. Vertical transport of energy averaged for 28-days for (a) entire water column. (b) Pressure transport below mixed layer with expanded scale. Diamonds are pressure transport during day 63, and dotted curves are plus and minus one standard deviation.

modeling the mixed layer, the system has often been approximated as closed, without energy escaping below the entrainment zone. Hence, to predict entrainment, a closed-system TKE budget is invoked that balances entrainment damping with net production minus dissipation. In such a system, transport redistributes TKE within the mixed layer and increases mixed layer potential energy by penetrative convection; however, energy that escapes below the entrainment zone into the pycnocline has been neglected.

The energy that escapes the mixed layer and the entrainment zone may be small compared with the total TKE. However, the escaped energy may be significant for the ambient internal wave energy in the pycnocline. The issue in this paper concerned the propagation or transport of TKE below the entrainment zone, energizing the internal wave field and possibly causing dissipation and mixing in the pycnocline. For the Labrador Sea site, the deep stratified water column from -1000 m to -2300 m was examined, and the loss of energy into the interior averaged about 0.1 W/m^2 . This energy loss of less than 1% of the mixed layer and the entrainment zone energy is usually insignificant for mixed layer dynamics and the prediction of mixed layer depth and surface conditions including sea surface temperature. However, this is not a negligible energy flux with regard to the maintenance of the interior internal wave field when other sources of internal wave energy are minimal.

LES was demonstrated to be an effective tool to quantify the generation and vertical propagation of internal wave energy by local forcing. To include nonlocal sources of internal wave energy, including bottom boundary layer and inertial-gravity wave sources, a much larger horizontal model domain will be required. To still include the interaction between the internal waves and the turbulence, the grid resolution will have to be relatively high. The computing resources are sufficient today to tackle this problem in depth-limited domains, such as on the continental shelf. To further complete the problem, the roles of forced convection in shallow stable mixed layers and of surface gravity waves needs to be added (Watson, 1990) to this study which focused only on deep free convection.

Acknowledgments. The Office of Naval Research (Code 322OM) and the National Science Foundation (Award Number 9530530) sponsored this work, and the DOD HPC Center provided a grant of computing time. This support is gratefully acknowledged. We thank Peter Guest for providing the surface fluxes soon after completion of the winter 1997 field experiment, and we thank John Lazier for the hydrographic data to initialize the model. Discussions with Pascale Lherminier were very helpful.

References

- Carsey, F. D. and R. W. Garwood, Jr., Identification of modeled ocean plumes in Greenland Gyre ERS-1 SAR data, *Geophys. Res. Lett.*, 20, 2207-2210, 1993.
- D'Asaro, E. A., A Lagrangian float, *J. Atmos. Oceanic Technol.*, 13, 1230-1246, 1996.
- Davis, R. E., D. C. Webb, L. A. Regier, and J. Dufour, The autonomous Lagrangian circulation explorer (ALACE), *J. Atmos. Oceanic Technol.*, 9, 264-285, 1992.
- Deardorff, J. W., The use of subgrid transport equations in a three-dimensional model of atmospheric turbulence, *J. Fluids Engineering*, 429-438, 1973.
- Fritts, D. C., U.-P. Hoppe, and B. Inhester, A Study of the vertical motion field near the high-latitude summer menopause during MAC/SINE, *J. Atmos. Terres. Phys.*, 52, 927-938, 1990.
- Garwood, R. W., Jr., S. M. Isakari and P. C. Gallacher, Thermobaric convection, in *The Role of the Polar Oceans in Shaping the Global Environment*, Ed. by O. Johannessen, R. Muench and J. Overland, Am. Geophys. Union Monograph, Vol. 85, 199-209.
- Harcourt, R. R., Numerical simulation of deep convection and the response of drifters in the Labrador Sea, Ph. D. Dissertation, Univ. of California, Santa Cruz, 378 pp., 1999.
- Harcourt, R. R., L. Jiang, and R. W. Garwood, Jr., Numerical simulation of drifter response to Labrador Sea convection, Tech. Rep. NPS-OC-98-001, Naval Postgraduate School, Monterey, 71 pp., 1998.
- Lherminier, P., R. R. Harcourt, R. W. Garwood, Jr., and J.-C. Gascard, Interpretation of mean vertical velocities measured by isobaric floats during deep convective events, *J. Mar. Systems*, submitted, 1999.
- Moeng, C.-H., A large-eddy simulation model for the study of boundary-layer turbulence, *J. Atmos. Sci.*, 41, 2052-2062, 1984.
- Müller, P. and D. Henderson, Eds., *Dynamics of Oceanic Internal Gravity Waves, Proceedings 'Aha Huli'ko'a Hawaiian Winter Workshop*, University of Hawaii at Manoa, 15-18 January, 508 pp., 1991.
- Rosby, T., D. Dorson, and J. Fontaine, The RAFOS system, *J. Atmos. Oceanic Technol.*, 3, 672-679, 1986.
- Siegel, D. A. and J. A. Domaradzki, Large-eddy simulation of decaying stably stratified turbulence, *J. Phys. Oceanogr.*, 24, 2353-2386, 1994.
- Skyllingstad, E. D. and D. W. Denbo, An ocean large-eddy simulation of Langmuir circulation and convection in the surface mixed layer, *J. Geophys. Res.*, 100, 8501-8522, 1995.
- Stone, R. E., Entrainment, detrainment and large-scale horizontal gradients in oceanic deep convection, Ph.D. thesis, Naval Postgraduate School, Monterey, 123 pp., 1999.
- The Labrador Sea Group, The Labrador Sea deep convection experiment, *Bull. Am. Meteorol. Soc.*, 79, 2033-2058, 1998.
- Watson, K. M., The coupling of surface and internal gravity waves: Revisited, *J. Phys. Oceanogr.*, 20, 1233-1248, 1990.

Near-Inertial Wave Generation on an Unsteady Ocean Current

M.-Pascale Lelong [†], Timothy J. Dunkerton [†] and David S. Darr ^{*}

[†]Northwest Research Associates, Bellevue WA and ^{*}University of Washington, Seattle WA

Abstract. A high-resolution numerical simulation of baroclinic instability on a shallow ocean jet demonstrates the generation of near-inertial waves in regions of strong flow curvature.

Introduction

Although much has been learned about the structure of the oceanic internal wave field over the past 30 years, many questions remain pertaining to the sources and sinks of the waves. One of the persistent features of the observed wave field is the nearly universal nature of the energy spectra and levels, with nearly half of the energy contained in the near-inertial frequency range (Munk, 1981). The general consensus is that a variety of mechanisms (e.g., wind, tidal forcing, topography, geostrophic adjustment) contribute energy to the wave field but the relative importance of individual sources remains to be established.

In certain observational studies, enhanced wave activity can be related easily to atmospheric forcing events (e.g., Leaman and Sanford, 1975; Pinkel, 1984; D'Asaro, 1995) or to a topographic feature (Kunze, 1993). In other cases where the forcing mechanism is not so obvious, downward energy propagation is taken as evidence that the waves originated at the surface and were, therefore, wind-driven (e.g., Lee and Eriksen, 1997). Many observations show enhanced near-inertial wave activity in the vicinity of oceanic fronts (e.g., Tang, 1979; Kunze and Sanford, 1984; Mied et al., 1986; Merrifield and Pinkel, 1996). Tang (1979) observed near-inertial waves in the vicinity of the St. Lawrence current and suggested geostrophic adjustment of the mean flow as a potential wave source. Geostrophic adjustment following barotropic /baroclinic instability of the mean flow is also suspected to have forced some of the near-inertial waves observed in the North Pacific Subtropical Front (Kunze and Sanford, 1984). Perhaps the most compelling observational evidence supporting wave generation by local adjustment on large-scale ocean currents is found in satellite (SAR) images. These SAR images reveal the presence of intense internal solitons in the Yucatan and Luzon Straits (Apel, 1998). Both regions are characterized by strong Western boundary currents (the Gulf Stream and the Kuroshio respectively) in the process of turning from zonal to meridional flows, and

by relatively steep topography on the cyclonic boundary of the current. Interestingly, the observed internal solitons propagate in a direction approximately normal to the mean direction of the large-scale baroclinic flow and Apel speculates that strongly sheared baroclinic currents may act as sources for internal solitons.

Interpretation of observational data is often complicated by the scattering and refraction of waves by the mean shear. For instance, waves with downward/upward propagation may not always originate above/below the region of detection. In the same fashion, we cannot exclude the possibility that waves observed in a particular region may have propagated in from elsewhere. This behavior highlights the difficulties encountered when trying to isolate inertia-gravity waves (henceforth IGWs) produced as a result of large-scale instabilities in the observational data, given our incomplete knowledge of the excitation process and the possible contributions from other sources over a wide surrounding region. This problem is, however, ideally suited to a numerical study where such factors can be controlled. One can, for example, focus on the effect of mean flow forcing by turning off wind forcing in the numerical model.

The generation of IGWs during a baroclinic lifecycle on an atmospheric jetstream was modelled numerically by O'Sullivan and Dunkerton (1995). In their study, the waves developed rapidly in regions of strong parcel accelerations, primarily in the jetstream region of the upper troposphere.

Baroclinic instability in the ocean differs from its atmospheric counterpart in several ways. The most crucial difference for the generation of inertia-gravity waves is the relatively slow growthrate of oceanic baroclinic instability due to the much weaker shears encountered in the ocean than in the atmosphere. Whereas e-folding times for atmospheric baroclinic instability are on the order of 5 to 6 days, typical oceanic values are much longer, typically 50 to 60 days. The increased separation between the IGW timescale and the instability timescale makes it unlikely that rapid growth of the in-

stability will generate waves. This does not preclude, however, the *local* generation of IGWs in regions where the assumptions of geostrophy (e.g., $H/L \ll 1$ where H and L denote characteristic vertical and horizontal length scales) break down.

The generation of IGWs following a vacillating baroclinic instability was also demonstrated by *Lovegrove et al.* (1999) in a laboratory setting. Very-high resolution visualization techniques enabled them to detect the small-scale, high-frequency IGW signal which developed periodically in localized regions along the instability wave.

Finally, we note that the phenomenon of wave generation by large-scale unsteady flows is not confined to baroclinically unstable flows. Similar behavior has been reported by *Ford* (1994) in a barotropically unstable shallow-water flow. Ford refers to the ensuing radiation of waves as Lighthill radiation.

In order to examine whether large-scale instabilities can provide a viable source for ocean internal waves, we have simulated numerically the onset and subsequent nonlinear development of a baroclinically unstable shallow ocean jet in typical midlatitude conditions using moderately high spatial and temporal resolution. The principal objectives of this study have been (1) to determine whether slowly evolving, large-scale instabilities can excite higher frequency unbalanced motions and (2) to identify preferred generation sites. The propagation characteristics of the waves, once generated, are beyond the scope of the present study, but will constitute the basis for future work on this topic.

We now examine in more detail the similarities and differences between the problem of IGW generation following large-scale instabilities and classic Rossby geostrophic adjustment. Large-scale oceanic flows are characterized by a small aspect ratio of vertical to horizontal length scales and a persistent state of near-geostrophic equilibrium. Consequently, their dynamical behavior is often studied in the context of the small-Rossby-number approximation (e.g., a quasigeostrophic or a balanced formulation). When regions develop where this equilibrium is perturbed (as is the case when an instability develops), the flow adjusts *locally* in order to restore geostrophic balance. In the process of trying to restore geostrophy, some energy radiates away as IGWs. In this respect, the problem is analogous to Rossby adjustment (*Rossby*, 1938; *Cahn*, 1945). It differs, however, in that the final state to which the flow is adjusting is not steady as is assumed in the classic formulation; instead, it continually evolves over the course of the instability lifecycle. In this manner, we do not know a priori the structure of the final state to which the flow is relaxing. Furthermore, a tacit assumption

of the classic Rossby problem is that the waves generated during adjustment will eventually radiate away from the source region. In our problem, it is likely that some waves will remain trapped in the mean flow (e.g., *Kunze and Sanford*, 1984; *O'Sullivan and Dunkerton*, 1995; *Kunze and Boss*, 1998).

The rest of the paper is organized as follows: Section 2 briefly describes the numerical method and the initial configuration. Results of a frequency-filtering analysis designed to isolate the fast wave components are presented in section 3. Finally, preliminary conclusions as well as suggestions for future directions are given in section 4.

Numerical Methodology

As a prototype for the mechanism described above, we have simulated numerically a developing baroclinic disturbance on a shallow, upper-ocean jet.

The numerical model used is a free-surface isopycnal model (HIM) developed by *Hallberg*, 1995).

Our computational domain is a box on an f -plane with horizontal dimensions $1.25^\circ \times 3.8^\circ$ centered at 40° N with a resolution of 64×96 grid points in the zonal and meridional directions respectively. The vertical resolution consists of 20 upper layers with an average initial depth of 50 m and two 1000-m deep layers. Boundary conditions are periodic in the zonal direction and free-slip in the meridional direction. Coriolis and buoyancy frequencies f and N are 10^{-4} s^{-1} and $1.7 \times 10^{-2} \text{ s}^{-1}$ respectively. Initially, the fluid is at rest and the free surface is tilted latitudinally. This initial tilt induces a mean eastward jet which is largely confined to the upper layers. The flow is then seeded with the fastest growing baroclinic mode and the instability is allowed to develop. To maximize available resolution, the zonal extent of the computational domain is chosen to encompass exactly one wavelength of the baroclinic instability wave. The simulation was run over a period of 85 days. For the first 65 days, dynamical fields were saved every 24 hours. By day 65, the flow exhibited rapid change characteristic of nonlinear behavior. From this point on, dynamical fields were saved every 2.4 hours to ensure the capture of high-frequency motions.

Analysis of Results

The horizontal divergence provides a useful diagnostic quantity for identifying ageostrophic activity in a flow otherwise dominated by balanced motions. One must be careful, however, not to ascribe the entire divergence field to waves. Indeed, the quadrupole distribution that emerges at early times in the horizontal divergence field (Figure 1) is the characteristic signature

of the secondary ageostrophic circulation. Its purpose is to maintain thermal wind balance during the baroclinic instability lifecycle, and it should not be interpreted as radiating waves.

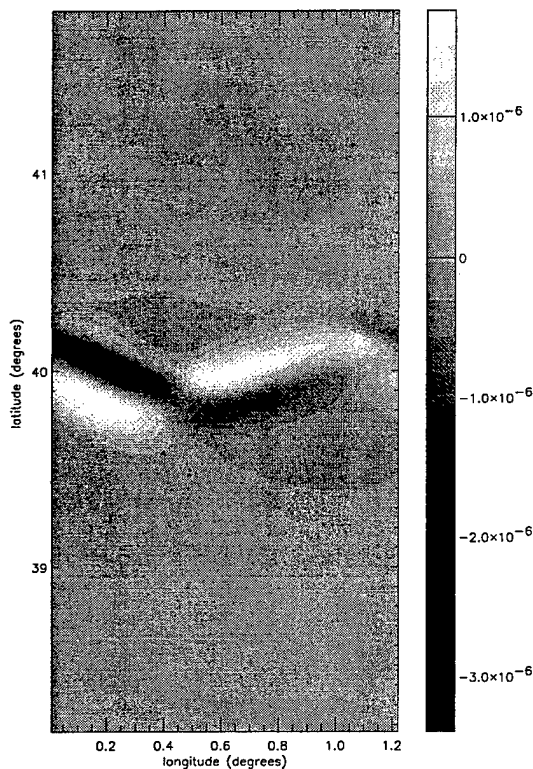


Figure 1. Horizontal divergence at day 40 in top layer.

Animation of the horizontal divergence, however, reveals the presence of smaller-scale, wave-like disturbances by day 65. Figure 2 shows the horizontal divergence field on days 65, 70 and 75. The dominant visible features are associated with the secondary ageostrophic circulation and follow the general pattern of the baroclinic instability wave. The small-scale signal appears to radiate in the northeast and southwest regions of the flow (Figure 2a).

To gain further information on the time scales involved, we performed a time-series analysis in the wave packet regions. The divergence power spectrum, averaged over the region between 39°N and 41°N, exhibits three distinct peaks (Figure 3).

The two lowest-frequency peaks clearly correspond to the secondary circulation of baroclinic instability. The highest, distinct frequency peak corresponds to a 3-day signal. There is no evidence of a peak in the inertial frequency range (the inertial period is 17 hours).

In order to isolate the 3-day signal, the dynamical fields were bandpass-filtered in frequency space with a

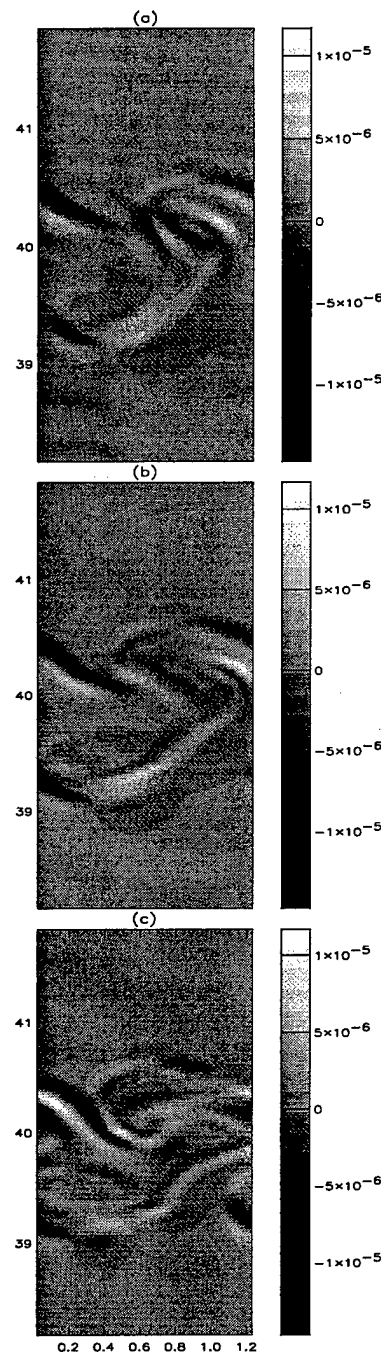


Figure 2. Horizontal divergence at days (a) 65, (b) 70 and (c) 75.

filter of the form,

$$\mathcal{F}(\omega) = \frac{2}{(1 + C_0(\omega_0/\omega)^2)(1 + C_0(\omega/\omega_0)^2)} \quad (1)$$

where ω is the frequency, $\omega_0 = 0.3$ is the frequency corresponding to the 3-day signal and $C_0 = 0.414$. The filter was applied recursively a total of 4 times to minimize contributions from neighboring peaks.

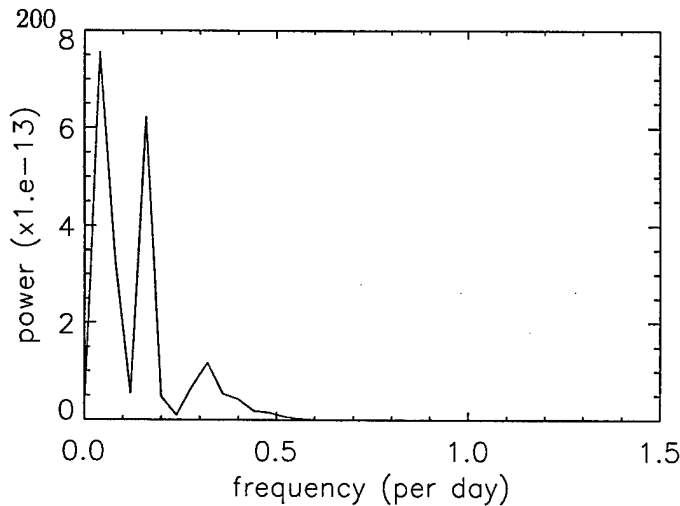


Figure 3. Frequency power spectrum for horizontal divergence averaged over northeast wave packet region.

The reconstructed, filtered divergence at days 65, 70 and 75 in the top layer is shown in Figure 4. At day 65, the larger scale features associated with the secondary ageostrophic circulation, have been filtered out and the two wavepackets detected during animation are clearly visible. By day 70, the southwest packet appears to be weakening but the northeast packet has strengthened. In addition, other disturbances are becoming visible in the central region. By day 75, the southeast packet has been refracted northeastward and, as a result of periodic boundary conditions, reappears below the jet region on the right-hand side of the domain. The activity in the center of the domain has intensified and another weaker disturbance appears to the south.

Zonal and meridional components of the bandpass-filtered velocity are elliptically polarized and, at any given point in the wavepacket regions, rotate anticlockwise in a manner consistent with the polarization relations for inertia-gravity waves (not shown).

The wavepackets appear to originate in regions of strong potential vorticity gradients (Figure 5). At day 65, the position of the two wavepackets corresponds to the presence of curved potential vorticity fronts. As the instability evolves, these frontal regions become distorted. For example, the northeast frontal region (Figure 5a) is eventually displaced and elongated westward (Figure 5b,c). The wave pattern which it spawned, on the other hand, continues to propagate northeastward (Figure 5b,c). Vector plots of the velocity field show that the waves originate in regions of high shear or where the flow changes direction rapidly (Figure 6).

Vertical cross sections of the horizontal divergence oriented in a direction perpendicular to the wave crests for the northeast disturbance reveal a complicated vertical structure (Figure 7). Clearly, the dominant

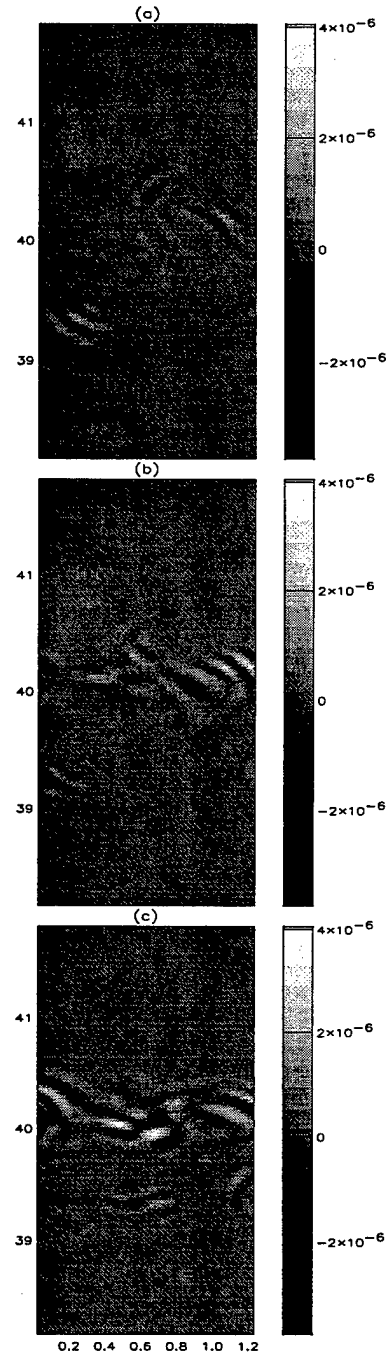


Figure 4. Filtered horizontal divergence at days (a) 65, (b) 70, (c) 75

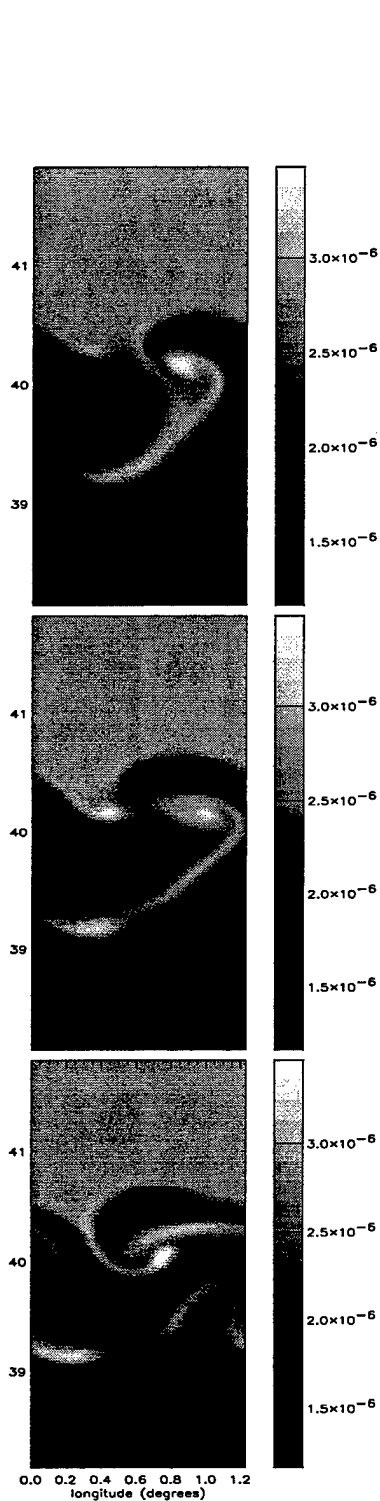


Figure 5. Potential vorticity at days (a) 65, (b) 70 and (c) 75 in top layer.

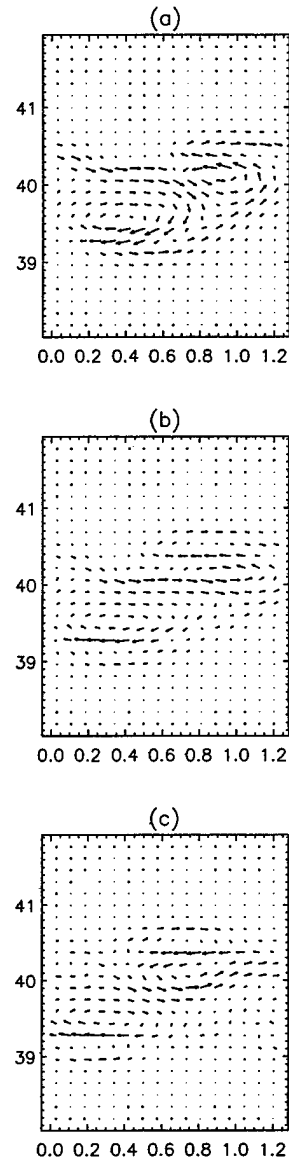


Figure 6. Velocity field at days (a) 65, (b) 70, (c) 75.

feature is the characteristic quadrupole of secondary ageostrophic circulation. Careful examination, however, reveals waves radiating away from the quadrupole structure on both sides. Figure 8 represents the vertical structure of the packet as it propagates in a relatively quiescent environment away from the front. The horizontal wavelength of the wavepacket is about 19 km. If the disturbance were a propagating inertia-gravity wave, we could use the dispersion relation

$$(\hat{\omega}^2 - f^2)m^2 = N^2 k_h^2$$

to determine its vertical wavelength. Here, $\hat{\omega}$ is the Lagrangian frequency; there is no evidence that Doppler-shifting by the mean flow is important and we may take

$\hat{\omega} = \omega$, the Eulerian frequency. m and k_h are vertical and horizontal wavenumbers. However, the disturbance frequency is much lower than the inertial frequency, implying that m must be imaginary. This behavior is reminiscent of evanescent waves (e.g., Gill, 1984). Vertically evanescent waves display the characteristics of propagating waves in the horizontal, but their amplitude decays exponentially in the vertical. The dispersion relation implies that the e-folding vertical scale should be around 12 meters. This is not currently resolved by the model, nor does the amplitude of the signal exhibit such rapid decay. There is also no clear evidence that the velocity vector rotates as a function of depth, as would be expected if the waves were pure inertia-gravity waves.

Several factors can produce inertia-gravity waves of lower frequency than predicted by the linear theory of freely propagating waves. For instance, Doppler-shifting by the mean flow can lower the Lagrangian frequency $\hat{\omega}$ to values below the Coriolis frequency. In our case, given the complicated nature of the velocity field in the late stages of the instability, it is unlikely that Doppler-shifting is very significant. Another more likely factor involves the lowering of the effective Coriolis frequency in regions by the ambient relative vorticity (Kunze, 1985; Kunze and Boss, 1998). This has the effect of broadening the range of frequencies that can support propagating inertia-gravity waves. It can also lead to wave trapping in regions of negative vorticity. The minimum values of relative vorticity in our simulation, however, are not sufficiently low to reconcile our results with propagating inertia-gravity waves. The lowest possible effective Coriolis frequency in our simulation is about $6 \times 10^{-5} \text{ s}^{-1}$, with a corresponding period of 29 hours. This falls short of the 72-hour period associated with ω_0 . Finally, the limited vertical resolution used in the present simulation will also influence the range of scales that can be modeled. In retrospect, given the horizontal scale of the dominant high-frequency motions, much finer vertical resolution will be needed to model accurately the generation of waves.

Conclusions

These preliminary results suggest that near-inertial waves can indeed be generated following the onset of baroclinic instability. The wavelike disturbances we have found exhibit properties of propagating waves in the horizontal, but their vertical structure remains unclear. Their subinertial frequency suggests evanescent behavior. It is also unclear, at this point, whether any waves can propagate out of the jet region. Higher-resolution runs are needed before these questions can be answered definitely.

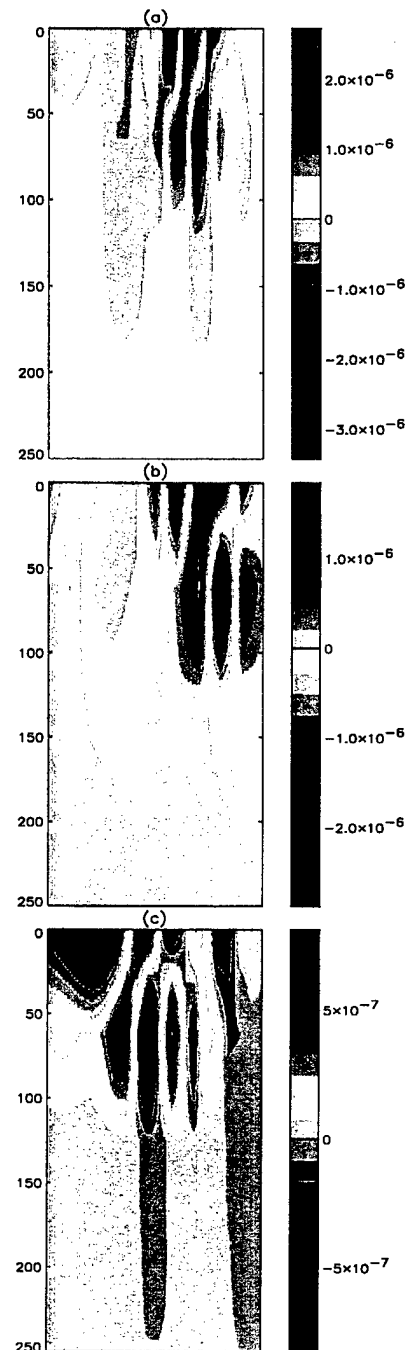


Figure 7. Vertical cross section of divergence through the wave packet at days (a) 65, (b) 70, (c) 75. Only the top 5 layers are shown.

The structure of the jet, its depth and its strength undoubtedly influence the nature of generated unbalanced motions. While it is expected that the baroclinic instability on a shallow jet will grow more rapidly than on a deep jet, a deep jet will present more possible loci for wave generation. Furthermore, since the vertical

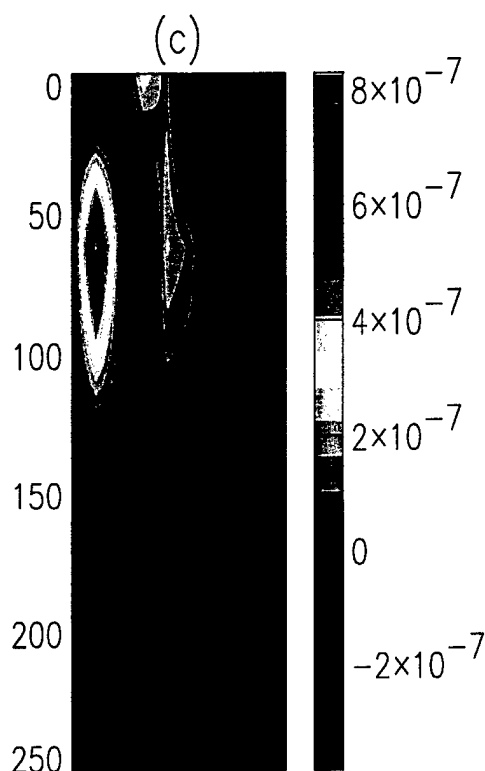


Figure 8. Vertical cross section of divergence through the wave packet at day 75 away from frontal region. Only the top 5 layers are shown.

scale of generated waves is expected to scale (at most) as the depth of the adjusting feature, our shallow jet may have generated waves with vertical structure that could not be captured with the present grid resolution.

Finally, differentiating waves from non-wave motions has proven to be quite difficult, given the complicated nature of the flow field in which the waves evolve. More work needs to be done to distinguish accurately balanced from unbalanced motions.

Acknowledgments

We thank Bob Hallberg for the gracious use of his numerical model and Eric Kunze for many stimulating discussions. This research was funded, in part, by NSF grant OCE-9811939.

References

- Apel, J.R., 1998: Are strongly sheared baroclinic currents sources for internal solitons? *paper presented at IOS/WHOI/ONR Internal Solitary Wave Workshop; Oct 27-29 1998. Sydney, British Columbia.*
- Cahn, A. Jr., 1945: An investigation of the free oscillations of a simple current system. *J. Meteorol.*, **2**, 113-119.
- D'Asaro, E.A., ed., 1995: Ocean Storms Experiment Special Issue. *J. Phys. Ocean.*, **25**.
- Ford, R., 1994: Gravity wave radiation from vortex trains in rotating shallow water. *J. Fluid Mech.*, **281**, 81-118.
- Gill, A.E. 1982: *Atmosphere-Ocean Dynamics*. Academic Press
- Hallberg, R., 1995: Some aspects of the circulation of ocean basins with isopycnals intersecting the sloping boundaries. *PhD Thesis, University of Washington.*
- Kunze, E., 1985: Near-inertial wave propagation in geostrophic shear. *J. Phys. Ocean.*, **15**, 544-565.
- Kunze, E., 1993: Submesoscale dynamics near a seamount. Part II: The partition of energy between internal waves and geostrophy. *J. Phys. Ocean.*, **23**, 2589-2601.
- Kunze, E. and E. Boss, 1998: A model for vortex-trapped internal waves. *J. Phys. Ocean.*, **28**, 2104-2115.
- Kunze, E. and T.B. Sanford, 1984: Observations of near-inertial waves in a front *J. Phys. Ocean.*, **14**, 566-581.
- Kunze, E., R.W. Schmitt and J.M. Toole, 1995: The energy balance in a warm-core ring's near-inertial critical layer, *J. Phys. Ocean.*, **25**, 942-957.
- Leaman, K.D. and T.B. Sanford, 1975: Vertical energy propagation of inertial waves: A vector spectral analysis of velocity profiles, *J. Geophys. Res.*, **80**, 1975-1978.
- Lee, C.M. and C.C. Eriksen, 1997: Near-inertial internal wave interactions with mesoscale fronts: Observations and models, *J. Geophys. Res.*, **102**, C2, 3237-325
- Lovegrove, A.F., P.L. Read and C.J. Richards, 1999: Generation of inertia-gravity waves in a baroclinically unstable fluid, *Q. J. R. Meteorol. Soc.*, in press.
- Merrifield, M.A. and R. Pinkel, 1996: Inertial currents in the Beaufort Sea: Observations of response to wind and shear. *J. Geophys. Res.*, **101**, C3, 6577-6590.
- Mied, R.P., C.Y. Shen, C.L. Trump and G.J. Lindemann, 1986: Internal-inertial waves in a Sargasso Sea front. *J. Phys. Oceanogr.*, **16**, 1751-1762.
- Munk, W.H., 1981: Internal waves and small-scale processes. *Evolution of Physical Oceanography*, B. Warren and C. Wunsch, eds. The MIT Press, 264-291.
- Orlanski, I., and M.D. Cox, 1973: Baroclinic instability in ocean currents. *Geophysical Fluid Dynamics*, **4**, 297-332.
- O'Sullivan D. and T. J. Dunkerton, 1995: Generation of inertia-gravity waves in a simulated lifecycle of baroclinic instability. *J. Atmos. Sci.*, **52**, 3695-3716.
- Pinkel, R., 1984, Doppler sonar observations of internal waves: The wavenumber-frequency spectrum. *J. Phys. Oceanogr.*, **14**, 1249-1270.
- Rossby, C.-G., 1938: On the mutual adjustment of pressure and velocity distributions in certain simple current systems, *J. Mar. Res.*, **1**, 239-263.
- Tang, C.L., 1979: Inertial waves in the Gulf of St. Lawrence: A study of geostrophic adjustment. *Atmos.-Ocean*, **17**, 135-156.
- M.-Pascale Lelong, Northwest Research Associates, PO Box 3027, Bellevue WA 98009-3027 USA

Model Predicted Distribution of Internal Wave Energy for Diapycnal Mixing Processes in the Deep Waters of the North Pacific

Toshiyuki Hibiya, Maki Nagasawa, and Yoshihiro Niwa

Department of Earth and Planetary Physics, Graduate School of Science, The University of Tokyo, Tokyo 113-0033, Japan

Abstract. Using a three-dimensional multi-level numerical model, we examine the distribution of internal wave energy available for diapycnal mixing in the deep waters of the North Pacific. It is demonstrated that energetic low-vertical-mode, near-inertial internal waves are excited in the latitudes 30–45°N in the western-central North Pacific by traveling midlatitude storms during winter and at around 20°N in the western North Pacific by tropical cyclones during fall. Thus-excited waves propagate equatorward down to the latitudes 10–15°N where the frequencies become twice the local inertial frequencies so that a large amount of energy is considered to be transferred across the local internal wave spectrum down to small dissipation scales by the mechanism of parametric subharmonic instability causing enhanced diapycnal mixing. The calculated results show that the low-vertical-mode, double-inertial-frequency internal waves are very weak at the times and locations of previous microstructure measurements, which suggests that the observed value of diapycnal diffusivity of about $10^{-5} \text{ m}^2 \text{ s}^{-1}$, an order of magnitude lower than required to satisfy the large-scale advective-diffusive balance of the thermohaline circulation, is not representative.

1. Introduction

It is demonstrated in the results from the oceanic general circulation models that the strength of the large-scale thermohaline circulation is intimately bound up with the distribution and intensity of diapycnal mixing [Bryan, 1987, Garrett, 1984]. A recent numerical experiment, in particular, has shown that in order to reproduce the observed meridional overturning circulation, a diapycnal diffusivity of the order of $10^{-4} \text{ m}^2 \text{ s}^{-1}$ is necessary just below the thermocline [Tsujino *et al.*, 1999]. In contrast, previous microstructure measurements including dye release experiments in the ocean interior show that diapycnal diffusivity within the thermocline is about $10^{-5} \text{ m}^2 \text{ s}^{-1}$ [Toole *et al.*, 1994; Sherman and Davis, 1995; Ledwell *et al.*, 1993], an order of magnitude lower than the value required to satisfy the large-scale advective-diffusive balance of the thermohaline circulation [Munk, 1966]. Previous microstructure measurements, however, have been carried out only in limited times and locations [Gregg, 1998] so that the global distribution of diapycnal mixing rates remains unknown.

The mechanical energy to drive the ocean interior mixing is considered to be originally supplied at large scales by atmospheric forcing [Kundu, 1993; Rubenstein, 1994; Nilsson, 1995; Niwa and Hibiya, 1997] and tide-topography interactions [Sjöberg and Stigebrandt, 1992], and then transferred across the local internal wave spec-

trum down to small dissipation scales by nonlinear interactions amongst internal waves. An important fact to be noted is that the deep-ocean internal wave spectrum has much the same shape and level wherever it is observed, unless the observations are made close to a strong source of internal waves [Müller *et al.*, 1978; Wunsch and Webb, 1979]. This universal spectrum was empirically modeled as the Garrett and Munk spectrum (hereafter referred to as the GM spectrum) [Garrett and Munk, 1972, 1975; Munk, 1981] which is believed to reflect the spectral features of the internal wave climate in the deep ocean.

Hibiya *et al.* [1996] succeeded in numerically reproducing the quasi-equilibrium internal wave field having the actually observed GM-like spectrum with the roll-off at vertical wavenumber 0.06 cycles per meter by calculating the nonlinear interactions over 7 inertial periods among randomly phased linear internal waves with amplitudes determined from the GM model. Hibiya *et al.* [1998] then applied forcing to the low-frequency and low-vertical-wavenumber portion of the reproduced internal wave spectrum in the form of a spectral bump as an initial condition and showed that the main energy for mixing processes is supplied by low-vertical-wavenumber double-inertial-frequency internal waves and is transferred across the internal wave spectrum down to small dissipation scales by the resonant interaction termed parametric subharmonic instability (hereafter referred to as PSI)

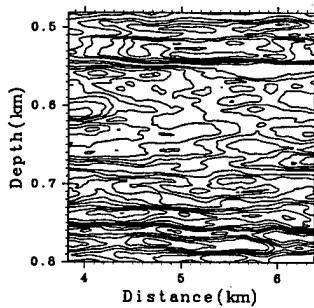


Figure 1. Contours of the horizontal current velocity with the interval of 1 cm s^{-1} in the numerically reproduced GM-like internal wave field [Hibiya *et al.*, 1998]. Horizontally elongated structures of strong vertical shear with vertical scale of a few tens of meters are found to develop in association with the energy transfer under the PSI mechanism. These pancake-like structures are considered to play an important role as critical layers in diapycnal mixing processes.

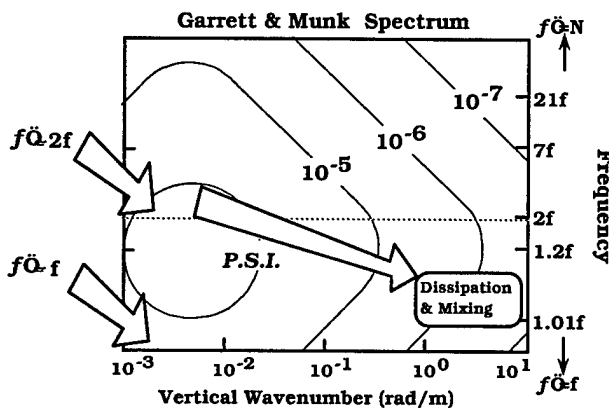


Figure 2. Schematic figure showing the dynamic balance of the internal wave spectrum wherein a downscale energy flux into the high-vertical-wavenumber near-inertial portion of the spectrum under the PSI mechanism is balanced by energy dissipation at critical layers formed by high-vertical-wavenumber, near-inertial flows [Hibiya *et al.*, 1996].

[McComas, 1977; McComas and Bretherton, 1977; McComas and Müller, 1981; Pomphrey *et al.*, 1980]. It was also shown that, in association with this energy transfer, horizontally elongated structures of strong vertical shear with vertical scale of a few tens of meters gradually develop in the velocity field which must play a crucial role as critical layers in diapycnal mixing processes (Figure 1). This implies the dynamic balance of the internal wave spectrum such that, with the increase of energy sup-

ply at low-vertical wavenumber double-inertial frequency, high-vertical-wavenumber near-inertial current shear is enhanced so that the rate of energy dissipation at critical layers increases (Figure 2). Understanding of the sources and variability of low-vertical-wavenumber double-inertial-frequency internal waves is therefore a key in constructing a predictive model of the rates of diapycnal mixing associated with internal wave breaking in the stratified interior of the world oceans.

In the present study, the generation and propagation of low-vertical-wavenumber low-frequency internal waves in the North Pacific are examined with the aid of a three-dimensional multi-level numerical model. Based on the numerically predicted energy distribution of low-vertical-wavenumber double-inertial-frequency internal waves, we discuss the spatial and temporal geography of diapycnal mixing rates in the deep waters of the North Pacific.

2. Numerical Experiment

Figure 3 shows the model North Pacific with the east-west and north-south sizes of 13000 km and 6600 km, respectively, covering the area from 120°E to 12°W and from 5°S to 55°N where realistic bottom topography from ETOPO5 of the National Geophysical Data Center is incorporated.

The governing equations are the three-dimensional Navier-Stokes equations under the hydrostatic, Boussinesq approximations in the orthogonal coordinate system given by

$$\begin{aligned} \frac{Du}{Dt} &= -\frac{1}{\rho_0} \frac{\partial p}{\partial x} + fv + A_H \nabla_H^2 u + A_V \frac{\partial^2 u}{\partial z^2} - ru \\ \frac{Dv}{Dt} &= -\frac{1}{\rho_0} \frac{\partial p}{\partial y} - fu + A_H \nabla_H^2 v + A_V \frac{\partial^2 v}{\partial z^2} - rv \\ -\frac{\partial p}{\partial z} &= \rho'g \end{aligned}$$

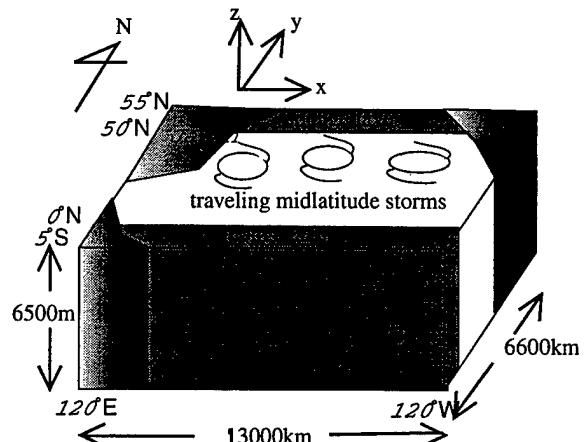


Figure 3. The North Pacific Ocean model used in the present study.

$$\frac{\partial u}{\partial x} + \frac{\partial v}{\partial y} + \frac{\partial w}{\partial z} = 0$$

$$\frac{D\rho'}{Dt} = \rho_0 w \frac{N^2}{g} + K_H \nabla_H^2 \rho' + K_V \frac{\partial^2 \rho'}{\partial z^2}$$

where t is time; u, v, w are the velocity components in the x, y, z directions, respectively; $D/Dt = \partial/\partial t + u\partial/\partial x + v\partial/\partial y + w\partial/\partial z$ is the total time derivative; $\nabla_H^2 = \partial^2/\partial x^2 + \partial^2/\partial y^2$; ρ' is the density perturbation from the background density profile; ρ_0 is the reference density; p is pressure; g is the acceleration due to gravity; N is the buoyancy frequency calculated from the background density profile; $f = 2\Omega \sin \phi$ is the Coriolis parameter with Ω the angular velocity of rotation of the earth and ϕ the latitude; r is the Newtonian damping coefficient assumed only in the sponge layers near the north and south boundaries, respectively; horizontal eddy viscosity A_H and horizontal eddy diffusivity K_H are both assumed to be $1 \text{ m}^2 \text{ s}^{-1}$; vertical eddy viscosity A_V and vertical eddy diffusivity K_V are determined following the Richardson-number formulation of Pacanowski and Philander [1981] such that

$$A_V = \frac{A_{V0}}{(1 + 5R_i)^2} + A_{Vb},$$

$$K_V = \frac{A_V}{(1 + 5R_i)} + K_{Vb},$$

$$R_i = \frac{N^2}{(u_c^2 + v_c^2)}$$

where $u_c = \partial u/\partial z$ and $v_c = \partial v/\partial z$, and we assume $A_{V0} = 10^{-2} \text{ m}^2 \text{ s}^{-1}$ and $A_{Vb} = K_{Vb} = 10^{-4} \text{ m}^2 \text{ s}^{-1}$. Background density field for each season is calculated from the salinity and temperature data of the National Oceanographic Data Center's World Ocean Atlas [Levitus and Boyer, 1994; Levitus et al., 1994]. The obtained seasonal density profile is then linearly interpolated to each time-step.

We employ the wind vectors at 10 m height above sea surface U_{10} for September 1991 - October 1992 from the Global Objectively Analyzed Data compiled by the Japan Meteorological Agency that is available at time intervals of 6 hours with grid spacings of $1.875^\circ \times 1.875^\circ$. The surface wind stress is calculated using the bulk transfer formula,

$$\tau = \rho_a C_D U_{10} U_{10}$$

where ρ_a is the density of air, U_{10} is the 10 m wind speed. Following Large and Pond [1981], the drag coefficient

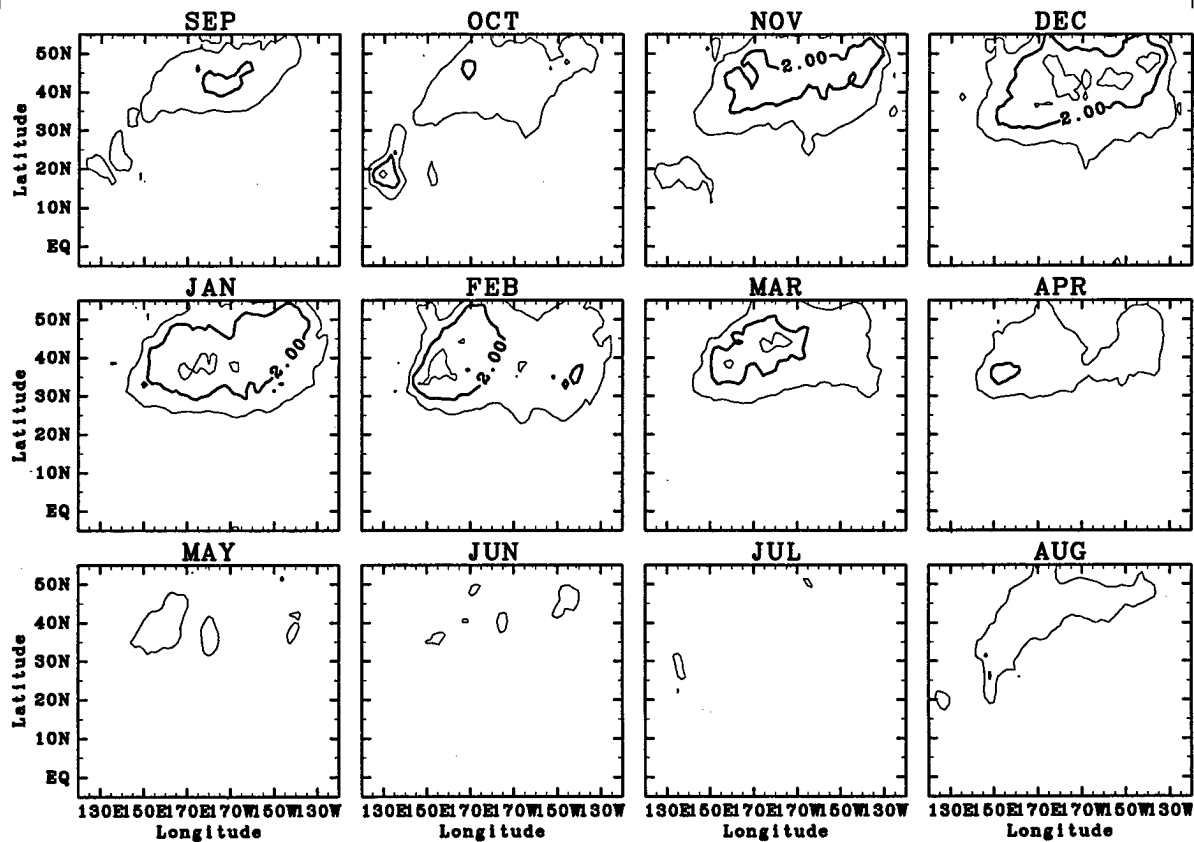


Figure 4. Monthly-averaged distribution of wind stress magnitude (dyn cm^{-2}) where the components with timescales longer than 6 days are filtered out. Contour interval is 1 dyn cm^{-2} .

C_D is given by

$$C_D = 1.14 \times 10^{-3} \quad U_{10} \leq 10 \text{ ms}^{-1}$$

$$C_D = (0.49 + 0.065 U_{10}) \times 10^{-3} \quad U_{10} > 10 \text{ ms}^{-1}$$

Figure 4 shows the monthly-averaged distribution of the wind stress magnitude where the components with timescales longer than 6 days are filtered out. We can find strong wind stress forcing in 30–45°N in the western-central North Pacific from November to March associated with traveling midlatitude storms. In addition, some local wind stress forcing of significant magnitude is found in October at around 20°N in the western North Pacific which is associated with tropical cyclones.

The governing equations are solved by using finite-difference method on $708 \times 360 \times 28$ grids with horizontal resolution of 18.5 km ($1^\circ/6$) and vertical resolution varying from 25 m for each of the top four levels up to 1600 m at depth. The sidewalls are assumed to be rigid. To eliminate the reflection of internal waves from the north and south boundaries, the Newtonian damping rate r in the sponge layer of 550 km (5°) width is increased linearly up to $1/(24\text{h})$ as each boundary is approached.

The model is run from an initial state of rest with a time-step of 600 s under wind stress forcing applied as a surface boundary condition. To avoid nonlinear numerical instability, the Euler-backward scheme is applied 5 times successively every 60 time-steps.

3. Results and Discussion

(a) Midlatitude storms in the western-central North Pacific

As has been theoretically shown by many investigators [Geisler, 1970; Price, 1983; Gill, 1984; Price *et al.*, 1994; Greatbatch, 1983, 1984], near-inertial internal waves are left behind the traveling atmospheric disturbances so that significant near-inertial energy is considered to be excited in the midlatitude band during winter. Figure 5 shows an example for the propagation of the first-vertical-mode near-inertial internal waves excited behind the traveling midlatitude storms in December where areas of significant wave energy are shaded. Superimposed are the contours of wind stress curl. We can see that large-amplitude

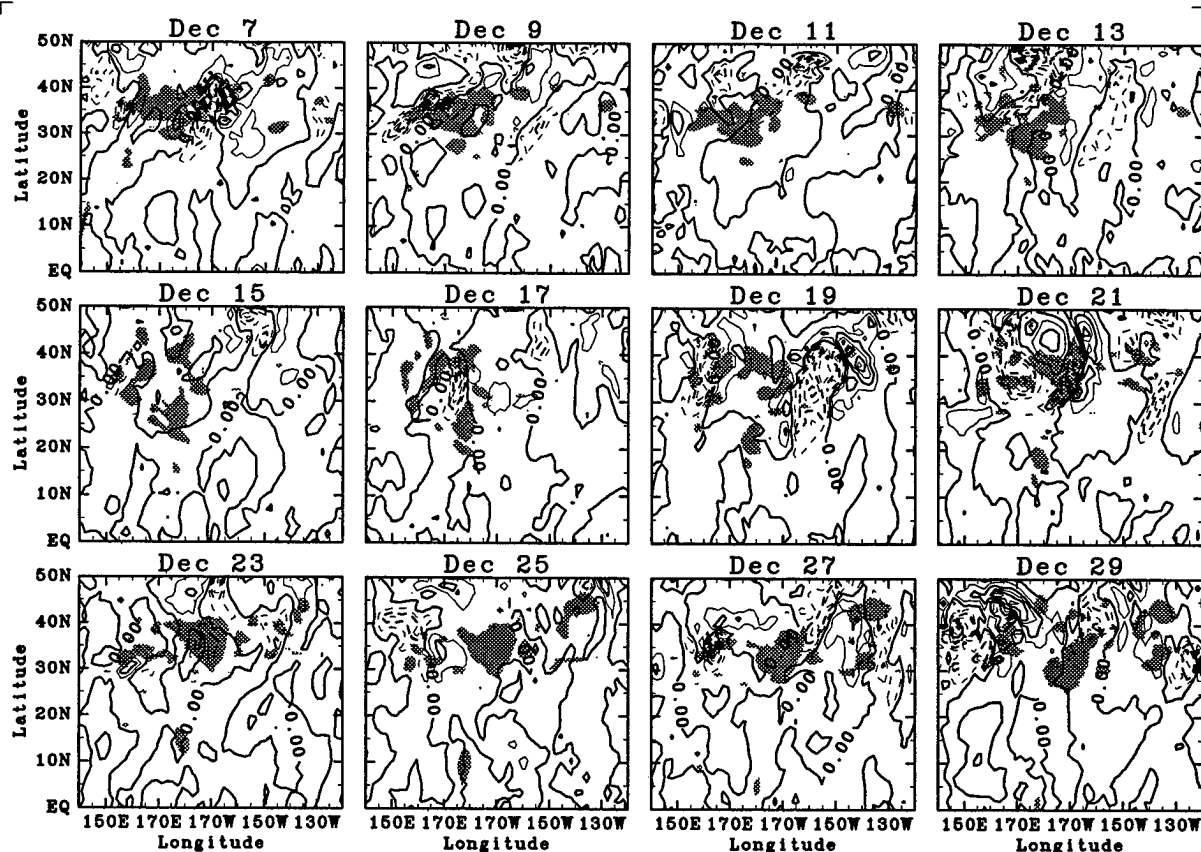


Figure 5. The propagation of the first-vertical-mode near-inertial internal waves excited behind the traveling midlatitude storms in December 1991. Areas where the vertically integrated internal wave energy is more than 10^6 erg cm^{-2} are shaded. Superimposed are contours of wind stress curl with the interval of $6.5 \times 10^{-8} \text{ dyn cm}^{-3}$. Negative values are denoted by dashed contours.

first-vertical-mode near-inertial internal waves are generated behind the midlatitude storm on December 7 and thereafter propagate equatorward because the poleward propagation is limited by the β effect.

The propagation of the first-vertical-mode near-inertial internal waves generated at midlatitudes (30–45°N) can be clearly tracked in the two-dimensional horizontal-wavenumber energy spectra calculated for various latitudinal bands in 155°E–165°W (Figure 6). On December 7, the spectral peak corresponding to the excited near-inertial internal waves is found in the spectrum for 30–40°N. As time proceeds, the spectral peak can be found in successively lower latitudinal band with the magnitude slowly decreasing and the corresponding north-south wavenumber gradually increasing. By December 21, the spectral peak can be tracked down to the latitudes 10–20°N. A particularly noticeable fact is that the frequencies of these propagating internal waves become twice the local inertial frequencies in 10–15°N in the western-central North Pacific, so that a large amount of energy is

considered to be transferred across the local internal wave spectrum down to small dissipation scales by the PSI mechanism causing enhanced diapycnal mixing.

(b) Tropical cyclones in the western North Pacific

Nearly the same situation is found to occur at low latitudes in the western North Pacific in October. As is shown in Figure 7, large-amplitude first-vertical-mode near-inertial-frequency internal waves are excited behind the tropical cyclone at around 20°N in October. These excited internal waves thereafter propagate equatorward down to the latitudes around 10°N where the wave frequencies become twice the local inertial frequency as is clearly identified in the corresponding two-dimensional horizontal-wavenumber energy spectra for various latitudinal bands in 140–180°E (Figure 8). At around 10°N in the western North Pacific, therefore, large amount of energy is considered to be transferred across the local internal wave spectrum down to small dissipation scales by the

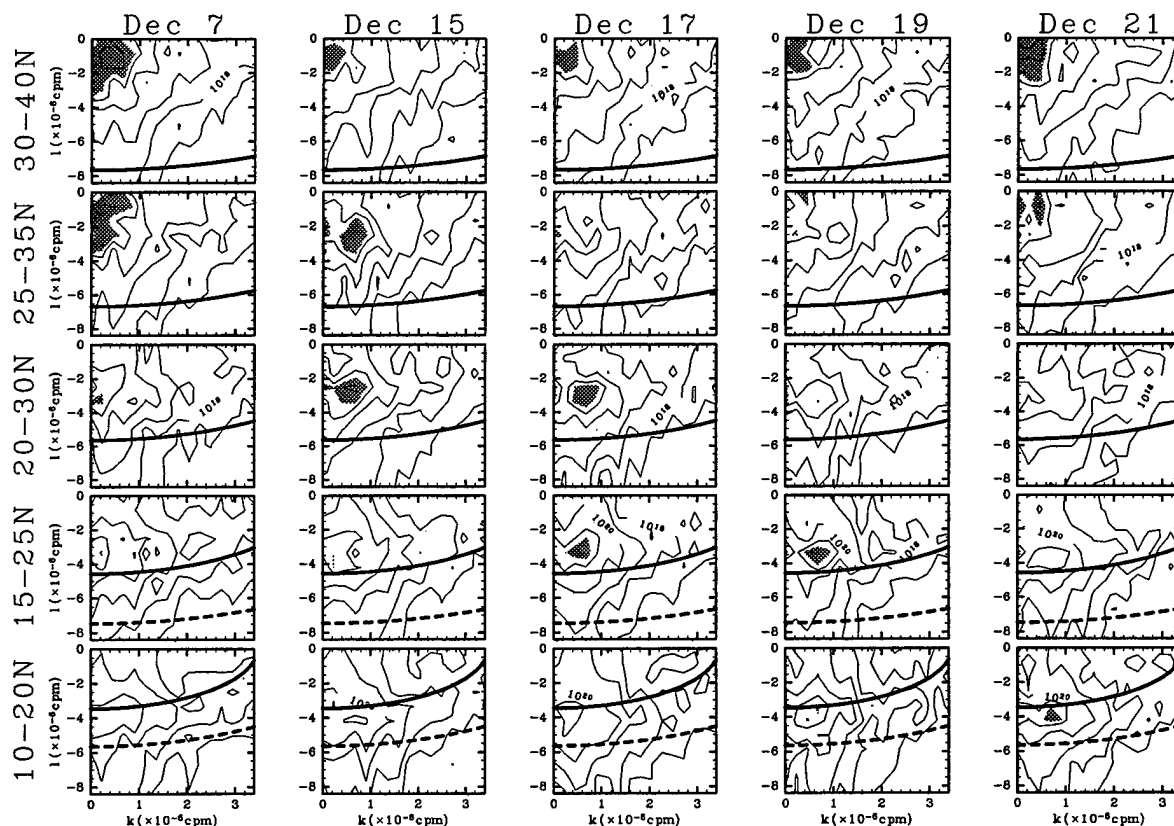


Figure 6. Two-dimensional horizontal-wavenumber spectra ($\text{erg cm}^{-2} \text{cpm}^{-2}$) of the vertically integrated energy of the first-vertical-mode near-inertial internal waves excited at midlatitudes (30–45°N) that are calculated for various latitudinal bands in 155°E–165°W. Note that spectral values are contoured with intervals of 1.0 in the logarithm (i.e., a factor of 10). Spectral values more than 10 % of the maximum over December 7–21 are shaded. Superimposed on each spectrum is the dispersion curve for the first-vertical-mode internal wave with the frequency $\omega=2f$ (solid line) and $\omega=3f$ (dashed line) where f is the local inertial frequency.

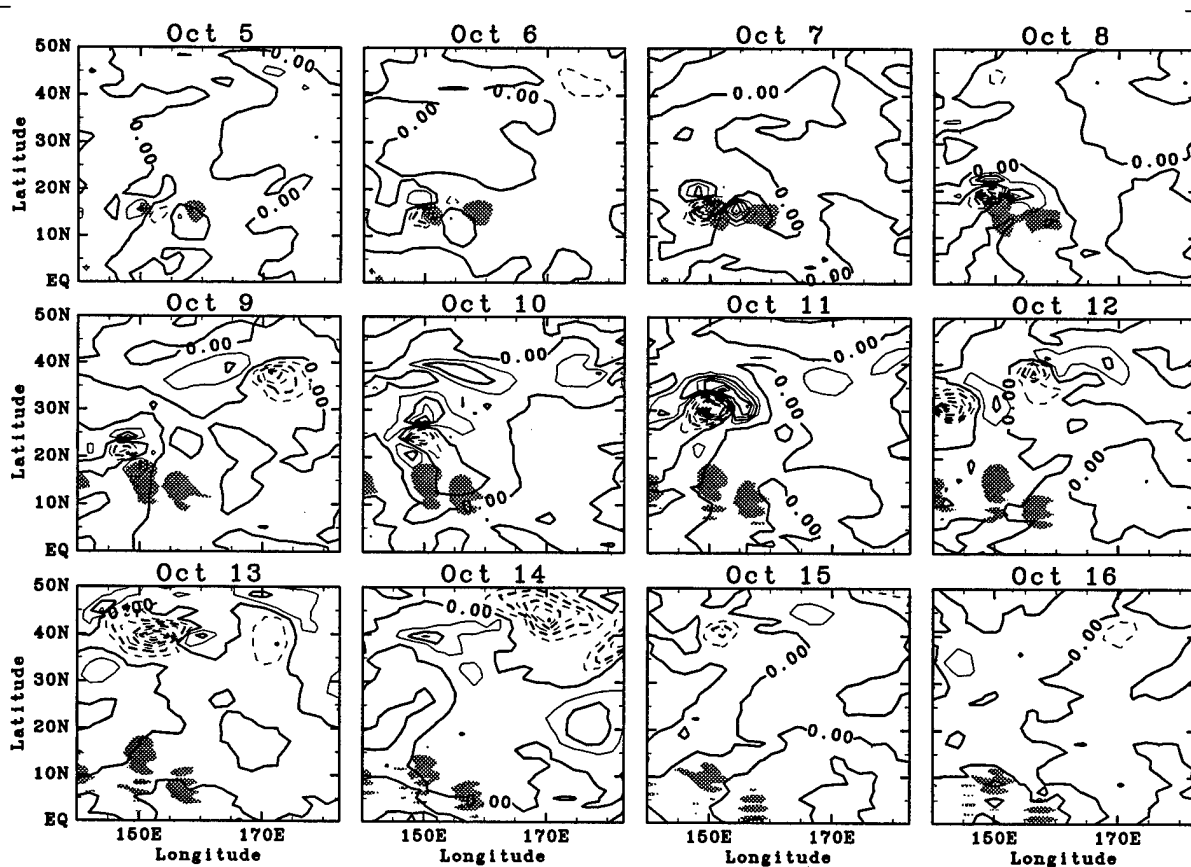


Figure 7. The propagation of the first-vertical-mode near-inertial internal waves excited behind the tropical cyclone at around 20°N in October 1991. Areas where the vertically integrated internal wave energy is more than 10^6 erg cm $^{-2}$ are shaded. Superimposed are contours of wind stress curl with the interval of 6.5×10^{-8} dyn cm $^{-3}$. Negative values are denoted by dashed contours.

PSI mechanism causing enhanced diapycnal mixing.

(c) Spatial and temporal distribution of double-inertial frequency waves

Figure 9 shows the monthly-averaged energy distribution for the low-vertical-modes double-inertial-frequency internal waves in the North Pacific from September 1991 through August 1992 which is predicted from the present numerical experiment. As is mentioned above, energetic near-inertial-frequency waves are generated in 30–45°N in the western-central North Pacific by traveling midlatitude storms during winter and at around 20°N in the western North Pacific by tropical cyclones during fall. The internal waves thus excited then propagate equatorward down to the latitudes where the frequencies become twice the local inertial frequencies. In particular, the vertically integrated energy of the low-vertical-modes internal waves with the frequency $2f < \omega < 3f$ (f is the local inertial frequency) in 10–15°N in the central North Pacific reaches about three times the corresponding value for the GM internal wave field in January, and that in 5–10°N in the western North Pacific reaches about ten times the corre-

sponding value for the GM internal wave field in October. Large amount of energy is thus available for diapycnal mixing in 10–15°N in the western-central North Pacific during winter and at around 10°N in the western North Pacific during fall.

Now the locations of previous microstructure measurements [Gregg, 1998] are superimposed on the energy distribution of the low-vertical-modes double-inertial-frequency internal waves in Figure 9. Previous microstructure measurements in the ocean interior were carried out in the eastern North Pacific or north of 27°N in the western-central North Pacific mostly during spring and summer and showed a diapycnal diffusivity of about 10^{-5} m 2 s $^{-1}$, an order of magnitude lower than the value predicted by most thermohaline ocean circulation models. The present numerical experiment provides a possible explanation for this discrepancy because the numerically predicted energy levels for the low-vertical-modes double-inertial-frequency internal waves are shown to be extremely low at the times and locations of the previous microstructure measurements (Figure 9).

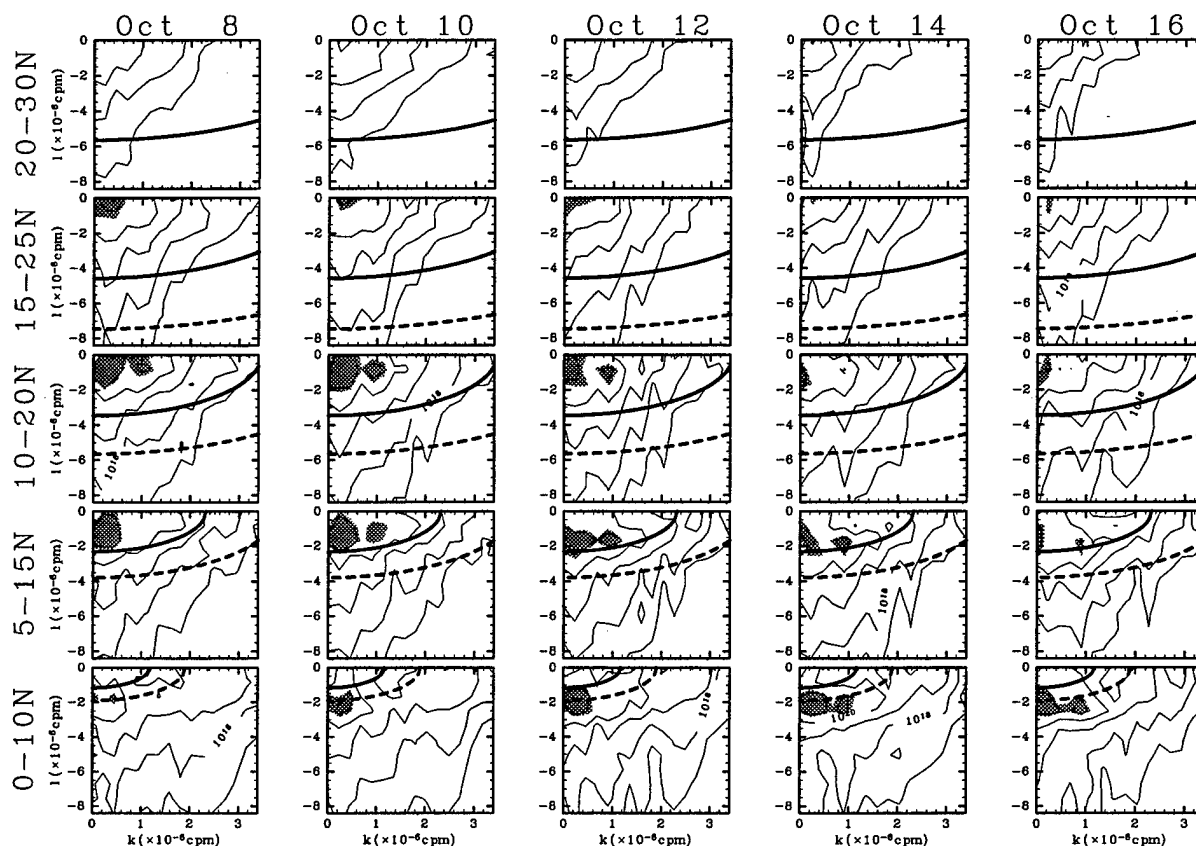


Figure 8. Two-dimensional horizontal-wavenumber spectra ($\text{erg cm}^{-2} \text{cpm}^{-2}$) of the vertically integrated energy of the first-vertical-mode near-inertial internal waves excited behind the tropical cyclone at around 20°N that are calculated for various latitudinal bands in $140\text{--}180^\circ\text{E}$. Note that spectral values are contoured with intervals of 1.0 in the logarithm (i.e., a factor of 10). Spectral values more than 20 % of the maximum over October 8-16 are shaded. Superimposed on each spectrum is the dispersion curve for the first-vertical-mode internal wave with the frequency $\omega = 2f$ (solid line) and $\omega = 3f$ (dashed line) where f is the local inertial frequency.

4. Conclusion

Energy applied to the internal wave spectrum at large scales is most effectively transferred to small dissipation scales by parametric subharmonic instability. The low-vertical-modes double-inertial-frequency waves, therefore, provide main energy for diapycnal mixing processes in the deep ocean. The present numerical experiment has clearly shown that energy distribution of low-vertical-modes double-inertial-frequency waves in the North Pacific exhibits significant spatial and temporal variability; they become energetic in the latitudes $10\text{--}15^\circ\text{N}$ in the western-central North Pacific during winter and at around 10°N in the western North Pacific during fall.

Previous microstructure measurements in the ocean interior were carried out in the eastern North Pacific or north of 27°N in the western-central North Pacific mostly during spring and summer. Considering that the numerically predicted energy levels of the low-vertical-modes double-inertial-frequency internal waves are extremely

low at these times and locations of the previous microstructure measurements, the observed value of diapycnal diffusivity of about $10^{-5} \text{m}^2 \text{s}^{-1}$, an order of magnitude lower than required to satisfy the large-scale advective-diffusive balance of the thermohaline circulation, cannot be representative.

It is believed that the barotropic tidal current interacting with bottom topography can be another important source of the mechanical energy to drive diapycnal mixing. In particular, semidiurnal internal tides generated at latitudes lower than 30° are considered to be significant [Munk, 1997], since the spectral cascade of their energy down to small dissipation scales is promoted by the PSI mechanism.

Continuing with this line of approach, we are currently examining the spatial and temporal energy distribution of low-vertical-modes double-inertial-frequency internal waves in the world oceans with the aid of three-dimensional numerical model which takes account of realistic atmospheric forcing as well as tide-topography

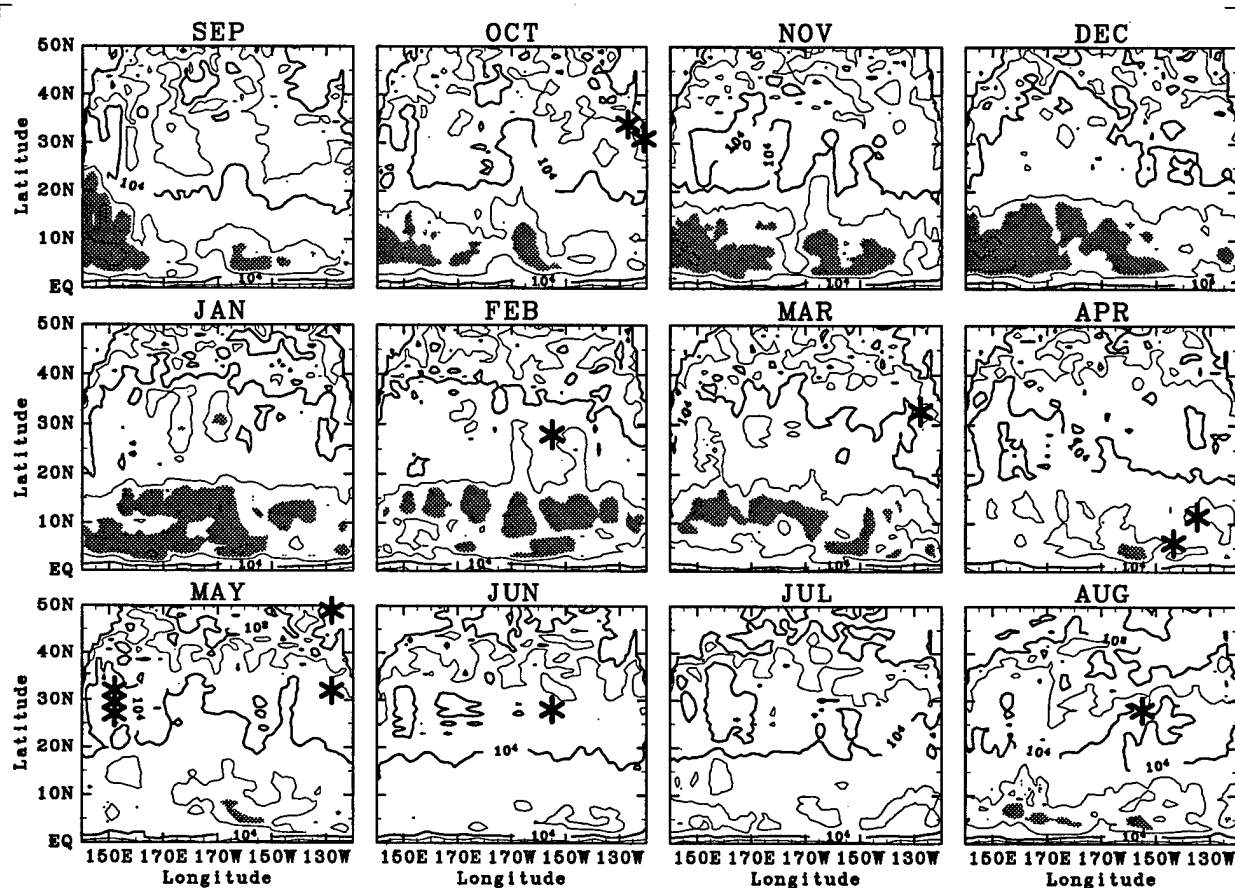


Figure 9. Monthly averaged distribution of the vertically integrated energy (erg cm^{-2}) of the low-vertical-modes (first-third vertical-modes) internal waves with the frequency $2f < \omega < 3f$ (f is the local inertial frequency) in the North Pacific predicted from the present numerical experiment. Note that energy values are contoured with intervals of 1.0 in the logarithm (i.e., a factor of 10). Areas where the value is more than 5 % of the maximum over September 1991 to August 1992 are shaded. Superimposed by crosses are the locations of previous microstructure measurements.

interactions. The results of these numerical experiments will guide attempts to determine the global structure of diapycnal mixing prerequisite for the realistic parameterization that can be incorporated into the oceanic general circulation models.

Acknowledgment. One of the authors (T. Hibiya) expresses his gratitude to Prof. Peter Müller for the kind invitation to the workshop. This work was supported in part through a Grant-in-Aid for Scientific Research to T. Hibiya by the Ministry of Education, Science, Sports and Culture of Japan (09640520).

References

- Bryan, F., 1987: Parameter sensitivity of primitive equation ocean general circulation models, *J. Phys. Oceanogr.*, 17, 970-985.
- Gargett, A. E., 1984: Vertical eddy diffusivity in the ocean interior, *J. Mar. Res.*, 42, 359-393.
- Garrett, C. J. R., and W. H. Munk, 1972: Space-time scales of internal waves, *Geophys. Fluid Dyn.*, 2, 225-264.
- Garrett, C. J. R., and W. H. Munk, 1975: Space-time scales of internal waves: A progress report, *J. Geophys. Res.*, 80, 291-297.
- Geisler, J. E., 1970: Linear theory of the response of a two layer ocean to a moving hurricane, *Geophys. Fluid Dyn.*, 1, 249-272.
- Gill, A. E., 1984: On the behavior of internal waves in the wake of storms, *J. Phys. Oceanogr.*, 14, 1129-1151.
- Greatbatch, R. J., 1983: On the response of the ocean to a moving storm: The nonlinear dynamics, *J. Phys. Oceanogr.*, 13, 357-367.
- Greatbatch, R. J., 1984: On the response of the ocean to a moving storm: Parameters and scales, *J. Phys. Oceanogr.*, 14, 59-77.
- Gregg, M. C., 1998: Estimation and geography of diapycnal mixing in the stratified ocean, in *Physical Processes in Lakes and Oceans (Coastal and Estuarine Studies, Vol. 54)*, edited by J. Imberger, pp. 305-338, American Geophysical Union, Washington D. C..
- Hibiya, T., Y. Niwa, K. Nakajima, and N. Sugimotohara, 1996: Direct numerical simulation of the roll-off range of internal

- wave shear spectra in the ocean, *J. Geophys. Res.*, 101, 14123-14129.
- Hibiya, T., Y. Niwa, and K. Fujiwara, 1998: Numerical experiments of nonlinear energy transfer within the oceanic internal wave spectrum, *J. Geophys. Res.*, 103, 18715-18722.
- Kundu, P. K., 1993: On internal waves generated by traveling wind, *J. Fluid Mech.*, 254, 529-559.
- Large, W. G., and S. Pond, 1981: Open ocean momentum flux measurements in moderate to strong winds, *J. Phys. Oceanogr.*, 11, 324-336.
- Ledwell, J. R., A. J. Watson, and C. S. Law, 1993: Evidence for slow mixing across the pycnocline from an open-ocean tracer-release experiment, *Nature*, 364, 701-703.
- Levitus, S., R. Burgett, and T. P. Boyer, 1994: World Ocean Atlas 1994, Vol. 3, Salinity: NOAA Atlas NESDIS 3, U. S. Dep. of Commer., Washington, D. C..
- Levitus, S., and T. P. Boyer, 1994: World Ocean Atlas 1994, Vol. 4, Temperature: NOAA Atlas NESDIS 4, U. S. Dept. of Commer., Washington, D. C..
- McComas, C. H., 1977: Equilibrium mechanisms within the oceanic internal wave field, *J. Phys. Oceanogr.*, 7, 836-845.
- McComas, C. H., and F. P. Bretherton, 1977: Resonant interaction of oceanic internal waves, *J. Geophys. Res.*, 82, 1397-1412.
- McComas, C. H., and P. Müller, 1981: The dynamic balance of internal waves, *J. Phys. Oceanogr.*, 11, 970-986.
- Müller, P., D. J. Olbers, and J. Willebrand, 1978: The IWEX spectrum, *J. Geophys. Res.*, 83, 479-500.
- Munk, W., 1966: Abyssal recipes, *Deep Sea Res.*, 13, 707-730.
- Munk, W. H., 1981: Internal waves and small-scale processes, in *Evolution of Physical Oceanography*, edited by B. S. Warren and C. Wunsch, pp. 264-291, MIT Press, Cambridge, Mass.
- Munk, W., 1997: Once again: once again-tidal friction, *Prog. Oceanogr.*, 40, 7-35.
- Nilsson, J., 1995: Energy flux from traveling hurricanes to the oceanic internal wave field, *J. Phys. Oceanogr.*, 25, 558-573.
- Niwa, Y., and T. Hibiya, 1997: Nonlinear processes of energy transfer from traveling hurricanes to the deep ocean internal wave field, *J. Geophys. Res.*, 102, 12469-12477.
- Pacanowski, R. C., and S. G. H. Philander, 1981: Parameterization of vertical mixing in numerical models of tropical oceans, *J. Phys. Oceanogr.*, 11, 1443-1451.
- Pomphrey, N., J. D. Meiss, and K. M. Watson, 1980: Description of nonlinear internal wave interactions using Langevin method, *J. Geophys. Res.*, 85, 1085-1094.
- Price, J. F., 1983: Internal wave wake of a moving storm, Part I: Scales, energy budget and observation, *J. Phys. Oceanogr.*, 13, 949-965.
- Price, J. F., T. B. Sanford, and G. Z. Forristall, 1994: Forced stage response to a moving hurricane, *J. Phys. Oceanogr.*, 24, 233-260.
- Rubenstein, D., 1994: A spectral model of wind-forced internal waves, *J. Phys. Oceanogr.*, 24, 819-831.
- Sherman, J. T., and R. E. Davis, 1995: Observations of temperature microstructure in NATRE, *J. Phys. Oceanogr.*, 25, 1913-1929.
- Sjöberg, B., and A. Stigebrandt, 1992: Computations of the geographical distribution of the energy flux to mixing processes via internal tides and the associated vertical circulation in the ocean, *Deep Sea Res.*, 39, 269-291.
- Toole, J. M., K. L. Polzin, and R. W. Schmitt, 1994: Estimates of diapycnal mixing in the abyssal ocean, *Science*, 264, 1120-1123.
- Tsujino, H., H. Hasumi, and N. Sugimotohara, 1999: Deep Pacific circulation controlled by depth-dependent vertical diffusivity, submitted to *J. Phys. Oceanogr.*.
- Wunsch, C., and S. Webb, 1979: The climatology of deep ocean internal waves, *J. Phys. Oceanogr.*, 9, 235-243.

What is the "Near-Inertial" Band and Why is it Different?

Chris Garrett

Department of Physics and Astronomy, University of Victoria, Victoria, British Columbia, Canada

Abstract. The "near-inertial" part of the internal wave continuum is both dominant and different. A simple possible reason for the difference is that waves generated at the surface are not reflected or scattered from the sea floor until they have propagated equatorward to a latitude where their frequency exceeds the local inertial frequency. This excess is easily estimated and is of the order of 10% of f at mid-latitudes. The estimate is in reasonable agreement with data on the depth-dependent peak frequency and on the frequency band within which there is little upward propagating energy, suggesting that an increased research emphasis on the near-inertial band is warranted.

Introduction

Freely propagating internal waves are possible in the open ocean at all frequencies between the Coriolis frequency f and the buoyancy frequency N . Near f the fluid motion is close to horizontal, with the Coriolis force dominating, whereas near N the motion is close to vertical with buoyancy providing the main restoring force. There is a gradual transition between these two limits, with no obvious transition frequency separating different parts of the continuum.

On the other hand, it does seem that the "near-inertial" band of waves with a frequency close to f does have different characteristics from the rest of the frequency spectrum. In particular, near-inertial waves appear to have a predominance of downward propagating energy (e.g., *Leaman and Sanford, 1975; D'Asaro and Perkins, 1984; Sanford, 1991*) and to have a redder vertical wavenumber spectrum than the rest of the frequency spectrum (*Sanford, 1991*). Part of this different spectral slope was shown by *Sherman and Pinkel (1991)* to be a consequence of the vertical displacement, by the internal waves themselves, of a spectrum which is more nearly separable in a "semi-Lagrangian" frame in which the shear is referenced to isopycnals rather than fixed depths. Even in this frame, however, the vertical wavenumber spectrum is steeper at near-inertial frequencies than at high frequencies (see their Figure 8c).

These major differences, taken together with the fact that most of the energy in typical internal wave spectra is at frequencies close to f , make it particularly surprising that the so-called GM spectrum (e.g.,

Munk, 1981), which is vertically isotropic and has the same vertical wavenumber dependence at all frequencies, has been taken seriously for so long.

It may well be more appropriate to start treating the near-inertial band as different from the rest of the spectrum, thus introducing the questions asked in the title of this paper. The questions are, of course, connected, with many possible answers. Some, to be discussed in this paper, arise from consideration of the generation of inertial waves in the upper ocean, the types of nonlinear interaction that are possible, and the role of latitudinal turning points in wave propagation. The main suggestion to be made, though, is that the unique behaviour of near-inertial waves arises from the fact that they exist on a β plane and must therefore propagate equatorward. If they conserve their frequency, their frequency becomes greater than the local f . The amount by which the wave frequency exceeds the local f when the waves reach the sea floor may then be a measure of what determines the "near-inertial" band within which the energy propagates downward and has not had its vertical wavenumber spectrum modified by reflection and scattering off a sloping and irregular sea floor.

There is, of course, an extensive literature on near-inertial waves, including the papers referred to above and the comprehensive treatise of *Fu (1981)*. Details of these and other papers will be introduced as appropriate in later sections.

The "Near-Inertial" Bandwidth

Let us suppose that the near-inertial band extends from f to $(1 + \epsilon)f$ and ask what value ϵ might take. An obvious answer might be that ϵ is about 1, on the grounds that at a frequency $2f$ the Coriolis and buoyancy forces are of equal importance in determining the wave frequency. This answer, however, appears to lack any dynamical significance or implication. We seek alternatives.

Generation

Much of the internal wave activity in the ocean appears to originate with the wind and other surface forcing. As discussed by Gill (1984), Zervakis and Levine (1995), and others, the speed of atmospheric fronts is typically much faster than the phase speed of internal waves in the ocean, so that the oceanic response occurs in two stages. In the first, short, stage, currents are generated in the surface layer of the ocean, and in the second, longer, stage, after the forcing has ceased, these currents undergo "Rossby adjustment". In this process, waves of near-inertial frequency are generated, with the difference in frequency ω from the inertial frequency depending on the horizontal wavenumber (k, l) of the disturbance left behind by the storm, according to the formula

$$\omega^2 - f^2 = c_j^2(k^2 + l^2) \quad (1)$$

where c_j is the eigenvalue associated with the j th vertical mode. If $\omega = (1 + \epsilon)f$ and ϵ is small, then for the j th mode

$$\epsilon = \epsilon_j \simeq \frac{1}{2}(c_j/f)^2(k^2 + l^2) \quad (2)$$

where c_j/f is the associated Rossby radius. A typical mid-latitude value might be 30 km for the first mode, and less for higher modes, giving $\epsilon \simeq 0.05$ for mode 1 if $(k^2 + l^2)^{-1/2} \simeq 100$ km, decreasing with mode number.

Kundu (1993) shows that slower moving storms will tend to shift the peak of the generated internal wave spectrum to higher frequencies, but on the whole it can be argued that the dominant inertial peak is a consequence of the forcing, in which case the question becomes one of accounting for the rest of the frequency spectrum. We return to this later.

The latitudinal turning point

Near-inertial waves in a medium of constant f are really a theoretical idealization; they cannot exist in the ocean as their wavelength exceeds the distance over

which f varies significantly. In reality, waves propagating poleward in varying f will encounter a turning latitude where they will have a greatly enhanced energy, as discussed in detail by Fu (1981) and Munk (1980, 1981). Fu (1981) demonstrated, in fact, that in the deep ocean over smooth topography the near-inertial cusp in typical frequency spectra of horizontal kinetic energy is purely a turning point effect, as if the waves had been generated at lower latitudes at frequencies greater than the Coriolis frequency there, and had then freely propagated poleward. The reverse situation is also possible, with the waves being generated near their turning latitude and propagating freely equatorward, and this seems more likely. Over rough topography or in the upper ocean Fu (1981) found that the energy is enhanced more than for free propagation, suggesting the importance of some sort of local process for transferring energy out of the near-inertial band before it has propagated far.

The width of the near-inertial band associated with enhancement at the latitudinal turning point can be estimated by considering the distance from the turning point at which this distance is equal to the reciprocal of the wavenumber; this marks the transition from an equatorward zone where ray theory is appropriate to a poleward zone where solutions can be expressed in terms of Airy functions. We use the internal wave dispersion relation

$$\omega^2 - f^2 = \frac{N^2(k^2 + l^2)}{(k^2 + l^2 + m^2)} \simeq \frac{N^2(k^2 + l^2)}{m^2} \quad (3)$$

away from N , with $\omega - f \simeq \beta y'$ at a small distance y' equatorward of the latitude where $\omega = f$. Then, with $k = 0$ and taking $l = y'^{-1}$,

$$y' = \left(\frac{N^2}{2\omega\beta m^2} \right)^{1/3} = \left(\frac{N_0^2 b^2}{2\omega\beta j^2 \pi^2} \right)^{1/3} \quad (4)$$

where we have used the connection $m = j\pi N/(N_0 b)$ between the vertical wavenumber m and the mode number j for an ocean with $N = N_0 e^{z/b}$, with $z = 0$ at the surface and assuming that the ocean depth H is much greater than the scale depth b (Munk, 1981). The associated value of ϵ in $\omega = (1 + \epsilon)f$ is

$$\epsilon = \frac{1}{2} j^{-2/3} \pi^{-2/3} \left(\frac{N_0 b \cos \phi}{\Omega R \sin^2 \phi} \right)^{2/3} \quad (5)$$

for generation latitude ϕ and with $\Omega = 7.292 \times 10^{-5} \text{ s}^{-1}$ the angular rotation rate of the earth and $R = 6,371$ km its radius. Taking $N_0 = 5.24 \times 10^{-3} \text{ s}^{-1}$ and $b = 1.3$ km,

$$\begin{aligned} y' &= 112 j^{-2/3} (\sin 2\phi)^{-1/3} \text{ km}, \\ \epsilon &= 0.014 j^{-2/3} (\cos \phi / \sin^2 \phi)^{2/3} \end{aligned} \quad (6)$$

which are $120j^{-2/3}$ km and $0.032j^{-2/3}$ respectively at latitude 30° .

These rather small values for y' and ϵ suggest that ray theory is likely to be appropriate to within a fairly small distance of the turning latitude. Moreover, there seems to be no reason why the dynamics of the waves should change character as this boundary is crossed.

Nonlinear interactions

A possible dynamical reason for treating near-inertial waves separately from the rest of the spectrum is that only waves with frequency greater than $2f$ are susceptible to parametric subharmonic instability (PSI) (McComas and Müller, 1981) which transfers energy to waves with half the frequency of the original waves. The frequency band from f to $2f$ is thus different from the rest of the spectrum in that it can receive energy by PSI but cannot lose it. It is not clear, however, that this transfer could account for the observed predominance of downward propagating near-inertial energy, or for the redder vertical wavenumber spectrum. On the contrary, one might expect that PSI would generate high vertical wavenumber near-inertial energy giving rise to a less red, rather than redder, vertical wavenumber spectrum.

Overall, the behaviour of near-inertial waves in weak nonlinear wave-wave interaction theory seems uncertain. McComas and Müller (1981) find that induced diffusion also tends to transfer energy to lower frequency and higher wavenumber, but the rate at which this happens for a wavenumber-frequency spectrum that has different vertical wavenumber dependencies at near-inertial and higher frequencies requires further attention.

Noting that weak interaction theory breaks down for much of the internal wave field, Henyey et al. (1986) adopt an alternative approach in which high vertical wavenumber waves propagate through a much larger-scale background shear representing the rest of the internal wave field. They find a general tendency for refraction to higher vertical wavenumber, and higher frequency, leading ultimately to dissipation. The background shear is clearly provided to a large extent by the near-inertial waves, but the back effect of the interactions on them is unclear.

It seems that there are good grounds for revisiting the two different approaches to nonlinear internal wave interactions in the ocean, paying more attention to the energetically dominant near-inertial band, but this is not the immediate object of this short paper.

Meridional Propagation of "Near-Inertial" Waves

Several authors (e.g. Kroll, 1975; Gill, 1984; Zervakis and Levine, 1995) have used ray theory to trace the paths of near-inertial wave packets, but their emphasis has been largely on the escape of near-inertial energy from the near-surface region of the ocean. The point to be made here is illustrated in Figure 1: inertial energy generated at the sea surface at the turning latitude propagates equatorward and vertically downward until it reaches the sea floor where it is reflected and scattered. It then has the same frequency as at the generation site, but this is now larger than the local Coriolis frequency, by an amount ϵf , say, with ϵ a small number that varies with latitude. At any particular latitude, it is clear that waves in the frequency band from the local f to $(1+\epsilon)f$ near the sea floor are only propagating downward and, furthermore, have a vertical wavenumber spectrum that has not been modified by bottom reflection and scattering. The waves in this band are thus distinct from the rest of the internal wave continuum.

It is simple to use the ray equations to determine ϵ . The dispersion relation for internal waves is

$$\omega^2 \simeq f^2 + N^2(k^2 + l^2)/m^2 \quad (7)$$

for a frequency near f . We also assume $k = 0$ for simplicity. (This seems a reasonable approximation as l grows to exceed a typical k quite quickly as the waves propagate equatorward, but we will examine the effect of finite k later.) We also assume $l = 0$ at the generation site, i.e. that the wave packet originates right at the turning latitude, and return later to this assumption.

The equations for the ray are

$$\frac{dy}{dt} = \frac{\partial \omega}{\partial l} = \frac{N^2 l}{m^2 \omega}, \quad \frac{dz}{dt} = \frac{\partial \omega}{\partial m} = -\frac{N^2 l^2}{m^3 \omega} \quad (8)$$

and we take y positive poleward and z positive upward with the origin at the generation site. Locally $\omega^2 -$

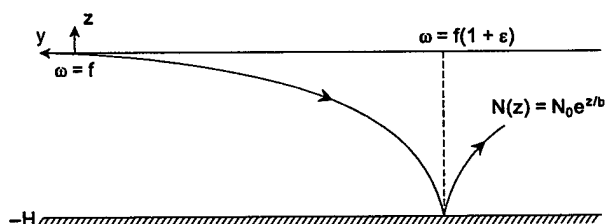


Figure 1. Schematic of the ray for inertial waves generated at the surface and propagating equatorward and downward.

$f^2 \simeq -2\omega\beta y$ for $f = \omega + \beta y$ where $\beta = fR^{-1}\cot\phi$ so that, writing $y' = -y$, we have

$$\frac{dy'}{dt} \simeq (2\omega\beta y')^{1/2} \frac{N}{\omega m}, \quad \frac{dz}{dt} \simeq \frac{-2\beta y'}{m}. \quad (9)$$

To solve for y' and z as functions of time t we also need an equation for m and will return to this later, but for now we just divide the group velocity equations to obtain

$$\frac{dy'}{dz} \simeq -\frac{N}{(2\omega\beta y')^{1/2}}. \quad (10)$$

For the model ocean already considered, with $N = N_0 e^{z/b}$, the ray reaches the sea floor at $z = -H$, for $H \gg b$, at $y' = Y$ where

$$Y \simeq \frac{1}{2} \left(\frac{9N_0^2 b^2}{\omega\beta} \right)^{1/3} \quad (11)$$

which is similar in form to (4). The corresponding value of ϵ is

$$\epsilon \simeq \frac{1}{2} \left(\frac{3N_0 b \cos\phi}{2\Omega R \sin^2\phi} \right)^{2/3} \quad (12)$$

which is likewise similar to (5). Taking $N_0 = 5.24 \times 10^{-3} \text{ s}^{-1}$ and $b = 1.3 \text{ km}$, we may write

$$Y = 315(\sin 2\phi)^{-1/3} \text{ km}, \quad \epsilon = 0.039(\cos\phi/\sin^2\phi)^{2/3} \quad (13)$$

as shown in Figure 2, and giving values of 330 km and 0.09 respectively at latitude 30° .

The formulae are similar to (6), but with larger values of both ϵ and Y , especially for high modes, thus

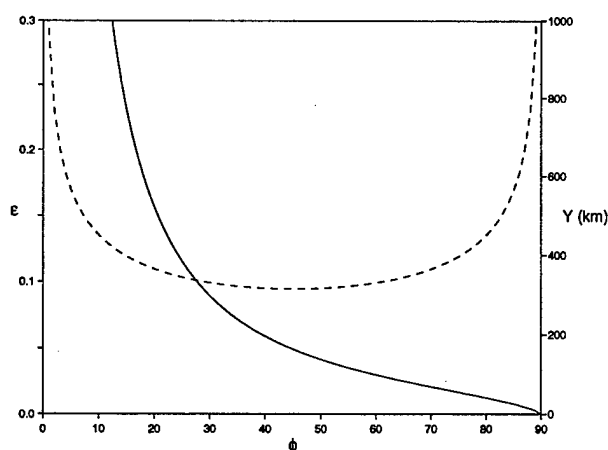


Figure 2. The equatorward propagation distance Y (dashed curve, right hand axis) and fractional frequency difference ϵ (solid line, left hand axis) as functions of the latitude ϕ .

illustrating the validity of ray theory over most of the ray path, at least as far as the meridional wavenumber l is concerned. Using ray theory is more questionable for low vertical modes for which the vertical wavelength is not small compared with the buoyancy scale height b . These formulae use the approximation $H \gg b$; for the assumed stratification both y' and ϵ are reduced at a depth of 4 km by a factor $(1 - e^{4/1.3})^{2/3} = 0.97$.

It should be remarked that while ϵ from (12) gives the bandwidth for downward-propagating waves observed near the bottom, upward-propagating waves will not be seen higher in the water column until the wave ray has progressed further equatorward. The reflected ray is described by (10) with the sign reversed since the vertical wavenumber is reversed on reflection at a flat bottom. Simple integration shows that the ray reaches the sea surface at a distance $2^{2/3}Y = 1.6Y$ from the generation site, with Y given by (11) or (13), corrected by a factor 0.97 for finite depth.

Effects of finite initial wavenumber

The above calculation has assumed that the initial wavenumbers are both zero. The zonal wavenumber k then remains zero while the meridional wavenumber l becomes increasingly negative as the wave group propagates equatorward. It is straightforward to allow for finite k and for finite initial l .

In the former case, but still with $l = 0$ initially, the waves originate equatorward of their origin for $k = 0$, but have a steeper ray and so actually reach the sea floor poleward of the position for $k = 0$. Assuming that this change is small, Y and ϵ as given by (11) and (12) are both reduced by a factor $1 - (4/9)(kY/j\pi)^2$, with Y from (11). If $k^{-1} \simeq 100 \text{ km}$, then the reduction is $0.49j^{-2}$ at latitude 30° . For low mode numbers this is not really small enough for the approximations used, but does suggest a significant reduction in the estimate of ϵ for the definition of the near-inertial band. The correction becomes much less for smaller k .

In the latter case, with a finite initial meridional wavenumber l_0 , a wave packet first propagates poleward if $l_0 > 0$. Assuming $k = 0$, the waves reach their turning latitude at a depth $z = -(N_0^2/3\omega\beta)(l_0 b/j\pi)^3$, which is $0.45j^{-3} \text{ km}$ for $l_0^{-1} = 100 \text{ km}$ at latitude 30° . The internally reflected ray then has less vertical distance to travel than if it started at the surface and reaches the bottom at a range given by Y from (11) reduced by a factor $1 - (16/81)(l_0 Y/j\pi)^3$, assuming a small correction. If $l_0^{-1} \simeq 100 \text{ km}$, then the reduction is $0.38j^{-3}$ at latitude 30° , again not small at low mode numbers for this value of l_0 , but much smaller for smaller l_0 .

The overall conclusion is that the bandwidth measure ϵ given in (11) will be reduced by an amount that might be some tens of percent for mode 1, much less for higher modes.

Evidence?

Fu (1981) examined the frequency of the peak of the internal wave spectrum using data from a variety of current meter moorings in the North Atlantic, finding a considerable scatter but with a definite tendency for the peak frequency to increase with depth. Fu (1981) attributes this to the fact that only waves with super-inertial frequency can propagate downwards. It seems quite likely, however, that the "blue shift" is a consequence of the β plane, as discussed above. At a depth of 4 km the average peak frequency for several data sets from moorings over smooth topography is about 1.05 times the local inertial frequency (see his Figure 5, upper panel). The moorings were at latitudes between 28°N and 38°N; at 33°N the value of ϵ from (13) with the correction factor 0.97 is 0.076. Comparing this with 0.05 assumes that the model stratification is reasonably appropriate, as seems to be the case. Quite possibly the reduced average blue shift is a consequence of waves being generated with non-negligible zonal and meridional wavenumbers, as discussed in the previous section.

Over rough topography Fu (1981) finds less of a tendency for a blue shift with depth; possibly the near-inertial waves are partially back-reflected or back-scattered from the topography, rather than being reflected equatorward, giving rise to deep energy closer to the local inertial frequency. It is worth remarking, in fact, that the bottom slope that would give back reflection is $\tan^{-1}(2\epsilon)^{1/2}(f/N)$. At latitude 33°N again, and with a typical bottom value of $5 \times 10^{-4} \text{ s}^{-1}$ for N , the critical slope is 0.06, smaller than the root mean square value of 0.2 calculated by Müller and Xu (1992) for Bell's (1975) model spectrum of seafloor topography truncated at a horizontal wavelength of 400 m.

The most compelling evidence for the suggestion of this paper comes from the analysis of D'Asaro and Perkins (1984) of data obtained in the Sargasso Sea from a current meter mooring at 30°29.7'N, 71°45.6'W and from surrounding vertical profiles of horizontal currents. The region is over the smooth Hatteras Abyssal Plain, so there should be no backscattered upward-propagating near-inertial waves. We should expect to see downward-propagating energy in the abyss only between f and about $1.085f$; near the surface where the data were obtained a further factor 1.6 expands the bandwidth to about $1.14f$ though this will, as discussed earlier, be reduced for low modes by

finite initial wavenumber.

Figure 3 here reproduces panels from Figures 7 and 8 of D'Asaro and Perkins (1984). They show a conspicuous lack of upward-propagating energy within a band from f to about $1.1f$. If anything, the bandwidth of this gap is a little wider for the first two modes than for modes 3 to 5, contrary to the expectations here of the effect of finite initial bandwidth, but this is a detail at this stage given that the authors estimate the frequency using an average of the fairly wide range of horizontal wavenumbers determined from the data.

Travel time versus interaction time

It begins to seem that much of the behaviour of the near-inertial band is determined by propagation and bottom reflection rather than by wave-wave interactions, even though the latter are sometimes thought to be important for near-inertial waves which have a very small vertical group velocity. In fact, waves propagating equatorward "escape" the inertial frequency on a spherical earth and so pick up a greater vertical speed with time. For our simple example of waves starting with $k = l = 0$, the travel time to the sea floor may easily be calculated by adding to (9) the equations for the rates of change of the wavenumbers l and m . Starting from the dispersion relation

$$\omega = \left(f^2 + \frac{N^2 l^2}{m^2} \right)^{1/2} = \Omega(l, m, f(y), N(z)), \quad (14)$$

we have for l

$$\frac{dl}{dt} = -\frac{\partial \Omega}{\partial y} = -\beta f / \omega \simeq -\beta, \quad l \simeq -\beta t. \quad (15)$$

The decrease of l with time because of the β effect is also implicit in the momentum equations as pointed out by D'Asaro (1989); initially unidirectional current vectors are rotated at different rates at different latitudes, generating a finite meridional wavenumber. Of course if l is finite, with value l_0 initially, the correct equation is $l \simeq l_0 - \beta t$.

In the vertical

$$\frac{dm}{dt} = -\frac{\partial \Omega}{\partial z} = \frac{N l^2}{m^2 \omega} \frac{dN}{dz} = \frac{m}{N} \frac{dN}{dz} \frac{dz}{dt} \quad (16)$$

so that

$$m \propto N \quad \text{or} \quad m = \frac{j\pi N}{N_0 b} \quad (17)$$

where j is the mode number in the model ocean chosen. These simple ray equations are not new (see, for example, Kroll (1975) or Zervakis and Levine (1995)), but using (15) and (17) in (8) gives

$$\frac{dy'}{dt} = \left(\frac{N_0 b}{j\pi} \right)^2 \frac{\beta t}{\omega}. \quad (18)$$

The travel time T to the latitude of bottom reflection is

$$T = 3^{1/3} j \pi \left(\frac{R^2 \sin \phi}{2 \Omega N_0^2 b^2 \cos^2 \phi} \right)^{1/3} \quad (19)$$

which is 8.3j days at latitude 30° .

This time does not seem particularly long but should be compared with the time for significant changes caused by nonlinear wave-wave interactions. As mentioned earlier, the details of these interactions

need reexamination for a spectrum in which the vertical wavenumber behaviour is different at near-inertial and higher frequencies. The main mechanism near f seems to be induced diffusion in which waves with a large vertical wavenumber are refracted by waves with a small vertical wavenumber; the effect on the lowest modes themselves is unclear. Nonetheless, we use the interaction times for a typical spectrum, as calculated by *McComas and Müller* (1981), discussed by *Müller et al.* (1986) and summarized by *Hirst* (1991). The time is a function of the vertical wavenumber, which changes during the propagation of a wave group because N varies with depth, but it seems that the interaction time is much longer than the propagation time for the lowest modes, becoming less than the propagation time at latitude 30° for mode number 5 and higher. The low mode near-inertial waves, which contain most of the energy in the internal wave spectrum, are thus affected more by bottom interactions than by wave-wave interactions.

Discussion

The main theme of this short note is the need to pay more attention to the near-inertial part of the internal wave spectrum as this is what seems to be primarily generated and contain most of the energy. Moreover, near-inertial waves seem to have a different vertical wavenumber content from the rest of the spectrum and have a predominantly downward energy flux (*Sanford*, 1991; *Sherman and Pinkel*, 1991; *D'Asaro and Perkins*, 1984). In discussing near-inertial waves, the key factor to recognize is that they propagate on a β plane, not an f plane, as is, of course, well-recognized in the literature (e.g. *Gill*, 1984). The suggestion here is that the main factor which defines the "near-inertial" band, and accounts for its different characteristics, is that by the time the waves reach the sea floor their frequency is greater than the local f . The excess varies with latitude, and with the initial horizontal wavenumbers, but is of the order of 10% of f .

The apparent success of this idea in accounting for some observed spectral features, as a consequence of propagation rather than nonlinear interaction, is encouraging, and suggests the need for a reappraisal of internal wave theories with an increased emphasis on the near-inertial band. Obvious questions include:

1) Can the steep vertical wavenumber spectrum of near-inertial waves reported by *Sanford* (1991) be attributed largely to generation and propagation? If not, at what vertical wavenumber do nonlinear interactions start to play a dominant role?

2) Is the whiter vertical wavenumber spectrum for higher frequency waves reported by *Sanford* (1991),

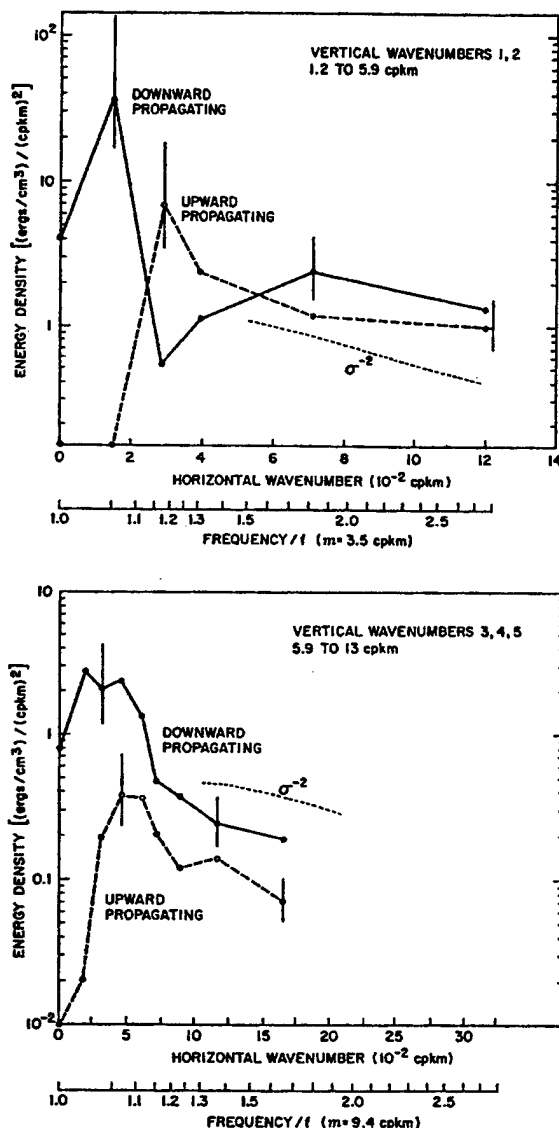


Figure 3. Energy spectra for upward and downward propagating internal waves as a function of horizontal wavenumber. The abscissa has also been presented as frequency, using an average of the vertical wavenumber over the range of vertical modes considered. From *D'Asaro and Perkins* (1984).

and by Sherman and Pinkel (1991) even in a semi-Lagrangian frame, a consequence of reflection and scattering off a rough sea floor of waves which have a frequency that is ever greater than the local f as they propagate south? Reexamination of the scattering results of Müller and Xu (1992) in the near-inertial limit would be interesting, though their model will need to be extended as their assumption that the bottom slope is much less than the wave slope is not valid near the inertial frequency.

3) What can we say about the general behaviour in wave-wave interactions of the near-inertial band, given that it is propagating on a β plane? Much of the previous theoretical work seems to take the inertial waves as a given background on an f plane, rather than the primary source on a β plane.

In a sense the view expressed here is just reinforcing the suggestion of D'Asaro (1991) that an emphasis be placed in future internal wave research on the large-scale "propagating" modes, though he was concerned that much of the near-inertial energy would be subject to refraction by weak ocean currents, as discussed by Kunze (1985), D'Asaro (1995) and Young and Jelloul (1997).

We are just beginning to address the major task of combining generation, propagation, nonlinear interactions and topographic interactions of internal waves. A preliminary concentration on the dominant near-inertial band may help to focus this discussion.

Acknowledgments

I thank Eric Kunze for useful comments and references. The support of the Office of Naval Research is also acknowledged with gratitude.

References

- Bell, T.H., Statistical features of sea-floor topography. *Deep-Sea Res.*, **22**, 883–892, 1975.
- D'Asaro, E.A., The decay of wind-forced mixed layer inertial oscillations due to the beta effect. *J. Geophys. Res.*, **94**, 2045–2056, 1989.
- D'Asaro, E.A., Upper-ocean inertial currents forced by a strong storm. Part III: Interaction of inertial currents and mesoscale eddies. *J. Phys. Oceanogr.*, **25**, 2953–2958, 1995.
- D'Asaro, E.A., A strategy for investigating and modeling internal wave sources and sinks. In *Dynamics of Oceanic Internal Gravity Waves, Proc. 'Aha Huliko'a Hawaiian Winter Workshop* (eds. P. Müller & D. Henderson), SOEST, 451–465, 1991.
- D'Asaro, E.A. and H. Perkins, A near-inertial internal wave spectrum for the Sargasso Sea in late summer. *J. Phys. Oceanogr.*, **14**, 489–505, 1984.
- Fu, L.-L., Observations and models of inertial waves in the deep ocean. *Rev. Geophys. Space Phys.*, **19**, 141–170, 1981.
- Gill, A.E., On the behavior of internal waves in the wakes of storms. *J. Phys. Oceanogr.*, **14**, 1129–1151, 1984.
- Heney, F.S., J. Wright, and S.M. Flatté, Energy and action flow through the internal wave field: An eikonal approach. *J. Geophys. Res.*, **91**, 8487–8495, 1986.
- Hirst, E., Internal wave-wave resonance theory: Fundamentals and limitations. In *Dynamics of Oceanic Internal Gravity Waves, Proc. 'Aha Huliko'a Hawaiian Winter Workshop* (P. Müller & D. Henderson, eds.), SOEST, 211–226, 1991.
- Kroll, J., The propagation of wind-generated inertial oscillations from the surface into the deep ocean. *J. Mar. Res.*, **33**, 15–51, 1975.
- Kundu, P., On internal waves generated by travelling wind. *J. Fluid Mech.*, **254**, 529–559, 1993.
- Kunze, E., Near inertial wave propagation in geostrophic shear. *J. Phys. Oceanogr.*, **15**, 544–565, 1985.
- Leaman, K.D. and T.B. Sanford, Vertical propagation of inertial waves: A vector spectral analysis of velocity profiles. *J. Geophys. Res.*, **80**, 1975–1978, 1975.
- McComas, C.H. and P. Müller, Time scales of interaction among oceanic internal waves. *J. Phys. Oceanogr.*, **11**, 139–147, 1981.
- Müller, P. and N. Xu, Scattering of oceanic internal gravity waves off random bottom topography. *J. Phys. Oceanogr.*, **22**, 474–488, 1992.
- Müller, P., G. Holloway, F. Heney, and N. Pomphrey, Nonlinear interactions among internal gravity waves. *Rev. Geophys.*, **24**, 493–536, 1986.
- Munk, W.H., Internal wave spectra at the buoyant and inertial frequencies. *J. Phys. Oceanogr.*, **10**, 1718–1728, 1980.
- Munk, W. H., Internal waves and small-scale processes. In *Evolution of Physical Oceanography* (B. A. Warren & C. Wunsch, eds.), The MIT Press, 264–291, 1981.
- Sanford, T.B., Spatial structure of thermocline and abyssal internal waves. In *Dynamics of Oceanic Internal Gravity Waves, Proc. 'Aha Huliko'a Hawaiian Winter Workshop* (P. Müller & D. Henderson, eds.), SOEST, 109–141, 1991.
- Sherman, J.T. and R. Pinkel, Estimates of the vertical wavenumber-frequency spectra of vertical shear and strain. *J. Phys. Oceanogr.*, **21**, 292–303, 1991.
- Young, W.R. and M.B. Jelloul, Propagation of near-inertial oscillations through a geostrophic flow. *J. Mar. Res.*, **55**, 735–766, 1997.
- Zervakis, V. and M.D. Levine, Near-inertial energy propagation from the mixed layer: Theoretical considerations. *J. Phys. Oceanogr.*, **25**, 2872–2889, 1995.

This preprint was prepared with AGU's L^AT_EX macros v4. File CHRIS9199 formatted September 1, 1999.

With the extension package 'AGU++' by P.W.Daly, version 1.5 from 1996/08/20

The Role of Vertical Divergence in Internal Wave/Wave Interactions

Eric Kunze

Applied Physics Laboratory University of Washington, 1013 NE 40th Street, Seattle, WA 98105-6698

Haili Sun

201-2525 NE 195th Street, Seattle, WA 98155

Abstract. Smallscale internal waves are numerically ray-traced through random 3-D Garrett and Munk (GM) internal wave backgrounds. Past ray-tracing investigations have considered only interactions with background vertical shear $V_z = (U_z, V_z)$. Our numerical simulations indicate a non-negligible role for vertical divergence W_z . The spectral transfer of internal-wave energy toward high vertical wavenumber k_z and turbulence production ϵ are 2–4 times shear-only predictions depending on the degree of vertical and horizontal scale-separation imposed. An upper limit is obtained by imposing vertical scale-separation $K_z < k_z$ and no restriction on horizontal wavenumber or frequency. This violates the WKB approximation in the horizontal and time. A lower limit is obtained by imposing stricter vertical scale-separation $K_z < 0.5k_z$ and horizontal scale-separation $K_H < k_h$ for background frequencies $\Omega > 11f$. Imposing WKB horizontal scale-separation at all background frequencies caused some test waves to get stuck at low horizontal wavenumber and low frequency. This is not realistic. The shear-and-strain lower limit produces turbulence production rates close to the upper limit of shear-only calculations and therefore consistent with observations.

1. Introduction

In the stratified ocean interior, internal waves are responsible for most turbulence production and mixing (Eriksen 1978; Munk 1981; Gregg *et al.* 1986; Gregg 1987). The turbulence production rate can be equated to the internal-wave spectral energy transfer rate toward high vertical wavenumber (McComas and Bretherton 1977) $\epsilon_p = \epsilon - \langle w' b' \rangle = (1 + \gamma)\epsilon = (1.0\text{--}1.2)\epsilon$ where the mixing efficiency $\gamma \leq 0.2$ from theory (Osborn 1980; Thompson 1980), laboratory work (McEwan 1983; Itsweire *et al.* 1986) and ocean observations (Oakey 1982). While there has been extensive investigation into the role that internal-wave vertical shear plays in spectral energy transfer in ray-tracing wave/wave simulations (Henyey *et al.* 1986; Gregg 1989), internal-wave vertical divergence has been neglected. In contrast, weak resonant-triad interaction theory (McComas and Müller 1981a, b; McComas and Bretherton 1977; Müller *et al.* 1986) suggests a potentially important role for vertical divergence.

McComas and Bretherton suggested that three classes of interaction dominate wave-triad interactions: (i) *induced diffusion* (ID) due to smallscale high-frequency waves interacting with larger-scale lower-frequency shear, (ii) *elastic scattering* which produces vertical symmetry in the internal wave field but causes no net spectral energy transfer, and (iii) *parametric subharmonic*

instability (PSI) when two smallscale waves interact with a wave of twice their frequency which induces time changes in the buoyancy frequency N through its vertical divergence W_z . Thus, vertical shear plays the major role in induced diffusion, and vertical divergence in parametric subharmonic instability. PSI and ID contribute about 60% and 40% of total spectral energy transfer in weak-triad interactions, respectively. Therefore, weak-triad results suggest that vertical divergence is potentially as important as vertical shear.

A role for high-frequency internal-wave vertical divergence in turbulence production is also implicated in recent oceanic observations. In regions of enhanced high-frequency internal-wave activity adjacent to topography, Padman *et al.* (1991), Wijesekera *et al.* (1993) and Polzin *et al.* (1995) report turbulent dissipation rates elevated above the predictions of the shear-only parameterization of Henyey *et al.* (1986) and Gregg (1989). They suggested that the shear-based parameterization for turbulent dissipation rate ϵ could be corrected with the observed strain variance $\langle \xi_z^2 \rangle$ to capture the high-frequency wave dynamics. However, in vertical wavenumber ray-tracing equation (2.4), it is vertical divergence W_z , not strain ξ_z , which contributes to the time rate of change of vertical wavenumber. We will examine the role of the vertical divergence term in the ray-tracing equations more closely.

Two finescale parameterizations for the turbulent dissipation rate ϵ developed for GM model spectral shapes have displayed some skill in reproducing ocean observations. The first is based on weak-triad interaction theory (McComas and Bretherton 1977; McComas and Müller 1981a, b) and the second on an eikonal (ray-tracing) interaction approach (Henyey *et al.* 1986). These agree with fine- and microstructure observations of the ocean (Gregg 1989; Polzin *et al.* 1995) in their dependence on spectral level E^2 and buoyancy frequency N^2 . But, when both models are adjusted to a Munk (1981) model spectrum, Henyey *et al.*'s predicted dissipation rate is 3–4 times weaker than the weak-triad rate.

1.1 McComas and Müller (1981b, MM)

Internal-wave spectral energy transfer rates from large to small scales can be calculated directly for each interaction triad,

$$Q_{\text{psi}} = \frac{E}{\tau_{\text{psi}}} \quad Q_{\text{id}} = \frac{E}{\tau_{\text{id}}}$$

where E is the canonical spectral energy density of the wave field, and τ_{psi} and τ_{id} are characteristic timescales of parametric subharmonic instability and induced diffusion, respectively. For a GM76 internal-wave spectra (Cairns and Williams 1976), McComas and Müller (1981b) predicted that the spectral energy transfer toward small scales (equivalent to the steady-state turbulence production rate) would be

$$\epsilon_{\text{MM}} = Q_{\text{psi}} + Q_{\text{id}} = \left(\frac{27\pi}{32\sqrt{10}} + 1 \right) \times \pi^2 b^2 j_*^2 f N^2 E_{\text{GM}}^2 \quad (1.1)$$

where $b = 1300$ m is the pycnocline's stratification lengthscale, f the Coriolis frequency, j_* the peak mode number, N the buoyancy frequency and E_{GM} the dimensionless spectral energy level (Table 1). Resonant-triad theory requires that the decorrelation time of the wave field be shorter than its interaction time (Müller *et al.* 1986) so that interactions must be weak.

1.2 Henyey, Wright and Flatté (1986, HWF)

Henyey *et al.* (1986) explored internal wave/wave interactions using ray tracing to overcome the questionable validity of weak interaction assumptions for finescale oceanic internal waves (Holloway 1980). This approach is referred to as *strong* wave/wave interaction by Müller *et al.* (1986) because it places no restrictions on the ratio of the decorrelation and interaction times in the

Table 1. Parameters in the Garrett and Munk internal wave model spectrum (Munk 1981).

$f = 7.3 \times 10^{-5} \text{ rad s}^{-1}$	Coriolis frequency at 30°N
$N_0 = 72f = 5.3 \times 10^{-3} \text{ rad s}^{-1}$	reference buoyancy frequency
$N(z) = N_0 e^{z/b}$	depth-dependent mean buoyancy frequency (z positive upward)
$N_i(x, y, z, t)$	instantaneous buoyancy frequency
$b = 1300 \text{ m}$	scale depth of thermocline
$E_{\text{GM}} = 6.3 \times 10^{-5}$	midlatitude dimensionless energy level
$j_* = 3$	peak vertical mode number
$k_{z_c} = \frac{1}{3j_* b E_{\text{GM}} Ri_c^{-1}} \text{ m}^{-1}$	high vertical wavenumber cutoff
$Ri_c = 2$	Richardson number at the cutoff vertical wavenumber k_{z_c}

wave field. However, ray tracing requires that (i) WKB scale-separated ($K_i < k_i$, $\Omega < \omega$) wave/wave interactions dominate, and (ii) the smallscale waves not significantly modify the larger-scale background. The internal-wave spectral energy transfer is calculated following smallscale test waves' propagation in a larger-scale background wave field described by the Garrett and Munk model spectrum (Munk 1981). Only interactions with background internal-wave vertical shear were presumed important in Henyey *et al.*'s (1986) calculations. They did not apply WKB scale-separation in time or the horizontal. They derived a parameterization for ϵ based on the spectral energy transfer rate toward high vertical wavenumber k_z

$$\epsilon(k_z) = \int S[E](k_z, \omega) \cdot \left\langle \frac{dk_z}{dt} \right\rangle \cdot d\omega \quad (1.2)$$

in terms of the energy spectra $S[E](k_z, \omega)$ and the ensemble-average time rate of change of vertical wavenumber k_z . The ray-tracing equation for vertical wavenumber k_z , including only vertical shear interactions, was expressed in terms of rms shear

$$\begin{aligned} \left\langle \frac{dk_z}{dt} \right\rangle &= \left\langle \frac{\partial(k_h \cdot V)}{\partial z} \right\rangle \sim \sqrt{k_h^2 \langle V_z^2 \rangle} \langle \cos^2 \theta \rangle \\ &\approx \frac{k_h N}{\sqrt{2} Ri_c} \sqrt{1 + \ln(k_z / k_{z_c})} \end{aligned} \quad (1.3)$$

where k_h is the horizontal wavenumber, θ the orientation of the horizontal wavevector, k_{z_c} the vertical wavenumber

of the finescale change in spectral slope ($= 0.08$ cpm in the GM model), and Ri_c the corresponding Richardson number. Finally, they derive a parameterization for the turbulent dissipation rate ϵ in a *Munk* (1981) GM internal-wave field

$$\epsilon_{\text{HWF}} = \frac{12 Ri_c^{1/2} b^2 j^* f N^2 E_{\text{GM}}^2 \left(\frac{k_{zc}}{k_z}\right)^2}{\sqrt{2\pi}} \times \sqrt{1 + \ln\left(\frac{k_z}{k_{zc}}\right) \left(\frac{1-r}{1+r}\right) \text{Arccosh}\left(\frac{N}{f}\right)} \quad (1.4)$$

where $r(k_z)$ is the ratio of up- to downscale spectral energy flux at vertical wavenumber k_z .

1.3 Gregg (1989)

Gregg (1989) introduced parameterizations for ϵ using 10-m vertical shear as a measure of the internal-wave energy level, that is, replacing E_{GM}^2 in *McComas and Müller* (1981b) and *Henyey et al.* (1986) with $\langle E_{\text{IW}}^2 \rangle = E_{\text{GM}}^2 \langle S_{10}^2 / S_{\text{GM}}^2 \rangle$ where S_{GM}^2 is the 10-m GM shear variance, $S_{10}^2 = 2.11[(\Delta U / \Delta z)^2 + (\Delta V / \Delta z)^2]$ the measured 10-m shear variance, $\Delta z = 10$ m and the 2.11 multiplier corrects for attenuation by the first-difference filter. With the assumption that $\langle S_{10}^4 \rangle = 2 \langle S_{10}^2 \rangle^2$ and $\langle S_{\text{GM}}^4 \rangle = 2 \langle S_{\text{GM}}^2 \rangle^2$, he rewrote *McComas and Müller's* (1981b) and *Henyey et al.'s* (1986) formulas as

$$\epsilon_{\text{MM}} = 1.1 \times 10^{-9} \frac{\langle N^2 \rangle \langle S_{10}^2 \rangle^2}{N_0^2 \langle S_{\text{GM}}^2 \rangle^2} \quad (\text{W kg}^{-1}) \quad (1.5)$$

$$\epsilon_{\text{HWF}} = 0.35 \times 10^9 \frac{\langle N^2 \rangle \langle S_{10}^2 \rangle^2}{N_0^2 \langle S_{\text{GM}}^2 \rangle^2} \quad (\text{W kg}^{-1}) \quad (1.6)$$

where we have adjusted ϵ_{MM} to be consistent with the *Munk* (1981) GM model spectrum used throughout this paper. The rewritten *Henyey et al.* (1986) model (1.6) collapsed PATCHEX and RING 82-I data sets to within a factor of two.

Gargett (1990) pointed out that the method used by *Gregg* (1989) to calculate the wave energy level E would underestimate E for $E > E_{\text{GM}}$ if Ek_{zc} is constant (*Smith et al.* 1987; *Duda and Cox* 1989). In addition, neither frequency nor wavenumber information were provided, so it is difficult to evaluate if and how the observations deviate from GM. *Polzin et al.* (1995) conjectured that “*Gregg* was able to collapse his PATCHEX and RING 82-I data sets under the $E^2 N^2$ scaling due to a cancellation between the underestimation of E and lower-than-

expected dissipations associated with lower-than-average wave frequency.”

1.4 Polzin et al. (1995)

Polzin et al. (1995) modified *Henyey et al.'s* (1986) formula following *Henyey* (1991) by rewriting (1.2) so that the spectral energy-flux through a fixed wavenumber can be estimated as

$$\epsilon(k_z) = \frac{1}{2k_z^2} \{S[V_z](k_z) + N^2 S[\xi_z](k_z)\} \times \left\{ \int_0^{k_z} S[V_z](k_z) dk_z \right\}^{1/2} \times k_z \left\langle \frac{\omega^2 - f^2}{N^2 - \omega^2} \right\rangle_E \times \frac{1}{\sqrt{2}} \left(\frac{1-r(k_z)}{1+r(k_z)} \right) \quad (1.7)$$

where $\langle \cdot \rangle_E$ is the expected value, $S[V_z](k_z)$ and $S[\xi_z](k_z)$ correspond to the GM76 (*Cairns and Williams* 1976; *Gregg and Kunze* 1991) vertical wavenumber spectra for shear and strain, and $k_z^{-2} \{S[V_z](k_z) + N^2 S[\xi_z](k_z)\}/2$ collapses the total energy spectra

$$\int_f^N S[E](k_z, \omega) d\omega.$$

Other terms in (1.7) come from rewriting the ray-tracing equation for vertical wavenumber k_z (2.4). The expected value for

$$\left\langle \frac{\sqrt{\omega^2 - f^2}}{\sqrt{N^2 - \omega^2}} \right\rangle_E$$

was estimated by *Polzin et al.* (1995) using the shear-to-strain variance ratio for a single internal wave,

$$R_\omega = \frac{S[V_z](k_z)}{N^2 S[\xi_z](k_z)} = \frac{(\omega^2 + f^2)(N^2 - \omega^2)}{N^2 (\omega^2 - f^2)}$$

which yields a biased estimator for frequency

$$\omega^2 = \frac{1}{2} \left[N^2 (1 - R_\omega) - f^2 + \sqrt{N^4 (R_\omega - 1)^2 + 2 f^2 N^2 (1 + 3 R_\omega) + f^4} \right]$$

(Appendix B of *Polzin et al.* 1995). *Polzin et al.* showed that the modified model (1.7) collapsed, to within a factor of two, data sets in both GM and weakly non-GM backgrounds.

1.5 Summary and Preamble

Using ray-tracing simulations, this paper formulates parameterizations for the turbulent production rate including interactions with both shear and vertical divergence. We restrict our analysis to *Munk* (1981) GM spectral shapes for comparison with *Henyei et al.*'s results. Our ray-tracing estimates of internal-wave spectral energy transfer imply turbulence dissipation rates ϵ that are 2–4 times those without vertical divergence (see Fig. 10 in Sec. 5.2) depending on the degree of scale-separation imposed between background and test waves.

WKB scale-separations are applied to get upper and lower limits for the spectral energy transfer rate. An upper limit is obtained by restricting the vertical wavenumbers of the background to be lower than those of the test waves ($K_z < k_z$) following *Henyei et al.* (1986). While this allows interactions with horizontal wavenumbers and frequencies that do not meet the WKB criterion, we include these for comparison with previous shear-only calculations. To get a lower limit, the background vertical wavenumber is restricted to be at most half that of the test wave ($K_z < 0.5k_z$), and the background horizontal wavenumber restricted to be lower than that of the test wave ($K_H < k_H$) for background frequencies $\Omega > 11f$. Applying WKB scale-separation in the horizontal at all frequencies or in frequency ($\Omega < \omega$) results in some test waves getting stuck at low horizontal wavenumber and frequency with no background to interact with. This is not realistic. The lower-limit criteria given above are a compromise in that wave frequencies $\Omega < 11f$ encompass 95% of the shear and 90% of the strain variance. It allows test waves to cascade to the small scale but omits the highest frequency contributions from the background.

Ray-tracing will not handle the upper-limit case accurately because the WKB approximation becomes questionable as the scales of the background and wave become comparable, and is invalid when test-wave scales are much larger than those of the background. Interactions with background waves with vertical scales comparable to the test waves ($k_z/2 < K_z < k_z$) account for a third of the total spectral energy transfer toward high wavenumber. This suggests that strong finescale wave/wave interactions do modify the background finescale field so the requirement that test waves not modify the background becomes questionable on the finescale. The factor of 2–4 uncertainty between the upper- and lower-limit estimates is comparable to the factor-of-two uncertainty in observations. Since very rapid fluctuations in the background should not contribute to the longterm evolution of test waves, we favor the lower-limit estimates for the turbulent production rate but caution that they may under- or overestimate the contribution from the finescale ($K_z \sim k_z$). Observations favor the lower limit (see

Fig. 14 in Sec. 6) except in data from the slope of a seamount where the frequency spectrum is decidedly non-GM (*Eriksen* 1998).

2. Ray-Tracing Equations

In this section, we examine the WKB ray-tracing equations for internal wave/wave interactions using the GM internal wave model (*Munk* 1981). The ray-tracing equations for tracking the evolution of smallscale test wavepackets' wavevector $\mathbf{k} = (k_x, k_y, k_z)$ and position $\mathbf{r} = (x, y, z)$ in a slowly-varying background are

$$\frac{D\mathbf{r}}{Dt} = \frac{\partial \omega_E}{\partial \mathbf{k}} = \frac{\partial \omega_i}{\partial \mathbf{k}} + \mathbf{V} = \mathbf{Cg} + \mathbf{V} \quad (2.1)$$

$$\frac{D\mathbf{k}}{Dt} = \nabla \omega_E = \frac{\partial \omega_i}{\partial N_i} \nabla N_i - \nabla(\mathbf{k} \cdot \mathbf{V}) \quad (2.2)$$

$$\frac{D\omega_E}{Dt} = \frac{\partial \omega_E}{\partial t} = \frac{\partial \omega_i}{\partial N_i} \frac{\partial N_i}{\partial t} - \mathbf{k} \cdot \frac{\partial \mathbf{V}}{\partial t} \quad (2.3)$$

(*Lighthill* 1978) where D/Dt is the time rate of change following the wave packet, $\omega_E = \omega_i + \mathbf{k} \cdot \mathbf{V}(\mathbf{r}, t)$ the wavepacket's Eulerian frequency, $\omega_i(N_i, f, \mathbf{k})$ its intrinsic (Lagrangian) frequency, $\nabla = (\partial/\partial x, \partial/\partial y, \partial/\partial z)$ a partial operator, \mathbf{V} the background wave-induced velocity and N_i the background instantaneous buoyancy frequency. The internal-wave intrinsic frequency is presumed to obey the linear intrinsic dispersion relation

$$\omega_i^2 = \frac{N_i^2 k_H^2 + f^2 k_z^2}{k^2}$$

where $k_H = \sqrt{k_x^2 + k_y^2}$ is the test wave's horizontal wavenumber. The intrinsic dispersion relation appears in the first terms of ray-tracing equations (2.1)–(2.3), that is, in terms of the form $\partial \omega_i / \partial(\mathbf{k}, \mathbf{r}, t)$. Finescale internal waves have very slow group velocities so their dispersion proves irrelevant compared to advection (see Appendix A and Fig. A1). Numerical simulations in which the finescale group velocity was either reduced or reversed [$\mathbf{Cg} = (0.1, -1)\mathbf{Cg}_{\text{IW}}$ for $\lambda_z \cdot 20$ m] while larger wavelengths propagated at their linear speed ($\mathbf{Cg} = \mathbf{Cg}_{\text{IW}}$ for $\lambda_z \geq 100$ m) produce spectral energy transfer rates indistinguishable from those using the linear dispersion relation above. Including the instantaneous N_i rather than mean \bar{N} also does not modify test-wave evolution significantly. This suggests that the choice of finescale test-wave dispersion relation is unimportant. The net spectral transfer of energy toward high vertical wavenumber is controlled by Doppler shifting and so depends more on the aspect ratio λ_z/λ_H of finescale variability than its intrinsic frequency. Thus, potential-

vorticity-carrying finestructure (vortical mode) should be transferred toward high vertical wavenumbers at the same rate as finescale internal waves of the same aspect ratio (see also *Haynes and Anglade 1997*).

The ray-tracing equation for a test wavepacket's vertical wavenumber (2.4) can be expanded to

$$\frac{dk_z}{dt} = -\frac{\partial\omega_E}{\partial z} = -k_x \frac{\partial U}{\partial z} - k_y \frac{\partial V}{\partial z} - k_z \frac{\partial W}{\partial z} - \frac{\partial\omega_i}{\partial N_i} \frac{\partial N_i}{\partial z} \quad (2.4)$$

I I II III

where

$$\frac{\partial\omega_i}{\partial N_i} = \frac{N_i k_H^2}{\omega_i k^2} \quad (2.5)$$

The WKB approximation requires that test-wave wavelengths λ be much smaller than those of the background Λ ($\lambda < \Lambda/2\pi$).

Scale analysis of vertical ray-tracing equation (2.4) would suggest that (i) the vertical shear V_z term, contributed mostly by near-inertial waves, dominates the evolution of high-frequency test waves, (ii) the vertical divergence W_z term, contributed by higher-frequency waves, dominates the evolution of near-inertial test waves, and (iii) the vertical buoyancy frequency gradient term can be neglected for all test-wave frequencies. Conclusions about the role of vertical divergence are qualitatively unchanged when high-frequency, high-horizontal-wavenumber contributions to the vertical divergence are excluded.

3. Numerical Simulations

3.1 The Background Wave Field

To numerically ray-trace smallscale waves in a larger-scale internal wave background, we first set up the background field. Following *Henyey et al. (1986)*, the background wave field is based on the *Munk (1981)* version of the Garrett and Munk model spectrum in (Ω, K_z) -space

$$S[V](\Omega, j, z) = \frac{2b^2 NN_0 E_{GM}}{\pi f} \times \frac{(j^2 + j_*^2)^{-1}}{\sum_{j=1}^{\infty} (j^2 + j_*^2)^{-1}} \frac{\Omega^2 + f^2}{\Omega^3 \sqrt{\Omega^2 - f^2}} \quad (3.1)$$

where the parameters are defined in Table 1. Vertical wavenumber K_z is related to the mode number j by

$$K_z = \frac{\pi j}{b} \sqrt{\frac{N^2 - \Omega^2}{N_0^2 - \Omega^2}}$$

The Monte-Carlo method is used to set up random GM backgrounds (Appendices B and D). Ensemble results will use up to 100 randomly generated backgrounds to ensure that all phases of the background wave field are sampled uniformly by the initial test waves, and to obtain statistical stability. Following *Henyey et al. (1986)*, the wave frequency $f \leq \Omega \leq N$, mode number j , amplitude V_0 , and horizontal wavevector direction $\theta = \text{Arctan}(K_y/K_x)$ are all randomly selected (Appendix B) so that the simulated background horizontal velocity field V is (i) 4-D, varying in time and space, (ii) horizontally isotropic and (iii) in agreement with GM.

Background vertical shear $V_z = (U_z, V_z)$, vertical divergence W_z , strain ξ_z and instantaneous buoyancy frequency N_i are derived from the horizontal velocity using linear internal-wave consistency relations (*Fofonoff 1969*)

$$V_z = (U_z, V_z) = iK_z V$$

$$W_z = -i(K_x U + K_y V)$$

$$\xi_z = \frac{1}{\Omega}(K_x U + K_y V)$$

$$N_i^2 = \bar{N}^2(z)[1 + \xi_z]$$

(Appendix D). The Monte-Carlo simulated spectra agree with GM (Fig. 1).

3.2 Coordinate Transformation

The GM model is a spectrum of Eulerian dependent variables (e.g., V, ξ, N_i) set in a Lagrangian coordinate frame [e.g., independent-variable particle labels $x', y', z'(\rho)$], that is, in a coordinate system following water parcels. Observations have shown that, although the ω^2 GM model does not describe the almost-flat finescale ($\lambda_z \approx 10$ –50 m) Eulerian frequency spectra for shear and strain (*Pinkel 1984*), it better describes spectra transformed into an isopycnal-following (or semi-Lagrangian) frame (*Sherman and Pinkel 1991; Anderson 1993*). In an Eulerian description, internal-wave shear and vertical divergence vary rapidly in time due to finestructure being swept past a fixed position by large-scale background velocities. Since finescale waves are advected with the background, such an Eulerian coordinate system is inappropriate for the test waves. In order to include background vertical divergence in ray-tracing calculations without Doppler-shift aliasing of high-wavenumber structure, we need either to (i) transform equations (2.1–2.2) into a Lagrangian frame or (ii) transform the Lagrangian particle label variables $x', y', z'(\rho), t'$ in V and N_i into Eulerian variables (*Henyey personal communication 1999*). As in *Henyey et al.*

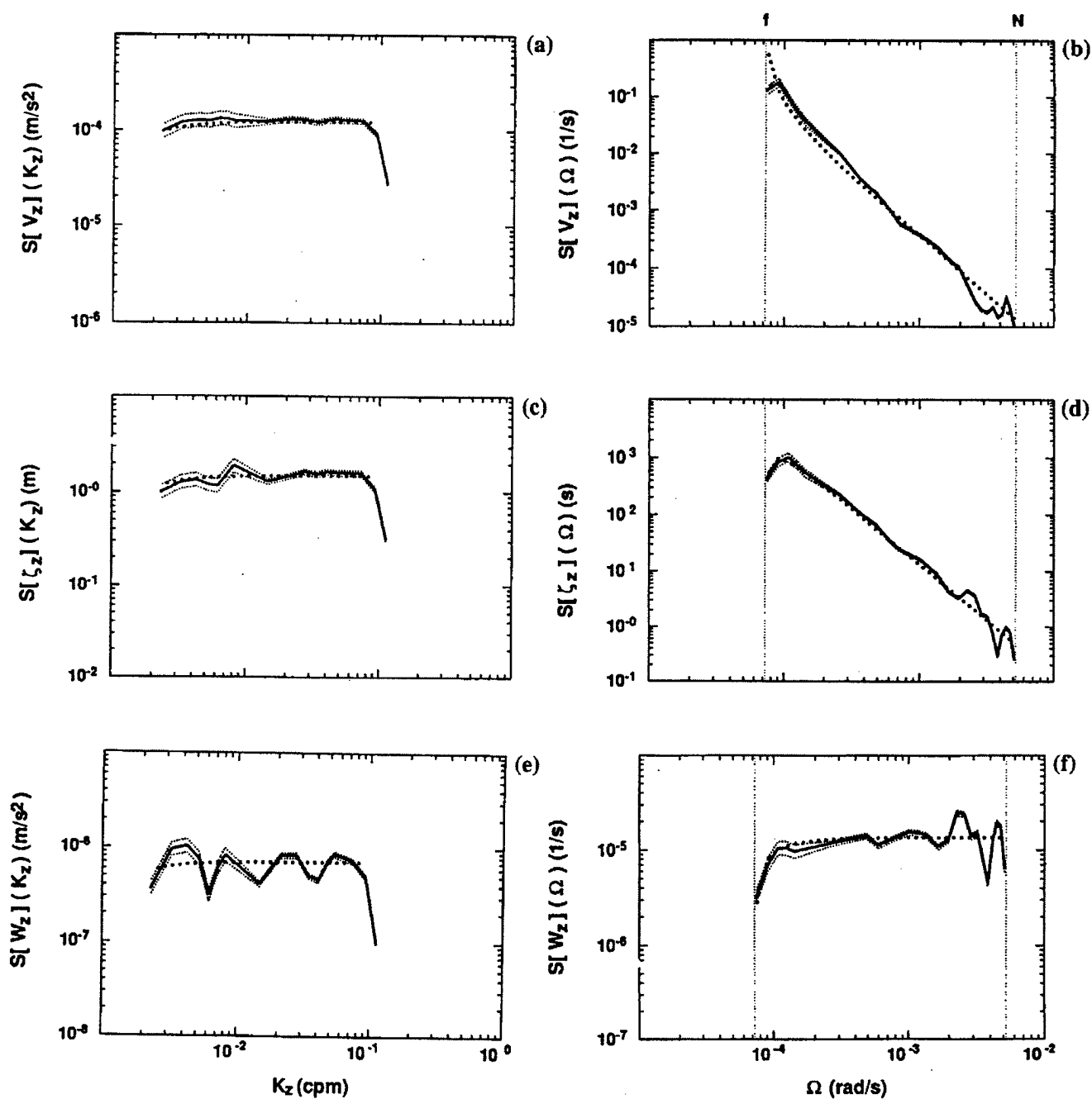


Figure 1. Monte-Carlo-simulated background GM internal-wave spectra (solid curves with 95% confidence limits as thin dotted curves) for vertical shear as functions of vertical wavenumber $S[V_z](K_z)$ (a) and frequency $S[V_z](\Omega)$ (b), strain spectra as a functions of vertical wavenumber $S[\xi_z](K_z)$ (c) and frequency $S[\xi_z](\Omega)$ (d), and vertical divergence spectra as a functions of vertical wavenumber $S[W_z](K_z)$ (e) and frequency $S[W_z](\Omega)$ (f). The simulated spectra agree well with the GM model (thick dotted).

(1986), we choose to transform the ray-tracing equations into a semi-Lagrangian frame (i) following vertical but not horizontal displacements by background waves (Appendix C), so that neither (i) nor (ii) are applied horizontally.

3.3 Numerical Simulation Results

Before looking at ensemble statistics, we examine a few typical test-wave trajectories selected from 100 runs. In the following simulations, we take the unperturbed buoyancy frequency to be constant, $\bar{N} = 40f = 2.9 \times 10^{-3}$ rad s⁻¹, which approximates the average buoyancy frequency in the upper ocean. We initialize the test-wave horizontal wavenumbers to be $k_x = 0.025$ rad m⁻¹ and $k_y = 0$. Test waves interact with the total GM vertical divergence in these calculations so will overestimate the role of divergence.

3.3.1 Typical test-wave trajectories. Following a typical test-wave trajectory (initially at $\omega_i = 9f$, $k_z = 0.12$ rad m⁻¹), Fig. 2 illustrates the evolution of test-wave

- (a) vertical wavenumber k_z ,
 - (b) intrinsic frequency ω_i ,
 - (c) contributions to the time rate of change of k_z by the zonal shear $k_x U_z$, vertical divergence $k_z W_z$ and buoyancy frequency gradient $(\partial \omega_i / \partial N_i)(\partial N_i / \partial z)$ terms in (2.4),
 - (d) their cumulative counterparts $\langle k_x U_z \rangle_t$, $\langle k_z W_z \rangle_t$ and $\langle (\partial \omega_i / \partial N_i)(\partial N_i / \partial z) \rangle_t$,
- and encountered background
- (e) shear magnitude $|V_z|$,
 - (f) buoyancy frequency anomaly $\delta N = N_i - N$, and
 - (g) vertical divergence W_z

where interactions with *total* background shear V_z , vertical divergence W_z and buoyancy frequency perturbations $\partial N_i / \partial z$ are allowed. When a test wave has low intrinsic frequency ($\omega_i < 4f$), evolution of its vertical wavenumber (8–12 h, Fig. 2c) is controlled mostly by the background vertical divergence term $k_z W_z$. When it has high frequency ($\omega_i > 16f$), the background shear term $k_x U_z$ dominates its behavior (1–3 h, Fig. 2c). For intermediate test-wave frequencies, background vertical divergence and shear have comparable contributions (3–6 h, Fig. 2c). The cumulative vertical divergence term $\langle k_z W_z \rangle_t$ is twice the cumulative vertical shear $\langle k_x U_z \rangle_t$ term, indicating that, despite being dominated by near-buoyancy frequencies, the vertical divergence term has a significant net impact over the lifespan of a test wave. We caution that these simulations include vertical divergence contributions that are not WKB scale-separated in the horizontal or time. The buoyancy frequency gradient term $\langle (\partial \omega_i / \partial N_i)(\partial N_i / \partial z) \rangle_t$ is everywhere negligible.

Figure 3 displays the evolution of

- (a) test-wave vertical wavenumber k_z ,
- (b) intrinsic frequency ω_i ,
- (c) the zonal shear term $k_x U_z$ in (2.4),
- (d) its cumulative form $\langle k_x U_z \rangle_t$, and
- (e) encountered background shear V_z

in the same background as Fig. 2 but allowing interactions only with vertical shear V_z . In this case, only background shear transfers test waves to smaller scale. It takes three times as long for the test wave's vertical wavelength to fall below 5 m in the absence of vertical divergence interactions.

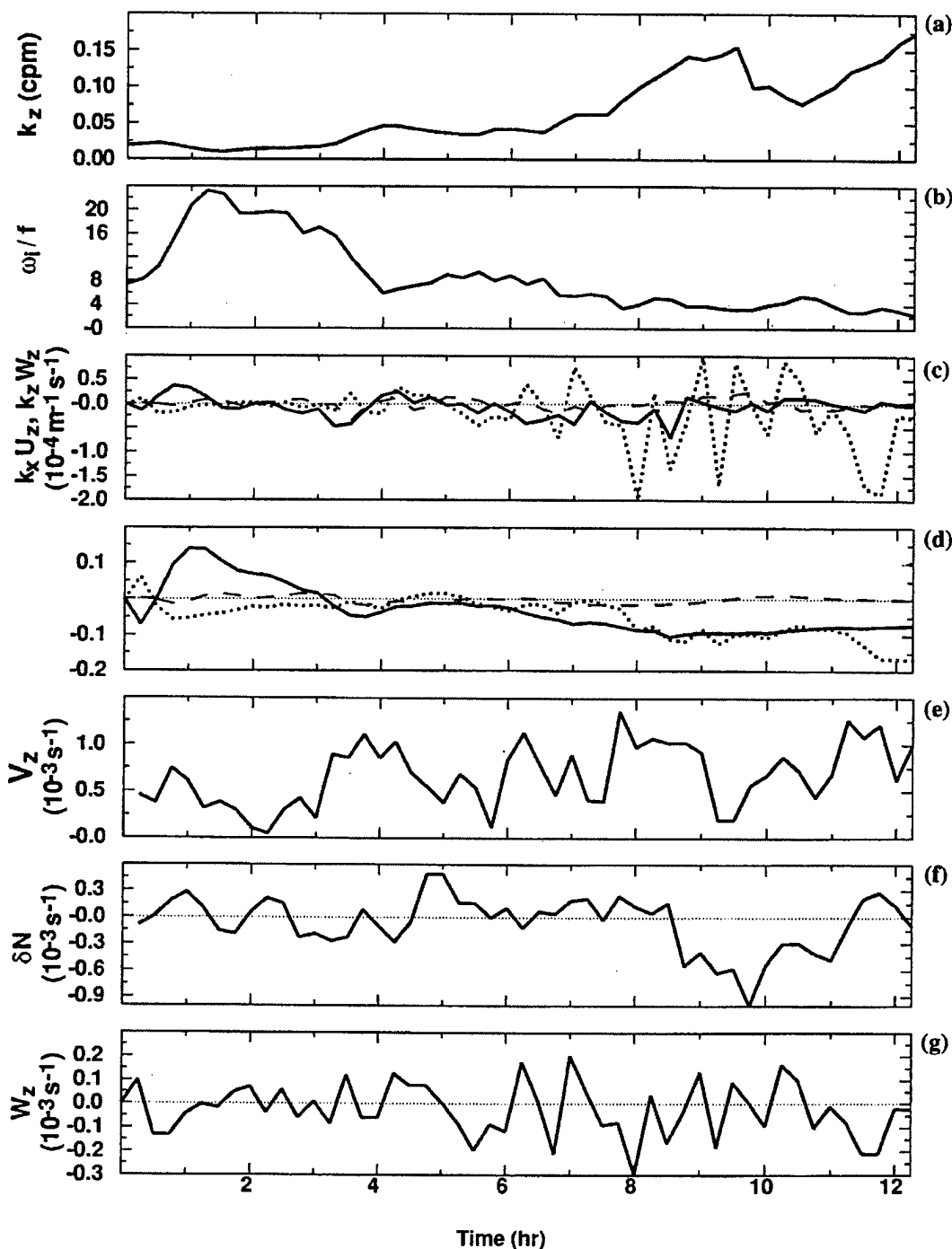


Figure 2. Following the evolution of a typical test wave in a GM background filtered only by vertical wavenumber ($K_z < k_z$). Panels display the evolution of test-wave vertical wavenumber k_z (a), intrinsic frequency ω_i (b), contributions to dk_z/dt from vertical shear $k_x U_z$ (solid), vertical divergence $k_z W_z$ (dashed) and vertical buoyancy frequency gradients $(\partial \omega_i / \partial N_i)(\partial N_i / \partial z)$ (dotted) (c), cumulative contributions $\langle k_x U_z \rangle_t$ (solid), $\langle k_z W_z \rangle_t$ (dashed) and $\langle (\partial \omega_i / \partial N_i)(\partial N_i / \partial z) \rangle_t$ (dotted) (d), encountered background shear magnitude $|V_z|$ (e), buoyancy fluctuations $\delta N = N_i - N$ (f), and vertical divergence W_z (g). Initial conditions for the test wave are $\omega_i = 9f$, $k_z = 0.12 \text{ rad m}^{-1}$, $k_x = 0.025 \text{ rad m}^{-1}$ and $k_y = 0$. The test wave interacts with background vertical shear V_z , vertical divergence W_z and vertical buoyancy frequency gradient $(\partial \omega_z / \partial N_i)(\partial N_i / \partial z)$. The background rms shear $\sqrt{\langle V_z^2 \rangle} = 1.83 \times 10^{-3} \text{ s}^{-1}$, rms vertical divergence $\sqrt{\langle W_z^2 \rangle} = 0.14 \times 10^{-3} \text{ s}^{-1}$, and rms strain $\sqrt{\langle \epsilon_z^2 \rangle} = 0.4$.

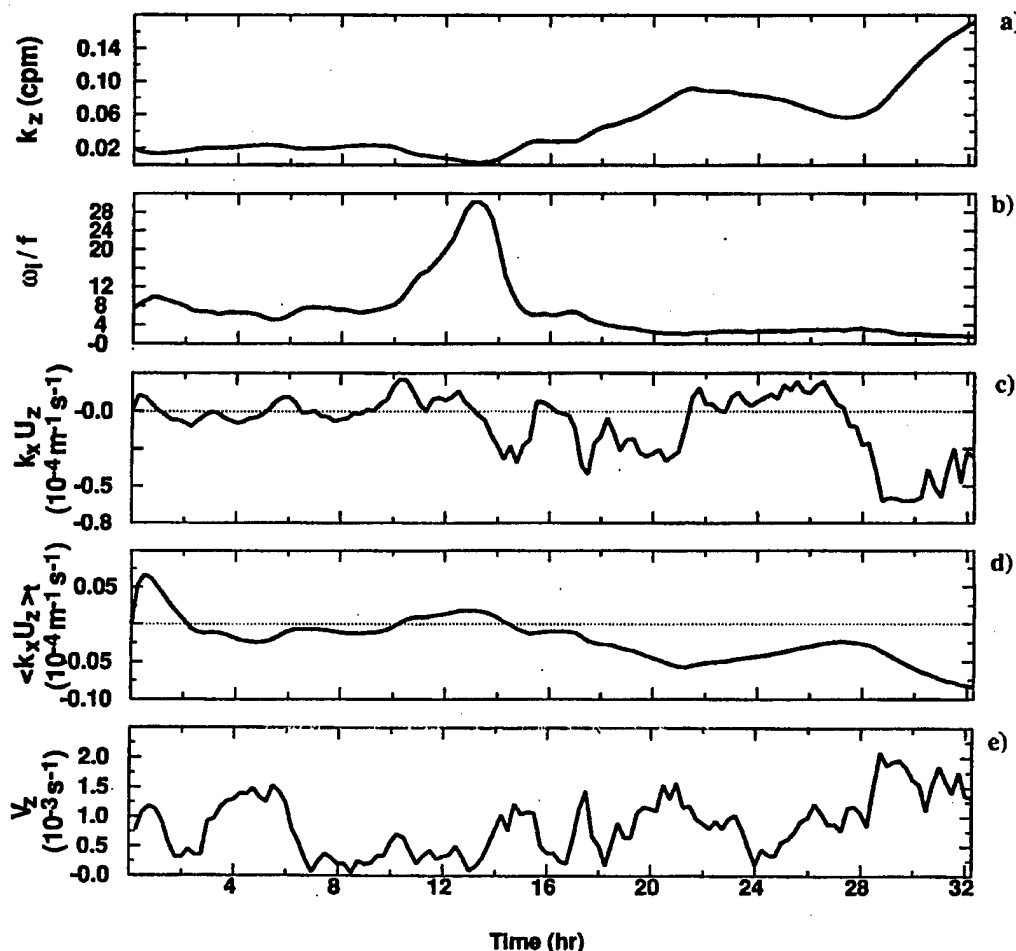


Figure 3. For the same initial conditions as in Fig. 2 but allowing interactions only with the background vertical shear V_z . The panels show evolution of test-wave vertical wavenumber k_z (a), intrinsic frequency ω_i (b), contributions to dk_z/dt from $k_x U_z$ (c), its cumulative counterpart $\langle k_x U_z \rangle_t$ (d), and background shear magnitude $|V_z|$ (e). Test-wave behavior differs from that in Fig. 2, taking longer to reach small vertical scales

3.3.2 Statistics. In the following, we present ensemble results based on test waves propagating in over 100 different Monte-Carlo backgrounds in order to sample the range of random phases and fluctuations present in the ocean and obtain stable statistics.

3.3.2.1 Test-wave breaking frequency. Figures 4 and 5 display histograms of test-wave intrinsic frequency at the instant their vertical wavelengths λ_z fall below the “breaking” wavelength of 5 m. Test-wave breaking histograms are independent of initial test-wave frequency (Fig. 4), implying an equilibrium finescale frequency spectrum. The histograms fall off more gently than the expected ω_i^{-1} distribution for an ω_i^{-2} spectrum (dotted curves), indicating that, for interactions involving all shear and vertical divergence, ray tracing suggests a gentler equilibrium spectral slope than GM.

In Fig. 5, simulations are considered which include interactions with (a) only background shear, (b) both background shear and vertical divergence, and (c) both background shear and vertical divergence but imposing frequency scale-separation $\Omega < \omega_i$ between the test wave and the background. Test waves that stall at low horizontal wavenumber because of the frequency scale-separation are not included in the statistics of (c). When only interactions with shear (a), or when frequency scale-separation (c), are imposed, test-wave breaking is more tightly confined to near-inertial frequencies, implying a test-wave spectral energy-flux toward low frequency and high vertical wavenumber. Figure 5c indicates that background vertical divergence plays an order-one role only when its frequency is higher than the test-wave intrinsic frequency. In strict WKB scale-separation, this

would imply that only shear drives a spectral energy transfer to high vertical wavenumber. But this contradicts observations of turbulent mixing in excess of that predicted by shear-only models in the presence of elevated high-frequency internal waves (Wijesekera *et al.* 1993; Polzin *et al.* 1995).

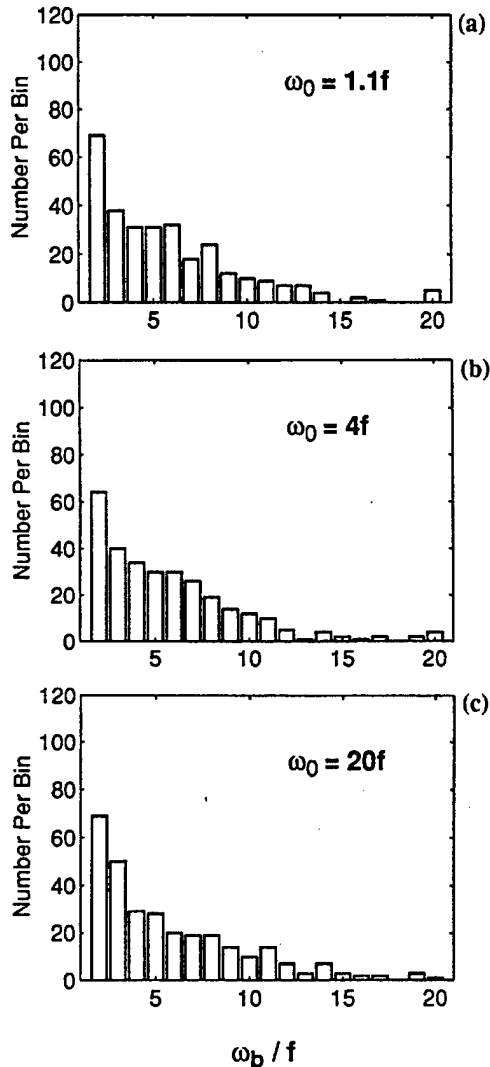


Figure 4. Histograms of the test-wave breaking frequencies for initial test-wave frequencies (a) $\omega_i = 1.1f$, (b) $\omega_i = 4f$ and (c) $\omega_i = 20f$. The histograms are independent of initial test-wave frequency.

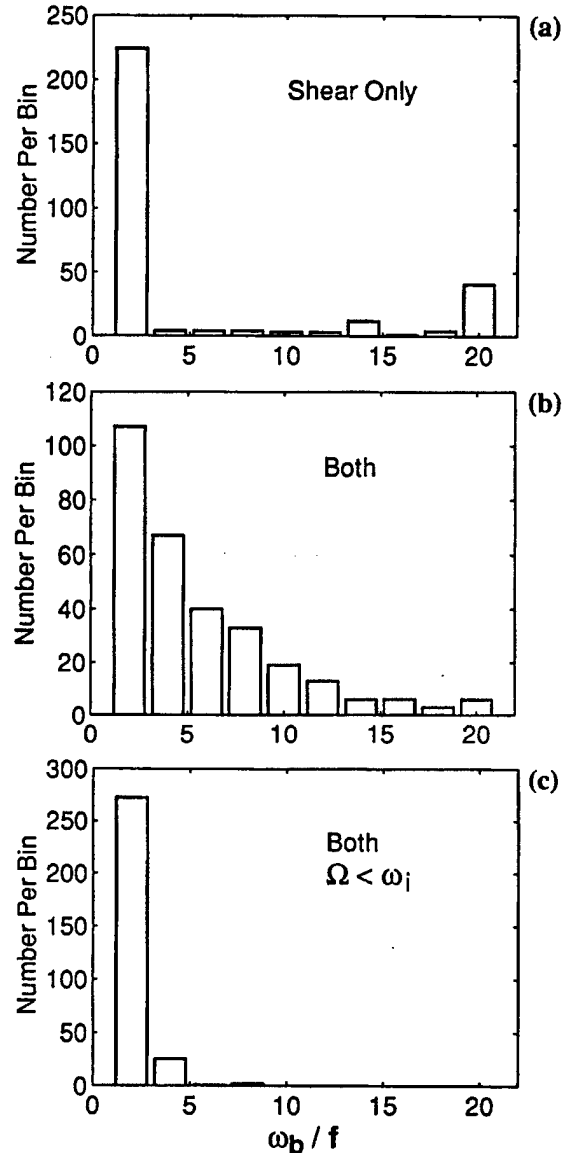


Figure 5. Histograms of test-wave frequencies at the instant of breaking ($\lambda_z < 5$ m) for test waves interacting with (a) only background shear, (b) both shear and vertical divergence, and (c) both shear and vertical divergence but restricting interactions to background frequencies lower than the test waves' ($\Omega < \omega_i$). Test waves are initialized with intrinsic frequencies $\omega_i = 21f$ and vertical wavenumbers $k_z = 0.05 \text{ rad m}^{-1}$. Test waves interacting with vertical divergence as well as vertical shear (b) break at higher frequencies than those interacting with shear only (a). However, if frequency scale-separation is imposed between the test waves and background ($\Omega < \omega_i$) (c), the histograms of breaking frequency with and without vertical divergence are similar.

3.3.2.2 Test-wave lifespans. Figure 6 shows test-wave lifespans (while $\lambda_z > 5$ m) versus background spectral energy level E without (a) and with (b) frequency scale-

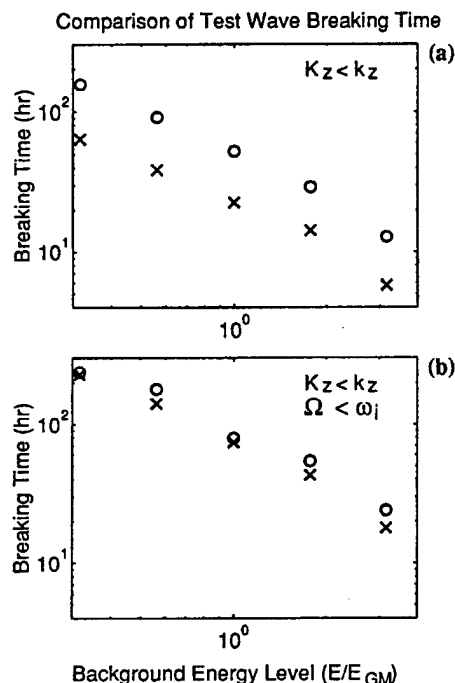


Figure 6. Test-wave lifespans (while $\lambda_z > 5$ m) versus background energy level E without (a) and with (b) frequency scale-separation ($\Omega < \omega_i$). Test waves are initialized with intrinsic frequencies $\omega_i = 9f$ and vertical wavenumbers $k_z = 0.12$ rad m^{-1} . The "x" denotes average test-wave lifespans for interactions with both background vertical divergence and shear, and "o" for interactions only with shear. The difference in lifespans with and without vertical divergence is a constant ratio of 2, independent of the background energy level (a). With frequency separation ($\Omega < \omega_i$) (b), test-wave lifespans are little affected by vertical divergence interactions.

separation $\Omega < \omega_i$ between the test wave and background. Each average includes simulations with 100 different backgrounds. Again, test waves that get stuck at low horizontal wavenumber are excluded from the statistics of Fig. 6b. The difference in average lifespan $\langle \Delta t \rangle$ between simulations with and without vertical divergence interactions is a constant ratio of ~ 2 , independent of the background energy level (Fig. 6a). Increasing the background energy level causes the breaking time to decrease smoothly. Consistent with Fig. 5c, imposing WKB frequency scale-separation ($\Omega < \omega_i$) results in almost identical average test-wave lifespans with and without background divergence W_z interactions.

Test-wave lifespans and frequencies at the time of breaking (when λ_z falls below 5 m) are not sensitive to the

number of waves comprising the background, provided the background wave field reproduces the GM model spectrum (Fig. 7). Turbulence production rates $\epsilon(1 + \gamma)$ should likewise be insensitive to the exact number of waves making up the background.

The above conclusions are based on the GM model and cannot be extrapolated to non-GM internal wave fields without additional numerical simulations. Polzin *et al.*

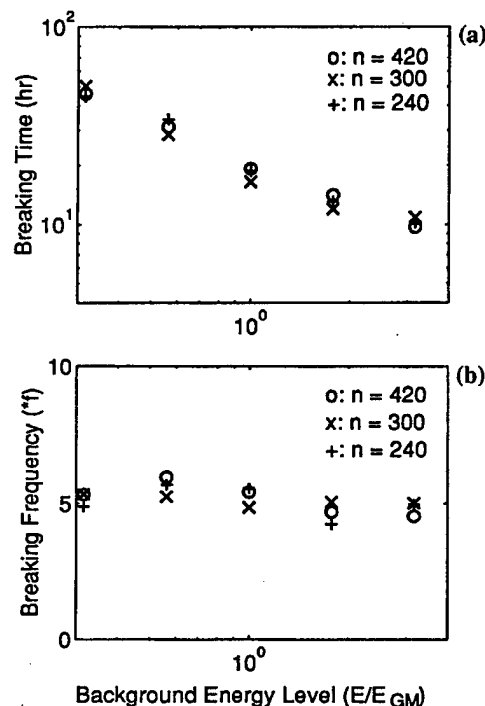


Figure 7. Test-wave lifespans (a) and frequencies (b) as a function of spectral energy level E/E_{GM} at the time λ_z falls below 5 m for different numbers of waves comprising the background. Test-wave lifespans and frequencies are insensitive to the number of background waves NW provided the background wave field reproduces the GM model spectrum.

(1995) suggest that non-GM frequency spectral shapes will have more impact on the relative roles of shear and vertical divergence than non-GM wavenumber spectral shapes.

3.3.2.3 Test-wave breaking. Figure 8 compares probability density functions (pdf) of background vertical divergence W_z (a), shear V_z (b) and strain ξ_z (c) at (i) the instant test-wave vertical wavelengths fall below 5 m (solid), (ii) throughout the test-wave trajectories ($\lambda_z > 5$ m) (dotted), and (iii) randomly sampling the background fields [dashed, not in (d)]. That these three sets of curves are not identical points to strong correlations between the test waves and background

overcoming the initial random phasing. Waves tend to “break” while encountering higher-than-average shear, vertical divergence and buoyancy frequency (solid curves, Fig. 8) as also reported from observations (Alford and Pinkel 1999). Prior to “breaking,” test waves experience lower-than-average shear, vertical divergence and buoyancy frequency (dotted, Fig. 8).

Taken together, Figs. 2–3 and 8 suggest the following wave/wave interaction scenario. While in lower-than-average shear and vertical divergence, test waves slowly migrate toward higher wavenumber (around $k_z = 0.05$ cpm) (1–2 h in Fig. 2). Upon encountering higher-than-average background shear, vertical divergence or strain, these finescale waves are rapidly forced toward even higher vertical wavenumber where they are assumed to break for $\lambda_z < 5$ m. Wave-induced variations in the vertical gradient of background buoyancy frequency are negligible. This scenario might also explain the change in spectral slope at $\lambda_z \sim 10$ m and the steeper finescale spectral slope for shear than strain.

4. Parameterizing the Turbulent Production Rate

Following Henyey *et al.* (1986), we ray-trace small-scale waves (referred to as test waves) in larger-scale Garrett and Munk (Munk 1981) internal-wave backgrounds (Appendices B and D, and Fig. 1) using (2.1)–(2.2).

It is not necessary to track individual test-wave amplitudes to estimate the spectral energy-flux by ray-tracing (Henyey *et al.* 1986; section 5). In order to parameterize the turbulence production rate $\epsilon(1 + \gamma)$ using eikonal techniques, one quantifies the rate at which energy is fluxed toward high vertical wavenumber in the internal wave spectrum. Then the time rate of change of energy in the spectral interval $dk_z d\omega$ is

$$\frac{d\{S[E](k_z, \omega) dk_z d\omega\}}{dt} = S[E](k_z, \omega) \left\langle \frac{dk_z}{dt} \right\rangle d\omega + S[E](k_z, \omega) \frac{d\omega}{dt} dk_z, \quad (4.1)$$

assuming the energy density spectra $S[E](k_z, \omega)$ is invariant. The time rate of change of the vertical wavenumber $\langle dk_z/dt \rangle$ is a function of both vertical wavenumber k_z and intrinsic frequency ω . In a steady state, the left-hand side of (4.1) vanishes. For an equilibrium spectrum, the second term of (4.1) vanishes so the first term of (4.1) can be equated to the turbulence production rate

$$\epsilon - \langle w'b' \rangle = \epsilon(1 + \gamma) = \int_f^N S[E](k_z, \omega) \left\langle \frac{dk_z}{dt} \right\rangle d\omega. \quad (4.2)$$

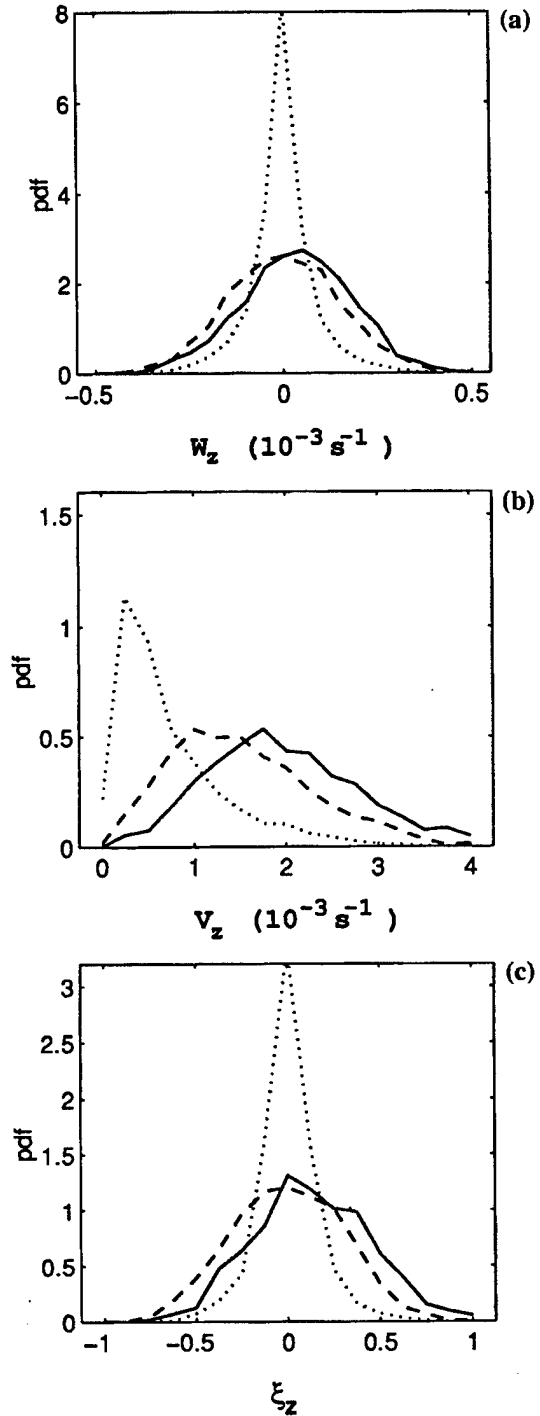


Figure 8. Comparison of probability density functions for background vertical divergence W_z (a), vertical shear V_z (b) and strain ξ_z (c) at sites where the test-wave vertical wavelength λ_z falls below 5 m (solid), throughout the test-wave trajectories (dotted), and randomly sampling the background (dashed). Test-wave “breaking” ($\lambda_z < 5$ m) tends to occur at higher-than-average background shear, vertical divergence and buoyancy frequency (solid curves). Prior to “breaking” (dotted), test waves tend to propagate through lower-than-average shear, vertical divergence and buoyancy frequency.

4.1 Parameterizing Turbulent Production Rate With Both Shear and Vertical Divergence Variances

To include interactions with internal-wave vertical divergence W_z in the parameterization of the turbulence production rate $\varepsilon(1 + \gamma)$ (4.2), the vertical wavenumber k_z ray-tracing equation (2.4) is used. The $(\partial\omega_i/\partial N_i)(\partial N_i/\partial z)$ term is negligible so will not be included here. Part of the high-frequency and high-horizontal-wavenumber vertical divergence term in dk_z/dt is reversible. In the following discussion, we first include the reversible part of dk_z/dt by estimating the ensemble time rate of change of the vertical wavenumber $\langle dk_z/dt \rangle$ in (4.2) from its rms value. This includes interactions with background waves that do not satisfy the WKB approximation. In section 4.2, we successively filter out reversible high-frequency and high-horizontal-wavenumber contributions to better satisfy WKB scale-separation.

First, following *Henyey et al.* (1986), we estimate $\langle dk_z/dt \rangle$ by its rms value

$$\begin{aligned} \left\langle \frac{dk_z}{dt} \right\rangle &\sim \sqrt{\left\langle \left(\frac{dk_z}{dt} \right)^2 \right\rangle} \\ &\sim r_1(k_z)k_z \sqrt{\langle V_z^2 \rangle} \left[\frac{k_h}{k_z} + r_2(k_z) \sqrt{\frac{\langle W_z^2 \rangle}{\langle V_z^2 \rangle}} \right] \\ &\sim r_1(k_z)k_z \sqrt{\langle V_z^2 \rangle} \left[\sqrt{\frac{\omega^2 - f^2}{N^2 - \omega^2}} + r_2(k_z) \sqrt{\frac{\langle W_z^2 \rangle}{\langle V_z^2 \rangle}} \right] \end{aligned} \quad (4.3)$$

where functions $r_1(k_z)$ and $r_2(k_z)$ indicate correlations between test waves and background. It has been assumed that the shear and vertical divergence terms are uncorrelated. Including vertical divergence in the ray-tracing equation augments the shear-only $\langle dk_z/dt \rangle$ with the term involving the ratio of the rms vertical divergence to rms shear $\sqrt{\langle W_z^2 \rangle / \langle V_z^2 \rangle}$.

Following *Henyey et al.* (1986), the spectral density $S[E](k_z, \omega)$ is described by the *Munk* (1981) GM model (with an additional k_z^{-1} dependence for wavenumbers $k_z > k_{zc} \approx 0.08$ cpm to simulate the finescale oceanic spectra, *Gargett et al.* 1981; *Gregg et al.* 1993)

$$S[E](\omega, k_z) = \frac{4fN^2bj_*E_{GM}}{\pi} \frac{1}{\omega\sqrt{\omega^2 - f^2}} \frac{k_{zc}}{k_z^3}. \quad (4.4)$$

GM model parameters are defined in Table 1. Substituting $\langle dk_z/dt \rangle$ from (4.3) and $S[E](\omega, k_z)$ from (4.4) into (4.2),

$$\begin{aligned} \varepsilon_1(1 + \gamma) &= \frac{12Ri_c f N^2 b^2 j_*^2 E_{GM}^2}{\pi} \\ &\times \left(\frac{k_{zc}}{k_z} \right)^2 r_1(k_z) \frac{\sqrt{\langle V_z^2 \rangle}}{N} \\ &\times \left[\text{Arccosh}\left(\frac{N}{f}\right) + r_2(k_z) \frac{N}{f} \text{Arccos}\left(\frac{f}{N}\right) \sqrt{\frac{\langle W_z^2 \rangle}{\langle V_z^2 \rangle}} \right] \end{aligned} \quad (4.5)$$

I II

expressed in terms of the internal-wave shear variance $\langle V_z^2 \rangle$ (I) and vertical divergence variance $\langle W_z^2 \rangle$ (II). Ignoring the vertical divergence term (II) reproduces *Henyey et al.*'s (1986) shear-based model, where $\sqrt{\langle V_z^2 \rangle}/N^2$ is equivalent to their $\langle Ri \rangle^{-1/2} = Ri_c^{-1/2} [1 + \ln(k_z/k_{zc})]^{1/2}$. Correlation $r_1(k_z)$ between test-wave vertical wavenumber and background shear is equivalent to their constant ratio $(1-r)/[\sqrt{2}(1+r)]$ related to the ratio of up- and down-wavenumber spectral energy-flux in k_z -space. In GM, the relationship between the wavenumber of the finescale change in spectral slope k_{zc} and the associated Richardson number Ri_c is $Ri_c^{-1} = 3j_*bk_{zc} E_{GM}$ (*Munk* 1981; *Henyey et al.* 1986).

The spectral energy-flux toward high wavenumber $\varepsilon(1 + \gamma)$ is independent of k_z for the GM model spectrum, as will be verified with numerical simulations (see Fig. 11 in Sec. 5.2); otherwise, energy would accumulate or deplete from intermediate wavenumbers. This eliminates the k_z dependence in (4.5)

$$\begin{aligned} \varepsilon_1(1 + \gamma) &= \frac{12Ri_c b^2 j_*^2 f N^2 E_{GM}^2}{\pi} \\ &\times \left(\frac{k_{zc}}{0.2\pi \text{ rad m}^{-1}} \right)^2 r_1 \frac{\sqrt{\langle V_z^2 \rangle}}{N} \\ &\times \left[\text{Arccosh}\left(\frac{N}{f}\right) + r_2 \frac{N}{f} \text{Arccos}\left(\frac{f}{N}\right) \sqrt{\frac{\langle W_z^2 \rangle}{\langle V_z^2 \rangle}} \right] \Big|_{k_z=0.2\pi \text{ rad/m}} \end{aligned} \quad (4.6)$$

where correlation coefficients $r_1 = 0.022$ and $r_2 = 1.7$ for the upper limit ($K_z < k_z$, no restriction on background horizontal wavenumber and frequency) are determined numerically (see dotted line in Fig. 10, Sec. 5.2). For the *Munk* (1981) model spectrum, the total rms ratio

$$\sqrt{\frac{\langle W_z^2 \rangle}{\langle V_z^2 \rangle}} = \sqrt{\frac{\int_f^N S[W_z](\Omega) d\Omega}{\int_f^N S[V_z](\Omega) d\Omega}} = \sqrt{\frac{4f}{3\pi N}}. \quad (4.7)$$

Equation (4.7) indicates that (II)/(I) is proportional \sqrt{N} , that is, the contribution from vertical divergence has a 0.5 stronger dependence on N than the shear. This extra \sqrt{N} scaling in (II) arises from the contribution of near-buoyancy frequency waves in the GM spectra to the vertical divergence W_z . It is not consistent with the N^2 dependence in observations (Polzin *et al.* 1995).

Because near-buoyancy background wave periods are much shorter than test-wave lifespans, and their horizontal wavenumbers much higher than those of finescale near-inertial test waves, including their rms variance will overestimate the spectral energy transfer. That is, the upper bound (4.6) with the given correlation coefficients is not realistic. These simulations include waves that do not satisfy WKB scale-separation in time or the horizontal. In section 4.2, we examine the effect of averaging vertical divergence over test-wave lifespans and applying WKB scale-separation in the horizontal. This leads to a parameterization in terms of shear and strain variances.

4.2 Parameterizing Turbulent Production Rate With Shear and Strain Variances

As mentioned in section 4.1, there is concern about parameterizing $\langle dk_z/dt \rangle$ and $\epsilon(1 + \gamma)$ in terms of the rms variance of vertical divergence $\langle W_z^2 \rangle$ in (4.5) and (4.6) because vertical divergence is dominated by near-buoyancy waves of short time- and horizontal lengthscales that do not satisfy the WKB approximation. Near-buoyancy waves dominate the rms $k_z W_z$, but not the test-wave lifespan average $\langle k_z W_z \rangle$ if high-frequency variations are reversible. Therefore, estimating $\langle dk_z/dt \rangle$ by the rms variance $k_z W_z$ exaggerates the role of high-frequency waves in spectral energy transfer.

To filter out high-frequency fluctuations which do not contribute to the ensemble average $\langle dk_z/dt \rangle$, we first estimate $\langle dk_z/dt \rangle$ from the ensemble average changes in test-wave vertical wavenumber Δk_z over the lifespans of the test waves Δt , that is,

$$\left\langle \frac{dk_z}{dt} \right\rangle \approx \left\langle \frac{\Delta k_z}{\Delta t} \right\rangle = \left\langle \frac{1}{\Delta t} \int_0^{\Delta t} \frac{dk_z}{dt} dt \right\rangle, \quad (4.8)$$

and later impose horizontal scale-separation. Test-wave lifespans (while wavelength $\lambda_z > 5$ m) in the numerical simulations vary from of order an hour at the base of the mixed-layer to tens of hours at 2000-m depth. During the lifespan of test waves, test-wave wavenumbers k_h, k_z and encountered background vertical shear V_z vary much more slowly than background vertical divergence W_z . Thus, the influence of high-frequency ($> 2\pi/\Delta t$) internal waves is filtered out in (4.8). We estimate

$$\left\langle \frac{\Delta t}{0} \int_0^{\Delta t} (dk_z/dt) dt \Delta t \right\rangle$$

by the rms

$$\left\{ \frac{\Delta t}{0} \int_0^{\Delta t} (dk_z/dt) dt \right\} / \Delta t$$

To zero order,

$$\begin{aligned} \left\langle \frac{dk_z}{dt} \right\rangle &\approx \text{rms } k_h \cdot V_z + \text{rms } \frac{k_z \xi_z}{\Delta t} \\ &= \sqrt{\langle (k_z V_z)^2 \rangle} \left[\frac{k_h}{k_z} + \frac{1}{\Delta t} \sqrt{\frac{\langle \xi_z^2 \rangle}{\langle V_z^2 \rangle}} \right] \\ &= r_1(k_z) k_z \sqrt{\langle V_z^2 \rangle} \left[\sqrt{\frac{\omega^2 - f^2}{N^2 - \omega^2}} + r_2(k_z) \sqrt{\frac{f^2 \langle \xi_z^2 \rangle}{\langle V_z^2 \rangle}} \right] \end{aligned} \quad (4.9)$$

where $r_2(k_z)$ is related to the ratio of the test-wave lifetime Δt to the inertial timescale f^{-1} as well as the correlation between test-wave vertical wavenumber and background vertical strain.

As in Polzin *et al.* (1995), it is assumed that the turbulence production rate can be parameterized in terms of internal-wave shear $\langle V_z^2 \rangle$ and strain $\langle \xi_z^2 \rangle$ variances. With $\langle dk_z/dt \rangle_E$ from (4.9), the turbulence production rate (4.2) independent of k_z is given by

$$\begin{aligned} \epsilon_2(1 + \gamma) &= \frac{12 Ri_c b^2 j^{*2} f N^2 E_{GM}^2}{\pi} \\ &\times \left(\frac{k_{zc}}{0.2\pi \text{ rad m}^{-1}} \right)^2 r_1 \cdot \frac{\sqrt{\langle V_z^2 \rangle}}{N} \\ &\times \left[\text{Arccosh} \left(\frac{N}{f} \right) + r_2 \cdot \text{Arccos} \left(\frac{f}{N} \right) \sqrt{\frac{N^2 \langle \xi_z^2 \rangle}{\langle V_z^2 \rangle}} \right] \end{aligned} \quad (4.10)$$

where $\langle V_z^2 \rangle / (\bar{N}^2 \langle \xi_z^2 \rangle)$ ($= 3$ in GM) is the shear-to-strain ratio, and correlation coefficients $r_1 = 0.22$ and $r_2 = 25$ are determined numerically by carrying out simulations with and without interactions with vertical divergence as in (4.6).

No frequency or horizontal wavenumber filtering were applied to the numerical simulations to obtain the r_1 and r_2 correlation coefficients for ϵ_2 so these represent another upper limit for turbulence production; indeed, the numerical simulations to obtain the upper limit of (4.10) were identical to those for (4.6). A lower limit ϵ_2 is obtained by applying stricter vertical scale-separation K_z

$< 0.5k_z$ and horizontal scale-separation $K_H < k_h$ for frequencies

$\Omega > 11f$. This yields correlation coefficients $r_1 = 0.01$ and $r_2 = 10$ in (4.10). The upper and lower limits of (4.10) differ by a factor of four.

Parameterizing $\epsilon(1 + \gamma)$ with shear and strain variances (4.10) predicts an N^2 scaling, consistent with the predicted scalings of *Heney et al.* (1986) and weak-triad interactions (*McComas and Müller* 1981b), and observations (*Polzin et al.* 1995). Replacing vertical divergence by the test-wave time-averaged change in strain filters out the high-frequency contributions to vertical divergence which produced a stronger dependence on N in (4.6). Thus, we suggest that the lower limit of (4.10) is a more reasonable parameterization. It averages over test-wave lifespans and better satisfies the WKB approximation and observations. However, although (4.10) is expressed in terms of strain, it should be emphasized that *physically* it is vertical divergence that induces internal-wave spectral energy transfer.

4.3 Summary

Several parameterizations for the turbulent production rate $\epsilon(1 + \gamma)$ have been presented (Table 2). Equation (4.6) parameterizes the turbulent production rate in terms of the total internal-wave vertical divergence $\langle W_z^2 \rangle$ and vertical shear $\langle V_z^2 \rangle$ variances so represents an upper

the total vertical divergence variance which contains significant contributions from wave periods shorter than test-wave lifespans and horizontal wavelengths smaller than those of the test waves, in violation of the WKB approximation. To overcome this failing, equation (4.10) parameterizes $\epsilon(1 + \gamma)$ with the vertical strain $N^2 \langle \xi_z^2 \rangle$ and vertical shear $\langle V_z^2 \rangle$ variances by filtering out the reversible high-frequency parts of vertical divergence in dk_z/dt . An upper limit from (4.10) is obtained from the same numerical simulations used to estimate the correlation coefficients in (4.6), that is, by applying scale-separation only in the vertical ($K_z < k_z$). A lower limit is obtained by applying stricter scale-separation in the vertical ($K_z < 0.5k_z$) and scale-separation in the horizontal ($K_H < k_h$) for frequencies $\Omega > 11f$. Applying horizontal scale-separation $K_H < k_h$ at all background frequencies, or frequency scale-separation $\Omega < \omega$, causes many test waves to get stuck at low horizontal wavenumber and low frequency with no background to interact with. This is not realistic. Placing no horizontal restrictions on backgrounds with $\Omega < 11f$ is a compromise which allows test waves to interact with 95% of the shear and 90% of the strain. Observations lie between the upper and lower limits of (4.10) (see Fig. 14b in Sec. 6), roughly consistent with measurement uncertainty.

5. Numerically Simulating the Spectral Energy Transfer

Following *Heney et al.* (1986), we calculate the GM spectral energy transfer (assumed equal to the turbulence production rate, $\epsilon_p = \epsilon + \langle w' b' \rangle$). In a steady state, the spectral energy transfer rate through a fixed vertical wavenumber can be expressed by the energy transfer rate following vertical wavenumber changes of the wavepackets. Procedure details follow.

From the ocean surface to 2000-m depth, 20 test-wave trajectories are released every 200 m in depth with fixed initial horizontal wavenumbers $(k_x, k_y) = (10^{-3} \text{ cpm}, 0)$ and vertical wavenumbers ranging from $k_z = -0.1$ to 0.1 cpm ($k_z \cdot 0$) in steps of $\Delta k_{z0} = 0.01 \text{ cpm}$, corresponding to vertical wavelengths $\lambda_z = 10\text{--}100 \text{ m}$. Test waves are released in Monte Carlo background internal-wave fields described by the Garrett and Munk model spectrum (*Munk* 1981) in an exponential mean buoyancy frequency profile ranging from $4.9 \times 10^{-3} \text{ rad s}^{-1}$ at 100-m depth to $1.1 \times 10^{-3} \text{ rad s}^{-1}$ at 2000-m depth (Table 1). When test-wave vertical wavelengths fall below $\lambda_z = 5 \text{ m}$ ($k_z \cdot 0.2 \text{ cpm}$), they are defined to "break" and lose their energy to turbulence. At this wavenumber, stability parameters, such as Richardson number and instantaneous buoyancy, approach criticality in the ocean (*Munk* 1981; *Müller et al.* 1986; *Polzin* 1996). A total of 4000 test waves are propagated in 20 different Monte Carlo simulations of a

Table 2. Correlation coefficients for turbulence production rate parameterizations (4.6) and (4.10) based on numerical ray-tracing simulations with various assumptions.

Model Assumptions	r_1	r_2
1. (4.6) V_z, W_z ($K_z < k_z$)	0.022	1.7
2. (4.10) V_z ($K_z < k_z$)	0.022	0
3. (4.10) V_z ($K_z < 0.5k_z$) $K_H < k_h$ (or $\Omega < 11f$)	0.010	0
4. (4.10) V_z, ζ_z ($K_z < k_z$)	0.022	25
5. (4.10) V_z, ζ_z ($K_z < 0.5k_z$) $K_H < k_h$ (or $\Omega < 11f$)	0.010	10
	c_I	r_2
6. (6.1) V_z, ζ_z ($K_z < k_z$)	1.0×10^{-8}	25
7. (6.1) V_z, ζ_z ($K_z < 0.5k_z$) $K_H < k_h$ (or $\Omega < 11f$)	0.4×10^{-8}	10

limit. The problem with this parameterization is that it expresses test-wave lifespan average $\langle dk_z/dt \rangle$ in terms of

GM background (Fig. 1) to obtain stable ensemble averages that span all phases of the initial background wave field.

To calculate the spectral energy-flux toward high wavenumber k_z in the high-wavenumber domain ($0.01 \text{ cpm} < k_z < 0.2 \text{ cpm}$, $k_h > 10^{-3} \text{ cpm}$), we assign an initial spectral action-flux into this spectral domain at the fixed initial horizontal wavenumber $k_{h0} = 10^{-3} \text{ cpm}$. This initial spectral action-flux will be redistributed by smallscale test wavepackets in phase space. How much action should be initially assigned to each test wave is determined by $q \cdot S[A](k_{h0}, k_{z0}) \cdot \Delta k_{z0} \cdot dk_{h0}/dt|_{t=0}$, where $S[A](k_h, k_z)$ is the GM action spectrum in terms of horizontal and vertical wavenumber, dk_{h0}/dt the initial horizontal wavenumber flux (to be discussed later), q a constant chosen such that the sum over all the test waves has the same total action as the high-wavenumber part of GM spectra

$$\begin{aligned} q \sum_{i=1}^{NW} S[A](k_{h0}, k_{z0}) \Delta k_{z0} \frac{dk_{h0}}{dt} \Big|_{t=0} \cdot \Delta t_i \\ = \int_{k_{h0}}^{\infty} \int_{k_{zlow}}^{k_{zb}} S[A](k_h, k_z) dk_z dk_h, \end{aligned} \quad (5.1)$$

NW the number of test waves, Δt_i the lifetime of the i th test wave, $k_{zlow} = 0.01 \text{ cpm}$ is the lowest and $k_{zb} = 0.2 \text{ cpm}$ the highest (final or "breaking") test-wave vertical wavenumbers.

Since the spectral action-flux $S[A](k_{h0}, k_{z0}) \Delta k_{z0} dk_{h0}/dt|_{t=0}$ is conserved following a test wave (Lighthill 1978), the spectral energy transfer rate through $k_z = 0.2 \text{ cpm}$ (\equiv turbulence production rate) can be calculated from the spectral action-flux multiplied by the intrinsic frequencies of the test waves as they break ($k_z \cdot k_{zb}$), that is,

$$\varepsilon(1 + \gamma) = q \sum_{i=1}^{NW} \left\{ S[A](k_{h0}, k_{z0}) \Delta k_{z0} \frac{dk_{h0}}{dt} \Big|_{t=0} \right\} \omega_{bj} \quad (5.2)$$

where ω_{bj} is the j th test-wave breaking frequency, ε the turbulent kinetic energy dissipation rate and $\gamma = -\langle w'b' \rangle / \varepsilon \cdot 0.2$ the mixing efficiency.

Three approaches are used to select the initial horizontal wavenumber flux rate $dk_{h0}/dt|_{t=0}$ for (5.2):

- for the shear and vertical divergence parameterization (4.6), evaluating the rms horizontal wavenumber ray-tracing equation

$$\frac{dk_{h0}}{dt} \Big|_{t=0} \sim k_{h0} \sqrt{\langle (\nabla_h V_h)^2 \rangle} + k_{z0} \sqrt{\langle (\nabla_h W)^2 \rangle}, \quad (5.3)$$

where $\sqrt{\langle (\nabla_h V_h)^2 \rangle}$ and $\sqrt{\langle (\nabla_h W)^2 \rangle}$ are calculated from GM model spectrum (Munk 1981), but with an extra factor $(N^2 - \omega^2)/(N^2 - f^2)$ in $S[W](\omega, k_z)$ to be consistent with the nonhydrostatic internal-wave equations of motion.

- for shear-and-strain parameterization (4.10), test-wave lifespan-averaged dk_h/dt is evaluated, that is,

$$\begin{aligned} \frac{dk_{h0}}{dt} \Big|_{t=0} &\sim \text{rms} \left\{ \frac{1}{\Delta t} \int_0^{\Delta t} \frac{dk_h}{dt} dt \right\} \\ &\sim k_{h0} \sqrt{\langle (\nabla_h V_h)^2 \rangle} + \frac{k_{z0}}{\langle \Delta t \rangle} \sqrt{\langle (\nabla_h \xi)^2 \rangle}, \end{aligned} \quad (5.4)$$

where $\langle \Delta t \rangle$ is the ensemble-averaged lifespan of the test waves. In this case, $dk_{h0}/dt|_{t=0}$ is independent of N . The distinction between (5.3) and (5.4) was discussed in connection with (4.6) and (4.10).

- constant so that $dk_{h0}/dt|_{t=0}$ is independent of both test-wave initial wavenumber and background buoyancy frequency N . (5.5)

Numerically-simulated test-wave vertical wavenumber spectral shapes for action (Fig. 9) prove insensitive to the choice of initial conditions (5.3–5.5). Because of the normalization q in (5.1) and (5.2), the simulated $\varepsilon(1 + \gamma)$ are independent of the magnitude of $dk_{h0}/dt|_{t=0}$ (Fig. 10). However, whether the calculated $\varepsilon(1 + \gamma)$ varies as $N^{2.5}$ or N^2 (Fig. 10) depends on how $dk_{h0}/dt|_{t=0}$ varies with N [as \sqrt{N} for (5.3), or independent of N for (5.4) and (5.5)]. In the following, numerical results are ensemble-averaged over all backgrounds and trajectories.

5.1 The High-Wavenumber Spectra

Figure 9 displays numerically-simulated test-wave vertical wavenumber spectra for action $S[A](k_z)$ normalized by GM at vertical wavenumbers $0.01 \text{ cpm} < k_z < k_{zb} = 0.2 \text{ cpm}$ ($100 \text{ m} > \lambda_z > 5 \text{ m}$) for vertical scale-separation $K_z < k_z$ and horizontal scale-separation $K_H < k_h$ for $\Omega > 11f$. When interactions with both shear and vertical divergence are included, the spectral slope is $k_z^{-1/2}$ steeper than GM (k_z^{-2}) below the finescale cutoff wavenumber $k_{zc} = 0.08 \text{ cpm}$. In the absence of vertical divergence interactions, the wavenumber spectral slope is the same as the GM model. These results are consistent with weak-triad interaction theory. McComas and Müller (1981a) argued that, to maintain a spectral action transfer independent of vertical wavenumber, requires a $k_z^{-2.5}$ dependence at low frequencies ($\omega_i < 4f$) and a k_z^{-2} dependence at high frequencies ($\omega_i > 5f$)—where interactions with vertical shear control the spectral action transfer. Since the ω^{-3} action spectra is dominated by low-frequency waves, it should display a $k_z^{-2.5}$ dependence. A

$k_z^{-2.5}$ high-wavenumber ($0.01 \text{ cpm} < k_z < 0.1 \text{ cpm}$) energy spectra was observed by *Leaman and Sanford (1975)* and *Pinkel (1984)* but is less discernible in other observations (e.g., *Gregg et al. 1993*; *Polzin et al. 1995*). Whether ocean spectra behave as $k_z^{-2.5}$ or k_z^{-2} may depend on the strength of interactions with the high-frequency wave field.

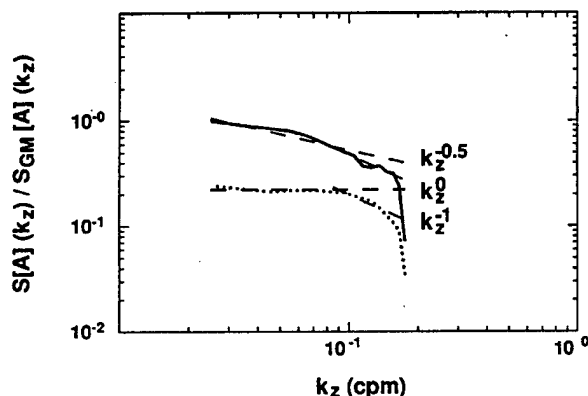


Figure 9. Vertical wavenumber spectra for test-wave action normalized by the GM model spectrum. Solid (dotted) curves include (exclude) vertical divergence $k_z W_z$ interactions. Dashed lines indicate labeled k_z power laws. Magnitudes of the two test-wave action spectra have been arbitrarily shifted vertically to make the plot clearer. With vertical divergence $k_z W_z$ interactions, the vertical wavenumber spectra is $k_z^{-0.5}$ steeper than GM at low wavenumbers ($0.01 \text{ cpm} < k_z < 0.08 \text{ cpm}$), consistent with weak-triad theory. At wavenumbers $k_z > 0.08 \text{ cpm}$ ($\lambda_z < 12 \text{ m}$), test-wave spectral slopes are k_z^{-1} steeper than at lower wavenumbers, that is, have a k_z^{-3} dependence, consistent with observed finescale spectra.

The GM-normalized test-wave action spectra steepen at finescale wavenumbers above $k_{zc} = 0.08 \text{ cpm}$ ($\lambda_z = 12 \text{ m}$; Fig. 9) whether interactions with background vertical divergence are included or not. The high-wavenumber test-wave spectra are k_z^{-1} steeper than the low-wavenumber GM spectra, that is, finescale action spectra have a k_z^{-3} dependence, consistent with observed finescale spectra (*Gargett et al. 1981*; *Gregg et al. 1993*). The change in spectral slope can be interpreted as arising from strong interactions between test waves and the background when test waves reach high wavenumbers and come in direct contact with the breaking wavenumber sink (*Hines 1991*; Fig. 3).

5.2 Simulated Turbulence Production Rates $\epsilon(1 + \gamma)$

Figure 10 displays profiles of the turbulence production rate $\epsilon(1 + \gamma)$ under various filtering assumptions. Coefficients r_1 and r_2 for the different assumptions are

listed in Table 2. Upper limits for the shear-and-strain predictions are consistent with weak-triad results (*McComas and Müller 1981b*). However, both weak-triad and ray-tracing approaches are in violation of their assumptions in this limit.

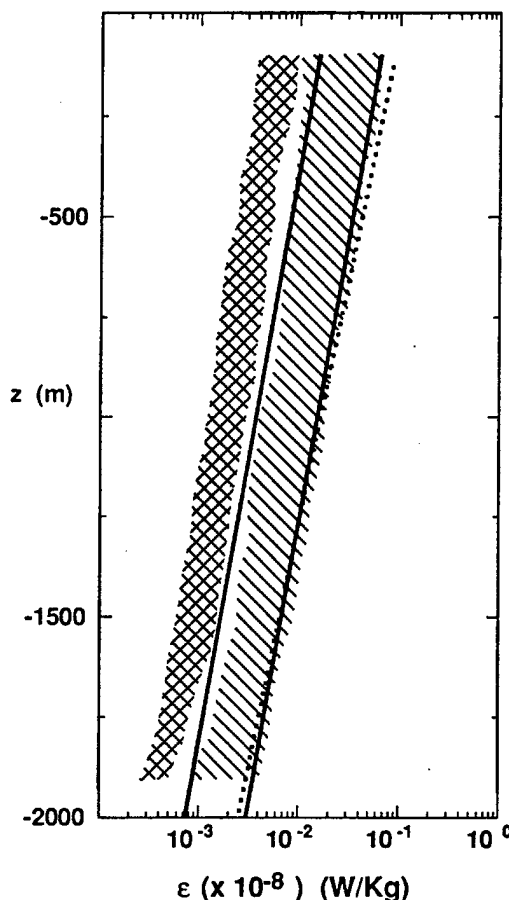


Figure 10. Profiles of predicted turbulent dissipation rate ϵ [converted from turbulent production rate $\epsilon(1 + \gamma)$ using $\gamma = 0.2$] in stratification $N(z) = N_0 e^{z/b}$ (Table 1). Crosshatching spans the upper and lower limits of shear-only simulations, stippling the upper and lower limits of shear-and-strain simulations. Upper limits include all interactions satisfying $K_z < k_z$, lower limits restrict $K_H < k_h$ for $\Omega > 11f$ and $K_z < 0.5k_z$. The dotted curve is parameterization (4.6) in terms of shear and vertical divergence, the right solid curve the shear-and-strain upper limit of (4.10), and the left solid curve the shear-only upper limit of (4.10). The upper limit of the predicted shear-and-strain ϵ is close to the weak-triad result (*McComas and Müller 1981b*) and 3–4 times the shear-only upper limit (*Heney et al. 1986*). The lower limit of the predicted shear-and-strain ϵ is close to the shear-only upper limit (*Heney et al. 1986*).

Applying WKB scale-separation to horizontal wavenumbers $K_H < k_h$ for $\Omega > 11f$, and more strictly to

vertical wavenumber $K_z < 0.5k_z$, reduces shear-and-strain turbulence production rates by a factor of four and shear-only predictions by a factor of two. Turbulence production rate estimates with $K_z < 0.5K_z$ are a third those with $K_z < k_z$ (see Fig. 12 in Sec. 5.3), so horizontal scale-separation accounts for the remaining difference. The lower-limit shear-and-strain values are consistent with upper-limit shear-only predictions (Henyey *et al.* 1986) and therefore observations (Gregg 1989; Polzin *et al.* 1995).

The simulated spectral energy transfer is not sensitive to the magnitude of the initial $dk_{h0}/dt|_{t=0}$ [because of normalizing factor q in (5.1)], initial test-wave wavenumber or initial frequency. But the buoyancy frequency scaling of $\epsilon(1 + \gamma)$ is sensitive to the N dependence of $dk_{h0}/dt|_{t=0}$ (Fig. 10). The test-wave lifespan-averaged or constant $dk_{h0}/dt|_{t=0}$ in both (5.4) and (5.5) are independent of N and give the same numerically calculated $\epsilon(1 + \gamma)$ with N^2 scaling (4.10). But the rms $dk_{h0}/dt|_{t=0}$ in (5.3) has a \sqrt{N} dependence, due to $\sqrt{\langle (\nabla_h W)^2 \rangle}$ being dominated by near-buoyancy waves in the GM model, and results in an $N^{2.5}$ dependence in the numerically-calculated $\epsilon(1 + \gamma)$ (4.6) which is not consistent with the observed N^2 dependence (Polzin *et al.* 1995).

We speculate that the lower limit of parameterization (4.10), expressed in terms of shear and lifespan-averaged vertical divergence, that is, strain, is the more reasonable choice since instantaneous high-frequency high-horizontal-wavenumber vertical divergence fluctuations do not necessarily contribute to the net spectral energy transfer. The lower limit is also more consistent with the WKB approximation and most of the observations (see Fig. 14). These speculations await further observational or numerical testing.

The numerically-calculated spectral energy transfer is independent of the breaking wavenumber k_b (Fig. 11). Therefore, the GM vertical wavenumber spectra is in equilibrium with respect to ray-tracing wave/wave interactions at high wavenumber, consistent with our assumptions. Figures 4 and 5 suggest that the finescale equilibrium frequency spectra has a gentler spectral slope than GM.

5.3 Sensitivity to Vertical Scale-Separation

The WKB approximation, and the requirement that test waves not modify the background during interactions, are two crucial assumptions for ray-tracing wave/wave interactions. Their validity requires scale-separation ($\lambda < \Lambda$) between test waves and background. The degree of scale-separation required is uncertain. In particular, our simulations show a strong contribution for waves with $\lambda \sim \Lambda$ which may not satisfy WKB scale-separation.

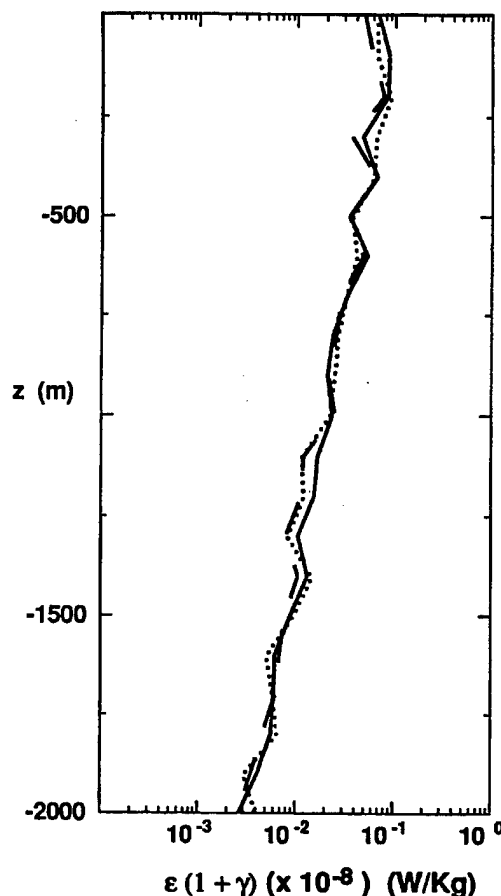


Figure 11. Numerically-simulated spectral energy transfer rate $\epsilon(1 + \gamma)$ profiles for different test-wave breaking wavenumbers, $k_z = 0.1$ cpm (solid), $k_z = 0.2$ cpm (dotted) and $k_z = 0.5$ cpm (dashed). Energy transfer rates, and their dependence on buoyancy frequency N , are independent of the assumed test-wave breaking vertical wavenumber.

Figures 12 and 13 examine the sensitivity of upper-limit spectral energy transfer rates to different vertical scale-separations between test waves and background. When vertical wavenumbers of the background are restricted merely to be lower than those of the test waves ($K_z < k_z$, max $K_z = k_z$, solid), the simulated turbulence production $\epsilon(1 + \gamma)$ is 1.6 times greater than when background vertical wavenumbers are restricted to be at most half ($K_z < 0.5k_z$, dotted), and 4.7 times greater than when background vertical wavenumbers are at most a fifth the test waves' ($K_z < 0.2k_z$, dashed). These results are independent of buoyancy frequency (Fig. 13). Since the background shear and vertical divergence variances $\int_0^{\max K_z} S(k_z) dk_z$ are proportional to max K_z , Figs. 12 and 13 indicate that the spectral energy transfer rate is slightly

less sensitive to variance at higher wavenumbers than lower wavenumbers. That is, interactions between waves of similar scale partially cancel on average. This implies that the turbulence production rate might be sensitive to the wavenumber-content of the wave field as well as the frequency-content (discussed in section 4, see also Polzin *et al.* 1995). This raises doubts about finescale parameterizations such as (4.6) and (4.10) which do not take into account which vertical wavenumbers contribute to shear and strain variances. Further work is needed to quantify these uncertainties.

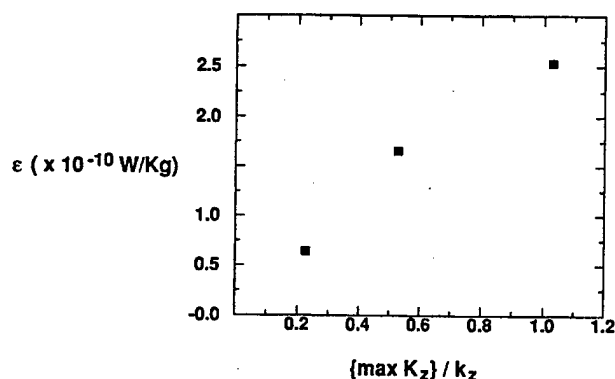


Figure 12. Numerically-simulated depth-averaged energy transfer rates $\epsilon(1 + \gamma)$ as a function of imposed separation between background and test-wave vertical wavenumbers $\{\max K_z\}/k_z$. For a greater degree of vertical scale-separation, the simulated energy transfer rate drops off. The calculated ϵ when $K_z < k_z$ is a factor of 1.6 greater than when $K_z < 0.5k_z$, and 4.6 times greater than when $K_z < 0.2k_z$. Because the variances in the GM spectra are proportional to $\max K_z$, the horizontal axis can be thought of as background shear or strain variance. Thus, energy transfer rates are slightly less sensitive to background variance at higher wavenumbers K_z .

As discussed by Henyey (1984), a factor-of-two separation in vertical wavenumbers might be sufficient to ensure (i) validity of the WKB approximation and (ii) the assumption that the background is not altered by wave/wave interactions. However, interactions between waves with less than a factor-of-two scale-separation contribute significantly (a third) to the ray-tracing spectral energy transfer rate (Figs. 12 and 13). In Henyey *et al.* (1986) and the upper-limit numerical simulations presented here, vertical wavenumbers of the background are merely restricted to be lower than those of the test waves ($K_z < k_z$), so the calculated $\epsilon(1 + \gamma)$ in Fig. 10 includes all such interactions. Figure 12 can be interpreted as implying that one third of the upper-limit ray-tracing spectral energy transfer is associated with waves that are not strictly WKB scale-separated in the vertical ($K_z >$

$0.5k_z$). Whether oceanic interactions are stronger or weaker than WKB for these waves is unknown.

5.4 Sensitivity to Horizontal Scale-Separation

Applying WKB horizontal scale-separation ($K_H < k_h$) as well as stricter vertical scale-separation ($K_z < 0.5k_z$) reduces the shear-and-strain predictions by a factor of four (2/3 due to horizontal and 1/3 due to vertical scale-separation) and the shear-only predictions by a factor of two compared to simulations that allow interactions with background waves of all horizontal wavenumbers. This suggests that, even for shear-only calculations, the issue of horizontal scale-separation cannot be ignored as was done by Henyey *et al.* (1986) and Polzin *et al.* (1995).

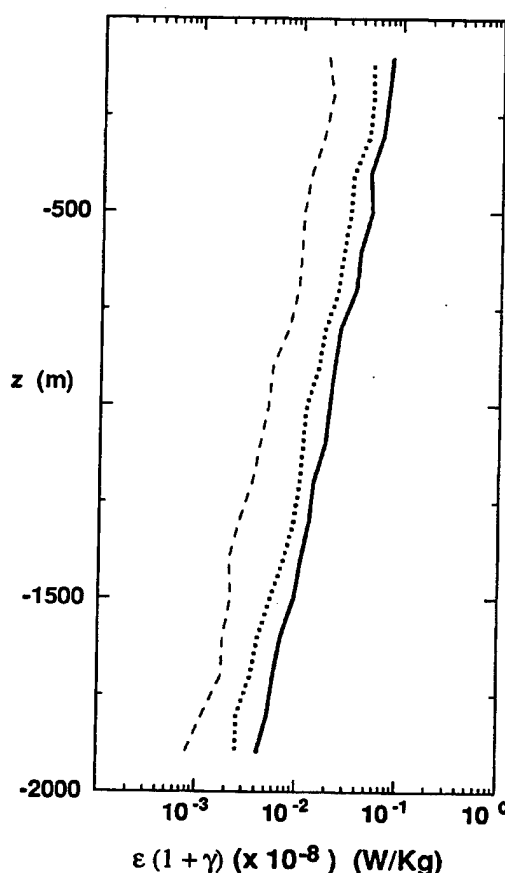


Figure 13. Numerically-simulated spectral energy transfer rate $\epsilon(1 + \gamma)$ profiles when background vertical wavenumbers K_z are restricted to be lower ($K_z < k_z$; solid), no more than half ($K_z < 0.5k_z$; dotted) and no more than one fifth ($K_z < 0.2k_z$; dashed) those of the test waves. The dependence on buoyancy frequency N is independent of the degree of vertical scale-separation.

6. Can GM-based Models be Simplified and Extended to non-GM?

Parameterizations (4.6) and (4.10) are convenient for comparison with *Heney et al.*'s (1986) GM-based model (1.4), but not oceanic observations because: (i) model parameters such as Ri_c , j^* , E_{GM} and k_{zc} can be difficult to estimate from observations, are not independent (*Munk* 1981; *Duda and Cox* 1989; *Smith et al.* 1987) and are not fundamental controlling dynamical variables, and (ii) oceanic internal wave fields deviate from GM. To apply the model to the range of internal wave fields observed in the ocean, *Gregg* (1989), *Wijesekera et al.* (1993) and *Polzin et al.* (1995) re-expressed *Heney et al.*'s (1986) GM model in terms of either shear variance, strain variance or both, then compared them to nearly GM and non-GM observations. We will refer to these rewritten parameterizations as *extended* models.

In this section, we formulate and compare extended parameterizations with each other and the observations of *Polzin et al.* (1995). Some of the difficulties in applying these models to the real ocean will be revealed in the process. We express the GM-based parameterizations (4.10) with shear and strain variances to facilitate comparison with *Gregg* (1989), *Wijesekera et al.* (1993) and *Polzin et al.* (1995).

Variances of shear $\langle V_z^2 \rangle$ and vertical strain $\langle \xi_z^2 \rangle$ are substituted for the GM model parameters j^* , E_{GM} and k_{zc} in (4.10) using GM model relations to yield

$$\epsilon(1 + \gamma) = c_1 f N^2 b^2 \left(1 + \frac{N^2 \langle \xi_z^2 \rangle}{\langle V_z^2 \rangle} \right)^2 \left(\frac{\sqrt{\langle V_z^2 \rangle}}{N} \right)^4 \times \left[\text{Arccosh} \left(\frac{N}{f} \right) + r_2 \text{Arccos} \left(\frac{f}{N} \right) \sqrt{\frac{N^2 \langle \xi_z^2 \rangle}{\langle V_z^2 \rangle}} \right] \quad (6.1)$$

where $\sqrt{\langle V_z^2 \rangle}/N = 0.7$ and $\langle V_z^2 \rangle/(N^2 \langle \xi_z^2 \rangle) = 3$ in the GM model (*Munk* 1981). We choose shear and strain variances because they appear as fundamental physical parameters in the test-wave lifespan-averaged vertical ray-tracing equation and are readily measured. Doing so eliminates dependence on large-scale quantities j^* and E .

We have replaced the $\sqrt{\langle V_z^2 \rangle}/N$ in (4.10) arising from dk_z/dt with $Ri_c^{-1/2} [1 + \ln(k_z/k_{zc})]^{1/2}$, where $Ri_c = 2$ and $k_z/k_{zc} = 2$, consistent with *Heney et al.* (1986). If it were retained, (6.1) would depend on $(\sqrt{\langle V_z^2 \rangle}/N)^5$ with coefficients little changed. Comparison with shear-only and shear-and-strain numerical simulations gives correlation coefficients $c_1 = 1.0 \times 10^{-8}$ and $r_2 = 25$ for the upper limit, $c_1 = 0.4 \times 10^{-8}$ and $r_2 = 10$ for the lower limit

(Table 2). That lower-limit spectral transfer rates are smaller than the upper limit indicates that interactions with background scales smaller than those of the test wave do not average to zero in ray-tracing simulations.

Parameterization (6.1) compares favorably with previous shear- and strain-based scaling and *Polzin et al.*'s (1995) observations (Fig. 14). For the models, the ratio R_ω is varied by fixing the shear variance at its GM value and varying the strain variance. Observations are normalized by measured $\langle V_z^2 \rangle^2$ to compensate for nonconstant shear spectral levels. Two points relevant to this as well as previous papers (*Gregg* 1989; *Wijesekera et al.* 1993; *Polzin et al.* 1995) must be stressed:

- extensions of GM-based parameterizations to non-GM spectral shapes have not been theoretically or numerically justified. All existing numerical or theoretical analyses are only applicable to exact GM spectra with $R_\omega = 3$.
- GM-based parameterizations [e.g., our (4.6) and (4.10); *Heney et al.* 1986; *McComas and Müller* 1981b] can be arbitrarily rewritten in different forms (e.g., based on shear or strain variance) using relationships specific to GM model. While these alternate expressions agree with each other for GM spectral shapes, they give different predictions for ϵ if the internal wave field deviates from GM (for example, through varying shear-to-strain ratio, Fig. 14a).

With these two caveats in mind, Fig. 14 shows that *Polzin et al.*'s (1995) observations lie between the upper and lower limits of the shear-and-strain parameterization (6.1). Near the GM shear-to-strain ratio ($R_\omega = 2.9$), the observations agree with our upper limit and with *McComas and Müller*'s (1981b) weak-triad predictions. They are significantly larger than *Heney et al.* and *Polzin et al.*'s predictions. However, these data come from a decidedly non-GM wave field on the flanks of Fieberling Seamount where critical reflection and lee-wave generation elevate the high-frequency part of the spectrum (*Eriksen* 1998; *Toole et al.* 1997). Higher-than-GM shear-to-strain ratios are typical of the open ocean ($4.6 \cdot R_\omega \cdot 17$). That is, the ocean interior internal wave field is more inertial than the GM model. At these higher shear-to-strain ratios, the observations approach the lower limit of (6.1) and better agree with *Polzin et al.*'s extended model. Additional observations are needed to test the parameterizations over a broader range of shear-to-strain ratio.

7. Discussion

Ray tracing has been used to study internal wave/wave interactions and estimate the rate of spectral energy transfer toward high vertical wavenumber and turbulence

production (Henyey *et al.* 1986). Whether a test wave's evolution is controlled by background near-inertial shear or higher-frequency vertical divergence in this approach depends on its frequency compared to those of the dominant background shear and vertical divergence. Vertical divergence dominates the evolution of near-inertial waves even if only low-frequency vertical divergence is considered.

7.1 Comparison with Weak-Triad Method

7.1.1 Differences. The ray-tracing approach differs from weak-triad interaction theory in its assumptions and methodology for calculating the spectral energy transfer. Ray-tracing is not restricted to resonant-triad interactions. Nor does it require that the interaction timescale be long compared to the decorrelation timescale of internal wave field. However, ray-tracing does require that test waves be smaller than the background ($\Omega < \omega$, $K_i < k_i$) and that smallscale test waves not modify the larger-scale background while weak-triad interaction theory does not have these limitations. Ambiguity in applying WKB scale-separation for $\Omega < \omega$, $K_i < k_i$ versus omitting some interactions introduces factor-of-two uncertainty in shear-only estimates of the spectral energy transfer rate, and factor-of-four uncertainty in shear-and-vertical-divergence estimates. It is also unclear whether the parametric subharmonic instability mechanism finds expression in the ray-tracing approach.

Ray tracing examines the energy transfer from large to small scales by following the evolution of smallscale test waves in GM background wave fields. Tracking the spectral action-flux of test waves leads to an estimate of the spectral energy transfer rate toward high vertical wavenumber. In the weak-triad method, spectral energy transfer through a fixed vertical wavenumber is calculated from the timescales for induced diffusion and parametric subharmonic instability.

7.1.2 Similarities. Despite differences in their assumptions and methodology, the results of ray-tracing and weak-triad interaction theory share

- low-frequency shear controlling the behavior of high-frequency waves and higher-frequency vertical divergence playing an important role in the evolution of near-inertial waves;
- net spectral energy transfer toward high vertical wavenumber; and
- similar dependence of the spectral transfer rate on buoyancy frequency and spectral energy levels. Ray tracing provides a clear scenario of how background vertical divergence and shear affect smallscale test-wave behavior (Figs. 2–3). It reveals that low-frequency shear transports higher-frequency waves toward smaller scale and near-

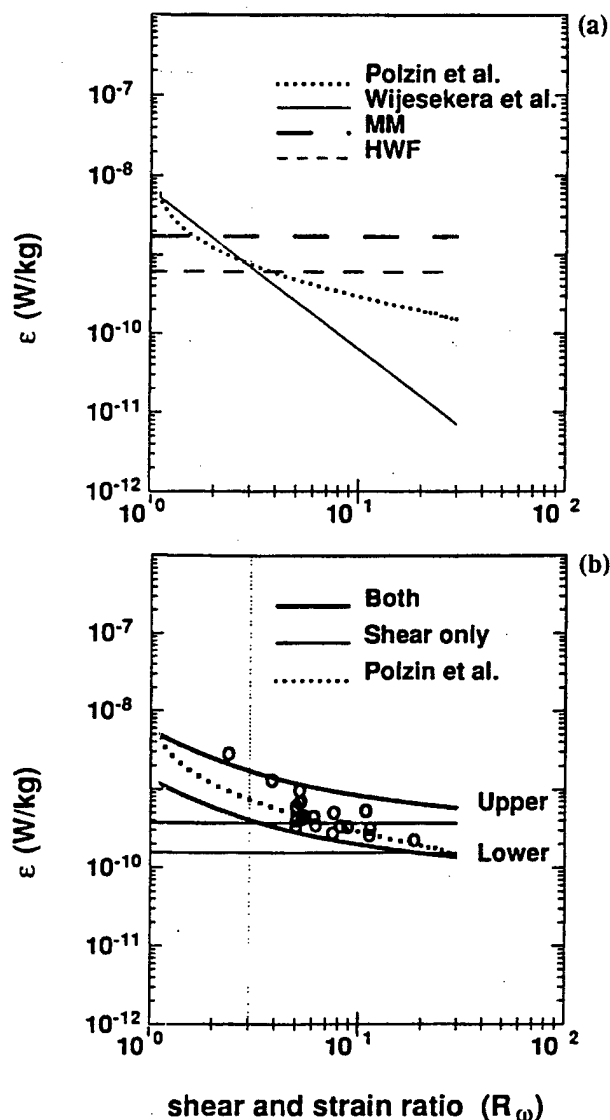


Figure 14. (a) Comparison of GM-based turbulent production models as functions of shear-to-strain ratio R_ω where shear variance is kept fixed at the GM value and strain varied. Models include strain-independent *McComas and Müller* (MM, 1981b) [thick dashed], strain-independent *Henyey et al.* (HWF, 1986) [thin dashed], shear- and strain-dependent *Polzin et al.* (PTS, 1995) [dotted], and strain-dependent *Wijesekera et al.* (WPDLP, 1993) [thin solid]. At non-GM shear-to-strain ratios, GM-based parameterizations are assumed valid without verification. (b) Comparison of upper and lower limits of shear-only parameterization (4.10) [thin horizontal lines], upper and lower limits of shear-and-strain parameterization (4.10) [thick solid curves], *Polzin et al.*'s (1995) observations (o) and *Polzin et al.*'s parameterization [dotted curve]. Observed dissipation rates have been normalized by $\langle V_z^2 \rangle^2 / \text{GM} \langle V_z^2 \rangle^2$ to compensate for nonconstant shear spectral levels. Observed ϵ fall between the upper and lower limits of our shear-and-strain parameterization, lying close to the lower limit and *Polzin et al.*'s parameterization for typical higher ratios.

inertial frequency. Once near-inertial, vertical divergence acts most effectively to force finescale test waves toward breaking wavenumbers. Weak-triad interaction theory mathematically isolates the mechanisms of vertical divergence (PSI) and shear (ID) to represent total spectral energy transfer by the two triad interactions. However, as in the ray-tracing approach, these two transfer mechanisms are coupled. Induced diffusion first sends higher-frequency internal waves toward low frequency. Then parametric subharmonic instability transfers small-scale, low-frequency waves to even smaller scale. Thus, weak-triad interactions imply a similar physical scenario as ray tracing. We caution that, while there are broad similarities between ray-tracing and weak-triad results, there is no rigorous justification for equating the mechanisms in the two approaches.

7.2 Implications of Vertical Divergence Interactions

Inclusion of interactions with vertical divergence as well as shear leads to predicted turbulence production rates for a GM internal wave field that are 2–4 times larger than shear-only ray-tracing predictions (Henyey *et al.* 1986). This might resolve the discrepancy between observed dissipation rates and the shear-only parameterization in the presence of enhanced high-frequency wave activity (Padman *et al.* 1991; Wijesekera *et al.* 1993; Polzin *et al.* 1995). In these papers, strain was proposed to capture the high-frequency dynamics in turbulent production missed by shear-only models. The work presented here suggests that it is vertical divergence that is *physically* responsible for transferring energy to high wavenumber. However, if the reversible part of vertical wavenumber flux (dk_z/dt) due to high-frequency vertical divergence is filtered over during a test wave's lifespan, a parameterization for the turbulent production can be expressed in terms of shear V_z and strain divided by the test-wave lifespan $\xi_z/\Delta t$ (4.10).

Recognizing the contribution from internal-wave vertical divergence in turbulence production may help understand the role of internal tides. At low and midlatitudes, internal tides have intrinsic frequencies higher than f and much lower than N . They can have broad wavenumber ranges depending on the topography that generates them and the oceanic conditions they propagate through (Prinsenbergh and Rattray 1975; Baines 1982; New 1988). Based on discussions in this paper, we speculate that internal-tide vertical divergence might interact with smallscale near-inertial waves to produce intensified turbulence. This scenario is consistent with recent theoretical work on parametric subharmonic instability of internal tides by Hirst (1996) and observations by Sun *et al.* (1996).

8. Summary

Numerical simulation indicates that the internal-wave spectral energy transfer rate toward high vertical wavenumber is controlled by vertical divergence W_z as well as vertical shear V_z . For interactions with the total GM model spectrum (Munk 1981), ray-tracing calculations that include vertical divergence predict turbulence production rates four times those of a shear-only ray-tracing model (Henyey *et al.* 1986) and observations. However, these estimates include interactions with background waves of higher horizontal wavenumber and frequency than the test waves, in violation of the WKB approximation. Confining interactions to background waves of larger vertical and horizontal scale, more commensurate with WKB scaling, reduces the shear-only contribution to ϵ by a factor of two and the shear-and-vertical-divergence contribution by a factor of four, implying shear-and-strain production rates consistent with upper-limit shear-only values (Henyey *et al.* 1986) and observations (Gregg 1989; Polzin *et al.* 1995).

A number of assumptions have been made for our ray-tracing internal wave/wave interactions. Fundamental to the ray-tracing approach are

- dominance of scale-separated wave/wave interactions so that the WKB approximation ($\lambda < \Lambda$) is applicable;
- smallscale test waves not significantly modifying the background.

The degree of scale-separation necessary for the validity of the WKB results is uncertain. As a sizable fraction of the net spectral energy transfer is associated with fine-scale waves that are not well scale-separated ($k_z \approx K_z$), this leads to uncertainty in quantitative estimates from the ray-tracing approach.

Following Henyey *et al.* (1986), Gregg (1989) and Polzin *et al.* (1995), we have assumed that

- the net rate of spectral energy transfer toward high vertical wavenumber is identical to the turbulence production rate $\epsilon(1 + \gamma)$;
- the turbulence production rate can be parameterized in terms of shear and strain variances;
- background vertical shear V_z and vertical divergence W_z are uncorrelated;
- all test waves lose their energy to turbulence when their vertical wavelength λ_z is forced below 5 m — simulations show little sensitivity to the breaking wavenumber;
- the spectral action-flux can be expressed with (5.1);
- finescale test-wave behavior can be described by the linear internal-wave dispersion relation.

The Munk (1981) version of the GM model spectrum was assumed to adequately describe the finescale internal wave field. This implies

- the internal-wave spectrum is separable in frequency and vertical wavenumber so that shear, strain and vertical divergence variances are dominated by the same high vertical wavenumber band;
- for wavenumbers, $k_z < k_{zc} = 0.08$ cpm, the internal-wave energy density spectrum has k_z^{-2} dependence on vertical wavenumber and ω^{-2} dependence on frequency so that shear is dominated by near-inertial frequencies, strain by higher but still low frequencies, and vertical divergence by high frequencies;
- at fine scales, $k_z > k_{zc} = 0.08$ cpm, the energy density spectra has a k_z^{-3} dependence on vertical wavenumber, but the same ω^{-2} intrinsic frequency dependence as at lower wavenumber.

The Munk model has less finescale variance than the GM76 model (Gregg and Kunze 1991). The intrinsic frequency spectrum is not well-known at the finescale because of Doppler-shifting (Kunze *et al.* 1990; Sherman and Pinkel 1991; Anderson 1993). Figures 4 and 5 suggest that the equilibrium finescale frequency spectrum may have a gentler slope than GM.

Unlike previous ray-tracing internal wave/wave investigations, we have

- included interactions with background internal wave vertical divergence,
- used test-wave lifespan averages to filter out the highest frequency contributions to the vertical divergence, and
- explored the consequences of applying WKB scale-separation to the horizontal wavenumbers $K_H < k_h$ for background frequencies $\Omega > 11f$.

Parameterizations (4.6) and (6.1) [derived from (4.10)] of the turbulence production rate $\epsilon(1 + \gamma)$ were proposed for GM spectral shapes with coefficients deduced from numerical ray-tracing simulations. Equation (4.6) expresses the turbulence production rate in terms of shear and vertical divergence. It assumes that total GM variances contribute to spectral energy transfer.

Since some high-frequency vertical divergence effects may be reversible over test-wave lifespans, and the simulations do not satisfy WKB scale-separation in the horizontal or time, (4.6) is likely an overestimate. To account for averages over test-wave lifespans, (6.1) expresses the turbulence production rate in terms of shear and strain. Two sets of coefficients were obtained for (6.1) from numerical simulations: an upper limit where interactions are allowed with the total background GM

wave field except background vertical wavenumbers $K_z > k_z$, and a lower limit restricting background vertical wavenumbers $K_z < 0.5k_z$ and horizontal wavenumbers $K_H < k_h$ for frequencies $\Omega > 11f$. Application of strict WKB scale-separation, $K_H < k_h$ or $\Omega < \omega$, caused a significant fraction of test waves to stall at low k_h and low ω before reaching the breaking wavenumber. Thus, strict WKB scale-separation cannot be realistically applied to the wave/wave ray-tracing problem. The above lower-limit criteria are used as a compromise.

We speculate that the lower-limit predictions from (6.1) are more realistic because they exclude reversible high-frequency contributions, are more consistent with WKB scale-separation, and are consistent with ocean interior observations (Fig. 14b). This is by no means certain, however, because interactions between finescale test waves and finescale backgrounds that cannot be described reliably under the WKB approximation may contribute a significant fraction of the total spectral energy transfer. This introduces a factor-of-four uncertainty in the shear-and-strain turbulence production rate estimates, and factor-of-two uncertainty in the shear-only estimates. While our upper-limit turbulence production rates are consistent with weak-triad results (McComas and Müller 1981b), weak-triad assumptions likewise break down on the finescale.

Although shear and vertical divergence are physically responsible for transferring internal waves to smaller scales (through dk_z/dt), it is unclear whether shear, strain (or vertical divergence) variances are sufficient to parameterize the spectral energy transfer rate $\epsilon(1 + \gamma)$. Both our numerical simulations and weak-triad interactions (McComas and Bretherton 1977) suggest that it is not be the highest frequency vertical divergence (section 4), nor the smallest-scale shear and vertical divergence (Fig. 13), that are most effective in transferring energy toward high vertical wavenumbers. The frequency- (section 4) and wavenumber-contents (Fig. 13) of the variances are also important. Our results, and those of Polzin *et al.* (1995), suggest that turbulence production is more sensitive to frequency-content. Nevertheless, it may be necessary to know frequency spectral shapes for shear and vertical divergence, and the degree of separability of the vertical wavenumber/frequency spectra, to accurately parameterize the turbulent production rate for the broad range of internal wave fields found in the ocean. Unfortunately, the finescale intrinsic frequency spectrum is difficult to measure directly because of both vertical and horizontal Doppler-smearing (Kunze *et al.* 1990; Sherman and Pinkel 1991; Anderson 1993; Sun *et al.* 1996).

This paper suggests a significant role for low-frequency vertical divergence in the production of

turbulence. Parameterization (6.1) in principle incorporates non-GM spectral shapes and compares favorably with observations (Fig. 14b). However, further work is needed to address the above issues and develop a robust turbulent production rate parameterization for the range of non-GM internal wave spectral shapes found in the ocean. Without a robust approach for treating oceanic internal wave/wave interactions, the lower-limit parameterization is our best estimate. But it should be applied to non-GM fields with caution. Numerical primitive-equation models are one promising approach. Although not yet able to span the full range of scales involved in oceanic internal waves, Winters and D'Asaro (1997) found spectral energy transfer rates consistent with observations and our lower-limit estimates.

Acknowledgments. We are grateful to Frank Henyey for providing the basic numerical simulation code and much helpful guidance. We acknowledge valuable discussions with Kurt Polzin, Eric D'Asaro, Jim Riley, and Kraig Winter. This work is based on Haili Sun's Ph.D. dissertation and two accepted papers (Sun and Kunze 1999a,b) which were supported by NSF grant OCE 94-16056.

References

- Alford, M., and R. Pinkel, 1999: Observations of overturning in the thermocline: The context of ocean mixing. *J. Phys. Oceanogr.*, submitted.
- Anderson, S.P., 1993: Shear, strain and thermohaline vertical shear in the upper ocean. Ph.D. thesis, University of California, San Diego, 143 pp.
- Baines, P.G., 1982: On internal tide generation models. *Deep-Sea Res.*, **29**, 307–338.
- Bouleau, N., and D. Lepingle, 1993: Numerical methods for stochastic processes. John Wiley and Sons, New York, 351 pp.
- Briscoe, M.G., 1977: Gaussianity of internal waves. *J. Geophys. Res.*, **82**, 2117–2126.
- Cairns, J.L., and G.O. Williams, 1976: Internal wave observations from a midwater float, 2. *J. Geophys. Res.*, **81**, 1943–1950.
- Duda, T.F. and C.S. Cox, 1989: Vertical wave number spectra of velocity and shear at small internal wave scales, *J. Geophys. Res.*, **94**, 939–950.
- Eriksen, C.C., 1978: Measurements and models of finestructure, internal gravity waves, and wave breaking in the deep ocean. *J. Geophys. Res.*, **83**, 2989–3009.
- Eriksen, C.C., 1998: Internal wave reflection and mixing at Fieberling Guyot. *J. Geophys. Res.*, **103**, 2977–2994.
- Fofonoff, N.P., 1969: Spectral characteristics of internal waves in the ocean. *Deep-Sea Res.*, **16**(Suppl.), 58–71.
- Gargett, A.E., 1990: Do we really know how to scale the turbulent kinetic energy dissipation rate ϵ due to breaking of oceanic internal waves? *J. Geophys. Res.*, **95**, 15,971–15,974.
- Gargett, A.E., P.J. Hendricks, T.B. Sanford, T.R. Osborn, and A.J. Williams III, 1981: A composite spectrum of vertical shear in the ocean. *J. Phys. Oceanogr.*, **11**, 1258–1271.
- Gregg, M.C., and E. Kunze, 1991: Internal wave shear and strain in Santa Monica basin. *J. Geophys. Res.*, **96**, 16,709–16,719.
- Gregg, M.C., D.P. Winkel, and T.B. Sanford, 1993: Varieties of fully resolved spectra of vertical shear. *J. Phys. Oceanogr.*, **23**, 124–141.
- Gregg, M.C., E.A. D'Asaro, T.J. Shay, and N. Larson, 1986: Observations of persistent mixing and near-inertial internal waves. *J. Phys. Oceanogr.*, **16**, 856–885.
- Gregg, M.C., 1987: Diapynal mixing in the thermocline: A review. *J. Geophys. Res.*, **92**, 5249–5286.
- Gregg, M.C., 1989: Scaling turbulent dissipation in the thermocline. *J. Geophys. Res.*, **94**, 9686–9698.
- Haynes, P., and J. Anglade, 1997: Vertical-scale cascade in atmospheric tracers due to large-scale differential advection. *J. Atmos. Sci.*, **54**, 1121–1136.
- Henyey, F.S., 1984: Transport of small-scale internal waves toward microstructure. *Proc. 'Aha Huliko'a Hawaiian Winter Workshop*, P. Müller and D. Henderson, Eds., U. of Hawaii, Honolulu, pp. 201–219.
- Henyey, F.S., J. Wright, and S.M. Flatté, 1986: Energy and action flow through the internal wave field: An eikonal approach. *J. Geophys. Res.*, **91**, 8487–8495.
- Henyey, F.S., 1991: Scaling of internal wave model predictions for ϵ . *Proc. 'Aha Huliko'a Hawaiian Winter Workshop*, P. Müller and D. Henderson, Eds., U. Hawaii, Honolulu, pp. 233–236.
- Hines, C.O., 1991: The saturation of gravity waves in the middle atmosphere. Part II: Development of Doppler-spread theory. *J. Atmos. Sci.*, **48**, 1360–1379.
- Hirst, E.V., 1996: Resonant instability of internal tides. Ph.D. thesis, University of Washington, Seattle, WA, 92 pp.
- Holloway, G., 1980: Oceanic internal waves are not weak waves. *J. Phys. Oceanogr.*, **10**, 906–914.
- Itsweire, E.C., K.N. Helland and C.W. Van Atta, 1986: The evolution of grid-generated turbulence in a stably stratified fluid. *J. Fluid Mech.*, **162**, 299–238.
- Kunze, E., A.J. Williams III and M.G. Briscoe, 1990: Observations of shear and vertical stability from a neutrally buoyant float. *J. Geophys. Res.*, **95**, 18,127–18,142.
- Leaman, K.D., and T.B. Sanford, 1975: Vertical energy propagation of inertial waves: A vector spectral analysis of velocity profiles. *J. Geophys. Res.*, **80**, 1975–1978.
- Lighthill, J., 1978: *Waves in Fluids*. Cambridge University Press, Cambridge, 504 pp.
- McComas, C. H., and F.P. Bretherton, 1977: Resonant interactions of oceanic internal waves. *J. Geophys. Res.*, **83**, 1397–1412.
- McComas, C.H., and P. Müller, 1981a: Time scales of resonant interactions among oceanic internal waves. *J. Phys. Oceanogr.*, **11**, 139–147.
- McComas, C.H., and P. Müller, 1981b: The dynamic balance of internal waves. *J. Phys. Oceanogr.*, **11**, 970–986.
- McEwan, A.D., 1983: Internal mixing in stratified fluids. *J. Fluid Mech.*, **128**, 59–80.

- Müller, P., G. Holloway, F. Henyey and N. Pomphrey, 1986: Non-linear interactions among internal gravity waves. *Rev. Geophys.*, **24**, 493–536.
- Munk, W., 1981: Internal waves and small-scale processes. *Evolution of Physical Oceanography*, B.A. Warren and C. Wunsch, Eds., The MIT Press, pp. 264–291.
- New, A.L., 1988: Internal tidal mixing in the Bay of Biscay. *Deep-Sea Res.*, **35**, 691–709.
- Oakey, N.S., 1982: Determination of the rate of dissipation of turbulent kinetic energy from simultaneous temperature and velocity shear microstructure measurements. *J. Phys. Oceanogr.*, **12**, 256–271.
- Osborn, T.R., 1980: Estimates of the local rate of vertical diffusion from dissipation measurements. *J. Phys. Oceanogr.*, **10**, 83–89.
- Padman, L., T.M. Dillon, H.W. Wijesekera, M.D. Levine, C.A. Paulson and R. Pinkel, 1991: Internal wave dissipation in a non-Garrett-Munk ocean. *Proc. 'Aha Huliko'a Hawaiian Winter Workshop*, P. Müller and D. Henderson, Eds., U. of Hawaii, Honolulu, pp. 31–51.
- Pinkel, R., 1984: Doppler sonar observations of internal waves: The wavenumber-frequency spectrum. *J. Phys. Oceanogr.*, **14**, 1249–1270.
- Polzin, K., J.M. Toole and R.W. Schmitt, 1995: Finescale parameterizations of turbulent dissipation. *J. Phys. Oceanogr.*, **25**, 306–328.
- Prinsenbergh, S.J. and M. Rattray, 1975: Effects of continental slope and variable Brunt-Vaisala frequency on the coastal generation of internal tides. *Deep-Sea Res.*, **22**, 251–263.
- Sherman, J.T., and R. Pinkel, 1991: Estimates of the vertical wavenumber-frequency spectra of vertical shear and strain. *J. Phys. Oceanogr.*, **21**, 292–303.
- Smith, S.A., D.C. Fritts and T.E. Van Zandt, 1987: Evidence of a saturation spectrum of atmospheric gravity waves. *J. Atmos. Sci.*, **44**, 1404–1410.
- Sun, H., E. Kunze and A.J. Williams III, 1996: Vertical heat-flux measurements from a neutrally buoyant float. *J. Phys. Oceanogr.*, **26**, 984–1001.
- Sun, H., and E. Kunze, 1999a: Internal wave/wave interactions: Part I. The role of internal wave vertical divergence. *J. Phys. Oceanogr.*, **29**, in press.
- Sun, H. and E. Kunze, 1999b: Internal wave/wave interactions: Part II. Spectral energy transfer and turbulence production. *J. Phys. Oceanogr.*, **29**, in press.
- Thompson, R.O.R.Y., 1980: Efficiency of conversion of kinetic to potential energy by a breaking internal gravity waves. *J. Geophys. Res.*, **85**, 6631–6635.
- Toole, J.M., R.W. Schmitt, K.L. Polzin and E. Kunze, 1997: Near-boundary mixing above the flanks of a mid-latitude seamount. *J. Geophys. Res.*, **102**, 947–959.
- Wijesekera, H., L. Padman, T. Dillon, M. Levine, C. Paulson and R. Pinkel, 1993: The application of internal-wave dissipation models to a region of strong mixing. *J. Phys. Oceanogr.*, **23**, 269–286.
- Winters, K.B., and E.A. D'Asaro, 1997: Direct simulation of internal wave energy transfer. *J. Phys. Oceanogr.*, **27**, 1937–1945.

Appendix A: Scaling the Nonlinear Terms in the Equations of Motion

In this appendix, we scale the internal-wave equations of motion to determine which nonlinearities dominate the evolution of finescale waves in a GM background field. The scaling will assume the finescale motions scale with the internal-wave dispersion relation. This is not strictly correct but is a reasonable starting point (Fig. A1). The following relations will be used

$$\frac{w}{u} \sim \frac{k_h}{k_z} = \sqrt{\frac{\omega^2 - f^2}{N^2 - \omega^2}} \quad (\text{A1})$$

from continuity and the linear dispersion relation,

$$\frac{b}{u} \sim \frac{N^2 w}{\omega u} \sim \frac{N^2}{\omega} \sqrt{\frac{\omega^2 - f^2}{N^2 - \omega^2}} \quad (\text{A2})$$

from conservation of buoyancy and the linear dispersion relation, and

$$\frac{p}{u} \sim \frac{\sqrt{N^2 - \omega^2} \sqrt{\omega^2 - f^2}}{\omega k_z} \quad (\text{A3})$$

from conservation of vertical momentum.

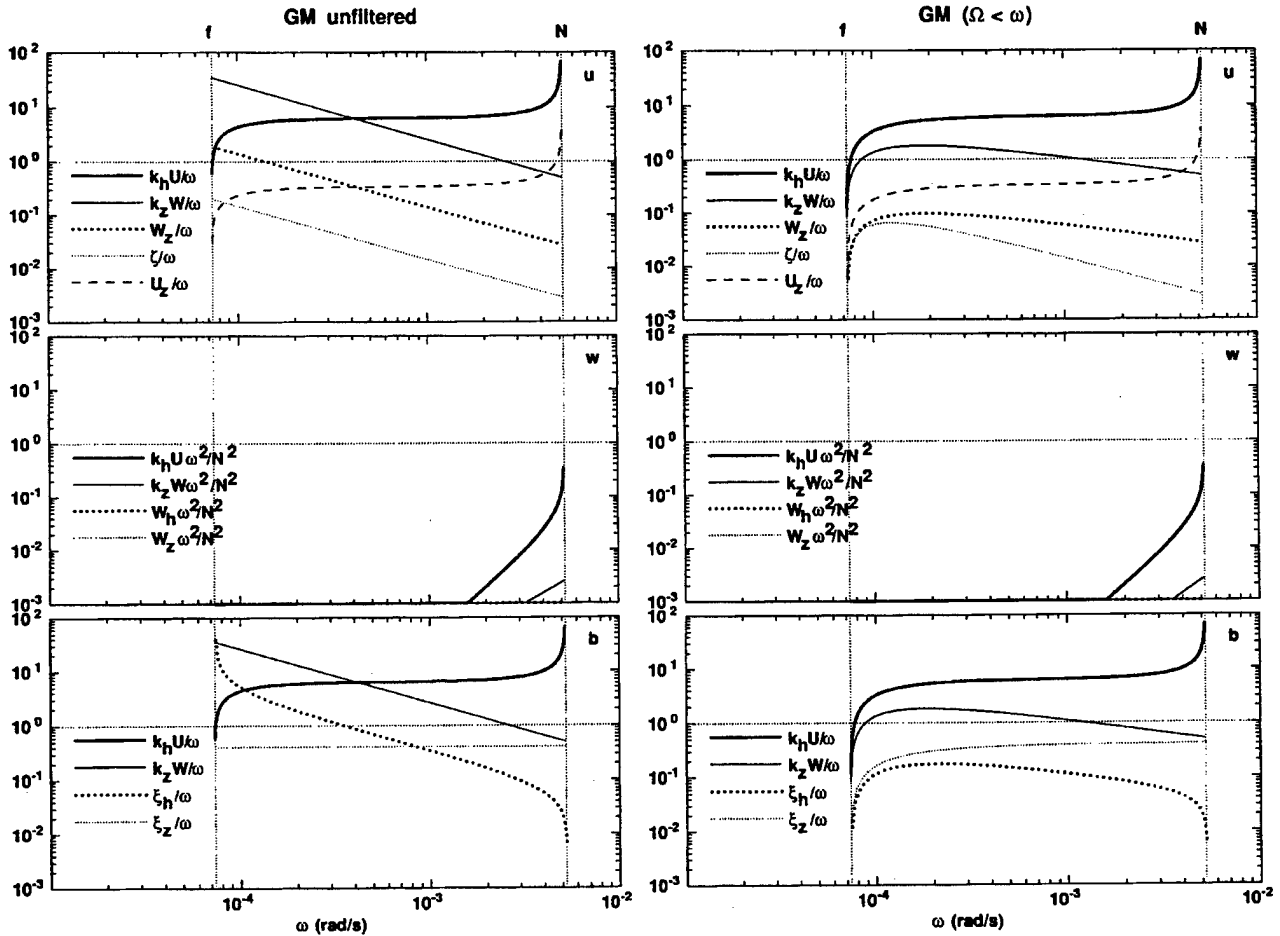


Figure A1. The normalized magnitude of nonlinear terms as a function of test-wave intrinsic frequency ω for a 10-m vertical wavelength test wave in a GM background internal wave field. Magnitudes are shown for nonlinear terms in conservation of horizontal momentum [upper panels, (A4)], vertical momentum [center panels, (A5)] and buoyancy [lower panels, (A6)]. In left panels, unfiltered rms backgrounds are used (all frequencies and horizontal wavenumbers), constrained only by the background vertical wavenumber being lower than the test wave's, $K_z < k_z$. In right panels, temporal filtering is applied ($\Omega < \omega$); this also guarantees horizontal filtering. In all cases, advection (solid curves) dominates over background gradient terms (dotted and dashed). In the strict WKB-filtered case (right panels), horizontal advection is 3–8 times larger than vertical advection and test-wave intrinsic frequency except at very near-inertial frequencies.

A.1 Horizontal Momentum

The zonal momentum balance can be expressed

$$u_t + (\mathbf{V}_H \cdot \nabla)u + W u_z + U_x u + U_y v \\ + U_z w - f v = -p_x$$

where lowercase variables represent the finescale test wave and uppercase the background wave field. The meridional conservation equation is similar. Substituting wave-like solutions and normalizing by the time rate of change, individual terms scale as

$$1; \frac{U k_z}{\omega} \sqrt{\frac{\omega^2 - f^2}{N^2 - \omega^2}}; \frac{W k_z}{\omega}; \frac{W_z}{2\omega}; \frac{\zeta}{2\omega}; \\ \frac{V_z}{2\omega} \sqrt{\frac{\omega^2 - f^2}{N^2 - \omega^2}}; \frac{f}{\omega} \sim \frac{N^2}{\omega^2} \frac{\omega^2 - f^2}{N^2 - \omega^2} \quad (\text{A4})$$

where U represents the background horizontal velocity, W the background vertical velocity, $-W_z$ the background horizontal divergence, ζ the rms vertical vorticity and V_z the background vertical shear. The second through sixth terms are nonlinear.

A.2 Vertical Momentum

The vertical momentum balance can be expressed

$$w_t + (\mathbf{V}_H \cdot \nabla)w + W w_z + W_x u + W_y v + W_z w \\ = -p_z + b.$$

which scales as

$$\frac{\omega^2}{N^2}; \frac{\omega U k_z}{N^2} \sqrt{\frac{\omega^2 - f^2}{N^2 - \omega^2}}; \frac{\omega W k_z}{N^2}; \\ \frac{\omega \nabla_H W}{N^2} \sqrt{\frac{N^2 - \omega^2}{\omega^2 - f^2}}; \frac{\omega W_z}{N^2} \sim \sqrt{\frac{\omega^2 - f^2}{N^2 - \omega^2}}; 1 \quad (\text{A5})$$

where $\nabla_H W$ represents the background horizontal shear of vertical velocity and W_z the background vertical divergence.

A.3 Buoyancy

Conservation of buoyancy can be expressed

$$b_t + (\mathbf{V}_H \cdot \nabla)b + W b_z + B_x u + B_y v \\ + N^2 w - N^2 Z_z w = 0$$

which scales as

$$1; \frac{U k_z}{\omega} \sqrt{\frac{\omega^2 - f^2}{N^2 - \omega^2}}; \frac{W k_z}{\omega}; \nabla_H Z_z \sqrt{\frac{N^2 - \omega^2}{\omega^2 - f^2}}; \\ 1; Z_z \sim 0 \quad (\text{A6})$$

where $\nabla_H Z$ represents the background isopycnal slope and Z_z the background vertical strain.

Figure A1 displays the magnitudes of the nonlinear terms in (A4–A6) as functions of test-wave intrinsic frequency ω . Background quantities were estimated as rms values from the Munk (1981) GM model spectrum. Test-wave wavenumber is $k_z = 2\pi/10$ m. Two cases are displayed. The ‘unfiltered’ case satisfies the vertical WKB constraint only (left panels) with background vertical wavenumber $K_z < k_z$. The ‘filtered’ additionally satisfies the temporal WKB constraint $\Omega < \omega$ (right panels, filtered).

Temporal and horizontal WKB approximation are both satisfied by choosing $\Omega < \omega$. From the internal-wave dispersion relation

$$K_H = \sqrt{\frac{\Omega^2 - f^2}{N^2 - \Omega^2}} K_z < \sqrt{\frac{\omega^2 - f^2}{N^2 - \omega^2}} k_z = k_h \quad (\text{A7})$$

provided $K_z < k_z$ and $\Omega < \omega$; $\Omega < \omega$ implies numerators $(\Omega^2 - f^2) < (\omega^2 - f^2)$ and denominators $(N^2 - \Omega^2) > (N^2 - \omega^2)$.

The vertical momentum equation is linear for all frequencies (Fig. A1). In both the filtered and unfiltered cases, advective nonlinear terms in the horizontal momentum and buoyancy equations exceed the intrinsic frequency by factors of at least 5 (except for very-near-inertial waves in the filtered case). This demonstrates that advection by background internal waves greatly exceeds the phase and group velocities of finescale internal waves at all but very-near-inertial frequencies. In the WKB-filtered case, horizontal advection dominates over vertical advection by factors of 3–30. While smaller than horizontal advection, vertical advection is significant at lower test-wave frequencies. Deforming or gradient nonlinear terms are smaller. In the unfiltered case, vertical divergence, vertical shearing and isopycnal tilting exceed the intrinsic frequency in different frequency bands. In a Lagrangian frame, where advection is absent, only vertical shearing and straining compare to the intrinsic frequency in magnitude for the WKB frequency scale-separated case.

Appendix B: Monte-Carlo Simulations of a Garrett-Munk Internal Wave Field

Density spectra can be treated as a probability density functions using Monte-Carlo methods (Bouleau and Lepingle 1993) to find random sampling schemes for background wave frequency Ω , mode number j , and amplitude V_0 in such a way as to reproduce the GM model spectrum for horizontal velocity (3.1).

B.1 Sampling Frequency Ω

The frequency dependence of (3.1) contains two terms, $(1 + f^2/\Omega^2)$ and $1/\Omega/\sqrt{\Omega^2 - f^2}$. We will utilize the first term to constrain the amplitudes of the U and V components based on the equations of motion for linear internal waves on the rotating earth. The second term will be used for the Monte-Carlo selection of wave frequencies. Integrating and normalizing the second term,

$$\frac{\int_{f_*}^f \frac{d\Omega}{\Omega \sqrt{\Omega^2 - f^2}}}{\int_{f_*}^f \frac{d\Omega}{\Omega \sqrt{\Omega^2 - f^2}}} = \frac{\cos\left(\frac{f}{\Omega}\right)}{\cos\left(\frac{f}{N_0}\right)} = \text{rnd}(e_1) \quad (\text{B1})$$

where $\text{rnd}(e_1)$ represents a random number in $[0, 1]$. In the following, we will use $\text{rnd}(e_1)$, $\text{rnd}(e_2)$...to indicate different random number sequences. Inverting (B1) for Ω , the sample scheme for background wave frequencies should be

$$\Omega = \frac{f}{\text{Arccos}[\cos(f/N_0)\text{rnd}(e_1)]} \quad (\text{B2})$$

B.2 Sampling Mode Number j

For numerical efficiency, mode numbers for background waves are divided into low ($j_* < j < j_{\text{sep}}$, $j_{\text{sep}} = 10$) and high ($j_{\text{sep}} < j < j_c$) mode number regimes. Low mode numbers, which dominate the background kinetic energy, are more densely sampled than high mode numbers. As with the frequency sampling (B2), we invert the normalized integration of the vertical mode number spectral shape

$$\frac{\int_{j_*}^j \frac{dj}{j^2 + j_*^2}}{\int_{j_*}^{j_{\text{sep}}} \frac{dj}{j^2 + j_*^2}} = \frac{\text{Arctan} \frac{j}{j_*} \frac{\pi}{4}}{\text{Arctan} \frac{j_{\text{sep}}}{j_*} \frac{\pi}{4}} \text{rnd}(e_2) \quad (\text{B3})$$

for j . The sampling scheme for low mode number j is then

$$j = j_* \tan \left[\frac{\pi}{4} + \text{Arctan}(j_{\text{sep}}/j_*) \text{rnd}(e_2) \right] \approx j_* \tan [\text{Arctan}(j_{\text{sep}}/j_*) \text{rnd}(e_2)] \quad (\text{B4})$$

for $j_* < j < j_{\text{sep}}$. Similarly, the sampling scheme for high mode number j is

$$j = j_{\text{sep}} \tan \left[\frac{\pi}{4} + \text{Arctan}(j_c/j_{\text{sep}}) \text{rnd}(e_3) \right] \approx j_{\text{sep}} \tan [\text{Arctan}(j_c/j_{\text{sep}}) \text{rnd}(e_3)] \quad (\text{B5})$$

for $j_{\text{sep}} < j < j_c$.

After selecting wave frequency Ω and mode number j , the horizontal wavenumber is determined from the internal-wave dispersion relation, with the direction of horizontal wavevector $\theta = \text{Arctan}(K_y/K_x)$ randomly chosen from $[0, 2\pi]$ to ensure horizontal isotropy.

B.3 Sampling Wave Amplitude

Background wave horizontal velocity amplitudes are sampled according to an exponential law approximating a Gaussian distribution (Briscoe 1977), i.e.,

$$V_0 = C \sqrt{\frac{2 \text{Arctan}(j_{\text{sep}}/j_*)}{\pi n_1}} \sqrt{-2 \ln[\text{rnd}(e_4)]} \quad \text{for } j < j_{\text{sep}} \\ = C \sqrt{\frac{2 \text{Arctan}(j_c/j_{\text{sep}})}{\pi n_2}} \sqrt{-2 \ln[\text{rnd}(e_5)]} \quad \text{for } j > j_{\text{sep}} \quad (\text{B6})$$

where coefficient $C = b \sqrt{N_0 N E_{\text{GM}}}$, n_1 and n_2 are the numbers of low and high mode-number waves selected in the Monte-Carlo process, respectively, such that $n_1 + n_2 = NW$, NW being the total number of background waves selected for the Monte-Carlo simulation.

Having selected NW wave frequencies Ω , vertical wavenumbers K_z and amplitudes V_0 , we can construct the 3-D wave field with Lagrangian variables $(x', y', z'(\rho), t')$. Defining the horizontal phase, vertical phase and horizontal propagation direction

$$\phi = K_x x' + K_y y' - \Omega t'$$

$$\psi = K_z z' = \frac{j\pi}{b} \sqrt{\frac{N^2 - \Omega^2}{N_0^2 - \Omega^2}} z'$$

$$\theta = \text{Arctan} \left(\frac{K_y}{K_x} \right) = 2\pi \text{rnd}(e_6)$$

then

$$U = \sum_{n=1}^{NW} (U_{rx} \cos \phi - U_{ix} \sin \phi) \cos \psi \quad (\text{B7})$$

$$V = \sum_{n=1}^{NW} (V_{ry} \cos \phi - V_{iy} \sin \phi) \cos \psi \quad (\text{B8})$$

where the amplitudes are

$$U_{rx} = V_0 \left[\frac{K_x}{K_h} \cos \theta + \frac{f}{\Omega} \frac{K_y}{K_h} \sin \theta \right] \quad (\text{B9})$$

$$U_{ix} = V_0 \left[\frac{K_x}{K_h} \sin \theta - \frac{f}{\Omega} \frac{K_y}{K_h} \cos \theta \right] \quad (\text{B10})$$

$$V_{ry} = V_0 \left[\frac{K_y}{K_h} \cos \theta - \frac{f}{\Omega} \frac{K_x}{K_h} \sin \theta \right] \quad (\text{B11})$$

$$V_{iy} = V_0 \left[\frac{K_y}{K_h} \sin \theta + \frac{f K_x}{\Omega K_h} \cos \theta \right] \quad (\text{B12})$$

The simulated background spectra reproduce the GM model spectrum (Fig. 1).

Appendix C: Coordinate Transformations

Here, we transform the ray-tracing equations into a semi-Lagrangian frame following wave-induced vertical displacements of isopycnals ξ but not horizontal internal-wave displacements χ and η . Assuming x', y', z', t' are Lagrangian variables, and x, y, z, t Eulerian, the semi-Lagrangian transform is

$$x' = x, y' = y, z' = z - \xi, t' = t$$

where the vertical displacement $\xi = \xi_0(x', y', z', t')$. The transformed derivatives are

$$\frac{\partial}{\partial x} = \frac{\partial}{\partial x'} - s \frac{\partial}{\partial z'} \xi_{x'}$$

$$\frac{\partial}{\partial y} = \frac{\partial}{\partial y'} - s \frac{\partial}{\partial z'} \xi_{y'}$$

$$\frac{\partial}{\partial z} = s \frac{\partial}{\partial z'}$$

$$\frac{\partial}{\partial t} = \frac{\partial}{\partial t'} - s \frac{\partial}{\partial z'} \xi_{t'}$$

where the Jacobian of the transformation is $s = 1/(1 + \xi_{z'})$. After transforming, the ray equations become

$$\frac{d'x'}{dt'} = \frac{\partial \omega_i}{\partial k_x} + U \quad (\text{C1})$$

$$\frac{d'y'}{dt'} = \frac{\partial \omega_i}{\partial k_y} + V \quad (\text{C2})$$

$$\frac{d'z'}{dt'} = \frac{\partial \omega_i}{\partial k_z} \quad (\text{C3})$$

$$\begin{aligned} \frac{d'k_x}{dt'} = & - \frac{\partial \omega_i}{\partial N_i} \frac{\partial N_i}{\partial x'} - k_x U_{x'} - k_y V_{x'} - k_z W_{x'} \\ & + s \xi_{x'} \left[\frac{\partial \omega_i}{\partial N_i} \frac{\partial N_i}{\partial z'} + k_x U_{z'} + k_y V_{z'} + k_z W_{z'} \right] \end{aligned} \quad (\text{C4})$$

$$\begin{aligned} \frac{d'k_y}{dt'} = & - \frac{\partial \omega_i}{\partial N_i} \frac{\partial N_i}{\partial y'} - k_x U_{y'} - k_y V_{y'} - k_z W_{y'} \\ & + s \xi_{y'} \left[\frac{\partial \omega_i}{\partial N_i} \frac{\partial N_i}{\partial z'} + k_x U_{z'} + k_y V_{z'} + k_z W_{z'} \right] \end{aligned} \quad (\text{C5})$$

$$\frac{d'k_z}{dt'} = -s \left[\frac{\partial \omega_i}{\partial N_i} \frac{\partial N_i}{\partial z'} + k_x U_{z'} + k_y V_{z'} + k_z W_{z'} \right]. \quad (\text{C6})$$

Here, $N_i^2 = N^2(1 + \xi_{z'})$ is the instantaneous buoyancy frequency squared, $N = N_0 e^{z/b}$ the background buoyancy frequency, d'/dt' the ray-following time derivative in semi-Lagrangian coordinates, and

$$\frac{\partial N_i}{\partial x'} = \frac{N^2}{2N_i} \xi_{x'z'}$$

$$\frac{\partial N_i}{\partial y'} = \frac{N^2}{2N_i} \xi_{y'z'}$$

$$\frac{\partial N_i}{\partial z'} = \frac{N^2}{2N_i} \xi_{z'z'} + \frac{N}{N_i} \frac{\partial N}{\partial z'} (1 + \xi_{z'})$$

where x', y', z' are Lagrangian variables following the vertical movement of the water.

Appendix D: GM Shear, Strain, Vertical Divergence and Action Spectra

The background GM shear, strain and vertical divergence spectra following Munk (1981) are

$$S[V_z](\Omega, K_z) = \frac{\pi}{b} A(\Omega) \frac{K_z^2 dK_z}{K_z^2 + K_z^2}$$

$$S[\xi_z](\Omega, K_z) = \frac{1}{N^2} \frac{\Omega^2 - f^2}{\Omega^2 + f^2} \cdot S[V_z](\Omega, K_z)$$

$$S[W_z](\Omega, K_z) = \frac{\Omega^2}{N^2} \frac{\Omega^2 - f^2}{\Omega^2 + f^2} \cdot S[V_z](\Omega, K_z)$$

where the frequency spectrum

$$A(\Omega) = \frac{4b^2 j^* f N_0 N^2 E_{GM}}{\pi^2} \left(1 + \frac{f^2}{\Omega^2} \right) \frac{1}{\Omega \sqrt{\Omega^2 - f^2}}$$

To compare test-wave action density spectra with the GM model, and to assign test waves an initial spectral action flux in section 3, the GM action density spectra

$$\begin{aligned} S[A](k_h, k_z, z) &= S[E/\omega](k_h, k_z, z) \\ &= \frac{4j^* b f N^2 E_{GM}}{\pi} \frac{k_z^2}{k_z^2 + k_z^2} \frac{\sqrt{N(z)^2 - f^2}}{[N(z)^2 k_h^2 + f^2 k_z^2]^{3/2}} \end{aligned}$$

Observations of Fine-Scale Richardson Number, Strain, and Effective Strain Rate Conditions Accompanying Overturning Events in the Thermocline

Matthew Alford

Applied Physics Laboratory, University of Washington, Seattle, WA

Robert Pinkel

Marine Physical Laboratory of the Scripps Institution of Oceanography, University of California San Diego, La Jolla, CA

Abstract. In an attempt to observe the time sequence of events which lead to internal wave breaking and ocean turbulence, a repeat profiling CTD and a coded-pulse doppler sonar are used in conjunction to sample the upper thermocline (100-400 m) during Feb/Mar 1995. The instruments were deployed from R/P FLIP, 30 km west of Point Argüello, CA, as an aspect of the Marine Boundary Layer Experiment. Depth/time series of 6.4-m shear S , 2-m strain ($\gamma \equiv \frac{N^2}{S^2}$, where N is the buoyancy frequency), 6.4-m gradient Richardson number $Ri \equiv \frac{N^2}{S^2}$ and 2-m "effective strain rate" $\frac{\partial \hat{w}}{\partial z} = \frac{1}{\gamma} \frac{\partial \gamma}{\partial t}$ (the depth derivative of CTD-inferred vertical velocity \hat{w}) are obtained at 4 minute intervals over a 9-day, 100-400 m domain. The occurrence of overturns, static instabilities of vertical scale ≥ 2 m in the observed density profiles, is monitored. Data are examined in both Eulerian and isopycnal following (semi-Lagrangian) reference frames. Over two thousand overturns are detected and mapped relative to the background shear, strain, Ri and strain rate fields. Correspondence between low values of 6.4-m Ri and overturns is indeed significant. However, 2-m γ and $|\frac{\partial \hat{w}}{\partial z}|$ appear to be better indices of overturning. $\gamma \geq 2$ in 60% of all overturning events. $|\frac{\partial \hat{w}}{\partial z}|$ is greater than average in 80% of overturns. Depth/time maps of effective strain rate show wave-like features on vertical scales 5-20 m, which extend coherently across isopycnal surfaces. We suggest that the overturns seen at this site result from breaking of these high $\frac{\partial \hat{w}}{\partial z}$ waves.

1. Introduction

Breaking internal waves appear to be the dominant source of ocean turbulence. Though open-ocean thermocline measurements of diapycnal diffusivity of $K_\rho \approx 10^{-5} \text{m}^2 \text{s}^{-1}$ from tracers [Ledwell et al., 1993] and microstructure (e.g., Gregg [1989]) are an order of magnitude too low to maintain the ocean's abyssal stratification (Munk [1966]; Munk and Wunsch [1999]), mixing near boundaries and topography can be much stronger. Intensified mixing (K_ρ up to $10^{-3} \text{m}^2 \text{s}^{-1}$) near, but hundreds of meters above, seamounts and ridges [Polzin et al., 1997] appears due to breaking of topographically generated, upward-propagating internal waves. In these

"hot-spot" locations as well as in the open ocean, we require a better understanding of the processes by which internal waves become unstable and break.

Observational [Gregg et al., 1986; Marmorino et al., 1987; Hebert et al., 1992; Moum et al., 1992] and theoretical [Henyey et al., 1986; Broutman and Young, 1986] studies have sought to identify the sequence of events which transfer energy from internal wave scales (vertical length scales of kilometers to a few meters, frequencies from f to N) to turbulent scales (meters to millimeters, frequencies higher than N). With quasi-continuous, semi-Lagrangian measurements of shear, strain, Ri and "effective strain rate," $\frac{\partial \hat{w}}{\partial z}$, which span 300 m in the ver-

tical and 9 days in time, we pursue this investigation. In particular, our goal is to determine the relationship between these fine-scale fields and the occurrence of large (≥ 2 m) overturns, static instabilities in the density field. Since they highlight the leadup to, rather than the aftermath of mixing, overturns provide a view of mixing which complements that gained by microstructure measurements. Microconductivity data from the same experiment are discussed in *Alford and Pinkel [1999b]*.

This paper presents a subset of the results of *Alford and Pinkel [1999a]*, henceforth AP99. Our approach is to present depth-time maps of the fine-scale quantities, on which the locations and times of overturns have been plotted. Anticipating a bit, we find correspondence between overturning and low 6.4-m Ri, supporting the well-documented importance of shear instability. However, high "effective strain rate" magnitude $|\frac{\partial \bar{w}}{\partial z}|$ is a better index of overturns than 6.4-m Ri, in our data. Depth-time maps of effective strain rate show coherent, wave-like features which cross isopycnals. If linear internal waves, they have wavelength ≈ 200 m and periods ≈ 7 hours. Instability of these waves (very possibly through shear instability) appears to be the most important cause of overturning at this site.

2. Observations and Methods

2.1. Experiment

An eight-beam Doppler sonar system and a repeat-profiling CTD (Fig. 1) were operated for 12 days during the first leg of the Marine Boundary Layer Experiment (MBL I), which took place in February and March of 1995. The experiment was sited approximately 30 km west of Point Argüello, California, in 1.5 km of water (Fig. 2). The 9-day mean buoyancy frequency profile (Fig. 3, heavy line) peaks at 7 cph at 30 m, dropping approximately exponentially to 2 cph at 400 m. The Research Platform FLIP was secured with a one-point mooring during the first part of the experiment (Fig. 2, "o"). Five days before the end of the experiment, on March 6 (yearday 66), the mooring was released and FLIP drifted freely towards the northwest (Fig. 2, "x").

Oceanographic conditions during the experiment, described in detail in AP99, are discussed briefly here. High shears and large baroclinic tidal displacements were present throughout the experiment. RMS 6.4-m shear was about 1.4 times the Garrett-Munk 1975 (GM) value, for depths above 250 m. Below this, mean shear increased with depth (RMS shear was 3 times the GM value at 400 m), suggesting a deep source of wave energy at the site. RMS baroclinic tidal displacements were typically 20-30 m. Larger (40-50 m) displacements occurring in a limited depth range near 150 m during

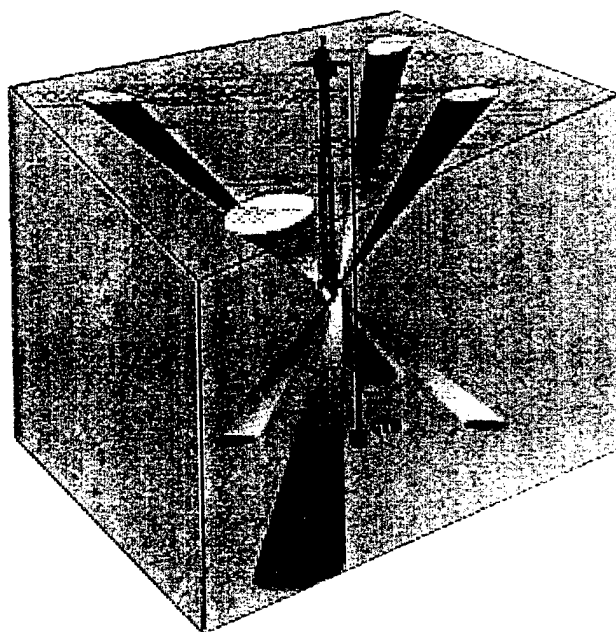


Figure 1. Schematic diagram of CTD and Doppler sonar aboard FLIP.

UTC 60-62 were associated with the passage of baroclinic energy along a tidal ray, presumably stemming from nearby topography.

2.2. CTD Observations

The CTD, a modified Sea-Bird Instruments SBE-9, profiles the upper 415 m of the water column every 4 minutes. The fall rate of the instruments is approximately 3.6 ms^{-1} . At this rate it is not necessary to pump the conductivity cell to assure adequate flushing. Data are sampled at 24 Hz, providing a measurement every 15 cm. Only the downcast of each drop is suitable for analysis; during the upcast the sensors are in the wake of the package. A Macintosh computer controls the CTD winch, reads and stores the data, and displays them in real time. An external clock ensures that the profiles are synchronized to the sonar, as well as to other onboard sensors.

To reduce the effects of salinity spiking, the cross spectrum between conductivity and temperature is estimated, using data from a region of near-uniform salinity. The data are corrected for effects of the thermal inertia of the conductivity cell, as described in *Lueck and Picklo [1990]* and *Morison et al. [1994]*. Temperature and conductivity are then low-pass filtered with a 2-m cutoff, and salinity and density are computed. The matching technique is described in more detail in *Anderson [1993]* and *Sherman [1989]*.

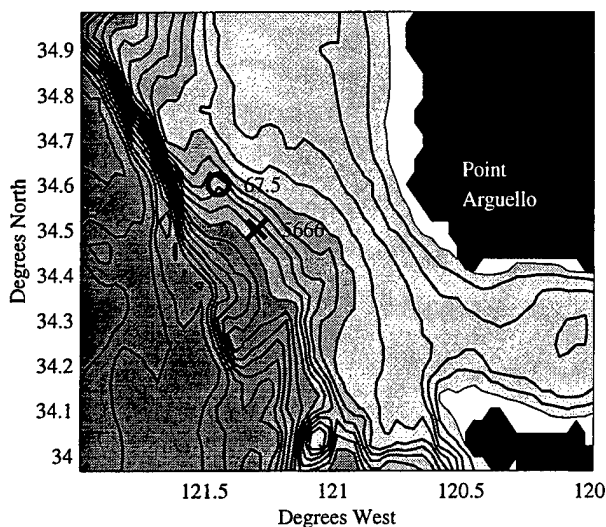


Figure 2. Location of the Marine Boundary Layer Experiment (MBL). Bathymetry contours in meters [Sandwell and Smith, 1996] are shown. The contour interval is 200 m, with 1000 m intervals indicated by increasing gray shading. FLIP was moored for the first portion of the experiment (black "x"). At UTC 66, the mooring line was severed. By UTC 67.5, FLIP had drifted to the position indicated by the black circle.

2.3. OvertURNS

Thermohaline intrusions, sensor noise and salinity spiking all make determination of the location and vertical extent of overturns from CTD data non-trivial (e.g., Galbraith and Kelley [1996]). Our procedure is described in more detail in AP99. Briefly, we compute composite Thorpe displacement [Thorpe, 1977] records from each profile of density ρ , temperature T , and electrical conductivity C . Only regions for which ρ , T and C invert, and which have a maximum Thorpe displacement $L_{\max} \geq 2m$, are termed overturns (Fig. 4). In all, we detected 2227 overturns over the 9-day period from 200-350 m, occupying 2.96% of the water column.

2.4. Sonar Observations

Designed and constructed at the Marine Physical Laboratory of the Scripps Institution of Oceanography, the Doppler sonar was mounted on the stern of FLIP at approximately 87 m depth (Fig. 1). It consists of four upward-looking (170 kHz) and four downward-looking (140 kHz) beams directed 30° from vertical. Only the downward-looking portion of the sonar data is used here. A repeat sequence code [Pinkel and Smith, 1992] consisting of 4 repeats of a 7 bit Barker code is transmitted. The bandwidth of the transmitted code is 1/(60

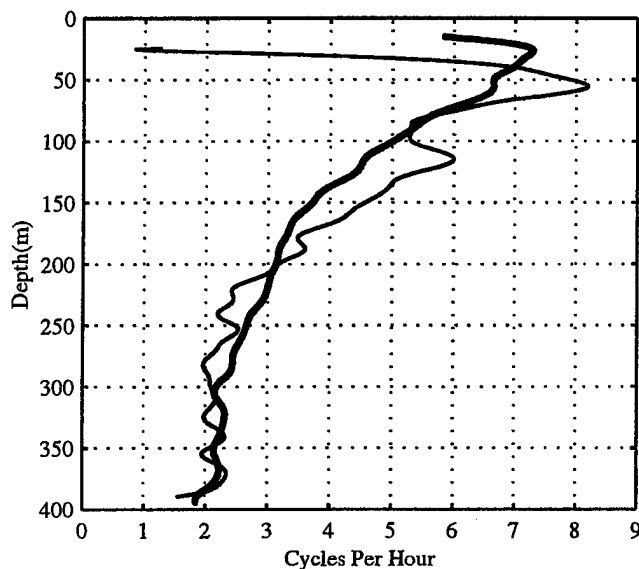


Figure 3. MBL 9-day (solid line) and 12-hour (yearday 67.5-68) mean (light line) buoyancy frequency profile.

ms). Vertical resolution is 3.2 m (data are sampled every 1.6 m). Transmissions are made every 1 s, and estimates recorded every minute. To improve precision and to enable integration with CTD data, 4-min averages are subsequently formed. These are aligned in time with the downward section of each CTD profile. The RMS precision of these 4 minute averages, estimated from frequency spectra, is 1.1 cm s^{-1} . The usable range of depths sampled by the downward-looking sonar is 100-500 m. Horizontal velocities are computed by averaging back-to-back beam velocities. Shear magnitude, S , is computed by differencing velocities over 6.4 m and then smoothing with a 6.4-m convolution filter.

The high quality of the MBL sonar enables the present examination of finescale Ri . Still, two aspects of the sonar affect S^2 (and therefore Ri) estimates. The horizontal separation of the beams biases S^2 low, since shear on horizontal scales comparable to the beam separation is underrepresented. Instrument noise biases S^2 high. These competing effects are discussed in detail in AP99.

3. Depth/Time Maps

3.1. Eulerian Maps

Representative 12-hour depth/time series of Eulerian 2-m strain $\gamma_{Eul}(t, z) \equiv [\frac{N^2(t, z)}{N^2(\rho(t, z))}]^{-1}$, 6.4-m shear squared anomaly $\hat{S}^2_{Eul}(t, z) \equiv \frac{S^2(t, z)}{S^2(\rho(t, z))}$ and 6.4-m $Ri_{Eul} = N^2/S^2$ are presented in Fig. 5. Twenty-three such 12-hour periods have been examined. Each 12 hour map

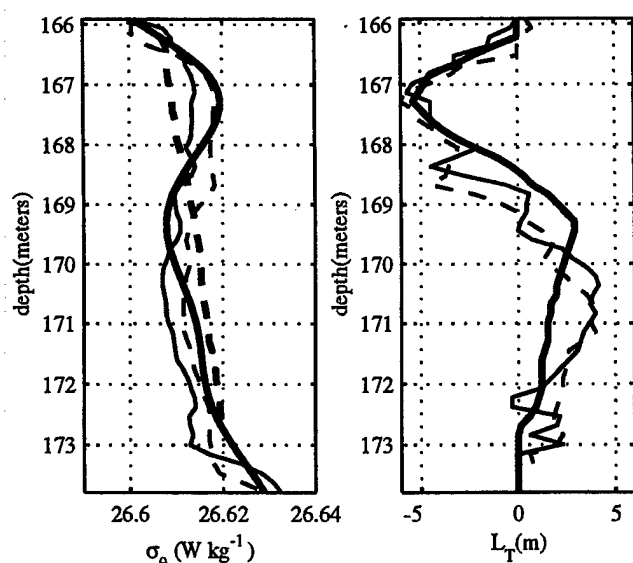


Figure 4. a. Full-resolution temperature (light solid line), conductivity (light dashed line) and 2-m density (heavy solid line) profiles for a sample overturn. T and C are expressed as equivalent densities $\rho_T = \alpha_T T + \beta_T$, $\rho_C = \alpha_C T + \beta_C$. The sorted density profile is plotted with a heavy dashed line. b. Thorpe displacements computed from temperature (light solid line), conductivity (light dashed line) and density (heavy solid line). All three measures of L_T must be comparable before the inversion is considered an overturn.

comprises 180 4-min profiles.

The 2-m Eulerian γ_{Eul} (Fig. 5a) represents the distortion of the water column by passing waves (It is also affected to a smaller degree by lateral intrusions – see AP99). By and large, strain features are advected vertically with the displacement field. However, some cross-isopycnal migration is seen (this aspect of the strain field will be seen more clearly in the s-L view). Notice the tendency of overturns (yellow-green dots) to lie in regions of high strain, low N .

The 64-m \hat{S}^2_{Eul} is characterized by “layers” of several hours duration (Fig. 5b). These are advected vertically by the isopycnal displacement field, as observed by Anderson [1993]. High frequency features are reproduced in the shear and displacement fields (e.g., the “wiggles” at yearday 67.63–67.65, 150 m).

Contributions to Ri may be examined separately in Figs. 5a and 5b; jointly in Fig. 5c. Layers of low Ri migrate vertically with time with an apparent (advection-affected) time scale of a few hours. By and large, these layers follow isopycnal surfaces. However, there are notable exceptions, which will be more apparent in the close-ups and semi-Lagrangian maps which follow.

Many overturns (black dots) lie in regions of low 6.4-

m Ri (e.g., yearday 67.93, 350 m, yearday 67.93, 350 m and yearday 67.94, 300 m). Larger scale internal waves vertically advect the latter region and associated overturns. In the large overturning region beginning at yearday 67.75, 375 m is centered on a low Ri , high shear layer but moves relative to it.

Some layers of 6.4-m Ri remain low for hours without any observed 2-m overturning (e.g., yearday 67.8–67.9, 350 m). Ri must remain sub-critical long enough for instability to develop, a time of order $\frac{4}{(|S|-2N)}$ [Hazel, 1972]. Therefore a one-to-one relationship between low Ri and overturning is not expected: for example, Kunze *et al.* [1990] noted a lack of one meter overturns in unstable 1-m Ri regions. But the lack of 2-m overturns in low 6.4-m Ri regions is surprising, and implies a significant separation between the scale of the unstable Ri and that of the resulting overturning. Alternately, $Ri \leq Ri_c$ (where Ri_c is a critical Richardson number) may be necessary, but not sufficient, for instability, as suggested by linear theory [Miles, 1961; Howard, 1961].

Seventy-four percent of overturns lie in regions of 6.4-m $Ri \geq 1$, 50% where 6.4-m $Ri \geq 2$. Regions at (67.75, 150 m), (yearday 67.95, 160 m) and (yearday 67.73, 340 m) are examples. Many such overturns lie in regions of either high strain or high effective strain rate magnitude (described below).

Recall that shear estimates (on which 6.4-m Ri is based) are increased by instrument noise and decreased by the finite beam separation of the sonar (AP99). We estimate that 6.4-m Ri estimates might be large by as much as a factor of $1/(0.6)$ relative to a “true” 6.4-m Ri estimate. In addition, vertical resolution is a concern: Ri decreases with decreasing vertical scale (e.g., Kunze *et al.* [1990]). Assuming a “canonical” shear spectrum white out to vertical wavenumber $m = 0.1$ cpm and falling off as m^{-1} thereafter [Gargett *et al.*, 1981], 6.4-m S^2 is only 55% of 2-m S^2 . Nevertheless, the observed large scale patterns are intriguing. Is (unresolved) shear between 6.4 m and 2 m sufficient to trigger 2-m overturns? The observations of extended regions of low 6.4-m Ri with no 2-m overturning, by contrast, are robust with respect to instrument concerns.

Apparent time variability in Fig. 5 and subsequent figures is due to true temporal modulation, as well as the advection of features past FLIP (AP99). FLIP-relative currents are $\approx 20 \text{ cm s}^{-1}$ toward the south-southwest during this period. In the absence of intrinsic temporal changes, an observed hour-long feature would correspond to a 720-m long structure drifting past at 20 cm s^{-1} . Attempts in later sections (3.4, 4.2) to assess the relative contributions of intrinsic and advective variability suggest that neither can be ignored.

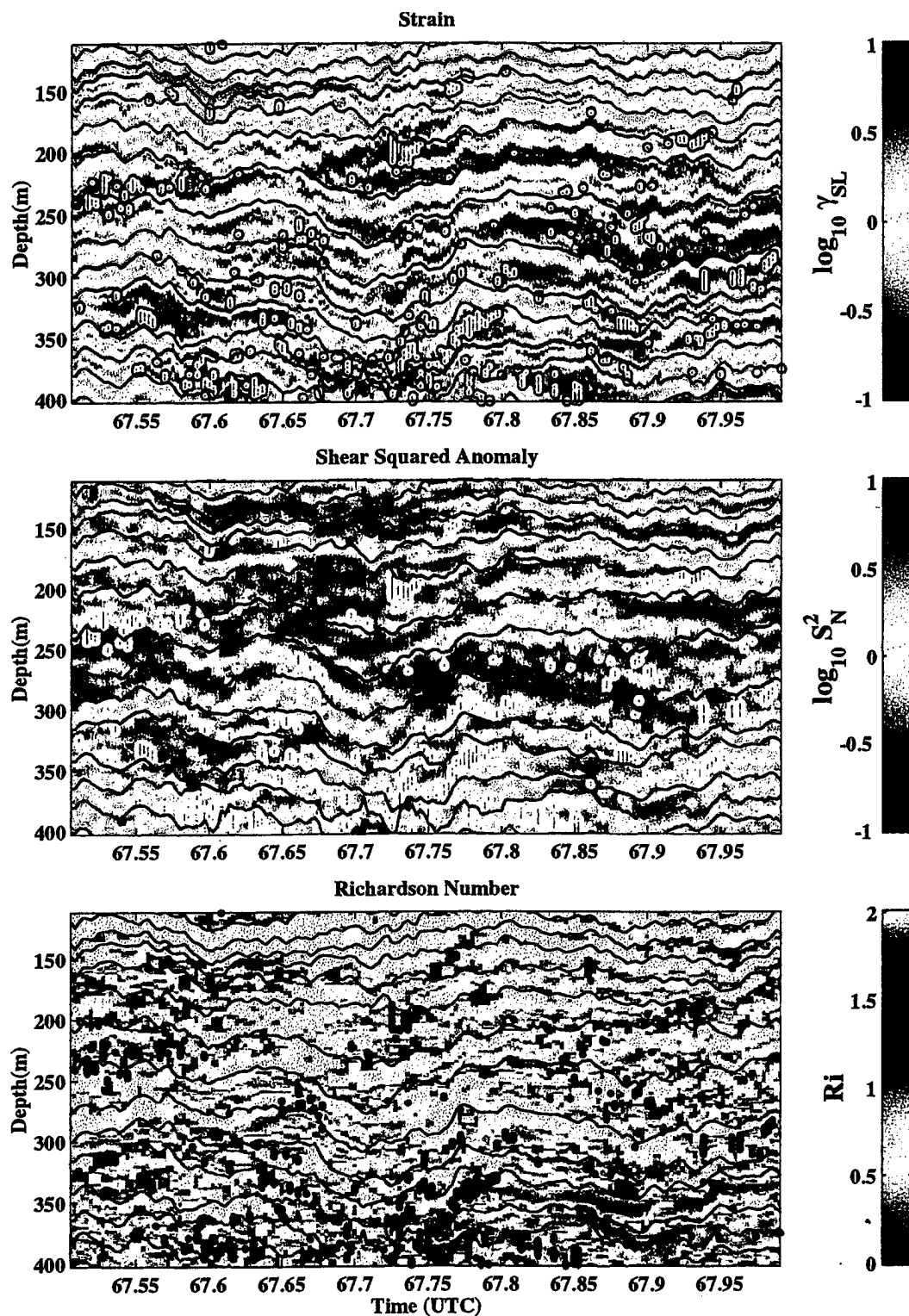


Figure 5. Eulerian 2-m strain $\gamma_{Eul} = \frac{\overline{N^2}}{N^2(z,t)}$ (a), 6.4-m shear squared anomaly (b) and 6.4-m $Ri \equiv \frac{N^2}{\overline{S^2}}$ (c), from yearday 1995 67.5–68.0 (12 hours). Each has been averaged over 12 min (3 profiles) in time prior to plotting. Blue colors in (a) indicate lower than average buoyancy frequency; red colors in (b) indicate higher-than-average shear; red colors in (c) indicate low 6.4-m Ri. Yellow-green (a,b) and black (c) dots mark the locations of overturns whose maximum Thorpe displacement $L_{max} \geq 2$ m. Solid black lines are isopycnal depths (20-m mean spacing).

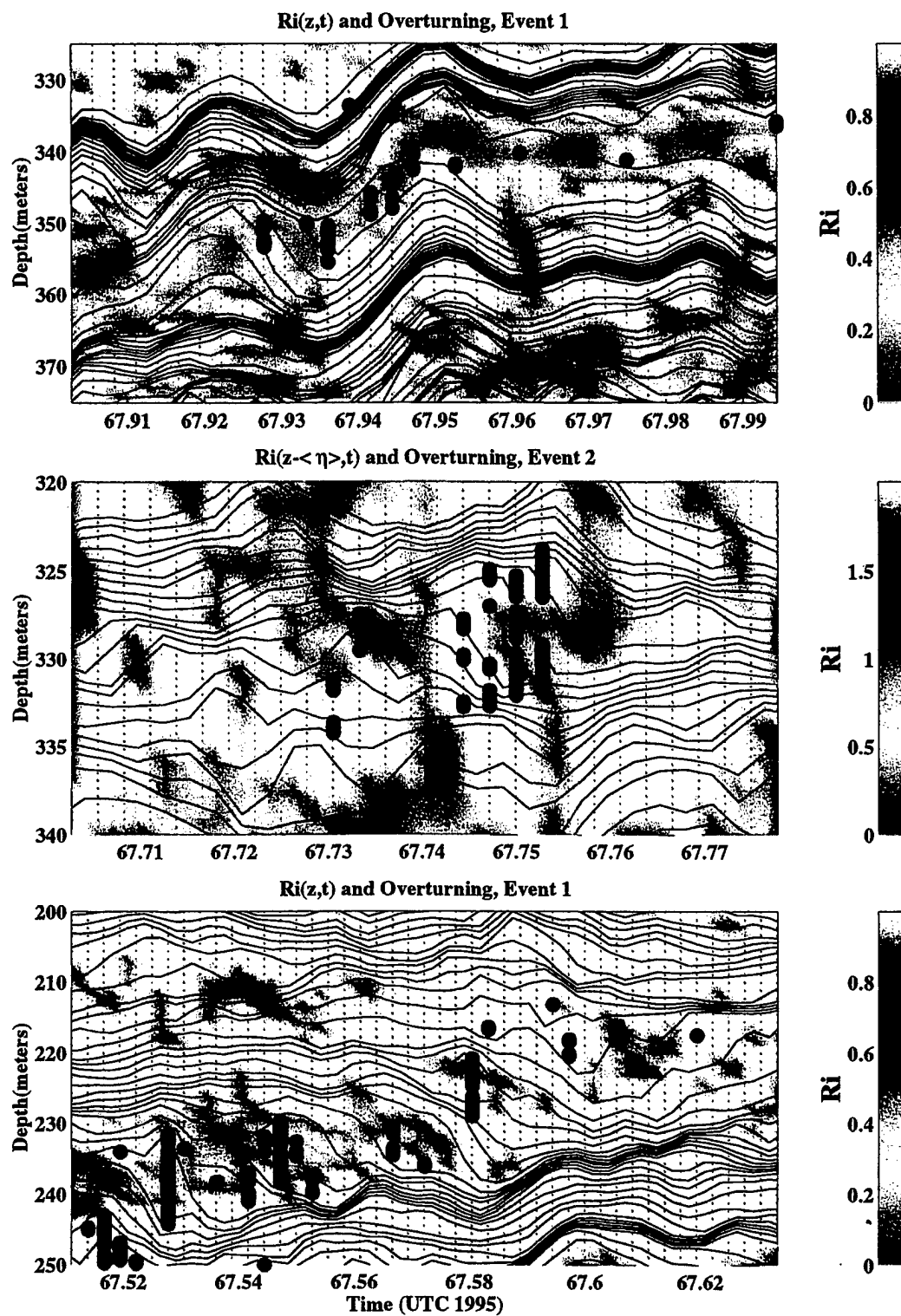


Figure 6. Close-ups of individual events. 6.4-m Ri is contoured, and isopycnals (1-m mean spacing) and overturn locations are plotted for three events. Note the increased color scale in (b). In (b) and (c) the depth-mean has been removed at each time. Blue dotted lines indicate times of individual CTD drops, spaced 4 minutes apart.

3.2. Case Studies of Instabilities

It is of value to examine several individual overturning events in detail. In Fig. 6, we present close-ups in depth (≤ 50 m) and time (≤ 3 hours) centered around three different overturning events seen in Fig. 5.

Figure 6a shows a series of overturning events associated with low 6.4-m Ri. Shear is high in this region, as evident from Fig. 5b. In addition, the buoyancy frequency is low, as indicated by a larger than average spacing between isopycnals. The region is sandwiched between higher gradient regions above and below. The feature crosses 5 isopycnals (moving towards less dense water) over the 3 hour period. It is also advected vertically with the background flow. Intermittent overturning is approximately centered on the shear maximum. We interpret Fig. 6a as a "classic" shear instability, caught in the act.

Figure 6b depicts a second event, where 6.4-m Ri is not low (The color scale has been extended so that white indicates $Ri \geq 2$, instead of $Ri \geq 1$ as in 6a and 6c). Scale differences (6.4 m for Ri, 2 m for overturns) and/or beam separation effects may be responsible for the poor correspondence. However, the event is also associated with the passage of a strain feature across these isopycnals, as seen by the large isopycnal separation. High wavenumber, high frequency motions make the isopycnals appear "jittery" in this region; these motions will be explored in detail in section 3.4. Overturning ceases when the feature propagates (or is advected) away.

A third example of an instability event is presented in Fig. 6c. It is associated with low 6.4-m Ri, as in Fig. 6a, and with the passage of a small scale disturbance as in Fig. 6b. Very large overturns are co-located with a high strain feature, which "peels off" isopycnals from above as it migrates vertically. Reminiscent of a spilling surface wave, overturning follows the wave feature as it migrates upwards.

3.3. Semi-Lagrangian Maps

It is also instructive to examine time variability in a semi-Lagrangian (isopycnal following, s-L) reference frame. The s-L frame is established by a set of reference isopycnals, $\{\rho_i\}$, whose mean depths are separated by 1 meter. The depth $z(t, \rho_i)$ and displacement $\eta(t, \rho_i) \equiv z(t, \rho_i) - \bar{z}(\rho_i)$ of each isopycnal are computed from each density profile (after sorting to remove inversions) by linear interpolation. Observations are expressed in an s-L frame by linear interpolation of the Eulerian data to the depths of the specific reference isopycnals.

In Fig. 7, semi-Lagrangian maps of strain, shear squared anomaly and Ri are presented from the same

time and depth range as the Eulerian fields in Fig. 5. Each map has been averaged over 24 min (6 profiles) in time prior to plotting (longer time averaging is possible in the s-L frame since smearing of features by vertical advection is avoided). The ordinate is not depth, but rather the isopycnal whose mean depth is indicated. Vertical excursions on a s-L plot imply cross-isopycnal migration, while horizontal variations indicate change at fixed density.

Contours surrounding regions of 6.4-m $Ri \leq 1$ have been plotted on Figs. 7a and 7b. Low-Ri regions are formed by both high shear and low strain; ignoring variations in either constituent is not justifiable.

The 2-m γ_{SL} features (Fig. 7a) slowly migrate across isopycnal surfaces; *e.g.*, at (yearday 67.77, 330 m) and (yearday 67.52, 250 m). They persist for several hours on average. Advection affects perceived cross-isopycnal migration: observed vertical excursions can represent true propagation, or sampling of spatially tilted features as they drift past.

Overturns, marked with yellow-green spots, demonstrate a clear tendency to lie in regions of high strain. Persistent, high strain features which exhibit overturning are reminiscent of the low-gradient, high-dissipation "patches" observed by Gregg *et al.* [1986] and by Marmorino *et al.* [1987]. Relative to 6.4-m shear (Fig. 5b) and 6.4-m Ri (Fig. 5c), changing (propagating) strain is often the best indicator of overturn locations.

3.4. Effective Strain Rate

An "effective strain rate" can be defined as

$$\frac{\partial \hat{w}}{\partial z} \approx \frac{\Delta \hat{w}}{\Delta z} = \frac{\partial / \partial t (\Delta z)}{\Delta z} = \frac{1}{\gamma} \frac{\partial \gamma}{\partial t}. \quad (1)$$

Here, Δz is the instantaneous separation between two isopycnals. To estimate $\frac{\partial \hat{w}}{\partial z}$, strain observations are differenced in time and divided by the normalized separation. Involving both the depth and time derivatives of isopycnal displacement, the effective strain rate, $\frac{\partial \hat{w}}{\partial z}$ emphasizes higher-frequency, higher-wavenumber constituents in the resolved displacement field.

Note that the lateral advection of horizontal structure complicates interpretation of this "strain rate." In fact,

$$\frac{\partial \hat{w}}{\partial z} = \frac{\partial w}{\partial z} + \partial / \partial z (\bar{u} \cdot \nabla_H \eta) \quad (2)$$

In the absence of horizontal advection, $\frac{\partial \hat{w}}{\partial z}$ equals the "vertical divergence" $\frac{\partial w}{\partial z}$, which appears in the ray-tracing equation governing the time rate of change of the vertical wavenumber of a Henyey/Broutman "test wave" [Sun and Kunze, 1998]. While $\frac{\partial \hat{w}}{\partial z}$ (computed here) is affected by horizontal advection, it is worth

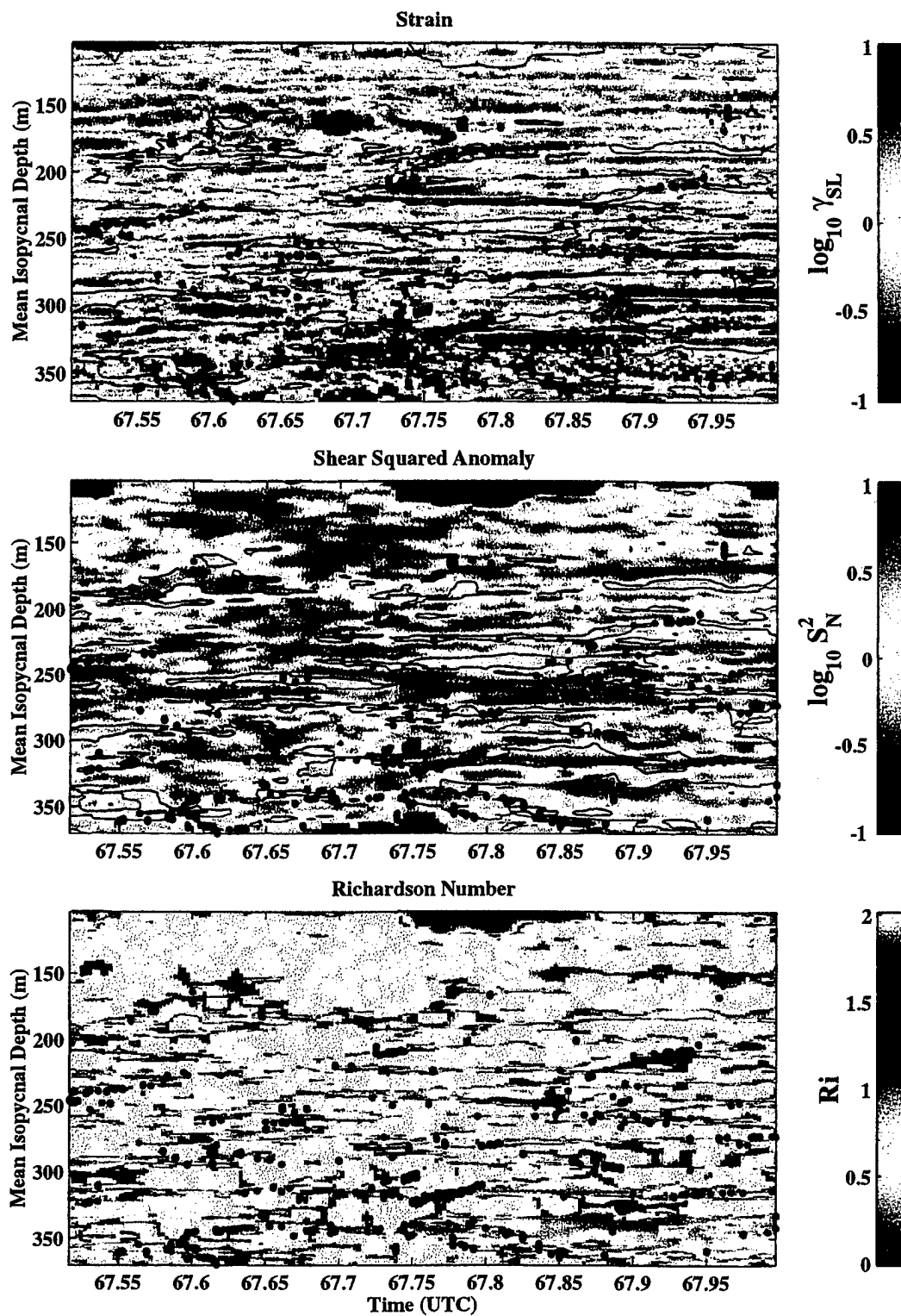


Figure 7. Semi-Lagrangian strain, 6.4-m shear squared anomaly and 6.4-m Ri , for the same depth range and period as in 5. Ordinate is the isopycnal whose mean depth is shown. Yellow-green (a,b) and black (c) dots indicate overturn locations as in 5. Solid black lines surround regions where $Ri \leq 1$.

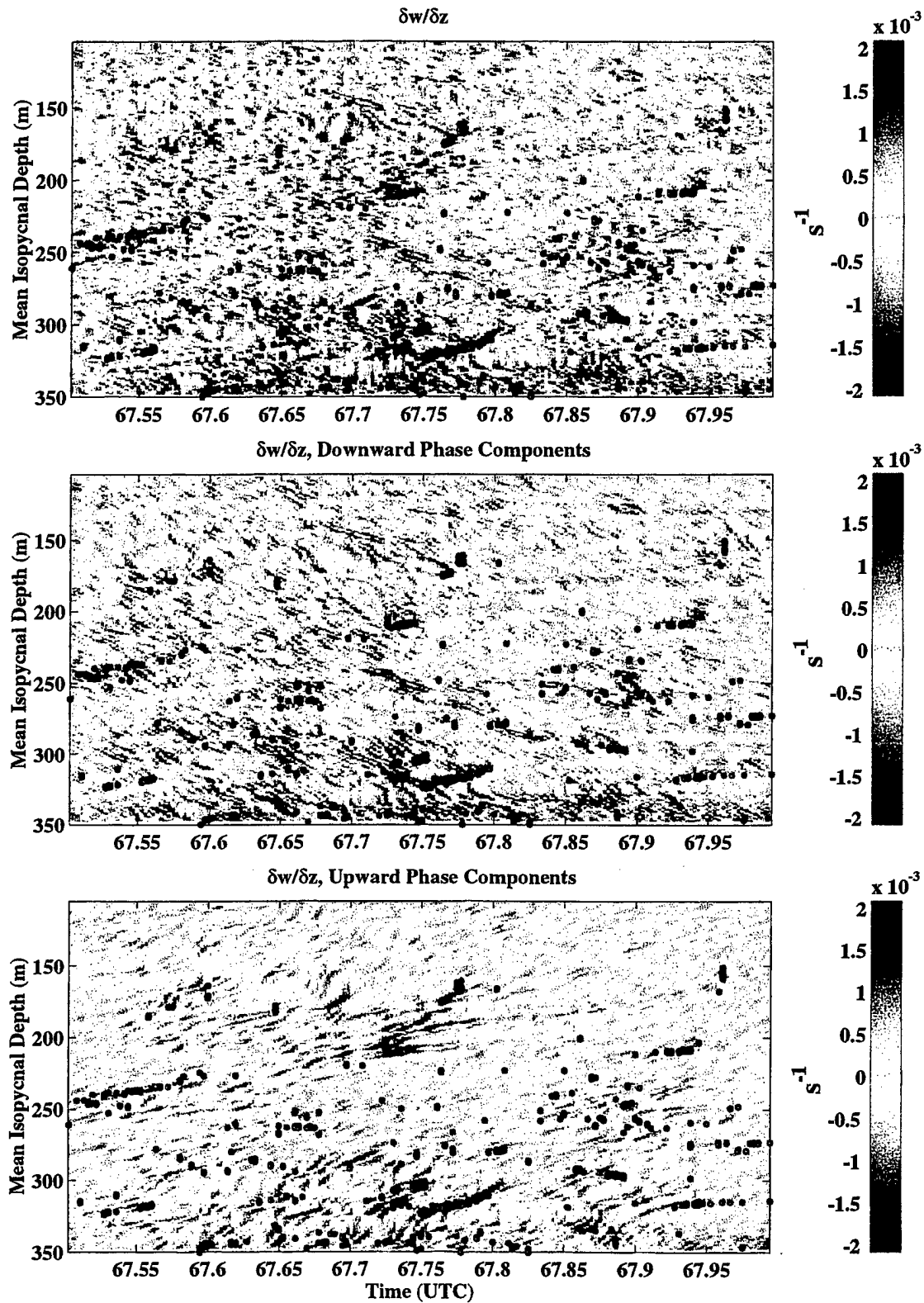


Figure 8. Depth/time map of s-L effective strain rate $\frac{\partial \hat{w}}{\partial z}$ (a). $\frac{\partial \hat{w}}{\partial z}$ is computed from s-L γ using equation 1, and smoothing over 2 bins in time, and 2 bins in depth. Wave propagation is more apparent when the field is separated into downward- (b) and upward-propagating (c) phase components. Yellow-green dots indicate overturn locations as in fig. 7.

pointing out that it is related to a quantity of dynamical interest.

Wavelike motions are seen in the $\frac{\partial \hat{w}}{\partial z}$ field (Fig. 8a)¹. Anticipated propagation phase speeds ($0.5 - 5 \text{ cm s}^{-1}$, see Appendix A) are lower than typical advective velocities (20 cm s^{-1}). Apparent sloping features may therefore represent sampling of slanted wave crests, in addition to true upward/downward propagation. These maps may thus be viewed as a combination of a "snapshot" of a frozen wavefield, swept past FLIP, and a "movie" of propagating waves.

To focus on the wavelike aspects of the $\frac{\partial \hat{w}}{\partial z}$ field, components of downward-propagating (Fig. 8b) and upward-propagating phase (Fig. 8c) are separated. These are formed by two-dimensional Fourier transform filtering of the depth/time series depicted in Fig. 8a.

Clear "groups" may be seen in both upward and downward fields, apparent as localized bursts of higher-amplitude wave crests. Notice the presence of upward-traveling groups, with downward-traveling phases (consistent with internal wave propagation): *e.g.*, Fig. 8b (yearday 67.73, 300 m), (yearday 67.53, 240 m) and (yearday 67.57, 170 m). Also common, however, are regions where group and phase are both up (*e.g.*, yearday 67.72, 200 m) or both down (*e.g.*, yearday 67.73, 250 m). These apparent non-propagating features are consistent with internal wave groups swept past FLIP.

Many ocean observations of internal wave groups have been made, some of which are discussed in the introduction. Still, our interpretation of the observed features as small-scale internal wave groups deserves comment. Other interpretations are possible, such as horizontal advection of quasipermanent density structures. However, it is hard to imagine how such explanations can account for the observed regular crest/trough patterns, groupiness and the presence of up/down features in the same region. The following two paragraphs examine in more detail the simpler interpretation of the features in these maps as internal wave groups. The skeptical reader is invited to regard this interpretation as a hypothesis to be tested with further observations.

First, what is the waves' frequency? The intrinsic frequency ω_{int} is difficult to determine, given the Doppler shifting of the waves by background currents and larger waves (Doppler shifting due to vertical motions is removed in an s-L frame). Still, simple estimates of horizontal wavenumber k and ω_{int} may be made by assuming a linear internal wave dispersion relation and advection by observed horizontal currents (Appendix

A). In a current of 20 cm s^{-1} , a typical wave of vertical wavenumber 0.08 cpm (12 m) and observed frequency 4 cph (like the feature at yearday 67.73, 300 m) would have ω_{int} near 0.14 cph (7 hours time scale) and k near $5.7 \times 10^{-3} \text{ cpm}$ (180 m wavelength), for a variety of propagation directions relative to the current. Advection can shift such waves from intrinsic time scales of hours to observed frequencies near N and higher. Uncertainties in velocity and encounter angle affect these estimates.

It is also instructive to consider the magnitude of fluctuations which would result from a single internal wave with displacement $\eta = a \sin(kx + mz - \omega t)$; k and m are horizontal and vertical wavenumbers, and ω is the intrinsic frequency. Then, $|\frac{\partial \hat{w}}{\partial z}| = am\omega$. To prevent isopycnals from crossing, $am = |\hat{\gamma}| \leq 1$. $\omega \leq N$ implies $|\frac{\partial \hat{w}}{\partial z}| \leq N = 5 \times 10^{-3} \text{ s}^{-1}$ (3 cph), representing an upper bound on single-wave "intrinsic" contributions to $\frac{\partial \hat{w}}{\partial z}$. Observed values are in this range (Fig. 8). On the other hand, the same wave swept past FLIP at velocity U would produce $|\frac{\partial \hat{w}}{\partial z}|_{adv}$ (the second term on the right hand side of equation 2) = $Ukma$. Taking $U = 20 \text{ cm s}^{-1}$ and $k = 1/(300 \text{ m})$, $|\frac{\partial \hat{w}}{\partial z}|_{adv} \leq 4 \times 10^{-3} \text{ s}^{-1}$ – the same order as the intrinsic term.

Based on the extremely simplistic considerations in the previous two paragraphs, the observed $\frac{\partial \hat{w}}{\partial z}$ features appear consistent with Doppler-shifted internal waves of intermediate frequencies. Still, their short duration and limited vertical propagation range suggest that they could be significantly nonlinear, violating the assumptions made in the intrinsic frequency calculation. A more detailed study of the dynamics of these waves is clearly called for, and will be the subject of a future paper.

Whatever their nature, overturns are much more likely to occur in their presence, which is indexed by high effective strain rate magnitude (Fig. 9), which highlights the envelopes of the small scale wave packets. For example, the instability event shown in close-up (Fig. 6c) is shown on this plot as a feature which begins at yearday 67.5, isopycnal number 250, and migrates upward. Most overturns lie inside the packet envelopes (yellow regions): 80% of observed overturns occur where $|\frac{\partial \hat{w}}{\partial z}| \geq 1.73 \times 10^{-6} \text{ s}^{-2}$, the 9-day mean value from 200-350 m. Regions with $6.4\text{-m Ri} \leq 1$ are also contoured in blue in each panel. Almost every overturn is encircled by either a blue or a yellow contour. Based on these observations, two types of phenomena appear to result in 2-m overturns: high 6.4-m shear layers, which are well resolved by the sonar, and internal wave groups, which are better indexed by CTD-inferred $|\frac{\partial \hat{w}}{\partial z}|$.

¹Imprecision in density estimates introduces $\text{RMS } |\frac{\partial \hat{w}}{\partial z}|_{\text{noise}} = 3.2 \times 10^{-4} \text{ s}^{-1}$ (AP99). The color scale of Fig. 8 is such that strong blue/red features are well above noise levels.

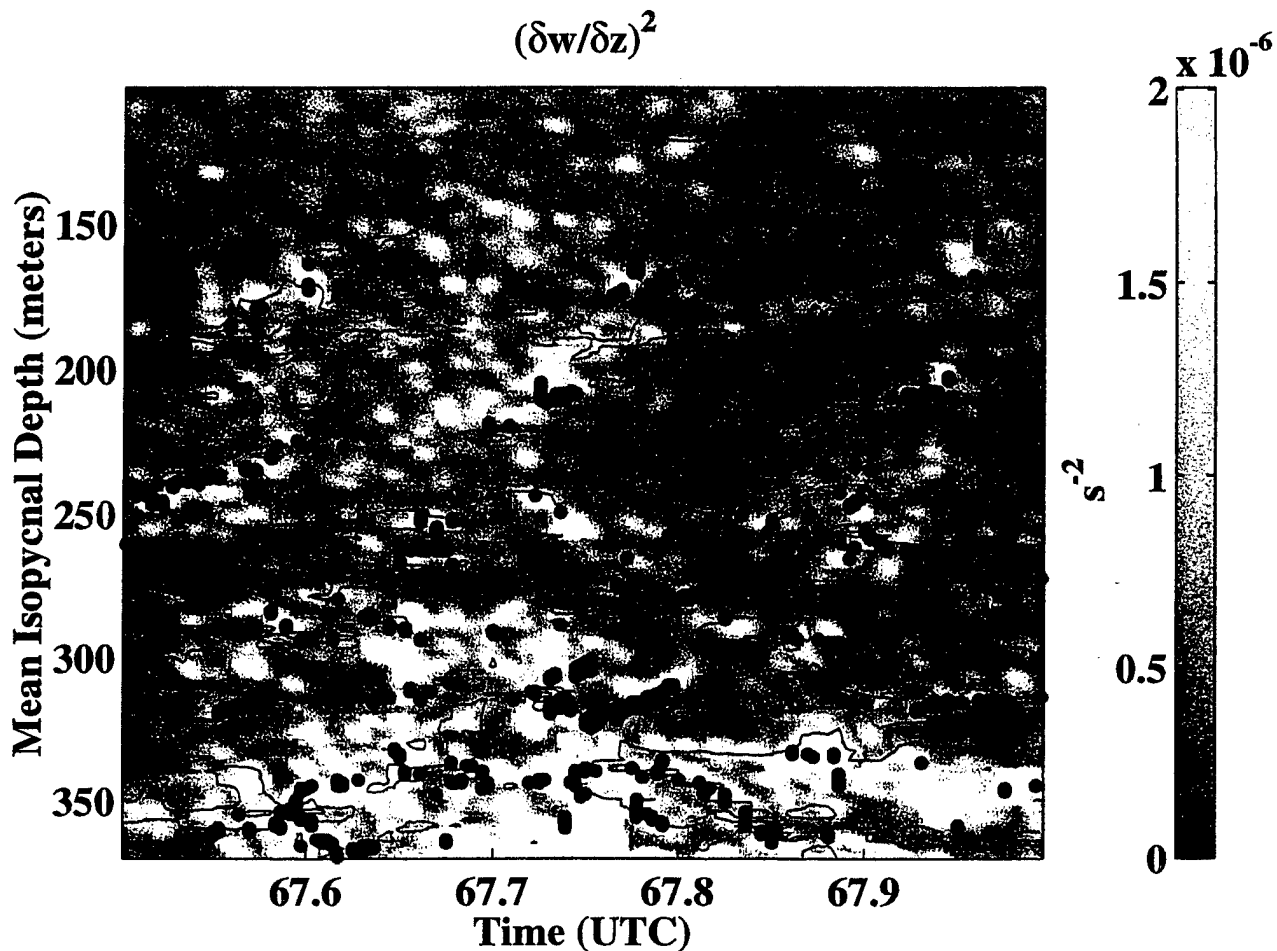


Figure 9. Effective strain rate squared, $(\frac{\partial \bar{w}}{\partial z})^2$. Data are smoothed over 4 isopycnals and 16 minutes in time, highlighting wave envelopes. Blue contours surround regions of $Ri \leq 1$. Black dots indicate overturns as in figs. 5-8.

4. A Statistical Summary of Overturning

Due to the size of the MBL data set, it is not possible to display depth/time maps of the entire cruise with the necessary detail. The last section examined one representative 12-hour period in detail. Here, general trends are summarized with statistical measures which employ the entire 9-day records. The analysis in this section centers around formation of probability density functions of the fine-scale quantities, using all observations from the 9-day, 200-350 m domain. These are then compared to corresponding PDF's computed using only observations at observed overturns (section 4.1), as well as before/after them (4.2). An analogous procedure using joint (rather than 1-D) probability density functions (PDF's) is employed in AP99.

4.1. Fine-scale Statistics: Overturns

To quantify the relationship between the various finescale fields and overturning, PDF's of Richardson number, strain, and effective strain rate are estimated. Separate PDF's of the total field (259,856 Eulerian data; 339,599 s-L data) and the subset of observed overturns (10,422 Eulerian data; 5522 s-L data) are created. The overturning totals are greater than the number of observed overturns (2227), since overturns can span multiple isopycnals and depth bins.

The PDF's of inverse Richardson number in the s-L frame (Fig. 10a) and the Eulerian frame (Fig. 10b) are in qualitative agreement with results of *Pinkel and Anderson* [1997]. In both reference frames, high values of Ri^{-1} are more likely when overturns are present (light black lines): 37% of overturns, compared with 30% of all observations, have $Ri_{s-L}^{-1} \geq 1$. In the Eulerian frame, 23% of overturns have $Ri_{Eul}^{-1} \geq 1$, compared with 16%

of all observations.

The PDF's of inverse strain for all data (Fig. 10c, heavy line) are qualitatively consistent with the gamma distribution of *Pinkel and Anderson [1992]*. When only overturning data are sampled (light line), the distribution is shifted towards lower values of inverse strain: overturns are much more likely to lie in regions which are less stratified than average. This is consistent with the conclusion drawn visually from the depth/time maps (Figs. 5a, 7a).

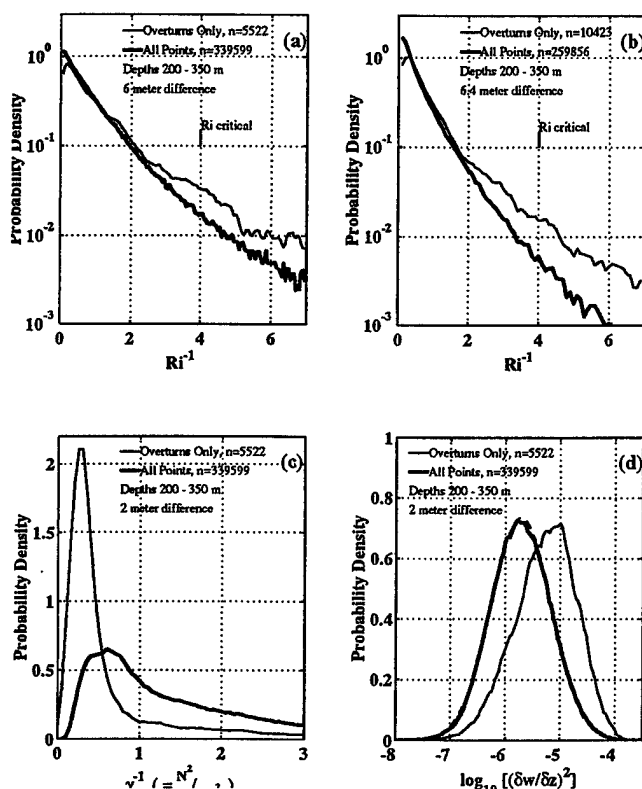


Figure 10. Probability density functions of s-L Ri^{-1} (a), Eulerian Ri^{-1} (b), s-L γ^{-1} (c) and $\log_{10}[(\partial w/\partial z)^2]$ (d). Heavy lines are computed using all observations from 200-350 m. Light lines represent observations at overturning regions. Overturning PDF's have been smoothed over $\Delta(Ri^{-1}) = 0.25$, $\Delta(\gamma^{-1}) = 0.25$ and $\Delta(\log_{10}[(\partial w/\partial z)^2]) = 0.20$, respectively. In (d) the dashed line (nearly obscured by the heavy line) is a Gaussian distribution with $\bar{y} = -5.67$, $\sigma = 0.56$.

The PDF of $\log_{10}[(\partial w/\partial z)^2]$ is presented in Fig. 10d. It is intriguing to observe that a quantity that seems to be intimately implicated with mixing should have a distribution indistinguishable from lognormal (dashed line). The PDF of $(\partial w/\partial z)^2$, considering overturning data only, is also roughly lognormal, but peaks at a higher value, demonstrating the tendency of overturns to occur where effective strain rate magnitude is large.

4.2. Fine-scale Statistics: Before and After Overturns

The previous section examined differences in statistics of finescale variables under "normal" and "unstable" conditions. That analysis is here extended to include not only overturns, but periods just before and just after overturns as well. The goal is to use statistics of many overturns to construct a schematic picture of finescale conditions before and after a representative "event". Can differences be detected between "leadup" and "aftermath" of overturns? Relevant issues are the degree to which observed before/after data represent the time history of one event (rather than just upstream/downstream samples of drifting features), and the amount by which overturns alter the surrounding flow.

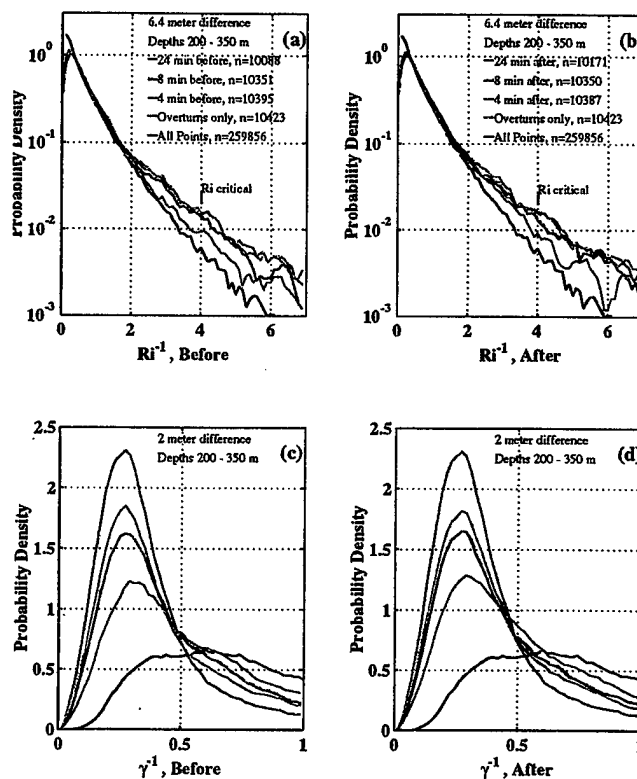


Figure 11. Probability density functions of Eulerian Ri^{-1} (a,b) and s-L γ^{-1} (c,d), computed using data before (a,c), and after (b,d) observed overturning events. In each, the black line is computed using all data. The red line is computed using data at overturning locations. Magenta, blue and green lines are computed using data 24, 8 and 4 min before/after observed overturns, respectively. Overturning and before/after PDF's have been smoothed as in figure 10.

Before/after PDF's of Ri^{-1} and γ^{-1} are presented in

Fig. 11, $(\frac{\partial \bar{w}}{\partial z})^2$ in Fig. 12. "Leadup" PDF's of Ri^{-1} (Fig. 11a), γ^{-1} (Fig. 11c) and $\frac{\partial \bar{w}}{\partial z}$ (Fig. 12a) are computed from data sampled 4 min (magenta line), 8 min (blue line), and 24 min (approx. one buoyancy period $1/N$, green line) before observed overturning events. PDF's of all data and overturning data (last section) are replotted in black and red, respectively. Figs. 11b,d and Fig. 12b are the corresponding "aftermath" PDF's, computed using data sampled after overturning events. The number of observations used in forming the various PDF's (noted in the legends of Fig. 11a,b) differs slightly, since overturns at the very beginning/end of the record cannot be used to form before/after PDF's, respectively.

The Ri^{-1} and γ^{-1} PDF's (Fig. 11) each comprise a family of curves leading smoothly from "normal" to "unstable" conditions (before: 11a,c), and back again (after: 11b,d). Conditions one buoyancy period before overturns (magenta line) are already distinguishable from "normal" conditions (black line): the probability of higher Ri^{-1} and lower γ^{-1} values is elevated. γ^{-1} PDF's continue a steady progress toward "unstable" conditions. By contrast, the 4-min and 8-min before Ri^{-1} PDF's are similar to the overturning PDF. Apparently, Ri^{-1} reaches the overturning value 4-8 min before a 2-m overturn is detectable.

No asymmetry is distinguishable between "before" and "after" in the Ri^{-1} and γ^{-1} curves. Two interpretations are possible. First, that true time dependence is not being observed. In this scenario, "before" and "after" represent spatially offset "upstream" and "downstream" samples. In an isotropic ocean, no asymmetry would be seen. Alternately, the similarity between the curves can mean that overturns affect the larger scale flow only little, as in spilling surface waves. Overturns occur without drastically affecting the Ri^{-1} and γ^{-1} fields.

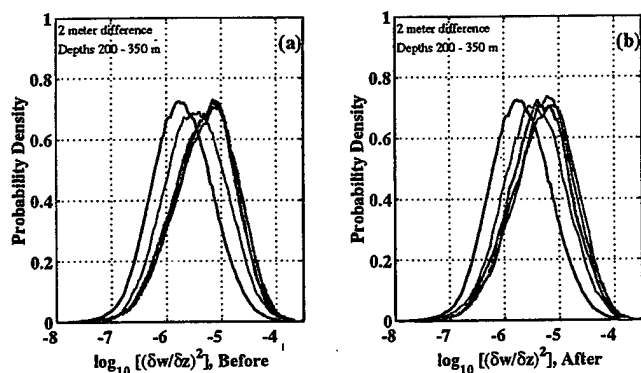


Figure 12. Probability density functions of $\frac{\partial \bar{w}}{\partial z}$, computed using data before (a), and after (b) observed overturning events. Colors are the same as in 11.

For effective strain rate, by contrast, differences are observed between before (12a) and after (12b) periods. Relative to the curve representing normal conditions, the 24-min before curve is shifted to the right. The 4,8-min before curves overlie the overturning curve, indicating that "overturning" conditions are present 8 min before overturns actually occur, as in the Ri^{-1} curves. After overturns, however, the behavior is different. A more rapid transition back to normal conditions is seen: the PDF's 4-min and 8-min after are shifted relative to the overturning curve. That is, $\frac{\partial \bar{w}}{\partial z}$ drops immediately after overturning occurs. The difference between before and after effective strain rate PDF's suggests that perceived variability is due to true temporal evolution, in addition to horizontal advection. Evidently, the $\frac{\partial \bar{w}}{\partial z}$ field is affected by overturning. Does instability in the small-scale waves result in their destruction, while leaving the larger-scale scale flow relatively unaffected?

5. Discussion

We have presented depth/time maps of fine-scale strain, shear, Ri and $\frac{\partial \bar{w}}{\partial z}$ from an energetic coastal site. The large range of depths (100-400 m) and lack of internal wave aliasing (Nyquist frequency $7.5 \text{ cph} \geq N$ for all depths) allow a unique view of fine-scale variability. Viewing these data in a semi-Lagrangian reference frame, we observe cross-isopycnal migration of wave-like disturbances.

Effective strain rate, $\frac{\partial \bar{w}}{\partial z}$, is the best index of such features. Though our relative lack of dynamical information about these "waves" is irksome, the observations themselves are robust. We have interpreted them as internal wave groups, a hypothesis that we hope will be tested with further observations. If they do have period 7 hours and horizontal wavelength $\lambda = 200 \text{ m}$ as we have calculated by assuming linearity, then their associated $Ri = 0.14$ (AP99) indicates that they are very susceptible to shear instability. Another consequence of their observed small vertical wavelengths, and implied small horizontal wavelengths, is that their shear is poorly resolved by the sonar ².

Our observations of increased overturning where 6.4-m Ri is low indicate that shear instability is indeed an important instability mechanism. Were the sonar able to fully resolve the shear associated with the $\frac{\partial \bar{w}}{\partial z}$ waves, the correlation would likely be much higher. However, even though at present they are only well resolved by the CTD, the $\frac{\partial \bar{w}}{\partial z}$ waves appear to be the ones which ac-

²The sonar does detect some of the waves' signature: s-L records of "slant shear" obtained from individual sonar beams (which suffer from limited vertical, but not horizontal, resolution) show clear correspondence with the CTD-based observations.

tually break. It is essential to understand the dynamics of these small-scale, vertically and diapycnally propagating waves.

6. Acknowledgments

The authors are indebted to Eric Slater, Lloyd Green, Mike Goldin, and Chris Neely for the design, construction, deployment, and at-sea operation of the sonar and CTD systems. The help and support of the captain and crew of FLIP is appreciated.

Appendix A: Estimating Intrinsic Frequency

Are the high frequency waves seen in MBL really high frequency? Advection by larger waves and background currents can cause a wave's observed frequency ω_{obs} to differ from its intrinsic frequency ω_{int} . The frequency shift depends on horizontal wavenumber k , the magnitude of the advective velocity \vec{U} , and the angle between current and wave propagation directions, θ :

$$\omega_{int} = \omega_{obs} - |k||U|\cos\theta \quad (A1)$$

Intrinsic frequency and horizontal wavenumber may be estimated using the dispersion relation for linear internal waves

$$\omega_{int} = \sqrt{\frac{N^2 k^2 + f^2 m^2}{k^2 + m^2}} \quad (A2)$$

Here, f is the Coriolis frequency, N the buoyancy frequency, and m the vertical wavenumber. θ is the angle between current and wave propagation directions. N , f , m , and ω_{obs} are observed quantities. Consider a representative, well-defined wave packet (Fig. 8b, 300 m and yearday 67.72), with $m = 0.08$ cpm, $\omega_{obs} = 4$ cph. Typical values of $|U|$ are 20 cm s^{-1} . Using $N = 2$ cph, $f \approx 1/24$ cph, and these values of m , ω_{obs} and $|U|$, curves A1 and A2 are plotted on the same axes, for different values of θ (Fig. A1). All frequencies and wavenumbers are expressed in cyclic units. The intersections of the colored curves with the gray one yield values of ω_{int} and k which are consistent with linear theory, for the indicated value of θ . Some Doppler shifting must have occurred, for the observed frequency $\omega_{obs} = 4$ cph is higher than local $N = 2$ cph. The minimum value of ω_{int} (assuming maximum Doppler shifting) is 0.14 cph (7 hour period). A lower bound on k is 5.7×10^{-3} cpm (180-m wavelength), implying a horizontal phase velocity $c_p = \omega/k = 0.7 \text{ cm s}^{-1}$. If angles of incidence were uniformly distributed, half of all values would lie between the 0° and 45° curves (less than a factor-of-two difference). Higher assumed values of θ result in lower

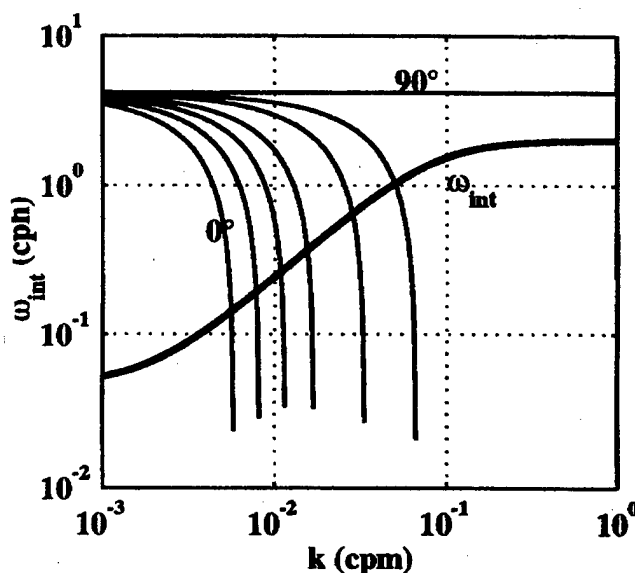


Figure A1. Equation A1 (light black lines) and A2 (heavy black line) are plotted versus horizontal wavenumber. Different light lines refer to different assumed angles ($0, 45, 60, 70, 80, 85, 90$) between wave vector \vec{k} and advective velocity \vec{U} . Assumed values are $U = 0.2 \text{ ms}^{-1}$, $m = 0.08 \text{ cpm}$, $N = 2 \text{ cph}$, $f = 1/24 \text{ cph}$, $\omega_{obs} = 4 \text{ cph}$. Intersections correspond to inferred values of k , ω_{int} consistent with linear internal waves Doppler shifted by the indicated amount.

estimates of ω_{int} . Assuming $|U| = 30 \text{ cm s}^{-1}$, for example, places maximally Doppler shifted waves of the dimensions above at near-tidal frequencies, with horizontal wavelength around 270 m.

References

- Alford, M., and R. Pinkel, Observations of overturning in the thermocline: the context of ocean mixing, *J. Phys. Oceanogr.*, in press, 1999a.
- Alford, M., and R. Pinkel, Patterns of turbulent and double diffusive phenomena: Observations from a rapid profiling conductivity probe, *J. Phys. Oceanogr.*, in press, 1999b.
- Anderson, S. P., Shear, strain and thermohaline vertical fine structure in the upper ocean, Ph.D. thesis, Univ. California San Diego, 1993.
- Broutman, D., and W. R. Young, On the interaction of small-scale oceanic internal waves with near-inertial waves, *J. Fluid Mech.*, 166, 341–358, 1986.
- Galbraith, P. S., and D. E. Kelley, Identifying overturns in CTD profiles, *J. Atmos. Ocean. Tech.*, 13, 688–702, 1996.
- Gargett, A. E., P. J. Hendricks, T. B. Sanford, T. R. Osborn, and A. J. Williams, III, A composite spectrum of vertical shear in the upper ocean, *J. Phys. Oceanogr.*, 11, 1258–1271, 1981.
- Gregg, M. C., Scaling turbulent dissipation in the thermocline, *J. Geophys. Res.*, 94(C7), 9686–9698, 1989.

- Gregg, M. C., E. A. D'Asaro, T. J. Shay, and N. Larson, Observations of persistent mixing and near-inertial waves, *J. Phys. Oceanogr.*, **16**, 856–885, 1986.
- Hazel, P., Numerical studies of the theory of inviscid stratified shear flows, *J. Fluid Mech.*, **51**, 39–61, 1972.
- Hebert, D., J. N. Moum, C. A. Paulson, and D. R. Caldwell, Turbulence and internal waves at the equator. part II: Details of a single event., *J. Phys. Oceanogr.*, **22**, 1346–1356, 1992.
- Heney, F. S., J. Wright, and S. M. Flatté, Energy and action flow through the internal wave field, *J. Geophys. Res.*, **91**, 8487–8495, 1986.
- Howard, L. N., Note on a paper of John W. Miles, *J. Fluid Mech.*, **10**, 509–512, 1961.
- Kunze, E., M. G. Briscoe, and A. J. Williams III, Observations of shear and vertical stability from a neutrally buoyant float, *J. Geophys. Res.*, **95**(C10), 18127–18142, 1990.
- Ledwell, J. R., A. Watson, and C. Law, Evidence for slow mixing across the pycnocline from an open-ocean tracer-release experiment, *Nature*, **364**, 701–703, 1993.
- Lueck, R. G., and J. J. Picklo, Thermal inertia of conductivity cells: Observations with a Sea-Bird cell, *J. Atmos. Ocean. Tech.*, **7**, 756–768, 1990.
- Marmorino, G. O., L. J. Rosenblum, and C. L. Trump, Fine-scale temperature variability: The influence of near-inertial waves., *J. Geophys. Res.*, 1987.
- Miles, J. W., On the stability of heterogeneous shear flows, *J. Fluid Mech.*, **10**(4), 496–508, 1961.
- Morison, J., R. Anderson, N. Larson, E. D'Asaro, and T. Boyd, The correction for thermal-lag effects in Sea-Bird CTD data, *J. Atmos. Ocean. Tech.*, **11**(4), 1151–1164, 1994.
- Moum, J. N., D. Hebert, C. A. Paulson, and D. R. Caldwell, Turbulence and internal waves at the equator. part I: Statistics from towed thermistors and a microstructure profiler, *J. Phys. Oceanogr.*, **22**, 1330–1345, 1992.
- Munk, W., and C. Wunsch, Abyssal recipes II, *Deep-Sea Res.*, **163**, 27–58, 1999.
- Munk, W. H., Abyssal recipes, *Deep-Sea Res.*, **13**, 707–730, 1966.
- Pinkel, R., and S. Anderson, Toward a statistical description of finescale strain in the thermocline, *J. Phys. Oceanogr.*, **22**, 773–795, 1992.
- Pinkel, R., and S. Anderson, Shear, strain and Richardson number variations in the thermocline: Part I, statistical description, *J. Phys. Oceanogr.*, **26**, 264–281, 1997.
- Pinkel, R., and J. A. Smith, Repeat sequence coding for improved precision of doppler sonar and sodar, *J. Atmos. Ocean. Tech.*, **9**, 149–163, 1992.
- Polzin, K. L., J. M. Toole, J. R. Ledwell, and R. W. Schmitt, Spatial variability of turbulent mixing in the abyssal ocean, *Science*, **276**, 93–96, 1997.
- Sandwell, D. T., and W. H. F. Smith, Marine gravity anomaly from Geosat and ERS-1 altimetry, *J. Geophys. Res.*, *in press*, 1996.
- Sherman, J. T., Observations of fine scale vertical shear and strain in the upper ocean, Ph.D. thesis, Univ. California San Diego, 1989.
- Sun, H., and E. Kunze, Internal wave/wave interactions: Part I. the role of internal wave vertical divergence, submitted to *J. Phys. Ocean.*
- Thorpe, S., Turbulence and mixing in a Scottish Loch., *Philos. Trans. R. Soc. London Ser. A*, **286**, 125–181, 1977.

M Alford, Applied Physics Laboratory, 1013 E 40th St, Seattle WA, malford@apl.washington.edu

Received October 1997, May 1998; revised February 1999

This preprint was prepared with AGU's L^AT_EX macros v5.01, with the extension package 'AGU++' by P. W. Daly, version 1.6a from 1999/05/21.

Waves, Turbulence, and Mixing Parameterizations

E. A. D'Asaro

Applied Physics Laboratory, University of Washington, Seattle, WA

R. C. Lien

Applied Physics Laboratory and School of Oceanography, University of Washington, Seattle, WA

Abstract. Recent measurements of Lagrangian frequency spectra in both the open ocean and Knight Inlet have led to a new way to separate internal waves and turbulence. Internal waves are found to have Lagrangian frequencies greater than N , while turbulence has Lagrangian frequencies less than N . This also leads to a new understanding of how mixing changes with increasing energy, i.e., decreasing Richardson number. At high Richardson number, mixing is controlled by interactions between internal wave modes. At Richardson number of order 1, mixing is controlled by instabilities of the wave modes. A "wave-turbulence" (W-T) transition separates these two regimes. As viewed in terms of vertical wavenumber spectra, the W-T transition occurs when the internal wave bandwidth becomes small, thus suppressing wave-wave interactions. As viewed in terms of Lagrangian (intrinsic) frequency spectra, the transition occurs when the inertial subrange of turbulence, confined to frequencies greater than N , reaches the level of the internal waves, confined to frequencies less than N . Present parameterizations of oceanic turbulence predict that these two singularities in the spectra occur at the same energy level. At internal wave energies below the W-T transition, dissipation rate depends on the internal wave energy squared; above the transition the dependence is linear. The finite depth of the water is crucial to the transition; the transition occurs at a lower shear and dissipation rate in shallower water. Traditional turbulence closure models, i.e., Mellor-Yamada and its relatives, ignore internal waves and will be accurate only at energies above the W-T transition.

Introduction

Two very different classes of models have been used to understand turbulence and mixing in stratified geophysical flows. One approach attempts to extrapolate the physics of unstratified turbulence into the stratified regime. Such "Stratified Turbulence" models [Mellor and Yamada, 1982; Luyten *et al.*, 1996] work well if the stratification is not too strong and the flow remains highly turbulent, but fail if the stratification is too strong [Simpson *et al.*, 1996]. A second approach attempts to extrapolate the physics of waves into a partially turbulent regime. Such "wave-wave interaction" models [Müller *et al.*, 1986] work well in the weakly turbulent ocean thermocline [Gregg, 1989; Polzin *et al.*, 1996] and have not been well tested in other regimes.

The two classes of models are fundamentally different in physical assumptions and mathematical form and will yield very different results if applied to the same flow.

The two different classes of models are designed to operate in different Richardson number regimes. Wave-wave interaction models assume that the flow can be expressed as the sum of interacting internal waves, each of which is a solution to the inviscid linear internal wave equations. Energy transfer and fluxes occur through the interactions of these waves. This approach is appropriate at high Richardson number, where the waves are stable and interact only weakly. Stratified turbulence models generally parameterize fluxes by assuming a local turbulent eddy viscosity, or similar closure, whose strength depends on the local length and time scales of

the flow. This approach is appropriate at low Richardson number where the flow is mostly turbulent and waves play only a minor role [Heney, 1989]. A transition from the high Richardson number wave physics to the low Richardson number turbulent physics should occur at some intermediate Richardson number. We will call this the *wave to stratified turbulence transition* or W-T transition.

We will study the W-T transition from an oceanographic viewpoint, considering how the physics of a broadband, high Richardson number, internal wave field, such as that in the open ocean thermocline, changes as its energy increases. The analysis is based on the observed shapes of oceanic spectra and existing parameterizations of dissipation rate. We first consider the Lagrangian frequency spectra of velocity, a recently measured quantity, first briefly describing the recent observations. We then consider the Eulerian wavenumber spectra of shear, a quantity that is well measured and modeled in the oceanic thermocline. Neither spectra can maintain its low energy form at high energy, implying that a transition must occur. We then quantify the transition and find that both spectra lose their low energy form at the energy level at which the large-scale Richardson number drops below 1.

Lagrangian Frequency Spectrum

Lien *et al.* [1998] and D'Asaro and Lien [1999] describe frequency spectra ($\Phi_u(\omega)$, $\Phi_v(\omega)$, $\Phi_w(\omega)$) [m^2s^{-1}] of velocity (u, v, w) as a function of Lagrangian frequency, ω [s^{-1}], as observed by neutrally buoyant floats in regions of both strong and weak turbulence. Their key diagnostic is the internal wave consistency relationship [Fofonoff, 1969; Calman, 1978],

$$\frac{\Phi_w^{iw}}{\Phi_H^{iw}} = \frac{\omega^2(\omega^2 - f^2)}{(N^2 - \omega^2)(\omega^2 + f^2)}, \quad (1)$$

where $\Phi_H^{iw} = \Phi_u^{iw} + \Phi_v^{iw}$.

Figure 1 shows spectra of horizontal and vertical velocity from an open ocean site. The spectra lie very close to the Garrett-Munk spectrum (orange dashed line) for frequencies below N . The vertical velocity spectrum falls rapidly above N . The black line marked W_{iw} shows the vertical velocity spectrum computed from (1) assuming that the horizontal velocity spectrum is entirely due to internal waves. If (1) is true, W_{iw} should equal W . W_{iw} lies within the error bars for W up to about $0.4 N$. Velocity fluctuations at this open ocean site are therefore dominated by internal waves, as expected. Analyses like this are the major reason why we think that internal waves dominate high frequency fluctuations in the open ocean.

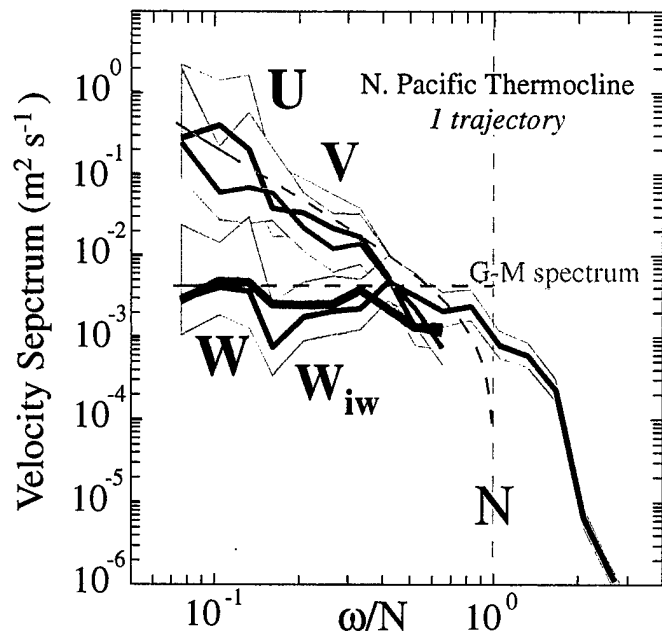


Figure 1. Normalized east (red), north (green) and vertical (blue) velocity spectra from the North Pacific thermocline. Shading represents the 95% confidence interval. Black line (W_{iw}) is the vertical velocity spectrum computed from (1). Orange dashed lines are the GM spectrum.

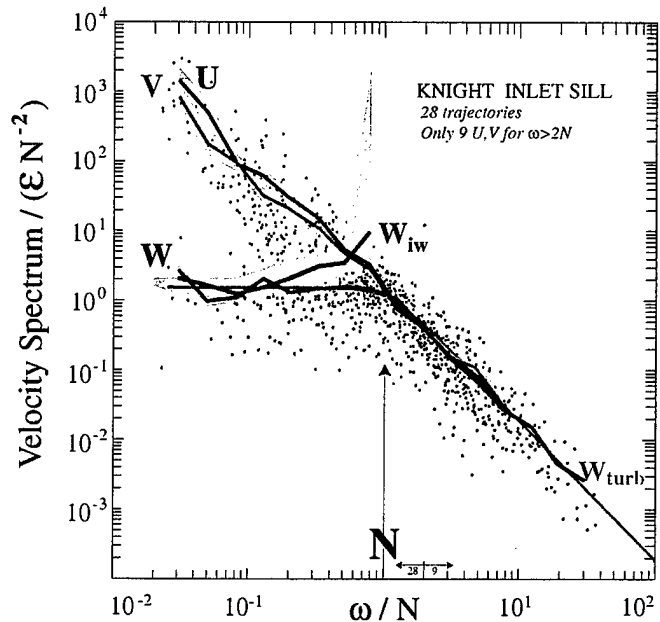


Figure 2. Normalized east (red), north (green), and vertical (blue) velocity spectra from the Knight Inlet sill. Dots are individual spectral estimates corrected for instrumental response; lines are average of these; shading represents the 95% confidence interval. Black line (W_{iw}) is the vertical velocity spectrum computed from (1) assuming that horizontal spectra are entirely due to internal waves.

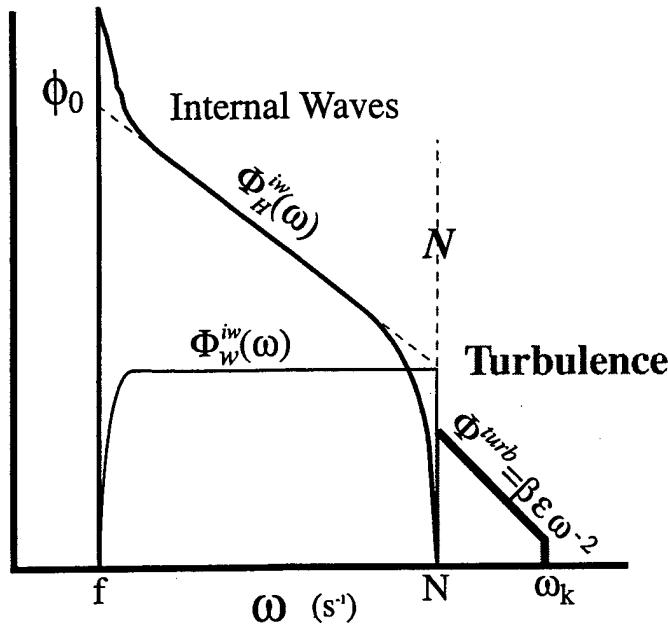


Figure 3. Model Lagrangian frequency spectra of vertical (w) and horizontal (H) velocity. The model consists of separate internal wave and turbulent components.

Figure 2 shows 28 spectra taken near the sill of Knight Inlet, a region of strong turbulence and mixing. The motions with frequencies below N have the properties expected of internal waves: they are anisotropic, approximately as specified by (1), and they have approximately the Garrett-Munk spectral shape characteristic of internal waves. This is truly remarkable; The sill of Knight Inlet is not where you would expect to find a Garrett-Munk spectrum! The motions with frequencies above N have the properties expected of homogeneous turbulence: their spectra are isotropic, and they have the -2 spectral shape characteristic of homogeneous turbulence. Based on these results *D'Asaro and Lien* [1999] hypothesize that the buoyancy frequency, measured in Lagrangian coordinates, separates waves and turbulence.

Based on these observations, we propose the Lagrangian frequency spectrum shown in Figure 3. It is the sum of internal wave and turbulent components. We model the internal wave horizontal velocity spectrum following GM76 [*Gregg and Kunze*, 1991], a traditional combination of *Garrett and Munk* [1975] and *Cairns and Willaims* [1976],

$$\Phi_H^{iw}(\omega) = \phi_0 \frac{f^2}{\omega(\omega^2 - f^2)^{1/2}} B\left(\frac{\omega}{N}\right) \quad (2)$$

where ϕ_0 is a constant which sets the internal wave energy, and B describes the shape of the spectrum near N . For $N \gg \omega \gg f$, Φ_H^{iw} has a -2 slope and Φ_w^{iw} is

white. Observed Φ_w sometimes show peaks near $\omega = N$. We will ignore these and choose

$$B(\omega) = (N^2 - \omega^2)/N^2 \quad (3)$$

so as to make Φ_w^{iw} white near N . Accordingly, Φ_H^{iw} falls below Φ_w^{iw} between $N/2^{1/2}$ and N .

Motions with Lagrangian frequencies above N are due to turbulence. We assume isotropic turbulence, $\Phi_H^{turb}/2 = \Phi_w^{turb} \equiv \Phi^{turb}$. For $\omega > N$, the spectrum is described by an inertial subrange [*Corrsin*, 1963; *Lien et al.*, 1998],

$$\Phi^{turb}(\omega) = \frac{\beta \epsilon}{\omega^2}, \quad (\omega > N) \quad (4)$$

with a Kolmogorov constant β , which has a value between 1 and 2 [*Lien et al.*, 1998]. We use $\beta = 1.8$. The inertial subrange form should be correct only for frequencies much larger than a "Large-Eddy" frequency, here taken to be N , and much less than a Kolmogorov frequency $\omega_k = (\epsilon/\nu)^{1/2}$. *D'Asaro and Lien* [1999] give analytical forms for the exact spectral shape of the spectrum near N . We assume no turbulent energy for frequencies below N

$$\Phi^{turb}(\omega) = 0 \quad (\omega < N) \quad (5)$$

although this must certainly be an approximation.

Figure 4 shows the evolution of the model $\Phi_w(\omega)$ as a function of internal wave energy. For typical oceanic, i.e., Garrett-Munk or GM, energy levels, (spectrum A), the internal wave spectrum has far more energy than the turbulence spectrum. This results in the sharp drop in the spectrum near N . This drop is particularly sharp when observed from neutrally buoyant floats [*Cairns*, 1975; *D'Asaro and Lien* 1999; *Kunze et al.*, 1990], i.e., for Lagrangian spectra. However, since the value of ϵ increases quadratically with wave energy [*Gregg*, 1989; *Polzin et al.*, 1995], the ratio $\Phi_w^{turb}(N)/\Phi_w^{iw}(N)$ will be proportional to $\Phi_w^{iw}(N)$. At low energies (spectrum A), the ratio will be small. As the internal wave energy increases (spectrum B), the ratio will increase until it reaches 1 (spectrum C). At this energy, which will turn out to mark the W-T transition, the drop in spectral level at N has disappeared.

If the energy is increased above the W-T transition level there are two possibilities: Φ_w^{turb} could continue to increase quadratically, as shown in spectrum E (Fig. 4, insert), leading to a sharp increase in spectral level at N , or it could remain at the same level as Φ_w^{iw} as shown in spectrum D. *D'Asaro and Lien* [1999] (Fig. 2) find no spectra which look like E, but many spectra which look like D. We therefore assume that only spectrum D occurs. *D'Asaro and Lien* [1999] assume this and using

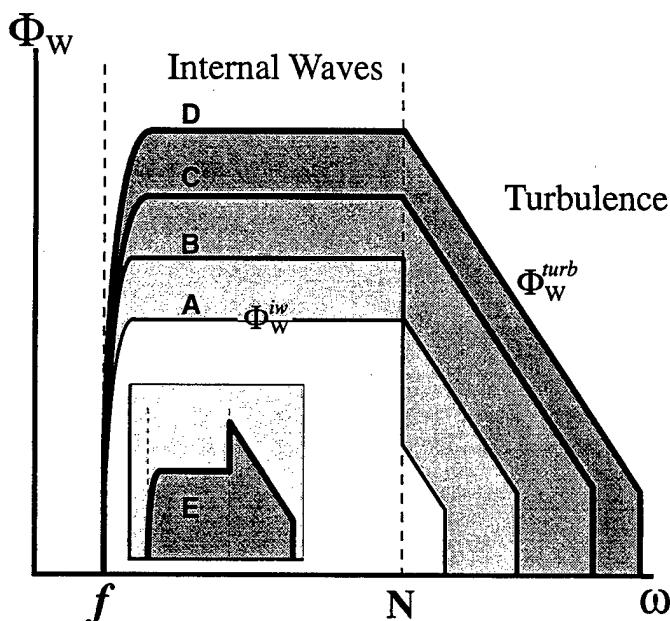


Figure 4. Evolution of Lagrangian frequency spectrum of vertical velocity with increasing energy. Spectra A and B are below the W-T transition energy. Spectrum C is just at the transition energy. Spectra D and E are two possible spectra above the transition energy. Spectrum E is not observed to occur.

the analytical spectral shapes near N , find

$$\varepsilon = 1.2 \beta^{-1} \Phi_w^{iw} N^2 = 0.6 \beta^{-1} \sigma_w^2 N \quad (6)$$

where σ_w^2 is the total vertical velocity variance. This relationship, valid at or above the W-T transition, shows a linear relationship between energy and dissipation. Thus the W-T transition marks a change from a quadratic to a linear relationship between energy and turbulent dissipation rate.

Eulerian Wavenumber Spectrum

Spectral Form

The vertical wavenumber spectrum, $\Phi_{SS}(m)$, of horizontal shear, S , in the ocean thermocline has been measured by many investigators using vertical profilers [Gregg, 1991]. Measurements have been mostly at near-GM energy levels. The basic form, first proposed by Garrett et al. [1981], is shown in Figure 5. There are three wavenumber bands: a low wavenumber "internal wave" band, a high wavenumber "turbulence" band and an intermediate "-1" band named for its spectral slope. We will extrapolate this form to energies much higher than GM and show how it eventually fails.

The low wavenumber band is believed to be dominated by internal waves [Müller et al., 1978]. We as-

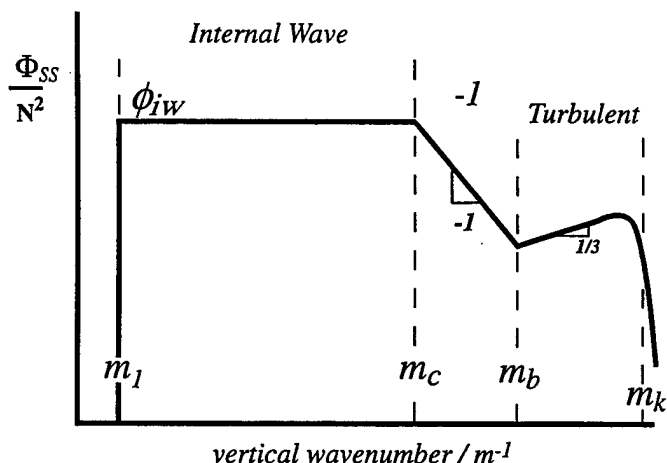


Figure 5. Model spectra of vertical wavenumber spectrum of shear.

sume a white normalized shear spectrum, $\Phi_{SS}(m)/N^2$ with a level ϕ_{iw} , consistent with numerous observations [Gregg et al., 1993; Polzin et al., 1995]. The lower end of the internal wave band is set by the WKB-stretched wavelength of the gravest internal wave mode, m_1 . For the open ocean, this is set by the thermocline depth; we assume the GM76 value $m_1 = 2\pi/b$ [m^{-1}] with $b = 1300$ m. For the continental shelf, this is set by the water depth; we will use $b = 100$ m. In the Garrett-Munk spectrum the shear spectral slope changes from white to +2 below vertical mode number j^* . GM76 uses $j^* = 3$. Levine et al. [1997] show evidence that j^* is large for low energy internal wave fields. Measurements under a storm [D'Asaro, 1985] and on the continental shelf (M. Levine, personal communication 1999) suggest that j^* is small for high energy internal wave fields. The data therefore suggest that at energies substantially above GM, j^* probably falls below 1 and the spectrum is white down to the lowest mode. We therefore ignore the j^* factor in GM76 and retain a white shear spectrum all the way to the lowest mode.

The upper end of the internal wave band is set by a critical wavenumber, m_c [Munk, 1981; Sherman and Pinkel, 1991] at which the Richardson number becomes small. More formally, the value of m_c is set so that the Froude function

$$Fr(m) = \int_{m_1}^m \frac{\Phi_{SS}(m)}{N^2} dm \quad (7)$$

equals a critical value, i.e. $Fr(m_c) = Fr_c$. Polzin et al. [1995] use $Fr_c = 0.7$. This yields

$$\phi_{iw}(m_c - m_1) = Fr_c. \quad (8)$$

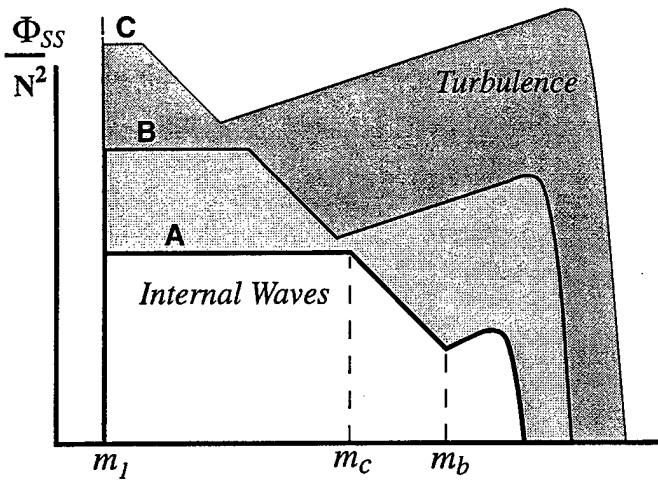


Figure 6. Evolution of model vertical wavenumber spectra of shear with increasing energy. Spectrum A is close to GM energy. With increasing energy the bandwidth of the internal waves shrinks and the bandwidth of turbulence increases. Spectrum D is close to the Wave-Turbulence transition.

Previous investigators have ignored the finite depth of the ocean, assuming $m_1 \ll m_c$, and thus written (8) with $m_1 = 0$. We will show that the W-T transition occurs when m_1 and m_c become comparable. Computationally, however, there is little advantage to including m_1 in (7) and (8), since it only becomes important when the model fails. Furthermore, including it leads to violation of Ozmidov scaling at high energies which seems unphysical. We therefore set $m_1 = 0$ and extrapolate the model to high energy to find how this, and other assumptions, fail.

At wavenumbers above m_c the spectral slope changes to -1 . At wavenumbers above $m_b = (N^3/\epsilon)^{1/2}$, corresponding to the inverse Ozmidov and overturning [Dillon, 1982] length scales, the spectrum assumes the form of the turbulent “ $-5/3$ ” inertial subrange

$$\Phi_{SS}^{turb} = m^2 \Phi_u^{turb} = \alpha_E \epsilon^{2/3} m^{1/3} \quad (9)$$

out to the Kolomogorov (viscous) wavenumber $m_k = (\epsilon/\nu^3)^{1/4}$. The Kolmogorov constant is $\alpha_E = 0.5$, to an accuracy of 10% [Sreenivasan, 1995]. The dynamical nature of the “ -1 ” range, intermediate between the internal waves and turbulence, remains elusive despite numerous observations of its existence in the ocean and atmosphere [Gregg et al., 1993].

Figure 6 shows the evolution of the vertical wavenumber spectrum with increasing energy as in Fig. 4. At the GM level (spectrum A), the internal wave bandwidth, $m_c - m_1$ is large, since $m_c \gg m_1$ and the turbulence bandwidth is small, since m_k is not very much bigger than m_b . With increasing energy (spectra B-C), the

internal wave bandwidth shrinks as m_c approaches m_1 and the turbulence bandwidth increases. The theory fails when m_c and m_1 become comparable so that the internal wave bandwidth becomes small. This will occur at the W-T transition.

Quantification

Dissipation Closure

We now compute the internal wave energy at which the transitions in wavenumber and frequency spectra occur. This requires a relationship between the internal wave energy and the energy dissipation rate ϵ , which we derive here, and a relationship between the level of the frequency spectrum and that of the wavenumber spectrum, which we derive in the next section.

We use the dissipation rate expression of Henyey et al. [1986], as expanded by Henyey [1991], implemented by Polzin et al. [1995], and explained by Winkel [1998]. The dissipation rate is computed as the net energy fluxing past vertical wavenumber m_c and is written as the product of three terms:

$$\epsilon = \underbrace{\frac{\phi_{iw} N^2}{2m_c^2} \alpha}_{\text{energy density}} \underbrace{\frac{k_H}{m_c} m_c N F \tau_c^{1/2}}_{|\frac{dm}{dt}|} \underbrace{\frac{1-\tau}{1+\tau}}_{\text{reflection}} \quad (10)$$

The first term expresses the energy density at m_c as the product of horizontal kinetic energy and the ratio α of total to horizontal kinetic energy. The second and third terms approximate the net rate at which wave packets cross wavenumber m_c under the influence of vertical shear, S . It uses the ray approximation $\frac{dm}{dt} = -k_H S$, where k_H is the horizontal wavenumber, and a reflection coefficient τ , set to 0.4. S is computed from (7). Combining terms, using single wave approximations for α and k_H/m_c , using (8) and referencing to the GM76 spectrum

$$\epsilon = \epsilon_0 \frac{m_{cGM}^2}{m_c(m_c - m_1)} \frac{N^2}{N_{GM}^2} \frac{f}{f_{GM}} \Gamma = \epsilon_0 \frac{m_{cGM}^2}{m_c(m_c - m_1)} \Gamma^* \quad (11)$$

where $\epsilon_0 = 6.7 \times 10^{-10} \text{ W kg}^{-1}$ is a reference dissipation rate for the GM spectrum, $m_{cGM} = 0.1 \text{ cpm} = 0.628 \text{ m}^{-1}$ is the value of m_c for the GM spectrum, f_{GM} is evaluated at 27°N and $N_{GM} = 0.00524 \text{ s}^{-1}$. Variations in the energy and wavenumber ratios and the amount of reflection are combined into the Γ factor which equals 1 for a GM spectrum. Similarly, Γ^* absorbs the additional deviations of N and f from GM values. Expression (11) is accurate to about a factor of 2 [Polzin et al., 1995; Winkel, 1998, if the variations in Γ are included. For completeness, we have not yet assumed $m_1 = 0$.

Substituting for ϕ_{iw} from (8) into (11)

$$\varepsilon = \phi_{iw}^2 \varepsilon_0 \frac{N^2}{N_{GM}^2} \frac{m_{cGM}^2}{Fr_c^2} \frac{f}{f_{GM}} \Gamma = \phi_{iw}^2 \varepsilon_0 \frac{m_{cGM}^2}{Fr_c^2} \Gamma^*. \quad (12)$$

The dissipation rate is proportional to the internal wave spectral level squared.

Spectral Normalization

The wavenumber and frequency spectra can be predicted as a function of ε using (11), (8) and the forms of $\Phi_{SS}(m)$ (Fig. 5) and $\Phi_u^w(\omega)$ (Fig. 3). The frequency spectrum is normalized by equating its horizontal kinetic energy in the internal wave band to that in the wavenumber spectrum. The resulting expressions are sensitive to the low mode and low frequency parts of the spectra, which seems unphysical. This, however, is necessary since we do not know the form of the Lagrangian frequency spectra of shear. Integrating (2)

$$\langle U^2 \rangle_L = \int_f^N \Phi_u(\omega) d\omega = \phi_0 f \sec^{-1} \left(\frac{N}{f} \right). \quad (13)$$

Integrating Φ_{SS}/m^2 in Fig. 5 while extending the “-1” range to infinity and ignoring the small effect of the B factor in (2), yields

$$\frac{\langle U^2 \rangle_E}{N^2} = \int_{m_1}^{m_b} \frac{\Phi_{uu}(m)}{m^2} dm = \phi_{iw} \left(\frac{1}{m_1} - \frac{1}{2m_c} \right) \quad (14)$$

Solving for ϕ_0 from (13) and (14) with $m_c \gg m_1$ yields

$$\phi_0 = \frac{\phi_{iw} N^2}{m_1 f \sec^{-1}(N/f)}. \quad (15)$$

The W-T Transition Energy

Combining (15), (4), (2), and (11) and assuming $m_1 = 0$ where possible gives

$$\frac{\Phi_w^{turb}(N)}{\Phi_w^{iw}(N)} = \frac{m_1}{m_c} \left[\frac{\pi \beta \varepsilon_0 m_{cGM}^2 \Gamma}{2 Fr_c N_{GM}^2 f_{GM}} \right]. \quad (16)$$

The bracketed expression has a value of 0.6, with an uncertainty of at least 50%. The ratios m_1/m_c and $\Phi_w^{turb}(N)/\Phi_w^{iw}(N)$ are nearly equal. The first ratio equals one when the turbulent and internal wave spectra merge in the Lagrangian frequency spectrum. The second equals one when the extrapolated internal wave bandwidth in the Eulerian wavenumber spectrum goes to zero. Both singularities occur at nearly the same internal wave energy, the W-T transition energy. This is the main result of this paper.

Physics

The W-T transition, as computed here, marks the energy level where the basic assumptions of GM-based wave-wave interaction theories fail. At open ocean energy levels and water depths, almost all of the energy is in the internal wave wavenumber band. The transfer of this energy to the smaller scale turbulence is due to wave-wave interactions. *Henye et al.* [1986]’s model of this (12) assumes the interaction of individual “test” waves with the “internal wave” band of wavenumbers in Fig. 5. At the W-T transition, m_c and m_1 become nearly equal, this band becomes small and the wave-wave interaction theory becomes ill-posed. In addition, the Richardson number of the lowest wavenumbers, i.e., m_1 , becomes order 1 on average. In places, the Richardson number will be less than critical. The large scale motions are thus locally unstable to shear instability and can thus directly transfer energy to turbulence. This is the physics of stratified turbulence. Thus, the W-T transition marks a change from energy transfer controlled by wave-wave interaction to that controlled by instability and turbulence.

The Transition Energy Level

The energy and spectral level of the W-T transition can be predicted by setting $m_1 = 0$ in (8) and then by finding the internal wave spectral level that sets $m_c = m_1$. This yields

$$\frac{\phi_{trans}}{\phi_{GM}} = \frac{m_{cGM}}{m_1} \quad (17)$$

where ϕ_{GM} is the value of ϕ_{iw} for the GM spectrum. Note that this is an extrapolation from low energy and thus only tells us when this theory fails.

Similarly, the internal wave energy at the transition is proportional to $N^2 \phi_{iw}/m_1$ by (14), so the wave energy of the transition, relative to GM, is

$$\frac{E_{trans}}{E_{GM}} = \frac{N^2}{N_{GM}^2} \frac{m_{cGM}}{m_1} \quad (18)$$

where m_{1GM} and E_{GM} are the values of m_1 and integrated internal wave energy for the GM spectrum.

Turbulent kinetic dissipation rate is proportional to $N^2 \phi_{iw}^2$ by (12) so

$$\frac{\varepsilon_{trans}}{\varepsilon_0} = \frac{N^2}{N_{GM}^2} \frac{m_{cGM}^2}{m_1^2}. \quad (19)$$

For deep ocean depths ($m_1 = 2\pi/1300\text{m}$, $m_{cGM} = 2\pi/10\text{m}$), the W-T transition is predicted at 130 times the GM spectral level, 130 times the GM energy level and $\varepsilon = 10^{-5} \text{W kg}^{-1}$. This seems unlikely to occur

over the entire water column. However, on a continental shelf ($m_1 = 2\pi/100$ m), with $N = N_{GM}$, the W-T transition is predicted at 10 times the GM spectral level, 130 times the GM energy level and $\epsilon = 7 \times 10^{-8} \text{ W kg}^{-1}$. (Moum and Nash, Topographically induced mixing on a small bank on the continental shelf, manuscript in preparation, 1999) report values of ϵ much larger than this over rough topography on the Oregon Shelf. —it Gregg et al., [this volume] describe significantly larger values on the shelf of Monterey Bay.

Equation (17) predicts that the W-T transition will occur at a lower spectral energy level in shallow water than in deep water. The transition occurs when motions with the same scale as the water depth, i.e., m_1 , have a Richardson number near one. We assume $m_c = 0.1$ cpm, a 10-m wavelength, so in a GM ocean, with m_1 corresponding to a 1300-m wavelength, the internal wave band is a factor of 130 wide. On a 100-meter deep continental shelf, the internal wave band is only a factor of 10 wide, so an increase in internal wave spectral energy level by a factor of 10 above GM will reduce the bandwidth to zero and cause the W-T transition. Note that the same effect does not occur with total internal wave energy density (18) because the total energy is inversely proportional to the water depth (15).

Parameterizations

Quadratic

The change from wave to turbulent physics at the W-T transition implies a change from a quadratic relationship between energy and ϵ (11) to a linear one (6). In the low energy wave regime, with high Richardson number, dissipation rate is set by wave-wave interactions which are quadratic in wave energy [Müller et al., 1986]. There is ample evidence for this scaling in the ocean thermocline [Gregg, 1989; Polzin et al., 1995; Winkel, 1998; Winters and D'Asaro 1997]. Mixing occurs when the wavefield intermittently decreases the Richardson number below critical, creating turbulence which then restores the Richardson number to above critical. The resulting statistics of Richardson number arrange themselves so that the rate of turbulence generation by instability just matches that set by the wave interactions [Polzin, 1996; Pinkel and Anderson, 1997]. The Richardson number of the large-scale energy containing waves is not important.

Linear

In the high energy, stratified turbulence regime, the dissipation rate is proportional to the energy

$$\epsilon = C\sigma_w^2 N. \quad (20)$$

Equation (6) implies $C = 0.3 - 0.6$ with the uncertainly set by uncertainty in β . Parameterizations of this form are common in the literature. Weinstock [1981] suggests $C = 0.4 - 0.5$ as a good predictor of dissipation in the stratosphere. Moum [1996] finds $C = 0.73 \pm 0.06$ for turbulent patches in the ocean thermocline. His measurement of σ_w^2 is biased low by an instrumental high pass filter; this is consistent with an estimate of C which is biased high. Observations in the upper equatorial Pacific, a region of high mean shear and turbulence, show strong linear relationships between turbulent dissipation rate and several measures of internal wave energy (wave isotherm displacement, wave slope, and wave potential energy) [Moum et al., 1992; Lien et al., 1996]. We have analyzed the data presented by Lien et al. [1996] and find a strong linear relationship ($r^2 = 0.64$) between σ_w^2 , measured from isothermal displacement rate, and ϵ . The estimated $C = 0.1$, which could easily be biased low by horizontal advection of temperature.

N-scaling of Diffusivity

The diapycnal diffusivity of mass due to internal-wave-driven turbulence is often computed from $\gamma\epsilon/N^2$, where the mixing efficiency γ is about 0.2 [Imberger and Ivey, 1991]. For energies below the W-T transition, (11) leads to a diffusivity independent of N and proportional to the internal wave energy squared. For energies above the W-T transition, (6) leads to a diffusivity proportional to $\sigma_w^2 N^{-1}$. Gargett [1984] showed that seasonally averaged diffusivities in lakes and fjords scaled as N^{-1} and proposed this scaling for the ocean interior. Subsequent measurements have showed this to be inappropriate for the ocean. Fjords are usually mixed by vigorous turbulence at a sill [D'Asaro and Lien, 1999; Farmer and Freeland, 1983], while lakes are often mixed by the rapid breakdown of intermittent wind-generated seiches [Imberger, 1994]. We suggest that Gargett's [1984] scaling is appropriate for fjords and lakes because they are mixed by strong turbulence above the W-T transition and inappropriate for the open ocean because it is mixed by motions below the W-T transition.

Summary

Measurements of Lagrangian frequency spectra from neutrally buoyant floats suggest that internal waves are confined to Lagrangian frequencies below N , not surprisingly, and that turbulence is confined to Lagrangian frequencies above N , a stronger statement. Examination of the resulting spectra leads to the hypothesis of two distinct dynamical regimes for mixing in stratified flows. At low energies, flow evolution is controlled by interactions between internal wave modes. At high energies flow evolution is controlled by instabilities of the

wave modes. The "wave-turbulence" transition, separating these regimes is marked by

- the merging of the internal wave and turbulence spectra at Lagrangian frequency N (Fig. 4)
- the decrease of the large scale Richardson number to near one
- the reduction of the internal wave vertical wavenumber bandwidth to a small value (Fig. 6)
- A change from a quadratic relationship between wave energy and dissipation rate at low energies (11), to a linear relationship at high energies (6).

Existing parameterizations of the Lagrangian and Eulerian wavenumber spectral shapes (Figs. 3,5), combined with the Polzin *et al.* [1995] parameterization of dissipation rate (11), predict that all of the above will occur at the same internal wave energy. The shape of the Lagrangian and Eulerian spectra (Figs. 4 and 6) may be useful diagnostics as to whether a given flow is above or below the W-T transition.

The W-T transition is predicted to occur at lower average dissipation rate and internal wave shear, but similar energy density, in shallow water than in deep water (Eqs. 17,18,19). It seems unlikely to occur for the full water depth in the open ocean but seems likely to occur at times on the continental shelves. Turbulence parameterization schemes which ignore internal waves will be accurate only for energies above the transition.

References

- Cairns, J., Internal wave measurements from a midwater float, *J. Geophys. Res.*, **80**, 299–306, 1975.
- Cairns, J. L., and G. O. Williams, Internal wave observations from a midwater float, *J. Geophys. Res.*, **81**, 1943–1950, 1976.
- Calman, J., On the interpretation of ocean current spectra. part II: Testing dynamical hypotheses, *J. Phys. Oceanogr.*, **8**, 644–652, 1978.
- Corrsin, S., Estimates of the relations between Eulerian and Lagrangian scales in large Reynold's number turbulence, *J. Atmos. Sci.*, **20**, 115, 1963.
- D'Asaro, E., Upper ocean temperature structure, inertial currents and Richardson numbers during strong meteorological forcing, *J. Phys. Oceanogr.*, **15**, 943–962, 1985.
- D'Asaro, E. A., and R. C. Lien, Lagrangian measurements of waves and turbulence in stratified flows, *J. Phys. Oceanogr.*, Submitted, 1999.
- Dillon, T. M., Vertical overturns: A comparison of Thorpe and Ozmidov length scales, *J. Geophys. Res.*, **87**, 9601–9613, 1982.
- Farmer, D. M., and H. J. Freeland, The physical oceanography of fjords, *Prog. Oceanogr.*, **12**, 147–220, 1983.
- Fofonoff, N. P., Spectral characteristics of internal waves in the ocean, *Deep-Sea Res.*, **16S**, 59–71, 1969.
- Gargett, A. E., Vertical eddy diffusivity in the ocean interior, *J. Mar. Res.*, **42**, 359–393, 1984.
- Gargett, A. E., P. J. Hendricks, T. B. Sanford, T. R. Osborn, and A. J. Williams, III, A composite spectrum of vertical shear in the upper ocean, *J. Phys. Oceanogr.*, **11**, 1258–1271, 1981.
- Garrett, C. J. R., and W. H. Munk, Space-time scales of internal waves: A progress report, *Ann. Rev. Fluid Mech.*, **11**, 339–369, 1975.
- Gregg, M. C., Scaling turbulent dissipation in the thermocline, *J. Geophys. Res.*, **94**, 9686–9698, 1989.
- Gregg, M., The study of mixing in the ocean: A brief history, *Oceanography*, **4**, 39–45, 1991.
- Gregg, M., and E. Kunze, Shear and strain in Santa Monica Basin, *J. Geophys. Res.*, **96**, 16,709–16,719, 1991.
- Gregg, M., D. Winkel, and T. Sanford, Varieties of fully resolved spectra of vertical shear, *J. Phys. Oceanogr.*, **23**, 124–141, 1993.
- Gregg, M. C., D. W. Winkel, J. A. MacKinnon, and R. C. Lien, Mixing over shelves and slopes, in *Internal Wave Modelling, Proceedings, 'Aha Huliko'a Hawaiian Winter Workshop, University of Hawaii at Manoa*, edited by P. Müller, and D. Henderson, p. in press, Hawaii Institute of Geophysics, 1999.
- Heney, F., Why eddy diffusivity doesn't work, in *Internal Gravity Waves and Small-Scale turbulence, Proceedings, 'Aha Huliko'a Hawaiian Winter Workshop, University of Hawaii at Manoa*, edited by P. Müller, and D. Henderson, pp. 245–250, Hawaii Institute of Geophysics, 1989.
- Heney, F., Scaling of internal wave predictions for ϵ , in *Internal Gravity Waves and Small-Scale turbulence, Proceedings, 'Aha Huliko'a Hawaiian Winter Workshop, University of Hawaii at Manoa*, edited by P. Müller, and D. Henderson, pp. 233–236, Hawaii Institute of Geophysics, 1991.
- Heney, F. S., J. Wright, and S. M. Flatté, Energy and action flow through the internal wave field: An Eikonal approach, *J. Geophys. Res.*, **91**, 8487–8495, 1986.
- Imberger, J., Transport processes in lakes: A review, in *Limnology Now: A Paradigm of Planetary Problems*, edited by R. Margalef, pp. 99–193, Elsevier-Science, New York, 1994.

- Imberger, J., and G. N. Ivey, On the nature of turbulence in a stratified fluid, I. The energetics of mixing, *J. Phys. Oceanogr.*, **21**, 650–658, 1991.
- Kunze, E., M. G. Briscoe, and A. J. W. III, Interpreting shear and strain from a neutrally buoyant float, *J. Geophys. Res.*, **95**, 18,111–18,125, 1990.
- Levine, M., L. Padman, R. D. Muench, and J. H. Morrison, Internal waves and tides in the western Weddell sea: Observations from ice station Weddell, *J. Geophys. Res.*, **102**, 1073–1089, 1997.
- Lien, R., M. McPhaden, and M. Gregg, High-frequency internal waves at 0 degrees, 140 degrees w and their possible relationship to deep-cycle turbulence, *J. Phys. Oceanogr.*, **26**, 581–600, 1996.
- Lien, R. C., E. A. D'Asaro, and G. T. Dairiki, Lagrangian frequency spectra of vertical velocity and vorticity in high-Reynolds number oceanic turbulence, *J. Fluid Mech.*, **362**, 177–198, 1998.
- Luyten, P., E. Deleersnijder, J. Ozer, and K. Ruddick, Presentation of a family of turbulence closure models for stratified shallow water flows and preliminary application to the Rhine outflow region, *Cont. Shelf Res.*, **16**, 101–130, 1996.
- Mellor, G. L., and T. Yamada, Development of a turbulence closure model for geophysical fluid problems, *Rev. Geophys. Space Phys.*, **20**, 851–875, 1982.
- Moum, J. N., Energy-containing scales of turbulence in the ocean thermocline, *J. Geophys. Res.*, **101**, 14,095–14,110, 1996.
- Moum, J. N., D. Herbert, C. A. Paulson, and D. R. Caldwell, Turbulence and internal waves at the equator 1. statistics from towed thermistors and a microstructure profiler, *J. Phys. Oceanogr.*, **22**, 1330–1345, 1992.
- Müller, P., D. J. Olbers, and J. Willebrand, The IWEX spectrum, *J. Geophys. Res.*, **83**, 479–500, 1978.
- Müller, P., G. Holloway, F. Henyey, and N. Pomphrey, Nonlinear interactions among internal gravity waves, *Rev. Geophys.*, **24**, 493–536, 1986.
- Munk, W. H., Internal waves and small-scale processes, in *Evolution of Physical Oceanography*, edited by B. A. Warren, and C. Wunsch, pp. 264–291, MIT Press, Cambridge, MA, 1981.
- Pinkel, R., and S. Anderson, Shear, strain and Richardson number variations in the thermocline. part II : Modelling mixing, *J. Phys. Oceanogr.*, **27**, 282–290, 1997.
- Polzin, K., Statistics of the Richardson number: Mixing models and finestructure, *J. Phys. Oceanogr.*, **26**, 1409–1425, 1996.
- Polzin, K., J. Toole, and R. Schmitt, Finescale parameterizations of turbulent dissipation, *J. Phys. Oceanogr.*, **25**, 306–328, 1995.
- Sherman, J., and R. Pinkel, Estimates of the vertical wavenumber-frequency spectrum of vertical shear and strain, *J. Phys. Oceanogr.*, **21**, 292–302, 1991.
- Simpson, J., W.R. Crawford, T. Rippeth, A. Campbell, and J. Cheok, The vertical structure of turbulent dissipation in shelf seas, *J. Phys. Oceanogr.*, **26**, 1579–1590, 1996.
- Sreenivasan, K., On the universality of the Kolmogorov constant, *Phys. Fluids*, **7**, 2788–2784, 1995.
- Weinstock, J., Energy dissipation rates of turbulence in the stable free atmosphere, *J. Atmos. Sci.*, **38**, 880–883, 1981.
- Winkel, D., Influences of mean shear in the Florida current on turbulent production by internal waves, Ph.D. thesis, Univ. of Washington, Seattle, WA 98105, 1998.
- Winters, K. E., and E. A. D'Asaro, Direct simulation of internal wave energy transfer, *J. Phys. Oceanogr.*, **27**, 1937–1945, 1997.
- E. A. D'Asaro, Applied Physic Laboratory and School of Oceanography, University of Washington, Seattle, WA
- R. C. Lien, Applied Physic Laboratory, University of Washington, Seattle, WA

This preprint was prepared with AGU's L^AT_EX macros v5.01, with the extension package 'AGU++' by P. W. Daly, version from

Large Eddy Simulation of Oceanic Fine Structure

G.F. Carnevale

Scripps Institution of Oceanography, University of California San Diego, 9500 Gilman Drive, La Jolla, California 92093, USA

M. Briscolini

IBM Italia S.p.A., Via Shangai 53, 00144 Roma, Italy

Abstract. Internal wave activity accounts for much of the variability of ocean density and velocity fields on vertical length scales greater than about 10 m. At scales below about 1 m and down to a viscous or diffusive cutoff, the flow appears to be dominated by isotropic turbulence. Between these wave and turbulence ranges there is a transition fine-structure range, sometimes called the 'buoyancy range,' in which waves and turbulence compete. The nature of the dynamics in this range is a controversial matter. The results of an attempt to numerically model the flow in the buoyancy range are presented here. The so-called cusp subgrid-scale model is used in the hope that it will correctly withdraw energy from the inertial range scales of motion while perturbing the buoyancy range scales as little as possible. The numerical grid used is isotropic and the forcing is supplied only at large-scale in the form of a standing internal wave. If the amplitude of the forcing is low, the spectra of the resolved scales approximates that in the 'buoyancy range,' while for sufficiently high amplitude forcing, the spectra indicate a fully turbulent range. In between these extremes, the results are somewhat ambiguous, but some evidence for a spectral break between the buoyancy and inertial ranges is presented.

Introduction

The spectra of density fluctuations and kinetic energy in the ocean have several distinguishable ranges. As a guide to discussing these ranges, consider the schematic diagram in Figure 1, which is based on a similar figure in *Holloway* (1981). Here ϕ is meant to be the one-dimensional spectrum of either the vertical shear or the vertical gradient of temperature. To facilitate the discussion, the vertical wavenumber axis is labeled in terms of vertical wavelengths. At vertical scales greater than λ_G , which is $O(10\text{ m})$, much of the variability in ocean currents, temperatures and salinities is associated with internal waves. In the open ocean, at these scales, the shear and vertical density gradient spectra seem to be well described by the *Garrett-Munk* (1975) (GM) spectra. The GM shear and gradient density spectra are relatively flat. Then the spectra fall off for scales less than λ_G . It seems that energy levels comparable to those in the GM spectrum at wavelengths less than λ_G would require internal waves of amplitudes too

high to be stable (cf. *Holloway* 1981). Thus λ_G can be crudely thought of as the wavelength below which internal waves "break." At scales from $O(10\text{ m})$ to $O(1\text{ m})$ the vertical gradient spectra fall off like k_z^{-1} . This is the buoyancy range. It terminates at the Ozmidov scale, the scale at which eddies have enough kinetic energy to overturn in the face of the background stratification. This scale forms the boundary between the transitional buoyancy range and the turbulent inertial range. An estimate for the Ozmidov wavenumber can be given in terms of the rate of energy dissipation ϵ and the Väisälä frequency N , which measures the effect of stratification. The Väisälä frequency is defined by

$$N^2 = -\frac{g}{\rho_0} \frac{\partial \bar{\rho}}{\partial z}. \quad (1)$$

The Ozmidov (or buoyancy) wavenumber is then estimated to be $k_b = (N^3/\epsilon)^{1/2}$ with the corresponding wavelength given by $\lambda_b = 2\pi/k_b$ (cf. *Holloway*, 1981; *Gibson*, 1986). At scales smaller than λ_b , if the kinetic energy dissipation rate ϵ is large enough, the current

and temperature spectra look like the vertical gradient versions of the Kolmogorov ($\epsilon^{2/3}k^{1/3}$) or Obykhov ($\epsilon^{-1/3}k^{1/3}$) spectra respectively. In much of the ocean, the Kolmogorov dissipative scale is a few centimeters, which is smaller than the typical Ozmidov scale.

Our objective is a numerical simulation of statistically stationary, forced and dissipating flow in which the buoyancy range is well represented. Two essential questions must be faced: (1) what kind of forcing would best allow the formation of flow structures that may be typical in the oceanic buoyancy range? and (2) what kind of subgrid-scale model will least perturb the dynamics of the buoyancy range while still properly dissipating in the inertial range? The answers to both of these questions are constrained by the availability of computer resources measured in numerical resolution and speed. Because we desired to run long simulations to achieve a reasonable degree of statistical stationarity, we decided to use a moderate numerical resolution of 64^3 grid points in our preliminary numerical simulations. We also decided to use 10 m as the length of one side of our computational cube. This places our cutoff or smallest resolved wavelength at about 30 cm, which we take as being in the inertial range. For the forcing, we use a large-scale standing internal wave. This kind of forcing will not introduce artificial noise at the large scale as a randomly generated force would do, and so it should better permit us to investigate the transition from waves to turbulence in the buoyancy range.

In the next section, we will present details of the numerical model focusing on the type of forcing and subgrid-scale model that are used. Then in section 3, we shall describe the results of three numerical simulations. Finally, in the last section, we will discuss some of the failings of the model and our plans for future development.

The numerical model

For the range of parameters involved in our studies, the Boussinesq approximation is appropriate. Following the notation of *Herring and Metals* (1992) with regard to dissipation, we have the following set of equations:

$$\frac{\partial \mathbf{u}}{\partial t} + \mathbf{u} \cdot \nabla \mathbf{u} + \frac{1}{\rho_0} \nabla p' - \frac{\rho'}{\rho_0} \mathbf{g} = \nu (\nabla^2) \mathbf{u}, \quad (2)$$

$$\nabla \cdot \mathbf{u} = 0. \quad (3)$$

$$\frac{\partial \rho'}{\partial t} + \mathbf{u} \cdot \nabla \rho' + w \frac{\partial \bar{\rho}}{\partial z} = \kappa (\nabla^2) \rho', \quad (4)$$

where $\nu(\cdot)$ and $\kappa(\cdot)$ are considered functions of the Laplacian operator and are used to represent eddy parameterizations in general, and $\mathbf{g} = -g\hat{\mathbf{z}}$. We have neglected the effect of rotation, which should not play a

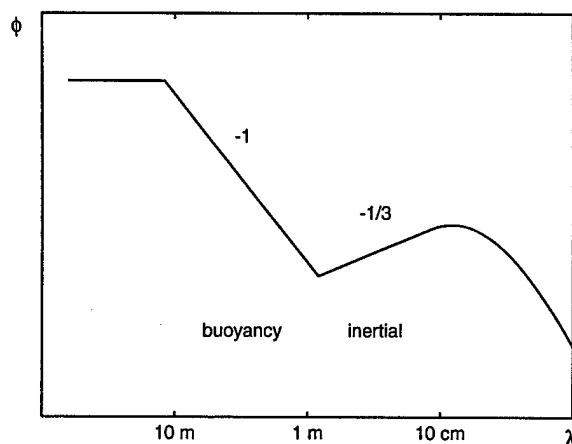


Figure 1. Schematic of the oceanic horizontal shear spectrum. The horizontal axis is labeled in terms of wavelength for convenience, but it is actually the k_z wavenumber axis. The slopes corresponding to the k_z^{-1} buoyancy range and the $k_z^{-1/3}$ inertial range are labeled by the exponents.

significant role at the small scales with which we are concerned. The total density is given by

$$\rho = \bar{\rho}(z) + \rho'(x, y, z, t), \quad (5)$$

where $\bar{\rho}(z)$ is the horizontally averaged background density assumed constant in time, and $\rho'(x, y, z, t)$ is the deviation from that mean. ρ_0 is the average of $\bar{\rho}(z)$ over z . The pressure p' is the deviation from the background mean pressure. p' can be determined in terms of \mathbf{u} by taking the divergence of (2) under the assumption that the velocity field is divergenceless.

We have written a spectral code to simulate these dynamical equations. The boundary conditions in this code are triply periodic. The code is a pseudo-spectral code de-aliased by the method of *Patterson and Orszag* (1971). The time stepping algorithm used to advance the velocity field is a second-order leap-frog scheme. This code is conservative, that is total energy is conserved if no viscosity or diffusivity is applied and if the time step is taken sufficiently small. See *Briscolini and Santangelo* (1992) for further details. As a sub-grid scale parameterization, we have used *Lesieur and Rogallo* (1989), which is based on the eddy viscosity theory of *Kraichnan* (1976). This model is referred to as the cusp model since the eddy viscosity (a function of wavenumber) has a cusp behavior at the highest allowed wavenumber, the spectral cutoff k_c . The eddy viscosity $\nu_t(k)$ can be defined by use of two-point Markovian closure theory (cf., *Kraichnan*, 1976; *Chollet*, 1980). For unstratified turbulence, an approximation based on assuming k_c is in the inertial energy range proves very

satisfactory. This approximation is

$$\nu_t(k) = (a_1 + a_2 \exp(-a_3 k_c/k)) \sqrt{E(k_c)/k_c}, \quad (6)$$

where $E(k)$ is the isotropic energy spectrum. The study of *Lesieur and Rogallo* (1989) suggests the optimal choices for the coefficients a_i for the problem of truncating an infinitely long inertial range. In general, the best choice of the coefficients will depend on the extent of the inertial range spectrum being modeled (*Chollet*, 1980). In our work, however, we have simplified things by just fixing the choice for these parameters for all simulations. We have used the values *Lesieur and Rogallo* (1989) found appropriate for a 64^3 simulation of infinite Reynolds number turbulence. Specifically, we take $a_1 = 0.15$, $a_2 = 5$ and $a_3 = 3.03$. In Figure 2, we show a graph of $\nu_t/\sqrt{E(k_c)/k_c}$. Note that there is a long plateau for large scales with the value $\nu_{t0} = a_1 \sqrt{E(k_c)/k_c}$. This is the eddy viscosity that acts on large-scales due to eddies of a far smaller scale. It seems reasonable in modeling the buoyancy range to use such a model that does not completely neglect the effects of small scale eddies on much larger scales, but at the same time puts the strongest eddy viscosity in the inertial range.

The choice of turbulent diffusion depends on the choice of values for various parameters that enter into the turbulence closure model for stratified turbulence. *Chollet* found that $\kappa_t(k)$ is similar to $\nu_t(k)$ to the extent that it also has a plateau at small k and a cusp at the spectral cutoff. The value of the turbulent Prandtl number $Pr_t \equiv \nu_t/\kappa_t$ as a function of k for one set of closure model parameters is found to vary from about 0.5 to 0.6. For simplicity we have just taken $Pr_t(k)$ to be a fixed constant independent of k in our simulations. We determined this constant by examining the evolution of the potential energy spectrum for decaying stratified turbulence that is initially highly excited at all scales. More specifically, we started with an initial spectrum in which the GM spectrum was continued to all scales below 10 m as in the decay simulations of *Siegel and Domaradski* (1994). With $Pr_t = 0.55$ our simulations of decaying turbulence produced spectra with the high wavenumbers obeying the $k^{-5/3}$ law for both velocity and density fluctuations. Thus we adopted this value of Pr_t for all of the simulations reported here.

Next we turn to the question of the forcing. The large-scale flows that actually drive the buoyancy range are the waves of the Garrett-Munk range. The full range where internal wave dynamics dominates includes scales of tens of kilometers in the horizontal and kilometers in the vertical. Because of lack of resolution, we cannot provide a full representation of the effects of large scale internal wave forcing on fine structure. In our model, we replace the driving of all of the GM waves by a

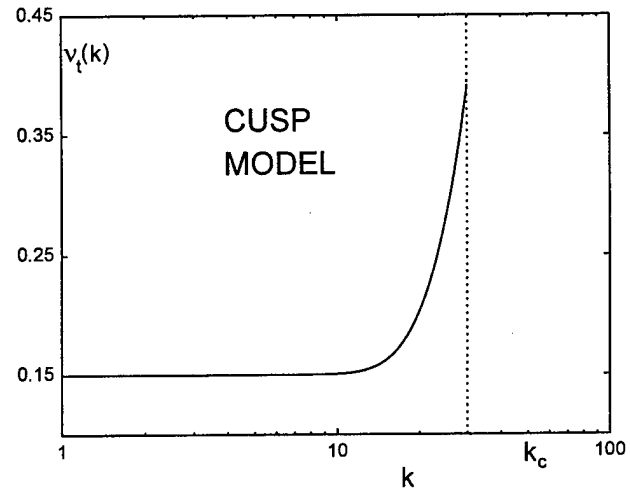


Figure 2. Graph of the eddy viscosity divided by $(E(k_c)/k_c)^{1/2}$, where k_c is the numerical cutoff or truncation wavenumber.

standing wave at one wavelength. This kind of forcing was previously used successfully by *Bouruet-Aubertot et al.* (1995, 1996) in two-dimensional simulations of stratified turbulence.

To give the form of the forcing used, let us first introduce nondimensional units. We will take all lengths to be scaled by $2\pi/L$, where L is the length of one side of our computational domain. Time will be scaled by $1/N$. Then the frequency of linear internal waves is given by

$$\sigma = \pm \frac{k_h}{k}, \quad (7)$$

where $k_h = \sqrt{k_x^2 + k_y^2}$ is the horizontal wavenumber. One particular standing wave is

$$\mathbf{u} = A \frac{g^*}{\sqrt{2}} (0, \sin y \sin z, \cos y \cos z) \sin \frac{t}{\sqrt{2}}, \quad (8)$$

$$\frac{\rho'}{\rho_0} = A \cos y \cos z \cos \frac{t}{\sqrt{2}}, \quad (9)$$

where A is an arbitrary amplitude and g^* is the nondimensional gravity. To give some idea of the structure of this standing wave, we show in Figure 3 a contour plot of the density field in a vertical $y-z$ cross section. Note that the density field in this standing wave has no variation along the x direction. In this figure, we see an instantaneous representation of the iso-density surfaces. When $t/\sqrt{2}$ is an odd multiple of $\pi/2$, these isopycnals will all be flat. The degree to which they deviate from that at other times depends on the value of A . Note however that there are two node lines in the domain which represent flat iso-density surfaces that remain flat during the complete cycle of the forcing.

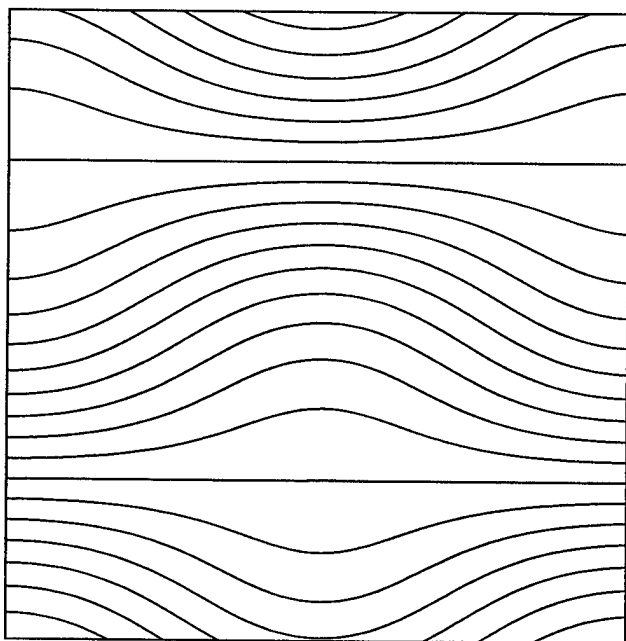


Figure 3. Contour plot of the density field in a vertical $y - z$ cross section through the center of the domain. The width and height of the cross section are each 10 m. The instant shown corresponds to maximum displacement of the isopycnals for the forcing of medium strength, $0.33S_{GM}(10 \text{ m})$.

In two-dimensional numerical studies of *Bouruet-Aubertot et al.* (1996), the standing wave becomes unstable and generates turbulence. This would also happen in our three-dimensional simulation, but the turbulence would be highly constrained since there is no source of x -variation in our flow. To break the two-dimensional symmetry of the flow, we have added a weak component of the force with x -variation. To preserve the nature of the forcing, this additional weak component is also taken as a large-scale standing internal wave. Specifically, we have added to the forcing another standing wave similar to (8) and (9) but with amplitude 0.014 and with the y dependence replaced by an x dependence. This is enough of a perturbation to break the artificial two-dimensional symmetry while leaving the shape of the isosurfaces of density of the standing waves still nearly two-dimensional with cross section as in Figure 3.

Numerical experiments

With the numerical model presented above, we ran a series of numerical experiments in which the amplitude of the forcing varied from one experiment to the next. One of the main issues was whether we could demonstrate the existence of a transition from a steep (buoyancy) spectral range to the shallower inertial range.

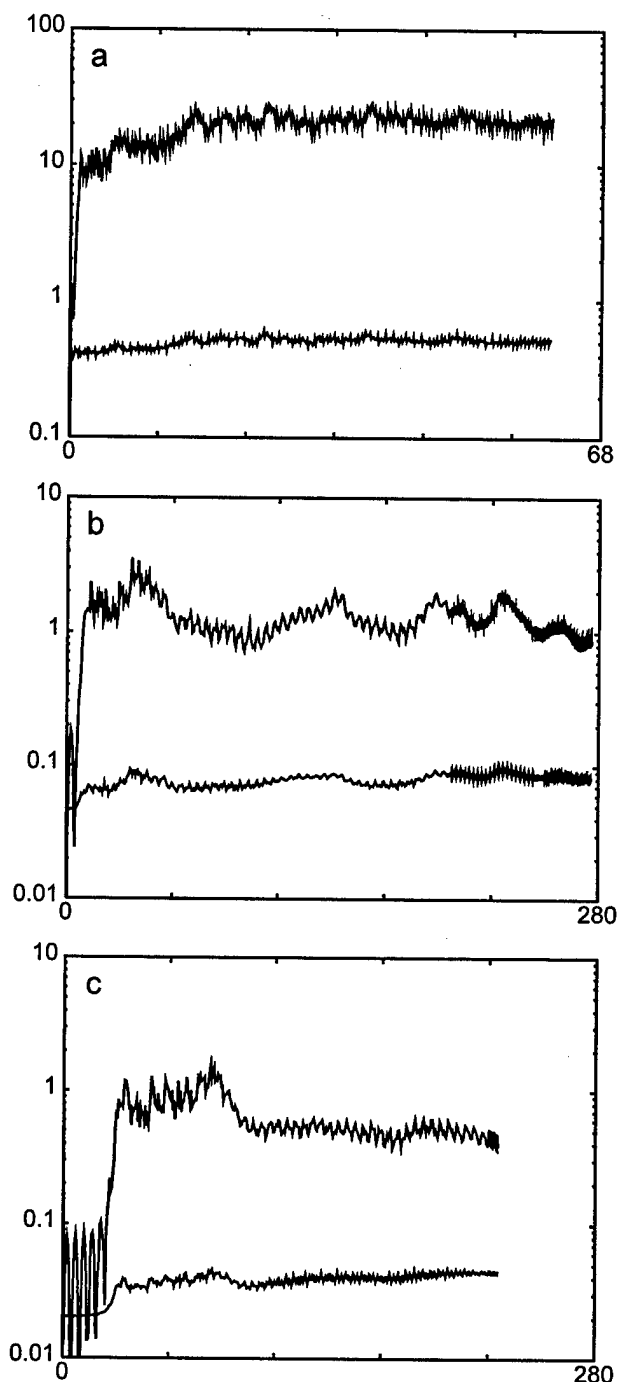


Figure 4. Graph of the evolution of the total energy and total enstrophy in non-dimensional units. The upper curve in each panel corresponds to the enstrophy. The three panels correspond to the three forcing levels (a) $1.2S_{GM}(10 \text{ m})$, (b) $0.33 S_{GM}(10 \text{ m})$, and (c) $0.25 S_{GM}(10 \text{ m})$. The unit for the horizontal time axis is the period of the cyclic forcing, that is $(2)^{1/2} 2\pi/N$.

Here we will present results from three of these experiments representing strong, medium and weak forcing. In each case the computational domain represents a cube 10 m long in each direction. The computational grid is isotropic with 64 points in each direction. An isotropic spectral cutoff at wavenumber 30 is imposed. Thus the smallest resolved wavelength is about 33 cm. In each case, the Väisälä frequency is taken to be 3 cycles per hour, which is a typical oceanic value. As a measure of the strength of the forcing, we can compare the maximum shear that occurs in our standing wave to the net rms shear of the GM spectrum integrated from kilometer scale down to the 10-m scale. This value is $S_{GM}(10\text{ m}) = 4.4 \times 10^{-3} \text{ s}^{-1}$ (cf., Gregg, 1989). Our representative of a strong wave forcing has its maximum shear given by $S/S_{GM} = 1.2$. This forcing is sufficiently strong that the standing wave itself actually overturns, that is, there are times during the cycle in which heavy fluid appears above light fluid. This overturning results in a convective instability which generates small scale turbulence. For the medium forcing, we will show the case with $S/S_{GM} = 0.33$. In this case, the wave itself is not unstable by either the Richardson number criterion for shear instability nor the stable stratification criterion for convective instability. However, it is unstable to wave-wave interactions that produce smaller scale structures that can satisfy these criteria. Finally, weak forcing will be represented by a wave with $S/S_{GM} = 0.25$. In this case, the motions generated never appear to be vigorously turbulent on any resolved scale.

As a first diagnostic of what occurs in these wave-forced flows, we consider the evolution of their energy and enstrophy. This is shown in separate panels in Figure 4 for each of the three cases. In each panel, there are two curves. The top one is the enstrophy and the bottom the energy, both in non-dimensional units. The horizontal axis measures time in number of cycles of the forcing. In each case, there is a relatively short transient period before the energy and enstrophy saturate at what we may think of as near equilibrium values. The time span of the transient is larger for weaker forcing, ranging roughly from something like 5 cycles for the strong forcing to more than 30 cycles for the weak forcing. Also note that in each case strong fluctuations in the energy and enstrophy levels persist through the course of the simulation. In the strong-forcing case, the time scale of these fluctuations is on the order of about 5 cycles, while in the medium forcing case, the time scale is about 30 cycles. Actually, in the weak-forcing case there are still some long term trends that persist, even after 250 cycles of forcing. These trends are perhaps not properly thought of as fluctuations, but clearly a much longer record length would be required to investigate that question. Please note that in panels (b) and (c)

the short period oscillations observed on the curves are due to aliasing of the much shorter period of the forcing due to insufficient sampling of the energy and enstrophy during much of the history of these simulations. The later portions of the curves were sampled more frequently and do not show these spurious oscillations.

Next we consider the energy spectra produced by our three representative forcing levels. We will only show spectra that have been temporally averaged over the last five cycles in the simulation record for each of the runs. The total time for each run is indicated in Figure 4. In Figure 5, we show the isotropic kinetic energy spectra $KE(k)$. The units for the energy and wavenumber are nondimensional. The wavenumber marked as 1 corresponds to the 10 m wavelength and that marked by 10 corresponds to the 1 m wavelength. In each panel, in addition to the kinetic energy spectrum (solid curve), the dashed straight lines have slopes appropriate to the ranges k^{-3} and $k^{-5/3}$ and are provided as a guide for pure buoyancy and inertial ranges. Owing to the lack of resolution, it is difficult to precisely define a slope. There is evidence, however, for a spectral break between a steep buoyancy range and a transition to a shallower inertial range at small scale in Figure 5b. This transition wavenumber (inverse Ozmidov scale) moves to higher/lower wavenumber as the forcing becomes weaker/stronger as we would expect.

Unfortunately, the picture arising from the corresponding isotropic potential energy spectra $PE(k)$ is far less clear or at least less amenable to interpretation. The results from our three representative cases are shown in Figure 6. The PE spectra in the strong and weak forcing cases are similar to the corresponding KE spectra. The medium-forcing case presents a puzzle, however. Perhaps some shallowing of the spectral slope occurs in going from large to small scale, but, overall, it seems that the spectrum has a slope of about -2.4, intermediate between -5/3 and -3. This is particularly surprising since the kinetic energy spectrum does show a clear spectral break and a relatively well defined portion of the $k^{-5/3}$ range.

Although we expect the flow to be statistically isotropic in the turbulent inertial range, this is not the case in the buoyancy range. Further, as in the schematic shown in Figure 1, the observational data are usually given in terms of one dimensional spectra depending on the vertical wavenumber only. For each of our three representative cases we have also calculated the one-dimensional vertical shear and density gradient spectra for the same time period as was used to calculate the isotropic spectra shown in Figures 5 and 6. The results are shown in Figure 7. The panels correspond again to the strong, medium and weak-forcing cases. In

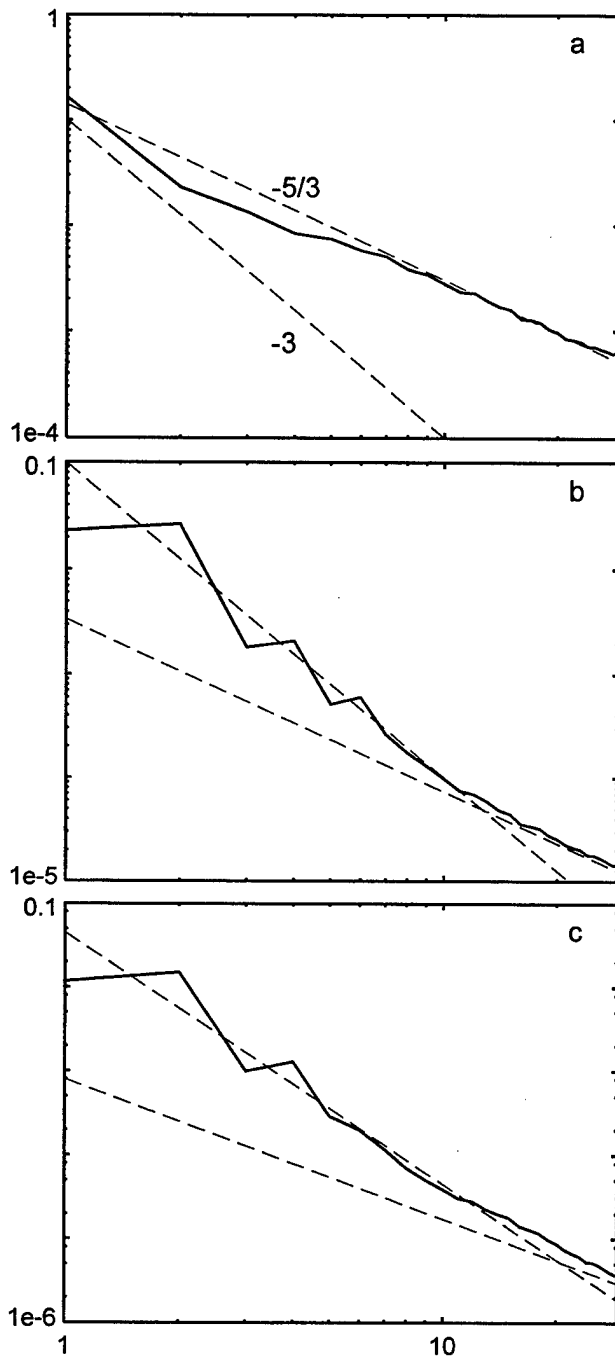


Figure 5. Isotropic kinetic energy spectra (non-dimensional) averaged over five cycles of the forcing for forcing levels (a) $1.2S_{GM}(10\text{ m})$, (b) $0.33S_{GM}(10\text{ m})$, and (c) $0.25S_{GM}(10\text{ m})$. The dashed lines show the functions $k^{-5/3}$ and k^{-3} . The horizontal axis is the wavenumber scaled so that $k = 1$ corresponds to a wavelength of 10 m.

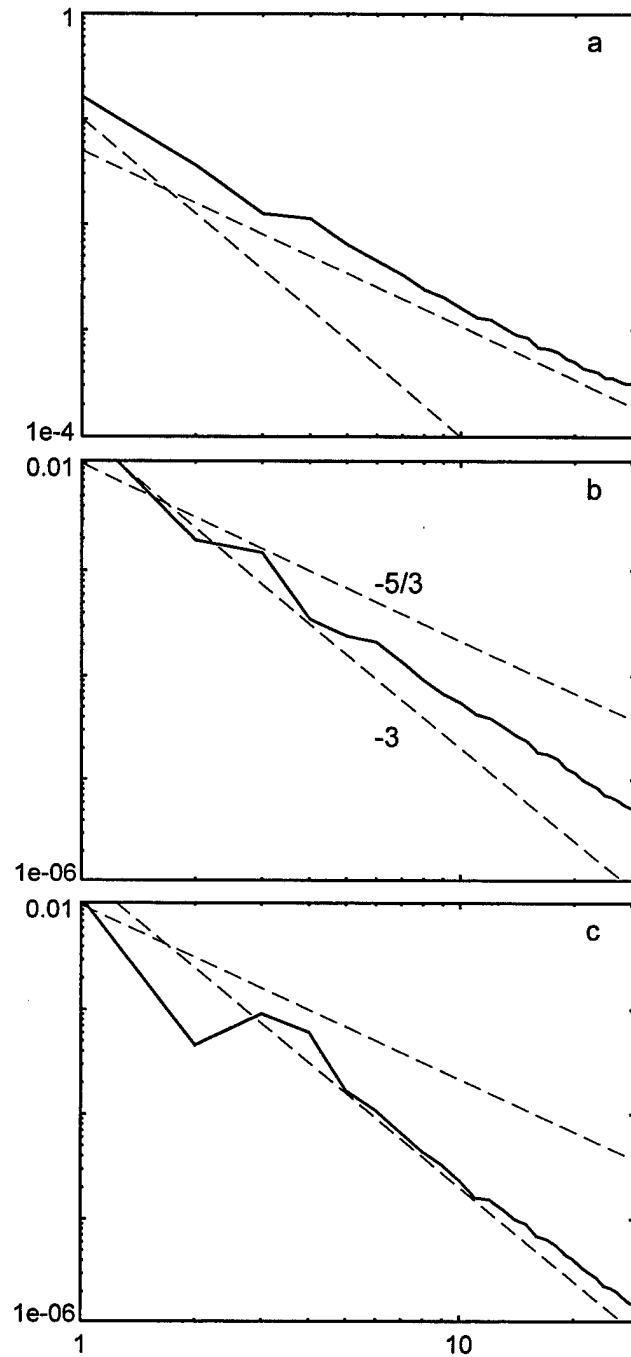


Figure 6. Isotropic potential energy spectra (non-dimensional) averaged over five cycles of the forcing for forcing levels (a) $1.2S_{GM}(10\text{ m})$, (b) $0.33S_{GM}(10\text{ m})$, and (c) $0.25S_{GM}(10\text{ m})$. The dashed lines show the functions $k^{-5/3}$ and k^{-3} . The horizontal axis is the wavenumber scaled so that $k = 1$ corresponds to a wavelength of 10 m.

each panel, we draw as a solid curve the spectrum of horizontal shear ($\frac{\partial u_h}{\partial z}$). Also in each panel we draw as a long-dashed curve the spectrum of the vertical gradient of density normalized by a factor of g/N (i.e., the spectrum of $\frac{g}{\rho_0 N} \frac{\partial \rho}{\partial z}$). For these gradient spectra, the buoyancy range is expected to have a k^{-1} spectrum and the inertial range a $k^{1/3}$ spectrum. Only in the strong-forcing case, panel (a), do we see a good representation of the inertial range, and then only for the shear spectrum. At first this seems surprising. Given that the kinetic energy spectrum in the medium-forcing case does show a significant piece of the inertial range, should we not expect to see a corresponding $k^{1/3}$ in the shear spectrum? Actually this is not the case. The degree to which one will observe the "spectral bump" corresponding to an inertial range depends very much on the length of the inertial range. If that range is very short either because of artificial spectral truncation as in our case, or because the Kolmogorov dissipation scale is too close to the Ozmidov scale, as is often the case in observations, then the "inertial range bump" will be diminished. To illustrate this, consider taking an isotropic modal energy spectrum $U(k)$, where the total energy is given by $E_{tot} = \int U dk_x dk_y dk_z$. Let U be such that the isotropic spectrum follows the k^{-3} law from 10 m down to 1 m, and then follows the $k^{-5/3}$ law to the spectral cutoff. This modal spectrum is then

$$U(k_x, k_y, k_z) = k^{-5} \quad \text{for } 1 < k < k_b \quad (10)$$

and

$$U(k_x, k_y, k_z) = ak^{-11/3} \quad \text{for } k_b < k < k_c \quad (11)$$

where $k_b = 10$ and $a = k_b^{-4/3}$. The theoretical one-dimensional gradient spectra for various values of the spectral cutoff are then obtained by integrating $k_z^2 U(k)$ over all values of k_x and k_y , for fixed k_z , subject to the constraint that $1 < k < k_c$. We multiply the result by a factor of two to account for the contributions from both positive and negative k_z . The theoretical one-dimensional gradient spectra for various values of the spectral cutoff are graphed in Figure 8. The figure shows that even in this ideal case the corresponding gradient spectra cannot be expected to have an "inertial range bump" that is any more than just a flattening of the spectrum if the spectral cutoff is at $k = 30$ ($\lambda = 33$ cm). Resolution corresponding to a $k = 60$ ($\lambda = 16$ cm) would just show some portion of positive slope, but nothing approaching the $+1/3$ value. We see that only at $k_c = 200$ ($\lambda = 5$ cm) do we have a very good representation of a $+1/3$ slope.

Next we turn to the question of the kind of density structures present in these flows. In Figure 9, we show density profiles taken at one horizontal location.

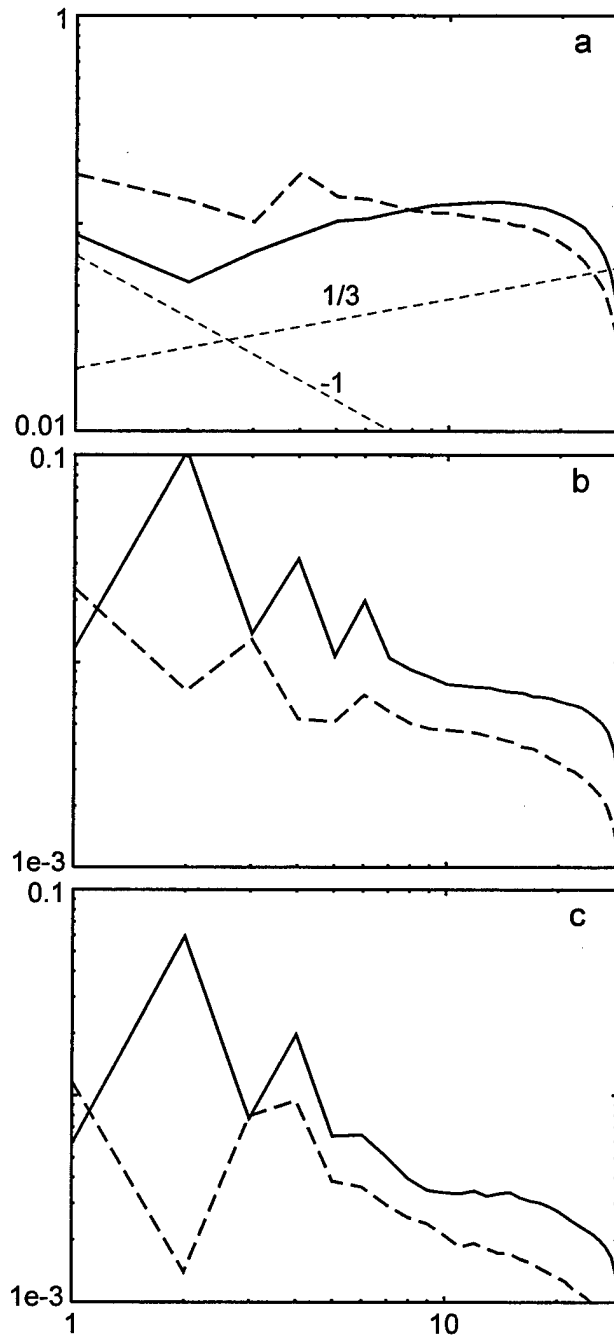


Figure 7. One dimensional kinetic (solid) and potential (long dashed) energy spectra (non-dimensional units) averaged over five cycles of the forcing for forcing levels (a) $1.2S_{GM}$ (10 m), (b) $0.33S_{GM}$ (10 m), and (c) $0.25S_{GM}$ (10 m). The short dashed lines show the functions $k_z^{1/3}$ and k_z^{-1} . The horizontal axis is the vertical wavenumber k_z scaled so that $k_z = 1$ corresponds to a wavelength of 10 m.

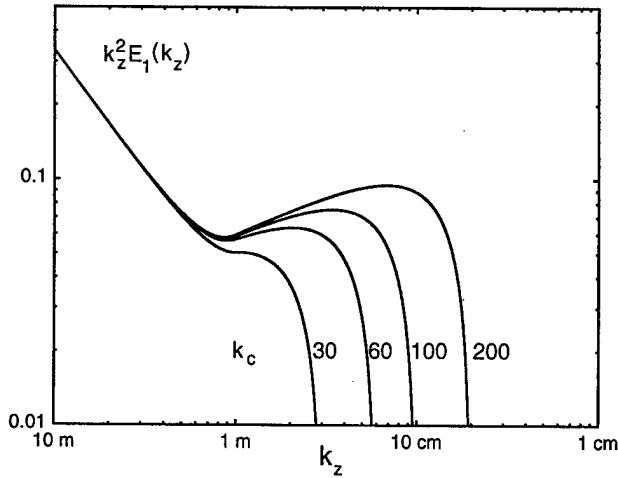


Figure 8. Graphs of 1-d energy spectra assuming an isotropic buoyancy range from 10 m to 1 m and an inertial range from 1 m down to a cutoff wavelength λ_c . The four curves represent the results for $\lambda_c = 33, 17, 10, 5$ cm corresponding to nondimensional wavenumber cutoffs of $k_c = 30, 60, 100$, and 200 .

More specifically, we plot ρ/ρ_0 as a function of z at the horizontal location $(x, y) = (0, 0)$. The profiles are taken from the very last instant of the numerical simulations for the strong and medium-forcing cases. In the case of the strong forcing, shown in panel (a), there is a well defined overturn with a vertical height of 2 or 3 meters. This is similar in scale to overturns found in oceanographic measurements in the buoyancy range (Alford and Pinkel, 1999). At this point in the evolution of our strong-forcing case, about 28% of the fluid volume is convectively unstable with $\partial\rho/\partial z > 0$. On the other hand, in the case with medium-forcing, we see only much smaller scale overturns. In that case only about 1% of the fluid has $\partial\rho/\partial z > 0$. We have not displayed the profile for the weak forcing case simply because there is very little structure and no overturns in that case.

One obtains a fuller understanding of the density field by examining vertical cross sections of the flow. In Figure 10 we display contour plots of the density field in two-dimensional cross sections. Specifically, we show the $y-z$ plane at x -position $x = 0$. For the strong forcing case (panel a), we see a few large (≈ 3 m) overturns and numerous smaller scale overturns. For the medium-forcing case (panel b), there is only one overturn evident, and that is at very small scale (≈ 30 cm). And no overturns are present in the weak-forcing case (panel c).

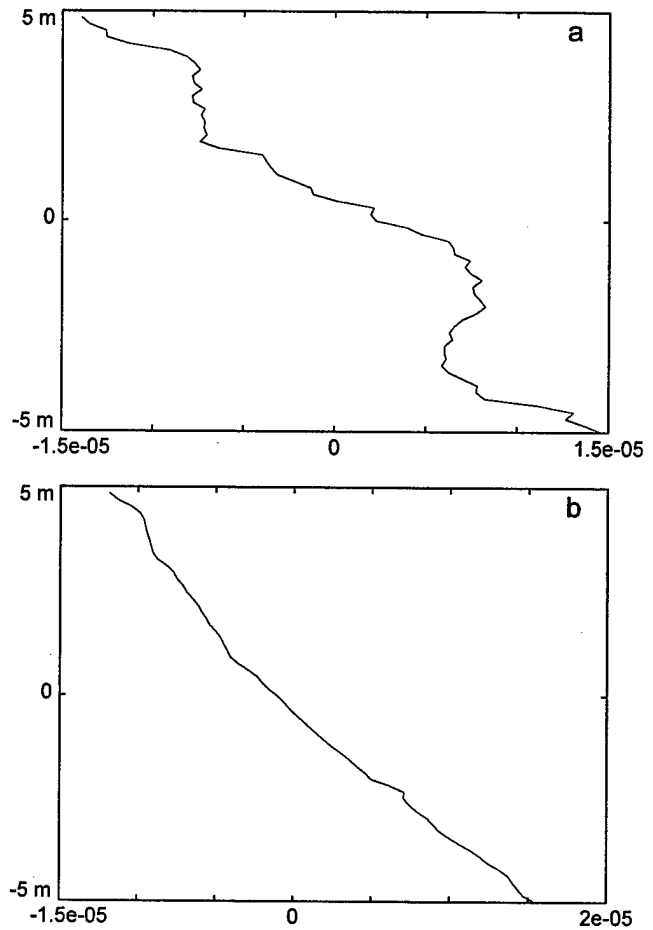


Figure 9. Vertical profiles of the density ρ/ρ_0 at the horizontal position $(x, y) = (0, 0)$. The two panels correspond to the forcing levels (a) $1.2S_{GM}$ (10 m), and (b) $0.33S_{GM}$ (10 m).

Discussion

Through the low resolution (64^3) simulations presented here, we have seen that it is possible to observe the transition from buoyancy to inertial range, at least in the kinetic energy spectrum, by using the cusp eddy viscosity model. The results suggest that it should be possible to move the transition point or Ozmidov scale by adjusting the strength of the wave forcing. For a forcing with shear comparable to the integrated rms shear of the waves in the Garrett-Munk spectrum, we found well defined overturns at scales on the order of 3m, which is consistent with oceanographic observations (Alford and Pinkel, 1999).

On the other hand, when we turn to quantitative measurements, we find some inconsistencies. For example, our estimate of the Ozmidov scale in the strong forcing case gives $k_b = 6$ corresponding to a wavelength of 1.7 m. This is perhaps not inconsistent with the

scale of the overturning structures that we observed in the strong-forcing case (see fig. 10); however, when we turn to the medium-forcing case, the Ozmidov scale is much smaller with $k_b = 70$ which means that it is unresolved. This is not consistent with the observation of a spectral break in Figure 5b at around $k = 15$ but perhaps is consistent with the rarity of even small scale overturns in that case. Also, we find that the strength of the turbulence generated in all cases presented was below that predicted by theory. This strength can be measured by estimating the Kolmogorov constant C_K where $E(k) = C_K \epsilon^{1/3} k^{-5/3}$. In observations and laboratory experiments this constant is about 1.5. For our strong forcing-case we found $C_K \approx 0.7$, about half the expected value. For the medium forcing case, the comparison is even worse with $C_K \approx 0.3$.

Thus the results at this point are somewhat ambiguous. Perhaps these ambiguities can be resolved by going to a larger domain size. We have begun to rerun these numerical experiments with the forcing at the 20-m scale, but with the cutoff still at the 33-cm scale. This requires a numerical grid of 128^3 points. The results so far are encouraging, especially from the point of view of the quantitative analysis. Also we have indications that the phenomenon of the spectral break is rather intermittent. This is quite sensible because at times there will be vigorous convective instability that will produce a significant inertial range, and at other times the flow will be more quiescent. Hopefully our current investigations will lead to a less ambiguous portrait of dynamics in the buoyancy range.

Acknowledgments

This research has been supported by Office of Naval Research grant N00014-97-1-0095. The numerical simulations were performed at the San Diego Super Computer Center. We thank Matthew Alford, Myrl Hendershott, James Lerczac, Robert Pinkel and David Siegel for very helpful discussions.

References

- Alford, M and R. Pinkel, 1999: Observations of overturning in the thermocline: the context of ocean mixing. *J. Phys. Oceanog.*, in press. (preprint, 31 pp.)
- Bouruet-Aubertot, P, J. Sommeria, and C. Staquet, 1995: Breaking of standing internal gravity waves through two-dimensional instabilities. *J. Fluid Mech.*, 285, 265-301.
- Bouruet-Aubertot, P, J. Sommeria, and C. Staquet, 1996: Stratified turbulence produced by internal wave breaking: Two-dimensional numerical experiments. *Dyn. Atmos. Oceans*, 23, 357-369.
- Briscolini, M. and P. Santangelo, 1992: Numerical simulations of three-dimensional homogeneous isotropic flows. In *Proc. Conf. on Parallel Computing: Problems, Meth-*

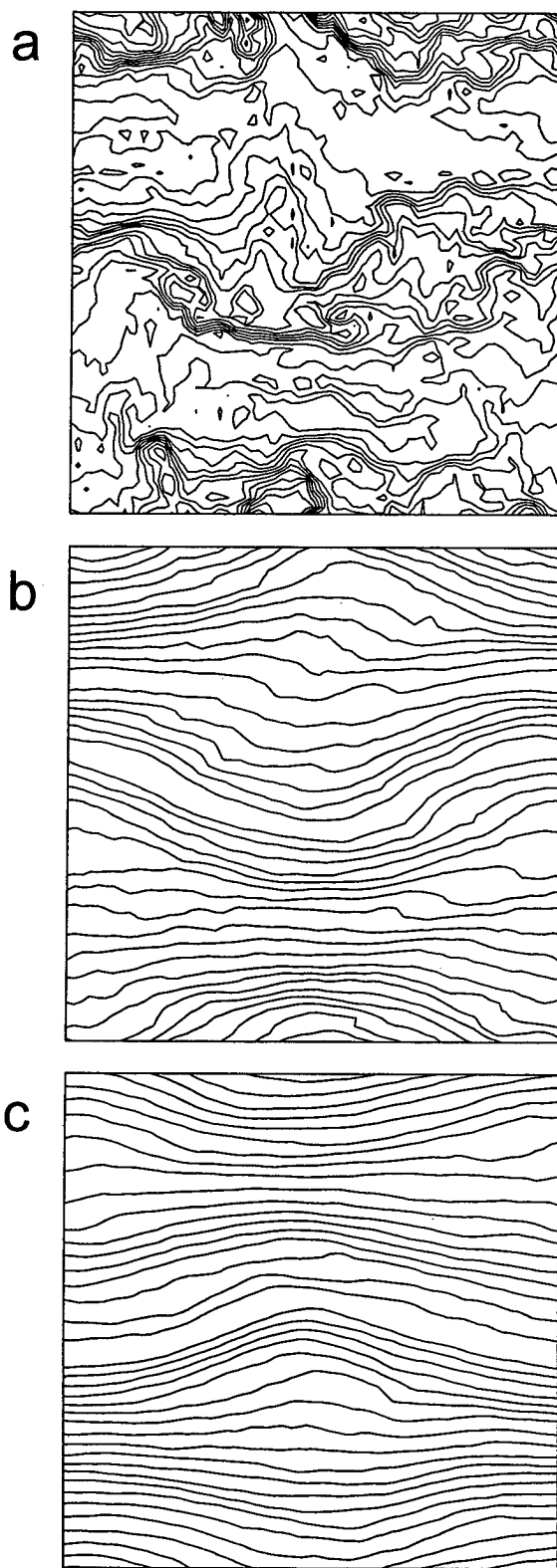


Figure 10. Contour plots of density in vertical y - z cross sections through the center of the domain. The three panels correspond to the three forcing levels (a) $1.2S_{GM}(10\text{ m})$, (b) $0.33S_{GM}(10\text{ m})$, and (c) $0.25S_{GM}(10\text{ m})$.

- ods and Applications*, (ed. P. Messina & A. Murli), Elsevier.
- Garrett, C. and W. Munk, 1975: Space-time scales of internal waves: A progress report. *J. Geophys. Res.*, 80, 291-297.
- Gregg, M.C. 1989: Scaling turbulent dissipation in the thermocline. *J. Geophys. Res.*, 94, 9686-9698.
- Herring, J.R. and O. Metais, 1992: Spectral transfer and bispectra for turbulence with passive scalars. *J. Fluid Mech.*, 235, 103-121.
- Holloway, G. 1981: Theoretical approaches to interactions among internal waves, turbulence and finestructure. In *Nonlinear Properties of Internal Waves*, AIP conference proceedings No. 76, (ed. B.J. West. AIP, New York.)
- Kraichnan, R.H. 1976: Eddy viscosity in two and three dimensions. *J. Atmos. Sci.*, 33, 1521-1536.
- Lesieur, M. and R. Rogallo, 1989: Large-eddy simulation of passive scalar diffusion in isotropic turbulence. *Phys. Fluids A*, 1, 718-722.
- Patterson, G.S. and S.A. Orszag, 1971: Spectral calculations of isotropic turbulence, efficient removal of aliasing interactions, *Phys. Fluids*, 14, 2538-2541.
- Siegel, D.A. and J.A. Domaradzki, 1994: Large-eddy simulation of decaying stably stratified turbulence, *J. Phys. Oceanogr.*, 24, 2353-86.

G.F. Carnevale, Scripps Institution of Oceanography,
University of California San Diego, La Jolla, California
92093, USA

Diapycnal Mixing and Internal Waves

Peter Müller

Department of Oceanography, School of Ocean and Earth Science and Technology, University of Hawaii, 1000 Pope Road, Honolulu, Hawaii 96822

Melbourne Briscoe

Ocean, Atmosphere, and Space Department, Office of Naval Research, 800 N Quincy Street, Arlington, VA 22217

Diapycnal mixing is an integral factor in the meridional overturning circulation of the ocean. The slow upwelling in the ocean interior across density surfaces requires counteracting diapycnal diffusion. Diapycnal diffusion in a stably stratified fluid requires mechanical energy and the availability of this energy might well be the controlling factor in setting the strength of the overturning circulation as, e.g., discussed by *Munk and Wunsch* (1998). The conventional wisdom is that

- Diapycnal mixing in the ocean interior is driven by intermittent patches of small scale turbulence.
- The turbulent patches have a vertical extent of up to a few meters and are caused by breaking internal gravity waves.
- Internal waves break by either shear or convective instabilities that are caused by chance superpositions or encounters with critical layers.

Confirming this connection between oceanic internal gravity waves and diapycnal mixing motivates and leads to funding for a large part of internal wave research. By understanding the internal wave field we may understand diapycnal mixing. Diapycnal mixing can also be caused by double diffusion, but this process will not be considered here.

What is the state of our understanding of the oceanic internal wave field? This was the task put before the participants of the eleventh 'Aha Huliko'a Hawaiian Winter Workshop, held from January 18 to 22, 1999, in Honolulu, Hawaii. The meeting came at an opportune time. Major field programs had just been completed (e.g., the Littoral Internal Wave Initiative (LIWI), the Brazil Basin Experiment, the Internal Tide Experiments (ITEX), the Internal Waves on the Continental Margin (IWAVES) experiment). The interaction of internal waves with topography had extensively been studied and the significance of internal wave induced boundary mixing had been explored. It was hoped that formerly incongruent pieces could be synthesized into a coherent and consistent picture of internal wave dynamics and internal wave induced mixing. However, the pieces still do not fit together. There was a feeling at the workshop that perhaps a break with basic underlying assumptions, a change of paradigm, is necessary. Below is the more detailed story.

The Garrett and Munk Spectrum

Much of internal wave research has been organized around the Garrett and Munk spectrum. More than twenty five years ago *Garrett and Munk* (1972) synthesized existing observations into a kinematic model spectrum that describes the observed distribution of internal wave energy in wavenumber and frequency space. Most of the detailed features of this spectrum were confirmed by the tri-moored internal wave experiment IWEX (*Müller et al.*, 1978). The GM spectrum, as it is known now, describes a wave field that is horizontally isotropic (waves coming in from all horizontal directions equally) and vertically symmetric (as many waves are propagating downward as upward). Often upward and downward propagating waves are assumed to be phase-locked and to produce vertically standing "normal modes." The most significant and surprising aspect of the GM spectrum is its universality. To observe significant (say larger than a factor of three) deviations from the GM spectrum one has to go to very special places such as the Arctic Ocean or submarine canyons. Figure 1 shows a typical example of how well the GM model represents an observed frequency spectrum.

It should be stressed that the GM spectrum does not describe all of the variance of the internal wave field. It only describes the "continuum," the broad background with a minus two slope in Figure 1, and the inertial peak. It does not account for the tidal peaks, which contain a considerable but highly variable fraction of the variance. In addition, the GM spectrum does not properly represent many of the observed properties of the inertial peak. It neither reflects its large temporal variability, nor its strong dependence on depth, nor its vertical asymmetry (most near-inertial waves are observed to propagate downward).

Since the formulation of the GM spectrum the focus has shifted from measuring the energy of the wave field, which is determined by the velocity and displacement variance, to measuring dynamically more active quantities, such as the shear or rate of strain. As observational techniques were developed to explore the wavenumber-frequency regions where the variance of these quantities is concentrated, it was found that other aspects of the GM spectrum also did not hold up, such as the separability of

wavenumber and frequency dependence. We will not dwell on these aspects here.

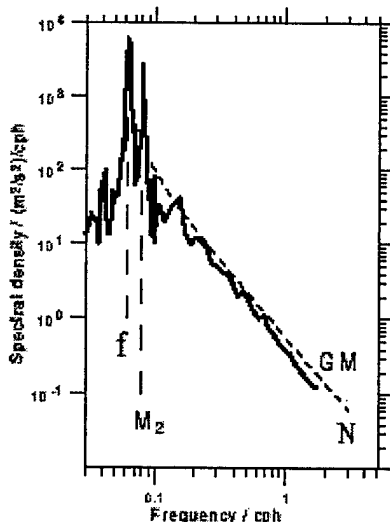


Figure 1. Frequency spectrum of horizontal velocity at 140 m depth at a site in the North-East Pacific during the Ocean Storms Experiment, 1987-88. Internal waves exist between the Coriolis frequency f and the buoyancy frequency N . M_2 is the semi-diurnal tidal frequency. The dashed line labeled GM is the Garrett and Munk model prediction. (courtesy of M. Levine).

The Dynamic Balance

Given a kinematic description of the internal wave field, the community started to search for a dynamical explanation of the spectrum as a balance of generation, transfer and dissipation processes. There are many dynamical processes that affect internal waves. A suitable theoretical framework for their quantitative calculation is the radiation balance equation, which describes the evolution of the wave spectrum along wave group trajectories. The dynamic balance that came out of these efforts is depicted in Figure 2.

This conventional dynamic balance has only two energy sources for internal waves: (i) Changes in the atmospheric windstress cause inertial oscillations in the oceanic surface mixed layer; part of their energy propagates into the ocean interior as large-scale, near-inertial internal waves; (ii) barotropic tidal currents impinging on topography in a stratified ocean generate internal waves of tidal frequency, the baroclinic tides. Their large-scale components propagate into the ocean interior. There is good observational evidence for both these generation processes. Near-inertial internal waves have been observed to

propagate away from the surface underneath storm and cyclone tracks. Baroclinic tidal beams have been observed to emanate from certain topographic features and can often be traced for hundreds of kilometers. As these large-scale waves propagate away from their generation region, they are assumed to interact nonlinearly with themselves and other internal waves and to scatter at fronts, mesoscale eddies, and topography. These nonlinear interaction and scattering processes transfer energy out of the large-scale waves into ever smaller scale waves that eventually break and cause turbulence and mixing. In a breaking event, the wave energy is partly dissipated into heat and partly converted to potential energy, since the mixing of a stably stratified fluid increases its potential energy. This nonlinear cascade to small scales has been theoretically investigated, using different approaches such as resonant wave-wave interaction and ray tracing. Attempts to observationally confirm the nonlinear cascade by bi-spectral analysis have failed because the nonstationarity and inhomogeneity of the ocean environment masked the expected signal.

Conventional dynamic balance

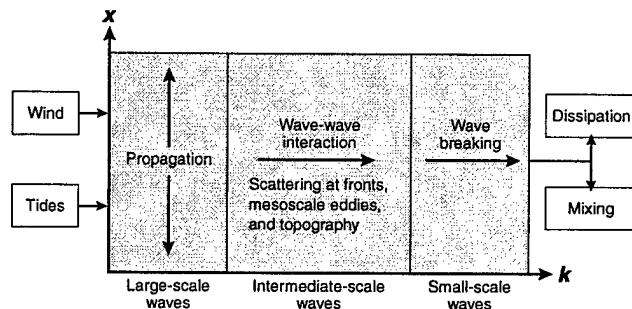


Figure 2. The conventional dynamic balance of the oceanic internal wave field in physical (x) and wavenumber (k) space. The wind and tides generate large-scale waves of near inertial and tidal frequencies. These large-scale waves propagate away from their sources in physical space and cascade towards small-scale waves in wave-number space. The cascade is caused by wave-wave interactions and scattering at fronts, mesoscale eddies, topography, and other scatterers. The small-scale waves break and cause turbulence and mixing.

The major confirmation of the scenario shown in Figure 2 comes from microstructure measurements. Over the last two decades microstructure measurements have been collected in a wide variety of ocean conditions, in conjunction with internal wave measurements. From microstructure measurements dissipation and mixing rates can be inferred. It was found that these dissipation rates scale with the internal wave energy and shear level as predicted by the nonlinear cascade calculations. This quantitative connection between microstructure measurements and

internal wave calculations is what gave credibility to the scenario in Figure 2. It also revived the concept of boundary mixing, as we will discuss next.

Boundary Mixing

The measured and deduced dissipation or mixing rates are equivalent to a diapycnal diffusivity of $10^{-5} \text{ m}^2 \text{ s}^{-1}$. This is one order of magnitude smaller than the value of $10^{-4} \text{ m}^2 \text{ s}^{-1}$, which has been inferred from the abyssal oceans' mass and heat balances and is required to maintain the abyssal stratification. Internal wave induced mixing in the ocean interior is not efficient enough to provide the mixing that is needed. The main mixing areas must lie elsewhere. The sloping side boundaries were immediately suspected as these mixing areas and this suspicion was nurtured by recent observations that show highly elevated dissipation levels near topography, as in Figure 3.

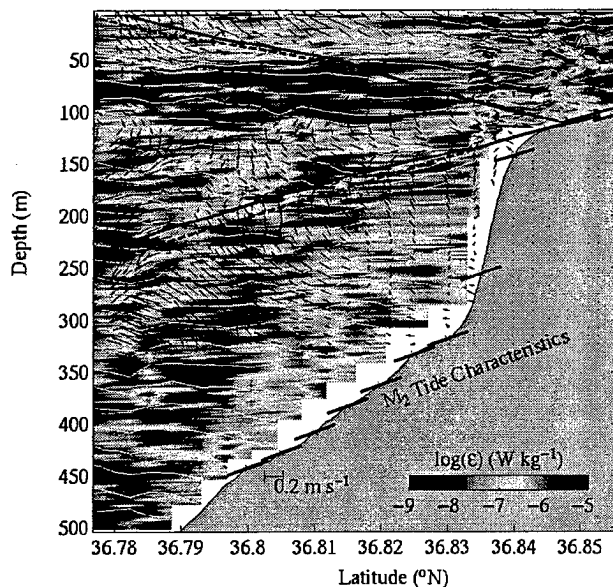


Figure 3. Section of the dissipation rate and velocity along the ridge of a sea fan outside Monterey Bay, California. Solid and dashed lines are characteristics of the internal tide, using different values of the buoyancy frequency. The dissipation rates are high along the internal tide characteristics and in a thick layer of strongly stratified water above the bottom, indicating zones of intense mixing. (Courtesy of M. Gregg)

Internal waves can easily be implicated in causing this boundary mixing. Internal waves radiate a sufficiently large energy flux onto topography, about 20 mW m^{-2} for the GM spectrum. It has been estimated that if only 1 mW m^{-2} or 5% of this flux could be converted to mixing it would sustain a diapycnal diffusivity of $10^{-4} \text{ m}^2 \text{ s}^{-1}$ in the ocean interior. This conversion might be facilitated by a peculiar property of internal waves. When reflecting from a sloping surface the wave vector of an internal wave

maintains its angle with the vertical rather than with the normal vector of the reflecting surface, as in specular reflection. This reflection law implies "critical reflection" when this angle becomes equal to the angle of the normal vector. The reflected wave then has an infinite wavenumber and zero group velocity. Energy and shear increase beyond bound at the reflecting surface. Wave breaking and mixing occurs. Thus reflection or, more generally, scattering at topography is a way to make internal wave energy available for mixing. It was hoped that such scattering in conjunction with suitable processes that will re-stratify the mixed water and communicate the mixing to the interior would account for an effective diapycnal diffusivity of $10^{-4} \text{ m}^2 \text{ s}^{-1}$. One such process is flow separation, a vigorous process that sweeps the mixed water into the interior and replenishes it with stratified water.

This is, in broad strokes, the current state of the relation between internal waves and diapycnal mixing and the state critically reviewed by the participants of the workshop. Of course, this review showed that the situation is not this simple.

Interaction with Topography

First, the interaction of internal waves with topography is an extremely complex problem. Even the reflection at an infinite sloping plane becomes somewhat involved when non-normal incidence is considered. Once finite topography in a finite-depth ocean is considered one must resort to numerical procedures, even for the linear problem. Results depend sensitively on the characteristics of the topography, such as the curvature and the amount and type of small-scale irregularities. Once nonlinear effects are included, a whole suite of new processes emerges, as depicted in Figure 4, involving secondary and tertiary, Lagrangian and Eulerian, and cross and along-slope flows. Again, non-normal incidence is the most challenging problem. Overall, it is fair to say that we have only started to identify and quantify all the different types of possible interactions. Given a topography, we cannot yet reliably estimate the amount of boundary mixing caused by an incident internal wave field. The interaction of internal waves with topography remains an active and important research area.

Second, the new research results presented at the workshop also questioned the conventional dynamic balance shown in Figure 2. It needs to be replaced by the extended dynamic balance shown in Figure 5, which clearly distinguishes between the baroclinic tides, the inertial peak and the continuum.

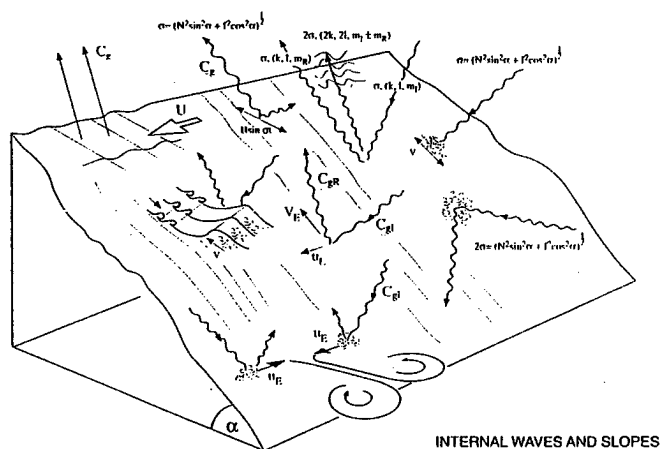


Figure 4. Physical processes involving the interaction of internal waves on sloping topography. Moving from the top left to right these are (i) lee wave generation by flow over topography, (ii) wave generation by oscillatory flow, particularly those of tidal period, (iii) resonant interaction between incident and reflected waves and, (iv) wave breaking when the incident is near or at critical frequency. The second row, left to right, shows (v) wave steepening and the formation of fronts upon reflection, (vi) the generation of upslope Eulerian flows, V_E , and along-slope Lagrangian flows, U_L , as waves reflect, and (vii) mixing produced by reflecting subcritical waves when the first harmonic is near critical. The final illustration, bottom left, represents Eulerian flows, U_E , generated by waves, which break and lose momentum at the boundary. (Courtesy of S. Thorpe)

The Baroclinic Tides

When the surface or barotropic tides impinge on continental slopes, mid-ocean ridges, sills or other topographic features, they generate a variety of baroclinic wave motions. These baroclinic wave motions contain the fundamental tidal frequency and all of its harmonics. The baroclinic waves propagate away from the topography or are trapped to it. The trapped waves dissipate their energy locally at the topography and contribute to boundary mixing. The propagating waves become part of the radiative internal wave field in the ocean interior. These energy pathways are depicted in Figure 5. The baroclinic tidal box is denoted by " M_2 ", the major tidal constituent. The details of the conversion of barotropic to baroclinic tidal energy and the associated mixing depend on the details of the topography and are not fully understood yet. The conversion is particularly efficient at critical slopes where the bottom slope matches the slope of the internal tide characteristics, (see Figure 3). The study and quantification of these conversion and mixing processes is the goal of the Hawaiian Ocean Mixing Experiment (HOME) which commenced this year.

Baroclinic tides propagating onto the shelf often steepen as they shoal and form bores, solitons, and other interesting nonlinear waveforms. The observations and theories of these nonlinear waveforms were the exclusive topic of the 1998 IOS/WHOI/ONR Internal Solitary Wave Workshop in Victoria, British Columbia, Canada, and were only briefly reviewed at the workshop.

Extended dynamic balance

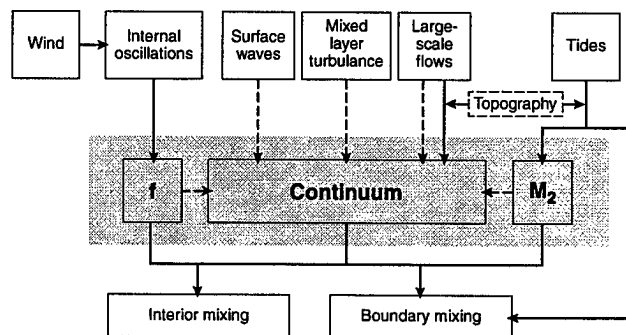


Figure 5. The extended dynamic balance of the oceanic internal wave field. The large dashed box represents the internal wave field, consisting of near inertial internal waves (f), the continuum, and the tides (M_2). The wind causes inertial oscillations in the surface mixed layer. Part of their energy leaks into the ocean interior as near inertial internal waves. Surface waves can resonantly interact to generate internal waves. Turbulent eddies in the surface mixed layer generate internal waves when they bounce onto the mixed layer bottom. The continuous geostrophic adjustment of large-scale flows causes emanation of internal waves. Flow over rough topography generated internal lee waves. Surface tides impinging on topography generate baroclinic tides and their higher harmonics, either trapped or radiating. All internal wave motions contribute to interior and boundary mixing. Near-inertial internal waves and baroclinic tides may also convert part of their energy to the continuum. The dashed lines indicate conjectured energy pathways.

Near-Inertial Waves

Near-inertial internal waves also deserve their own box in Figure 5, denoted by " f ". They are generated by the wind, most vigorously under storm tracks in winter and cyclone tracks in fall. Thereafter they propagate equatorward. A particular scenario suggests that these waves propagate equatorward until their frequency exceeds twice the local Coriolis frequency. Then the waves become susceptible to parametric sub-harmonic instability and subsequent wave breaking. Numerical modeling of these processes in the North Pacific shows that a very fragmented internal wave field emerges from this scenario, with internal-wave energy and mixing only occurring in certain parts of the Pacific Ocean in certain seasons. This energy pathway may, however, be obstructed. Near-inertial waves scatter off bottom topography many times

before they get far enough equatorward to undergo instability.

Near-inertial waves are also observed in the vicinity of the equator, generated by westerly wind bursts. Though these waves have periods of weeks and wavelengths of hundreds of kilometers, they are internal gravity waves. They obey the internal wave propagation laws just as their shorter period and smaller wavelength manifestations at midlatitudes.

The Continuum

The dynamic balance of the continuum is much less understood. The link that is holding up the most is the calculation of the nonlinear energy flux from low to high wavenumbers within the continuum. There are still some numerical differences between the different theories, but it was felt that these discrepancies will resolve themselves when a clearer account is taken of what interactions are included and excluded in the various approaches. Within the conventional balance the energy of the continuum is assumed to come from the baroclinic tides and from inertial waves. However both these sources are highly localized. Near-inertial internal waves are mostly generated at the surface under storm and cyclone tracks. Baroclinic tides only emanate from certain topographic features. This strong localization of the sources does not immediately square with the universal, horizontally isotropic, and vertically symmetric GM spectrum.

The conventional way out of this dilemma is to argue that large-scale near-inertial waves and baroclinic tides propagate long distances, thereby obscuring their sources and providing more uniformly distributed sources for the continuum. However, these assertions have not been substantiated as yet. There have been no systematic studies of which parts of the ocean are "illuminated" by the assumed internal wave sources; nor have the mechanisms been identified by which energy is extracted from the large-scale propagating waves and transferred to the continuum. A variant of this scenario is to assume that there exist scatterers in the ocean, also not identified, that turn an internal wave beam into an isotropic wave field, similar to the way water droplets in a cloud turn the incoming sun light into diffuse light.

Another way out of this dilemma is that there exist strong but yet overlooked sources for the continuum that are more evenly distributed. Several such sources were presented at the workshop.

Generation of internal lee waves by flows over rough topography. There is observational evidence from the Brazil Basin Experiment that this mechanism is indeed a significant source of internal wave energy and that this energy is dissipated in the water column above.

- Generation of internal waves by the continuous geostrophic adjustment of large-scale flows.
- Generation by turbulent eddies in the mixed layer. As these eddies bounce onto the mixed layer bottom, they generate interfacial waves, which then propagate into the interior. Turbulence can thus be a source rather than a sink of internal wave energy.
- Generation by surface waves. Two interacting swell components can interact resonantly to generate one internal wave. This is a somewhat forgotten but potentially efficient process, depending on the stratification and swell characteristics (Watson, 1990). The upper ocean internal wave energy level has been observed to vary with the swell intensity, however with an eleven day lag (Briscoe, 1983).

All these processes are shown in the extended energy diagram, Figure 5.

There was also a more radical fraction at the workshop that argued that perhaps the universal isotropic GM spectrum is a myth, that the oceanic internal wave field consists instead of highly intermittent and directional wave groups. Perhaps the universality and isotropy are just a consequence of the way we analyze and present data. Stable spectral estimates require considerable averaging, thereby eliminating finegrained information about the wave field. Also, log-log representations of spectra, as in Figure 1, tend to emphasize power laws and the continuum. The exact kinematic structure of the internal wave field also has dynamical implications. The extent of "groupiness" affects the patterns and observable signatures of wave breaking.

In order to resolve the discrepancy between the stationary, homogeneous, and isotropic GM spectrum and the highly localized energy sources we need to continue to study environments where the internal wave spectrum deviates from the GM spectrum (Wunsch, 1976). Indeed, the workshop saw many new observations of internal waves and microstructure in canyons, fjords, and inlets and on the continental slope and shelf and theoretical and numerical efforts to understand the dynamics of internal waves in these peculiar environments.

Summary and Outlook

The eleventh 'Aha Huliko'a Workshop reviewed our understanding of the oceanic internal wave field and internal wave induced diapycnal mixing. It became clear at the workshop that a clear distinction needs to be made between the inertial peak, the tidal peak and the continuum. The energy in the inertial and tidal peaks is highly variable; the energy level of the continuum is "universal" and represents a stationary, homogeneous, isotropic wave field that is well described by the Garrett and Munk kinematic model spectrum, subject to minor modifications.

There are well identified energy sources for the inertial and tidal peaks: fluctuations in the atmospheric windstress and the barotropic tide interacting with topography. The energy source for the continuum has not been identified yet. It has been conjectured that energy is scattered out of the inertial and tidal peaks into the continuum, although detailed mechanisms and quantitative estimates are lacking. Other possible sources are surface waves, bottom flow over rough topography, and continuous geostrophic adjustment of large-scale flows.

Internal waves support diapycnal mixing in the ocean interior, at a rate equivalent to a diapycnal diffusivity of $10^{-5} \text{ m}^2 \text{ s}^{-1}$. This is consistent with estimates inferred from microstructure measurements but insufficient to maintain the abyssal stratification which requires a value of $10^{-4} \text{ m}^2 \text{ s}^{-1}$, one order of magnitude larger. Microstructure measurements near topography indicate that boundary mixing may account for the required value in deep abyssal basins with their abundant topography but probably not in the pycnocline, unless observations have missed mixing "hot spots". Internal waves reflecting off and scattering at topography can provide the mechanical energy source for boundary mixing, but the exact mechanisms and their exact contribution have not been reliably determined yet.

Most of the energy sources in Figure 5 are external or boundary sources. Wind, surface waves, mixed layer turbulence, and tides and currents interacting with topography all generate internal waves at the boundaries of the ocean. The waves then propagate into the ocean interior. Only the generation due to continuous geostrophic adjustment is an interior source. This has important consequences for the parameterization of internal wave induced fluxes and internal wave induced mixing in oceanic general circulation models. If continuous geostrophic adjustment is the primary energy source, then perhaps classical cascade arguments apply and the effect of internal waves might be parameterized solely in terms of local mean flow quantities. If boundary sources are dominant, this cannot be expected. Instead, the fluxes and flux divergences need to be calculated from the solution of a radiative transport equation for the internal wave field. Internal waves then represent an additional radiative field in oceanic general circulation models in the same way that light from the sun is treated as an additional radiative field in atmospheric general circulation models. To do such a radiative transport calculation requires that we know the energy pathways through the internal wave field. To understand these pathways is the primary focus of current internal wave research.

Acknowledgments. We thank the participants of the workshop for their input into this report and for their permission to quote unpublished material. Copies of the proceedings are available from Peter Müller, University of Hawaii, School of Ocean and Earth Science, and Technology, Department of Oceanography, 1000 Pope Road, Honolulu, Hawaii, 96822. The eleventh 'Aha Huliko'a Hawaiian Winter Workshop was supported by the Department of the Navy grant number N00014-98-1-0207, issued by the Office of Naval Research. The United States Government has a royalty free license throughout the world in copyrightable material contained herein.

References

- Briscoe, M. G., 1983: Observations on the energy balance of internal waves during Jasin. *Phil. Trans. R. Soc. London*, **A308**, 427-444.
- Garrett, C. J. R. and W. H. Munk, 1972: Space-time scales of internal waves. *Geophys. Fluid Dyn.*, **2**, 225-264.
- Müller, P., D. Olbers and J. Willebrand, 1978: The IWEX spectrum. *J. Geophys. Res.*, **83**, 479-500.
- Munk, W. and C. Wunsch, 1998: Abyssal recipes II: energetics of tidal and wind mixing. *Deep-Sea Res.* **45**, 1997-2010.
- Watson, K. M., 1990: The coupling of surface and internal gravity waves. *J. Phys. Oceanogr.*, **20**, 1233-1248.
- Wunsch, C., 1976: Geographical variability of the internal wave field: A search for sources and sinks. *J. Phys. Oceanogr.*, **6**, 471-485.